Transactions of the ASME®

Journal of Engineering for Gas Turbines and Power

Published Quarterly by The American Society of Mechanical Engineers

VOLUME 112 • NUMBER 4 • OCTOBER 1990

TECHNICAL PAPERS

Contents continued on p. 485

Technical Editor,
G. K. SEROVY
Associate Technical Editors
Advanced Energy Systems
M. J. MORAN
Environmental Control
H. E. HESKETH
Fuels and Combustion Technologies
D. W. PACER
Gas Turbine
S. A. MOSIER
Internal Combustion Engine
J. A. CATON
Nuclear Engineering
S. M. CHO
Power
R. W. PORTER

BOARD ON COMMUNICATIONS
Chairman and Vice-President
M. E. FRANKE

Members-at-Large
W. BEGELL
T. F. CONRY
T. DEAR
R. L. KASTOR
R. MATES
E. M. PATTON
R. E. REDER
R. D. ROCKE
A. VAN DER SLUYS
A. J. WENNERSTROM
W. O. WINER
B. ZIELS

President, **A. E. BERGLES**
Executive Director,
D. L. BELDEN
Treasurer, **ROBERT A. BENNETT**

PUBLISHING STAFF
Mng. Dir., Publ.
CHARLES W. BEARDSLEY
Managing Editor,
CORNELIA MONAHAN
Sr. Production Editor,
VALERIE WINTERS
Production Assistant,
MARISOL ANDINO

Transactions of the ASME, Journal of Engineering for Gas Turbines and Power (ISSN 0022-0825) is published quarterly (Jan., Apr., July, Oct.,) for $125.00 per year by The American Society of Mechanical Engineers, 345 East 47th Street, New York, NY 10017. Second class postage paid at New York, NY and additional mailing offices. POSTMASTER: Send address changes to Transactions of the ASME, Journal of Engineering for Gas Turbines and Power, c/o THE AMERICAN SOCIETY OF MECHANICAL ENGINEERS, 22 Law Drive, Box 2300, Fairfield, NJ 07007-2300. **CHANGES OF ADDRESS** must be received at Society headquarters seven weeks before they are to be effective. Please send old label and new address. **PRICES:** To members, $36.00, annually: to *nonmembers*, $125.00. Add $15.00 for postage to countries outside the United States and Canada.

STATEMENT from By-Laws. The Society shall not be responsible for statements or opinions advanced in papers or . . . printed in its publications (B 7.1, para. 3), **COPYRIGHT © 1990** by The American Society of Mechanical Engineers. Reprints from this publication may be made on condition that full credit be given the TRANSACTIONS OF THE ASME—JOURNAL OF ENGINEERING FOR GAS TURBINES AND POWER, and the author, and date of publication be stated.

INDEXED by Applied Mechanics Reviews and Engineering Information, Inc.

Downloaded 03 Jun 2010 to 171.66.16.159. Redistribution subject to ASME license or copyright; see http://www.asme.org/terms/Terms_Use.cfm

(Contents continued)

ANNOUNCEMENTS

J. H. Wang
Professor.

F. M. Shih
Graduate Student.

Department of Power Mechanical
Engineering,
National Tsing-Hua University,
Hsinchu, Taiwan 30043

Threshold Performance Optimization of a Rotor-Bearing System Subjected to Leakage Excitation

Fluid leakage in blade tips in turbomachinery may induce instability and limit and output rating. In this work, the optimization technique has been used to find diameters of shaft elements and bearing supports so that the optimized rotor-bearing system can sustain a larger fluid leakage force. The results show that the threshold performance of rotor-bearing systems can be significantly improved by slight modifications of the shaft diameters. The results also indicate that the threshold performance can be improved more significantly by the combination of optimum bearing supports and optimum shaft diameters.

Introduction

One of the most important instability mechanisms found in turbomachinery is the excitation force owing to the fluid leakage in blade tips (Thomas, 1958; Alford, 1965). The magnitude of the leakage excitation force is approximately proportional to the output power of the turbomachine, so the instability caused by fluid leakage becomes one of the most important factors that restrain the output rating of a high-output turbomachine. Since 1958, many papers have been presented on how to improve the threshold performance of a turbomachine. Some of the work suggested that the stability of a turbomachine can be improved by the anisotropy of bearings or bearings supports (Warner et al., 1975; Kurohashi, 1984; Ebner, 1985; Wang and Tsai, 1988). Among them, Ebner (1985) observed that the external anisotropic stiffnesses would elongate the rotor whirling orbits, and as a consequence, would decrease the work done by the leakage excitation forces. An advanced study on this phenomenon was made by Wang and Tsai (1988). The results of the previous work (Wang and Tsai, 1988) showed that the external anisotropy cannot always decrease the work done by the leakage forces, and it might increase or decrease the energy dissipated by the system dampings. Only when the work done by the leakage excitation force is reduced more than the decrease of the energy dissipated by the system damping can the threshold performance be improved. According to the above discussions, one can see that the stability of a rotor system is strongly dependent on the work done by all nonconservative forces of the system. All the damping forces and the leakage excitation force belong to the nonconservative forces. The work done by the leakage forces is proportional to the unstable whirl orbit area of the points at which the forces act. Furthermore, the unstable whirl orbits are related to the modal shapes of the rotor system. The modal shapes are functions of the rotor stiffness and mass distributions.

Although the previous work (Wang and Shih, 1990) has used an optimization technique to find the optimum diameters of the shaft, it does not consider the effect of the bearing supports. In this work, the optimization technique was used to find the optimum parameters of the rotor-bearing system so that the optimized system can sustain much larger excitation. The parameters include the shaft diameters and the stiffness of the bearing supports.

Analysis

Usually, a rotor-bearing system is modeled as an assemblage of concentrated rigid disks, discrete bearings, and rotor segments with distributed mass and elasticity, and it would also contain the model of leakage excitation in this analysis. Since the finite element discretization procedure is well documented in the literature (Nelson, 1976, etc.), the details will be omitted here. The rotor segments were considered as Euler beam elements in the present work. In the following section, the model of leakage excitation and model of linear bearing will first be discussed briefly, and then the sensitivity analysis and optimization procedure will be presented in detail.

Model of Leakage Force. The leakage excitation force is caused by the working fluid passing the uneven blade-tip clearance when the rotor position has an eccentricity caused by any disturbance. The working fluid may leak through the clearance and causing a net unbalanced force F_q acting on the rotor. Furthermore, the experimental data indicated that the net un-

---

Contributed by the International Gas Turbine Institute and presented at the 34th International Gas Turbine and Aeroengine Congress and Exhibition, Toronto, Ontario, Canada, June 4-8, 1989. Manuscript received at ASME Headquarters January 24, 1989. Paper No. 89-GT-126.

balanced force is always in the direction normal to the rotor displacement, and its magnitude is approximately a linear function of rotor eccentricity (Wohlrab, 1975; Thomas, 1975). Hence, the mathematical formulation of the leakage excitation force of a turbine may be expressed as

$$\begin{Bmatrix} F_{qx} \\ F_{qy} \end{Bmatrix}_i = -\begin{bmatrix} 0 & q_i \\ -q_i & 0 \end{bmatrix} \begin{Bmatrix} u \\ v \end{Bmatrix}_i \tag{1}$$

where F_{qx}, F_{qy} are the leakage excitation forces acting in the x, y directions, and u, v are the rotor displacements in the x, y directions, respectively. The q is called the clearance excitation factor and the subscript i indicates the node where the leakage excitation acts. In general, the clearance excitation factor is approximately a linear function of the turbine output, and can be expressed as (Alford, 1965; Thomas, 1975)

$$q = \frac{\beta T}{D_p H} \tag{2}$$

where T is the turbine torque, D_p is the average pitch diameter of the turbine blades, H is the average height of the blades, and β is a coefficient, which can be determined experimentally (Wohlrab, 1975).

Linear Bearing Model. The nonlinear characteristics of the bearings can be linearized at the static equilibrium position under the assumption of small vibration. The dynamic characteristics of bearing can be represented by eight stiffness and damping coefficients. The interactive forces between journal and bearing can be expressed as

$$\begin{Bmatrix} F_{jx} \\ F_{jy} \end{Bmatrix} = \begin{bmatrix} k_{xx} & k_{xy} \\ k_{yx} & k_{yy} \end{bmatrix} \begin{Bmatrix} u_j - u_b \\ v_j - v_b \end{Bmatrix} + \begin{bmatrix} c_{xx} & c_{xy} \\ c_{yx} & c_{yy} \end{bmatrix} \begin{Bmatrix} \dot{u}_j - \dot{u}_b \\ \dot{v}_j - \dot{v}_b \end{Bmatrix} \tag{3a}$$

$$\begin{Bmatrix} F_{bx} \\ F_{by} \end{Bmatrix} = \begin{bmatrix} k_{xx} & k_{xy} \\ k_{yx} & k_{yy} \end{bmatrix} \begin{Bmatrix} u_b - u_j \\ v_b - v_j \end{Bmatrix} + \begin{bmatrix} c_{xx} & c_{xy} \\ c_{yx} & c_{yy} \end{bmatrix} \begin{Bmatrix} \dot{u}_b - \dot{u}_j \\ \dot{v}_b - \dot{v}_j \end{Bmatrix} \tag{3b}$$

where F_{jx}, F_{jy}, F_{bx}, and F_{by} are the forces acting on the journal and bearing in the x, y directions, respectively, and u_j, v_j, u_b, and v_b, are the journal and bearing displacements in the x, y directions, respectively. If a journal bearing is considered, the bearing coefficients are functions of Sommerfeld number (Glienicke et al., 1980); if a rolling bearing is considered, the bearing coefficients can be assumed to be constant and with the cross-coupling coefficients equal to zero.

Stability Analysis. The assembled system equation of motion is generally represented by the form (Wang et al., 1989)

$$[M]\{\ddot{p}\} + ([C] - \Omega[G])\{\dot{p}\} + [K]\{p\} = \{F\} \tag{4}$$

Note that the system damping comes only from the bearings in this study. In order to analyze the stability of a rotor-bearing system, the system eigenvalues must be solved at first. To set up the eigenvalue problem for a system governed by equation (4), it is convenient to write the system equation in the state space form

$$[A]\{\dot{z}\} + [B]\{z\} = \{R\} \tag{5}$$

Due to the damping matrix $[C]$ and the asymmetric stiffness matrix $[K]$, the eigenvalues σ_i of equation (5) are generally written in complex conjugate form

$$\lambda_i = \sigma_i \pm j\omega_i \qquad i = 1, \ldots, N \tag{6}$$

where ω_i are known as the natural frequencies of the system, and σ_i are the system damping factors. It is known that the stability of a linear autonomous system depends on the growth factors σ_i, and the following statement concerning the stability of the system can be made: When all the eigenvalues of equation (5) have nonpositive real parts but some of the eigenvalues have vanishing real parts, the system is said to be at the *threshold state*. For a given rotor-bearing system, the growth factors σ_i are functions of the clearance excitation factor q, which is contained in the $[K]$ matrix of equation (4). At the threshold state the q is called the *threshold performance* $q_{\max}$, which is the maximum clearance excitation that the system can sustain in a stable manner. According to the relation of equation (2), $q_{\max}$ can also be used to judge the maximum torque that the turbomachinery can generate while maintaining stability.

Sensitivity Analysis. In order to provide the gradient information of the constraint functions concerning the system eigenvalues in the following optimization procedures, the method of the eigenvalue sensitivity analysis (Fox et al., 1968; Rajan et al., 1986) is introduced. In the state formulation, the left and right eigenvectors $\{x_i\}$, $\{y_i\}$ of equation (5), with $\{R\} = 0$, satisfy the biorthogonality relation

Nomenclature

$[A]$, $[B]$ = system state matrices
c_{xx}, c_{xy}, c_{yx}, c_{yy} = damping coefficients of bearing
$[C]$ = damping matrix
d_{Oi}, d_{Ii} = outer and inner shaft diameters
D_p = pitch diameter
E = modulus of elasticity
f = objective function
$\{F\}$ = force vector
$[G]$ = gyroscopic matrix
H = blade height
I_p = disk polar inertia
I_d = disk diametral inertia
k_x, k_y = stiffness of bearing support
k_{xx}, k_{xy} k_{yx}, k_{yy} = stiffness coefficient of bearing
$[K]$ = stiffness matrix
l = element length
$[M]$ = mass matrix
m_b = mass of bearing housing
N = degrees of freedom of system
N_e = number of rotor element
N_p = number of design variables
$\{p\}$ = displacement vector
q = leakage excitation factor
$q_{\max}$ = threshold performance
$\{R\}$ = state force vector
R_i = system state modal norm
T = torque
u, v = displacement in the x, y directions
$\{V\}$ = vector of design variable
v_j = design variable
W = total mass of rotor elements
$\{x_i\}$ = left eigenvector
$\{y_i\}$ = right eigenvector
$\{z\}$ = generalized coordinate in state space
β = leakage coefficient
δ_{ij} = Kronecker delta
λ = eigenvalue
ρ = mass per unit volume
σ = growth factor
ω = natural frequency
Ω = rotation speed

Subscripts

b = bearing
d = rigid disk
j = journal

Superscript

T = transpose

$$\{x_j\}^T[A]\{y_i\} = R_i\,\delta_{ij} \qquad (7)$$

$$\{x_j\}^T[B]\{y_i\} = -\lambda_i R_i \delta_{ij} \qquad (8)$$

where the left and right eigenvectors $\{x_i\}$, $\{y_i\}$ are defined as

$$(\lambda_i[A] + [B])\{y_i\} = \{0\} \qquad (9)$$

$$\{x_i\}^T(\lambda_i[A] + [B]) = \{0\}^T \qquad (10)$$

Premultiplication of equation (9) by $\{x_i\}^T$ results in the scalar equation

$$\{x_i\}^T(\lambda_i[A] + [B])\{y_i\} = 0 \qquad (11)$$

By differentiating equation (11) with respect to a system parameter v_j and introducing equations (7), (9), and (10), one can derive the following expression for the eigenvalue derivative:

$$\frac{\partial\lambda_i}{\partial v_j} = \frac{-\{x_i\}^T\left(\lambda_i\dfrac{\partial[A]}{\partial v_j} + \dfrac{\partial[B]}{\partial v_j}\right)\{y_i\}}{R_i} \qquad (12)$$

Since $[A]$ and $[B]$ are the system state matrices formed by the superposition of the system element matrices, the state matrices derivatives $\partial[A]/\partial v_j$ and $\partial[B]/\partial v_j$ can be expressed in terms of the element matrices derivative.

Optimization Analysis. The main object of this work is to find the optimum parameters such that the optimized rotor system can sustain the maximum leakage excitation. The objective function to be maximized can be expressed as

$$\text{Maximize } f_1 = q_{\max} \qquad (13)$$

The main design variables considered in this optimization problem are the diameters of the shaft elements and bearing support stiffness. A close form relationship between $q_{\max}$ and the diameters of the shaft elements does not exist. Hence, the following analysis one may introduce the clearance excitation factor q as one of the design variables, and choose the objective function alternatively as:

$$\text{Maximize } f_2 = q \qquad (14)$$

or it can be expressed in a standard form:

$$\text{Minimize } f = -q \qquad (15)$$

The formulation of equation (15) would be equivalent to that of equation (13) when the following stability constraint was introduced:

$$\sigma_i \leq 0 \qquad i = 1, \ldots N \qquad (16)$$

where σ_i is the growth factor in equation (6); N is the degrees of freedom of the system.

In practice, the diameters of the shaft elements cannot be sharply changed from the original designed values due to the strength consideration. In the following studies, the outer diameters of the shaft elements are allowed to vary from 80 to 120 percent of the original designed values

$$0.8d^*_{Oi} \leq d_{Oi} \leq 1.2d^*_{Oi},\; i = 1, \ldots, N_e \qquad (17)$$

where d_{Oi} are the outer diameters of the shaft element, d^*_{Oi} is the original designed value of the outer diameters, and N_e is the number of shaft elements.

For an aeroengine rotor, another factor that should be considered is the weight of the rotor. Hence, the total weight of the rotor should be kept under a certain limit during the process of finding the maximum threshold performance. This constraint can be expressed as

$$\sum_{i=1}^{N_e} \rho l_i[\pi(d^2_{Oi} - d^2_{Ii})/4] - W_o \leq 0 \qquad (18)$$

where ρ is the mass per unit volume of the shaft, l_i is the length of the ith shaft element, and d_{Ii}, d_{Oi} are the inner and outer diameters of the corresponding shaft element. N_e is the number of shaft elements and W_o is the limited weight of the rotor.

If an anisotropic bearing support is used, then the stiffnesses of the bearing support also should be limited in a reasonable range

$$\begin{matrix} \underline{k}_{xi} \leq k_{xi} \leq \bar{k}_{xi} \\ \underline{k}_{yi} \leq k_{yi} \leq \bar{k}_{yi} \end{matrix} \quad i = 1, 2, \ldots, N_f \qquad (19)$$

where k_{xi} and k_{yi} are the stiffnesses of bearing supports in the x and y directions, respectively; $\underline{k}_{xi}$, $\underline{k}_{yi}$ are the lower limits and $\bar{K}_{xi}$, $\bar{k}_{yi}$ are the upper limits. The N_f is the number of bearings supported with anisotropic stiffness.

From equation (15) to equation (19), we have completed the optimization formulation, which is cast as a nonlinear programming problem and can be solved by the method of feasible direction (Kirsch, 1981). The design variables of this optimization problem contain the outer shaft diameters d_{Oi}, the stiffnesses of bearing support k_{xi}, k_{yi}, and the clearance excitation factor q, and can expressed as

$$\begin{aligned} \{V\}^T &= \{v_1, v_2, \ldots, v_{N_p}\} \\ &= \{q, k_{x1}, k_{x2} \ldots k_{y1}, k_{y2} \ldots, d_{O1}, d_{O2} \ldots d_{ON_e}\} \end{aligned} \qquad (20)$$

The derivations of all constraints with respect to design variables, except for the constraint of equation (16), are quite straight forward and will not be discussed here. The derivative of equation (16) with respect to v_j can be derived from equation (12), and can be expressed as

$$\frac{\partial\sigma_i}{\partial v_j} = \text{Re}\left(\frac{\partial\lambda_i}{\partial v_j}\right) = \text{Re}\left(\frac{-\{x_i\}^T\left(\lambda_i\dfrac{\partial[A]}{\partial v_j} + \dfrac{\partial[B]}{\partial v_j}\right)\{y_i\}}{R_i}\right)$$

Finally, since the objective function f is a linear function of the clearance excitation factor q only, its gradient expression is simply

$$\nabla f = \{-1, 0, 0, \ldots\ldots 0\} \qquad (22)$$

Note that because the vector of design variables $\{V\}$ contains different kinds of physical quantities, which are quire different in magnitude, they must be scaled in the optimization procedures so that their magnitudes are all of the same order.

Results and Discussion

Two numerical examples are shown and discussed below to illustrate the proposed method. During the optimization procedure, the feasible direction method (Kirsch, 1981) and one-dimensional search were employed in this work.

Example 1. The original design rotor of this example is a two-bearing rotor with the configuration shown in Fig. 1. This

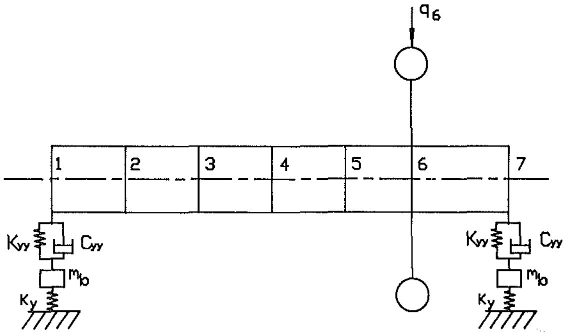

Fig. 1 The configuration of the two-bearing rotor

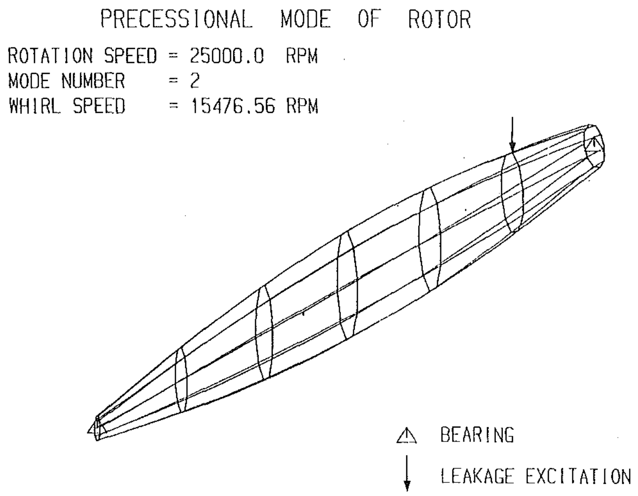

Fig. 2(*a*) The unstable mode of the original two-bearing rotor with rigid bearing support

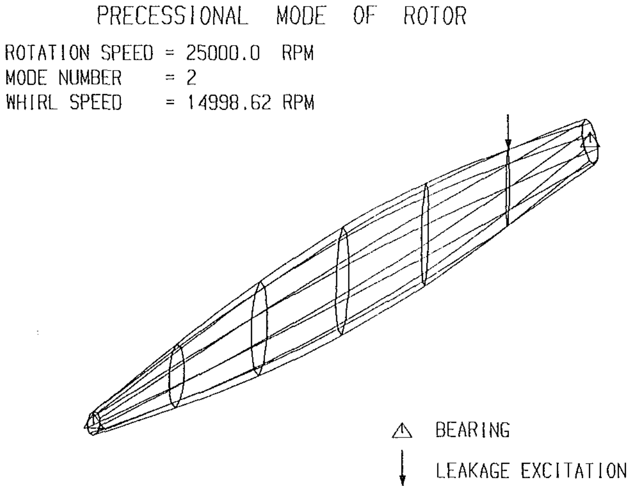

Fig. 2(*b*) The unstable mode of the two-bearing rotor with optimal bearing support stiffness

rotor has been used by Alam and Nelson (1985) to study the blade loss response. The rotor was slightly modified in this example, namely, a bearing housing mass m_b and anisotropic bearing stiffnesses k_x, k_y (only k_y is shown in Fig. 1) were added to the rotor. If the k_x and k_y are set to a very large value ($\geq 10^{11}$ N/m), then the rotor system can practically be considered as the same system with rigid bearing supports used by Alam. For space reasons, the system data are not given here, but may be found in the work of Alam (1985). If the leakage excitation force was assumed to act on the rigid disk, then the threshold performance of the original rotor with rigid bearing supports was found to be $q_{\max} = 9.28 \times 10^5$ N/m. The rotation speed was assumed to be 25,000 rpm, and k_x, k_y were set to a large value, 10^{11} N/m, to simulate rigid bearing supports. The procedure to find the $q_{\max}$ of the original rotor is straightforward; that is, one can increase the q value until the equation (5) reaches its threshold state. The unstable mode shape is shown in Fig. 2(*a*). Note that the unstable mode is the second natural mode, but it is the first forward natural mode. Three cases will be discussed below with three different solutions to increase the threshold performance of the original rotor with rigid bearing supports.

Case A. In this case only the stiffnesses of the bearing supports k_x and k_y will be considered as design variables, and the shaft diameters were held to the original design value, 5.08 cm. Due to the deadweight of the rotor, if the support stiffnesses of the vertical direction (y direction) were held constant for all bearings, then the alignment of the rotor and other construction would be easier to do in practice. So, in this case the stiffnesses of the bearing supports in the y direction, k_{y1} and k_{y2}, were fixed at 10^{10} N/m while the stiffnesses in the x direction, k_{x1} and k_{x2}, were considered as two independent design variables. The lower and upper limits $\underline{k}_x$ and $\bar{k}_x$ were set at 10^6 N/m and 10^9 N/m, respectively. In this case only equations (15), (16), and (19) should be used to find the optimum result. The results of optimum stiffnesses of bearing supports and $q_{\max}$ are listed in Table 1. As indicated before, the threshold performance of the original rotor with rigid bearing supports was found to be $q_{\max} = 9.28 \times 10^5$ N/m. The results of Table 1 show that the $q_{\max}$ of the rotor with optimal bearing support is 4.852×10^6 N/m, which is a 420 percent improvement. The unstable mode shape of the rotor with the optimum anisotropic bearing support is shown in Fig. 2(*b*). The reason for this improvement can be explained from the energy point of view (Wang, 1988) by comparing the unstable mode shapes of Figs. 2(*a*) and 2(*b*). The whirl orbit of the disk is elongated by the anisotropic bearing supports. As a consequence, the positive work done by the leakage excitation force is reduced, and the system becomes more stable.

Table 1 Optimal bearing support stiffness and $q_{\max}$ with optimal stiffness

k_y (N/m)	k_{x1} (N/m)	k_{x2} (N/m)
10^{10}	4.956×10^7	0.962×10^7

$q_{\max}$ (N/m)	Improvement
4.852×10^6	420.1 %

Table 2 Optimal and original shaft diameter, case B, example 1

Rotor Element Data

Element No.	Length (cm)	Original Diameters (cm)	Optimal Diameters (cm)
1	8.47	5.08	4.06
2	8.47	5.08	4.75
3	8.47	5.08	6.10
4	8.47	5.08	6.10
5	8.47	5.08	6.10
6	8.47	5.08	4.06

$E = 20.69 \times 10^6$ N/cm^2, $\rho = 8304$ kg/m^3, $m_b = 1.0$ kg

$q_{\max}$ (N/m) Original Design	$q_{\max}$ (N/m) Optimal Design	mass increment
9.28×10^5	2.88×10^6	7.89 %

Case B. In this case only the shaft diameters were taken as the design variables, and the bearings supports were assumed to be rigid ($k_x = k_y = 10^{11}$ N/m). The total mass of the rotor was not constrained in this case. The diameters of the six shaft elements were allowed to vary from 80 to 120 percent of the original value. Then equations (15), (16), and (17) were used to find the optimum diameters and $q_{\max}$ by the feasible direction

Table 3 Optimal bearing support stiffness for optimal diameter rotor (case C, example 1)

k_y (N/m)	k_{x1} (N/m)	k_{x2} (N/m)
10^{10}	4.197×10^7	1.731×10^7

q_{max} (N/m)	Improvement
10.63×10^6	1045.3 %

Table 4 Optimal and original shaft diameter of the dual rotor

Rotor Element Data				
Element No.	Length (cm)	Inner Dia. (cm)	Original Outer Dia. (cm)	Optimal Outer Dia. (cm)
1	7.62	0.00	3.048	3.071
2	8.89	0.00	3.048	3.369
3	8.89	0.00	3.048	3.661
4	7.62	0.00	3.048	3.661
5	7.62	0.00	3.048	3.661
6	5.08	0.00	3.048	3.660
7	5.08	0.00	3.048	3.468
8	5.08	3.81	5.08	4.530
9	7.62	3.81	5.08	4.531
10	7.62	3.81	5.08	4.529
11	5.08	3.81	5.08	4.060

$E=20.69 \times 10^6$ N/cm^2, $\rho=8304$ kg/m^3

q_{max} (N/m) Original Design	q_{max} (N/m) Optimal Design
5.66×10^5	11.68×10^5

method. The results of the optimum diameter and $q_{\max}$ are shown in Table 2, and the configuration of the optimized rotor is shown in Fig. 3. The improvement of threshold performance is also very significant, 210 percent in comparison with the original design. This improvement is partly due to less work done by the leakage exciting force, and partly due to more energy dissipated by the bearings. Note that the diameter at the shaft ends of the optimized rotor becomes smaller, but the diameter at the shaft middle becomes larger. The first critical speed of the optimized rotor increases about 2 percent in comparison with the original design. The results of this case demonstrate that the threshold performance can be improved very significantly by only slight modification of the shaft diameters. Although the total mass of the rotor was not constrained in this case, the mass increment is only 7.89 percent, as shown in Table 2.

Case C. Although the results of cases A and B show that the threshold performance can be improved significantly either by optimum anistotropic bearing supports or slight modification of shaft diameters, if necessary, this improvement can be further increased by the combination of optimum anisotropic support and optimum shaft diameter. If the rotor with optimum diameter of case B is further supported with anisotropic bearing stiffnesses, then the optimum stiffnesses k_{x1} and k_{x2} can be found by the same procedure as in case A. The results of the optimum k_{x1}, k_{x2} and $q_{\max}$ are listed in Table 3. The improvement, in comparison with the original rotor with rigid support, is 1045.3 percent. In this case, the optimum shaft diameters were found at first, and then the optimum anisotropic supports were calculated. Of course, one can consider the shaft diameters and the stiffnesses of supports as design variables simultaneously.

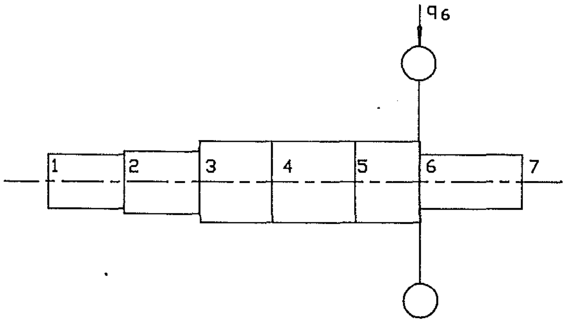

Fig. 3 The configuration with the optimal shaft diameters, case B, example 1

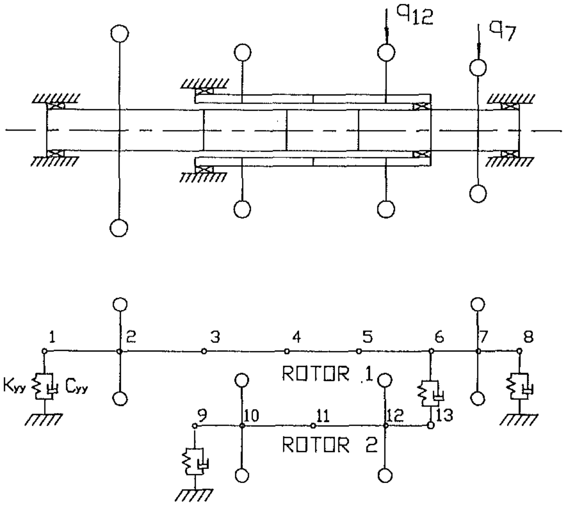

Fig. 4 The configuration and model of the dual rotor

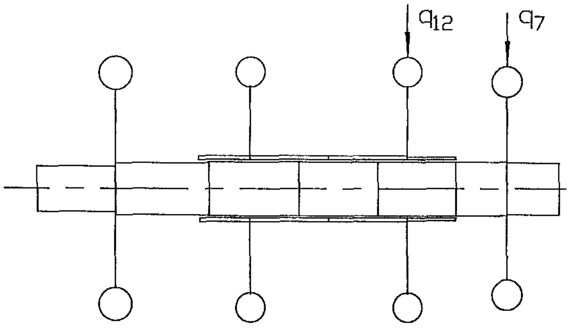

Fig. 5 The configuration with optimal shaft diameters, example 2

The above three cases show that, according to the practical or necessary limitation, one can use different solutions to overcome the instability caused by fluid leakage excitation.

Example 2. In this example, the dual rotor system previously used by Rajan and Nelson (1986) was analyzed. This rotor is shown in Fig. 4. A shaft speed of 8000 rpm for the inner low-speed rotor 1 and 12,000 rpm for the outer high-speed rotor 2 were used. This system was modeled as 11 finite elements and with 52 degrees of freedom. The leakage excitations were assumed to act on the low and high-pressure turbines with the ratio of q_{12} : $q_7=0.5$:0.5. The threshold performance 0.5 $q_{\max}=(q_{12})_{\max}=(q_7)_{\max}$. The threshold performance of the original design was found to be

$q_{max} = 5.66 \times 10^5$ N/m. Now it is desirable to increase the threshold performance by allowing the outer diameter of the shaft elements to vary from 80 to 120 percent of the original design values. In this example, the mass constraint, equation (18), was introduced to ensure that the total mass of the optimized rotor is less than or equal to that of the original rotor. Then equations (15)-(18) were used to find the optimum outer diameters of rotors 1 and 2. The results of optimum shaft outer diameters of the dual rotor are shown in Table 4, and the configuration of the optimized rotor is shown in Fig. 5. The threshold performance of the optimized rotor was found to be $q_{max} = 11.68 \times 10^5$ N/m, which is a 106 percent improvement in comparison with the original rotor. This significant improvement is partly due to more energy dissipated by the bearing damping, and partly to less work done by the leakage exciting forces. The unstable whirl speed of the original rotor is 8693 rpm, while the unstable whirl speed of the optimized rotor is 9847 rpm. The results of this example demonstrate that, even without any increase of the total mass, the threshold performance can be increased significantly by slight modification of the outer diameters. This is very important for the aeroengine, which is very sensitive to the total weight of the rotor.

From the above two examples, one can see that the method of feasible direction had been successfully applied to find out the optimum rotor that can sustain larger leakage excitation. The results show that when the diameters of the shaft elements of rotors are slightly modified (±20 percent in this study) and even without any increase of the total mass, the threshold performance can be improved significantly. This indicates that when the optimum shaft configuration is used, one can increase the ratio of power generated per pound of rotating elements in a significant manner without an instability problem.

Although the bearings used in the above two examples were rolling bearings without cross-coupling coefficients, a journal bearing with cross-coupling coefficient has also been used in the rotor model of example 1 and investigated. The result indicates also that a slight modification of shaft diameters can significantly increase the stability of rotor system.

Conclusions

In this work, an optimization technique has been used to find an optimum shaft configuration and bearing support stiffness so that the optimized rotor-bearing system can sustain larger fluid leakage excitation. The results show that, even without the increase of the total mass of the rotor system, the threshold performance of the rotor-bearing systems can be significantly improved by slight modification of the shaft diameters. Although the modification of the shaft diameters may be difficult to do for an existing rotor, the suggested method of this work can be used very well in the design phase. The results also show that, according to the practical requirement and limitation, one can select optimum anisotropic bearing support, optimum shaft diameters, or a combination to overcome the instability caused by fluid leakage excitation. For example, as indicated by the previous work (Wang and Tsai, 1988) that the threshold performance of some rotor systems cannot be improved by anisotropic bearing support, then the method of slight modification of the rotor diameters can be selected to overcome this difficulty.

Acknowledgments

This work was supported by the National Science Council, Republic of China (Contract No. NSC77-0401-E007-17). This support is hereby gratefully acknowledged.

References

Alam, M., and Nelson, H. D., 1985, "A Blade Loss Response Spectrum for Flexible Rotor Systems," ASME JOURNAL OF ENGINEERING FOR GAS TURBINES AND POWER, Vol. 107, pp. 187-195.

Alford, J. S., 1965, "Protecting Turbomachinery From Self-Excited Rotor Whirl," ASME JOURNAL OF ENGINEERING FOR POWER, Vol. 77, pp. 333-343.

Ebner, F. L., 1985, "Stability Behavior of Clearance-Excited Turborotors With External Anisotropy," ASME Paper No. 85-DET-149.

Fox, R. L., and Dapoor, M. P., 1968, "Rates of Change of Eigenvalues and Eigenvectors," *AIAA Journal*, Vol. 6, No. 12, pp. 2426-2429.

Glienicke, J., Han, D. C., and Leonhark, H., 1980, "Practical Determination and Use of Bearing Dynamic Coefficients," *Tribology International*, pp. 297-309.

Hauck, L. H., 1982, "Strömungsvorgänge in den Labyrinth-dichtungen von Turbinenstufen," Dissertation TU München, Federal Republic of Germany.

Kirsch, U., 1981, *Optimum Structure Design*, McGraw-Hill, New York, Chap. 8.

Kurohashi, M., et al., 1984, "Stability Analysis of Rotor Bearing System Subjected to Cross Coupling Force," Paper No. C266/84, Third International Conference on Vibrations in Rotating Machinery, University of York, United Kingdom.

Nelson, H. D., and Macvaugh, J. M., 1976, "The Dynamics of Rotor-Bearing Using Finite Elements," ASME *Journal of Engineering for Industry*, Vol. 88, pp. 593-600.

Rajan, M., Nelson, H. D., and Chen, W. J., 1986, "Parameter Sensitivity in the Dynamics of Rotor-Bearing Systems," ASME *Journal of Vibration, Acoustics, Stress, and Reliability in Design*, Vol. 108, pp. 197-206.

Thomas, H.-J., 1958, "Instabile Eigensch-wingungen von Turbinenlaufern, angefacht durch die Spaltströmung in stopfbuchsen und Besch-auflungen," *Bull. de l'AIM 71*, Vol. 11/12, pp. 1039-1063.

Thomas, H.-J., 1975, *Thermische Kraftanlagen*, Springer-Verlag, Berlin, Chap. 7.

Wang, J. H., and Tsai, M. T., 1988, "The Effect of Anisotropic Support on Rotor Instability Due to Fluid Leakage," ASME JOURNAL OF ENGINEERING FOR GAS TURBINES AND POWER, Vol. 110, pp. 585-591.

Wang, J. H., and Tsai, M. T., 1989, "Instability Due to Fluid Leakage of a Rotor System With Anisotropic Support," ASME *Journal of Vibration, Acoustics, Stress, and Reliability in Design*, Vol. 111, No. 1, pp. 27-34.

Wang, J. H., and Shih, F. M., 1990, "Improve the Stability of Rotor Subjected to Fluid Leakage by Optimum Diameter Design," ASME *Journal of Vibration and Acoustics*, Vol. 112, pp. 59-64.

Warner, R. E., and Soler, A. I., 1975, "Stability of Rotor-Bearing Systems With Generalized Support Flexibility and Damping and Aero Dynamic Cross Coupling," ASME *Journal of Lubrication Technology*, Vol. 97, pp. 461-471.

Wohlrab, R., 1975, "Spalterregung bei thermischen Turbomaschinen," Dissertation, TU München, Federal Republic of Germany.

Unbalance Response of a Jeffcott Rotor Incorporating Short Squeeze Film Dampers

A. El-Shafei
Assistant Professor,
Department of Mechanical
Design and Production,
Cairo University,
Cairo, Egypt

The steady-state unbalance response of a Jeffcott rotor incorporating short squeeze film dampers executing circular centered whirl is obtained by a fast algorithm. Savings in execution time of the order of fifty times are gained over numerical integration. Fluid inertia forces are included in the model of the squeeze film dampers. The fast algorithm allows parametric studies to be performed. It is shown that fluid inertia results in the excitation of a second mode for the Jeffcott rotor, decreases the possibility of jump resonance, and decreases the useful range of vibration isolation of the dampers. It is also shown that a squeeze film damper with no centering spring (or a very soft spring) may be advantageous with regards to the unbalance response and the vibration isolation capability of the dampers.

Introduction

Squeeze film dampers (SFDs) were introduced approximately 25 years ago (Cooper, 1963), and nowadays they find wide use in aircraft gas turbine engines. Their ability to attenuate the amplitude of engine vibrations and to decrease the magnitude of the force transmitted to the engine frame makes them an attractive rotor support. Yet, SFD behavior proved to be very difficult to predict analytically, because of their nonlinear nature.

In his experiments, Cooper (1963) observed "bistable" operation of a rotor incorporating a SFD; that is, the rotor would exhibit a jump from a certain whirling orbit to another at some frequency. This is the classical jump phenomenon, and perhaps this was the first indication of the nonlinear behavior of squeeze film dampers. White (1972) studied theoretically and experimentally the dynamics of a rigid rotor on squeeze film dampers. He was able to calculate the forces acting in the damper based on Reynolds equation of fluid lubrication. He predicted three steady-state orbits of the rotor journal at the same frequency, but using a stability analysis he found that only two of them were stable. This confirmed Cooper's predictions for the jump phenomenon.

Mohan and Hahn (1974) studied the dynamics of a rigid rotor in squeeze film dampers. They obtained the steady-state response by assuming a circular whirl, and they did parametric studies to determine the effect of the damper on the dynamics of the rotor, and the force transmitted to the engine frame, and also to determine the maximum rotor unbalance at which the damper is effective. They concluded that the squeeze film damper is generally an effective damping device, but for a badly designed damper, the transmitted force can be magnified rather than attenuated, and this could lead to the failure of the engine.

Cunningham et al. (1975) demonstrated the possibility of using design data for a SFD designed on the basis of single mass flexible rotor analysis, and applying it for the design of a SFD for a multimass flexible rotor. In an experimental parametric study, Tonnesen (1976) was able to show that the forces in the damper agree with the π-film theory. Gunter et al. (1977) numerically studied the nonlinear response of aircraft engines incorporating SFDs, and they were able to show that the rotor exhibits the jump phenomenon, and, under unidirectional loading, subharmonic whirl motion may exist. This was later verified experimentally by Sharma and Botman (1977), who observed nonsynchronous whirl in their test rig, although they did not associate it with unidirectional loading.

Rabinowitz and Hahn (1977a) studied the steady-state orbits for a flexible rotor incorporating SFDs. They did a parametric study to determine regions of unacceptable behavior of rotors due to SFDs. They also did a stability analysis of the steady-state orbits they obtained (Rabinowitz and Hahn, 1977b). Taylor and Kumar (1980) did an investigation of the numerical integration techniques used to determine the response of a rigid rotor in SFDs. They were able to demonstrate the drawbacks of numerical integration, and this motivated them (Taylor and Kumar, 1983) to find closed-form steady-state solutions for a rigid rotor in squeeze film dampers by assuming a circular orbit. More recently, Guang and Zhong-Qing (1985) used a similar technique to do a parametric study of a flexible rotor incorporating SFDs.

The above-mentioned analyses are all based on the Reynolds equation, which neglects the effects of fluid inertia. This has been a good assumption, since the dampers usually operate at a very low squeeze Reynolds number. But as the speed of aircraft engines increases and as the trend of using lighter viscosity oils prevails, the values of Reynolds number for SFDs in practice have been continually increasing, and the need for a model that includes fluid inertia becomes a necessity.

Recently, in their experiments on squeeze film dampers Tecza

Contributed by the International Gas Turbine Institute and presented at the 34th International Gas Turbine and Aeroengine Congress and Exhibition, Toronto, Ontario, Canada, June 4–8, 1989. Manuscript received at ASME Headquarters January 13, 1989. Paper No. 89-GT-75.

et al. (1983) showed that fluid inertia may be a significant factor in determining the dynamic characteristics of squeeze film dampers. This has prompted several investigations of the effects of fluid inertia in squeeze film dampers. Tichy (1983) provided an explanation for the importance of fluid inertia in squeeze film dampers versus journal bearings. San Andrés and Vance (1988) obtained the steady-state response of a rotor incorporating SFDs, including fluid inertia effects, by using an averaged momentum approximation (San Andrés and Vance, 1986).

Perhaps one of the first attempts to study the effects of fluid inertia in hydrodynamic bearings is the work of Smith (1964-1965). Using a unique form of Reynolds equation, he was able to obtain inertia force coefficients for journal bearings, and his conclusion was that the effect of fluid inertia in oil film bearings is to introduce an added mass to the rotor. This may affect the dynamics of the rotor especially for short stiff rotors on wide bearings. Approximately a decade later Reinhardt and Lund (1975) used a perturbation solution for small Reynolds number to obtain the force coefficients of journal bearings. They showed that fluid inertia introduces rather small corrections to the damping and stiffness coefficients of journal bearings and they also provided plots of inertia coefficients versus the eccentricity. They had to solve a set of differential equations numerically to arrive at these plots. Another notable paper is the work of Szeri et al. (1983). They used a technique based on averaging the inertia forces across the film to obtain the force coefficients in a squeeze film damper. They also had to solve the resulting differential equations numerically. A recent paper by Ramli et al. (1987) compares the results of Smith, Reinhardt and Lund, and Szeri et al., and concludes that they are in good agreement, especially for short bearings. It is pointed out, however, that Smith's approach has the advantage of computational simplicity, and leads to fairly simple asymptotic analytical expressions for very short and very long bearings.

The results of all these researchers indicate that the classical lubrication theory is in error with respect to the pressure field and the inertia forces, which can dominate at higher Reynolds numbers. On the other hand, they all seem to indicate that the velocity field predicted by the classical lubrication theory is not greatly affected by fluid inertia for Reynolds number in the range of usual application of squeeze film dampers. In fact, the method of averaged momentum is based on the assumption that the velocity profiles predicted by the classical lubrication theory are not changed much by fluid inertia.

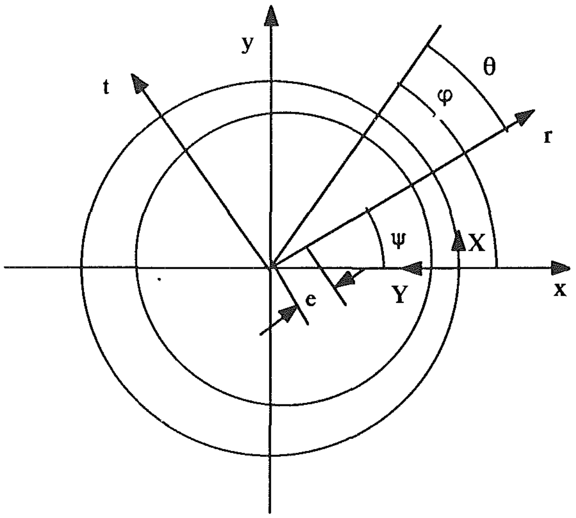

Fig. 1 Squeeze film damper

A recently developed model of fluid inertia in SFDs (El-Shafei, 1988, 1989) is also based on the assumption that the velocity field predicted by the classical lubrication theory is not changed much by fluid inertia. This permits the kinetic coenergy of the fluid to be calculated, and the inertia forces to be obtained by Lagrange's equations as applied to an open system. This model is used in this paper to predict the fluid inertia forces in short SFDs. The damping forces in the SFDs are predicted by the Reynolds equation. These damping and inertia forces are then used to obtain the unbalance response of a Jeffcott rotor incorporating SFDs. By assuming that the orbit of the journal in the damper is circular and centered, the differential equations describing the system are reduced to algebraic equations. Further manipulation of the algebraic equations results in a single eighth-order polynomial in the speed of rotation, which is then solved by the IMSL routine ZPOLR. This permits all the solutions to be found without trial and error, and results in a huge savings in computation time over numerical integration of the equations of motion, and permits parametric studies of the rotor-damper system to be performed.

Nomenclature

B = $\mu RL^3/m\omega_n c^3$ = bearing parameter
c = clearance, m
C = half damping coefficient, Ns/m
C_{rr}, C_{tt}, C_{tr}, C_{rt} = damping coefficients, Ns/m
C^*_{rr}, C^*_{tt}, C^*_{tr}, C^*_{rt} = nondimensional damping coefficients
d = rotor deflection at midspan, m
D = d/c = nondimensional deflection
e = eccentricity, m
$F_{i,r}$ = radial inertia force, N
$F_{i,t}$ = tangential inertia force, N
F_r = radial force, N
F^*_r = $F_r/mc\omega_n^2$ = nondimensional radial force
F_{rc} = radial damping force, N
F_{ri} = radial inertia force, due to fluid within control volume, N
F_t = tangential force, N
F^*_t = $F_t/mc\omega_n^2$ = nondimensional tangential force
F_{tc} = tangential damping force, N
F_{ti} = tangential inertia force, due to fluid within control volume, N
h = film thickness, m
i = $(-1)^{1/2}$
K = half rotor stiffness, N/m
K^* = $K/m\omega_n^2$ = nondimensional rotor stiffness
K_{eq} = $K_r K/(K_r+K)$ = equivalent stiffness of the rotor and retainer spring, N/m
K^*_{eq} = $K_{eq}/m\omega_n^2$ = nondimensional equivalent stiffness
K_r = retainer spring stiffness, N/m
K^*_r = $K_r/m\omega_n^2$ = nondimensional retainer spring stiffness
L = damper length, m
m = half mass of disk, kg
m_{rr}, m_{tt}, m_{rt} = inertia coefficients, kg
m^*_{rr}, m^*_{tt}, m^*_{rt} = nondimensional inertia coefficients
m_{11}, m_{22}, m_{12}, m_{21} = supplemental inertia coefficients, kg
m^*_{11}, m^*_{22}, m^*_{12}, m^*_{21} = nondimensional supplemental inertia coefficients
M = $\rho RL^3/mc$ = inertia parameter
$\hat{n}$ = outward normal on control surface
p = pressure, N/m^2

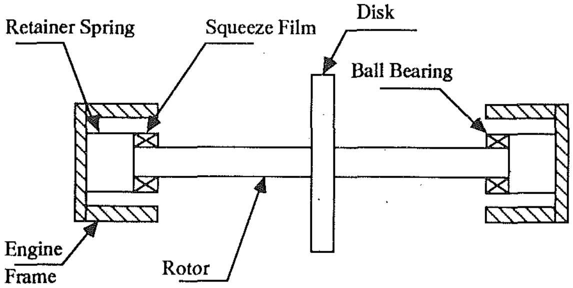

Fig. 2 Jeffcott rotor on squeeze film dampers

Squeeze Film Dampers

Figure 1 shows a SFD, and the coordinate system used. The film thickness h at any given location is given by

$$h=c-e\cos\theta \tag{1}$$

where e is the eccentricity of the journal and θ is measured from the positive r axis of the whirling coordinate system (r, t, z). The z axis is perpendicular to the plane of the paper. Also shown in Fig. 1 are the stationary coordinate system (x, y, z) and the angle φ, which is measured from the positive x axis, and $\theta=\varphi-\psi$. For a steady circular whirl $\psi=\omega t$, where ω is the whirling frequency of the journal and t is time. The flow in the damper is described with respect to the stationary coordinate system (X, Y, Z) shown in Fig. 1.

If the inertia of the fluid is neglected, then the Reynolds equation is the equation governing the pressure in the damper, and for a short damper is given by

$$\frac{\partial}{\partial z}\left(\frac{h^3}{\mu}\frac{\partial p}{\partial z}\right)=-12(e\dot\psi\sin\theta+\dot e\cos\theta)$$

which when integrated gives the pressure as

$$p=\frac{6\mu}{h^3}\left(\frac{L^2}{4}-z^2\right)(e\dot\psi\sin\theta+\dot e\cos\theta) \tag{2}$$

where $\dot e$ is the radial velocity and $e\dot\psi$ is the tangential velocity of the journal in the damper.

The damping forces can be obtained by integrating the pressure equation (2). Thus the radial and tangential damping forces F_{rc} and F_{tc} acting on the journal are given by

$$F_{rc}=-C_{rr}\dot e-C_{rt}e\dot\psi \tag{3}$$

$$F_{tc}=-C_{tr}\dot e-C_{tt}e\dot\psi \tag{4}$$

where the coefficients C_{rr}, C_{tt}, C_{tr}, and C_{rt} are the damper's damping coefficients. For a cavitated damper we are going to use the π-film theory, which assumes that the film extends for π radians in the region of positive pressure.

Thus for a π-film, with the journal executing a nearly circular counterclockwise whirl, the coefficients C_{rr}, C_{tt}, C_{tr}, and C_{rt} are given by

$$C_{rr}=\frac{\mu RL^3}{c^3}C^*_{rr},\quad C_{tt}=\frac{\mu RL^3}{c^3}C^*_{tt},\quad C_{rt}=C_{tr}=\frac{\mu RL^3}{c^3}C^*_{rt}$$

$$C^*_{rr}=\frac{\pi}{2}\frac{(1+2\epsilon^2)}{(1-\epsilon^2)^{5/2}} \tag{5}$$

$$C^*_{tt}=\frac{\pi}{2}\frac{1}{(1-\epsilon^2)^{3/2}} \tag{6}$$

$$C^*_{rt}=\frac{2\epsilon}{(1-\epsilon^2)^2} \tag{7}$$

Fluid Inertia Forces in SFDs

For a short damper, the axial velocity profile is given by

$$w=\frac{6z}{h}\left(\frac{Y}{h}-\frac{Y^2}{h^2}\right)(e\dot\psi\sin\theta+\dot e\cos\theta) \tag{8}$$

and thus the kinetic coenergy of the fluid in the damper, which is defined by

$$T^*=\frac{1}{2}\int_{\theta_1}^{\theta_2}\int_0^h\int_{-\frac{L}{2}}^{\frac{L}{2}}\rho\, w^2R\, d\theta\, dY\, dZ \tag{9}$$

can be calculated as

$$T^*=\frac{1}{2}m_{rr}\dot e^2+\frac{1}{2}m_{tt}(e\dot\psi)^2+m_{rt}\dot e e\dot\psi \tag{10}$$

where m_{rr}, m_{tt}, and m_{rt} represent the inertia coefficients of the short damper. For a cavitated damper we are also going to assume the π-film theory. Including inertia in the analysis, we anticipate that the extent of the positive pressure in the film should be different from π, yet because the π-film theory is the most acceptable cavitation theory for rotordynamic analysis (Burrows et al., 1987), and to have results compatible with the damping analysis, we are going to use the π-film theory here also.

Nomenclature (cont.)

r = runout at rotor center, m
R = journal radius, m
R^* = nondimensional runout
R_k = K_r/K = stiffness ratio
R_{ri} = radial inertia force, due to flux of fluid through control surface, N
R_{ti} = tangential inertia force, due to flux of fluid through control surface, N
S = control surface area, m^2
t = time, s
t^* = kinetic coenergy of fluid per unit volume, N/m^2
Tr = transmissibility
T^* = kinetic coenergy of fluid in control volume, Nm
u = unbalance, m
U = u/c = nondimensional unbalance
$\mathbf{V}$ = fluid velocity vector at control surface, m/s
w = axial fluid velocity, m/s
α, β = phase angles, rad
ϵ = e/c = eccentricity ratio
ζ = position vector in complex plane, m

η = $C/m\omega_n$ = damping loss factor
θ = angle (Fig. 1), rad
μ = fluid dynamic viscosity coefficient, Ns/m^2
π = 3.14159265.....
ρ = fluid density, kg/m^3
τ = $\omega_n t$ = nondimensional time
φ = angle (Fig. 1), rad
ψ = angle (Fig. 1), rad
ω_n = $(K_{eq}/m)^{1/2}$ = natural frequency of rotor-bearing system, rad/s
Ω = rotor speed, rad/s
Ω^* = Ω/ω_n = nondimensional rotor speed
$(\dot{\ })$ = denotes differentiation with respect to t
$(\ )'$ = denotes differentiation with respect to τ

Reference frames

(x, y, z) = stationary frame (Fig. 1)
(r, t, z) = whirling frame (Fig. 1)
(X, Y, Z) = stationary frame (Fig. 1)

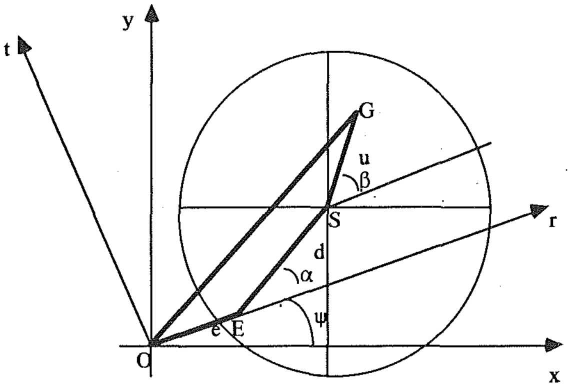

Fig. 3 Side view of rotor

For a π-film, with the journal executing a nearly circular counterclockwise whirl, the coefficients m_{rr}, m_{tt}, and m_{rt} are given by

$$m_{rr}=\frac{\rho RL^3}{c}m_{rr}^*,\quad m_{tt}=\frac{\rho RL^3}{c}m_{tt}^*,\quad m_{rt}=\frac{\rho RL^3}{c}m_{rt}^*$$

where

$$m_{rr}^*=\frac{1}{10}\frac{\pi}{\epsilon^2}\left[\frac{1}{(1-\epsilon^2)^{1/2}}-1\right] \tag{11}$$

$$m_{tt}^*=\frac{1}{10}\frac{\pi}{\epsilon^2}[1-(1-\epsilon^2)^{1/2}] \tag{12}$$

$$m_{rt}^*=-\frac{1}{10}\frac{1}{\epsilon}\left[\frac{1}{\epsilon}\log\left(\left|\frac{1-\epsilon}{1+\epsilon}\right|\right)+2\right] \tag{13}$$

The inertia forces in the damper can be obtained by Lagrange's equations, but since the damper is an open system (because of the fluid being squeezed out axially), the Reynolds transport theorem (see for instance Potter and Foss, 1982) must be used in conjunction with Lagrange's equations. Thus the radial and tangential inertia forces become

$$F_{i,r}=F_{ri}+R_{ri} \tag{14}$$

and

$$F_{i,t}=F_{ti}+R_{ti} \tag{15}$$

where $F_{i,r}$ is the radial inertia force and $F_{i,t}$ is the tangential inertia force, R_{ri} and R_{ti} are the inertia forces due to the flux of the fluid particles across the control surface in the r and t directions, respectively, and F_{ri} and F_{ti} are obtained by Lagrange's equations and are given by

$$F_{ri}=-\frac{d}{dt}\left(\frac{\partial T^*}{\partial \dot{e}}\right)+\frac{\partial T^*}{\partial e} \tag{16}$$

and

$$F_{ti}=-\frac{1}{e}\frac{d}{dt}\left(\frac{\partial T^*}{\partial \dot{\psi}}\right)+\frac{1}{e}\frac{\partial T^*}{\partial \psi} \tag{17}$$

The flux terms R_{ri} and R_{ti} are given by

$$R_{ri}=-\int_{cs}\frac{\partial t^*}{\partial \dot{e}}\mathbf{V}\cdot\hat{n}\,dS+\int_{cs}t^*\frac{\partial(\mathbf{V}\cdot\hat{n})}{\partial e}dS$$

$$R_{ti}=-\frac{1}{e}\int_{cs}\frac{\partial t^*}{\partial \dot{\psi}}\mathbf{V}\cdot\hat{n}\,dS+\frac{1}{e}\int_{cs}t^*\frac{\partial(\mathbf{V}\cdot\hat{n})}{\partial \psi}dS$$

where t^* is the kinetic coenergy per unit volume; $\mathbf{V}$ is the velocity of the fluid with respect to the control surface S; $\hat{n}$ is the outward normal vector on the control surface. On calculating the above equations, for a π-film, with the journal executing a circular centered whirl, we get for the radial and tangential forces

$$F_r=(m_{rr}-m_{12})e\dot{\psi}^2-C_{rt}e\dot{\psi} \tag{18}$$

$$F_t=(m_{rt}-m_{22})e\dot{\psi}^2-C_{tt}e\dot{\psi} \tag{19}$$

with

$$m_{22}=\frac{\rho RL^3}{c}m_{22}^*,\quad m_{12}=\frac{\rho RL^3}{c}m_{12}^*$$

where

$$m_{22}^*=-\frac{17}{70}\frac{1}{\epsilon}\left[4+\frac{2}{\epsilon}\log\left(\left|\frac{1-\epsilon}{1+\epsilon}\right|\right)\right] \tag{20}$$

$$m_{12}^*=-\frac{17}{70}\frac{\pi}{\epsilon^2}\left[2-\frac{(2-\epsilon^2)}{(1-\epsilon^2)^{1/2}}\right] \tag{21}$$

Jeffcott Rotor Incorporating SFDs

Figure 2 shows a Jeffcott rotor mounted on two identical ball bearings, each of which is surrounded by a squeeze film. The outer race of each ball bearing, which is assumed rigid and massless, is constrained from rotating by a retainer spring of stiffness K_r, which also acts to center the journal in the clearance of the oil film. The rotor is assumed massless with stiffness of $2K$, the disk is assumed rigid with mass $2m$, and the damping acting at the rotor center has a damping coefficient of $2C$.

Figure 3 shows a side view of the Jeffcott rotor of Fig. 2. Point O represents the center of bearings, while point E represents the center of the journal. Thus the distance OE is equal to the eccentricity (e) of the journal in the damper. Point S represents the geometric center of the disk, thus the distance SE is the deflection (d) of the rotor at its midspan; and point G represents the center of mass of the disk; thus the distance GS is the unbalance (u). Since the rotor is symmetric, the eccentricities of the journals in each bearing are the same.

Figure 3 also shows the notation and the coordinate frames used in the analysis of the rotor. The (x, y) frame is a stationary frame whose center is at the bearing center O. The rotating (r, t) frame is rotating at the whirl frequency of the journal in the damper. The positive r axis joins the center of the bearing O and the center of the journal E, and makes an angle ψ with the positive x axis. The rotor deflection d can in general be in a direction making an angle α with the positive r axis, and the unbalance u makes an angle β with the positive r axis as shown in Fig. 3.

We can consider the (x, y) plane of Fig. 3 to be a complex plane, in which the position vector of a point in the plane is determined by a complex number $\zeta=x+iy$. Then the equations of motion of the rotor become

$$\begin{aligned}&m\{\ddot{e}-e\dot{\psi}^2+i(e\ddot{\psi}+2\dot{e}\dot{\psi})+\\&\quad[(\ddot{d}-d(\dot{\alpha}+\dot{\psi})^2)+i(d(\ddot{\alpha}+\ddot{\psi})+2\dot{d}(\dot{\alpha}+\dot{\psi}))]e^{i\alpha}\\&\quad+[-u(\dot{\beta}+\dot{\psi})^2+iu(\ddot{\beta}+\ddot{\psi})]e^{i\beta}\}+\\&\quad C\{\dot{e}+ie\dot{\psi}+[\dot{d}+id(\dot{\alpha}+\dot{\psi})]e^{i\alpha}\}+Kde^{i\alpha}=0\end{aligned} \tag{22}$$

and

$$Kde^{i\alpha}-K_re+F_r+iF_t=0 \tag{23}$$

where the forces F_r and F_t are the forces generated in the squeeze film dampers. Equation (22) is the equation of motion of the disk, while equation (23) represents the force balance at the center of the journal. Also the condition that the unbalance u is rotating at the speed of rotation of the rotor Ω is given by

$$\dot{\beta}+\dot{\psi}=\Omega \tag{24}$$

which gives an additional condition on the motion of the system.

It is desirable to nondimensionalize equations (22), (23), and (24) to generalize the analysis and to reduce the number of independent parameters. To do so, we divide each of equations (22) and (23) by $m\,\omega_n^2c$. It should be noted that since we chose to nondimensionalize the parameters by using the natural frequency ω_n, then K^* and K_r^* are determined completely by the knowledge of R_k; since $K_{eq}^*=1$, then

$$K^* = 1 + 1/R_k$$

and

$$K_r^* = 1 + R_k$$

This is a restriction that conveniently results in a reduction of the number of parameters under investigation. It is not necessary to use such a nondimensionalizing scheme; we could have chosen any other datum frequency (although in this case the undamped critical speed will not be at $\Omega^* = 1$), if it is required to study the effects of the rotor stiffness and the retainer spring stiffness separately.

Thus equations (22) and (23) become

$$\begin{aligned} &\epsilon'' - \epsilon\psi'^2 + i(\epsilon\psi'' + 2\epsilon'\psi') + \\ &\quad [D'' - D(\alpha' + \psi')^2 + i(D(\alpha'' + \psi'') + 2D'(\alpha' + \psi'))]e^{i\alpha} \\ &\quad + [-U(\beta' + \psi')^2 + iU(\beta'' + \psi'')]e^{i\beta} \\ &\quad + \eta\{\epsilon' + i\epsilon\psi' + [D' + iD(\alpha' + \psi')]e^{i\alpha}\} + K^*De^{i\alpha} = 0 \end{aligned} \tag{25}$$

and

$$K^*De^{i\alpha} - K_r^*\epsilon + F_r^* + iF_t^* = 0 \tag{26}$$

Dividing equation (24) by ω_n, we get

$$\beta' + \psi' = \Omega^* \tag{27}$$

where ()′ denotes differentiation with respect to τ.

Substituting for ψ' from equation (27) into equations (25) and (26), they become two complex differential equations, i.e., four real differential equations, in four unknowns: ϵ, D, α, and β. They are nonlinear equations since F_r^* and F_t^* are nonlinearly dependent on the position of the journal in the damper. These equations are difficult to solve analytically, and it has been reported (Taylor and Kumar, 1980) that they exhibit the following problems, when solved numerically:

(*a*) false convergence to steady state;

(*b*) regions of multiple solution tend to involve a tedious and time-consuming trial and error process;

(*c*) only stable solutions can be found; and

(*d*) the particular algorithm and convergence criteria used in the iterative approach determine the accuracy and credibility of the results.

Also if these algorithms are used for multimass rotor systems, they will become very time consuming.

Fortunately since the rotor of Fig. 2 is symmetric, we can assume that at steady state, the points E, S, and G execute circular centered whirling orbits, at the frequency of the rotation of the rotor Ω^* (since this is a forced response due to unbalance). Thus the polygon OESG of Fig. 3 is locked at steady state and is not changing, and rotating at a constant frequency Ω^*. In this case the forces generated by the damper on the journal are given by equations (18) and (19). Also at steady state $\epsilon' = \epsilon'' = D' = D'' = \alpha' = \alpha'' = \beta' = \beta'' = 0$. Applying these conditions and substituting (27) into equations (25) and (26), their real and imaginary parts become

$$\Omega^{*2}U\cos\beta = -\epsilon\Omega^{*2} + (K^* - \Omega^{*2})D\cos\alpha - \eta\Omega^*D\sin\alpha \tag{28}$$

$$\Omega^{*2}U\sin\beta = \eta\Omega^*\epsilon + (K^* - \Omega^{*2})D\sin\alpha + \eta\Omega^*D\cos\alpha \tag{29}$$

$$K^*D\cos\alpha = K_r^*\epsilon + BC_{rt}^*\epsilon\Omega^* - Mm_r^*\epsilon\Omega^{*2} \tag{30}$$

$$K^*D\sin\alpha = BC_{tt}^*\epsilon\Omega^* + Mm_t^*\epsilon\Omega^{*2} \tag{31}$$

where $m_r^* = (m_{rr}^* - m_{12}^*)$ and $m_t^* = (m_{22}^* - m_{rt}^*)$.

Equations (28)–(31) are four nonlinear algebraic equations in the four unknowns ϵ, D, α, and β. Instead of solving these equations numerically using a nonlinear equation solver like the Newton–Raphson technique, which will involve a tedious trial and error process in regions of multiple solution, we are going to manipulate equations (28)–(31) further. The goal is to obtain a polynomial in Ω^* whose coefficients are functions of ϵ. Taylor and Kumar (1983) were successful in doing so, for a rigid rotor mounted on squeeze film dampers. They solved the resulting fourth-order polynomial in closed form to obtain the unbalance response.

Squaring (28) and (29) and adding, we get

$$\begin{aligned} U^2\Omega^{*4} = {} & (\eta^2 + \Omega^{*2})\epsilon^2\Omega^{*2} + [(K^* - \Omega^{*2})^2 \\ & + \eta^2\Omega^{*2}]D^2(\cos^2\alpha + \sin^2\alpha) \\ & + 2\epsilon\Omega^*[\eta K^*D\sin\alpha + \Omega^*(\eta^2 - K^* + \Omega^{*2})D\cos\alpha] \end{aligned}$$

Substituting for $D\cos\alpha$ and $D\sin\alpha$ from equations (30) and (31), respectively, into the above equation, and after some extensive algebraic manipulation we get

$$\begin{aligned} & a_1\Omega^{*8} + a_2\Omega^{*7} + a_3\Omega^{*6} + a_4\Omega^{*5} + a_5\Omega^{*4} \\ & \quad + a_6\Omega^{*3} + a_7\Omega^{*2} + a_8\Omega^* + a_9 = 0 \end{aligned} \tag{32}$$

where

$$\begin{aligned} a_1 &= \frac{M^2}{K^{*2}}(m_t^{*2} + m_r^{*2}) \\ a_2 &= \frac{2MB}{K^{*2}}(C_{tt}^*m_t^* - C_{rt}^*m_r^*) \\ a_3 &= \frac{1}{K^{*2}}[B^2(C_{tt}^{*2} + C_{rt}^{*2}) - 2MK_r^*m_r^* - 2MK^*m_r^* \\ &\quad + M^2(\eta^2 - 2K^*)(m_t^{*2} + m_r^{*2})] \\ a_4 &= \frac{2B}{K^{*2}}[M(\eta^2 - 2K^*)(C_{tt}^*m_t^* - C_{rt}^*m_r^*) \\ &\quad + C_{rt}^*(K^* + K_r^*)] \\ a_5 &= 1 - \frac{U^2}{\epsilon^2} - \frac{2M\eta^2m_r^*}{K^*} + \frac{2K_r^*}{K^*} + \frac{K_r^{*2}}{K^{*2}} + M^2(m_t^{*2} + m_r^{*2}) \\ &\quad + 2Mm_r^* + \frac{(\eta^2 - 2K^*)}{K^{*2}}[B^2(C_{tt}^{*2} + C_{rt}^{*2}) - 2MK_r^*m_r^*] \\ a_6 &= 2Mm_t^*\eta + \frac{2BC_{rt}^*\eta^2}{K^*} + \frac{2(\eta^2 - 2K^*)K_r^*BC_{irt}^*}{K^{*2}} \\ &\quad - 2BC_{rt}^* + 2MB(C_{tt}^*m_t^* - C_{rt}^*m_r^*) \\ a_7 &= \eta^2 + 2BC_{tt}^*\eta + 2\eta^2\frac{K_r^*}{K^*} - 2K_r^* + B^2(C_{tt}^{*2} + C_{rt}^{*2}) \\ &\quad - 2MK_r^*m_r^* + (\eta^2 - 2K^*)\frac{K_r^{*2}}{K^{*2}} \\ a_8 &= 2K_r^*BC_{rt}^* \\ a_9 &= K_r^{*2} \end{aligned}$$

Equation (32) is an eighth-order polynomial in Ω^*, whose coefficients are functions of ϵ. This polynomial was solved numerically by the IMSL subroutine ZPOLR, which uses the Laguerre algorithm to obtain the roots of the polynomial. A value of ϵ is assumed and the subroutine is called to obtain the roots of equation (32). Complex roots were neglected, since they would not indicate a steady state. Since the rotor can rotate both in the clockwise and the counterclockwise directions, the routine obtained both positive and negative roots, which were mirror images. Knowing that, only the positive roots were retained, for counterclockwise rotation. If the rotor rotates in the clockwise direction, then the system will exhibit behavior similar to when the rotor rotates in the counterclockwise direction.

Knowing ϵ and Ω^*, it is possible to obtain the deflection D from equations (30) and (31), by squaring and adding, thus

$$\begin{aligned} D^2 = \frac{\epsilon^2}{K^{*2}}\{ & M^2(m_t^{*2} + m_r^{*2})\Omega^{*4} + 2K_r^*BC_{rt}^*\Omega^* + K_r^{*2} \\ & + 2MB(C_{tt}^*m_t^* - C_{rt}^*m_r^*)\Omega^{*3} \\ & + [B^2(C_{tt}^{*2} + C_{rt}^{*2}) - 2MK_r^*m_r^*]\Omega^{*2}\} \end{aligned} \tag{33}$$

Also if we divide equation (31) by (30), then α is

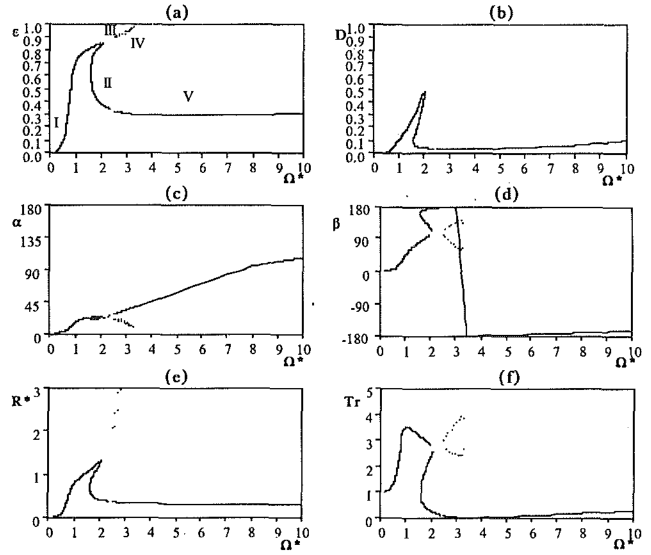

Fig. 4 Unbalance response of generic system

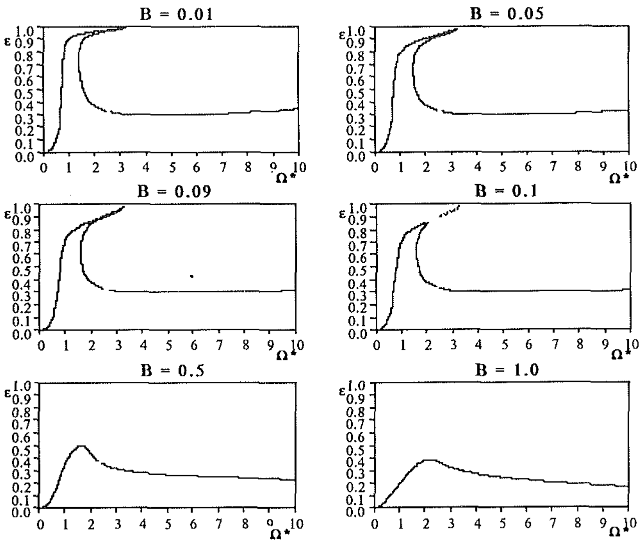

Fig. 5 Effect of B on the unbalance response of generic system, ϵ

$$\alpha=\tan^{-1}\left\{\frac{BC_{tt}^{*}\Omega^{*}+Mm_{t}^{*}\Omega^{*2}}{K_{r}^{*}+BC_{rt}^{*}\Omega^{*}-Mm_{r}^{*}\Omega^{*2}}\right\} \tag{34}$$

Similarly, dividing equation (29) by (28), then β is

$$\beta=\tan^{-1}\left\{\frac{\eta\Omega^{*}\epsilon+(K^{*}-\Omega^{*2})D\sin\alpha+\eta\Omega^{*}D\cos\alpha}{-\epsilon\Omega^{*2}+(K^{*}-\Omega^{*2})D\cos\alpha-\eta\Omega^{*}D^{*}\sin\alpha}\right\} \tag{35}$$

It is sometimes convenient to describe the motion of the rotor by the runout at the rotor center r, which is the distance OS in Fig. 3. If we define $R^{*}=r/c$, as a nondimensional runout, then

$$R^{*}=\sqrt{(\epsilon+D\cos\alpha)^{2}+D^{2}\sin^{2}\alpha} \tag{36}$$

Another quantity that is important in determining SFD performance is the transmissibility Tr. It is defined as the ratio of the magnitude of the force transmitted to the engine frame with SFD support, to the magnitude of the force transmitted to the engine frame if the support was rigid. Thus

$$Tr=\frac{\dfrac{\sqrt{F_{r}^{*2}+F_{t}^{*2}}}{K^{*}U\Omega^{*2}}}{\sqrt{(K^{*}-\Omega^{*2})^{2}+\eta^{2}\Omega^{*2}}} \tag{37}$$

If $Tr<1$, then the squeeze film damper is successful in attenuating the force transmitted to the engine frame. On the other hand, if $Tr>1$, then the SFD magnifies the force transmittted to the engine frame. The transmissibility serves to determine the regions of successful SFD operation.

It should be noted that in this analysis we are assuming that the eccentricities in both dampers have the same phase; thus we are neglecting the excitation of the odd modes for this system. One would expect that this system would have three modes because of the three lumped masses: one due to the disk, and one each due to fluid inertia in the two dampers. Thus we expect that we have two even modes and one odd mode, while the analysis here provides only the two even modes. For this system the odd mode, because of symmetry, would result in no whirl at the disk center and whirl primarily in the journals. It appears that this mode would be unimportant since the motion essentially occurs in the dampers, and thus would be highly damped, which would result in relatively small amplitudes, and thus its neglect would not affect the unbalance response.

The unbalance response of the system was obtained by a program UNBRES that employed the techniques described in the previous paragraphs. The program was extremely efficient, such that typically it took approximately 20 seconds to obtain the full steady-state unbalance response on a PDP-11/44 computer. It has been reported (Taylor and Kumar, 1980) that, using numerical integration, the unbalance response of a simpler system (rigid rotor, no fluid inertia) took about 15 minutes on a PDP-11/34 computer. This is a savings in computer time of the order of fifty times over numerical integration, which should be beneficial in the design process of squeeze film dampers.

The fast algorithm allowed parametric studies to be performed. In doing so, we took a datum system, whose parameters are close to those reported in Taylor and Kumar (1980), and varied each parameter of interest to determine its effect on the unbalance response, in particular on two variables: ϵ and Tr. This datum system exhibits the generic behavior resulting from the nonlinear characterisitics of SFDs. The unbalance response of this generic system is shown in Fig. 4, for a π-film short damper. The parameters defining the generic system are: $B=0.1$, $M=0.2$, $U=0.3$, $R_k=0.1$, and $\eta=0.01$.

Figure 4(a) illustrates the basic features of the unbalance response of the generic system. The eccentricity ratio ϵ is plotted versus the nondimensional frequency Ω^{*}. The jump phenomenon can be clearly seen in the figure, and also two high-eccentricity steady-state branches can be seen at Ω^{*} between 2.5 and 3.5. Regions II and III in the figure are unstable steady states (Taylor and Kumar, 1980), while regions I, IV, and V represent stable steady states that the rotor can achieve. Figure 4(b) shows the nondimensional deflection D versus Ω^{*}. Regions III and IV are at a much larger amplitude (of the order of 3. to 5.) than regions I, II, and V, and are not shown in the figure. Comparing Figs. 4(a) and 4(b), it can be seen that the rotor deflection D is much smaller than ϵ for regions I, II, and V, but for regions III and IV the deflection is much larger than ϵ and consequently the rotor will probably be deflected beyond its limit if it were to operate in region IV. Figures 4(c) and 4(d) show the angles α and β versus Ω^{*}, respectively. These figures help in visualizing the mode shape and the phase differences for the rotor. Figure 4(e) shows the nondimensional runout at the rotor center R^{*} versus Ω^{*}, from which the large deflections of the rotor in regions III and IV can be appreciated. Figure 4(f) shows the transmissibility Tr versus Ω^{*}, from which it can be seen that the SFD will be a superior rotor support if it operates on branch V.

Figures 5 and 6 illustrate the effects of changing the bearing parameter B on the unbalance response of the generic system. The bearing parameter, which was identified previously in the literature (White, 1972; Mohan and Hahn, 1974), is a measure of the amount of damping the SFD can provide. Figure 5 illustrates the effect of changing B on ϵ. For low values of B,

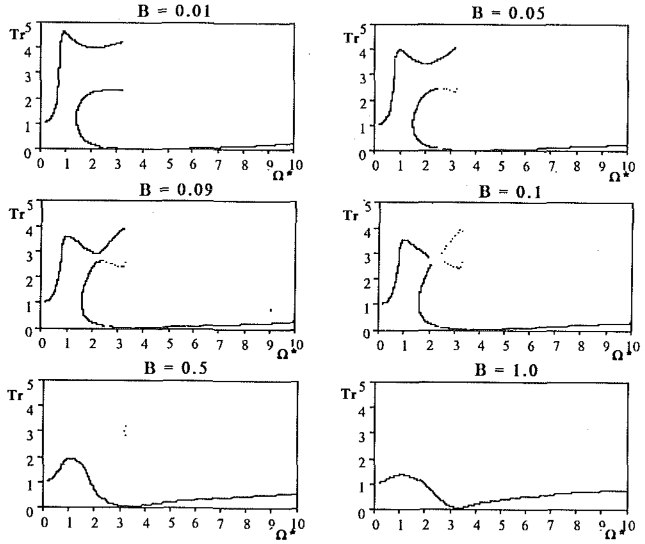

Fig. 6 Effect of B on the unbalance response of generic system, *Tr*

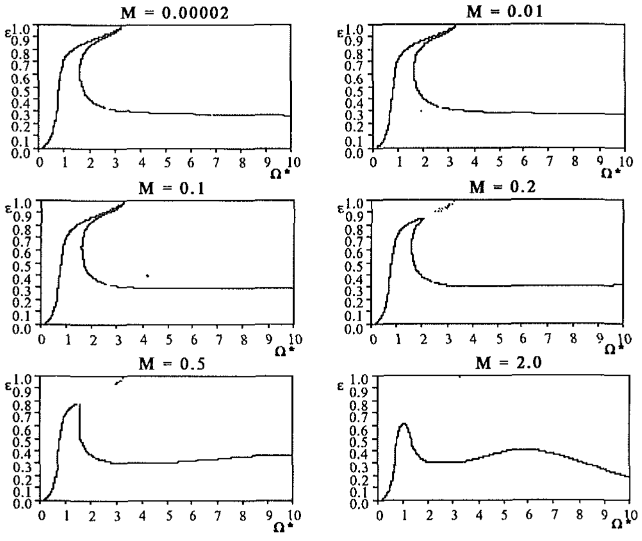

Fig.7 Effect of *M* on the unbalance response of generic system, ϵ

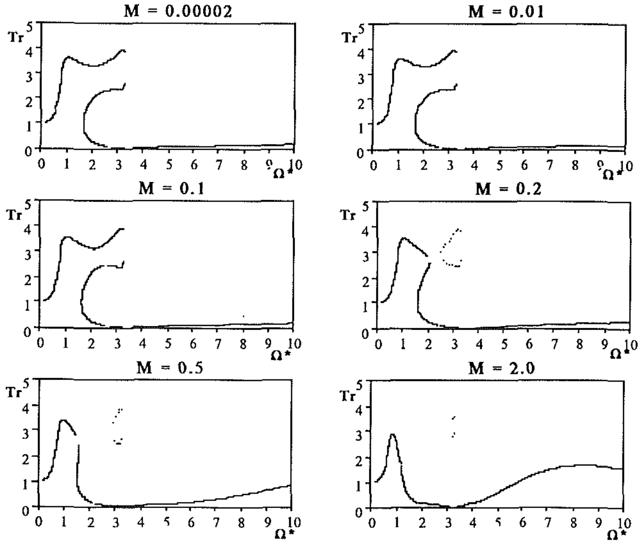

Fig. 8 Effect of *M* on the unbalance response of generic system, *Tr*

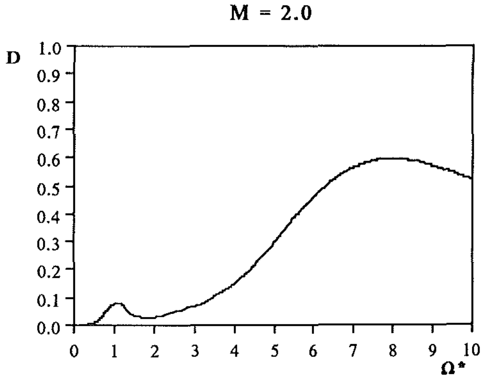

Fig. 9 Steady-state deflection of rotor at midspan, $M=2.0$

regions III and IV disappear, and the jump resonance attains large amplitudes. The values of $B=0.09$ is interesting: Regions III and IV are starting to appear, and are connected to regions I and II. It can be seen that region III is a continuation of region II and region IV is continuation of region I. Thus it is no surprise that region III is unstable, while region IV is stable. Increasing B further, the amplitude of the jump resonance decreases and regions III and IV separate from regions I and II. At large values of B, the jump resonance disappears and regions III and IV also decrease in size and eventually disappear. Figure 6 shows the effect of changing B on Tr. For low values of B the transmissibility is high in region I, and in region V the transmissibility is nearly zero. Thus low values of B result in a large speed range with low transmitted force. For large values of B the transmissibility is larger than 1.0 in region I (but with values less than those for small B), and the jump resonance does not occur. Regions III and IV diminish, although they exhibit large transmissibilities. Region V has sizable Tr, but still less than 1. Thus in the useful speed range, large values of B result in larger Tr than low values of B.

Figures 7 and 8 illustrate the effects of changing the inertia parameter M on the unbalance response of the generic system. Figure 7 illustrates the effect of changing M on ϵ. For low values of M, as for B, regions III and IV disappear and the jump resonance attains large amplitudes. The value of $M=0.00002$ should be considered to be similar to the case of no fluid inertia. We were not able to reduce M to zero, since the coefficient a_1, of equation (36) would be zero and in this case the routine ZPOLR was not able to obtain the roots of the polynomial. For large values of M, regions III and IV appear and as M is increased they diminish, and the jump resonance magnitude also decreases until it disappears. Thus it may be concluded that large values of M are beneficial with regard to the jump resonance. Also for large values of M, a second mode appears in the frequency range under consideration. This mode is essentially due to fluid inertia in the dampers, and it exhibits a smaller peak relative to that due to the first mode. Perhaps it should be pointed out that looking at the second critical speed (mode) from the point of view of ϵ would be quite misleading, as illustrated in Fig. 9, which shows the deflection D versus Ω^* at $M=2.0$. From this it is clear that the rotor is undergoing relatively large deflections at this mode, which have to be taken into consideration when designing the rotor. Nevertheless these deflections are much smaller than those corresponding to regions III and IV, and a rotor should not be allowed to operate in region IV (region III is unstable so the rotor will never operate there). Figure 8 illustrates the effect of changing M on Tr. It is clear that for large M, the useful transmissibility range ($Tr<1$) is reduced because of the second mode. For low values of M its effect is similar to that of B.

Another important parameter in determining the unbalance response of the rotor system is the unbalance. An important question in the design of a rotor is how much unbalance that rotor would tolerate. Figures 10 and 11 show the effect of

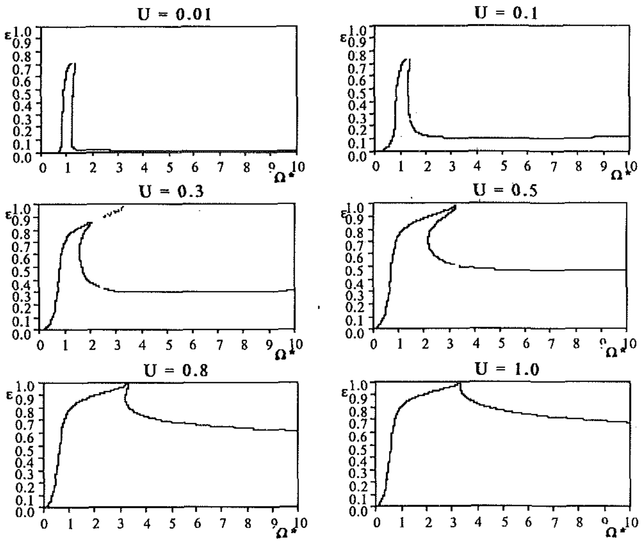

Fig. 10 Effect of *U* on the unbalance response of generic system, ε

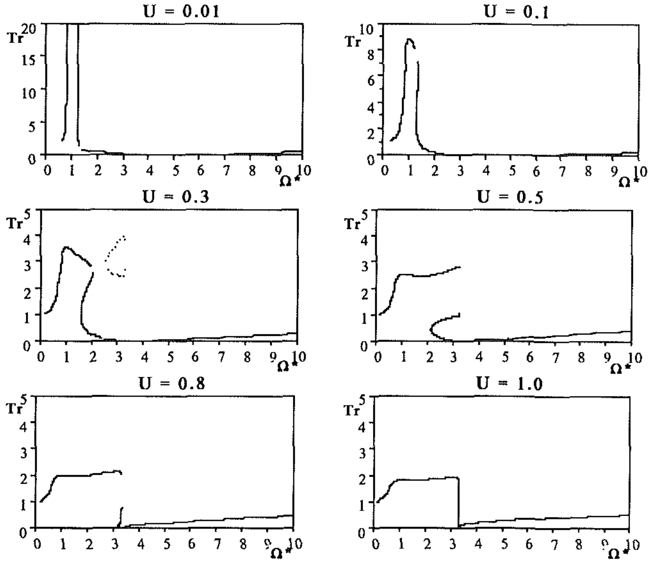

Fig. 11 Effect of *U* on the unbalance response of generic system, *Tr*

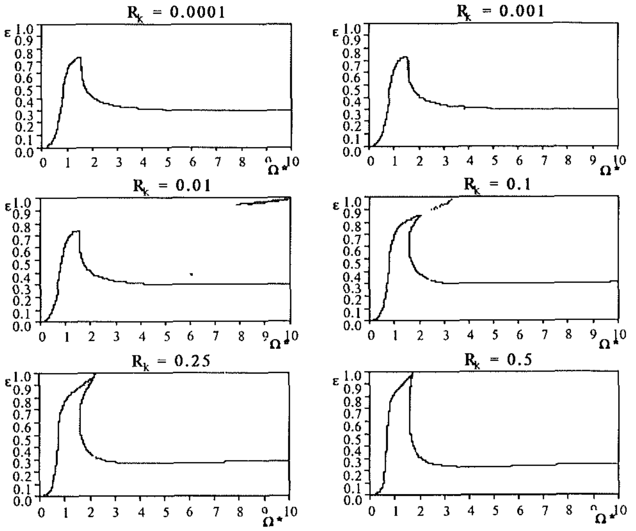

Fig. 12 Effect of R_k on the unbalance response of generic system, ε

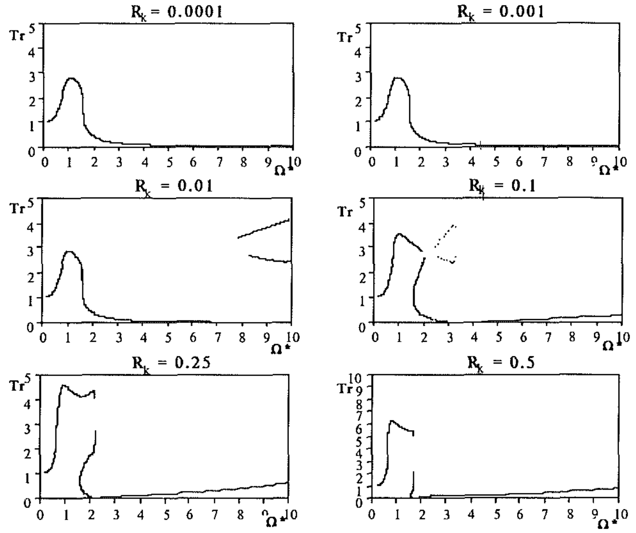

Fig. 13 Effect of R_k on the unbalance response of generic system, *Tr*

changing the unbalance U on the unbalance response of the system. Figure 10 illustrates the effect of changing U on ϵ. It can be seen that for low values of U the jump resonance is reduced in magnitude, but not totally eliminated for this system. Probably as we go to lower values of U than those shown in Fig. 10, the jump resonance would be eliminated. It has been reported in the literature (White, 1972; Mohan and Hahn, 1974) that decreasing the unbalance decreases the jump resonance, and would at a certain point disappear. Rotors incorporating SFDs are designed to operate at an unbalance that does not cause the rotor to exhibit the jump phenomenon. But apparently our generic system would exhibit the jump phenomenon at relatively low values of U. (Further investigation revealed that the jump could be eliminated by increasing B.) For large values of U, the jump becomes pronounced and regions III and IV appear, and as U is increased regions III and IV unite with regions II and I, respectively, to form an even sharper resonance. At even larger values of U, the rotor exhibits a totally unacceptable response. The same effects are illustrated in Fig. 11, which shows the effect of changing U on Tr and it reveals that, at low U, the SFD has a low transmissibility for nearly all the speed range, except at resonance. Curiously this large Tr at resonance increases with the decrease of U. This is because the force in the damper depends on ϵ and Ω^* only, which do not change much with decreasing U (see Fig. 10), but the damperless system would have a much lower force, and since we divide by the force in the damperless system to obtain the transmissibility, thus Tr increases. At large values of U, the transmissibility appears to be acceptable ($Tr < 1$) in a large range of speeds, but this is deceiving, since the amplitudes of motion were judged to be excessive.

Finally, we investigate the effect of changing the stiffness ratio R_k on the unbalance response of the rotor. Figure 12 shows the effect of changing R_k on ϵ. It can be seen that low values of R_k result in a decrease in the magnitude of the jump resonance and the gradual elimination of regions III and IV, i.e., a damper without a retainer spring exhibits a superior unbalance response for the parameters used in our generic system. For large values of R_k, the jump resonance becomes more pronounced. Figure 13 shows the effect of changing R_k on Tr, from which it can be also seen that a softer retainer spring results in better transmissibility characteristics.

Discussion and Conclusion

The steady-state unbalance response of a Jeffcott rotor incorporating short squeeze film dampers executing circular centered whirl is obtained. Fluid inertia forces are included in the model of the squeeze film dampers, using an energy approximation (El-Shafei, 1988). This approximation relies on the assumption that the fluid velocity profiles do not change much due to fluid inertia. This assumption was also used by San Andrés and Vance (1986) who used a momentum approximation to obtain the inertia forces in the damper. Both approximations yield similar results in simplified squeezing flows (El-Shafei, 1988). A comparison of the energy and momentum approximations of the inertia forces in SFDs (Crandall and El-Shafei, 1989) reveals that the energy approximation results in exactly the same forces in the dampers for small circular-centered whirl as those predicted by the full solution. The momentum approximation, although it gives similar results, predicts inertia forces that are 20 percent off, in this case, which implies that the energy approximation is more accurate. Also, it should be pointed out that, as illustrated in the literature (Reinhardt and Lund, 1975; San Andrés and Vance, 1986), fluid inertia has very little effect on the damping coefficients as long as the damper is in the laminar regime. This fortunate fact allows for the decoupling of the inertia and damping coefficients as we have done here.

The unbalance response is obtained by the fast algorithm described above. It relies on the assumption of circular centered whirl, which is supported by both numerical and experimental evidence (Taylor and Kumar, 1983). The following may be concluded from the paper:

1 Using the technique described in this paper in obtaining the steady-state unbalance response results in considerable savings of computer time and avoids trial and error procedures in regions of multiple steady states.

2 The requirements of good vibration isolation ($Tr < 1$) and attenuation of amplitude of response may conflict. In this case a compromise has to be made.

3 Fluid inertia introduces a second mode to the response of the Jeffcott rotor. This mode is well damped for short squeeze film dampers.

4 Fluid inertia tends to decrease the possibility of jump resonance for the first mode in short squeeze film dampers.

5 Fluid inertia results in a decrease of the useful range of vibration isolation ($Tr < 1$) of the dampers.

6 A system with no retainer spring (or a soft retainer spring) exhibits better steady-state unbalance response and vibration isolation capability than that with a retainer spring. This may not be the whole story since a system with no retainer spring would probably exhibit worse transient response than a system with a retainer spring.

7 The increase of the bearing parameter B results in better attenuation of vibration and worsens the vibration isolation capabilities of the damper, while a small B results in worse attenuation of amplitude of vibration and better vibration isolation.

References

Burrows, C. R., Sahinkaya, M. N., and Kucuk, N. C., 1987, "A New Model to Predict the Behaviour of Cavitated Squeeze Film Bearings," *Proc. R. Soc. Lond.*, Series A, Vol. 411, pp. 445–466.

Cooper, S., 1963, "Preliminary Investigation of Oil Films for the Control of Vibration," *Lubrication and Wear Convention*, I. Mech. E., pp. 305–315.

Crandall, S. H., and El-Shafei, A., 1989, "Energy and Momentum Approximations for the Inertia Forces in Squeeze Film Dampers," to appear.

Cunningham, R. E., Fleming, D. P., and Gunter, E. J., 1975, "Design of a Squeeze Film Damper for a Multimass Flexible Rotor," ASME *Journal of Engineering for Industry*, Vol. 97, pp. 1383–1389.

El-Shafei, A., 1988, "Dynamics of Rotors Incorporating Squeeze Film Dampers," Ph.D. Thesis, Department of Mechanical Engineering, Massachusetts Institute of Technology, Cambridge, MA.

El-Shafei, A., 1989, "Fluid Inertia Effects in Squeeze Film Dampers," presented at Damping 89, West Palm Beach, FL, Feb.

Guang, M., and Zhong-Qing, X., 1985, "Investigation on Steady State Response and Its Nonlinear Characteristics of Flexible Rotor Squeeze Film Damper Systems," ASME Paper No. 85-GT-141.

Gunter, E. J., Barrett, L. E., and Allaire, P. E., 1977, "Design of Nonlinear Squeeze Film Dampers for Aircraft Engines," ASME *Journal of Lubrication Technology*, Vol. 99, No. 1, pp. 57–64.

Mohan, S., and Hahn, E. J., 1974, "Design of Squeeze Film Damper Supports for Rigid Rotors," ASME *Journal of Engineering for Industry*, Vol. 96, pp. 976–982.

Potter, M. C., and Foss, J. F., 1982, *Fluid Mechanics*, Great Lakes Press, Inc., Okemos, MI.

Rabinowitz, M. D., and Hahn, E. J., 1977a, "Steady State Performance of Squeeze Film Damper Supported Flexible Rotors," ASME Journal of Engineering for Power, Vol. 99, No. 4, pp. 552–558.

Rabinowitz, M. D., and Hahn, E. J., 1977b, "Stability of Squeeze Film Damper Supported Flexible Rotors," ASME Journal of Engineering for Power, Vol. 99, No. 4, pp. 545–551.

Ramli, M. D., Ellis, J., and Roberts, J. B., 1987, "On the Computation of Inertial Coefficients in Squeeze-Film Bearings," *Proc. I. Mech. E.*, Vol. 201, No. C2, pp. 125–131.

Reinhardt, E., and Lund, J. W., 1975, "The Influence of Fluid Inertia on the Dynamic Properties of Journal Bearings," ASME *Journal of Lubrication Technology*, Vol. 97, No. 2, pp. 159–167.

San Andrés, L. A., and Vance, J. M., 1986, "Effects of Fluid Inertia and Turbulence on the Force Coefficients for Squeeze Film Dampers," ASME Journal of Engineering for Gas Turbines and Power, Vol. 108, No. 2, pp. 332–339.

San Andrés, L. A. and Vance, J. M., 1988, "Effect of Fluid Inertia on the Performance of Squeeze Film Damper Supported Rotors," ASME Journal of Engineering for Gas Turbines and Power, Vol. 110, No. 1, p. 51.

Sharma, R. K., and Botman, M., 1977, "An Experimental Study of the Steady-State Response of Oil-Film Dampers," ASME Paper No. 77-DET-33.

Smith, D. M., 1964–1965, "Journal Bearing Dynamic Characteristics—Effect of Inertia of Lubricant," *Proc. I. Mech. E.*, Vol. 179, pp. 37–44.

Szeri, A. Z., Raimondi, A. A., and Giron-Durate, A., 1983, "Linear Force Coefficients of Squeeze Film Dampers," ASME *Journal of Lubrication Technology*, Vol. 105, pp. 326–334.

Taylor, D. L., and Kumar, B. R. K., 1980, "Nonlinear Response of Short Squeeze Film Dampers," ASME *Journal of Lubrication Technology*, Vol. 102, pp. 51–58.

Taylor, D. L., and Kumar, B. R. K., 1983, "Closed Form Steady State Solution for the Unbalance Response of a Rigid Rotor in Squeeze Film Damper," ASME Journal of Engineering for Power, Vol. 105, No. 3, pp. 551–559.

Tecza, J. A., Giordano, J. C., Zorzi, E. S., and Drake, S. K., 1983, "Squeeze Film Damper Technology: Part 2—Experimental Verification Using a Controlled Orbit Test Rig," ASME Paper No. 83-GT-248.

Tichy, J. A., 1983, "The Effect of Fluid Inertia in Squeeze Film Damper Bearings: A Heuristic and Physical Description," ASME Paper No. 83-GT-177.

Tonnesen, J., 1976, "Experimental Parametric Study of a Squeeze Film Bearing," ASME *Journal of Lubrication Technology*, Vol. 98, pp. 206–213.

White, D. C., 1972, "The Dynamics of a Rigid Rotor Supported on Squeeze Film Bearings," *Conference on Vibrations in Rotating Machinery, Proc. I. Mech. E.*, pp. 213–229.

Optimum Weight Design of a Rotor Bearing System With Dynamic Behavior Constraints

Ting Nung Shiau

Jon Li Hwang

National Cheng Kung University,
Institute of Aeronautics and Astronautics,
Tainan, Taiwan

An efficient design algorithm for optimum weight design of a rotor bearing system with dynamic behavior constraints is investigated. The constraints include restrictions on stresses, unbalance response, and/or critical speeds. The system dynamic behaviors are analyzed by the finite element method. The exterior penalty function method is used as the optimization technique to minimize the system weight. The system design variables are the cross-sectional areas of the shaft and the stiffnesses of the bearings. The sensitivity analysis of the system parameters is also investigated. The example of a single spool rotor bearing system is employed to demonstrate the merits of the design algorithm with different combinations of dynamic behavior constraints. At the optimum stage, it is shown that the weight of the rotor system can be significantly reduced. Moreover, the optimum design weights are quite different for various combinations of dynamic behavior constraints.

Introduction

With increasingly improved performance, the design process of high-speed rotating machinery, such as gas turbine engines and generators, usually requires the integration of the design and the analysis. In addition, a number of sophisticated design modifications of system parameters may be needed. In general, the design objectives can be minimization of the bearing loads or unbalance response, optimum placement of critical speeds, optimization of system weight, etc.

Many authors (Lund and Sternlicht, 1962; Lund, 1963; Gunter, 1970; Dworski, 1964; Nelson, 1980; Childs and Graviss, 1982) have shown that the parameters including the geometry of the system, coefficients of bearings, inertia properties of rigid disks, and the distribution of the mass and stiffness of rotating assemblies, can significantly influence the dynamic characteristics of a rotor-bearing system.

The system sensitivity analysis has been studied for a rotor system using a state vector-transfer matrix approach (Lund, 1979), for a general vibrating system with application to simple rotor models (Fritzen and Nordman, 1982), and for complex nonconservative rotors using finite element discretization (Rajan et al., 1985). The optimal placement of critical speeds in rotor-bearing was investigated (Rajan et al., 1987) using a method of gradient projections.

Recently, structural designers have searched for efficient algorithms for optimum design of structures (Venkayya, 1971; Venkayya et al., 1973; Schmit and Farshi, 1974; Haug et al., 1972). Moreover, the increase of computational efficiency and economy of modern computers has led to the possibility of a automated design system process for large structural systems.

The minimization of response amplitudes within the operating range of a rotor system may be the most primary design objective. The problem of weight minimization usually arises from the revision of an existing rotor-bearing system to increase the system performance. The weight minimization of the rotor system with restrictions on critical speeds has been studied by Shiau and Hwang (1988). The objective of the present study is to develop an efficient design algorithm for minimum weight design of a rotor-bearing system under the requirements of dynamic behaviors such as critical speeds, dynamic stress, and/or steady-state unbalance response, to increase the performance of a rotor-bearing system.

Rotor Model

The equations of motion of a rotor-bearing system, using the finite element method, have been studied (Nelson and McVaugh, 1976; Nelson, 1980) both in fixed reference frame and in a whirl reference frame. The rotor bearing system may be modeled as an assemblage of rigid disks, flexible shaft elements with distributed mass and stiffness, and discrete bearings. Figure 1 shows the typical configuration of a rotor-bearing system. The local shaft element and the displacements q_i of the nodal points are shown in Fig. 2. A fixed reference X-Y-Z and a rotating reference x-y-z are utilized to describe the system motion. The X and x axes are collinear and coincident with the undeformed bearing centerline. The two reference frames have a single rotation ωt difference about X with ω denoting a precession speed. All deflections and forces are assumed to be parallel to the Y-Z plane and the rotor has four degrees of freedom at each finite-element station. For the convenience of analysis, the complex variables have been directly introduced to derive the equations of motion in the fixed ref-

---

Contributed by the International Gas Turbine Institute and presented at the 34th *International Gas Turbine and Aeroengine Congress and Exhibition*, Toronto, Ontario, Canada, June 4-8, 1989. Manuscript received at ASME Headquarters January 13, 1989. Paper No. 89-GT-74.

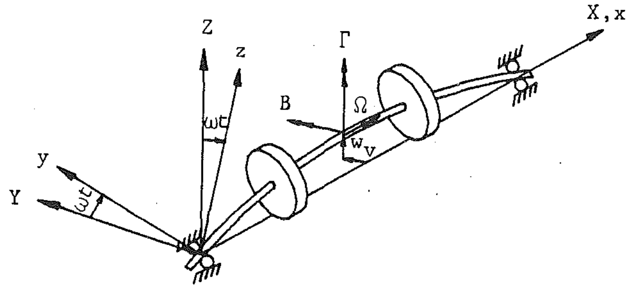

Fig. 1 Typical rotor configuration and coordinates

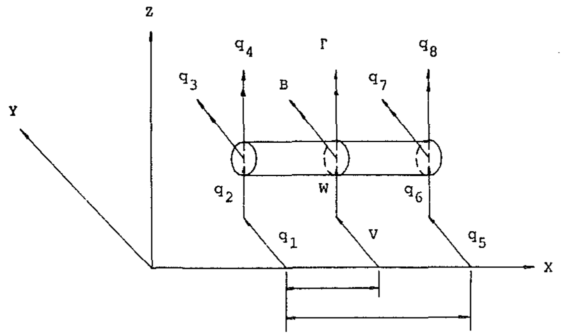

Fig. 2 Local shaft element and coordinates

erence frame. The equation governing the motion of the shaft element is obtained as:

$$([\mathrm{M}^e]+[\mathrm{N}^e])\{\ddot{p}^e\}-i\Omega[\mathrm{G}^e]\{\dot{p}^e\}+[\mathrm{K}^e]\{p^e\}=\{\mathrm{Q}^e\} \qquad (1)$$

where

$$\{p^e\}^T=\{p_1^e, p_2^e, p_3^e, p_4^e\}$$

$$p_1^e=q_1^e+iq_2^e; \quad p_2^e=q_4^e-iq_3^e$$

$$p_3^e=q_5^e+iq_6^e; \quad p_4^e=q_8^e-iq_7^e \qquad (2)$$

and the matrices [M^e], [N^e], [G^e], [K^e] are all 4 × 4 real symmetric matrices shown in the appendix with [G^e] = 2•[N^e]. Ω is the shaft rotational speed. Similarly, the equations governing the motion of the rigid disk are of the form

$$\begin{bmatrix}\mathrm{M}^d & 0\\ 0 & I_D^d\end{bmatrix}\begin{Bmatrix}\ddot{p}_1^d\\ \ddot{p}_2^d\end{Bmatrix}-i\Omega\begin{bmatrix}0 & 0\\ 0 & I_P^d\end{bmatrix}\begin{Bmatrix}\dot{p}_1^d\\ \dot{p}_2^d\end{Bmatrix}=\{\mathrm{Q}^d\} \qquad (3)$$

Moreover, the equation governing the characteristics of an isotropic, undamped bearing can be expressed as

$$k_i p_i^b=Q_i^b \qquad (4)$$

where k_i denotes the ith bearing stiffness; p_i^b and Q_i^b are the complex displacement and external force of ith bearing.

The system equations that describe the behavior of the entire rotor bearing system are formulated by taking into account the contributions from all the elements in the model. The assembled equation of motion with N_e elements in the whirl frame coordinates is of the form

$$([\mathrm{M}]+[\mathrm{N}])\{\ddot{p}\}-i\Omega[\mathrm{G}]\{\dot{p}\}+[\mathrm{K}]\{p\}=\{\mathrm{Q}^u\} \qquad (5)$$

where the matrices [M], [N], [G], and [K] are the real symmetric matrices of order $2\cdot(N_e+1)$. Since there are no external load considered in this study, the vector $\{\mathrm{Q}^u\}$ will be the self-excited force due to system unbalance.

Critical Speeds, Steady-State Response, and Normal Stress Analysis

1 Critical Speeds. Since it is often difficult to measure accurately the damping in the system, it is practical to restrict our attention to computing the undamped critical speeds. For the isotropic and undamped system, the system response can be assumed to be of the form

$$\{p\}=\{p_0\}e^{i\omega t} \qquad (6)$$

Substituting equation (6) into the homogeneous part of equation (5) yields the characteristic equation

$$([\mathrm{K}]-\omega^2([\mathrm{M}]+[\mathrm{N}]-\lambda[\mathrm{G}]))\{p_0\}=\{0\} \qquad (7)$$

where $\lambda = \Omega/\omega$ is the whirl ratio. By assigning a special whirl ratio and solving the eigenvalue problem of equation (7), one can obtain the whirl speeds associated with the whirl mode of the rotor bearing system. Attention in this study will focus on the system critical speeds as well as the correspondent mode shape of circular synchronous.

2 Steady-State Response. The mass unbalance forces $\{Q^u\}$ shown in equation (5) can be usually expressed as follows:

$$\{\mathrm{Q}^u\}=\{\mathrm{Q}_0\}\Omega^2e^{i\Omega t} \qquad (8)$$

where the vector $\{\mathrm{Q}_0\}$ is independent of time and rotating speed. The steady-state response due to mass unbalance is assumed of the form

$$\{p\}=\{p_s\}e^{i\Omega t} \qquad (9)$$

Substituting equations (8) and (9) into equation (5) for $\lambda=1$ yields

$$([\mathrm{K}]-\Omega^2([\mathrm{M}]+[\mathrm{N}]-[\mathrm{G}]))\{p_s\}=\Omega^2\{Q_0\} \qquad (10)$$

Nomenclature

d_i = design variables
$\bar{F}^b$, $\bar{F}^d$, $\bar{F}^e$ = external force vector of bearing, disk, and shaft element, respectively
[G] = gyroscopic matrix
g_j = constraint functions
J = number of constraint functions
[K] = stiffness matrix
l_i = length of ith shaft element
$\tilde{M}$ = bending moment acting on the shaft element
[M] = translational mass matrix
[N] = rotational mass matrix
N_e, N_b = number of shaft elements and bearings
$\bar{p}$ = displacement vector relative to rotating reference $\dot{x}-y-z$
$\{p_s\}$ = amplitude of steady-state response
r_i, r_{I_i} = outer radius and inner radius of the ith shaft element
v, w = translational displacements in the direction in y, z axes
$W(\mathbf{d})$, $W^*(\mathbf{d})$ = objective function and pseudo-objective function
β, γ = angle rotations about y, z axes
ζ = radius ratio = r_{oi}/r_{Ii}
κ' = shear factor
λ = whirl ratio = Ω/ω
μ = Poisson ratio
ν = eigenvalue of system = ω^2
ρ = mass density
σ_{xx} = normal stress
Ω = rotational speed
ω = precession speed

Then the steady-state response can be obtained by solving equation (10) for $\{p_s\}$.

3 Bending Stress Analysis. The bending stress resisted by the rotating flexible shaft is very important for the structural designer. It can be obtained by finding the external loads acting on the shaft elements. These loads can be calculated by solving equation (10) for the response and substituting that into each term of equation (1). In the left-hand side of equation (1), the first two terms will give the inertia forces and the third term represents the elastic restoring forces. The bending stress distribution in the shaft element excited by the elastic restoring forces can be obtained by using the classical beam theory, which is of the form

$$\sigma_{xx} = \frac{\tilde{M} r}{I} \tag{11}$$

where σ_{xx} is the normal bending stress, $\tilde{M}$ is the bending moment acting on the shaft element, I and r are the area of moment of inertia and the distance of that point relative to the neutral axis, respectively.

With the cubic polynomial interpolation functions of beam element, the moment distribution in the shaft element will be linear. This will lead to the maximum bending stress at the nodal point of shaft element. The bending stress at the nodal point can be obtained using equations (1), (10), and (11) as follows:

$$(\sigma)_{(1)}^{(i,m)} = \left[\sum_{j=1}^{4} K_{(2,\,j)}^{e(i)} \bullet p_{s(j)}^{(i,m)}\right] r_{oi}/I_i$$

$$(\sigma)_{(2)}^{(i,m)} = \left[\sum_{j=1}^{4} K_{(4,\,j)}^{e(i)} \bullet p_{s(j)}^{(i,m)}\right] r_{oi}/I_i \tag{12}$$

where the superscript i denotes the ith shaft element; the superscript m denotes when $\Omega = \Omega_m$, Ω_m is associated with the upper or the lower limit of the operating speed range; $\sigma_{(1)}^{(i,m)}$ and $\sigma_{(2)}^{(i,m)}$ represent the bending stress of a nodal point on the left-hand side and right-hand side of the shaft element; $p_{s(j)}^{(i,m)}$ represents the value of the $(4i - 4 + j)$th entry of the steady-state response vector $\{p_s\}$ as $\Omega = \Omega_m$, and $K_{(l,\,j)}^{e(i)}$ denotes the value of the stiffness matrix $[K^e]$ of ith shaft element at the lth row and the jth column.

Design Problem Statement and Optimization Algorithm

The weight minimization of a rotor bearing system under dynamic behavior constraints is investigated. The dynamic behavior constraints consist of the critical speeds, unbalance response, and bending stress. Usually, three major procedures have to be founded for an optimum design problem. The first is to set up the objective function, which is the total weight of the rotor bearing system. The second is to choose the design variables, which are practically the most sensitive parameters. The last is to decide the major design constraints of this problem, which may be the most difficult procedure.

The system design variables are the cross-sectional area of the shaft element (with outer radius fixed) and the stiffness of the bearings. The constraints, which are nonlinear functions in the design variables, have to be satisfied through the structural dynamic characteristic analysis. The optimum of the objective function, which is a linear explicit function in the design variables, can be reached using the optimum design algorithm.

The design problem posed in this paper may be stated as: Find the set of design variables d_i, $i = 1, 2, \ldots, N_t$, such that the weight of the rotor system, $W(\mathbf{d})$, is a minimum and the behavior constraints, $G_j(\mathbf{d})$, are satisfied at the same time. Mathematically, this can be written as: Find the set of d_i, such that

$$\text{minimize} \quad W(\mathbf{d}) = \sum_{i=1}^{N_e} \rho_i l_i A_i \tag{13}$$

$$\text{subject to} \quad G_j(\mathbf{d}) \leq 0, \quad j = 1, 2, \ldots, J \tag{14}$$

$$d_i^l \leq d_i \leq d_i^u, \; i = 1, 2, \ldots, N_t \tag{15}$$

where ρ_i, l_i, and A_i are the material mass density, the length, and the cross-sectional area of the ith shaft element, respectively. The vector $\mathbf{d}$ represents the set of design variables, d_i, $i = 1, 2, \ldots, N_t$. The number of design variables N_t is equal to the sum of the number of shaft elements N_e and the number of bearings N_b.

The decision of the cross-sectional area of the shaft element instead of the inner radius of shaft element (Shiau and Hwang, 1988) as the design variable leads to some extent to advantages in analysis. It makes the system weight function linear in the design variables. In addition, the order of the nonlinear behavior constraints is reduced. It is noted that the stiffness of the bearings do not affect the weight of the system. However they do play an important role in the placement of system critical speeds (Rajan et al., 1987). This suggests that the stiffnesses of bearings have to be taken into account when critical speed requirements are set as behavior constraints.

For the critical speed constrained case, the associated behavior constraint equations can be represented as

$$\begin{aligned} G_1(\mathbf{d}) &= \omega_2^c - \Omega_{\text{low}}/a_1 \leq 0 \\ G_2(\mathbf{d}) &= a_2 \bullet \Omega_{\text{high}} - \omega_3^c \leq 0 \end{aligned} \tag{16}$$

where Ω_{low} and Ω_{high} are the lower and upper limit of the operating range of the original system. For convenience, they are denoted by Ω_1 and Ω_2, respectively. The second and third critical speeds are denoted by ω_2^c and ω_3^c. Both are usually associated with the second rigid body mode and the first bending mode, respectively. In general, significant rotor bending may occur at all critical speeds for the rotor system studied. The constants a_1 and a_2 are some positive real numbers greater than one. Physically, equation (16) states that the second critical speed of the new system has to be lower than Ω_1 by a factor a_1 and the third critical speed has to be higher than Ω_2 by a factor a_2. This implies that the new system has a wider operating range and the performance is improved. If the limitations on bending stress and unbalance response are considered, the behavior constraint equations are expressed as follows:

$$\begin{aligned} G_j(\mathbf{d}) &= |(\sigma)_{(n)}^{(i,m)}| - \sigma^* \leq 0 \qquad j \in J \\ G_j(\mathbf{d}) &= |\delta| - \delta^* \leq 0 \qquad j \in J \end{aligned} \tag{17}$$

where δ denotes the steady-state response at the position of the rigid disk. σ^* and δ^* represent the allowable stress and allowable steady-state response, respectively.

The particular feature of this nonlinear optimization problem is that the initial design usually is infeasible. It has been shown by Shiau and Hwang (1988) that one of the Sequential Unconstrained Minimization Techniques (SUMT), namely the exterior penalty function method, will especially provide some advantages for this problem. Therefore, it will be employed to search for the optimum design of the present system. A general flow chart of this optimum design algorithm is shown in Fig. 3.

If the constraints of critical speeds, unbalance response, and/or bending stresses are all considered, special treatment during the optimum design process has to be overcome. This is because the unbalance response and the bending stresses will be extremely high when the rotating speeds pass the critical values. A simple way to overcome these barriers is to search for the optimum design only with critical speed constraints before doing the optimum design with all the constraints.

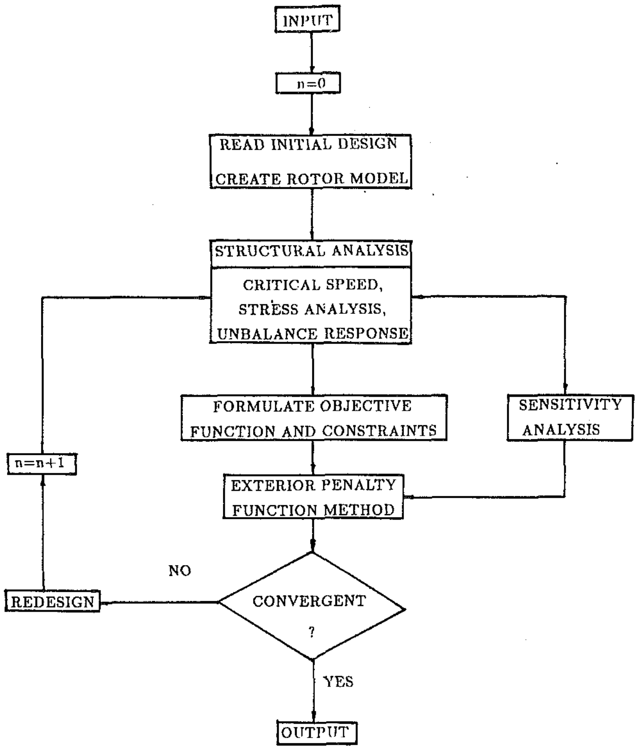

Fig. 3 Flow chart of optimum design algorithm

Sensitivity Analysis

To perform an optimum design, a sensitivity analysis is required, namely calculation of the derivative of the objective function and constraint functions with respect to the design variables for each iterative design.

The derivatives of the objective function can be obtained directly by differentiating equation (13) with respect to the design variable d_i

$$\frac{\partial W(\mathbf{d})}{\partial d_i}=\rho_i l_i \text{ for } d_i=A_i,\ i=1,2,\ldots,N_e \tag{18a}$$

$$\frac{\partial W(\mathbf{d})}{\partial d_i}=0 \text{ for } d_i=k_j,\ j=1,2,\ldots,N_b \tag{18b}$$

Similarly by differentiating equation (16) with respect to d_i, the derivatives of critical speed constraints can be obtained as

$$\frac{\partial G_1(\mathbf{d})}{\partial d_i}=\frac{\partial \omega_2^c}{\partial d_i} \tag{19a}$$

$$\frac{\partial G_2(\mathbf{d})}{\partial d_i}=\frac{-\partial \omega_3^c}{\partial d_i} \tag{19b}$$

The derivatives of critical speeds shown on the right-hand side of equation (19) can be obtained (Fox and Kapoor, 1968; Lund, 1979; Plaut and Huseyin, 1973) further as

$$\frac{\partial \omega_q^c}{\partial d_i}=\frac{1}{2\omega_q^c}\bullet\{p_q\}^T\left(\frac{\partial[\mathrm{K}]}{\partial d_i}-(\omega_q^c)^2\frac{\partial[\mathrm{B}]}{\partial d_i}\right)\{p_q\}$$

$$i=1,2,\ldots,N_t;\quad q=2,3 \tag{20}$$

where $[\mathrm{B}]=[\mathrm{M}]+[\mathrm{N}]-[\mathrm{G}]$, and $\{p_q\}$ is the natural mode corresponding to the critical speed ω_q^c. The gradients, $\partial[\mathrm{K}]/\partial d_i$ and $\partial[\mathrm{B}]/\partial d_i$, shown in equation (20) can be computed by the following processes:

(*i*) When the bearing stiffness is the design variable, i.e. $d_i=k_j$, it is simple to notice that $\partial[\mathrm{B}]/\partial d_i$ vanishes and $\partial[\mathrm{K}]/\partial d_i$ is of the form:

$$\frac{\partial[\mathrm{K}]}{\partial d_i}=\frac{\partial[\mathrm{K}]}{\partial k_j}$$

$$=\begin{bmatrix}0 & \cdots & \cdots & \cdots & 0\\ \vdots & \ddots & & & \vdots\\ \vdots & & {}^{0}1_{0} & & \vdots\\ \vdots & & & \ddots & \vdots\\ 0 & \cdots & \cdots & \cdots & 0\end{bmatrix}_{2(N_e+1)\times 2(N_e+1)} \tag{21}$$

The non-zero value in the matrix is the result of derivative of the term in [K] associated with the *j*th bearing stiffness.

(*ii*) When the cross-sectional area is the design variable, i.e., $d_i=A_i$, one can obtain

$$\frac{\partial[\mathrm{K}]}{\partial d_i}=\frac{\partial[\mathrm{K}]}{\partial A_j}$$

$$=\begin{bmatrix}0 & \cdots & \cdots & \cdots & \cdots & 0\\ \vdots & \ddots & & & & \vdots\\ \vdots & & 0 & [\mathrm{K},_{A_i}]_{4\times 4} & 0 & \vdots\\ \vdots & & & & \ddots & \vdots\\ 0 & \cdots & \cdots & \cdots & \cdots & 0\end{bmatrix} \tag{22a}$$

$$\frac{\partial[\mathrm{B}]}{\partial d_i}=\frac{\partial[\mathrm{B}]}{\partial A_i}$$

$$=\begin{bmatrix}0 & \cdots & \cdots & \cdots & \cdots & \cdots & 0\\ \vdots & \ddots & & & & & \vdots\\ \vdots & & 0 & [\mathrm{M},_{A_i}-\mathrm{N},_{A_i}]_{4\times 4} & 0 & & \vdots\\ \vdots & & & & & \ddots & \vdots\\ 0 & \cdots & \cdots & \cdots & \cdots & \cdots & 0\end{bmatrix} \tag{22b}$$

where

$$[\mathrm{M},_{A_i}]_{4\times 4}=C_1\left(\frac{1}{A_i}-\frac{2}{(1+\Phi_i)}\frac{\partial\Phi_i}{\partial A_i}\right)$$
$$\bullet([\mathrm{M}]_o+\Phi_i[\mathrm{M}]_1+\Phi_i^2[\mathrm{M}]_2)$$
$$+C_1([\mathrm{M}]_1+2\Phi_i[\mathrm{M}]_2)\bullet\frac{\partial\Phi_i}{\partial A_i} \tag{23a}$$

$$[\mathrm{N},_{A_i}]_{4\times 4}=C_2\left(\frac{r_{Ii}^2}{2I_i}-\frac{2}{(1+\Phi_i)}\bullet\frac{\partial\Phi_i}{\partial A_i}\right)$$
$$\bullet([\mathrm{N}]_o+\Phi_i[\mathrm{N}]_1+\Phi_i^2[\mathrm{N}]_2)$$
$$+C_2([\mathrm{N}]_1+2\Phi_i[\mathrm{N}]_2)\bullet\frac{\partial\Phi_i}{\partial A_i} \tag{23b}$$

$$[\mathrm{K},_{A_i}]_{4\times 4}=C_3\left(\frac{r_{Ii}^2}{2I_i}-\frac{1}{(1+\Phi_i)}\frac{\partial\Phi_i}{\partial A_i}\right)$$
$$\bullet([\mathrm{K}]_o+\Phi_i[\mathrm{K}]_1)+C_3([\mathrm{K}]_1\bullet\frac{\partial\Phi_i}{\partial A_i} \tag{23c}$$

The parameter Φ_i is the function Φ given in the appendix associated with the *i*th shaft element. The derivatives of Φ_i with respect to design variables are of the form

$$\frac{\partial\Phi_i}{\partial A_i}=-\Phi_i\left(\frac{1}{\kappa_i'}\frac{\partial\kappa_i'}{\partial \mathrm{A}_i}+\frac{\mathrm{A}_i}{4\pi I_i}\right)$$

where

$$\frac{\partial\kappa'}{\partial A_i}=\left[\frac{345(\zeta_i^4-1)\zeta_i}{(8.5(1+\zeta_i^2)^2+23\zeta_i^2)^2}\right]\bullet\frac{-\zeta_i}{2\pi r_{I_i}^2}$$

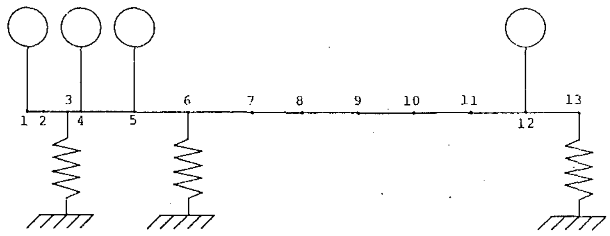

Fig. 4 Rotor schematic

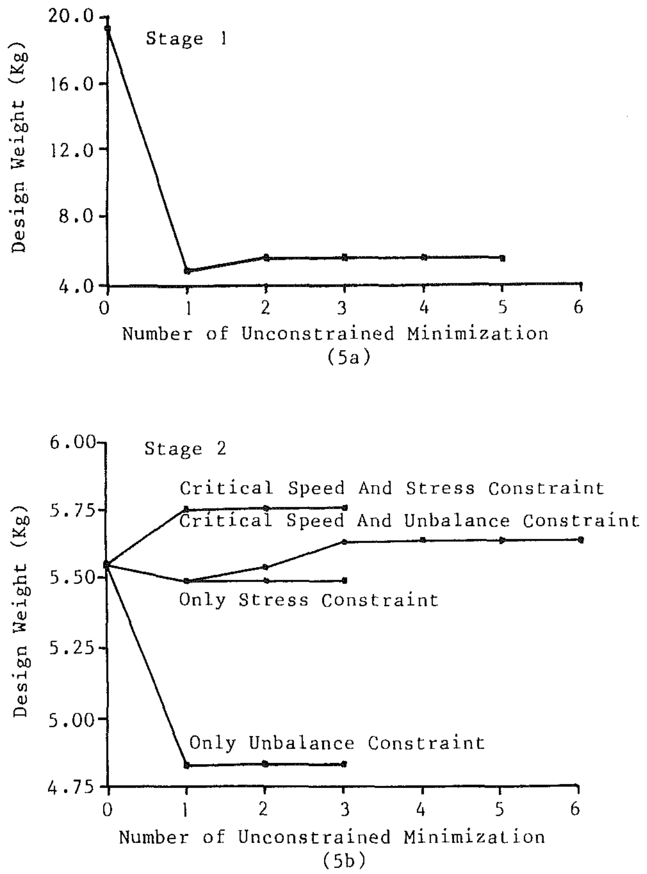

Fig. 5 Weight design history: (*a*) critical speed constraints; (*b*) combination of other constraints

is obtained for $\nu = 0.25$ and $\zeta_i = r_{I_i}/r_{oi}$.

Furthermore by differentiating equation (17) with respect to d_l, the derivatives of stress constraints can be obtained as

$$\frac{\partial G_j(\mathbf{d})}{\partial d_l} = \left| \frac{\partial (\sigma)^{(i,m)}_{(n)}}{\partial d_l} \right|, \quad j = 1, 2, \ldots, J$$
$$l = 1, 2, \ldots, N_l$$
$$J = 2 + i \cdot m \cdot n \qquad (24)$$

The derivatives of bending stress shown on the right-hand side of equation (24) can be obtained from equation (12) as

$$\frac{\partial (\sigma)^{(i,m)}_{(n)}}{\partial d_l} = \sum_{j=1}^{4} \left(K^{e(i)}_{(2n,\,j)} \cdot p^{(i,m)}_{s(j)}\right) \cdot \frac{\partial (r_{oi}/I_i)}{\partial d_l}$$
$$+ \sum_{j=1}^{4} \left(\frac{\partial K^{e(i)}_{(2n,\,j)}}{\partial d_l} \cdot p^{(i,m)}_{s(j)} \right) \cdot \frac{r_{oi}}{I_i}$$
$$+ \sum_{j=1}^{4} \left(k^{e(i)}_{(zn,\,j)} \cdot \frac{\partial p^{(i,m)}_{s(j)}}{\partial d_l} \right) \cdot \frac{r_{oi}}{I_i};$$
$$n = 1, 2; \quad i = 1, N_e, \quad m = 1, 2 \qquad (25)$$

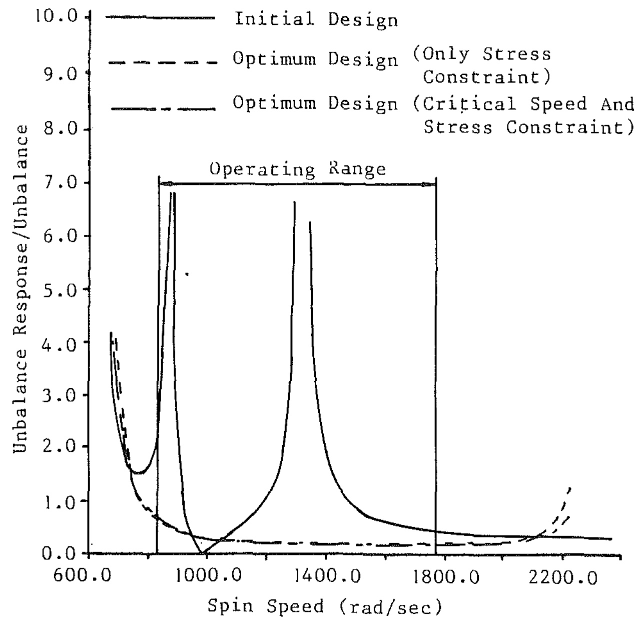

Fig. 6 Unbalance response of initial design and optimum design of the first disk, σ_{cr} = 150 MPa

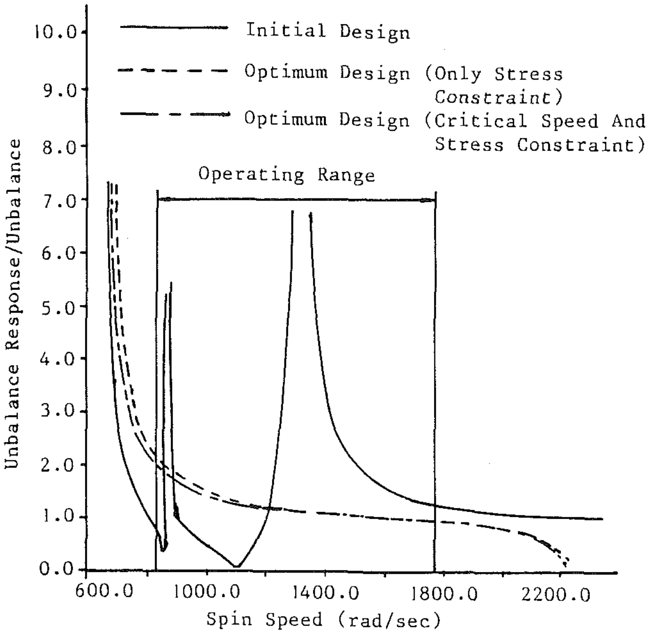

Fig. 7 Unbalance response of initial design and optimum design of the fourth disk, σ_{cr} = 150 MPa

and

$$\frac{\partial (r_{oi}/I_i)}{\partial d_l} = \begin{cases} -r_{oi} r_{I_l}^2 / 2(I_i)^2 & \text{when } d_l = A_l \text{ and } i = l \\ 0 & \text{otherwise} \end{cases} \qquad (26)$$

For calculating the gradients of unbalance response, equation (10) is employed. It yields

$$\frac{\partial \{p_s^{(m)}\}}{\partial d_l} = -[\mathrm{H}^{(m)}]^{-1} \cdot \frac{\partial [\mathrm{H}^{(m)}]}{\partial d_l} \cdot \{p_s^{(m)}\} \qquad (27)$$

where $[\mathrm{H}^{(m)}] = [\mathrm{K}] - \Omega_m^2([\mathrm{M}] + [\mathrm{N}] - [\mathrm{G}])$, and the gradients of $[\mathrm{H}^{(m)}]$ can be obtained using equations (21)–(23).

It is very interesting to point out that the derivatives of the critical speed with respect to the bearing stiffness are of the form

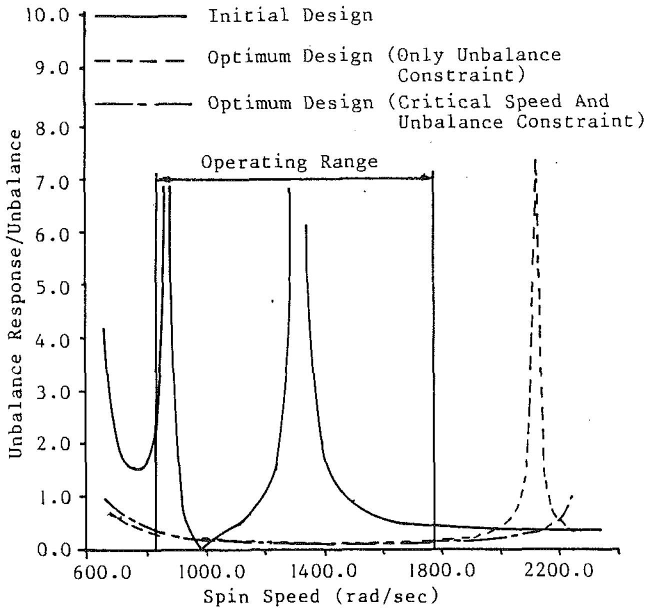

Fig. 8 Unbalance response of initial design and optimum design of the first disk with unbalance ratio = 1.5

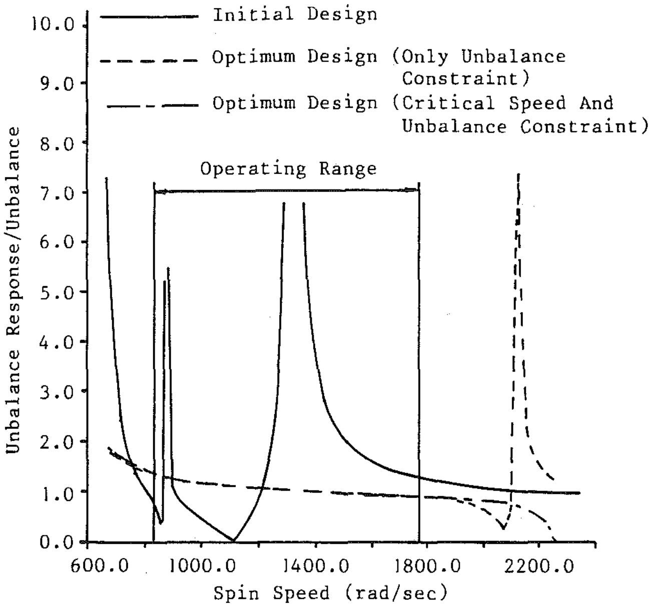

Fig. 9 Unbalance response of initial design and optimum design of the fourth disk with unbalance ratio = 1.5

$$\frac{\partial \omega_q^c}{\partial k_j} = \frac{\omega_q^c}{2k_j} \cdot U_q^j \qquad (28a)$$

where

$$U_q^j = \frac{k_j}{(\omega_q^c)^2} \{p_q\}^T \cdot \frac{\partial [\mathrm{K}]}{\partial k_j} \cdot \{p_q\} \qquad (28b)$$

Physically, U_q^j represents the ratio of the jth bearing strain energy with respect to the total strain energy of the qth mode.

Equation (28a) shows that the sensitivity of the critical speed with respect to bearing stiffness is proportional to the bearing strain energy ratio U_q^j. For the rigid body mode, the value of U_q^j will be very large. This implies that under this condition a small change in bearing stiffness may induce a large change in critical speed. On the other hand, when it is in the bending

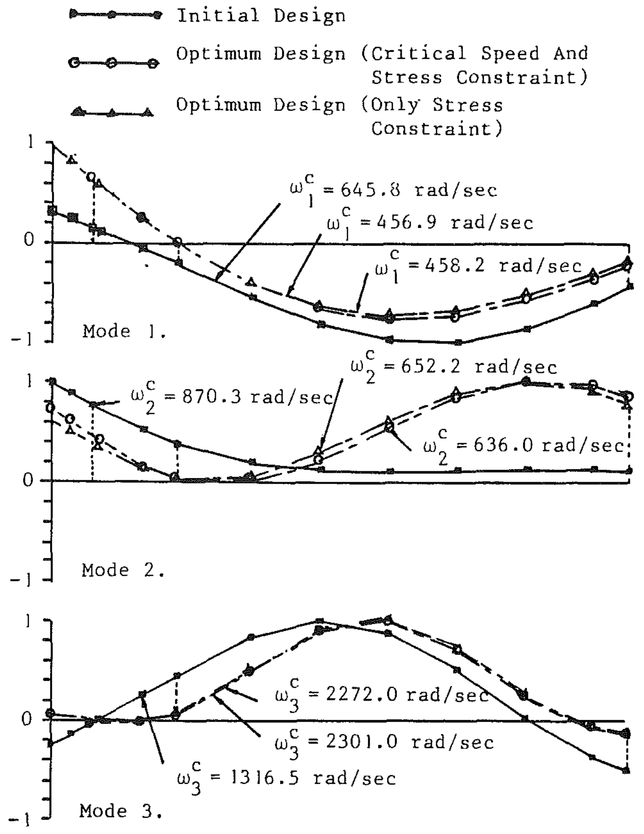

Fig. 10 Mode shapes of initial and optimum design with stress constraint and stress and critical speed constraints

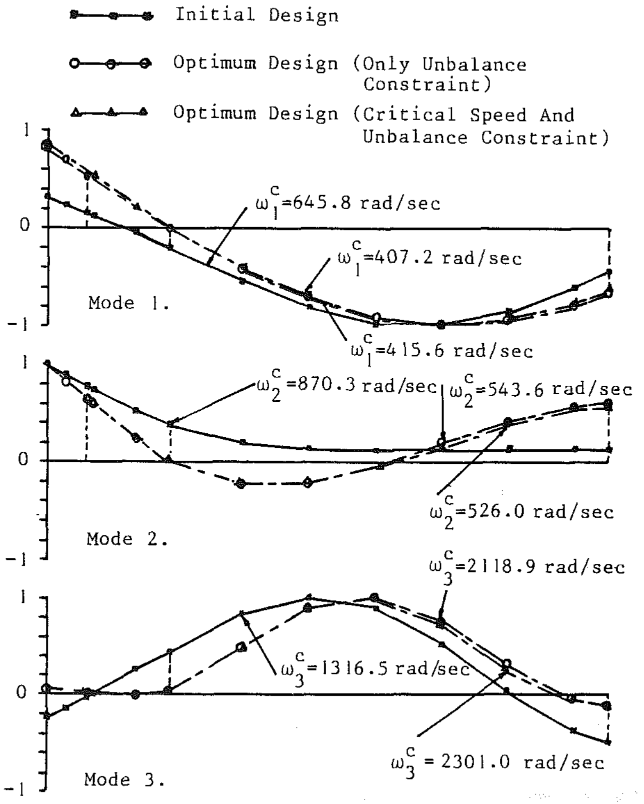

Fig. 11 Mode shapes of initial and optimum design with unbalance response constraint and unbalance and critical speed constraints

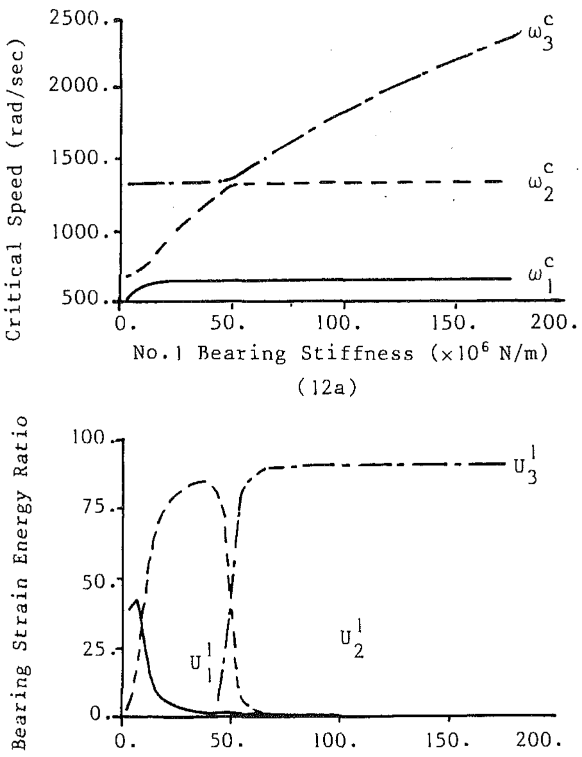

(12a)

(12b)

Fig. 12 Effect of No. 1 bearing stiffness on system properties: (*a*) critical speed sensitivity; (*b*) strain energy ratio with $k_2 = k_3 = 1.75 \times 10^7$ N/m for initial design

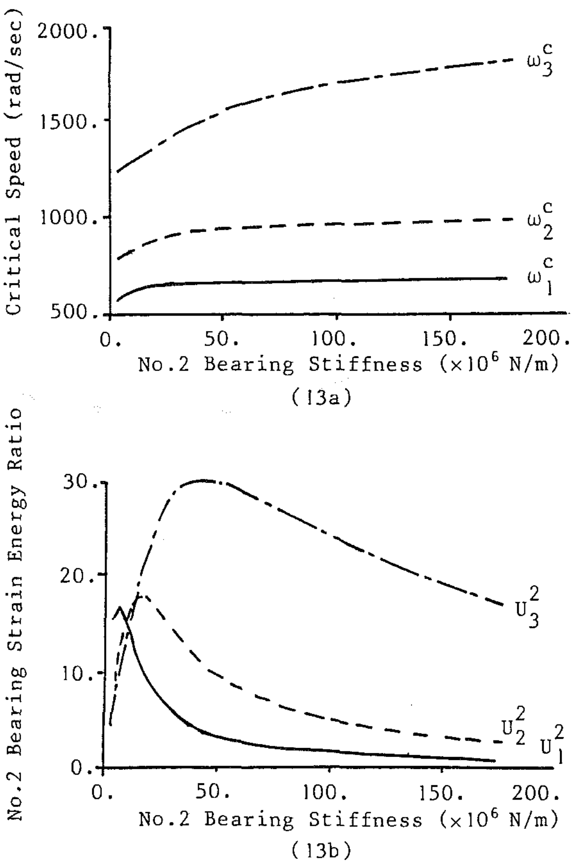

(13a)

(13b)

Fig. 13 Effect of No. 2 bearing stiffness on system properties: (*a*) critical speed sensitivity; (*b*) strain energy ratio with $k_1 = k_3 = 1.75 \times 10^7$ N/m for initial design

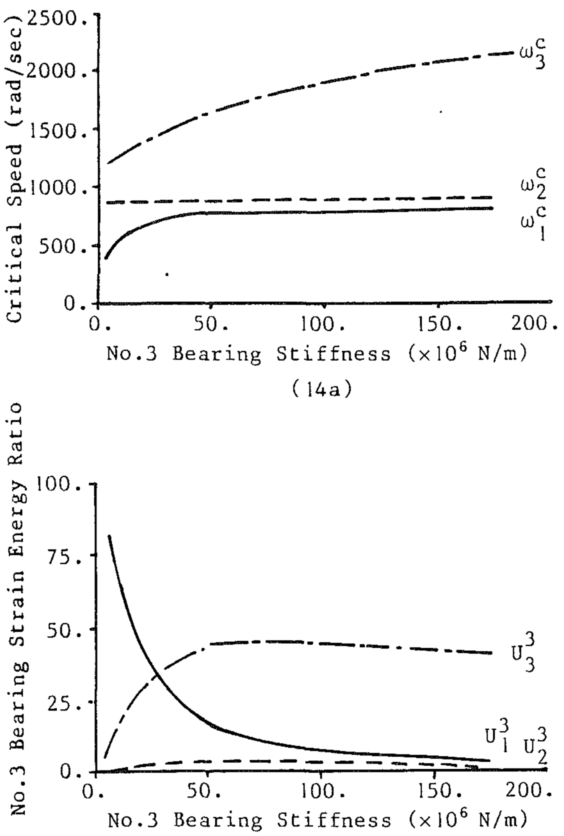

(14a)

(14b)

Fig. 14 Effect of No. 3 bearing stiffness on system properties: (*a*) critical speed sensitivity; (*b*) strain energy ratio with $k_1 = k_2 = 1.75 \times 10^7$ N/m for initial design

mode, the value of U_q^j will be small. Therefore the change of critical speeds is not as sensitive to the bearing stiffness in this mode.

Numerical Results

The rotor system used as an example to demonstrate the importance of the present study is schematically shown in Fig. 4. The system is a single spool supported by bearings at stations 3, 6, and 13. The bearings are denoted as No. 1, No. 2, and No. 3 with correspondent stiffnesses k_1, k_2, and k_3. In this model, there are 12 elements, 13 stations, and 26 degrees-of-freedom. In addition, four disks with fixed masses are located at stations 1, 4, 5, and 12. The details of the rotor configuration are listed in Tables 1 and 2. The design operating range is given by $\Omega_{\text{low}} = 830.0$ rad/s, $\Omega_{\text{high}} = 1770.0$ rad/s. The bending stress calculated is based on the external loads due to eccentricity of the value 0.718×10^{-3} m.

The optimum designs, which include the final weight and critical speeds, with stress constraint and/or critical speed constraints, are shown in Table 3. Similarly, Table 4 indicates the data at optimum design stage with constraints on unbalance response and/or critical speeds. The unbalance ratio shown in Table 4 is defined as the ratio between the steady-state unbalance response and unbalance value. Figure 5 shows the history of design weight with stress constraint 150.0 MPa and/or unbalance constraint 1.5. A comparison of the steady-state unbalance response of the first disk is shown in Fig. 6 for the initial design, optimum design with stress constraint, and optimum design with stress and critical speed constraints. Similarly, Fig. 7 indicates the comparison of the unbalance response of the fourth disk at the initial and optimum design stages.

Table 1 Fixed rigid disk data

Station No.	Mass (Kg)	Polar Inertia ($Kg - cm^2 \times 10^{-2}$)	Diametral Inertia ($Kg - cm^2 \times 10^{-2}$)
1	11.38	19.53	9.82
4	7.88	16.70	8.35
5	7.7	17.61	8.80
12	21.7	44.48	22.24

Table 2 Initial configuration data of rotor system

Station No.	Axial Distance to Station 1 (cm)	Shaft Element No.	Inner Radius (cm)
1	0.		
2	4.29	1	$r_{Ii} = 1.68$ $i = 1,12$
3	8.89	2	
4	10.49	3	
5	20.17	4	
6	27.69	5	
7	44.20	6	
8	59.44	7	
9	74.68	8	
10	89.92	9	
11	105.16	10	
12	120.14	11	
13	127.94	12	

Shaft Elastic Modulus $E = 20.69 \times 10^6$ N/cm^2
Density $\rho = 8193.0$ Kg/m^3
Outer Radius $r_{Oi} = 2.95$ cm $i = 1,12$

The unbalance response values of the first and fourth disk are shown in Figs. 8 and 9 for the cases with unbalance response constraint and unbalance and critical speed constraints. The mode shapes of the initial and optimum designs for the stress constraint and stress and critical speed constraints are shown in Fig. 10. Similarly, Fig. 11 indicates the mode shapes of designs for the unbalance response constraint and unbalance and critical speed constraints cases. Figures (12*a*), (13*a*), and (14*a*) show the sensitivity of the critical speeds with respect to the bearing stiffness for the initial design. Figures (12*b*), (13*b*), and (14*b*) show the bearing strain energy ratio for the initial design.

Conclusions

An efficient algorithm for minimizing the weight of an undamped, isotropic bearing supported rotor system with consideration of constraints on stress, steady-state unbalance response, and/or critical speeds has been investigated. The design variables are chosen to be cross-sectional areas of the shaft elements and the bearing stiffnesses. One of the advantages of choosing cross-sectional area as the design variable instead of inner radius is that the objective function is linear and the nonlinearity of the constraint functions can be reduced, which will save a lot of computing time. The results can be summarized as follows:

1 The weight of the original system can often be greatly reduced for the stress constraint, unbalance response constraint, and/or critical speed constraint cases.

2 For the stress constraint case, if the stress is higher up to a certain value, the system weight cannot be reduced any more. Similarly for the unbalance response constraint case, if the unbalance ratio is greater than 1.25, the minimum weight of the system will be constant.

3 When the unbalance ratio is lower than 1.0 for the unbalance constraint case and lower than 1.10 for the unbalance and critical speed constraint case, one may fail to achieve the minimum weight design. However, one can achieve a minimum weight design for the imposed different conditions.

Table 3 Data at optimum design stage with stress constraint and stress and critical speed constraints

Constraint / Optimum Design / Strength (Mpa)	Stress Constraint			Stress and Critical Speed		
	Weight (Kg)	ω_2^c (rad/sec)	ω_3^c (rad/sec)	Weight (Kg)	ω_2^c (rad/sec)	ω_3^c (rad/sec)
100.0	6.6441	527.7	2314.3	6.6363	527.8	2314.6
125.0	5.7694	539.3	2264.4	6.2681	523.7	2296.4
150.0	5.4835	652.2	2272.0	5.7543	636.0	2301.0
175.0	4.9071	645.0	2156.6	5.6310	671.4	2301.0
200.0	4.8289*	662.8	2132.1	5.5682	678.3	2298.9

Table 4 Data at optimum design stage with unbalance response constraint and unbalance and critical speed constraints

Constraint / Optimum Design / Unbalance Ratio	Unbalance Response			Unbalance and Critical Speed		
	Weight (Kg)	ω_2^c (rad/sec)	ω_3^c (rad/sec)	Weight (Kg)	ω_2^c (rad/sec)	ω_3^c (rad/sec)
1.00	8.4036	485.1	1877.6	—	—	—
1.10	6.3930	491.7	2307.8	6.8626	535.2	2315.4
1.25	4.8289*	510.6	2116.7	5.6884	521.0	2301.0
1.50	4.8289*	526.0	2118.9	5.6317	543.6	2301.0
1.75	—	—	—	5.5655	609.6	2299.1

4 The mode shapes at the optimum design stage are quite different from those of the original design. This implies that the percentage of the strain energy store in the shaft and the bearings will be different. This depends on the initial design selected.

References

Childs, D. W., and Graviss, K., 1982, "A Note on Critical Speed Solutions for Finite-Element-Based Rotor Models," ASME *Journal of Mechanical Design*, Vol. 104, pp. 412-416.

Cowper, G. R., 1966, "The Shear Coefficient in Timoshenko's Beam Theory," ASME *Journal of Applied Mechanics*, Vol. 33, pp. 335-341.

Dworski, J., 1964, "High Speed Rotor Suspension Formed by Fully Floating Hydrodynamic Radical and Thrust Bearings," ASME JOURNAL OF ENGINEERING FOR POWER, Vol. 86, No. 2, pp. 149-160.

Fritzen, C. P., and Nordman, R., 1982, "Influence of Parameter Changes to Stability Behavior of Rotor," NASA Conference Publication 2250, Rotor-Dynamic Instability Problems in High-Performance Turbomachinery, Texas A & M Univ., College Station, pp. 284-297.

Fox, R. L., and Kapoor, M. P., 1968, "Rates of Change of Eigenvalues and Eigenvectors," *AIAA Journal*, Vol. 6, No. 12, pp. 2426-2429.

Gunter, E. J., 1970, "Influence of Flexibility Mounted Rolling Element Bearings on Rotor Response, Part 1: Linear Analysis," ASME *Journal of Lubrication Technology*, Vol. 92, No. 1, pp. 59-75.

Haug, E. J., Pan, K. C., and Strecter, T. C., 1972, "A Computational Method for Optimal Structural Design. I. Piecewise Uniform Structures," *Int. J. Num. Meth. Engng.*, Vol. 5, pp. 171-184.

Kane, T. R., and Levinson, D. A., 1985, *Dynamics: Theory and Applications*, McGraw-Hill, New York.

Lund, J. W., and Sternlicht, B., 1962, "Rotor-Bearing Dynamics With Emphasis on Attenuation," ASME *Journal of Basic Engineering*, Vol. 84, No. 4, pp. 491-502.

Lund, J. W., 1963, "Attenuation of Bearing Transmitted Noise—Vol. 2, Part 1: Attenuation of Rotor Unbalance Forces by Flexible Bearing Supports," Report No. EC232, Bureau of Ships, Contract No. BS-86914.

Lund, J. W., 1979, "Sensitivity of the Critical Speeds of a Rotor to Changes in Design," ASME *Journal of Mechanical Design*, Vol. 102, pp. 115-121.

Nelson, H. D., and McVaugh, J. M., 1976, "The Dynamics of Rotor Bearing Systems Using Finite Elements," ASME *Journal of Engineering for Industry*, Vol. 93, No. 2, pp. 593-600.

Nelson, H. D., 1980, "A Finite Rotating Shaft Element Using Timoshenko Beam Theory," ASME *Journal of Mechanical Design*, Vol. 102, pp. 793-804.

Plaut, R. H., and Huseyin, K., 1973, "Derivatives of Eigenvalues and Eigenvectors in Non-Self-Adjoint Systems," *AIAA Journal*, Vol. 11, No. 2, pp. 250-251.

Rajan, M., Nelson, H. D., and Chen, W. J., 1986, "Parameter Sensitivity in Dynamics of Rotor-Bearing Systems," ASME *Journal of Vibration, Acoustics, Stress, and Reliability in Design*, Vol. 108, No. 2, pp. 197-206.

Rajan, M., Rajan, S. D., Nelson, H. D., and Chen, W. J., 1987, "Optimal Placement of Critical Speed in Rotor Bearing System," ASME *Journal of Vibration, Acoustics, Stress, and Reliability in Design*, Vol. 109, pp. 152-157.

Shiau, T. N., and Hwang, J. L., 1988, "Minimum Weight Design of a Rotor Bearing System With Multiple Frequency Constraints," ASME JOURNAL OF ENGINEERING FOR GAS TURBINES AND POWER, Vol. 110, No. 4, pp. 592-599.

Schmit, L. A., and Farshi, B., 1974, "Some Approximation Concepts for Structural Synthesis," *AIAA Journal*, Vol. 12, No. 5, pp. 692-699.

Vanderplaats, G. N., 1982, "Structural Optimization Past, Present, and Future," *AIAA Journal*, Vol. 20, No. 7, pp. 992-998.

Venkayya, V. B., 1971, "Design of Optimum Structures," *International Journal of Computers and Structures*, Vol. 1, pp. 265-309.

Venkayya, V. B., Khot, N. S., and Berke, L., 1973, "Application of Optimality Criteria Approaches to Automated Design of Large Practical Structures," presented at AGARD Second Symposium on Structural Optimization, Milan, Italy.

APPENDIX

The matrices shown by Nelson and McVaugh (1976) are generalized to yield the shaft element matrices $[\mathrm{M}^e]$, $[\mathrm{N}^e]$, $[\mathrm{G}^e]$, and $[\mathrm{K}^e]$, which are shown in equation (2). They are of the form for mass matrices

$$[\mathrm{M}^e] = C_1\{[\mathrm{M}]_0 + \Phi[\mathrm{M}]_1 + \Phi^2[\mathrm{M}]_2\}$$

$$C_1 = \frac{\rho\pi l(r_0^2 - r_I^2)}{420(1+\Phi)^2}$$

$$[\mathrm{M}]_0 = \begin{bmatrix} 156 & 22l & 54 & -13l \\ 22l & 4l^2 & 13l & -3l^2 \\ 54 & 13l & 156 & -22l \\ -13l & -3l^2 & -22l & 4l^2 \end{bmatrix}$$

$$[\mathrm{M}]_1 = \begin{bmatrix} 294 & 38.5l & 126 & -31.5l \\ 38.5l & 7l^2 & 31.5l & -7l^2 \\ 126 & 31.5l & 294 & -38.5l \\ -31.5l & -7l^2 & -38.5l & 7l^2 \end{bmatrix}$$

$$[\mathrm{M}]_2 = \begin{bmatrix} 140 & 17.5l & 70 & -17.5l \\ 17.5l & 3.5l^2 & 17.5l & -3.5l^2 \\ 70 & 17.5l & 140 & -17.5l \\ -17.5l & -3.5l^2 & -17.5l & 3.5l^2 \end{bmatrix}$$

$$[\mathrm{N}_e] = C_2\{[\mathrm{N}]_0 + \Phi[\mathrm{N}]_1 + \Phi^2[\mathrm{N}]_2\}$$

$$C_2 = \frac{\rho\pi(r_0^4 - r_I^4)}{120l\cdot(1+\Phi)^2}$$

$$[\mathrm{N}]_0 = \begin{bmatrix} 36 & 3l & -36 & 3l \\ 3l & 4l^2 & -3l & -l^2 \\ -36 & -3l & 36 & -3l \\ 3l & -l^2 & -3l & 4l^2 \end{bmatrix}$$

$$[\mathrm{N}]_1 = \begin{bmatrix} 0 & -15l & 0 & -15l \\ -15l & 5l^2 & 15l & -5l^2 \\ 0 & 15l & 0 & 15l \\ -15l & -5l^2 & 15l & 5l^2 \end{bmatrix}$$

$$[\mathrm{N}]_2 = \begin{bmatrix} 0 & 0 & 0 & 0 \\ 0 & 10l^2 & 0 & 5l^2 \\ 0 & 0 & 0 & 0 \\ 0 & 5l^2 & 0 & 10l^2 \end{bmatrix}$$

and for stiffness matrices

$$[\mathrm{K}^e] = C_3\{[\mathrm{K}]_0 + \Phi[\mathrm{K}]_1\}$$

$$C_3 = \frac{\pi E(r_0^4 - r_I^4)}{4l^3(1+\Phi)}$$

$$[\mathrm{K}_0] = \begin{bmatrix} 12 & 6l & -12 & 6l \\ 6l & 4l^2 & -6l^2 & 2l^2 \\ -12 & -6l & 12 & -6l \\ 6l & 2l^2 & -6l & 4l^2 \end{bmatrix}$$

$$[\mathrm{K}]_1 = \begin{bmatrix} 0 & 0 & 0 & 0 \\ 0 & l^2 & 0 & -l^2 \\ 0 & 0 & 0 & 0 \\ 0 & -l^2 & 0 & l^2 \end{bmatrix}$$

where

$$\Phi = \frac{12EI}{\kappa' GAl^2} = \frac{3E}{Gl^2}\cdot\frac{(r_0^2 - r_I^2)}{\kappa'}$$

$$\kappa' = \frac{6(1+\nu)(1+\zeta^2)^2}{(7+6\nu)(1+\zeta^2)^2 + (20+12\nu)\zeta^2}$$

κ is the shear factor (Cowper, 1966); ν is the Poisson ratio; $\zeta = r_o/r_I$.

M. E. F. Kasarda[1]
Rotor Bearing Dynamics, Inc.,
Wellsville, NY 14895

P. E. Allaire

R. R. Humphris

L. E. Barrett

Department of Mechanical and Aerospace
Engineering,
University of Virginia,
Charlottesville, VA 22901

A Magnetic Damper for First-Mode Vibration Reduction in Multimass Flexible Rotors

Many rotating machines such as compressors, turbines, and pumps have long thin shafts with resulting vibration problems. They would benefit from additional damping near the center of the shaft. Magnetic dampers have the potential to be employed in these machines because they can operate in the working fluid environment, unlike conventional bearings. This paper describes an experimental test rig that was set up with a long thin shaft and several masses to represent a flexible shaft machine. An active magnetic damper was placed in three locations: near the midspan, near one end disk, and close to the bearing. With typical control parameter settings, the midspan location reduced the first mode vibration 82 percent, the disk location reduced it 75 percent, and the bearing location attained a 74 percent reduction. Magnetic damper stiffness and damping values used to obtain these reductions were only a few percent of the bearing stiffness and damping values. A theoretical model of both the rotor and the damper was developed and compared to the measured results. The agreement was good.

Introduction

Compressors, turbines, and other rotating machines often have long thin shafts, which give rise to high vibration problems. Currently, many compressors operate above the first (Kludt, 1983) or second critical speed. Steam turbines also operate above several critical speeds. Seals inside compressors give rise to cross-coupled stiffness terms, which may drive a machine into large subsynchronous vibrations, as shown by Allaire (1987a). Nicholas et al. (1986) report on the effects of flexible supports, which tend to increase vibration levels in steam turbines. Generally it is desirable to increase the damping effects near the center of these long, thin shaft machines. One method of doing this is to place a damper inside the machine casing.

The concept of using a damper inside these machines is not new. Such a damper would be located somewhere between the bearings and apply damping, and perhaps stiffness, to the rotor. What has been lacking until recent years is a damper that could operate in the environment of the working fluid. Conventional rolling element and fluid film bearings require an oil supply. A central damper in a compressor would have to be sealed so that the oil does not contaminate the gas. In most cases, the additional complications do not warrant the damper. In steam turbines, the temperature is so high that an oil damper could not be used inside the turbine.

Magnetic dampers are now a real possibility for these types of machines. Commercial magnetic bearings (Foster, 1986; Hustak, 1986) are increasingly being used for compressors and other machines. These do not require oil and can operate at high temperatures, thus removing the limitations indicated above. To date, the authors are not aware of the use of a magnetic damper in a field application in North America.

A magnetic bearing can be used as a magnetic damper simply by having it carry no load. Thus the machine is completely supported in regular bearings. Typically these are oil-lubricated bearings. If the damper is not active, then the machine reverts to its normal behavior without a damper effect. Some early work on simple rotors with active control was reported by Allaire et al. (1981, 1983).

Studies have been carried out by both Nikolajsen (1979) and Gondhalekar (1984) on the suppression of vibrations in long transmission shafts. A magnetic damper was placed at various locations along the shaft to determine the reduction. These studies differ from the present paper because they did not address the vibration characteristics of many types of turbomachinery where there are large masses located along the shaft. Unlike previous works the current paper examines the effect of both active damping and active stiffness on a test rotor with vibration characteristics similar to that of a compressor or turbine.

A magnetic bearing/damper has been developed at the University of Virginia. It was used as the damper in this work, so the relevant publications are described in some detail here. The basic bearing geometry and control algorithm was described by Humphris et al. (1986). The effects of the bearing employed to support a flexible rotor were measured and reported by Allaire et al. (1986a, 1986b, 1987b). Adjustment of the bearing stiffness properties via the control system gains allowed movement of the rotor first critical speed from approximately 800 rpm to 2000 rpm, which is more than a factor of two. Variation of the bearing damping properties gave a reduction in rotor vibrations of as much as an order of magnitude. The first results using the magnetic bearing as a damper (not supporting

---

[1] Current address: Mechanical Engineer, E. I. du Pont de Nemours Co. Inc., Newark, DE 19714-6090.

Contributed by the International Gas Turbine Institute and presented at the 34th International Gas Turbine and Aeroengine Congress and Exhibition, Toronto, Ontario, Canada, June 4–8, 1989. Manuscript received at ASME Headquarters February 1, 1989. Paper No. 89-GT-213.

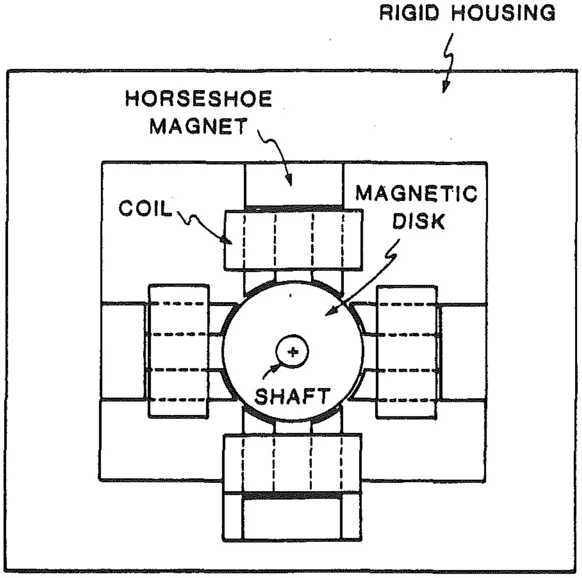

Fig. 1 Magnetic damper model

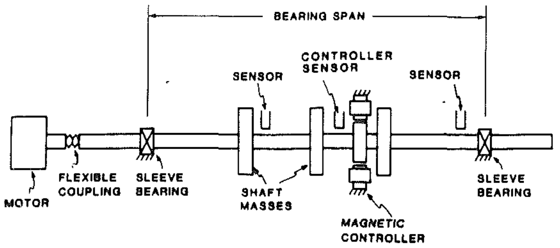

DAMPER AT MIDSPAN

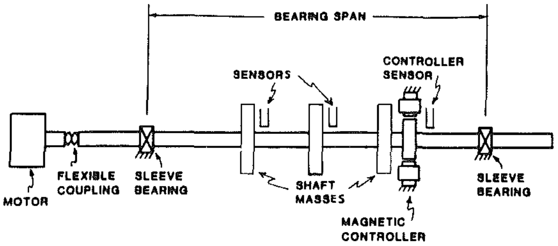

DAMPER AT DISK THREE

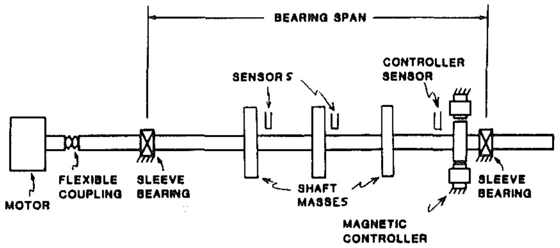

DAMPER AT BEARING

Fig. 2 Schematic of three-mass rotor with magnetic damper at three different locations (not to scale)

any steady state load) were reported by Allaire (1987c). Also, initial results of employing digital control to operate magnetic bearings were published by Keith (1988).

The purpose of this paper is to report on the use of an active magnetic damper in a multimass flexible rotor. Three large disks were placed on a shaft, supported in conventional bearings, to represent a multimass compressor or steam turbine. The magnetic damper was placed in various locations to observe the vibration reduction capabilities. The magnetic damper was placed near the midspan, near one end disk, and as close to the outboard bearing as possible.

Active Magnetic Damper

An active magnetic damper is essentially an active magnetic bearing with no load support capacity. The magnetic damper used in this analysis consists of four electromagnets located radially around the rotor shaft. The electromagnetic currents, which determine the force in each magnet, were determined by a controller, which maintained the shaft in the center of the damper by continuously monitoring the shaft position and adjusting the electromagnetic currents accordingly. There were air gaps between the shaft and the magnets and the shaft did not contact the magnets. The dynamic properties of the damper (i.e., damping and stiffness) were electronically regulated by the controller.

A diagram of the four electromagnets that made up the damper is shown in Fig. 1. They were located radially around a laminated ferromagnetic disk, which was attached to the rotor shaft. The purpose of this laminated disk was to provide a continuous flux path between the magnet pole faces with a minimum of eddy current losses.

Each electromagnet in the damper consisted of a solid soft iron core forming a horseshoe, with two pole faces cut to a diameter of 60.5 mm (2.38 in.). This gave a nominal radial clearance of 1.0 mm (0.040 in.). Each leg of the coil was wound with 920 turns of wire. All electromagnets were the same with equal steady-state currents. The theory of the damper characteristic is presented in Appendix A.

Two proximitor (eddy current) probes located vertically and horizontally near the damper (unless otherwise specified) were used as rotor position sensors for input to the electronic controller. Various tests were previously conducted to insure that the magnetic fields from the damper did not affect the readings of the probes.

Test Rig

A four-mass laboratory rotor was constructed with a 19.0 mm (0.75 in.) shaft supported in conventional sleeve bearings with a bearing span of 660.4 mm (26.0 in.). Three steel disks were placed 4 in. apart at the center of the shaft leaving 190.5

Nomenclature

A = area of magnetic pole face (one)
C = capacitance
c_{eq} = equivalent damping
F = force
G = controller transfer function
h = gap thickness
h_s = steady-state gap thickness
i = current
i_s = steady-state current
i_b = bottom magnet current
i_t = top magnet current
K_a = current amplifier gain
K_{eq} = equivalent stiffness
K_g = proportional gain
K_i = current stiffness
K_g = rate gain
K_t = controller total gain
K_y = position stiffness
M = mass
N = number of turns (per leg)
R = resistance
s = Laplace variable
W = weight
y = vertical position
μ_o = permeability of free space
τ = time constant
ϕ = magnetic flux
ω = angular velocity

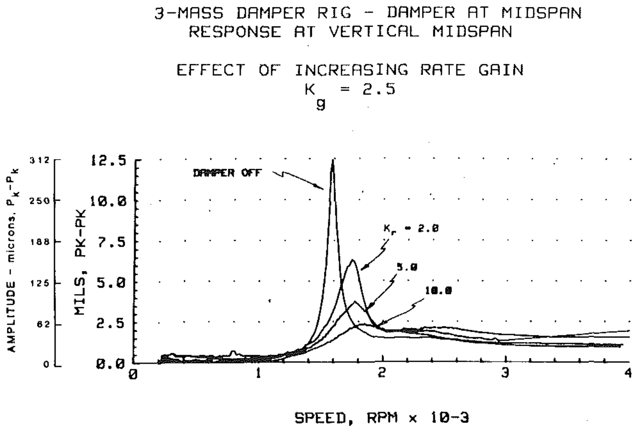

Fig. 3 Experimental results for the damper at midspan (increasing rate gain K_r) at the vertical midspan probe

mm (7.5 in.) between each outboard disk and the closest support bearing. Each of these three disks was 139.7 mm (5.5 in.) in diameter, 25.4 mm (1.0 in.) in thickness, and weighed 28.48 N (6.4 lb). The fourth mass was the laminated ferromagnetic damper disk, which weighed 4.90 N (1.1 lb) and was 58.4 mm (2.3 in.) in diameter with a thickness of 25.4 mm (1.0 in.). The total rotor length and weight, including the laminated magnetic disk, was 762 mm (30.0 in.) and 107.2 N (24.1 lb), respectively.

This damper disk was placed at three different locations on the rotor, illustrated in Fig. 2, depending on the desired location of the magnetic damper. The three locations were at the midspan near the center disk, near the third disk at the quarterspan of the rotor, and at a location just inboard of the outer bearing. These locations were chosen to demonstrate the effect of a damper at optimum and less than optimum rotor locations for control of one or more modes of vibration. These locations represent situations where there may be design constraints on an actual machine as to the placement of a magnetic damper on the rotor. As shown in Fig. 2, shaft displacement sensors were placed at three different locations to monitor shaft motion. These locations will be referred to from left to right as the disk 1 probe, midspan probe, and disk 3 probe, respectively. The four-mass rotor will now be referred to as the three-mass rotor, due to the relatively small mass of the laminated ferromagnetic disk compared to the three large steel disk masses.

The three-mass rotor was attached to an aluminum baseplate, which was fixed to a large concrete block by anchor bolts. Shim stock was placed underneath the aluminum baseplate to correct a slight bow in the baseplate. The shaft was also twisted (bowed) with a significant shaft bow, which could not be corrected. For example, when the shaft bow at the midspan probe was reduced to below 0.0254 mm (1 mil), the bow near the first disk was still close to 0.0508 mm (2 mils).

The rotor was driven by a 1/2 hp electric motor rated at 10,000 rpm. The motor transmitted power through a flexible rubber coupling as shown in Fig. 2.

A total of three vertical and three horizontal proximitor probes were used to monitor shaft displacements. A separate proximitor probe was used as a key phasor. Signals from the probes were run to two digital vector filters, where amplitude and phase information at the probes was determined. One set of proximitor probes was also used as input sensors for the magnetic damper controller. These sensors were always located close to the damper.

The three-mass experimental rotor was used to study the effects of a magnetic damper located at the three locations on the shaft. The magnetic damper was used in conjunction with an electronic controller. The current amplifier in the electronic controller was overloaded and unable to follow the conditioned signal for speeds greater than 4000 rpm and would saturate for moderate vibration levels above this speed. The problem was corrected after the completion of this study. Therefore, this paper will be limited to operation below 4000 rpm (66.7 Hz). The first rotor bending mode is located at about 1600 rpm (26.7 Hz), with all other modes located at frequencies greater than 4000 rpm (66.7 Hz).

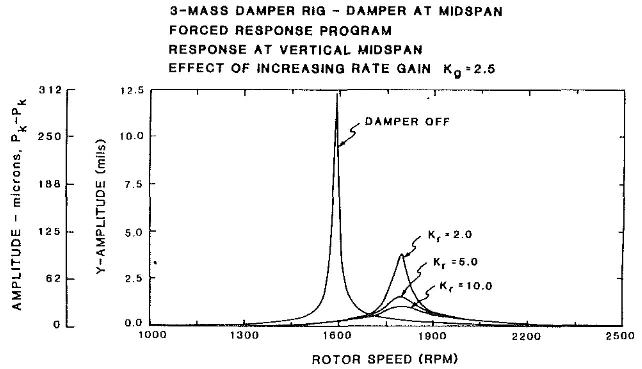

Fig. 4 Forced response program predictions for damper at midspan (increasing rate gain K_r) at vertical midspan probe

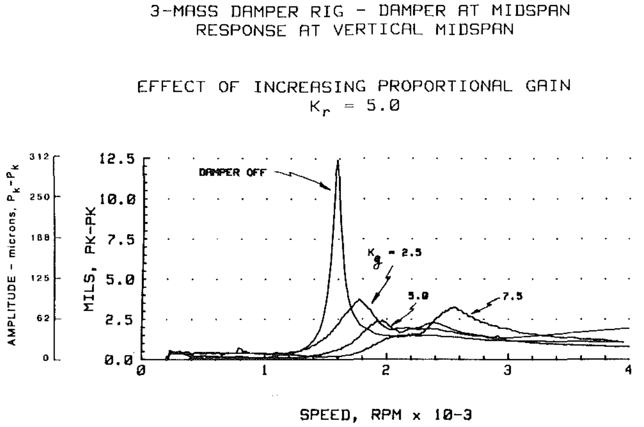

Fig. 5 Experimental results for the damper at midspan (increasing proportional gain K_g) at the vertical midspan probe

Damper at Midspan

The first location of the magnetic damper to be investigated was the midspan location, as shown in Fig. 2. This was expected to be the optimum position for control of first-mode vibrations.

The effect of increasing rate gain (K_r) or damping and proportional gain (K_g) or stiffness of the electromagnetic damper was studied at each location. The rate gain (K_r) was varied from a nominal value of 2.0 to a maximum value of 20.0. Due to stability problems, it was not possible to use this damper with pure damping or rate gain (K_r) and therefore, the controller was set with a nominal proportional gain (K_g) of 2.5, while the rate gain (K_r) was varied for analysis. Similarly, the electromagnetic damper could not be used with pure stiffness or proportional gain (K_g) and the controller was set with a nominal rate gain (K_r) of 5.0 while the proportional gain (K_g) was varied from 2.5 to 10.0. Finally, a comparison of the effect of the damper location for fixed values of rate gain (K_r) and proportional gain (K_g) was carried out.

The effect of using the damper at the midspan is shown in Fig. 3. The rotor was run with the damper off and with rate gain (K_r) equal to 2.0, 5.0, and 10.0. Proportional gain was held constant at 2.5. There was an 82 percent reduction in amplitude with a rate gain of 10.0 over the case with the damper off.

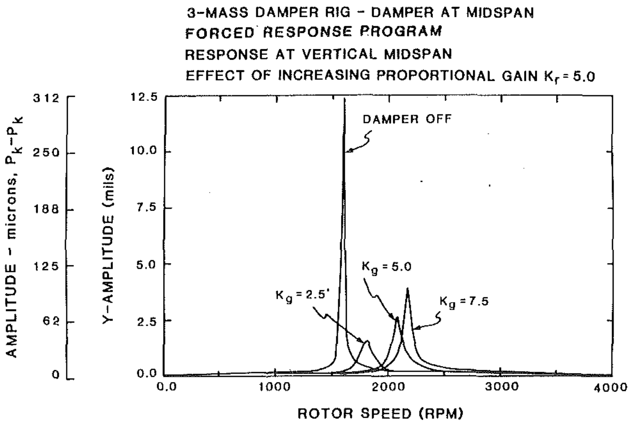

Fig. 6 Forced response program predictions for damper at midspan (increasing proportional gain K_g) at vertical midspan probe

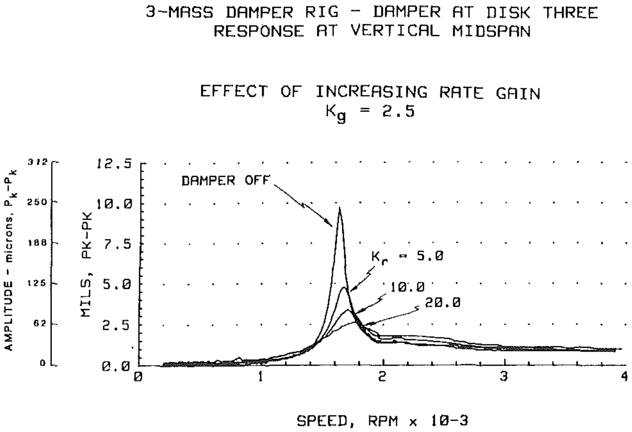

Fig. 7 Experimental results for the damper at disk three (increasing rate gain K_r) at the vertical midspan probe

An unbalance response model of the rotor was developed to compare to the measured data. Stiffness and damping coefficients were evaluated for the damper as described in Appendix B. Also, the unbalance level in the rotor was determined by balancing the rotor to a low level and then adding a known unbalance weight in the center disk.

The forced response predictions for the magnetic damper at the midspan of the three-mass rotor are plotted in Fig. 4 for cases with the magnetic damper off, and with the damper on with a rate gain (K_r) equal to 2.0, 5.0, and 10.0, respectively. A maximum reduction of 88 percent in the amplitude of vibration occurs theoretically with $K_r = 10$ as compared to the value of 82 percent for the measured case.

It may be seen from these results that even a small amount of damping can greatly reduce the vibration level. For $K_r = 2.0$, the estimated damping value was 31 N-s/m (0.18 lb-sec/in.), which produces a 49 percent decrease in amplitude at the rotor center. The estimated bearing damping was 1050 N-s/m (6.0 lb-sec/in.). Thus the actual midspan damping is only approximately 3 percent of the bearing damping. At $K_r = 10$, the estimated damping was 122 N-s/m (0.70 lb-sec/in.) or approximately 12 percent of the bearing damping. This produced an 82 percent reduction in amplitudes of vibration.

Figure 5 shows the experimental values for the midspan damper location as the proportional gain (K_g) had the values 2.5, 5.0, and 7.5. The rate gain was held constant at $K_r = 5.0$. The critical speed increased from 1600 rpm (26.7 Hz) to 2570 rpm (42.8 Hz) with $K_g = 7.5$. The value of $K_g = 7.5$ corresponds to a damper stiffness of 210,000 N/m (1200 lb/in.). This stiffness value is only about 10 percent of the bearing vertical stiffness.

The calculated forced response is shown in Fig. 6. The predicted increase in critical speed is 38 percent for $K_g = 7.5$. This is somewhat lower than the 60 percent measured increase in critical speed. Also, the theory predicted a steady increase in amplitude with increasing K_g, whereas the measured values decreased and then increased. Overall, however, the agreement is good.

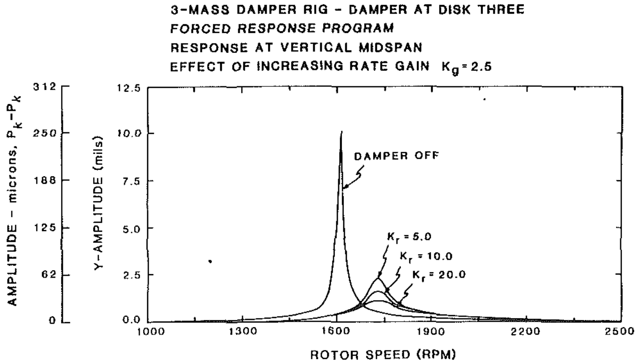

Fig. 8 Forced response program predictions for damper at disk three (increasing rate gain K_r) at vertical midspan probe

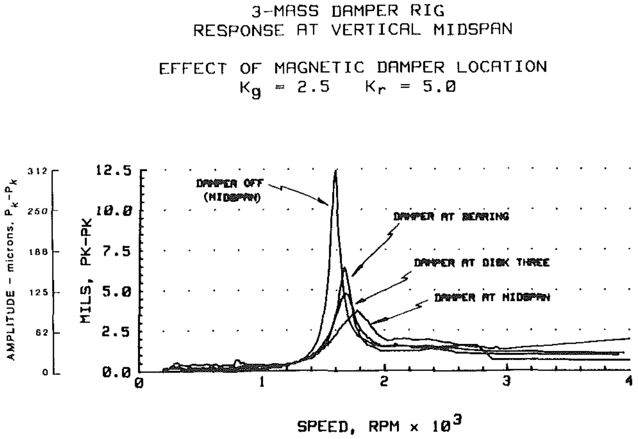

Fig. 9 Experimental results for the damper at three locations (proportional gain (K_g) equal to 2.5, rate gain (K_r) equal to 5.0)

Damper at Disk Three

The second location of the magnetic damper is the disk three location as shown in Fig. 2. This was expected to be the next best position for control of the first mode vibrations.

The effect of using the damper at disk three is shown in Fig. 7. The rotor was run with the damper off and the rate gain (K_r) equal to 5.0, 10.0, and 20.0. Proportional gain was held constant at 2.5. There is a 75 percent reduction in amplitude with a rate gain of 20.0 over the case with the damper off.

An unbalance response model of the rotor with the damper at disk three was also developed for comparison with the measured data. The forced response predictions for this configuration are plotted in Fig. 8 for cases with the magnetic damper off, and with the damper on, with a rate gain (K_r) equal to 5.0, 10.0, and 20.0, respectively. A maximum reduction of 85 percent in the amplitude of vibration occurred theoretically with $K_r = 20$, as compared to the value of 75 percent for the measured case.

Again, it may be seen from these results that even a small amount of damping can greatly reduce the vibration level. At $K_r = 20$, the estimated damping was 175 N-s/m (1.0 lb-sec/in.) or 17 percent of the bearing damping. This produced a 75 percent reduction in amplitudes of vibration.

Experimental data were also taken for the disk three damper location with proportional gain (K_g) values of 2.5, 7.5, and 10.0, while the rate gain (K_r) remained at 5.0. The critical speed

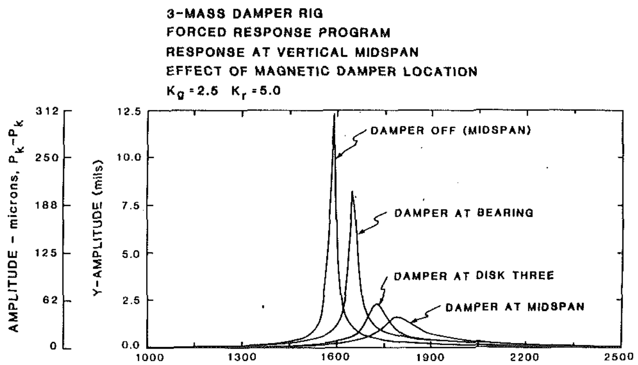

Fig. 10 Forced response predictions for the damper at three locations (proportional gain (K_g) equal to 2.5, rate gain (K_r) equal to 5.0)

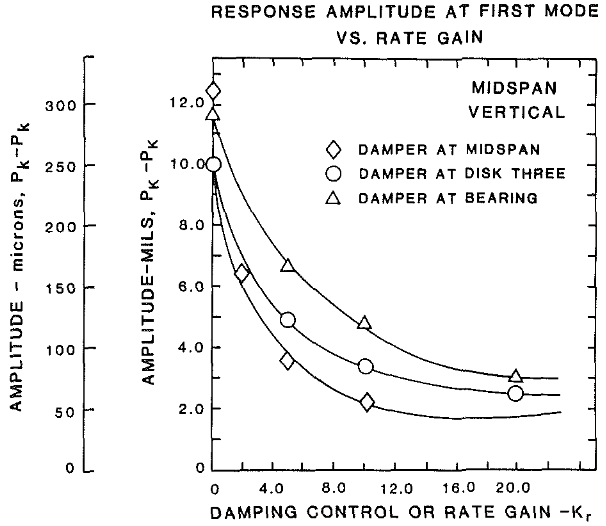

Fig. 11 Response amplitude at first mode versus rate gain (damper at midspan, disk three, and bearing location)

increased from 1600 rpm (26.7 Hz) to 1920 rpm (32 Hz) with $K_g = 10.0$. The value of $K_g = 10.0$ corresponded to a damper stiffness of 262,000 (1500 lb/in.). This stiffness value was only about 13 percent of the bearing vertical stiffness.

The corresponding forced response calculations predicted a 25 percent increase in the critical speed frequency for $K_g = 10.0$. This was somewhat higher than the measured value of 19 percent. Once again the theory predicted a steady increase in amplitude with increasing K_g, whereas the measured values decreased and then increased. In general, however, agreement was good.

Damper at Bearing

The third location of the magnetic damper to be investigated was the bearing location, as shown in Fig. 2. This was expected to be the least effective location for control of the first mode of vibrations.

The effects of using the damper at the bearing was similar to the effect of the damper at other locations. However, experimental data were taken for the rotor when the rate gain (K_r) was equal to 5.0, 10.0, and 20.0, while the proportional gain (K_g) equals 2.5. There was a significant 74 percent reduction in amplitude with a rate gain of 20.0, over the case with the damper off, whereas forced response calculations predicted only a 52 percent decrease.

Similar data were taken when the proportional gain (K_g) was set at 2.5, 7.5, and 10.0, with the rate gain (K_r) equal to 5.0. There was a measured 11 percent increase in the first critical speed from 1620 rpm (27 Hz) with the damper off to 1800 rpm (30 Hz) with the proportional gain (K_g) equal to 10.0. Forced response calculations predicted a 6 percent increase in critical speed.

Effect of Magnetic Damper Location

A summary of the measured effect of magnetic damper location is shown in Fig. 9, when the proportional gain (K_g) equals 2.5 and the rate gain (K_r) equals 5.0. As noted, the optimum control of the first mode vibrations occurs when the damper is at the midspan location, with a 70 percent reduction. The next best location is at disk three, with a 61 percent reduction in vibration. While the least optimum location for control of the first mode of vibrations is the bearing location, there is still a 48 percent reduction in vibrations over the case with no damper.

The corresponding forced response predictions are shown in Fig. 10. There is a predicted 84 percent reduction when the damper is at the midspan and an 81 percent reduction when the damper is at disk three. Also there is a 34 percent predicted reduction when the damper is at the bearing.

A summary of the overall measured responses at the first mode is shown graphically in Fig. 11 with $K_g = 2.5$. This figure shows the effect of the damper at various locations on the first mode response. It can also be noted that the vibration reduction approaches a minimum level as the damping is increased.

Conclusions

Overall, the magnetic damper achieves the desired result of a large reduction of first mode vibration at the center of the rotor. The largest reduction is 82 percent with the damper in the optimum location near the rotor center. These results indicate that even less than optimum placement or less than optimum control parameter setting values can produce very significant vibration reductions. This is very encouraging for the potential use of magnetic dampers in industrial applications.

It can also be noted, however, that there is a limit to the vibration reduction that can be attained by a single damper in the machine. Beyond a certain level, even a large increase in the stiffness and damping of the damper essentially produces very little further reduction in vibration.

Generally, the agreement between the theoretical modeling of the shaft/damper system compared to the measured results is good. The magnitudes are close and the trends in the results are consistent. This indicates that the design of magnetic dampers, done on a theoretical basis before construction, has a high probability of success.

References

Allaire, P. E., Lewis, D. W., and Jain, V. K., 1981, "Feedback Control of a Single Mass Rotor on Rigid Supports," *Journal of the Franklin Institute*, Vol. 312, pp. 1-11.

Allaire, P. E., Lewis, D. W., and Knight, J. D., 1983, "Active Vibration Control of a Single Mass Rotor on Flexible Supports," *Journal of the Franklin Institute*, Vol. 315, pp. 211-222.

Allaire, P. E., Humphris, R. R., and Barrett, L. E., 1986a, "Critical Speeds and Unbalance Response of a Flexible Rotor in Magnetic Bearings," *Proc. of European Turbomachinery Symposium*.

Allaire, P. E., Humphris, R. R., and Kelm, R. D., 1986b, "Dynamics of a Flexible Rotor in Magnetic Bearings," *Proc. of Rotordynamic Instability Problems in High-Performance Turbomachinery*, NASA Conference Publication 2443, pp. 419-430.

Allaire, P. E., Stroh, C. G., Flack, R. D., Kocur, J. A., and Barrett, L. E., 1987a, "Subsynchronous Vibration Problem and Solution in Multistage Centrifugal Compressor," *Proc. of 16th Turbomachinery Symposium*, sponsored by Texas A&M University, Dallas, TX.

Allaire, P. E., Humphris, R. R., and Imlach, J., 1987b, "Vibration Control of Flexible Rotors With Magnetic Bearing Supports," AFOSR/ARO Conference, Nonlinear Vibrations, Stability, and Dynamics of Structures and Mechanisms, Virginia Tech, Blacksburg, VA.

Allaire, P. E., Humphris, R. R., Kasarda, M. E. F., and Koolman, M. I., 1987c, "Magnetic Bearing/Damper Effects on Unbalance Response of Flexible Rotors," *Proc. AIAA Conference*, Philadelphia, PA.

Foster, E. G., Kulle, V., and Peterson, R. A., 1986, "The Application of Active Magnetic Bearings to a Natural Gas Pipeline Compressor," ASME Paper No. 86-GT-61.

Gondhalekar, V., and Holmes, R., 1984, "Design of an Electromagnetic Bearing for the Vibration Control of a Flexible Transmission Shaft," *Rotor Dynamics Instability Problems in High Performance Turbomachinery*, Texas A&M University.

Humphris, R. R., Kelm, R. D., Lewis, D. W., and Allaire, P. E., 1986, "Effect of Control Algorithms on Magnetic Journal Bearing Properties," ASME JOURNAL OF ENGINEERING FOR GAS TURBINES AND POWER, Vol. 108, pp. 624-632.

Hustak, J. F., Kirk, R. G., and Schoeneck, K. A., 1986, "Analysis and Test Results of Turbocompressors Using Active Magnetic Bearings," presented at ASLE Annual Meeting, Toronto, Ontario, Canada.

Keith, F. J., Williams, R. D., Allaire, P. E., and Schafer, R. M., 1988, "Digital Control of Magnetic Bearings Supporting a Multimass Flexible Rotor," presented at NASA Conference on Magnetic Suspension Technology, NASA Langley, VA.

Kludt, F. H., and Salamone, D. J., 1983, "Rotor Dynamics Modification of an Eight Stage Compressor for Safety/Reliability Improvement," *Twelfth Turbomachinery Symposium*, Texas A&M University, pp. 81-96.

Nicholas, J. C., and Barrett, L. E., 1986, "The Effect of Bearing Support Flexibility on Critical Speed Prediction," *ASLE Trans.*, Vol. 29, No. 3, pp. 329-338.

Nikolajsen, J. L., Holmes, R., and Gondhalekar, V., 1979, "Investigation of an Electromagnetic Damper for Vibration Control of a Transmission Shaft," *Proc. IMechE*, Vol. 193, No. 31, pp. 331-336.

APPENDIX A

Active Magnetic Damper

This appendix briefly discusses basic electromagnetic theory relating to the force and control of a magnetic damper. For an active magnetic damper there are four electromagnets located radially around the shaft. For the vertical direction there would be an identical top and bottom magnet and the force is

$$F_{\text{total}} = 2F_{g(\text{top})} - 2F_{g(\text{bottom})} = \frac{\mu_o A N^2 i_t^2}{h^2} - \frac{\mu_o A N^2 i_b^2}{h^2} \qquad (1)$$

In a damper, for steady-state conditions,

$$i_t = i_b$$

The total force or load capacity in a magnetic damper is thus equal to zero

$$F_{\text{total}} = W = 0$$

This, of course, would not be true in a magnetic bearing.

In an electromagnetic damper, two independent parameters can change: position y, and current i. The position and current stiffness are defined as

$$K_y = -\frac{\Delta F}{\Delta y} = \text{position stiffness}$$

$$K_i = -\frac{\Delta F}{\Delta i} = \text{current stiffness}$$

The gap thickness and current expressions are

$$h = h_s - \Delta y$$

$$i = i_s + \Delta i$$

for small changes about the steady state. The total force expression, equation (1), becomes

$$F_{\text{total}} = \left[\frac{\mu_o A N^2 (i_t + \Delta i)^2}{(h_s - \Delta y)^2}\right] - \left[\frac{\mu_o A N^2 (i_b - \Delta i)^2}{(h_s + \Delta y)^2}\right]$$

or approximating by the binomial expansion

$$F_{\text{total}} = \frac{\mu_o A N^2 i_t^2}{h_s^2}\left(1 + 2\frac{\Delta y}{h_s} + 2\frac{\Delta i}{i_s}\right) - \frac{\mu_o A N^2 i_b^2}{h_s^2}\left(1 - 2\frac{\Delta y}{h_s} - 2\frac{\Delta i}{i_b}\right)$$

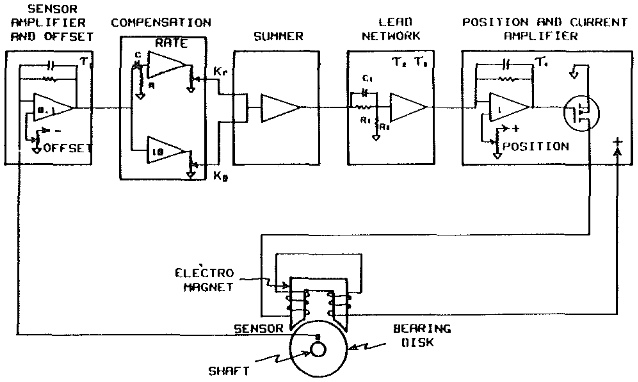

Fig. 12 Block diagram of control circuit

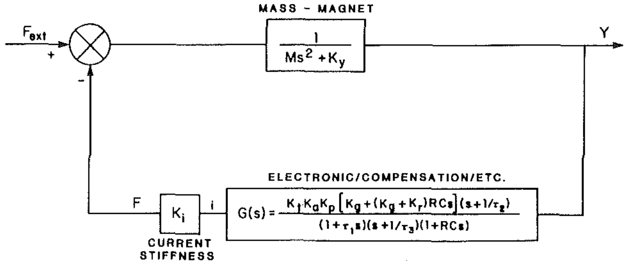

Fig. 13 Diagram of magnetic damper system for controller

For steady-state conditions

$$i_t = i_b = i_s$$

so the total force equation reduces to

$$F_{\text{total}} = \frac{\mu_o A N^2 i_s^2}{h_s^2}\left(\frac{4\Delta y}{h_s} + \frac{4\Delta i}{i_s}\right)$$

The two stiffnesses K_y and K_i can now be obtained.

First setting Δi to zero

$$F = W - K_y \Delta y = \frac{\mu_o A N^2 i_s^2}{h_s^2}\left(\frac{4\Delta y}{h_s}\right)$$

Recalling that W = zero for a damper, the total positive stiffness is

$$K_y = -\frac{4\mu_o A N^2 i_s^2}{h_s^3} \qquad (2)$$

Second, setting Δy to zero

$$F = W - K_i \Delta i = \frac{\mu_o A N^2 i_s^2}{h_s^2}\left(\frac{4\Delta i}{i_s}\right)$$

The total current stiffness is

$$K_i = -\frac{4\mu_o A N^2 i_s}{h_s^3} \qquad (3)$$

Both the position and current stiffnesses for the combination top and bottom electromagnets are simply two times the position and current stiffnesses for a single electromagnet, respectively.

The purpose of the electronic controller is to condition the position voltage signals from the proximitor probes and feed back the correct amount and phase of current to the magnets for optimum control of the rotor. The stiffness of the electromagnet damper is determined by the controller and can be varied by changing the proportional gain (K_g) of the controller. The damping of the electromagnetic damper is also determined by the controller. The position voltage signal from the proximitor probes is electronically differentiated so that the damping can be determined by the amount of velocity or rate signal

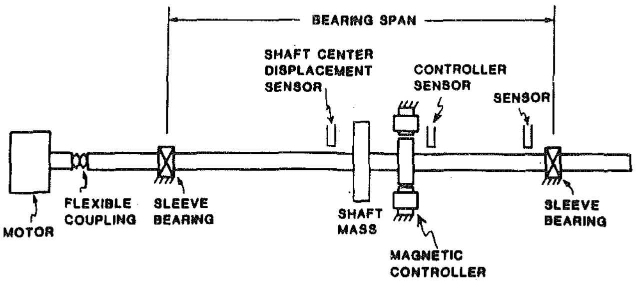

Fig. 14 Schematic of single-mass rotor with magnetic damper (not to scale)

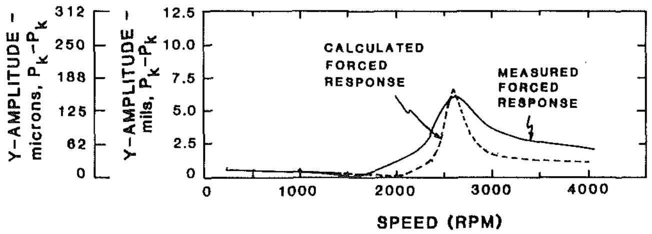

Fig. 15 *Comparison of calculated and experimentally measured forced response*

Table 1 Horizontal and vertical stiffness values of the magnetic damper at approximately 2500 rpm (41.7 Hz)

Proportional Gain (K_g)		0	2.5	5.0	7.5	10.0
K_x	(N/m)	-35,000	44,000	190,000	210,000	260,000
	(lb/in)	(-200)	(250)	(1100)	(1200)	(1500)
K_y	(N/m)	-35,000	70,000	175,100	210,100	263,000
	(lb/in)	(-200)	(400)	(1000)	(1200)	(1500)

Table 2 Horizontal and vertical damping values (lb-sec/in.) of the magnetic damper at N 2500 rpm (41.7 Hz)

K_r =	0.0	2.0	5.0	10.0
K_g	$\frac{\text{N-sec}}{\text{m}}\left(\frac{\text{lb-sec}}{\text{in}}\right)$	$\frac{\text{N-sec}}{\text{m}}\left(\frac{\text{lb-sec}}{\text{in}}\right)$	$\frac{\text{N-sec}}{\text{m}}\left(\frac{\text{lb-sec}}{\text{in}}\right)$	$\frac{\text{N-sec}}{\text{m}}\left(\frac{\text{lb-sec}}{\text{in}}\right)$
0.0	C_x=33(C_x=.19) C_y=30(C_y=.17)	-	-	-
2.5	U	C_x=49(C_x=.28) C_y=32(C_y=.18)	C_x=100(C_x=.62) C_y= 84(C_y=.48)	C_x≈150(C_x≈.85) C_y≈120(C_y≈.70)
5.0	U	U	C_x= 51(C_x=.29) C_y= 42(C_y=.24)	-
7.5	U	U	U	C_x= 47(C_x=.27) C_y= 47(C_y=.27)
10.0	U	U	U	U

U = Unstable

present. The damping can be varied by changing the rate gain (K_r) of the controller.

A block diagram for the controller is shown in Fig. 12. A feedback control diagram of the entire magnetic damper is shown in Fig. 13. The transfer function for the electronics from the sensor amplifier through the position and current amplifier is

$$G(s) = \frac{K_t K_a K_p [K_g + (K_g + K_r) RCs] (s + 1/\tau_2)}{(1 + \tau_1 s)(s + 1/\tau_3)(1 + RCs)} \tag{4}$$

Finally, the total transfer function for the magnetic damper is

$$\frac{y}{F_{\text{ext}}} = \frac{\dfrac{1}{Ms^2 + K_y}}{1 + \dfrac{K_i G(s)}{Ms^2 + K_y}}$$

Simplifying

$$\frac{y}{F_{\text{ext}}} = \frac{1}{Ms^2 + K_y + K_i G(s)} \tag{5}$$

It is easily seen that adjustment of controller proportional and rate gains (K_g and K_r) are used to adjust the stiffness and damping of the magnetic damper.

An effective damper stiffness and damping can also be obtained. The transfer function for an equivalent mass-spring-damper system is

$$\frac{y}{F_{\text{ext}}} = \frac{1}{Ms^2 + c_{eq}s + K_{eq}}$$

Equating this expression with equation (5) gives

$$K_{eq} = K_y + K_i Re\{G(j\omega)\}$$

$$c_{eq} = \frac{-K_i Im\{G(j\omega)\}}{\omega} \tag{6}$$

where s has been replaced by $j\omega$ for synchronous vibrations.

APPENDIX B

Determination of Damper Dynamic Properties

A single mass rotor as shown in Fig. 14 was used experimentally to evaluate the damping and stiffness characteristics of the magnetic damper for various settings of rate gain (K_r) and proportional gain (K_g). The effective stiffness of the damper is determined by the proportional gain (K_g) setting only. The effective damping of the magnetic damper is determined primarily by the rate gain (K_r) setting, but is also affected by the proportional gain (K_g) setting.

A rotor model of the single mass rotor was established, including support bearing characteristics, shaft bow, and unbalance in the rotor. The support bearings had a vertical stiffness of 4,030,000 N/m (23,000 lb/in.) and a vertical damping of 10,000 N-s/m (57 lb-sec/in.). This model was used in a forced response program and the predicted response was compared to experimentally measured rotor response. Various values of stiffness and damping were added to the rotor model at the electromagnetic damper location until predicted response (i.e., frequency and amplitude of the first mode response) matched the experimental rotor response to within approximately 5 percent. An example of experimental data and their corresponding or "matching" calculated response is shown in Fig. 15 for the case when the proportional gain (K_g) equals 2.5 and the rate gain (K_r) equals 2.0. In this manner stiffness and damping characteristics for the electromagnetic damper were determined for various values of rate gain (K_r) and proportional gain (K_g). The stiffness values are listed in Table 1 and the damping values are listed in Table 2.

The damping and stiffness characteristics of the magnetic damper determined in this manner were used in the rotor model of the three-mass rotor for forced response calculations.

A theoretical prediction of the vertical forced response is calculated when the proportional gain (K_g) equals 2.5 and the rate gain (K_r) equals 2.0 (corresponding to the measured results in Fig. 15). The theoretically predicted vertical response is 162 μm (6.5 mils) at approximately 2570 rpm.

Effective Tools for Diagnosing Elusive Turbomachinery Dynamics Problems in the Field

H. R. Simmons
Principal Engineer.

A. J. Smalley
Institute Engineer.

Southwest Research Institute,
San Antonio, TX 78284

This paper describes and discusses techniques that can effectively diagnose dynamics problems in turbomachinery. A variety of elusive dynamics problems are identified that require definition, quantification, diagnosis, and monitoring. The state of the art in measurement and signal processing techniques is discussed with reference to such factors as the directness of the measurement, the degree of intrusion required, the difficulty of installation, and the reliability or durability of the sensor. Several examples of techniques are provided that have proved to be effective in diagnosing elusive dynamics problems; some examples allow comparison of alternative techniques with different degrees of effectiveness. Problems addressed include rotating stall in the compressor section of a gas turbine, coupled lateral/torsional vibration in a gas turbine driven pipeline compressor, forced vibration of combustor parts, strain gage telemetry of blade vibrations, and nonintrusive measurement of blade vibrations using bearing-mounted accelerometers.

Introduction

Dynamics problems can be a serious but elusive cause for concern in gas turbines and their driven equipment. If not accurately diagnosed and corrected, such problems can lead to nuisance trips, fatigue failure, wear, reduced efficiency, excessive noise, and operator discomfort. The cause may be a design deficiency, an installation problem, operational damage, or progressive deterioration (wear, erosion, etc.). To diagnose machinery dynamics problems requires appropriate measurement, effective signal processing, and interpretation. As a general rule, measurements that most closely represent the failure mechanisms involved are also the most intrusive—that is, they require more penetration and machinery access for preparation. However, effective signal processing can greatly enhance the information obtained from less intrusive measurements, and can sometimes make them effective diagnostic tools.

Many of the dynamics problems encountered in gas turbine trains can be grouped under the headings Torsional Dynamics, Lateral Rotordynamics, Blade Vibrations, Compressor Stall, and Burner or Combustor Vibrations. Each class of problems has its own set of characteristics and constraints, which influence the choice of measurement technique.

Torsional dynamics problems are usually a system problem in which an inappropriate match in flexibility and inertia of system components (e.g., turbine, coupling, gear box) creates a system torsional natural frequency, which coincides with a strong excitation at some point in the desired operating speed range. Qualitative symptoms of torsional vibrations include noise from gear boxes, induced lateral motion at gear boxes, low or high cycle fatigue failures, fretting wear at gear teeth and couplings, etc.

The cure for a torsional vibration problem may be to change the natural frequency, to change the excitation frequency, to reduce the excitation magnitude, to strengthen weak components, or a combination of approaches. It is desirable to define the characteristics of the problem before deciding the course of action, but such characteristics are elusive because the vibrating parts are rotating, and because the twisting motion is difficult to detect with stationary sensors without some addition or modification to the rotating element.

The causes of lateral rotordynamics problems are too numerous to mention in their entirety; they include high unbalance, proximity of running speed to a lightly damped critical speed, destabilizing mechanisms at seals and bearings, rubs, misalignment, thermal distortion of rotor or casing, etc. Symptoms include high relative motion between shaft and bearing; high amplitudes at bearing housing or rotor casing; bearing damage; seal wear; increased leakage; and in some cases, seizure or permanent distortion of the rotor and destruction of turbine or compressor blades.

Measurement of vibration at bearings has become very commonplace and the increasing use of noncontact displacement sensors has improved understanding of many gas turbine lateral rotordynamics problems. However, the accurate definition of rotordynamics behavior at the point of highest vibration amplitude, where there is a significant potential for damage, often remains elusive.

Blade vibrations (stationary or rotating) are a major source of costly problems in gas turbines. They can arise for various reasons, including an order-related excitation, which falls unacceptably close to a sensitive blade natural frequency, stall

---

Contributed by the International Gas Turbine Institute and presented at the 34th International Gas Turbine and Aeroengine Congress and Exhibition, Toronto, Ontario, Canada, June 4–8, 1989. Manuscript received at ASME Headquarters January 13, 1989. Paper No. 89-GT-71.

Table 1 Torsional vibration measurement methods

Measurement	Comments
Keyphase	Essential time of arrival reference for signal processing.
Casing Acceleration	Usually installed on aeroderivative turbines. Limited sensitivity to torsional vibrations.
Motion at Opposing Locations	Signal difference indicates reactive torque of driving or driven components. Affected by lateral vibration.
Bearing Velocity	Usually installed on industrial gas turbines. Limited sensitivity to torsional vibrations.
Laser Velocimetry	Able to trace torsional mode shapes. Affected by lateral vibration. Not widely used.
Turbine or Compressor Bearing Displacement	Usually installed on industrial turbines. Limited sensitivity to torsional vibrations.
Pinion Bearing Displacement	Sensitive to some torsional modes. Provides lateral interaction information.
Instantaneous Generator or Motor Watts	Difficult to apply for high voltage systems. Useful for motor start-up diagnoses.
Gear Tooth Pulse Signal	Pulse signal demodulation required. Affected by tooth profile. Requires multiple sensors to discriminate lateral vibration.
Torsiograph (Velocity)	Needs free end attachment to shaft. Generally useful diagnostic tool.
Torsional Accelerometer	Needs free end attachment to shaft and telemetry or slip rings. Also useful for reactive motions of driving or driven components.
Shaft Encoder	Pulse signal demodulation required. Needs free end attachment to shaft. Useful tool for torsional diagnosis. Inexpensive and available.
Shaft Strain Gages	Can be located near high stress points. Requires strain gages and transmitter. Most effective for torsional diagnosis.

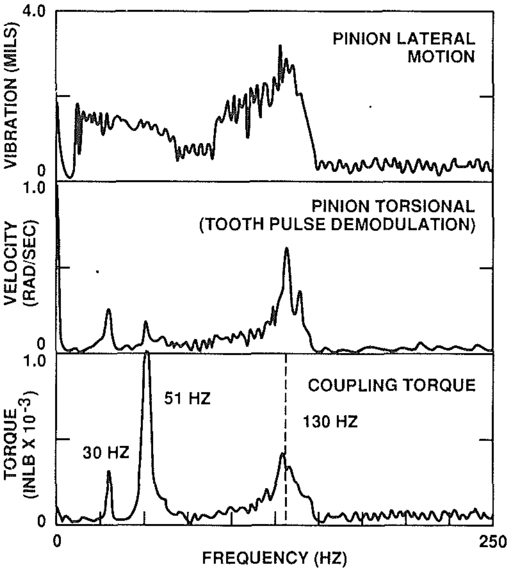

Fig. 1 Comparison of torsional and lateral vibration during turbine run-up

during off-design conditions, and flow-induced vibration (flutter) at very high flow rates.

Rotating blade vibrations are difficult to quantify directly because of the problems involved with routing signal leads along the rotor, and for providing a means for carrying the signals off the rotor. The blades are often in a difficult environment—hot and erosive.

Solutions to blade vibration problems include tuning blade resonant frequencies by changing stiffness or inertia, by addition of shroud bands to make blades vibrate together, and by changes in attachment of root or shroud. Before implementing such solutions, it is always desirable to characterize the blade vibrations—most often an elusive goal.

Rotating stall is commonly found in axial flow compressors at low flow conditions. Variable stator geometry and compressor bleed controls tend to mitigate the stall excitation levels, but extended operation at off-design conditions can lead to fretting of airfoil attachments.

Vibration is a source of fatigue cracking of burner internal components that can result in excessive maintenance or replacement requirements. The usual sources of burner vibration are flow turbulence, vortex shedding, blade passing, acoustic resonances, and mechanical excitation from the turbine rotors. We have documented one case where burner vibration responded to fuel line pulsation. Source identification techniques, such as signal coherence tracing, are useful diagnostic tools; but the burner vibration signals must be acquired from within an extremely hot and hostile environment.

Evaluation of Vibration Measurement Methods

Torsional Vibrations. Torsional vibration of a rotor system involves angular oscillations superimposed on the normal rotation in the system elements. In a gas turbine with a speed reducer or increaser, it is common to find one or more torsional critical speeds below the highest system speed; and if the system must run over a speed range, there is potential for torsional vibration problems. If such a problem is suspected, diagnosis requires identification of:

- Speeds and frequencies at which vibration is most severe.
- Severity of the peak vibration.
- Dependence of severity upon conditions.
- Location of high dynamic stress.
- Participating components (mode shape).

Some of the choices for torsional measurement are listed in Table 1, which includes a summary of applications, limitations, signal processing requirements, and other relevant comments on each measurement method. The choices are in approximate order of intrusiveness.

Figure 1 compares the signals obtained with three of these measurement methods as a function of speed, in a gas turbine driven pipeline compressor train (Simmons and Smalley, 1984). Strain gage telemetry provides very clear evidence of three torsional modes (30 Hz, 51 Hz, 130 Hz), one of which (51 Hz) was lightly damped (about 1 percent damping ratio) and generated stresses sufficient to be of considerable concern.

The tooth frequency demodulation (pinion torsional) is affected by mode shape, by gear machining imperfections, and by lateral motion of the pinion; a single sensor is unable to distinguish the different types of motion because they both have the same effect on the arrival time of the tooth. Although this measurement clearly does not accurately quantify severity and could not quantify damping for all modes, it was able to detect the same three torsional modes as the telemetry system.

The pinion lateral motion is not always a consistent measure of torsional vibration; however, it often supplies supporting information. Figure 1 clearly shows that lateral measurements produce no evidence of the most sensitive mode at 51 Hz, which is consistent with the low damping valve found for this mode due to the lack of radial motion of the pinion in its

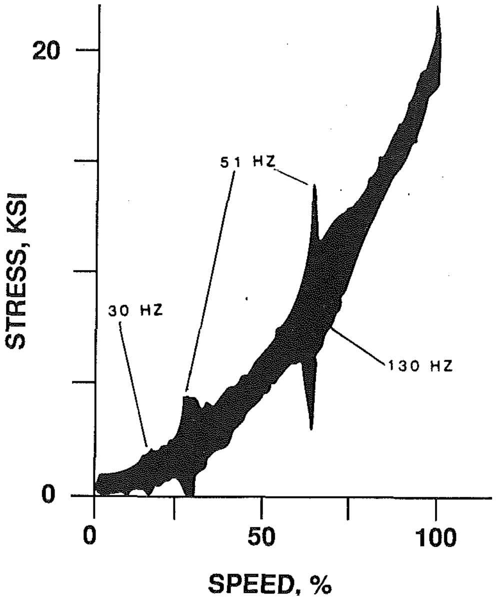

Fig. 2 Coupling strain gage signal during turbine run-up

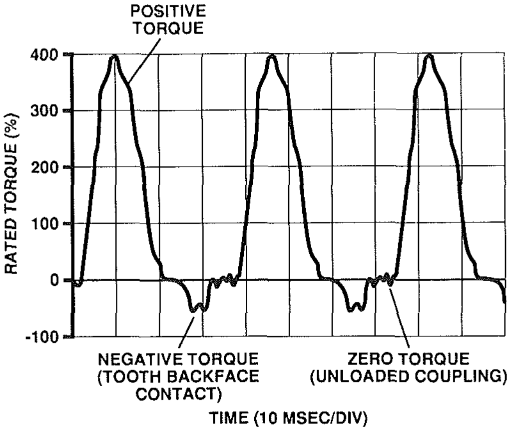

Fig. 3 Torsional strain gage signal showing backlash

bearings. Conversely, the torsional resonance at 130 Hz shows considerable evidence of coupling with lateral motion, which is the probable reason that its associated damping is relatively high.

The details of static and dynamic stresses available in strain gage telemetry signals are illustrated in Fig. 2. This figure plots total strain gage output against speed and provides very clear evidence that backlash at the coupling teeth prevents stress reversal at a major torsional resonance (51 Hz). The fidelity available in shaft strain gage data allows description of highly nonlinear response, such as tooth unloading and backface contact within the backlash event (Fig. 3).

Figure 4 shows a typical strain gage telemetry installation. Close inspection reveals shaft strain gages, the transmitter ring attached to the shaft, and the stationary antenna that picks up the transmitted signal.

Figure 5 shows the transient motion of a gear box pinion during a violent surge in an adjacent compressor. The journal impacts shown in this figure give clear evidence of the potential for bearing damage that can result from torsional lateral interaction during surge. In this case, the train consisted of a gas turbine, two compressors, a generator, and two gear boxes, which resulted in several torsional critical speeds below operating speed, as shown by the torsiograph data in Fig. 6. This figure also shows the severe torsional response measured during the surge event. Note that not only are the torsional resonances

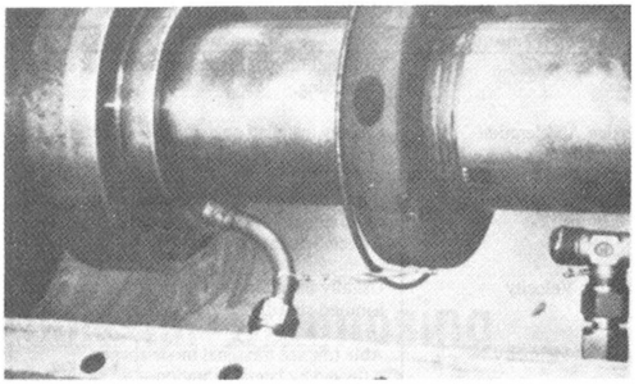

Fig. 4 Strain gage transmitter installed on compressor coupling

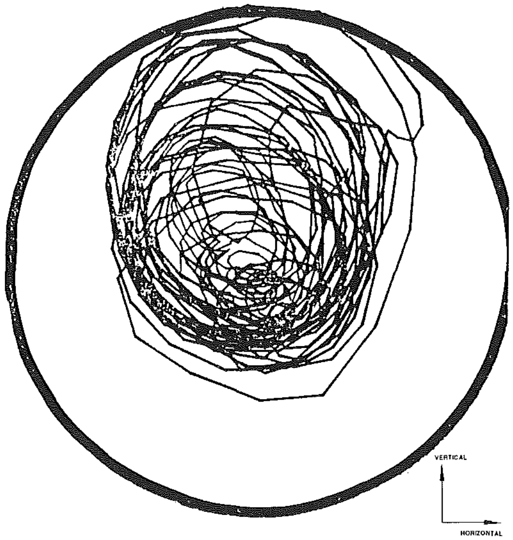

Fig. 5 Pinion lateral response (orbits) during compressor surge

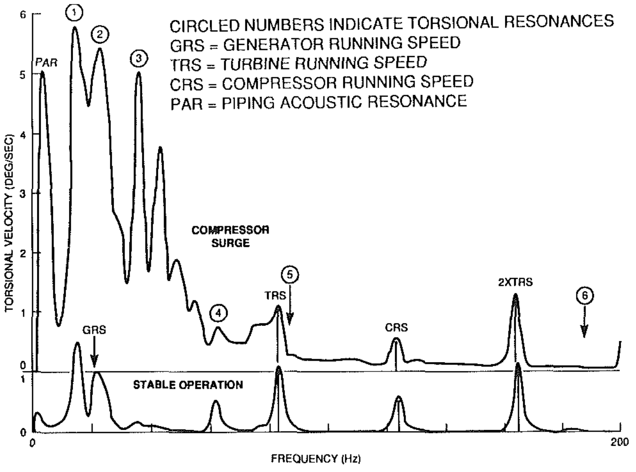

Fig. 6 Comparison of torsional spectra for stable operation and for compressor surge

strongly excited, but that a 3-Hz response appears in the spectra, which is indicative of acoustic resonances of the adjoining piping when excited by compressor surge.

In appropriate installations, the torsiograph provides good evidence of most torsional vibration modes. It is a moderately intrusive instrument, requiring access to a shaft free end. Its effectiveness is of course influenced by the extent of participation of the point of attachment in the torsional modes of interest. To the best of the authors' knowledge, the availability of torsiographs is limited.

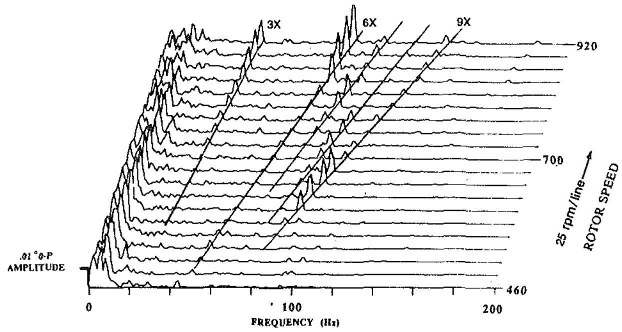

Fig. 7 Torsional response measurement using shaft encoder on diesel generator auxiliary drive system

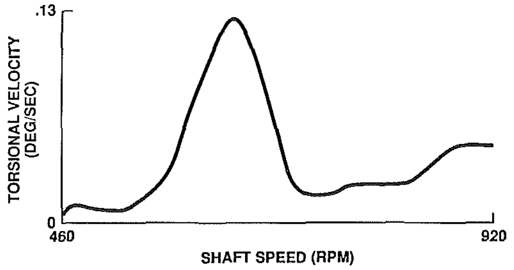

Fig. 8 Tracking analysis of 9th order excitation identifies torsional resonance at 97 Hz

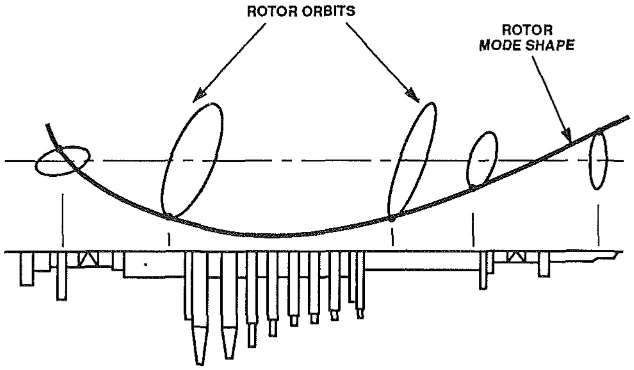

Fig. 9 Turbine vibration orbits near critical speed

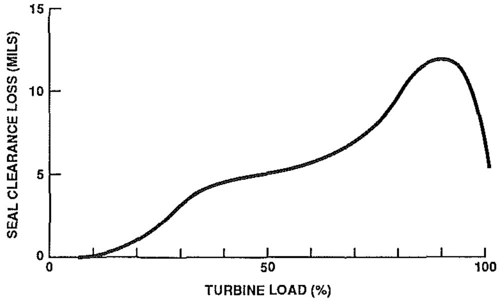

Fig. 10 Changes to turbine seal clearance during start-up

The shaft encoder is an attractive alternative to the torsiograph. While it also requires access to a shaft free end, it is proving increasingly reliable and has the advantage of low cost and ready availability such that several can be installed for a single test. The encoder provides a clean digital pulse train output and avoids inconsistencies due to gear tooth profile or shaft motion.

Typical test results from the auxiliary drive system of a diesel generator are presented in Fig. 7, where several shaft encoders and strain gage telemetry systems were installed. The demodulated encoder signal was integrated and amplified to one degree per volt, and provided a fidelity nearly equivalent to the strain gage signals. Cascade analysis of an engine acceleration run shows that the strongest excited orders (3rd and 6th) approach resonances just above running speed. The encoder signal strength was sufficient for a 9th order tracking analysis (Fig. 8) to identify a problem resonance at 97 Hz.

Often, only the inference of a torsional shaft resonance is necessary to instigate corrective action when obvious torsional problems such as keyway cracking or coupling fretting occur. An effective nonintrusive approach in this case is to mount matched vibration transducers in the vertical direction and equal distance from the shaft centerline on a driving or driven component. Subtraction of the signals provides an indication of the reactive torque absorbed by the component; synchronous tracking of the resultant signal and the reactions of other components during a start-up or shutdown transient usually provides sufficient evidence to discriminate between torsional and lateral responses.

Lateral Vibrations. In lateral rotordynamics problems, measurement of shaft displacement at fluid film bearings is a powerful diagnostic tool; with appropriate data recording and display, shaft sensors can reveal the nature of many lateral vibration problems, both steady state and transient.

Shaft displacement sensors are routinely deployed in X-Y arrangements by the petrochemical industry on critical machinery. On existing large industrial gas turbines for electrical power generation, displacement sensors at the bearings are found less frequently, but they are increasingly being included in new installations, particularly for cogeneration. Myrick (1988) provides examples of the benefits of shaft vibration monitoring on a large industrial gas turbine. Displacement sensors must be selected to survive the high-temperature environment of turbine end bearings, and care must be taken to account for the effects of temperature on the calibration; some users install redundant pairs of displacement sensors at hot end bearings, which helps compensate for thermal growth errors; one gas turbine supplier now offers a displacement sensor installation that allows the probe to be replaced from outside the turbine.

On turbines with a good experience base, it is possible to make reasonable judgments about machinery integrity from bearing displacement measurements; indeed, on some classes of gas turbines, one inch per second is widely used as a trip criterion for bearing housing velocity measurements. At the same time, the bearing housing vibration is distinctly limited in its ability to show clearly the nature of particular vibration problems. Even the use of a shaft sensor at the bearings can suffer this limitation.

When there is suspected high lateral vibration in gas turbines, likely concerns include bearing overload, loss of blade tip clearance, and seal rubs. In each case, to assess the severity of vibration requires knowledge of both static displacement and dynamic journal motions. As shown by McHugh (1983), bearing overload can occur in the bearings of a well-aligned rotor system with high vibration. In a misaligned rotor system, bearing overload can occur at lower vibration levels because the external load due to misalignment reduces the margin for dynamic loads. Thus, an ideal measurement and signal processing arrangement for gas turbine bearings will monitor the total output of the displacement sensors. If a proper reference is maintained, the average (DC level) signal reveals the mean shaft position while the dynamic signal shows how the shaft is moving relative to its mean position. This total information can be interpreted to indicate the severity of a static and dynamic load combination.

Assessing the likelihood of seal rubs is more difficult. The net seal clearance is the initial clearance at assembly modified by thermal growth of rotor and seal, change in bearing eccentricity, thermal bending and ovalling distortion of casing, thermal distortion of rotor, and shaft vibration at the seal location. In some rotor bearing systems, mode shapes reveal amplitudes near the shaft midspan that may be several times the amplitude at the bearing. The vibration may be a major contributor to seal clearance loss, but for accurate assessment of severity and quantitative diagnosis, the dynamic measurement should not be completely separated from the static problem. A similar argument prevails for blade tip clearance loss.

In summary, there is often a need for accurate assessment of static and dynamic deflection well inboard of the bearings. The state of the art in shaft displacement measurement can sometimes be exploited to expand upon bearing deflection measurement alone. Figure 9 shows the dynamic orbit obtained at five points along a high-speed turbine shaft. Figure 10 shows a corresponding plot of change in vertical clearance during start-up at one point. Such data can be interpreted to identify the net loss in clearance. A complicating factor in such measurements with eddy current sensors is often the influence of temperature on probe sensitivity (volts per mil) and on differential thermal growth of the probe. Users of such sensors should carefully review the likely influence of temperature on results.

It is not always possible to gain access in the midspan area of the shaft to mount a displacement sensor looking at the shaft; more often than not, the only possible targets are blade tips. At present, several feasibility investigations and sensor development efforts are underway to make dynamic measurements from blade tip targets. The touch probes used by Aoki et al. (1988) and Valentini et al. (1988) meet most of the requirements discussed above for blade tip clearance monitoring. This probe advances in small steps toward the target blade row until it gets within fractions of a thousandth of an inch of the closest blade. At this point, the probe's proximity is detected by discharge of a moderately high voltage (approximately 400 V), and the probe retracts to a reference location. The measurement system notes the radial distance between reference position and "contact point," which can be directly interpreted to assess clearance loss. The probe advance and retract cycle is continuously repeated.

The touch probe is seeing increasing use and is a valuable tool for tip clearance measurement. Its limitations from a diagnostic point of view are that it simply measures minimum clearance and does not distinguish blade-to-blade clearance variation.

The eddy current sensor, being a well-established product, is an attractive candidate for measurement of shaft vibration from signals obtained from blade tips. Questions to be carefully assessed are frequency response, temperature sensitivity, and survival at high temperatures. For the compressor section of a gas turbine, it may be an appropriate choice.

The capacitance sensor is available as a product, though not so widely used as the eddy current sensor. It offers potential advantages of high-frequency response, reduced temperature sensitivity, and ability to survive high temperatures, including the gas turbine hot section.

The optical sensor can also be constructed and cooled to handle hot section temperatures, and offers high-frequency response. The optical sensor is not presently available as a product.

Blade Vibrations. Blade vibrations are a significant source of gas turbine problems. One reason is the large number of different geometry blades (as many as 20 rotating blade stages in an axial compressor), and the large number of sources of forced excitation (the flow distortions encountered) are rich in harmonics. Another reason is the potential for flow instabilities (stall/surge) and for flow-induced aeroelastic (flutter) vibrations at high flow rates.

A frustrating fact about blade vibrations is the difficulty of making direct measurements—the blades are rotating and often in a hot and erosive environment. As a field diagnostic tool, strain gage measurement is rarely attempted. Telemetry of the signal is difficult and intrusive. When such measurement is undertaken, the strain gages can only be expected to last a limited time (Gabriel and Donato, 1986). Techniques have been developed for detecting blade vibration using probes that penetrate the case and sense blade time of arrival differences (Roth, 1980), or acoustic Doppler responses (Leon and Scheibel, 1986). Ideally, there would exist a nonintrusive measurement whose signals preserved high coherence with the blade vibration. Such is rarely if ever the case, but careful signal processing and system characterization can maximize the return from nonintrusive measurements.

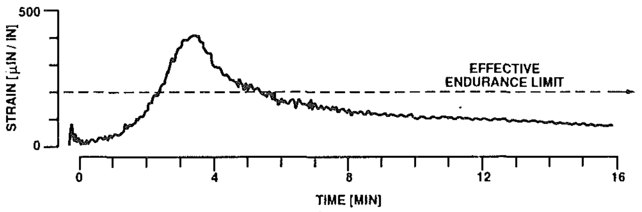

Fig. 11 Blade dynamic strain at three times running speed (3×r.s.) frequency during heat-up period

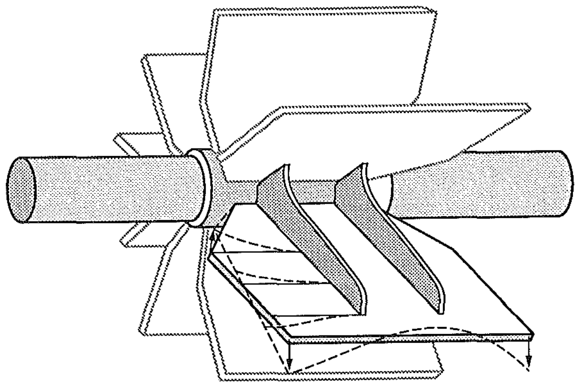

Fig. 12 Fan blade mode shape of 48 Hz resonance

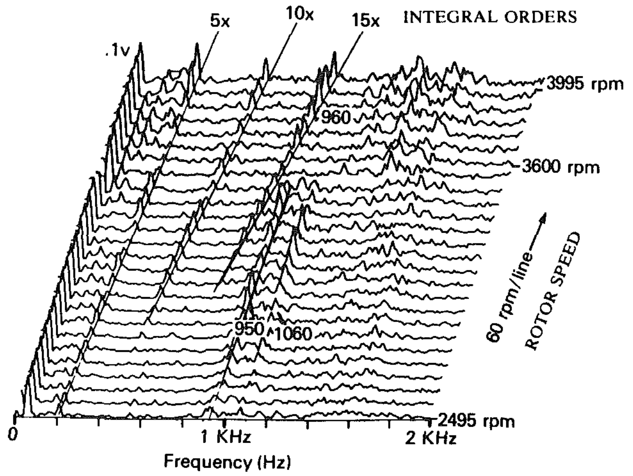

Fig. 13 Vibration cascade of rotor acceleration to overspeed showing blade resonances

Figure 11 shows the output of a rotating strain gage on a fan blade where resonant frequency reduced with load because of the temperature dependence of its Young's modulus, and momentarily matched with the three times running speed excitation. The resonant peak in the strain at constant running speed clearly proves the value of intrusive measurement. From the data obtained, it was possible to define the cause of high

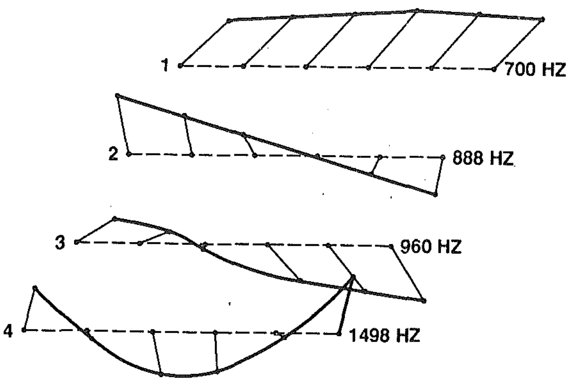

Fig. 14 Mode shapes of six-blade group resonances

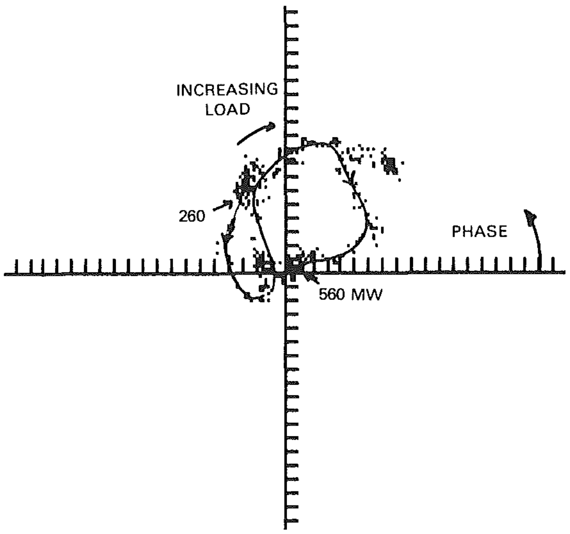

Fig. 15 Nyquist plot of 16th order bearing vibration during load ascent

cycle fatigue resulting from stress cycles during each heat-up cycle. The offending vibration occurred at the fundamental mode (48 Hz) illustrated in Fig. 12, which was defined by impact modal testing prior to the rotating strain gage tests.

As an example of useful though more inferential data (Simmons, 1986, 1987) obtained by nonintrusive testing, Fig. 13 presents a spectral cascade plot obtained during acceleration of a 550 MW steam turbine to overspeed (4000 rpm). The sensor used was an accelerometer mounted on the bearing housing. The increasing amplitude of the 15th order vibration at high speed is apparent. Figure 14 presents mode shape data from impact testing of a six blade group from the blade row where fatigue and fretting had been observed. There are two modes near 900 Hz that could be excited at 15th order, and that had modes consistent with the damage patterns (root fretting most common at outermost blades of group). Figure 15 presents a Nyquist plot of 16th order vibrations from the bearing mounted accelerometer during a load run from 260 MW to 560 MW. The 16th order data are phase referenced to a shaft once per rev signal. The data generate a resonant circle during the load change suggesting the potential for this signal as a diagnostic parameter. In the case of this nonintrusive measurement, effective signal processing has substantially increased the information obtained.

Rotating Stall. Rotating stall may cause compressor damage in gas turbines that are required to operate over a large speed range. At low flow conditions, some of the compressor stages may generate local stall cells that precess around the stage. Experience with turbomachinery from low-speed single-stage fans to high-speed aircraft engines shows that the precession rate for rotating stall is approximately 1/3 of rotor speed. Multiple stall cells are often encountered, however, such that rotor multiples near 2/3, 3/3, 4/3, etc., are observed.

An indication of rotating stall was detected by spectral analyses of vibration signals from the monitoring velocity transducers of an aeroderivative gas generator in gas processing service. A vibration peak at 36 percent and at 3 × 36 percent of rotor speed was observed in turbine and compressor transducers (Fig. 16) with the engine at idle. While these measure-

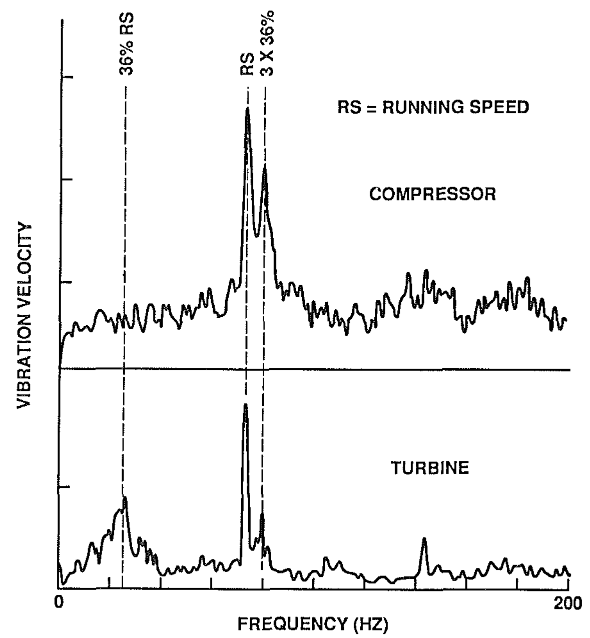

Fig. 16 Indications of rotating stall in engine vibration spectra at idle speed

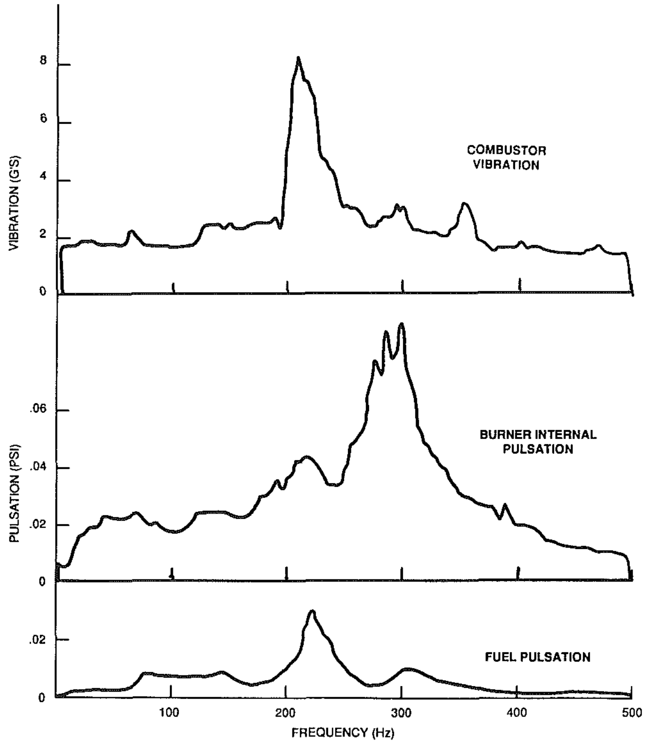

Fig. 17 Comparison of combustor vibration with pulsation inside burner and at fuel supply line

ments could not detect which compressor stage went into rotating stall, they were sufficient in a diagnostic study to confirm the operating conditions leading to fretting fatigue of airfoil attachments.

In cases where the rotating stall must be defined with greater detail, more intrusive measurements may be required. Strain gages on the airfoils, a distribution of dynamic pressure transducers, or casing mounted accelerometers are instrument choices to be considered depending on the degree of intrusion allowed versus the data fidelity required.

Burner Fatigue. Turbine burners are such a high maintenance item that special features are often provided in their design to facilitate quick inspection and field replacement. Excessive burner failures, or maintenance outside the norm for turbines of like manufacture and service, should be investigated for dynamic problems. A metallurgical examination at an early stage of the investigation provides evidence for differentiating between high cycle fatigue, low cycle fatigue, burner hot spots, etc. The construction, function, and environment of combustion chamber components make them especially vulnerable to failure. A number of dynamic sources such as turbulence, vortex shedding, and other pulsations make burner fatigue problems very difficult to solve such that "cut and try" solution approaches are often resorted to.

Fortunately, accelerometers and strain gages that can withstand elevated temperatures (1150°F and 2000°F, respectively) are available, but a dedicated effort is required if field installation and testing are to be carried out. Acoustic pulsation measurements are more easily made but still require moderate intrusion for meaningful signals.

An investigation of a small industrial gas turbine, where a number of significantly different burner designs provided no improvement to burner life, demonstrated the benefits of using high-temperature accelerometers and pressure transducers. Figure 17 compares the spectra obtained from an accelerometer mounted on the combustor, from a pressure sensor in the combustor itself, and from pressure sensor in the fuel line. These data reveal a prominent vibration peak at 210 Hz for combustion chamber components that had experienced repeated high cycle fatigue problems. This frequency was relatively close to a combustor structural resonance, and seemed to match pulsation frequencies measured inside the combustion chamber and in the fuel line.

The technique of coherence function analysis provides a means for defining causal linear relationships between suspected sources and combustor vibration. Coherence can be considered as a measure of the signal-to-noise relationship in the transfer of vibration or pulsation energy from one point to another. High values of coherence (near +1) imply strong causal relationships. Low coherence (near zero) implies a predominance of noise or excitation from other sources.

A survey of the coherence function between combustor vibration and all other pulsation and vibration signals eliminated compressor discharge and turbine inlet as sources of acoustic energy. The lack of a sharp spectral peak at 310 Hz eliminated the rotor as a source of mechanical excitation. The strongest coherence existed between combustor vibration and internal pulsation signal at 210 Hz, which confirms a structural/acoustic interaction with the combustion process. Close inspection of Fig. 17 reveals many spectral similarities between combustor vibration and internal pulsation.

The similarity in spectral data of fuel line pulsation and combustor vibration strongly suggested that the two signals were causally related. The fuel supply pulsation source was traced to an external fuel pump and was eliminated using a pulsation control bottle. The burners now survive until their normal maintenance period.

Vibration Criteria. There is considerable variation in the diagnostic capability of the various tools discussed. Each method of analysis will in general have a different approach to establishing criteria for acceptable levels, and for the type of information provided when compared to conventional measurement approaches using vibration transducers and proximity probes, as described by Blake (1964), Lifson et al. (1986, 1987), and Eshleman (1988). For example, there is not an immense body of readings available from torsional measurements, mostly because the special transducers and signal processing required impose a significant cost burden in acquiring this data. As a result, torsional vibrations are generally only made by specialists after a failure, such as a cracked shaft or a damaged gear box, has occurred.

Only recently have torsional vibration monitors been installed on steam turbine generators to monitor line-fault torsional response (Raczkowski and Kung, 1978; Rusche, 1983), and on reciprocating machinery to monitor engine performance (Jewitt and Lawton, 1986). Large quantities of data are seldom necessary for evaluating torsional vibrations because the type of problems associated with torsional vibrations can generally be related to a stress level, which is either measured directly via strain gages, deduced by comparison with a model, or estimated, based on some relatively simple analysis of the system. In other words, the criterion is much more deterministic and less statistically based than bearing vibration criteria. Virtually all strain gage measurements are of this nature, as the measurement is much more basic and judgments, based on engineering background, are all that is necessary for an evaluation of fatigue, load, etc.

Pulsation measurements are difficult to quantify for their potential for damaging structures such as gas turbine burners. Normally, axisymmetric pulsations, as experienced in piping at low frequencies, have very little direct affect on dynamic stresses; but it is the unbalanced excitation acting at elbows, tees, etc., that tend to create vibration and, hence, stresses. For these situations, the American Petroleum Institute (1986) has established general guidelines that limit pulsation levels to approximately 1 percent of static pressure.

Pulsations in a burner, or other turbomachinery structures, strongly depend upon the coincidence of the excitation frequency with a structural resonance, and the matching of acoustic modal patterns with structural mode shapes. The effects of damping for a particular mode are also very important. Fortunately, combustor components are readily amenable to finite element simulations, and modal testing provides an experimental approach to determining resonant frequencies, damping, and mode shapes. With these tools in hand and a reasonable estimate of the acoustic to structural interaction, stress levels can be estimated.

Shell structures, such as burners, have quite large surface areas that can absorb considerable acoustic energy, and thus, are quite susceptible to seemingly low pulsations under the right circumstances. High-frequency pulsations often encountered in combustion chambers are very difficult to detect with precision, as the transducer must be located in a relatively cool environment and the pulsation sensed with a lead line of some finite length, which itself will have a resonance that may attenuate the signal depending upon its acoustic response.

Oftentimes the most useful criterion is one that detects near coincidence of a source of excitation to a structural resonance. At resonances of blades, burners, impellers, stator vanes, etc., vibration strains can be amplified by a factor of 100 or more. Therefore, any indication of near incidence of resonance provides indications of operating conditions to be avoided, or structural degeneration related to impending failure. Properly interpreted, such information should be much more useful to an operator of turbomachinery than trending based on levels alone.

Summary

With increasing numbers of gas turbines going into service for power generation and for mechanical drive in pipeline and other applications, every opportunity to increase reliability and availability substantially should be pursued. The recent rise in popularity of predictive maintenance shows that there is a perceived economic benefit in this effort to avoid turbomachinery failures and associated outage costs. Such predictive maintenance programs are limited to detecting deterioration of rotordynamics components, e.g., bearing wear, unbalance accumulation, etc., and usually cannot identify specific causes of impending failure. The diagnostic techniques presented provide tools that augment predictive maintenance survey work by providing information that is more directly related to specific failure mechanisms.

Torsional vibrations are usually considered difficult measurements to make and beyond the scope of ordinary diagnostic work. A total of 12 torsional measurement methods are presented in the paper, some of which can provide useful torsional information with ordinary vibration instrumentation.

Blade problems are the most costly cause of turbine outage and repair cost; yet, they are not addressed by any monitoring programs except sometimes to indicate that a blade failure has occurred. New techniques are becoming available to sense blade vibration from probes mounted in the case. A nonintrusive technique is discussed that uses accelerometers mounted at the bearing to provide some capability for monitoring changes in blade resonance due to deterioration with time, or to temperature and speed variations.

On-site modal testing of turbomachinery components, such as blades, shafts, foundation, casing, burners, etc., provide many of the important clues regarding resonant frequencies, damping, and mode shapes as shown in Figs. 12 and 14. Impact techniques are usually used for on-site modal testing because of the speed and efficiency of such tests and the portability of the instrumentation. When necessary for heavier structures or data precision requirements, on-site shaker testing may be employed.

Oftentimes, effective diagnostic tools relate more to the analysis techniques than to the instrumentation used. The rotating stall experience presented in the paper is one example where a greater emphasis on spectral analyses of signals from the transducers already installed provided the important clues for diagnosing the problem. The experience on burner vibration exemplifies the use of coherence analyses for tracking down pulsation transmission paths leading to burner damage.

It is the ability to use a combination of approaches and instrumentation techniques that provides the greater guidance in developing an effective solution to a problem. Modal analysis testing by itself can only provide resonance information, and may not include the effects of temperature, pressure, speed, etc. Spectral cascades and order tracking analyses provide information on the actions of naturally occurring excitations as they interact with the structural resonances. Intrusive instrumentation, such as internal accelerometers or strain gages mounted on blades or shafts, requires a dedicated effort for installation and signal acquisition, but is occasionally necessary to provide the signal quality level and confidence necessary when onerous problems must be dealt with and effective solutions implemented.

References

Aoki, S., Teshima, K., Arai, M., and Yamao, H., 1988, "Results From the Phase II Test Using the High Temperature Developing Unit (HTDU)," ASME Journal of Engineering for Gas Turbines and Power, Vol. 110.

American Petroleum Institute, 1986, "Reciprocating Compressors for General Refinery Services," API Standard 618, 3rd ed.

Blake, M. P., 1964, "New Vibration Standards for Maintenance," *Hydrocarbon Processing and Petroleum Refinery*, Vol. 43, pp. 111-114.

Eshleman, R. L., 1988, "Machinery Condition Analysis," *Vibrations*, Vol. 4, No. 2, p. 3.

Gabriel, F. K., and Donato, V., 1986, "Telemetry Measurement of Combustion Turbine Blade Vibration in a High Temperature Environment," ASME Paper No. 86-GT-207.

Jewitt, T. H. B., and Lawton, B., 1986, "The Use of Speed Sensing for Monitoring the Condition of Military Vehicle Engines," *Proc. IMechE*, Vol. 200, No. D1, pp. 45-51.

Leon, R. L., and Scheibel, J. R., 1986, "Current Status of the EPRI Acoustic Doppler Blade Monitor," presented at the EPRI Steam Turbine Blade Reliability Workshop, Los Angeles, CA.

Lifshits (Lifson), A., Simmons, H. R., and Smalley, A. J., 1986, "More Comprehensive Vibration Limits for Rotating Machinery," ASME Journal of Engineering for Gas Turbines and Power, Vol. 108, pp. 583-590.

Lifson, A., Simmons, H. R., and Smalley, A. J., 1987, "Vibration Limits for Rotating Machinery," *Mechanical Engineering*, pp. 60-63.

McHugh, J. D., 1983, "Estimating the Severity of Shaft Vibrations Within Fluid Film Journal Bearings," ASME *Journal of Lubrication Technology*, Vol. 105, pp. 306-312.

Myrick, S. T., 1988, "Case Histories #1 and #2: Shaft Vibration Monitoring on a Large Industrial Gas Turbine Detects Problems Which Seismic Transducers Do Not and Sierra Pacific Power Company's ADRE 3 System Pays for Itself in 4 Months," *Orbit*, Vol. 9, No. 1, pp. 7-12.

Raczkowski, C., and Kung, G. C., 1978, "Turbine-Generator Torsional Frequencies—Field Reliability and Testing," *Proceedings of the American Power Conference*, Vol. 40, pp. 1117-1123.

Roth, H., 1980, "Vibration Measurements on Turbomachine Rotor Blades With Optical Probes," presented at the Joint Fluids Engineering Gas Turbine Conference and Products Show, New Orleans, LA.

Rusche, P. A. E., 1983, "Torsional Monitoring for Diagnosis and Surveillance Utility Experience," presented at the EPRI Workshop on Generator Monitoring & Surveillance, Dallas, TX.

Simmons, H. R., 1986, "A Non-intrusive Method for Detecting HP Turbine Blade Resonance," ASME Paper No. 86-JPGC-Pwr-36.

Simmons, H. R., 1987, "Nonintrusive Detection of Turbine Blade Resonance," presented at the Third EPRI Conference on Incipient Failure Detection in Power Plants, Philadelphia, PA.

Simmons, H. R., and Smalley, A. J., 1984, "Lateral Gear Shaft Dynamics Control Torsional Stresses in Turbine Driven Compressor Train," ASME Journal of Engineering for Gas Turbines and Power, Vol. 106.

Valentini, E., Laciligrola, P., and Casini, M., 1988, "Progress on Measurement Techniques for Industrial Gas Turbine Technology," ASME Paper No. 88-GT-113.

K. Mathioudakis
Lecturer.

E. Loukis
Research Assistant.

K. D. Papailiou
Professor.

National Technical University of Athens,
Laboratory of Thermal Turbomachines,
15710 Athens, Greece

Casing Vibration and Gas Turbine Operating Conditions

The results from an experimental investigation of the compressor casing vibration of an industrial gas turbine are presented. It is demonstrated that statistical properties of acceleration signals can be linked with engine operating conditions. The power content of such signals is dominated by contributions originating from the stages of the compressor, while the contribution of the shaft excitation is secondary. Using nonparametric identification methods, accelerometer outputs are correlated to unsteady pressure measurements taken by fast response transducers at the inner surface of the compressor casing. The transfer functions allow reconstruction of unsteady pressure signal features from the accelerometer readings. A possibility is thus provided for "seeing" the unsteady pressure field of the rotor blades without actually penetrating through the casing, but by simply observing its external surface vibrations.

1 Introduction

Recognition of the benefits from gas turbine condition monitoring has led to a rapid growth of related systems and techniques in recent years. Both gas path analysis and vibration techniques are in use. Vibration monitoring in particular provides important information about machinery health, as it can reveal the cause of potential problems and provide an early indication of incipient mechanical failures. This gives the possibility for diagnosing and correcting malfunctions, leading to an optimum management of engine operation with respect to engine shutdown and maintenance. In order to fulfill this purpose, before setting up a vibration monitoring system, the following items have to be studied:

- Selection of engine parts to be covered by the system and appropriate measuring locations.
- Measuring instruments to be used.
- Data evaluation procedures and criteria for deciding on the significance of collected data.
- Vibration limits and reference values that establish the condition of an engine.

A basis for selecting and justifying a vibration monitoring system has been provided in a recent paper (Lifson et al., 1989), where a number of case histories has also been presented. A discussion of vibration limits and vibration sources has been provided by Lifshits et al. (1986), while aspects of data evaluation and interpretation have been covered by Baines (1987), Bently et al. (1986), and Laws and Muszynska (1987). These authors also give an overview of recent progress in the area.

The aspects of malfunction covered in most of the recent publications refer mainly to problems showing up in shaft-related vibrations (the test cases presented by the abovementioned authors). Such problems are, for example, bearing failures, misalignment, shaft cracks, structural resonances, unbalance, shaft bow, fluid film and bearing instability, rubs, etc. Most of the published data and fault signatures discussed in the open literature refer to such cases. Identification of the condition of the blading itself has not received much attention, although blading problems have been reported by Barschdorff and Korthauer (1986) to rank among the most frequent faults. They presented a study related to blading problems and the emphasis was on pattern recognition, applied in identifying blade damages.

The investigation reported in the present paper is focused on studying the vibrational behavior of a gas turbine compressor casing, with respect to engine operating conditions. The purpose is to form a background for fault studies. Before the actual faults are studied, the dependence of casing vibration characteristics on engine operating conditions has to be examined. The reasons for proceeding that way are multiple: first, to understand the nature of sources exciting casing vibration, second, to study their behavior for different operating conditions of a healthy engine (baseline information), and third, to attempt to correlate engine outer surface measurements to events in engine interior. An industrial gas turbine has been used as a test engine.

In the following we start by describing the background reasoning, which leads to the choice of the particular measurements and the procedure we use. The experimental setup, results from the measurements, and conclusions from the data elaboration are given.

2 Background of the Investigation

The investigation was designed as a part of a more general study aiming at the identification of failures of compressor rotor blades, by means of vibration measurements. The measurements had therefore to be chosen in such a way that they are influenced by excitations originating from the rotating

---

Contributed by the International Gas Turbine Institute and presented at the 34th International Gas Turbine and Aeroengine Congress and Exhibition, Toronto, Ontario, Canada, June 4–8, 1989. Manuscript received at ASME Headquarters January 17, 1989. Paper No. 89-GT-78.

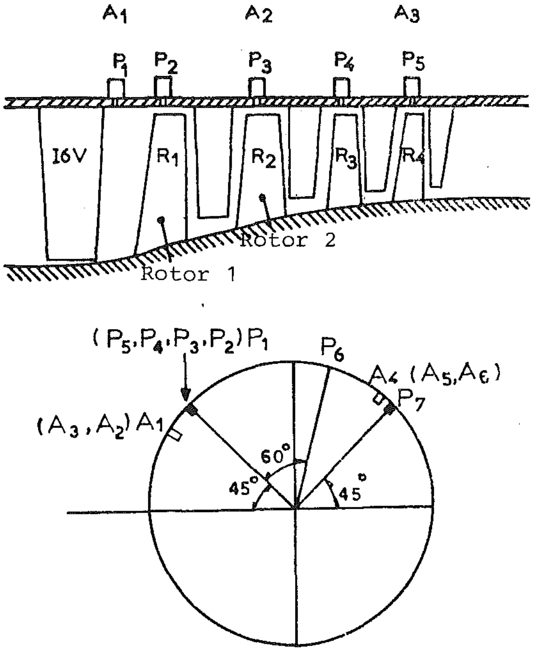

Fig. 1 Positions of pressure transducers and accelerometers on the compressor casing

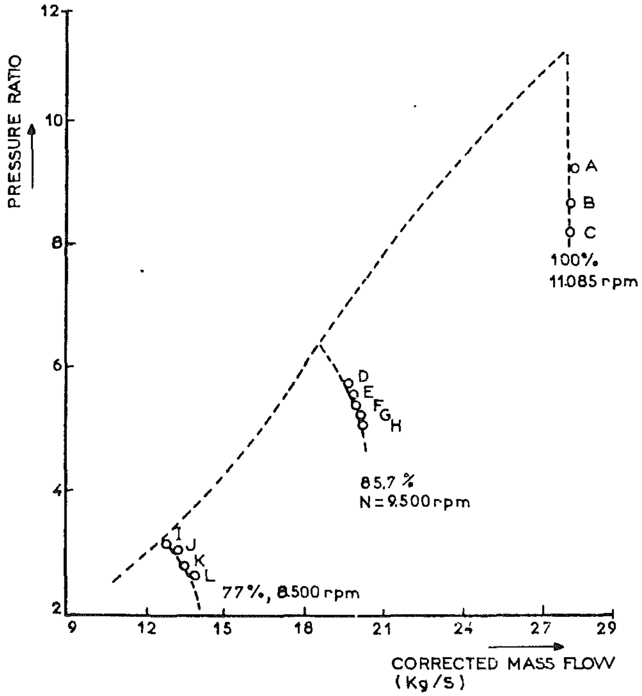

Fig. 2 Operating points for the experiments on the compressor map

blades. Suitable measuring positions for that purpose were chosen at the outer surface of the compressor casing.

The vibration of the casing surface is excited by forces of two kinds: (*a*) forces transmitted through its junctions to the intake and the rear part of the engine. They represent vibrations originating at different engine components, reaching the casing by transmission paths through the engine structure. (*b*) Forces of aerodynamic origin. They are created by (*i*) pressure fields of rotating blade rows, (*ii*) acoustic waves propagating inside the annulus, (*iii*) pressure fluctuations from turbulent flow phenomena, and (*iv*) unsteady forces from stator blades fixed on the casing. For all these forces, the fundamental cause is the rotation of the blade-to-blade pressure fields of rotors. This therefore is considered as the main exciting mechanism, as far as aerodynamic forces are considered.

The pattern of the blade-to-blade pressure field around a rotor circumference depends on the geometric shape of the blades, which reflects their mechanical condition. (It changes when blade faults occur, as for example blade bending, loss, or blade shape changes due to erosion or fouling.) On the other hand the change of the operating condition of a compressor blade row corresponds to a change in the pressure distribution along the blade surface. The casing vibrations are therefore expected to vary with the compressor operating point.

This variation needs to be studied for two main reasons: (*i*) In order to establish baseline information for casing vibration sensors, we should know how their readings vary for various operating points. Such variations are not due to any change in the mechanical conditions of the blades and should therefore be known in order to avoid misinterpretation of related shifts. (*ii*) Since the excitation and the resulting vibration change with the operating point, it will be useful to study how the casing response is influenced. We also want to examine whether a casing transfer function can be established.

In order to establish the relation between casing vibrations and excitations inside the engine, measurements must be performed of both the engine outer casing surface vibration and the internal pressure field. On the other hand, a complete experimental data set covering the entire operating range of the compressor that is as reliable as possible must be acquired.

We describe now the setup and the procedure for the experiments.

3 Experimental Setup and Procedure

The experiments were carried out on the single shaft version of the Tornado Gas Turbine, manufactured by Ruston Gas Turbines, with a nominal output of 6.2 MW at 11,085 rpm. A description of the engine has been given by Wood (1981).

Six accelerometers were mounted on the outer surface of the compressor casing. They were piezoelectric, manufactured by METRAVIB-RDS (model AM-109-MP) with a frequency range 1.5 Hz to 10 kHz, a linearity ±2 percent up to 1000*g*, and a minimum resonant frequency of 30 kHz. Fast response pressure transducers were flush mounted at the compressor inner casing wall. They were Kulite XST-190-25 SG. The positioning of the sensors on the compressor casing is shown schematically in Fig. 1.

Data were acquired through a data acquisition system manufactured by LMS, with a total capacity of 32 channels and maximum total sampling frequency of 960 kHz. A key phasor signal, bearing proximity probe signals from all engine bear-

Nomenclature

a = casing surface acceleration
A_i = accelerometer number i; Fig. 1
[H] = transfer matrix; equation (2)
p = internal casing wall static pressure
P_i = pressure transducer i; Fig. 1
S_{xx} = autospectrum of a system input x
S_{xy} = cross-spectrum of a system input x to an output y
[Y] = column vector consisting of the Fourier transforms Y of outputs y
[X] = column vector consisting of the Fourier transforms X of inputs x

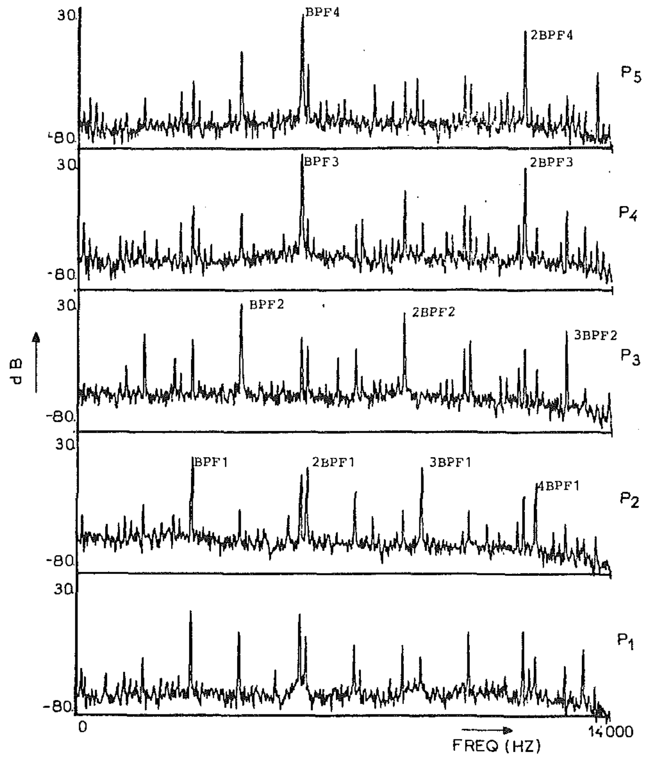

Fig. 3 Power spectra from pressure transducers at operating point F

ings, and acoustic signals from microphones placed around the engine, were acquired simultaneously with unsteady pressure and acceleration. Aerodynamic performance data were acquired by means of a data logging system described by Timperley and Smith (1983). Performance data provide information about operating conditions and cycle parameters for each operating point.

The engine operating points at which unsteady measurement data were acquired are shown on the compressor performance map (Carchedi and Wood, 1982) of Fig. 2. The results presented here were derived from data strings of 8192 samples per channel, with acquisition frequencies of 34 kHz (data at 9500 rpm, 11,085 rpm) and 24 kHz (data at 8500 rpm).

4 Accelerometers and Pressure Transducer Signal Features

The results of the measurements of unsteady pressure at the inner surface of the casing and acceleration on the outer surface are now presented. First the power spectra of the signals are discussed, while dependence on operating conditions is discussed afterward. Although only representative results are given here, the discussion is based on observations of the full amount of data.

4.1 Unsteady Pressure. Some sample power spectra of pressure signals are shown in Fig. 3. Since the frequencies excited by the individual rotor blade rows are known (blades/row × frequency of rotation), the relative importance of blade row interactions can be estimated from such spectra. It can be seen that the signal of each pressure transducer facing a rotor blade row is dominated by components with frequencies generated by the corresponding blade row. Harmonics corresponding to rotors of neighboring stages are also present, but they are of much smaller magnitude. This shows that the pressure field generated by a rotating blade row is not strongly influenced by the fields of the rotors of the neighboring stages. The presence of these harmonics, however, shows that they cannot be ignored, if one is interested in interpreting the data or possibly producing a model of the pressure field.

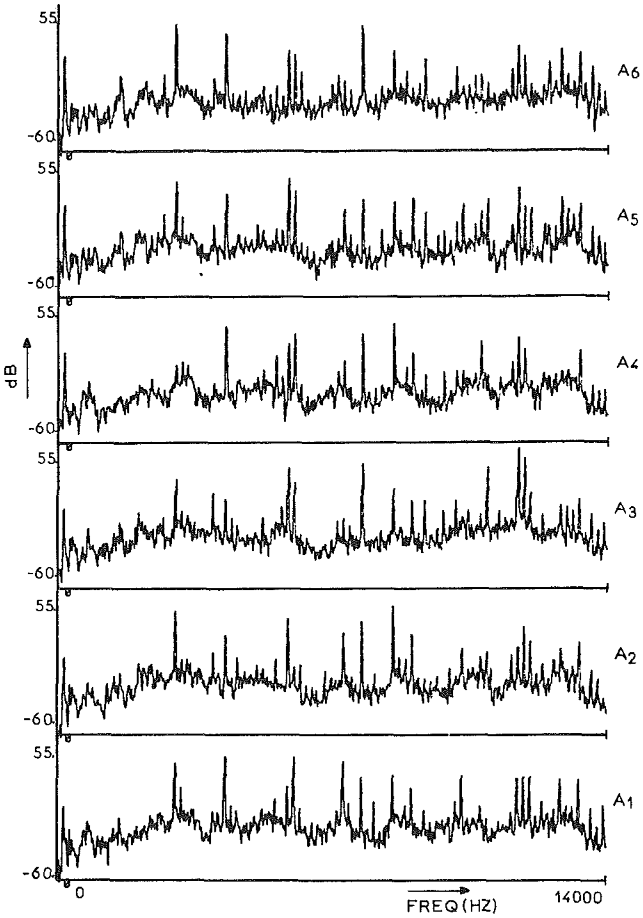

Fig. 4 Power spectra from accelerometers at operating point F

4.2 Accelerometer Signals. The spectra of the six casing accelerometers at the same operating point are shown in Fig. 4. Before commenting on these, it must be pointed out that they extend up to 14 kHz. Attention should be focused however on frequencies up to 10 kHz, since this is the useful range of the accelerometers. It can be noticed that in the spectra of all the accelerometers, peaks of comparable magnitude are present for the frequencies excited by different rotors. Therefore, vibrations measured at an axial location corresponding to a blade row are not necessarily dominated by the excitation of that row, but contain frequencies excited by the blade rows at other axial positions as well. On the other hand the relative importance of the harmonics is different for the different locations on the casing. This is interpreted as a consequence of the asymmetry of the casing geometry, which results in different transmission paths even for accelerometers placed at the same axial position.

These observations coming from a first glance at the signals indicate already that since the accelerometers contain information from adjacent blade rows, a suitable combination of accelerometer signals could be processed in order to derive information about what is happening in each blade row along the compressor.

Inspection of the spectra shows also that the signal energy is contained mainly in the higher frequencies and in particular, in frequencies corresponding to the blade passing of different rotors. Therefore, vibrations transmitted from the shaft through the bearings to the casing are of secondary importance. This picture changes slightly when we examine different operating points.

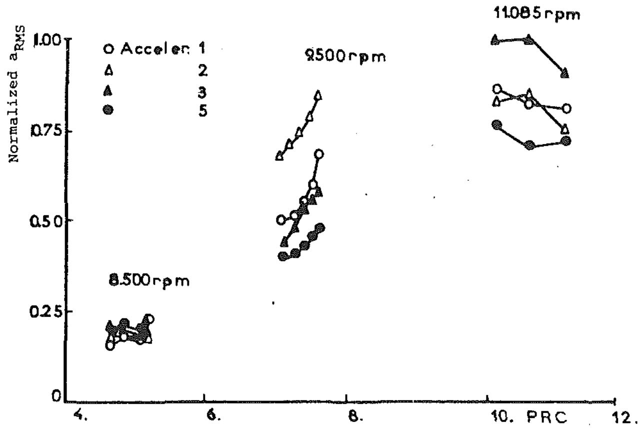

Fig. 5 The rms accelerometer readings as a function of compressor pressure ratio

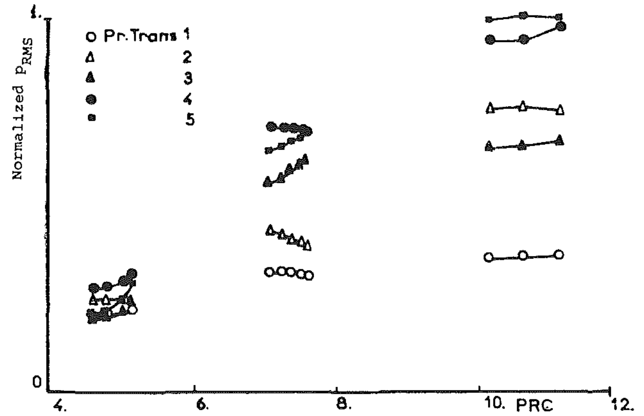

Fig. 6 The rms pressure transducer readings as a function of compressor pressure ratio

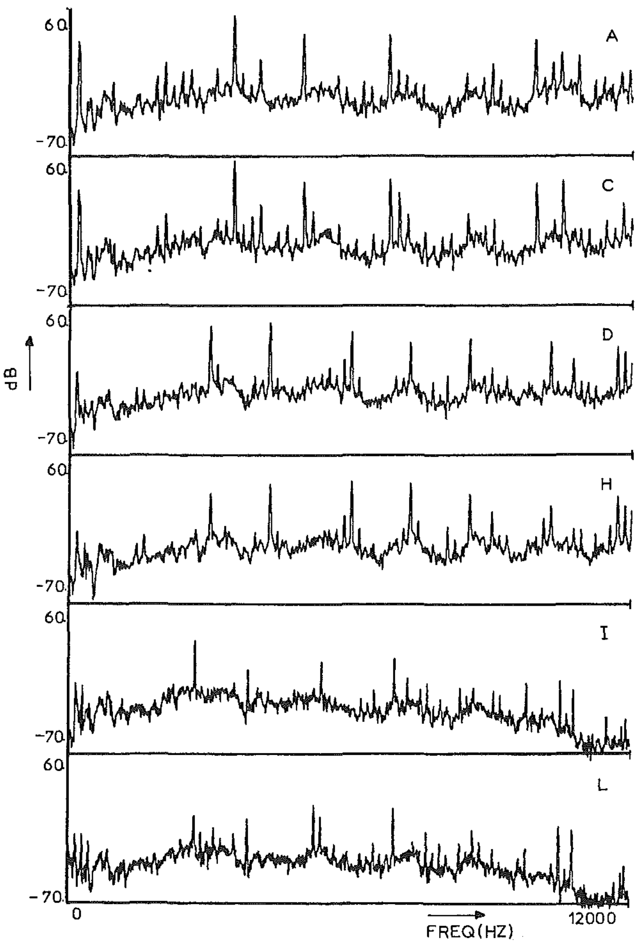

Fig. 7 Power spectra from accelerometer A1 at operating points A, C, D, H, I, and L

This leads to a conclusion about diagnostics: Casing acceleration measurements should be used very carefully when they are meant to detect shaft-related problems. Appropriate filtering should be employed in order to extract excitations from rotating blades, which contribute most of the signal energy.

4.3 Dependence on Operating Conditions. The observation that the accelerometer signals contain information from the excitation of the compressor blade rows suggests that the features of accelerometer signals depend on engine operating point (defined, for example, by rotational speed and output load).

A feature of the signals that we examine in this respect is the rms value, defined as follows:

$$X_{\rm rms} = \left|\frac{1}{N-1}\sum_{i=1}^{N}(x_i-\bar{x})^2\right|^{1/2} \quad \text{where } \bar{x} = \frac{1}{N}\sum_{i=1}^{N}x_i \qquad (1)$$

N is the number of points used. This quantity represents the energy content of the signal within the range of frequencies covered. It reflects changes in amplitudes of the different harmonics in a global manner, without showing how the changes are distributed among them. We shall first examine its variation with operating point and we will subsequently proceed in examining how its changes are distributed among individual harmonics.

The rms accelerometer signals for the different operating points of our experiments are shown in Fig. 5. This figure shows the following: (1) The overall level of the rms changes significantly from one speed to another, in comparison to smaller changes on each speedline. (2) At one operating speed the rms is changing with the pressure ratio. The change is monotonous for the cases of 8500 and 9500 rpm.

In order to examine whether the observed changes correspond to a similar behavior of the excitation forces from pressure transducers and bearings, the rms of the corresponding signals has also been examined as a function of the engine operating point.

Figure 6 shows the dependence of pressure transducer rms on operating point. It can be seen that the rms of the unsteady pressure signals is also varying with the operating point. In particular we observe that: (1) Changing the rotational speed gives a drastic increase of values of the rms, in comparison to the changes observed on one speedline. (2) The trends of the change at 8500 and 9500 rpm are monotonous, which is not the case for 11,085 rpm. From this point of view, the trends are similar to those of the accelerometers.

Finally, inspecting the rms values of signals from the bearing proximity probes showed that they do not exhibit a significant variation. These observations indicate that the vibrations of the casing outer surface are directly linked to the internal pressure field.

Further processing of the time domain signals of both the pressure transducers and accelerometers was done. Correlation functions and phase averages have been calculated and their dependence on operating point was examined. Results are not presented here due to space limitations. A conclusion drawn from this processing is that pressure transducer signals are far more suitable than accelerometer signals, for identifying blade

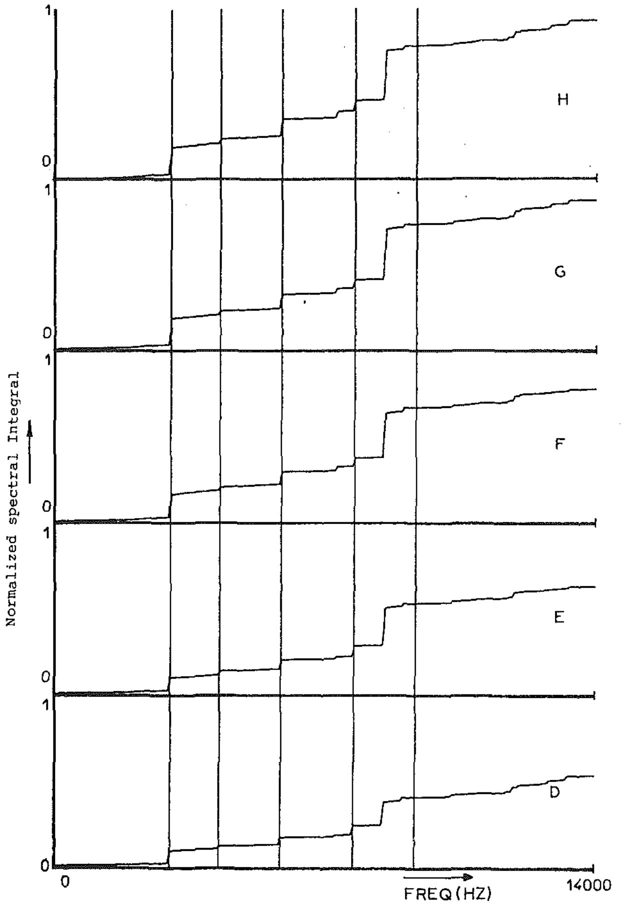

Fig. 8 Energy addition along the frequency range, for operating points D, E, F, G, and H. Accelerometer A2

operating conditions as well as blade faults. More details are given by Mathioudakis et al. (1988).

4.4 Power Spectra for Different Operating Conditions. We will examine now how the spectra change with the engine operating conditions. In Fig. 7 we show power spectra of signals from accelerometer A1 for two operating points on each speedline of Fig. 2. The spectra at one rotational speed show that the pattern of the harmonics remains basically the same, but their relative amplitudes are changing. Spectra at the different rotational speeds contain harmonics at the corresponding frequencies. It must be noted, however, that the "envelope" of the spectrum looks similar, for all these operating conditions.

In order to examine how the signal energy is distributed within the range of frequencies of interest, we integrate the spectra. An example of a result of the integration is shown in Fig. 8. The quantity on the Y axis is the integral of the spectral density from zero to a particular frequency f. This quantity is therefore the energy content of the signal in the frequency range from 0 to f Hz. Observing its evolution along the frequency range, we can see at what frequencies the energy is contained. It is seen that the energy is contained mainly in the frequencies of blade passing of the rotor blade rows, while the broadband contribution is rather minor. This observation confirms our previous comment, that the casing vibration is mainly excited by aerodynamic sources (unsteady pressure field) coming from the compressor interior. On the other hand, the change of the overall energy (equal to the variance) shown in Fig. 6 varies with operating conditions, due to a change of the contributions at the individual rotor blade passing frequencies. In Fig. 8, for example, the change of the total energy content is caused mainly by the change of the contribution of the second harmonic of the rotor 2 blade row.

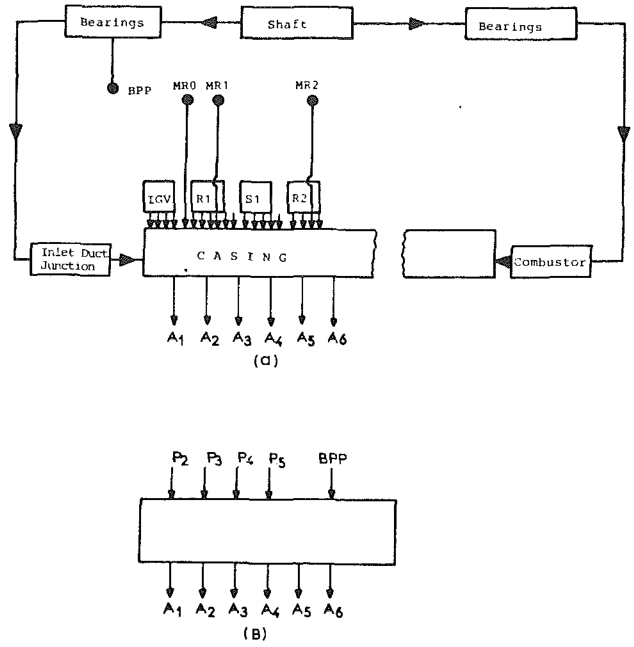

Fig. 9 The compressor casing as a linear system: *(a)* the full, distributed input-output system; *(b)* the lumped input-output system

5 Interrelation Between Unsteady Pressure Field and Acceleration Measurements

Having at our disposal measurements of both the exciting forces and the vibratory responses of the casing, its transmission characteristics can be established. Knowledge of them can be used for diagnostics, since it enables: (*i*) the calculation of the casing vibrations, when the excitations (rotor blade pressure field, associated with either "healthy" or "nonhealthy" engine operation) are known. This gives the possibility of simulating the effects of blade faults. (*ii*) The calculation of the excitations when the response is known, namely the reconstruction of the unsteady pressure signals, from acceleration measurements. This capability is very important from a diagnostics point of view. As we have seen, unsteady pressure signals are far more suitable for determining the stage where a fault or a defect has occurred, since they are influenced mainly by the corresponding blade row.

5.1 Transfer Function Considerations. The transmission characteristics of the compressor casing can be mathematically expressed as a set of vector transfer functions, if the compressor casing is modeled as a linear system.

The inputs of the linear system are all the excitations of the casing. They are continuously distributed over the internal surface of the casing and its connections to adjacent engine components. A schematic view of the system and the excitations is shown in Fig. 9(*a*). It is a distributed parameter, distributed input system. In order to study its characteristics, we lump the most important excitations and form an equivalent system with lumped inputs. The vibration of any point of the compressor casing can be considered as output of the linear system. The resulting simplified system is shown in Fig. 9(*b*).

The calculation of any of the vector transfer functions from time domain signals is based on a well-established method known from systems theory; see for example Bendat and Piersol (1971). The main equation employed is

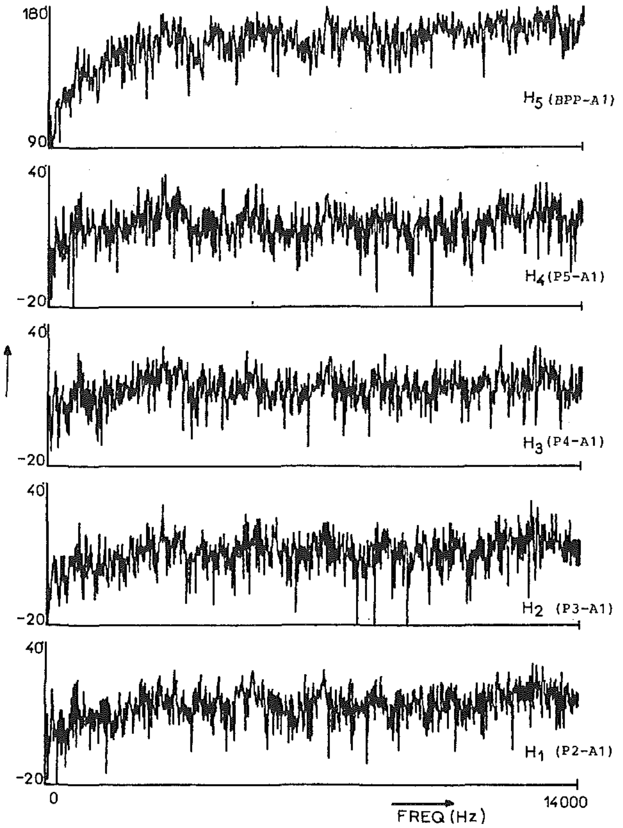

Fig. 10 Amplitudes (in db) of the three transfer function branches between accelerometer A2 and unsteady pressure transducers P2, P3, P4, and P5 and inlet bearing proximity probe: point F

$$[H(f)] = [S_{xy}(f)]^{-1}[S_{xx}(f)] \tag{2}$$

This equation has been implemented together with appropriate averaging procedures, in order to reduce the influence of stochastic noise in the signals (Mathioudakis et al., 1988).

The vector transfer functions are expected to depend on the dynamics of the compressor casing; dependence on operating point is envisaged, only as long as casing temperature variations occur.

Vector transfer functions were calculated from our data, according to the model of Fig. 9(*b*). A representative result is shown in Fig. 10, where we see the transfer function branches for the five inputs and accelerometer A1 as output, for operating point F. During our study we have examined various combinations of inputs and the corresponding transfer functions. The main contributors to a specific output can be determined by discarding some of the inputs and seeing whether significant changes in the result are produced. In this way we have found that the main contributors to each accelerometer are the pressure transducers P2, P3, and P4 (see Fig. 1).

5.2 Dependence on Operating Point. In Fig. 11 we see one branch of the vector transfer functions for operating points H, G, E, and D, which lie on the 9500 rpm speedline. A comparison between them shows that despite small differences, a general similarity exists. This conclusion has been found to be also valid for points on the other two speedlines of 8500 rpm and 11,085 rpm. Since visual inspection or crossplots do not form a proof of similarity, a more rigorous proof for this observation has been given through signal reconstruction, which will be discussed in the next section.

A comparison between corresponding branches for operating points of different speedlines has also been done. In Fig. 12 we can see the results for the operating points J and B, respectively. It is seen that between the 8500 rpm and 9500 rpm speedlines there is a lower degree of similarity, while between them and the 11,085 rpm the degree of similarity becomes even lower.

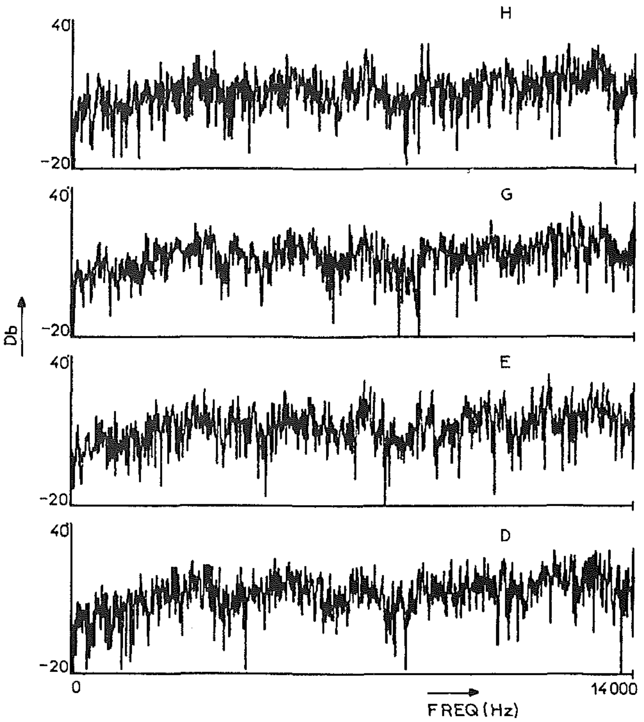

Fig. 11 Transfer function branch H2 for different operating points on the speedline at 9500 rpm

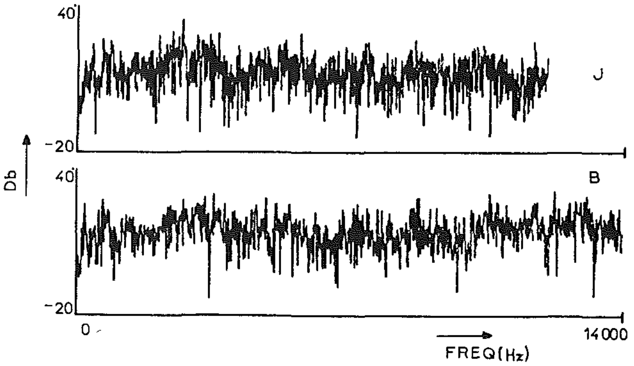

Fig. 12 Transfer function, branch H1, for 8500 rpm, 11,085 rpm

From the above discussion, we can conclude that the calculated transfer function is not fully independent of the operating point, but depends to some extent on the rotational speed and secondarily on the power level. A possible reason for this dependence is the change of temperatures associated with operation at different speeds. Changes of dimensions due to thermal expansion can, for example, reduce clearances between parts, and change the stiffness of the structure. Another possible reason is the bias errors due to our assumption about relations between the distributed inputs in lumping them. In reality the inputs taken into account are associated with the ones that are not, by nonlinear relations. Nonlinearities are expected to exist, mainly with respect to the operating point and aerodynamic excitations. Statistical reasons for this dependence are also present, due to errors resulting from noise in the inputs and the output. These errors decrease with the signal-to-noise ratio; therefore they are expected to be smaller

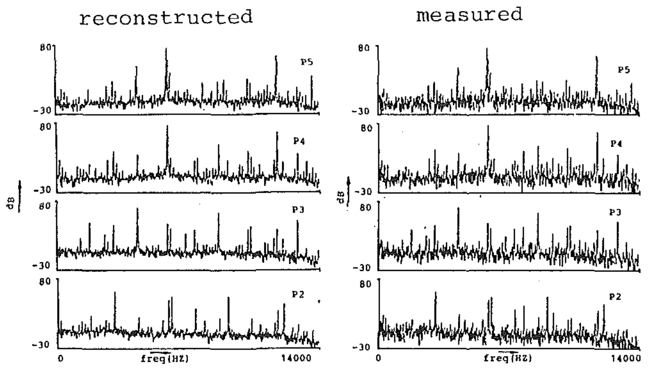

Fig. 13 Comparison between measured and reconstructed power spectra of pressure transducers

at the frequencies of the periodic components (peaks in the spectra) than at the frequencies of the broadband region.

6 Unsteady Pressure Signal Reconstruction

One of the purposes of the transfer function calculations is to enable the reconstruction of the casing excitations when the response is known. We present, now, how this is done.

The unsteady pressure signals of the first four stages' rotors have been reconstructed from the signals of accelerometers A1-A6 by employing the casing transfer function. The four unsteady pressure transducers P2-P5 have been regarded as outputs and the six accelerometers as inputs. This inverse direction modeling is a mathematical way devised to improve the accuracy of the calculations, by avoiding too many matrix inversions.

First the vector transfer functions $[H]$ are established, between each one of the unsteady pressure transducers P2-P5 (as output) and the six accelerometers A1-A6 (as inputs). The test data and relation (2) were used for this purpose. Then, using these transfer functions, the unsteady pressure transducer signal Fourier transforms are calculated. The Fourier transforms $[Y]$ of the pressure signals are calculated, from the transforms $[X]$ of the accelerometers, by means of the relation

$$[Y]=[H]\ [X] \tag{3}$$

Finally from the reconstructed Fourier transforms, the corresponding reconstructed spectral densities are calculated.

Using this procedure, the power spectra for the pressure transducers at the operating point F were reconstructed. The time domain signals of the accelerometers at that operating point were the inputs and a transfer function, resulting from an averaging of transfer functions at all operating points at that speed. A comparison with the corresponding directly calculated spectrum (Fig. 13) shows a very good agreement, particularly at frequencies corresponding to the periodic components of the signals.

The reason for the observed decrease in the level of the broadband random noise is probably the cross-multiplication averaging operations of the Fourier transforms in these frequencies. The corresponding Fourier transform values of the other unsteady pressure transducers or accelerometers involved in the calculation of cross-spectral densities are uncorrelated.

The same has been done for all the other available operating points. The general conclusion drawn is that for any operating point the spectral densities of unsteady pressure transducers P2-P5 can be satisfactorily reconstructed from the accelerometers' A1-A6 signals, using a complex average vector transfer function for the speedline of the operating point. This fact proves also rigorously the conclusion of the previous section, that transfer functions corresponding to different operating points of a speedline are similar. Thus, averaging over the different operating points does not influence the possibility of reconstructing features of the internal pressure signals.

Reconstruction of spectra at operating points on one speedline by using a transfer function evaluated at a different one was also attempted. The conclusion drawn is that, for any operating point, the reconstruction is not very successful when using an average transfer function from a different speedline. This fact confirms the conclusion of the previous section, that the transfer function similarity becomes weaker, when we change speedline. We can finally say that a single transfer function can be established for one rotational speed.

7 Conclusions

The experimental investigation reported above gives the possibility of drawing conclusions about the diagnostic value of the various measured quantities.

Unsteady pressure measurements can be used for identifying the operating condition of rotating blades. Such measurements are expected to provide a clear picture of blading faults.

Accelerometer measurements have the following features:

- The signals from accelerometers on the casing contain information about the operating conditions of compressor stages. Since the corresponding energy content is dominant along the frequency range, appropriate filtering should be employed, when shaft-related problems are considered.
- Each accelerometer signal carries information not only from the stage in its immediate vicinity, but also from other stages along the compressor.
- The vibrations of the compressor casing surface are not symmetrically distributed around the circumference. This fact is of diagnostic value, since accelerometers placed at the same axial location can provide information about stages at other axial locations.

Concerning the casing transfer characteristics:

- Transfer functions have been established, in order to relate pressure transducer outputs to those of accelerometers.
- Transfer functions from operating points at a certain speedline are similar, while transfer functions for different speeds show a smaller degree of similarity.

Using transfer functions, the power spectra of pressure transducers have been reconstructed using the accelerometer signals as inputs. It was shown that the reconstruction is successful by using one single transfer function for one rotational speed.

These last conclusions prove that: By following appropriate techniques, such as the ones we applied, it is possible to deduce information about phenomena at the engine interior, from measurements on the casing. In principle, it seems that it will be possible to diagnose engine condition from such measurements.

Acknowledgments

The work reported in this paper has been carried out within the frame of research contract BRITE No. RI 1B-0159-F(CD). The authors express their thanks to the Hellenic General Secretariat for Research and Technology and the European Communities, for their financial support. Thanks are expressed to METRAVIB RDS and RUSTON GAS TURBINES, for providing the instrumentation and the test engine. The experiments were possible only by their cooperation. Special thanks are due to Mr. M. K. Smith for valuable discussions and suggestions and to Dr. P. Wetta for his excellent cooperation in preparing and executing the experiments.

References

Baines, N., 1987, *Modern Vibration Analysis in Condition Monitoring Noise and Vibration Control Worldwide*, May, pp. 148-151.

Barschdorff, D., and Korthauer, R., 1986, "Aspects of Failure Diagnosis on Rotating Parts of Turbomachines Using Computer Simulation and Pattern Recognition Methods," Paper No. H1, International Conference on Condition Monitoring, Brighton, United Kingdom, May 21-23.

Bendat, J. S., and Piersol, A. G., 1971, *Random Data: Analysis and Measurement Procedures*, Wiley-Interscience, New York.

Bently, D., Zimmer, S., Palmatier, G., and Muszynska, A., 1986, *Interpreting Vibration Information From Rotating Machinery. Noise and Vibration Control Worldwide*, Part I, June, pp. 174-176; Part 2, July.

Carchedi, F., and Wood, G. R., 1982, "Design and Development of a 12:1 Pressure Ratio Compressor for the Ruston 6-MW Gas Turbine," ASME JOURNAL OF ENGINEERING FOR POWER, Vol. 104, pp. 823-831.

Laws, W., and Muszynska, A., 1987, "Periodic and Continuous Vibration Monitoring for Preventive/Predictive Maintenance of Rotating Machinery," ASME JOURNAL OF ENGINEERING FOR GAS TURBINES AND POWER, Vol. 109, pp. 159-167.

Lifshits, A., Simmons, H., and Smalley, A., 1986, "More Comprehensive Vibration Limits for Rotating Machinery," ASME JOURNAL OF ENGINEERING FOR GAS TURBINES AND POWER, Vol. 108, pp. 583-590.

Lifson, A., Quentin, G. H., Smalley, A. J., and Knauf, C. L., 1989, "Assessment of Gas Turbine Vibration Monitoring," ASME JOURNAL OF ENGINEERING FOR GAS TURBINES AND POWER, Vol. 111, pp. 257-263.

Mathioudakis, K., Loukis, E., Stamatis, A., and Papailiou, K. D., 1988, "Noise/Vibration Imaging Techniques for Gas Turbine Investigations," Project Report No. 3, BRITE project No. 1368, June.

Timperley, S., and Smith, M. K., 1983, "A Data-Logging and Performance Analysis System for Application to Industrial Gas Turbines," ASME Paper No. 83-GT-104.

Wood, G. R., 1981, "The Ruston Tornado. A 6-MW Gas Turbine for Industrial Application," ASME Paper No. 81-GT-171.

Some Composite Bearing and Seal Materials for Gas Turbine Applications—A Review

H. E. Sliney
NASA Lewis Research Center,
Cleveland, OH 44135

A review is given of the selection and tribological testing of materials for high-temperature bearings and seals. The goal is to achieve good tribological properties over a wide range of temperatures, because bearings and seals must be functional from low-temperature start-up conditions on up to the maximum temperatures encountered during engine operation. Plasma-sprayed composite coatings with favorable tribological properties from 25 to 900°C are discussed. The performance of these coatings in simple tribological bench tests is described. Examples are also given of their performance in high-speed sliding contact seals, as Stirling cylinder liner materials, and as backup lubricants for compliant foil gas bearings.

Introduction

As gas turbine engine designs become more complex, the need for high-temperature bearing and seal materials increases. For example, many modern gas turbine engines contain variable stator vanes (VSV) in the compressors (see Fig. 1). These vanes are nonrotating, but their angle of attack or pitch is variable. Each vane requires two sliding contact pivot seals that are basically cylindrical bearings with a thrust collar. In the downstream stages of the compressor, gas temperatures can be on the order of 540°C and the pivot seal material temperature is about 370°C (700°F). A high-temperature polyimide polymer with graphite fiber/fabric reinforcement is a material of choice for this application. This material was chosen after the results of extensive laboratory research at several laboratories, which demonstrated its favorable tribological properties, were reported (e.g., Giltrow and Lancaster, 1968; Sliney and Johnson, 1972; Sliney and Jacobson, 1975; Sliney, 1979a, 1979b; Fusaro and Sliney, 1978; Gardos and McConnell, 1982). Engine performance could be further improved by also employing variable stator vanes in the turbine section. Turbine VSV components will require self-lubricating pivot materials capable of operating at much higher temperatures, possibly up to 1500°C. This of course is well beyond the thermal capabilities of polymer composites. Satisfactory materials for turbine VSV bushings must have very good thermochemical stability and have sufficiently low friction and wear to allow actuation with modest forces and to provide adequate durability. The well-known graphite and molybdenum disulphide (MoS_2) solid lubricants are oxidatively unstable in air above about 300°C for long-duration applications and in some cases, can possibly be used at higher temperatures for a short duration (Sliney, 1982). The oxidation rate of carbon/graphite can be reduced by formulating the graphite with oxidation-inhibiting additives (Wedeven and Harris, 1987). The maximum service temperature in air for formulated long-life carbon/graphite components is generally accepted to be about 500°C.

For even higher temperature applications, more novel solid lubricating materials are needed. The materials must be chemically stable at high temperatures and must also have the physical properties needed to make them lubricative. The scope of this paper encompasses: (1) a discussion of the selection of

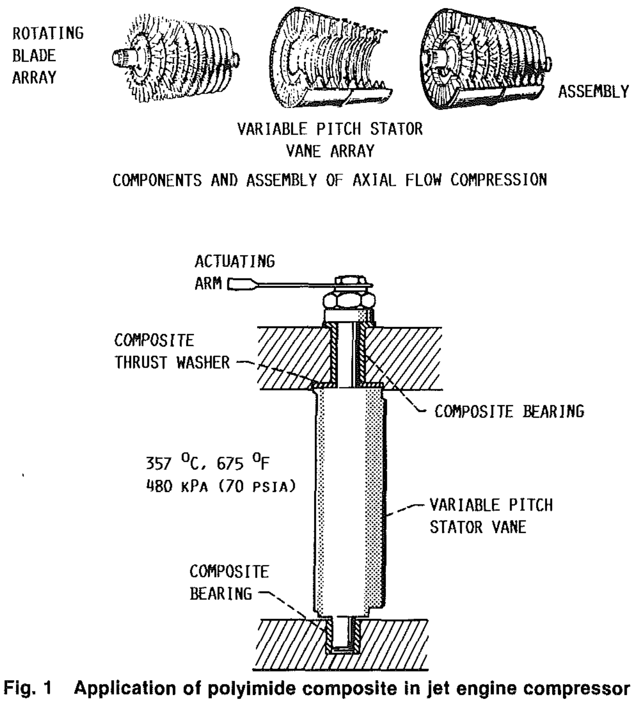

Fig. 1 Application of polyimide composite in jet engine compressor

---

Contributed by the International Gas Turbine Institute and presented at the 34th International Gas Turbine and Aeroengine Congress and Exhibition, Toronto, Ontario, Canada, June 4–8, 1989. Manuscript received at ASME Headquarters January 23, 1989. Paper No. 89-GT-144.

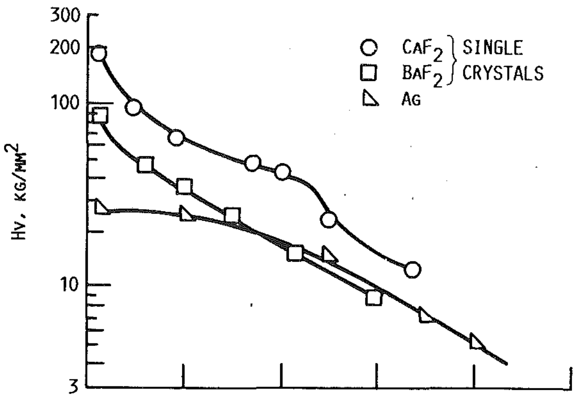

(A) HOT HARDNESS.

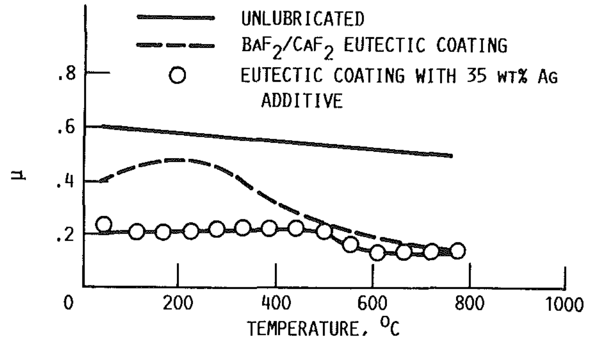

(B) FRICTION.

Fig. 2 Effect of temperature on microhardness and friction coefficients of coating materials

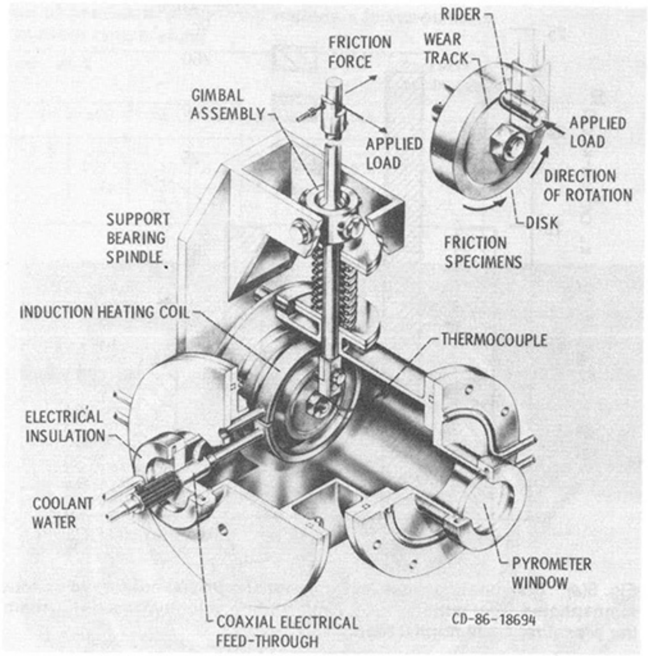

Fig. 3 Pin-on-disk tribometer

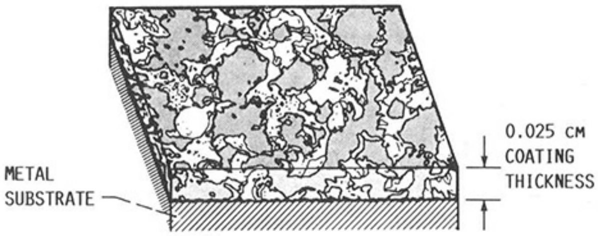

COMPOSITION	CHARACTERISTICS
32% Ni ALLOY 48% Cr_3C_2	WEAR AND OXIDATION RESISTANT METAL BONDED CARBIDE
10% Ag	LOW TEMPERATURE START UP LUBRICANT WITH HIGH TEMPERATURE OXIDATION RESISTANCE
10% BaF_2/CaF_2 EUTECTIC	HIGH TEMPERATURE LUBRICANT

● LUBRICATES IN AIR, HELIUM, OR HYDROGEN TO +900 °C

Fig. 4 Concept of PS200, a plasma-sprayed composite solid lubricant coating

such materials; (2) the formulation of self-lubricating plasma-sprayed composite coatings with wide temperature spectrum capability; (3) the basic friction and wear of these composites; and (4) examples of prototype applications.

Materials Selection

A solid lubricant material for high-temperature use must have good thermochemical stability, a stable crystal structure over the temperature range of interest, and an adequately high melting point. Solid lubricant coatings should be formulated to have a thermal expansion coefficient that reasonably matches the intended substrate in order to prevent spalling during temperature excursions. Important properties of solid lubricants in general are: They are soft; they have a high degree of plasticity (the plasticity must be associated with a low yield strength in shear for lubricity); and they must adhere tenaciously to the lubricated surfaces because the material cannot perform a lubricating function if it is not retained within the sliding interface.

We have used calcium fluoride, barium fluoride, and silver as solid lubricants in our high-temperature coatings. They satisfy the chemical and physical criteria over specific ranges of temperatures. Thermochemical calculations indicate that these materials should be chemically stable to high temperatures in air or in hydrogen and this has been experimentally verified. The hardness-temperature characteristics of these two fluorides and of metallic silver were reported by Deadmore and Sliney (1987) and are given in Fig. 2(*a*). Silver is very soft at room temperature with a hardness of about 30 kg/mm^2 and this continuously decreases to about 4 kg/mm^2 at 800°C. Thin films of silver lubricate quite well at temperatures up to about 500°C, but appear to have inadequate film strength to support a load at higher temperatures. The fluorides, on the other hand, are considerably harder than silver at the lower temperatures, but their hardness drops off rapidly with temperature and at about 400°C, their hardnesses are 30 kg/mm^2 or less. Also, brittle to ductile transition temperatures, at high strain rates, of 300 to 400°C have been reported for these fluorides (Phillips, 1961; Burn and Murray, 1962; Liu and Li, 1964). Fluoride coatings have been shown to be lubricious above 400°C, but ineffective as lubricants at lower temperatures (Sliney, 1986). Therefore, there is an apparent correlation of hardness-temperature characteristics and of the brittle to ductile transition temperature with the friction-temperature characteristics.

Since silver films are lubricative at the lower temperatures and the fluorides discussed are lubricative at higher temperatures than silver, it is reasonable that a composite coating containing silver and the fluorides might be lubricious over a wide temperature range, and this has been demonstrated repeatedly in our research (Sliney, 1979a, 1986). Figure 2(*b*) illustrates this point. The friction-temperature characteristics of 0.02-mm-thick fused fluoride coatings with and without silver, which were prepared by a process similar to porcelain enameling, are compared. The data were obtained with a pin-

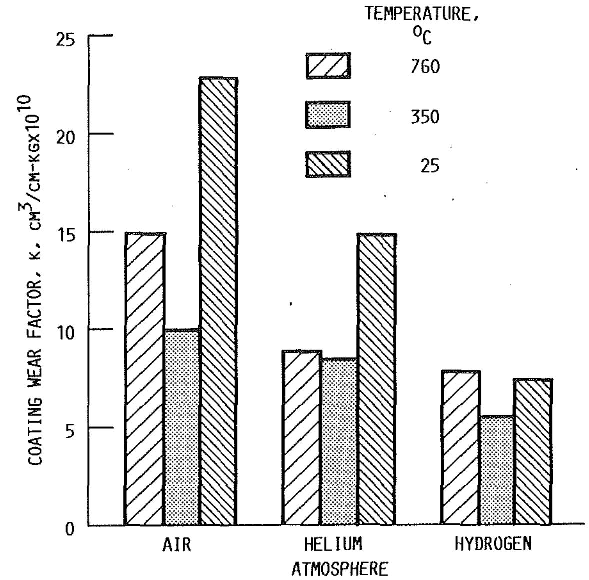

Fig. 5(*a*) Disk coating wear factor, *k*, for the PS200 coating in various atmospheres. Test conditions: 2.7 m/s sliding velocity, 38.97 kPa chamber pressure, 4.9 N normal load.

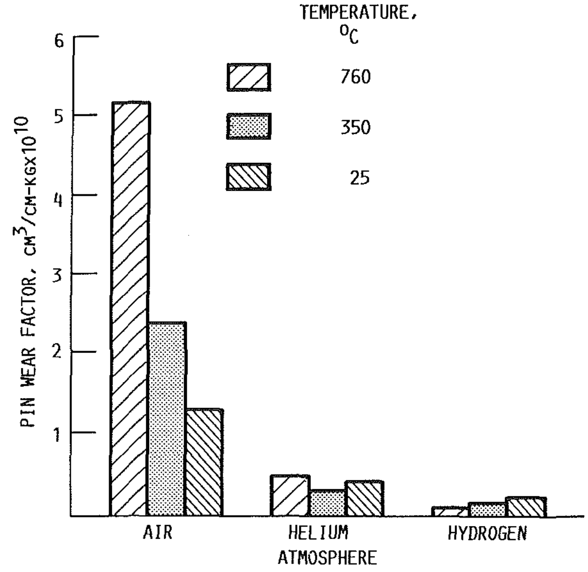

Fig. 5(*b*) Pin wear factor, *k*, for the hardened cobalt alloy tested against the PS200 coating in various test atmospheres. Test conditions: 2.7 m/s sliding velocity, 38.97 kPa chamber pressure, 4.9 N normal load.

on-disk tribometer illustrated in Fig. 3. The all-fluoride coatings were lubricious only above about 400°C, while the coatings that also contained silver lubricated from room temperature to 800°C. These results with relatively thin coatings were followed by research with thicker plasma-sprayed coatings.

Plasma-Sprayed Coatings

We have reported two series of plasma-sprayed coatings containing fluoride solid lubricants: the PS100 and the PS200 series (Sliney, 1979b; DellaCorte and Sliney, 1987). The PS100 series contains stable fluorides and silver with a nichrome binder; the PS200 series contains the same lubricants and chromium carbide with a nickel-cobalt alloy binder. The proportions of the components can be varied to optimize the coatings for various uses. In general, coatings in the PS100 series, which are softer, have been useful in applications where a slightly compliant, but nongalling coating is needed. One example of this type of application is a knife-edge high-speed shaft seal.

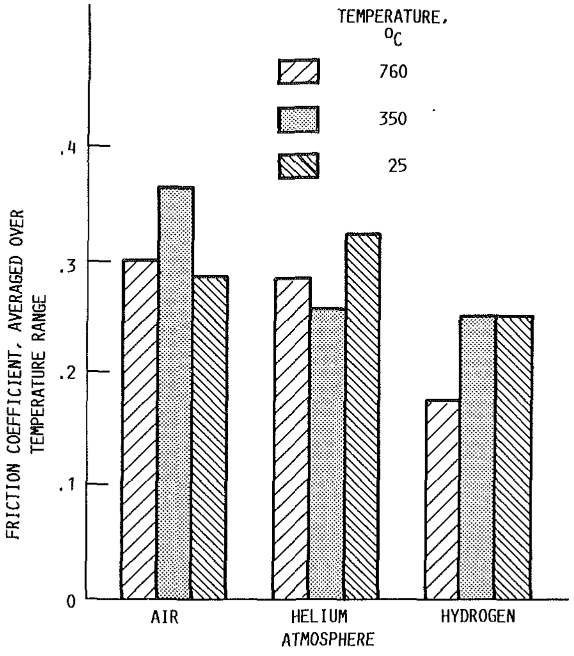

Fig. 6 Friction coefficient for PS200 sliding against hardened cobalt alloy in various atmospheres. Test conditions: 2.7 m/s sliding velocity, 38.97 kPa chamber pressure, 4.9 N normal load.

In this type of seal, circumferential raised knife edges on the shaft slide against a coated seal housing. Thermal expansion or run-out causes the knife edges to contact and deform the coating to provide a seal. This seal material is conformable and relatively dense rather than abradable, and therefore minimizes secondary leakage compared to that which occurs through porous abradable seals. The PS100 coating is also much more resistant to erosion by particulates carried in the gas path. The wear coefficient *k* for the PS100 series of coatings is on the order of 10^{-5} mm^3/Nm (moderate wear regime) and the friction coefficient is typically 0.21 to 0.25.

When more wear-resistant coatings are needed, the PS200 series is preferable. The PS200 concept is summarized in Fig. 4. As the sketch indicates, the coating is a composite material with the lubricating solids distributed throughout a wear-resistant chromium carbide/nickel alloy matrix. A typical composition consists of 10 wt percent each of silver and calcium fluoride/barium fluoride eutectic in the metal-bonded chromium carbide matrix.

Friction and Wear of PS200 Plasma-Sprayed Coatings

The wear and friction of PS200 coatings in sliding contact with Stellite 6B, a cobalt-chromium base alloy, in three different atmospheres—air, helium, and hydrogen—are given in Figs. 5 and 6 (from DellaCorte and Sliney, 1988). Tests in hydrogen give the lowest friction and wear. Friction coefficients are typically 0.23 ± 0.05. Coating wear factors (*k*) are about 6×10^{-6} mm^3/Nm and pin wear factors are in the 10^{-7} mm^3/Nm range. This is generally considered to be in the very mild to low wear regime. Friction and wear are moderately higher in helium and still higher in air. In general, friction and wear increase somewhat as the test atmosphere chemistry changes from reducing, to inert, to oxidizing. The maximum test temperature in these tests was 760°C. We have shown elsewhere that the PS200 coating has potential applicability to 900°C (Sliney, 1986). However, oxidative wear may limit coating durability in air above about 700°C.

In addition to Stellite 6B, several other alloys were tested as counterface pin materials for sliding against PS200. The nominal chemical compositions of these alloys are given in Table

Table 1 Nominal composition and Rockwell hardness of candidate piston ring materials [compositions are taken from manufacturers' data; hardness values at room temperature]

Pin material	Element. wt %														Rockwell hardness
	Ni	Cr	Co	C	Fe	Al	Si	Ti	Mo	Mn	B	W	N	Cb	
Inconel X-750	70	16	1	0.1	7.5	1	----	2.5	----	1	---	-	----	---	R_C40
XF818	18	18	--	.2	54.6	-	0.3	---	7.5	.15	0.7	-	0.12	0.4	R_C18
Stellite 6B	2.	30	59	1	1	-	.75	---	.75	1.25	---	4	----	---	R_C42
Nitronic 60	8	18	--	.1	61.8	-	4.0	---	----	.8	---	-	.12	---	R_C28

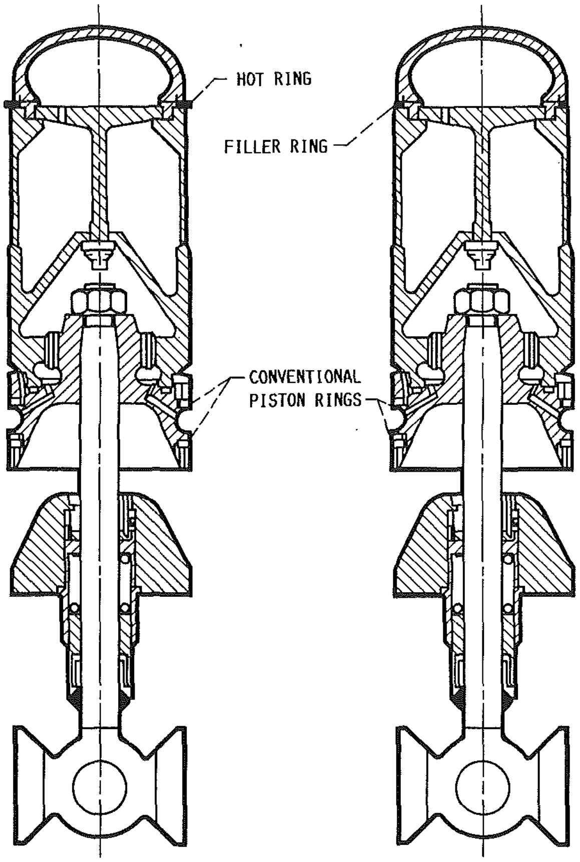

MOD I ENGINE PISTON WITH HOT RING

MOD I ENGINE PISTON WITH FILLER RING

Fig. 7 Piston configurations

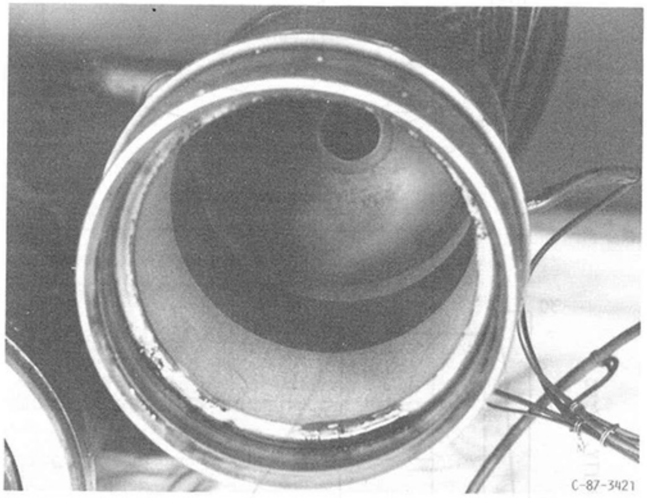

Fig. 8 PS200 coating on Stirling engine cylinder after 22-h engine test with "hot rings"

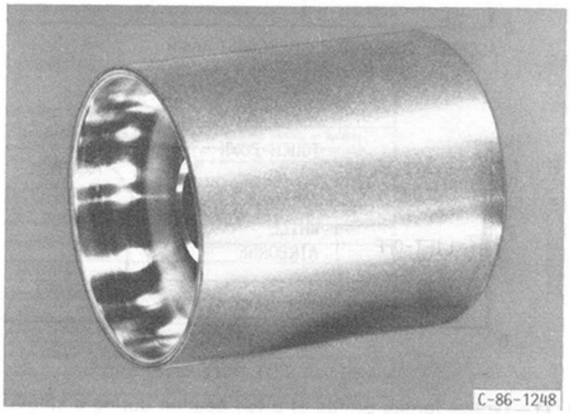

Fig. 9 Gas bearing journal coated with PS200 and finished by diamond grinding (successfully completed 10,000 start/stop rubs in a foil gas bearing at temperatures up to 650°C)

1. However, none of them were as effective as Stellite 6B on PS200. This material combination was subsequently selected as a piston ring/cylinder liner material combination for evaluation in a Stirling engine in a "Hot Piston Ring" development program. The results of this program are summarized below.

Application Tests of PS200

Stirling Engine Cylinder Liner. The lubrication of the piston ring/cylinder contacts in the Stirling automotive engine is a challenging high-temperature tribological problem. Metal temperatures are as high as 600 to 1000°C near the top of the cylinder walls. The working fluid in the engine thermodynamic cycle is hydrogen. The lubricant coating, therefore, must not only provide low friction and wear, but also must be thermochemically stable in a strongly reducing hydrogen atmosphere.

In current designs of the Stirling engine, the piston rings are made of reinforced polytetrafluoroethylene (PTFE). They are located in ring grooves near the bottom of the piston where the temperatures are relatively low and do not degrade the PTFE. This arrangement results in a long annular "appendix" gap from the top of the piston to the piston ring. This gap is the source of parasitic energy losses (Tomazic, 1985). It is therefore desirable to minimize the appendix gap by locating the top ring in a groove near the top of the piston. A schematic of the ring locations in a conventional baseline piston and in a piston with an added top (hot) ring are shown in Fig. 7.

A Mechanical Technology Inc. (MTI) designed Stirling engine was modified to allow the use of hot piston rings. The cylinders were bored out to allow for a PS200 coating thickness of 0.25 mm (0.010 in.) and the pistons were modified to accept the Stellite 6B piston rings. The coatings were sprayed on the cylinder walls to a thickness of about 0.35 mm (0.015 in.), then diamond ground to a final thickness of 0.25 mm. Engine tests reported by Sliney (1988) were run at a heater head temperature of 700°C and 5, 10, and 15 MPa mean operating pressure over a range of operating speeds. Tests were run both with the "hot rings" in place and without them to provide a baseline for comparison.

At some operating conditions, efficiency, as calculated from specific fuel consumption, increased slightly compared to the

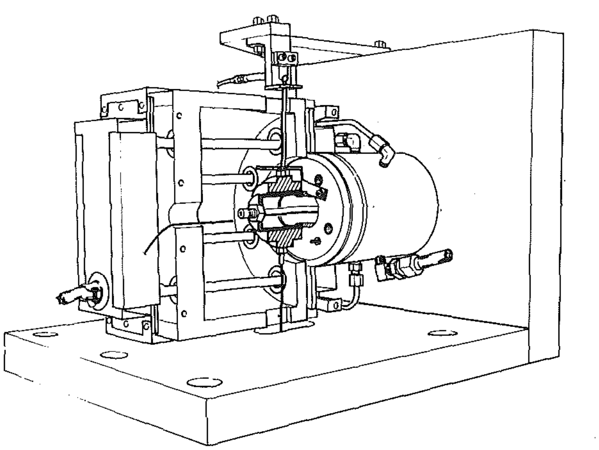

Fig. 10 Foil bearing test machine

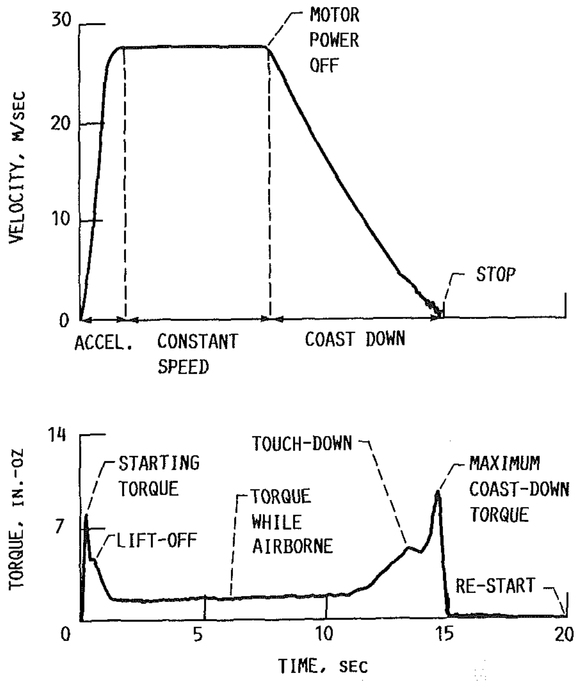

Fig. 11 Typical torque profile of a foil bearing during a single start/stop cycle

baseline engine. Under other conditions, no significant differences in efficiency were measured. The overall average indicated about a 3 percent increase in efficiency with the "hot rings" over the baseline configuration. This increase was over and above the additional friction loss introduced by the "hot rings." Seal leakage measurements showed a significant reduction in leakage with the "hot ring" in place. In addition, cylinder wall temperature measurements indicated less cylinder heating between the lower piston rings and the "hot ring." Approximately 22 h of ring-on-coating operation were recorded. Figure 8 is a photograph of the coated cylinder wall after the engine test. The dark, polished surface is the area swept by the piston ring. The results of applying PS200 to the Stirling Engine cylinder walls are encouraging. Overall engine efficiency was improved and post-test wear measurements indicate that the coated engine components could have been run considerably longer, at least several hundred hours. This solid lubricated Stirling Engine test indicates a potential usefulness of long life, self-lubricating materials for improved engine and mechanism efficiency and for other high-temperature applications such as gas bearings.

Gas Bearings. Figure 9 is a gas bearing journal coated with PS200 and finished by diamond grinding. Start-stop tests of this journal in a foil bearing were conducted in an air atmosphere using the test apparatus shown in Fig. 10 and reported by Wagner and Sliney (1986). The surface velocity and torque profiles during a typical start-stop cycle are shown in Fig. 11. The higher torque at the beginning and end of each cycle occurs during sliding contact when the surface velocity is below the critical lift-off velocity for the bearing. It is during these low operating speed periods that solid lubrication must be provided for the bearing. PS200 coatings on the journals provide this lubrication. Foil bearings with PS200 coated journals have routinely survived life tests in air consisting of 10,000 starts and stops (20,000 rubs) at bearing temperatures from 25 to 650°C.

Concluding Remarks

This paper has reviewed some of the high-temperature solid lubrication research performed at NASA Lewis Research Center that appears to be applicable to gas turbine technology. Some of the more significant considerations are the following:

1 For the high-temperature requirements in gas turbine engines, conventional solid lubricants such as graphite and molybdenum disulphide do not have the required thermal-oxidative stability. It is proposed that selection criteria for new solid lubricants must include chemical stability at high temperatures, plasticity, low yield strength in shear, and low hardness.

2 Mixtures of calcium fluoride, barium fluoride, and silver have shown promise in thin fused coatings and in plasma-sprayed coatings for lubricating from room temperature to at least 760°C in hydrogen, helium, and air. Lubrication is more effective in hydrogen than in air, but the coatings have been successful in long-term start-stop testing as air bearings at 650°C. The maximum useful temperature of these coatings is estimated to be about 900°C (just below the melting point of silver: 961°C).

3 Plasma-sprayed composite coatings of metal-bonded chromium carbide, calcium fluoride/barium fluoride eutectic, and silver have been successful as seal and bearing lubricants in component testing under conditions considered to be relevant to gas turbine applications.

References

Burn, R., and Murray, G. T., 1962, "Plasticity and Dislocation Etch Pits in CaF_2," *Journal of the American Ceramic Society*, Vol. 45, No. 5, pp. 251-252.

Deadmore, D. L., and Sliney, H. E., 1987, "Hardness of CaF_2 and BaF_2 Solid Lubricants at 25 to 670°C," NASA TM-88979.

DellaCorte, C., and Sliney, H. E., 1987, "Composition Optimization of Self-Lubricating Chromium Carbide Based Composite Coatings for Use to 760°C," *ASLE Transactions*, Vol. 30, No. 1, pp. 77-83.

Della Corte, C., and Sliney, H. E., 1988, "The Effects of Atmosphere on the Tribological Properties of a Chromium Carbide Based Coating for Use to 760°C," *Lubrication Engineering*, Vol. 44, No. 4, pp. 338-344.

Fusaro, R. L., and Sliney, H. E., 1978, "Friction and Wear Behavior of Graphite Fiber Reinforced Polyimide Composites," *ASLE Transactions*, Vol. 21, No. 4, pp. 337-343.

Gardos, M. N., and McConnell, B. D., eds., 1982, *Development of a High-Load, High-Temperature, Self-Lubricating Composite*, ASLE SP-9, American Society of Lubrication Engineering, Park Ridge, IL.

Giltrow, J. P., and Lancaster, J. K., 1968, "Carbon-Fiber Reinforced Polymer as Self-Lubricating Materials," *6th Tribology Group Convention*, Pitlochry, Scotland, Institute of Mechanical Engineers, England, pp. 149-159.

Liu, T. S., and Li, C. H., 1964, "Plasticity of Barium Fluoride Single Crystals," *Journal of Applied Physics*, Vol. 35, No. 11, pp. 3325-3330.

Phillips, W. L., Jr., 1961, "Deformation and Fracture Processes in Calcium Fluoride Single Crystals," *Journal of the American Ceramic Society*, Vol. 44, No. 10, pp. 499-506.

Sliney, H. E., and Johnson, R. L., 1972, "Graphite Fiber-Polyimide Composites for Spherical Bearings to 340°C," NASA TN D-7078.

Sliney, H. E., and Jacobson, T. P., 1975, "Performance of Graphite Fiber-

Reinforced Polyimide Composites in Self-Aligning Plain Bearings to 315°C," *Lubrication Engineering*, Vol. 31, No. 12, pp. 609-613.

Sliney, H. E., 1979, "Wide Temperature Spectrum Self-Lubricating Coatings Prepared by Plasma Spraying," *Thin Solid Films*, Vol. 64, pp. 211-217.

Sliney, H. E., 1979, "Some Load Limits and Self-Lubricating Properties of Plain Spherical Bearings With Molded Graphite Fiber-Reinforced Polyimide Liners to 320°C," *Lubrication Engineering*, Vol. 35, No. 9, pp. 497-502.

Sliney, H. E., 1982, "Solid Lubricant Materials for High Temperatures—A Review," *Tribology International*, Vol. 15, No. 5, pp. 303-315.

Sliney, H. E., 1986, "The Use of Silver in Self-Lubricating Coatings for Extreme Temperatures," *ASLE Transactions*, Vol. 29, No. 3, pp. 370-376.

Sliney, H. E., 1988, "Hot Piston Ring/Cylinder Liner Materials—Selection and Evaluation," SAE Paper 880544; NASA TM-100276.

Tomazic, W. A., 1985, "Stirling Engine Supporting Research and Technology," NASA TM-87175.

Wagner, R. C., and Sliney, H. E., 1986, "Effects of Silver and Group II Fluoride Solid Lubricant Additions to Plasma-Sprayed Chromium Carbide Coatings for Foil Gas Bearings to 650°C," *Lubrication Engineering*, Vol. 42, No. 10, pp. 594-600.

Wedeven, L. D., and Harris, T. A., 1987, "Rolling Element Bearings Operating at the Extremes," *Machine Design*, Vol. 59, No. 18, Aug. 6, pp. 72-76.

A Review of Failure Models for Ceramic Matrix Composite Laminates Under Monotonic Loads

D. E. Tripp[1]

J. H. Hemann

Department of Civil Engineering,
Cleveland State University,
Cleveland, OH 44115

J. P. Gyekenyesi

NASA Lewis Research Center
Cleveland, OH 44135

Ceramic matrix composites offer significant potential for improving the performance of turbine engines. In order to achieve their potential, however, improvements in design methodology are needed. In the past most components using structural ceramic matrix composites were designed by "trial and error" since the emphasis on feasibility demonstration minimized the development of mathematical models. To understand the key parameters controlling response and the mechanics of failure, the development of structural failure models is required. A review of short-term failure models with potential for ceramic matrix composite laminates under monotonic loads is presented. Phenomenological, semi-empirical, shear-lag, fracture mechanics, damage mechanics, and statistical models for the fast fracture analysis of continuous fiber unidirectional ceramic matrix composites under monotonic loads are surveyed.

Introduction

Ceramic matrix composites offer significant potential for improving the thrust-to-weight ratio of gas turbine engines by enabling higher cycle temperatures with the use of refractory, high specific strength material systems. Adding a reinforcing or toughening second phase with optimal interfacial bonding improves fracture toughness and decreases the sensitivity of the brittle matrix to pre-existing flaws. The reinforcing second phase can have a variety of shapes, ranging from nearly spherical particles, through wiskers and chopped fibers with various length-to-diameter ratios, to continuous fibers. Aveston et al. (1971) have shown, however, that the addition of continuous small-diameter fibers reinforces ceramics most efficiently since their orientation in the direction of the principal load significantly enhances the matrix cracking strain, as well as the ultimate load carrying capability of the composite.

The primary purpose of this increase in toughness is to allow for a "graceful" rather than catastrophic failure as opposed to an increase in the ultimate strength, although in high fiber volume fraction composites, that may also occur. Ceramic matrix composites retain substantial strength and strain capability beyond the initiation of first matrix cracking despite the fact that neither of its constituents would exhibit such behavior if tested alone. First matrix cracking occurs at a strain greater than that in the monolithic ceramic alone. As additional load is applied beyond first matrix cracking, the matrix will break in a series of transverse cracks bridged by reinforcing fibers. Additional load is borne by the fibers until the ultimate strength of the composite is reached. The desired design stress limit, however, should be less than the matrix cracking stress as cracking allows oxidation of the fibers, especialy at elevated temperatures, which causes increased fiber-matrix bonding and embrittlement of the composite.

In the past, most components using structural ceramic matrix composites were designed by "trial and error," since the emphasis was on feasibility demonstration rather than on fully understanding the parameters' controlling behavior. In addition, the continuous change and development of these material systems and the lack of standardized design data minimized the emphasis on mathematical modeling. To gain insight into the mechanisms of failure, and to understand the parameters' controlling response, development of structural failure models is required.

The objective of this survey is to investigate appropriate failure models, which may be applicable to the fast fracture analysis of continuous fiber unidirectional ceramic matrix composite lamina under monotonic loading, both for first matrix cracking and ultimate strength. Much of this methodology has been adapted from existing polymer matrix composites technology. Phenomenological, semi-empirical, shear-lag, fracture mechanics, damage mechanics, and statistical models are surveyed. Although semi-empirical models apply to multidirectional laminates, they are included here for completeness. The emphasis is not on evaluating the models in detail; more complete surveys are available elsewhere. Rather the ability of the models to predict the fast fracture of ceramic matrix composites is discussed.

Future work will selectively implement these models and others to be developed into an integrated composite design code for the reliability analysis of ceramic matrix composites for use by industry in designing heat engine components. Because a general purpose code is desired, failure criteria applicable to unidirectional lamina are preferred. Laminate failure

---

[1] NASA Resident Research Associate.

Contributed by the International Gas Turbine Institute and presented at the 34th International Gas Turbine Aeroengine Congress and Exhibition, Toronto, Ontario, Canada, June 4-8, 1989. Manuscript received at ASME Headquarters January 25, 1989. Paper No. 89-GT-153.

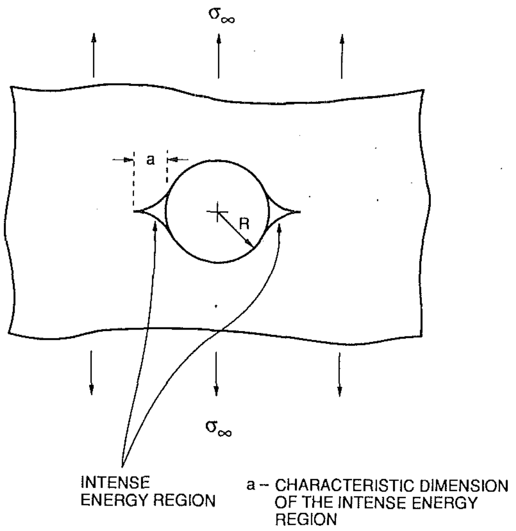

Fig. 1 Semi-empirical model for circular hole showing assumed intense energy region

criteria would require the characterization of each laminate configuration under consideration. Classical lamination theory can be used to determine the failure of the laminate from the failure of the individual lamina. The authors are aware (Labossiere and Neale, 1987) that variation of the stacking sequence will affect the strength of a laminate, while classical lamination theory predicts the same strength if the layers in a symmetric laminate are rearranged into another symmetric laminate. This issue will also be addressed in the future.

Phenomenological Failure Criteria

A number of theories exist to predict the failure of homogeneous isotropic materials under general states of stress using the material properties obtained from simple uniaxial tension, compression, and shear tests. Generalizations of these criteria for homogeneous, isotropic materials have been proposed as failure criteria for fiber-reinforced composites that are anisotropic and inhomogeneous. These phenomenological criteria are the most familiar to design engineers. Consequently, models such as maximum stress, maximum strain, Azzi–Tsai (Azzi and Tsai, 1965), and Tsai–Wu (Tsai and Wu, 1971) are currently the most frequently used in industry to design polymer matrix components according to a user survey by Burk (1983) and Soni (1983).

Two excellent reviews of phenomenological failure criteria are by Nahas (1986) and Labossiere and Neale (1987). Other surveys of phenomenological anisotropic failure theories exist (Sandhu, 1972; Bert et al., 1969; Kaminski and Lantz, 1969; Sendeckyj, 1972; Vicario and Toland, 1975; Rowlands, 1975; Tsai, 1984; Snell, 1978). Nahas, in his review, classifies failure criteria into four categories: direct laminate criteria, limit criteria, interaction criteria, and tensor polynomial criteria. In the direct laminate approach the failure criterion is applied to the entire laminate, which is considered homogeneous but anisotropic. This requires the strength characterization of each laminate under consideration; thus, these criteria are not amenable to a general purpose code as discussed earlier and are not considered further.

In the ply-by-ply approach, into which the other three categories fall, the lamina is considered to be homogeneous and orthotropic. Lamination theory is used to find the stresses in each lamina and these stresses are transformed to the lamina principal material axes before the failure criteria are applied. The direction of the principal stresses or strains have no significance for isotropic materials. However, strength varies with direction in composites, and generally the direction of maximum strength does not necessarily coincide with the direction of principal stress. Thus, the highest stress may not be the stress governing the design, and a comparison of the actual stress field with the allowable stress field is required. The allowable stress field for a unidirectional composite is given by the strengths in the principal material direction. They are the longitudinal tensile strength, longitudinal compressive strength, transverse tensile strength, transverse compressive strength, and in-plane shear strength.

Limit criteria, the first category in the ply-by-ply approach, assume that failure occurs when the stress in one of the principal material directions exceeds the allowable value. The maximum stress criterion and the maximum strain criterion are examples of limit criteria, that is

Maximum stress

$$X' \leq \sigma_1 \leq X, \quad Y' \leq \sigma_2 \leq Y, \quad |\tau_{12}| \leq S$$

Maximum strain

$$\epsilon'_{1U} \leq \epsilon_1 \leq \epsilon_{1U}, \quad \epsilon'_{2U} \leq \epsilon_2 \leq \epsilon_{2U}, \quad |\gamma_{12}| \leq \gamma_{12U} \tag{1}$$

where σ and τ are the stresses, ϵ and γ are the strains, X, Y, and S are the longitudinal, transverse and shear strengths, prime (′) denotes compressive strength, the subscripts 1 and 2 denote longitudinal and transverse directions, and U is the ultimate strength or strain.

Stowell and Liu (1961), Kelly and Davies (1965), and Prager (1969) suggested additional variations of the maximum stress criterion. Hu (1985), Wasti (1970), and Lance and Robinson (1971) have proposed generalizations of Tresca's maximum shear stress criterion for anisotropic materials.

Hill (1948) proposed an interactive criterion by generalizing the Von Mises Hencky maximum distortional energy theory to include anisotropy in metals such as cold rolled steel. It is assumed that the yield condition is a quadratic function of the stress components

$$\begin{aligned} 2f(\sigma_{ij}) \equiv F(\sigma_2-\sigma_3)^2 + G(\sigma_3-\sigma_1)^2 + H(\sigma_1-\sigma_2)^2 \\ + 2L\tau_{23}^2 + 2M\tau_{31}^2 + 2N\tau_{12}^2 = 1 \end{aligned} \tag{2}$$

where F, G, H, L, M, and N are material coefficients characteristic of the state of anisotropy, and the subscripts i and j refer to the material axes. Linear terms were not included since it was assumed that there is no Bauschinger effect. Hill showed that the material coefficients are functions of the material characteristic strengths, and that for plane stress the criterion reduces to

$$\left(\frac{\sigma_1}{X}\right)^2 + \left(\frac{\sigma_2}{Y}\right)^2 - \left(\frac{1}{X^2} + \frac{1}{Y^2} - \frac{1}{Z^2}\right)\sigma_1\sigma_2 + \left(\frac{\tau_{12}}{S}\right)^2 = 1 \tag{3}$$

Azzi and Tsai (1965) suggested that Hill's criterion be modified for composites by assuming that the material is transversely isotropic and setting $Y = Z$.

$$\left(\frac{\sigma_1}{X}\right)^2 + \left(\frac{\sigma_2}{Y}\right)^2 - \left(\frac{\sigma_1\sigma_2}{X^2}\right) + \left(\frac{\tau_{12}}{S}\right)^2 = 1 \tag{4}$$

This criterion is also referred to as the Tsai–Hill or maximum work criterion.

Hoffman (1967) modified Hill's criterion to take into account the differences between tensile and compressive strengths. Other interactive criteria similar to Azzi–Tsai have been proposed by Marin (1957), Franklin (1968), Norris and McKinnon (1946), Yamada and Sun (1978), Fischer (1967), Chamis (1969), and Griffith and Baldwin (1962). For various reasons they are not as widely used as accepted.

In the 1960s, the use of tensor polynomial criteria was motivated by the idea that the failure envelopes of fiber-reinforced materials should be invariant with respect to the choice of material axes. With that in mind Gol'denblat and Kopnov (1966) proposed the first tensor polynomial criterion for anisotropic materials, that is

$$(F_i\sigma_i)^\kappa + (F_{ij}\sigma_i\sigma_j)^\lambda + (F_{ijk}\sigma_i\sigma_j\sigma_k)^\mu + \ldots = 1 \qquad i, j = 1, 6 \tag{5}$$

where the F's denote strength tensors of various orders and κ, λ, and μ are experimentally determined constants.

Tsai and Wu (1971) later proposed a similar criterion, that is

$$f(\sigma) = F_i\sigma_i + F_{ij}\sigma_i\sigma_j = 1 \quad i, j = 1, 6 \tag{6}$$

To ensure that the failure criterion is physically meaningful, or that the failure surface is closed, the stability criterion, $F_{ii}F_{jj} - F_{ij}^2 > 0$ (no summation), must be satisfied. Under plane stress conditions the criterion reduces to

$$F_1\sigma_1 + F_2\sigma_2 + F_6\tau_{12} + F_{11}\sigma_1^2 + F_{22}\sigma_2^2 + 2F_{12}\sigma_1\sigma_2 + F_{66}\tau_{12}^2 = 1 \tag{7}$$

which is the Hill criterion with the addition of linear terms. The main disadvantage of the Tsai-Wu criterion is that F_{12} is determined from difficult biaxial tests. This theory has not been as widely accepted because of disagreements over the experimental methods to determine F_{12}. According to Narayanaswami and Adelman (1977), in the off-axis tests of four different fiber orientations, it was found that only one value satisfied the necessary stability criterion.

Wu (1974) claims that most phenomenological criteria are a degenerate case of the Tsai-Wu criterion. Ashkenazzi (1966), Malmeister (1967), and Huang and Kirmser (1975) have also proposed tensor polynomial failure criteria; however, they have only been used in special cases that reduce them to the Tsai-Wu theory.

Semi-Empirical Failure Criteria

It is natural to attempt to apply linear elastic fracture mechanics (LEFM) to tension-loaded composites with crack-like defects; however, according to Wu (1968) LEFM is valid only if:

1 The orientation of the flaws with respect to the principal axes of symmetry is fixed.

2 The stress intensity factor defined for anisotropic cases is consistent with the isotropic case in stress distribution and in crack displacement modes.

3 The critical orientation coincides with one of the principal directions of elastic symmetry. In general, however, significant amounts of damage growth at the crack tip precede fracture in a composite and self-similar crack growth is not likely to occur, even for unidirectional laminates.

To apply principles of LEFM to composites, the previously proposed fracture theories of Waddoups et al. (1971), Cruse (1973), Whitney and Nuismer (1974), and Nuismer and Whitney (1975) did not consider this complex pattern of crack tip damage. Instead the damage was modeled as an "intense energy" region that was assumed to grow in a self-similar manner. With these assumptions fracture mechanics models developed for isotropic materials were generalized for composites.

Consider the two fracture models proposed by Waddoups, Eisenmann, and Kaminski (WEK) (1971), one for laminates containing circular holes and one for laminates containing straight cracks. For circular holes, the WEK model assumes that regions of intense energy of length a transverse to the loading direction are developed at the edge of the hole, as shown in Fig. 1. From Bowie (1956) and Paris and Sih (1965) they solve for the opening mode stress intensity factor K_I

$$K_I = \sigma_N^\infty \sqrt{\pi a} f\left(\frac{a}{R}\right) \tag{8}$$

where R is the radius of the hole, a is the characteristic length of the intense energy region, and σ_N^∞ is the remote applied stress. Values of $f(a/r)$ can be found from Paris and Sih (1965). At failure the notched strength of the composite laminate, σ_N^∞, from equation (8) is

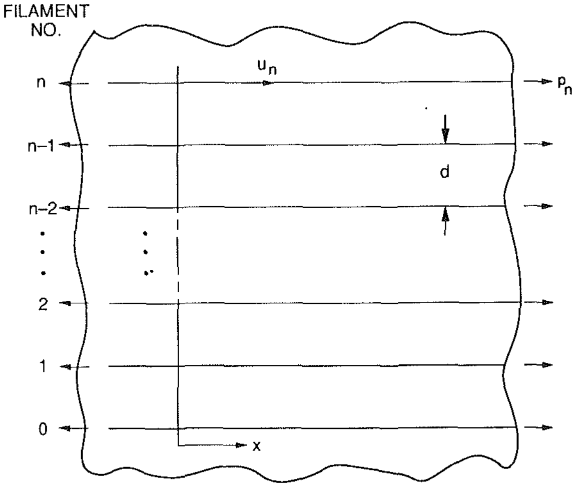

Fig. 2 Forces and displacements in filaments in Hedgepeth's shear-lag model

$$\sigma_N^\infty = \frac{K_{IC}}{\sqrt{\pi a}\, f(a/R)} \tag{9}$$

where K_{IC} is the composite critical stress intensity factor or toughness. For an unnotched specimen, that is for a composite with no hole,

$$\sigma_o = \sigma_N^\infty \Big|_{a/R=\infty} = \frac{K_{IC}}{\sqrt{\pi a}\ (1.00)} \tag{10}$$

Combining equations (9) and (10), the notched strength of the composite laminate is

$$\sigma_N^\infty = \frac{\sigma_o}{f(a/R)} \tag{11}$$

The WEK fracture model for straight cracks assumes that the half-crack length, c, is extended by the damage zone, a. This results in an effective half-crack length of $(c+a)$, similar to Irwin's plastic zone correction factor for isotropic materials. The resulting strength of the notched composite laminate is

$$\sigma_N^\infty = \sigma_o \sqrt{\frac{a}{C+a}} \tag{12}$$

Other similar semi-empirical models have been proposed by Whitney and Nuismer (1974), Nuismer and Whitney (1975), Karlak (1977), Pipes et al. (1979, 1980), Mar and Lin (1977), Poe and Sova (1980), Tan (1987), and Zhen (1983). A comprehensive review is given by Awerbuch and Madhukar (1985). Two excellent discussions of semi-empirical models are given by Kanninen et al. (1977) and Kanninen and Popelar (1985).

Shear-Lag Failure Criteria

Hedgepeth (1961) was the first to apply shear-lag models to unidirectional composites. The shear-lag models assume that the load is transferred from broken fibers to adjacent fibers by the matrix shear forces, which are assumed to be independent of the transverse displacements. This uncouples the longitudinal equilibrium equations from those in the transverse direction.

As shown in Fig. 2, Hedgepeth's model consists of a sheet of parallel filaments, which carry axial loads only in a matrix that carries only shear. Equilibrium of an element of the nth filament, for the static case, requires that

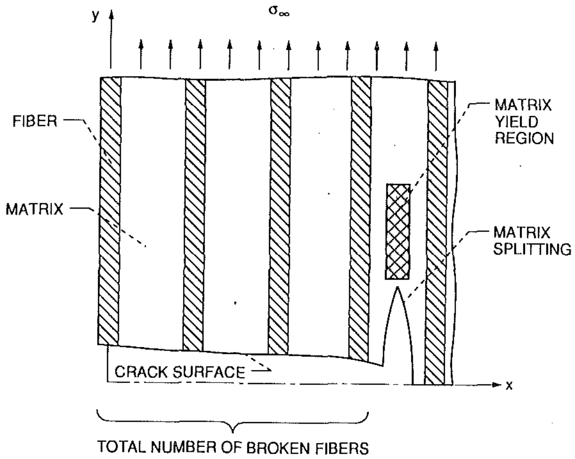

Fig. 3 Goree and Gross's shear-lag model showing matrix damage in the form of matrix yielding and matrix splitting

$$\frac{dp_n(x)}{dx}+s_n(x)-s_{n-1}(x)=0 \tag{13}$$

where $p_n(x)$ is the load in the nth filament and $s_n(x)$ is the matrix shear force per unit length between the nth and $(n+1)$th filaments. The force in the nth filament is

$$p_n(\mathrm{x})=\mathrm{EA}\frac{\mathrm{d}u_n(\mathrm{x})}{\mathrm{dx}} \tag{14}$$

where EA is the extensional stiffness and $u_n(x)$ is the displacement of the nth filament in the axial direction. The shear force per unit length can be calculated from

$$s_n(x)=\frac{Gh}{d}(u_{n+1}-u_n) \tag{15}$$

where G is the matrix shear modulus, h is the effective thickness of the matrix, and d is the centerline spacing between the filaments. Equations (15) is the shear-lag assumption, which assumes that the shear force is a function of the axial displacements only.

Substitution of equations (14) and (15) into equation (13) results in

$$EA\frac{d^2u_n}{dx^2}+\frac{Gh}{d}(u_{n+1}-2u_n+u_{n-1})=0 \tag{16}$$

Applying the boundary conditions for n broken fibers, Hedgepeth solved for the stress concentration in the first unbroken fiber as a function of the number of broken fibers.

Hedgepeth and Van Dyke (1967) extended the analysis to consider three-dimensional fiber arrays and an elastic–perfectly plastic matrix. Eringen and Kim (1974) further generalized Hedgepeth's model to include transverse loads in the matrix. Both of these models, however, only determined stress concentrations in unbroken fibers. Goree and Gross (1979) investigated the behavior due to broken fibers and matrix damage in the form of longitudinal yielding and matrix splitting, as shown in Fig. 3. A failure criterion for the matrix due to shear alone was assumed in attempting to predict the characteristic strength and fracture properties of unidirectional composite lamina. Further models by Dharani et al. (1983) and Kaw and Goree (1985) considered other forms of damage.

Fracture Mechanics Failure Criteria for First Matrix Cracking

According to Aveston, Cooper, and Kelly (ACK) (1971), if the fibers have a higher failure strain than the matrix, multiple fracture of the matrix will occur if

$$\sigma_{fu}V_f>\sigma_{mu}V_m+\sigma_f' V_f \tag{17}$$

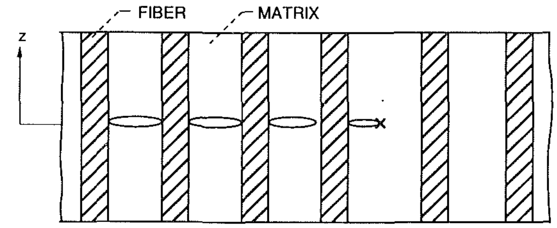

(a) PERFECTLY BONDED, NO SLIP FIBERS

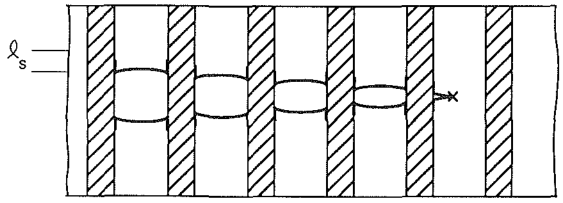

(b) UNBONDED, SLIPPING FIBERS

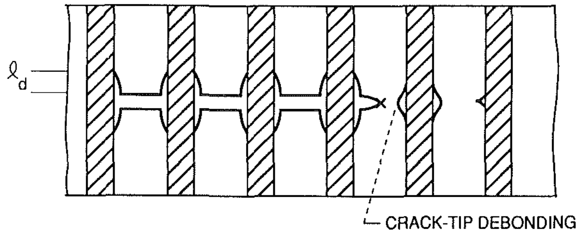

(c) INITIALLY BONDED, DEBONDING FIBERS

Fig. 4 Various assumed interface conditions for steady-state matrix cracking

where V_f and V_m are the fiber and matrix volume fractions, σ_{fu} and σ_{mu} are the ultimate strength of the fiber and matrix, and σ_f' is the stress on the fibers required to produce a strain equal to the failure strain of the matrix. Most ceramic matrix composites exhibit such multiple matrix cracking behavior where a crack propagates through the matrix and is bridged by reinforcing fibers. ACK assumed that the requirements necessary for the formation of such a matrix crack are that the stress in the matrix must be equal to the matrix breaking stress, and that the total energy of the specimen and the loading system must decrease as a result of crack formation.

The energy changes considered by ACK when a matrix crack is formed are: ΔW, the work done by the applied stress; γ_{db}, the work done in breaking the fiber-matrix interfacial bond; ΔU_m, the decrease in the matrix strain energy; ΔU_f, the increase in fiber strain energy; and U_s, the work done against frictional forces as the fiber moves relative to the matrix. The condition for the formation of a crack then is

$$2\gamma_m V_m+\gamma_{db}+U_s+\Delta U_f\leq\Delta W+\Delta U_m \tag{18}$$

where γ_m is the fracture surface work in forming a matrix crack. The energy terms can be calculated from

$$\begin{aligned}
\Delta W &= E_fE_mV_m\epsilon_{mu}^3\frac{\alpha r(1+\alpha)}{2\tau_s}\\
\Delta U_m &= E_fE_mV_m\epsilon_{mu}^3\frac{\alpha r}{3\tau_s}\\
\Delta U_f &= E_fE_mV_m\epsilon_{mu}^3\frac{\alpha r(1+\alpha/3)}{2\tau_s}\\
U_s &= E_fE_mV_m\epsilon_{mu}^3\frac{\alpha r(1+\alpha)}{6\tau_s}\\
\gamma_{db} &= 2\sigma_{mu}V_m\frac{G_{II}}{\tau_s}
\end{aligned} \tag{19}$$

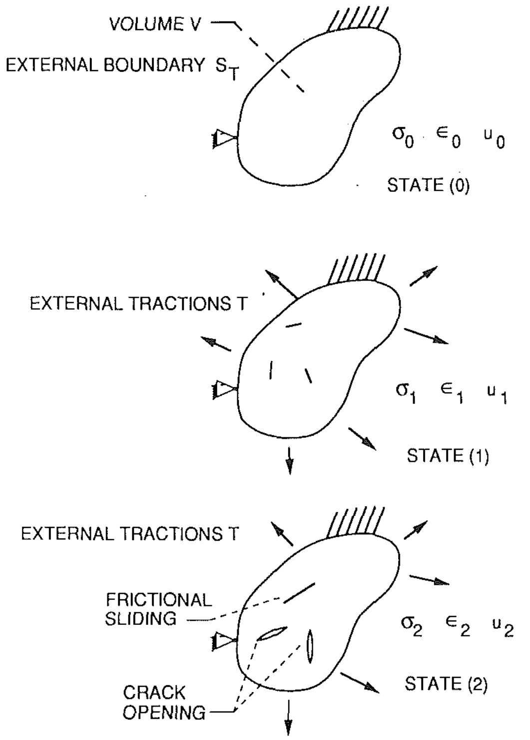

Fig. 5 Three states of energy in deriving Budiansky, Hutchinson, and Evans fracture model

where E_f and E_m are Young's modulus for the fiber and matrix, ϵ_{mu} is the failure strain of the matrix, τ_s is the fiber-matrix interfacial shear strength, G_{II} is the energy per unit area required to debond the fiber from the matrix, r is the fiber radius, and $\alpha = E_m V_m / E_f V_f$. For a purely frictional bond γ_{db} equals zero and the critical matrix cracking strain can be expressed as

$$\epsilon_{mu} = \left(\frac{12\tau_s \gamma_m E_f V_F^2}{E_c E_m^2 r V_m}\right)^{1/3} \tag{20}$$

where E_c is Young's modulus of the composite. Aveston and Kelly (AK) (1975) later extended the analysis to include an elastically bonded interface and an initially bonded, debonding interface, which are shown in Fig. 4 along with the unbonded, slipping fibers case.

ACK looked at the energy states before and after crack propagation, while Budiansky, Hutchison, and Evans (BHE) (1986) considered the case of steady-state cracking, which assumes that the stress necessary to propagate a crack larger than some characteristic dimension is constant. The assumption of steady-state cracking implies that the stress at the crack tip remains unchanged during crack growth and also that the upstream and downstream stresses, far ahead of and behind the crack, do not change.

BHE considered a body in three different states, shown in Fig. 5. In state (0) the body has no external applied loads but contains an initial stress distribution, σ_0. In state (1), with an external applied load T, the internal stress distribution becomes σ_l and additional strains ϵ_1 are produced. Obviously, these subscripts do not correspond to the previously introduced material axes directions. Open cracks as well as internal surfaces in which sliding has occurred may exist. In state (2) additional cracking and frictional sliding has occurred with no change in T. The stresses and strain are σ_2 and ϵ_2, respectively. The loss in potential energy in going from state (1) to state (2) may be written as

$$\pi_1 - \pi_2 = \frac{1}{2}\int_V (\sigma_1 - \sigma_2):(\epsilon_1 - \epsilon_2)dV + \xi_f \tag{21}$$

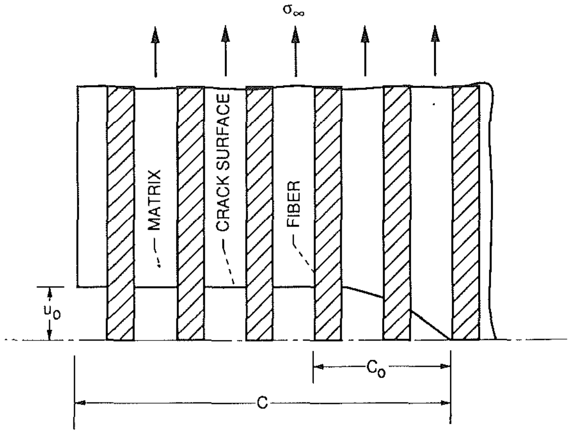

Fig. 6 Steady-state matrix cracking assumed by Marshall, Cox, and Evans

where π_1 and π_2 are the potential energies in states (1) and (2) and ξ_f is the frictional energy.

If no slipping occurs, Fig. 4(*a*), or if the fibers are slipping but frictionally constrained, Fig. 4(*b*), the potential energy release rate per unit crack extension per unit thickness is

$$P_u - P_d = \frac{1}{2A_c}\int_{-L}^{L}\int_{A_c}(\sigma_u - \sigma_d):(\epsilon_u - \epsilon_d)dA\ dz + \frac{\partial \epsilon_f}{\partial s} \tag{22}$$

where P_u and P_d are the upstream and downstream potential energies per unit cross-sectional area of composite crack extension, σ_u, ϵ_u, σ_d, and ϵ_d are the upstream and downstream stress and strain distributions and A_c is the representative cross section of the composite crack extension. The frictional energy dissipation rate associated with fiber-matrix slip is $\partial\epsilon_f/\partial s$.

BHE assume that the energy release rate, $P_u - P_d$, must be balanced by the sum of the frictional energy-dissipation rate and the critical matrix crack extension energy release rate, $V_m G_m$, where G_m is the critical matrix energy release rate. Thus,

$$\frac{1}{2}A_c\int_{-L}^{L}\int_{Ac}(\sigma_u - \sigma_d):(\epsilon_u - \epsilon_d)dA\ dz = V_m G_m \tag{23}$$

In the case of initially bonded, debonding fibers a term for the debonding energy release rate is included in the materials resistance to crack growth

$$\frac{1}{2}A_c\int_{-L}^{L}\int_{A_c}(\sigma_u - \sigma_d):(\epsilon_u - \epsilon_d)dA\ dz = V_m G_m + 4V_f\left(\frac{l_d}{r}\right)G_d \tag{24}$$

where l_d is the debond length, r is the fiber radius, and G_d is the critical debonding energy release rate.

The upstream stresses are given by the rule-of-mixtures relationship

$$\sigma_f^u = \left(\frac{E_f}{E_c}\right)\sigma + \sigma_f^I \quad \text{and} \quad \sigma_m^u = \left(\frac{E_m}{E_c}\right)\sigma + \sigma_m^I \tag{25}$$

where σ_f^I and σ_m^I are the initial residual axial fiber and matrix stresses in the unloaded composite, and σ is the average applied stress. The downstream stresses are determined from a shear-lag analysis of a composite cylinder. Substitution of the upstream and downstream stresses into equations (23) and (24) results in the matrix cracking condition. For unbonded frictionally constrained fibers the matrix cracking stress, σ_{cr}, is

$$\frac{\sigma_{cr}}{E_c} + \frac{\sigma_m^I}{E_m} = \left(\frac{V_f E_f G_m \rho}{r E_m E_c}\right)^{1/2} \tag{26}$$

where r is the fiber radius and ρ is defined by BHE as a function of constituent properties. The matrix cracking stress for unbonded slipping fibers is

$$\frac{\sigma_{cr}}{E_c}+\frac{\sigma_m^I}{E_m}=\left(\frac{6V_f^2E_f\tau_s}{V_mE_mE_c}\right)^{1/3}\left(\frac{G_m}{rE_m}\right)^{1/3} \tag{27}$$

where τ_s is the fiber-matrix interfacial shear stress. Equations (26) and (27) are identical to the AK/ACK results except for the initial matrix stresses. BHE also derive a parametric relationship for the results between the no-slip and large slip cases, and the matrix cracking stress for the case of initially bonded, debonding fibers. These cases were not considered by AK/ACK.

Marshall, Cox, and Evans (MCE) (1985) defined steady-state crack differently, distinguishing between large and small cracks, as shown in Fig. 6. Large cracks asymptotically approach the equilibrium separation, u_o, of the completely failed matrix bridged by reinforcing fibers. This equilibrium separation occurs a characteristic dimension, c_o, from the crack tip. Beyond this characteristic distance the net force in the fibers that bridge the crack exactly balances the applied force, and the stress needed to extend the crack is independent of the crack length. Crack growth in this region is defined by MCE as steady-state growth. On the other hand, for short cracks the entire crack contributes to the stress concentration, and the stress required to propagate a crack is sensitive to crack length.

Unlike BHE, MCE considered unbonded, frictionally constrained fibers only. The matrix cracking stress is evaluated using a stress intensity approach. The fibers and matrix are assumed to be cut, as shown in Fig. 7(*a*), and traction forces, *T*, are applied to the ends of the fibers so that they are rejoined. The crack surfaces are regarded as being subjected to a net opening pressure $[\sigma_\infty - p(x)]$ where σ_∞ is the applied load and $p(x)$ is the distribution of closure pressure on the crack surfaces defined as

$$p(x)=T(x)V_f \tag{28}$$

where x represents the position on the crack surface, as shown in Fig. 7(*b*). Therefore, MCE introduce the composite stress intensity factor

$$K^L=2\left(\frac{c}{\pi}\right)^{1/2}\int_0^1\frac{[\sigma_\infty-p(X)]}{\sqrt{1-X^2}}\,dX \tag{29}$$

for a straight crack or

$$K^L=2\left(\frac{c}{\pi}\right)^{1/2}\int_0^1\frac{[\sigma_\infty-p(X)]}{\sqrt{1-X^2}}X\,dX \tag{30}$$

for a penny shaped crack, where c is the crack length and $X=x/c$. MCE assume that the critical matrix stress intensity factor is related to the composite stress intensity factor by

$$K_c^m=\frac{K_c^LE_m}{E_c} \tag{31}$$

The steady-state matrix cracking stress is obtained by evaluating equations (29) or (30) and (31) and setting $\sigma_\infty=\sigma_{cr}$. After performing the indicated operations one obtains

$$\sigma_{cr}=\delta'\left[(1-\nu^2)K_c^{m2}\tau_sE_fV_f^2V_m\frac{(1+\eta)^2}{E_mr}\right]^{1/3} \tag{32}$$

where ν is the Poisson ratio, τ_s is the fiber-matrix interfacial shear stress, $\eta=E_fV_f/E_mV_m$, r is the fiber radius, and δ' is a dimensionless constant. The results are equivalent to those for the large slip case of ACK, where $\delta'=1.83$ from an MCE analysis and $\delta=6^{1/3}$ from an ACK analysis.

In subsequent papers Marshall and Cox (1987) generalized the analysis to include fiber failure in the wake of the crack, as shown in Fig. 8(*a*). In their model the fibers were assumed to have a single valued strength. In another model, Thouless and Evans (1988) assumed a statistical variation the fiber strength, which is also shown in Fig. 8(*b*), and examined the effects of pull-out when fibers fracture away from the crack plane.

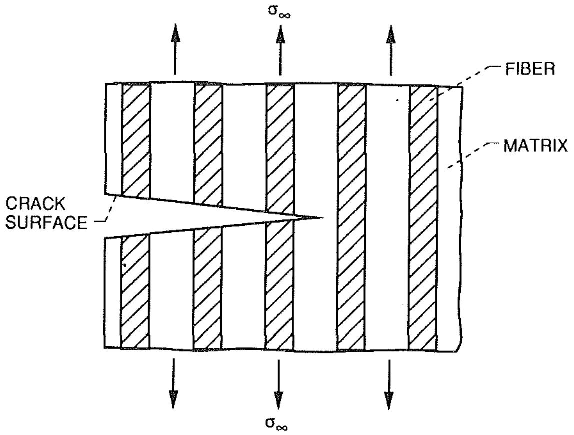

(a) Initially cracked fiber and matrix.

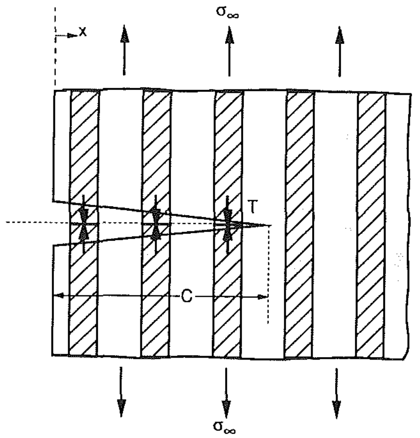

(b) Fiber and matrix after applying traction forces, T.

Fig. 7 Expected crack geometry before and after application of fiber forces to evaluate closure pressure in stress intensity analysis

Continuum Damage Mechanics

Continuum damage mechanics will now be discussed because it addresses local phenomena as did fracture mechanics previously and because it can be utilized to predict the failure of composites, especially time-dependent failure. However, it will only be briefly described here in general terms and will not be included in the subsequent discussion.

The basic idea of damage mechanics according to Sidoroff (1984) is the introduction of a damage variable describing at the macroscopic level the microscopic degradation occurring in the material. Like fracture mechanics, continuum damage mechanics considers the behavior of an imperfect body; however, while fracture mechanics deals with one dominant macrodefect, continuum damage mechanics considers a whole population of microdefects. In other words, where fracture mechanics starts with a cracked body, continuum damage mechanics starts with a perfect material and follows its damage accumulation to the appearance of a dominant macroscopic defect.

In the simplest case a single damage variable D is assumed to predict failure when $D=1$ or some other critical value D_c, and it is usually defined from some measurable macroscopic quantity ρ, which is hoped to be representative of the macroscopic degradation process. Hence

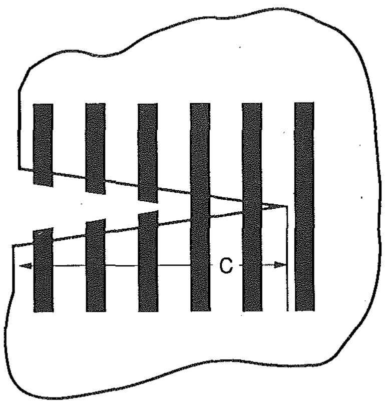

(a) Single valued fiber strength.

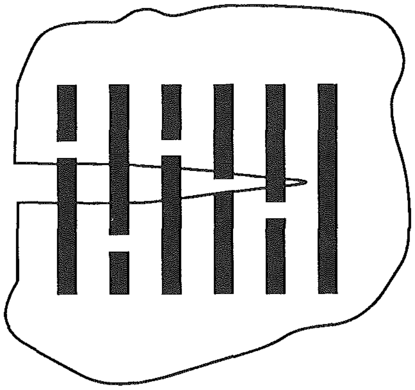

(b) Statistical variation in fiber strength.

Fig. 8 Crack configurations analyzed assuming fiber breaks in the wake of the crack tip

$$D=\frac{\rho_o-\rho}{\rho_o-\rho_R} \tag{33}$$

where ρ_0 and ρ_R denote the values of ρ in the initial undamaged state and at rupture. To complete the model a damage evolution law is needed to follow the damage process. A generalized evolution equation can be written in the form

$$\frac{dD}{dt}=H(\sigma,\ \dot{\sigma},\ D,\ .\ .\ .) \tag{34}$$

This one-dimensional scalar model, however, will not be sufficient for composite structures. Many mechanisms are known to be responsible for composite damage, i.e., fiber failure, matrix cracking, interfacial debonding, etc., and their interaction is not clearly understood. Averaging them in a single damage variable cannot be realistic. They are also strongly related to the anisotropy of composite materials. Consequently, anisotropic damage tensors and other damage descriptions have been proposed by Wnuk and Kriz (1985), Talreja (1986), Shen et al. (1987), Lene (1986), and others.

Statistical Failure Criteria

Purely statistical criteria have also been proposed for the failure characterization of ceramic matrix composites when the deterministic models do not adequately describe observed variation in composite strength. Because these criteria are purely statistical they can always be applied, but they do require a greater amount of test data.

The principle of independent action (PIA) (Wetherhold, 1983) is the statistical formulation of the maximum stress criterion. Using Weibull's weakest link statistic and a state of plane stress for a transversely isotropic material, the reliability due to intrinsic flaws in a composite can be calculated from

$$R=\exp\int_V-\left[\left(\frac{\sigma_1}{\beta_1}\right)^{\alpha_1}+\left(\frac{\sigma_2}{\beta_2}\right)^{\alpha_2}+\left(\frac{\sigma_6}{\beta_6}\right)^{\alpha_6}\right]dV \tag{35}$$

where the reliability R is the probability of no failure of the volume, α_i and β_i are the Weibull shape and scale parameters, σ_i are the in-plane material axes stresses, and σ_6 has been substituted from the previously used τ_{12}. The principle of independent action is a weakest link model, which assumes that volume V is divided into N elements where no failure of the volume requires no failure of any of the elements. The event of no failure of an element is the same as the event of no failure of an element by any of the stress components, which are assumed to act independently. A statistical equivalent of the maximum strain failure criterion has also been developed.

Wetherhold's other model (Wetherhold, 1983) is the probabilistic form of the maximum distortional energy (MDE) criterion. It also is a weakest link model where MDE is the criterion for failure of an element. The MDE criterion is given by

$$K^2_{\mathrm{MDE}}=\left(\frac{\sigma_1}{X_1}\right)^2-\frac{\sigma_1\sigma_2}{X_1^2}+\left(\frac{\sigma_2}{X_2}\right)^2+\left(\frac{\sigma_6}{X_6}\right)^2 \tag{36}$$

The reliability of the element is $P\{K<1\}$. To evaluate the reliability one needs to integrate the following equation:

$$R=\int_0^{i(1)}\int_0^{h(1;X_6)}\int_0^{g(1;X_2,\ X_6)}F_{X_1}(X_1)F_{X_2}(X_2)F_{X_6}(X_6) \bullet dx_1dx_2dx_6 \tag{37}$$

where F_{X_1}, F_{X_2}, and F_{X_6} are the probability density functions for strengths X_1, X_2, and X_6 and

$$g(1;\ X_2,\ X_6)=\sqrt{\frac{\sigma_1^2-\sigma_1\sigma_2}{1-(\sigma_2/X_2)^2-(\sigma_6/X_6)^2}}$$

$$h(1;\ X_6)=\sqrt{\frac{\sigma_2^2}{1-(\sigma_6/X_6)^2}}$$

$$i(1)=\sigma_6$$

The integral in equation (37) is intractable and can be evaluated only by using a Monte Carlo technique. Other statistical forms of phenomenological criteria are given by Cassenti (1984) and Sun and Yamada (1978).

The previous statistical criteria were based on the observed variation in composite strength. For composites with high fiber volume fractions and fully cracked matrices, three models (Jayatilaka, 1979) for the ultimate unidirectional strength have been proposed that are solely based on the variation in fiber strength of the composite. These models are based on the following assumptions:

1 The crack propagates catastrophically in a direction normal to the adjacent fibers following the fracture of a single fiber.

2 The crack may also propagate along the fiber-matrix interface and the composite behaves then as a bundle of unbound fibers.

3 The last model assumes that when the weakest fiber fails it is followed by additional fiber fracture at other weak sites as the load is increased. This is known as the cumulative damage failure model.

The strength of a single fiber varies with the length of the fiber and this is due to flaws present in the fiber. The average single fiber strength is given by

$$\bar{\sigma}_l=\beta(l)^{-1/\alpha}\Gamma\left(1+\frac{1}{\alpha}\right) \tag{38}$$

where α and β are the fiber Weibull shape and scale parameters, l is the fiber length, and Γ is the gamma function. The strength of a bundle of fibers in the second model is similar to the problems considered by Daniels (1945) where he studied the strength of a bundle of threads. The average bundle strength of the fibers is

$$\bar{\sigma}_b = \beta(l\alpha e)^{-1/\alpha} \tag{39}$$

where e is the base of the natural logarithm, that is $e = 2.7183$. These strengths are substituted into the rule-of-mixtures relationship to determine the ultimate strength of the composite assuming zero matrix strength.

The cumulative damage model assumes that when a fiber fractures, a portion of the fiber of length δ does not carry any load. The composite is divided into layers of length δ. Each layer is considered a bundle of links and the composite is a series of such bundles, or a chain of bundles. Failure of one bundle results in total failure of the composite. The average strength value from the cumulative damage model to be used in the rule-of-mixtures equation is

$$\bar{\sigma}_{fu} = \sigma_{\text{mode}} \cong \beta(\alpha\ \delta e)^{-1/\alpha} \tag{40}$$

where δ, the ineffective length, is a function of r, V_f, E_f, and the matrix shear modulus.

Other investigators have proposed models based on the cumulative damage model. Zweben and Rosen (1970) considered the chain-of-bundles model in discussing crack growth in unidirectional composites. The strength of each bundle was determined by bundle theory taking into consideration stress concentrations from the shear-lag model of Hedgepeth in fibers adjacent to broken fibers. Weakest link theory was used to determine the probability of failure of the chain of bundles. Zweben and Rosen did not succeed in establishing a usable failure criterion.

Harlow and Phoenix (1978) also utilized the chain-of-bundles model. They assumed that the strength of individual brittle fibers, embedded in a matrix having stiffness and strength far below that of the fibers, follows a Weibull distribution. Upon loading isolated fractures are observed in individual fibers. As the load is increased fiber fractures accumulate until the composite can no longer support the load. Two load sharing rules for the unbroken fibers were considered. The Equal Load Sharing (ELS) rule assumes that the load from the broken fibers is evenly distributed among the remaining fibers. The Local Load Sharing (LLS) rule assumes that the additional load is concentrated in the fibers adjacent to the broken fibers.

The Batdorf (1982) model, as opposed to the chain-of-bundles models, considers a composite containing N fibers of length l held together by a matrix. Damage resulting from loading is assumed to consist of breaks in the fibers. Single isolated breaks are called singlets, pairs are called doublets, or in general i-plets. The assumption is made that fiber failure conforms to a Weibull distribution where the cumulative probability of the fiber breaking is given by

$$P_f(\sigma) = 1 - \exp\left[-l\left(\frac{\sigma}{\beta}\right)^{\alpha}\right] \tag{41}$$

where α and β are the Weibull parameters. If there are N fibers of length l, the number of singlets at stress σ is

$$Q_1 = NP_f = Nl\left(\frac{\sigma}{\beta}\right)^{\alpha} \tag{42}$$

A singlet becomes a doublet when one of the neighboring fibers breaks. The probability that a singlet becomes a doublet, P_{1-2}, is

$$P_{1-2} = n_1\lambda_1\left(\frac{c_1\sigma}{\beta}\right)^{\alpha} \tag{43}$$

where n_1 is the number of fibers subjected to a stress concentration that varies from $c_1\sigma$ to σ relative to the nominal fiber stress and λ_1 is the effective length of this overstressed region. The number of doublets in loading to stress σ thus becomes

$$Q_2 = Q_1 n_1 \lambda_1\left(\frac{c_1\sigma}{\beta}\right)^{\alpha} \tag{44}$$

Generalizing this result gives

$$Q_{i+1} = Q_i n_i \lambda_i\left(\frac{c_i\sigma}{\beta}\right)^{\alpha} \tag{45}$$

Failure occurs when an i-plet becomes unstable and immediately becomes an $(i+1)$-plet, which immediately becomes an $(i+2)$-plet, etc., resulting in fracture of the composite.

Summary and Discussion

There are two general approaches to predicting failure. One is the phenomenological approach and the other is mechanistic. The phenomenological approach is strictly an empirical curve-fitting procedure that develops a surface in stress space to fit the available data. With enough constants the experimental data can always be adequately described. The phenomenological approach has been applied to homogeneous, isotropic materials such as metals with considerable success. If the strength of the metal, however, is sensitive to microstructural discontinuities, such as cracks, a mechanistic approach such as fracture mechanics is required. The mechanistic approach develops criteria that describe the mechanisms of failure in terms of microstructural variables and the use of engineering principles.

The complex mechanisms of failure in ceramic matrix composites such as matrix cracking, interfacial debonding, and fiber pull-out (Harris, 1986) are strongly affected by microstructural parameters such as fiber diameter or fiber–matrix interfacial shear strength. The macroscopic phenomenological criteria cannot account for these factors in predicting failure. In addition, mechanistic criteria can extrapolate beyond known test conditions to account for variations in these parameters. Thus, mechanistic criteria are necessary to understand the factors controlling the failure of ceramic matrix composites. On the other hand, they may become intractable when too many parameters control the materials failure behavior.

The semi-empirical failure criteria attempt to apply the mechanistic principles of linear elastic fracture mechanics to composites by assuming the existence of an "intense energy" region at the crack tip. In practice, however, because of unknown crack dimensions, they are two-parameter empirical correlations of test data much the same as the phenomenological criteria. The models were developed for polymer matrix composites where the assumption of an "intense energy" region may be acceptable, but is questionable for ceramic matrix composites. To apply these criteria certain characteristic parameters must be determined experimentally. These parameters are dependent upon the laminate configuration and material system. Like the phenomenological models, the semi-empirical criteria do not describe the mechanisms of failure.

The shear-lag failure criteria are mechanistic models that describe the behavior of the composite at the micromechanics level. The first models did not consider failure in a composite but simply the stress concentration due to broken fibers in adjacent unbroken fibers. Goree and Gross were the first to consider failure. The model included longitudinal yielding of the matrix and matrix splitting, two failure mechanisms seen in polymer matrix composites. Shear-lag models are not currently applicable to ceramic matrix composites. They assume that the tensile load is carried solely by the fibers, while actually, a ceramic matrix has significant load carrying capability.

The fracture mechanics failure criteria are also mechanistic models. The ACK model, based on energy principles, was originally developed for concrete and steel reinforcing wires, but is also applicable to ceramic matrix composites. The multiple matrix fracture and enhanced matrix cracking strain predicted by ACK is seen in many brittle matrix composites. The more rigorous energy analysis of BHE was developed specially for brittle matrix composites for the cases of frictionally constrained and initially bonded, debonding matrices. The model of primary interest, however, is that of MCE. It considers frictionally constrained, slipping fibers, which result in the desired "graceful" failure of the ceramic matrix composite. MCE also considers the transition from notch insensitive large crack behavior to notch sensitive short crack response. Failure due to transverse or compressive loads has not been addressed here. Fracture mechanics models are suitable only for tension loaded ceramic matrix composites. In addition, fracture mechanics models are based on the assumption of a constant interfacial shear strength. The validity of that assumption is being addressed by others.

The criteria discussed so far have all been deterministic. Some phenomenological and mechanistic models can also be expressed in statistical form. There is a great deal of intrinsic variability in the strength of each of the brittle constituents of a ceramic matrix composite but, depending on the composite system, the matrix cracking strength may be deterministic or probabilistic. The ultimate unidirectional composite strength, however, will always be probabilistic since its value is determined by the brittle fiber strength distribution. Thus, statistical models are required for those composite systems that possess a great deal of strength scatter or have linear stress-strain curves all the way to fracture.

The criteria of Wetherhold, Cassenti, and Sun and Yamada are purely statistical and are based on the distribution of composite strength data. Phenomenological models are used as criteria to predict probability of failure of the composite. The three models described by Jayatilaka for the ultimate unidirectional strength of a composite are also purely statistical, but are based on the variation in strength of only the composite fiber. In higher fiber volume fraction composites, the most conservative and accurate ultimate, longitudinal strength is a function of the bundle strength, provided that the fiber volume fraction and fiber strength are adequate to carry the load after matrix failure. The other two models are less conservative and more applicable to the behavior of polymer matrix composites.

A better approach would be to develop statistical failure criteria based on mechanistic models, as done for monolithic ceramics. These criteria could then be used to extrapolate beyond the range of observations, not on the basis that the distributions they produce can be fitted to existing test data, but that they are germane to the phenomena. These criteria currently do not exist. The most promising model to describe the variability in strength and the mechanisms of failure in ceramic matrix composites would be a statistical failure criteria based on the fracture mechanics models of ACK, BHE, and more specifically of MCE.

Fracture mechanics and statistical models, and combinations of these as required by the selected material system, will be incorporated in the near future into an integrated composite design program for component analysis.

Acknowledgments

This research was sponsored by the Structural Integrity Branch at NASA Lewis Research Center under cooperative agreement NCC-3-81.

References

Ashkenazi, E. K., 1966, "Problems of the Anisotropy of Strength," *Polymer Mechanics*, Vol. 1, No. 2, pp. 60-70.

Aveston, J., Cooper, G. A., and Kelly, A., 1971, "Single and Multiple Fracture," *The Properties of Fibre Composites*, IPC Science and Technology Press, Surrey, United Kingdom, pp. 15-26.

Aveston, J., and Kelly, A., 1975, "Theory of Multiple Fracture of Fibrous Composites," *Journal of Materials Science*, Vol. 8, No. 3, pp. 352-362.

Awerbuch, J., and Madhukar, M. S., 1985, "Notched Strength of Composite Laminates: Prediction and Experiments—A Review," *Journal of Reinforced Plastics and Composites*, Vol. 4, No. 1, pp. 3-159.

Azzi, V. D., and Tsai, S. W., 1965, "Anisotropic Strength of Composites," *Experimental Mechanics*, Vol. 5, No. 9, pp. 283-288.

Batdorf, S. B., 1982, "Tensile Strength of Unidirectionally Reinforced Composites—1," *Journal of Reinforced Plastics and Composites*, Vol. 1, No. 2, pp. 153-164.

Batdorf, S. B., and Ghaffarian, R., 1982, "Tensile Strength of Unidirectionally Reinforced Composites—2," *Journal of Reinforced Plastics and Composites*, Vol. 1, No. 2, pp. 165-176.

Bert, C. W., Mayberry, B. L., and Ray, J. D., 1969, "Behavior of Fiber-Reinforced Plastic Laminates Under Uniaxial, Biaxial, and Shear Loadings," U.S. Army Aviation Material Laboratory, USAAVLABS-TR-68-86 (available NTIS, AD-684321).

Bowie, O. L., 1956, "Analysis of an Infinite Plate Containing Radial Cracks Originating at the Boundary of an Internal Circular Hole," *Journal of Mathematics and Physics*, Vol. 35, pp. 60-71.

Budiansky, B., and Hutchison, J. W., and Evans, A. G., 1986, "Matrix Fracture in Fiber-Reinforced Ceramics," *Journal of Mechanics and Physics of Solids*, Vol. 34, No. 2, pp. 167-189.

Burk, R. C., 1983, "Standard Failure Criteria Needed for Advanced Composites," *Astronautics and Aeronautics*, Vol. 21, No. 6, pp. 58-62.

Cassenti, B. N., 1984, "Probabilistic Static Failure of Composite Materials," *AIAA Journal*, Vol. 22, No. 1, pp. 103-110.

Chamis, C. C., 1969, "Failure Criteria for Filamentary Composites," in: *Composite Materials: Testing and Design*, ASTM STP-460, American Society for Testing and Materials, Philadelphia, PA, pp. 336-351.

Cruse, T. A., 1973, "Tensile Strength of Notched Composites," *Journal of Composite Materials*, Vol. 7, pp. 218-229.

Daniels, H. E., 1945, "The Statistical Theory of the Strength of Bundles of Threads," *Proceedings of the Royal Society (London), Series A*, Vol. 183, No. 995, pp. 405-435.

Dharani, L. R., Jones, W. F., and Goree, J. B., 1983, "Mathematical Modeling of Damage in Unidirectional Composites," *Engineering Fracture Mechanics*, Vol. 17, No. 6, pp. 555-573.

Eringen, A. C., and Kim, B. S., 1974, "Stress Concentration in Filamentary Composites With Broken Fibers," *Letters in Applied and Engineering Science*, Vol. 2, pp. 69-89 (available NTIS, AD-785778).

Fischer, L., 1967, "Optimization of Orthotropic Laminates," ASME *Journal of Engineering for Industry*, Vol. 89, No. 3, pp. 399-402.

Franklin, H. G., 1968, "Classic Theories of Failure of Anisotropic Materials," *Fibre Science and Technology*, Vol. 1, pp. 137-150.

Gol'denblat, I. I., and Kopnov, V. A., 1966, "Strength of Glass Reinforced Plastics in the Complex Stress State," *Polymer Mechanics*, Vol. 1, No. 2, pp. 54-59.

Goree, J. G., and Gross, R. S., 1974, "Analysis of a Unidirectional Composite Containing Broken Fibers and Matrix Damage," *Engineering Fracture Mechanics*, Vol. 13, No. 3, pp. 563-578.

Griffith, J. E., and Baldwin, W. M., 1962, "Failure Theories for Generally Orthotropic Materials," *Developments in Theoretical and Applied Mechanics*, Vol. 1, Plenum Press, New York, pp. 410-420.

Harlow, D. G., and Phoenix, S. L., 1978, "The Chain-of-Bundle Probability Model for the Strength of Fibrous Materials—1. Analysis and Conjectures," *Journal of Composite Materials*, Vol. 12, pp. 195-215.

Harris, B., 1986, *Engineering Composite Materials*, The Institute of Metals North American Publication Center, Brookfield, VT.

Hedgepeth, J. M., 1961, "Stress Concentration for Filamentary Structures," NASA TN D-882.

Hedgepeth, J. M., and Van Dyke, 1967, "Local Stress Concentrations in Imperfect Filamentary Composite Materials," *Journal of Composite Materials*, Vol. 1, No. 3, pp. 294-309.

Hill, R., 1950, *The Mathematical Theory of Plasticity*, Oxford University Press, London, United Kingdom, pp. 318-320.

Hoffman, O., 1967, "The Brittle Strength of Orthotropic Materials," *Journal of Composite Materials*, Vol. 1, No. 2, pp. 200-206.

Hu, L. W., 1958, "Modified Tresca's Yield Condition and Associated Flow Rules for Anistropic Materials and Applications," *Journal of the Franklin Institute*, Vol. 265, No. 3, pp. 187-204.

Huang, C. L., and Kirmser, P. G., 1975, "A Criterion of Strength for Orthotropic Materials," *Fibre Science and Technology*, Vol. 8, No. 2, pp. 103-112.

Jayatilaka, A. S., 1979, *Fracture of Engineering Brittle Materials*, Applied Science Publishers, London, United Kingdom, pp. 249-257.

Kaminski, B. E., and Lantz, R. B., 1969, "Strength Theories of Failure for Anisotropic Materials," *Composite Materials: Testing and Design*, ASTM STP-460, American Society for Testing and Materials, Philadelphia, PA, pp. 160-169.

Kanninen, M. F., and Popelar, C. H., 1965, *Advanced Fracture Mechanics*, Oxford University Press, New York.

Kanninen, M. F., Rybicki, E. F., and Brinson, H. F., 1977, "A Critical Look at Current Applications of Fracture Mechanics to the Failure of Fibre-Reinforced Composites," *Composites*, Vol. 8, No. 1, pp. 17-22.

Karlak, R. F., 1977, "Hole Effects in a Related Series of Symmetrical Laminates," *Proceedings of Failure Modes in Composites, IV*, J. A. Cornie and F.

W. Crossman, eds., The Metallurgical Society of AIME, Warrendale, PA, pp. 105-117.

Kaw, A. K., and Goree, J. G., 1985, "Shear-Lag Analysis of Notched Laminates With Interlaminar Debonding," *Engineering Fracture Mechanics*, Vol. 22, No. 6, pp. 1013-1029.

Kelly, A., and Davies, G. J., 1965, "The Principles of the Fibre Reinforcement of Metals," *Metallurgical Reviews*, Vol. 10, No. 37, pp. 1-77.

Labossiere, P., and Neale, K. B., 1987, "Macroscopic Failure Criteria for Fiber Reinforced Composite Materials," *Solid Mechanics Archives*, Vol. 12, No. 2, pp. 65-95.

Lance, R. H., and Robinson, D. N., 1971, "A Maximum Shear Stress Theory of Plastic Failure of Fibre-Reinforced Materials," *Journal of Mechanics and Physics of Solids*, Vol. 19, No. 2, pp. 49-60.

Lene, F., 1986, "Damage Constitutive Relations for Composite Materials," *Engineering Fracture Mechanics*, Vol. 25, No. 5-6, pp. 713-728.

Malmeister, A., 1966, "Geometry of Theories of Strength," *Polymer Mechanics*, Vol. 2, No. 4, pp. 324-331.

Mar, J. W., and Lin, K. Y., 1977, "Fracture Mechanics Correlation for Tensile Failure of Filamentary Composites With Holes," *Journal of Aircraft*, Vol. 14, No. 7, pp. 703-704.

Marin, J., 1957, "Theories of Strength for Combined Stresses and Nonisotropic Materials," *Journal of the Aeronautical Sciences*, Vol. 24, No. 4, pp. 265-268, 274.

Marshall, D. B., and Cox, B. N., 1987, "Tensile Fracture of Brittle Matrix Composites: Influence of Fiber Strength," *Acta Metallurgica*, Vol. 35, No. 11, pp. 2607-2619.

Marshall, D. B., Cox, B. N., and Evans, A. G., 1985, "The Mechanics of Matrix Cracking in Brittle Matrix Fiber Composites," *Acta Metallurgica*, Vol. 33, No. 11, pp. 2013-2021.

Nahas, M. N., 1986, "Survey of Failure and Post-Failure Theories of Laminated Fiber-Reinforced Composites," *Journal of Composites Technology and Research*, Vol. 8, No. 4, pp. 138-153.

Narayanaswami, R., and Adelman, H. M., 1977, "Evaluation of Tensor Polynomial and Hoffman Strength Theories for Composite Materials," *Journal of Composite Materials*, Vol. 11, No. 4, pp. 366-377.

Norris, C. B., and McKinnon, P. F., 1946, "Compression, Tension, and Shear Tests on Yellow-Poplar Plywood Panels of Sizes That Do Not Buckle With Tests Made at Various Angles to the Face Grain," Report 1328, Forest Products Laboratory, Madison, WI.

Nuismer, R. J., and Whitney, J. M., 1975, "Uniaxial Failure of Composite Laminates Containing Stress Concentrations," *Fracture Mechanics of Composites*, ASTM STP-593, American Society for Testing and Materials, Philadelphia, PA, pp. 117-142.

Paris, P. C., and Sih, G. C. M., 1965, "Stress Analysis of Cracks," *Fracture Toughness Testing and Its Applications*, ASTM STP-381, American Society for Testing and Materials, Philadelphia, PA, pp. 30-83.

Pipes, R. B., Wetherhold, R. C., and Gillespie, J. W., Jr., 1980, "Macroscopic Fracture of Fibrous Composites," *Materials Science and Engineering*, Vol. 45, No. 3, pp. 247-253.

Pipes, R. B., Wetherhold, R. C., and Gillespie, J. W., Jr., 1974, "Notched Strength of Composite Materials," *Journal of Composite Materials*, Vol. 13, pp. 148-160.

Poe, C. C., Jr., and Sova, J. A., 1980, "Fracture Toughness of Boron/Aluminum Laminates with Various Properties of 0° and ±45° Plies," NASA TP-1707.

Prager, W., 1969, "Plastic Failure of Fibre-Reinforced Materials," *Journal of Applied Mechanics*, Vol. 36, No. 3, pp. 542-544.

Rowlands, R. E., 1975, "Flow and Failure of Biaxially Loaded Composites: Experimental-Theoretical Correlation," *Inelastic Behavior of Composite Materials*, C. T. Herakovich, ed., Vol. 13, American Society of Mechanical Engineers, New York, pp. 97-125.

Sandhu, R. S., 1972, "A Survey of Failure Theories of Isotropic and Anisotropic Materials," AFFL-TR-72-71, Air Force Flight Dynamics Laboratory," Wright Patterson Air Force Base, OH (available NTIS, AD-756889).

Sendeckyj, G. P., 1972, "A Brief Survey of Empirical Multiaxial Strength Criteria for Composites," *Composite Materials: Testing and Design (Second Conference)*, ASTM STP-497, American Society for Testing and Materials, Philadelphia, PA, pp. 41-51.

Shen, W., Peng, L., Yang, F., and Shen, Z., 1987, "Generalized Elastic Damage Theory and Its Application to Composite Plate," *Engineering Fracture Mechanics*, Vol. 28, No. 4, pp. 403-412.

Sidoroff, F., 1984, "Damage Mechanics and Its Application to Composite Materials," *Mechanical Characterization of Load Bearing Fibre Composite Laminates*, A. H. Cardon and G. Verchery, eds., Elsevier, New York, pp. 21-35.

Snell, M. B., 1978, "Strength and Elastic Response of Symmetric Angle-Ply CFRP," *Composites*, Vol. 9, No. 3, pp. 167-176.

Soni, S. R., 1983, "A Comparative Study of Failure Envelopes in Composite Laminates," *Journal of Reinforced Plastics and Composites*, Vol. 2, No. 1, pp. 34-42.

Stowell, E. Z., and Liu, T. S., 1961, "On the Mechanical Behaviour of Fibre-Reinforced Crystalline Materials," *Journal of Mechanics and Physics of Solids*, Vol. 9, No. 4, pp. 242-260.

Sun, C. T., and Yamada, S. E., 1978, "Strength Distribution of a Unidirectional Fiber Composite," *Journal of Composite Materials*, Vol. 12, No. 2, pp. 169-176.

Talreja, R., 1986, "Stiffness Properties of Composite Laminates With Matrix Cracking and Interior Delamination," *Engineering Fracture Mechanics*, Vol. 25, No. 5-6, pp. 751-762.

Tan, S. C., 1987, "Laminated Composites Containing an Elliptical Opening. I. Approximate Stress Analyses and Fracture Models," *Journal of Composite Materials*, Vol. 21, No. 10, pp. 925-948.

Tan, S. C., 1987, "Laminated Composites Containing an Elliptical Opening. II. Experiment and Model Modification," *Journal of Composite Materials*, Vol. 21, No. 10, pp. 949-968.

Thouless, M. D., and Evans, A. G., 1988, "Effects of Pull-Out on the Mechanical Properties of Ceramic Matrix Composites," *Acta Metallurgica*, Vol. 36, No. 3, pp. 517-522.

Tsai, S. W., 1984, "A Survey of Macroscopic Failure Criteria for Composite Materials," *Journal of Reinforced Plastics and Composites*, Vol. 3, No. 1, pp. 40-62.

Tsai, S. W., and Wu, E. M., 1971, "A General Theory of Strength for Anisotropic Materials," *Journal of Composite Materials*, Vol. 5, No. 1, pp. 58-80.

Vicario, A. A., Jr., and Toland, R. H., 1975, "Failure Criteria and Failure Analysis of Composite Structural Components," *Structural Design and Analysis*, Part 1, C. C. Chamis, ed. (*Composite Materials*, Vol. 7, L. J. Broutman and R. H. Krock, eds.), Academic Press, New York, pp. 51-97.

Waddoups, M. E., Eisenmann, J. R., and Kaminski, B. E., 1971, "Macroscopic Fracture Mechanics of Advanced Composite Materials," *Journal of Composite Materials*, Vol. 5, No. 4, pp. 446-454.

Wasti, S. T., 1970, "The Plastic Bending of Transversely Anisotropic Circular Plates," *International Journal of Mechanical Sciences*, Vol. 12, No. 1, pp. 109-112.

Wetherhold, R. C., 1983, "Statistics of Fracture of Composite Materials Under Multiaxial Loading," Ph.D. Dissertation, University of Delaware, Newark, DE.

Whitney, J. M., and Nuismer, R. J., 1974, "Stress Fracture Criteria for Laminated Composites Containing Stress Concentrations," *Journal of Composite Materials*, Vol. 8, No. 3, pp. 253-265.

Wnuk, M. P., and Kriz, R. D., 1985, "CDM Model of Damage Accumulation in Laminated Composites," *International Journal of Fracture*, Vol. 28, No. 3, pp. 121-138.

Wu, E. M., 1968, "Fracture Mechanics of Anisotropic Plates," *Composite Materials Workshop*, S. W. Tsai, J. C. Halpin, and N. J. Pagano, eds., Technomic Publication Co., Inc. Lancaster, PA, pp. 20-43.

Wu, E. M., 1974, "Phenomenological Anisotropic Failure Criterion," *Mechanics of Composite Materials*, G. P. Sendeckyj, ed. (Composite Materials, Vol. 2, L. J. Broutman, ed.), Academic Press, New York, pp. 353-431.

Yamada, S. E., and Sun, C. T., 1978, "Analysis of Laminate Strength and Its Distribution," *Journal of Composite Materials*, Vol. 12, No. 3, pp. 275-284.

Zhen, S., 1983, "The D Criterion Theory in Notched Composite Materials," *Journal of Reinforced Plastics and Composites*, Vol. 2, No. 2, pp. 98-110.

Zweben, C., and Rosen, B. W., 1970, "A Statistical Theory of Material Strength With Application to Composite Materials," *Journal of the Mechanics and Physics of Solids*, Vol. 18, pp. 189-206.

Fracture Energy for Short Brittle Fiber/Brittle Matrix Composites With Three-Dimensional Fiber Orientation

R. C. Wetherhold
Department of Mechanical and
Aerospace Engineering,
State University of New York at Buffalo,
Buffalo, NY 14260

Adding brittle fibers to a brittle matrix can create a composite that is substantially tougher than the monolithic matrix by providing mechanisms for energy dissipation during crack propagation. A model based on probabilistic principles has been developed to calculate the increased energy absorption during fracture for a brittle matrix reinforced with very short, poorly bonded fibers. This model, previously developed for planar fiber orientations, is extended to consider the three-dimensional fiber orientations that may occur during composite fabrication. The fiber pull-out energy is assumed to dominate other fracture energy terms, and simple parametric studies are performed to demonstrate the effect of fiber orientation, fiber length, fiber diameter, and fiber–matrix interfacial shear stress. In particular, the fiber orientation effects may be grouped into an effective "orientation parameter." The model predictions compare satisfactorily with the limited data available, and offer a conceptual framework for considering the effect of changing the physical variables on the fracture energy of the composite.

Introduction

Ceramic or glass–ceramic materials are recognized as providing high strength and microstructure stability at elevated temperatures, as well as possessing low density and chemical inertness. The traditional sudden, brittle fracture behavior of these materials may be made more "graceful" to some extent by the inclusion of a reinforcing second phase, which provides a variety of energy dissipation processes during fracture. For the case of weakly bonded, brittle fibrous reinforcement, the fibers decrease notch sensitivity and increase fracture energy absorption by means of fiber debonding, fiber pull-out, and crack blunting or deflection (Buljan and Sarin, 1987; Donald and McMillan, 1976; Faber and Evans, 1983). Since the overall fracture process involves little plasticity, the crack propagation energy and the energy absorbed during fracture surface creation may be assumed to be simply related (Phillips, 1974). This assumption appears both physically plausible and conservative.

The fracture toughness for any given specimen is the result of the interaction of an enormous number of reinforcing particles. Such a fracture process is best described in probabilistic terms based on a statistical knowledge of the orientation distribution and spatial location distribution of the fibers. This formulation is suited for systematically describing the effect of fiber orientation and other key variables on the fracture energy of reinforced brittle materials. This research, then, focuses on a probabilistic formulation for the energy contribution provided by the addition of short fibers to the work of fracture of a brittle matrix composite such as a ceramic matrix composite (CMC). Based on earlier work on planar fiber orientations (Wetherhold, 1989), we will consider three-dimensional fiber orientation in this paper.

Analytical Development

We cannot predict the failure load for a particular composite, since it depends on the location and distribution of flaws throughout the composite, as well as on an enormous number of fiber–fiber interactions. However, we may observe that after failure, the fracture surface is macroscopically roughly planar and on closer observation is seen to have fibers projecting out from the fracture surfaces (Phillips, 1974; Gadkaree and Chyung, 1986). The debonding and pull-out of these fibers contribute heavily to the dissipation of energy during fracture (Buljan and Sarin, 1987). The measure we choose here for the composite "toughness" during fracture is the integral of the force-displacement curve up to the final fracture condition. Since there is little plasticity in the constituents of these CMC systems, this force-displacement integral should equal the surface energy of the two created fracture surfaces under quasi-static loading-controlled fracture conditions (no kinetic effects). It is thus assumed that the surface energy may be simply related to the critical energy release rate G_{IC}. Using the findings of Phillips (1974) from controlled flexure and impact tests, we have

Contributed by the International Gas Turbine Institute and presented at the 34th International Gas Turbine and Aeroengine Congress and Exhibition, Toronto, Ontario, Canada, June 4–8, 1989. Manuscript received at ASME Headquarters January 23, 1989. Paper No. 89-GT-125.

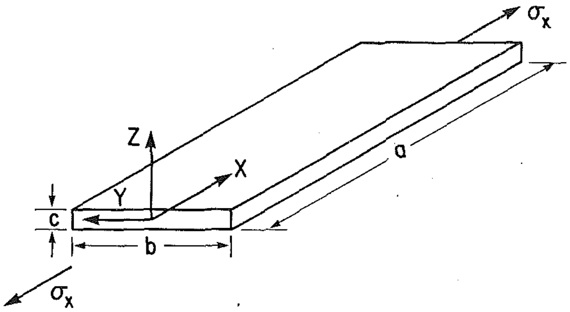

Fig. 1 Specimen dimensions and loading

$$G_{IC} = 2\gamma_c \tag{1}$$

where

G_{IC} = critical energy release rate for crack self-propagation
γ_c = composite surface energy

This generally assumes that the nature of the fracture phenomenon does not change as fracture cleavage continues.

The surface energy γ_c for the composite may be expressed by (Beaumont and Harris, 1972)

$$\gamma_c = \gamma_f + \gamma_r + \gamma_d + \gamma_p + \gamma_a \tag{2}$$

where

γ_f = fracture surface energy (fiber and matrix)
γ_r = released relaxation energy of fiber
γ_d = fiber-matrix debonding energy
γ_p = fiber pull-out energy
γ_a = matrix and fiber plastic deformation energy

As indicated, the plastic deformation term is normally negligible for brittle/brittle composites. The relaxation term refers to the "elastic recoil" of any fiber that is stretched, and then released while still remaining in the matrix, and is also assumed to be small. In this research, we shall restrict our consideration to short fibers whose length never exceeds the critical length. For this important limiting case, this requires that the fiber length be prescribed (Gadkaree and Chyung, 1986; Kelly and MacMillan, 1986)

$$l \le \frac{\sigma_u d}{2\tau_f} \tag{3}$$

where

l = fiber length
σ_u = fiber ultimate strength
d = fiber diameter
τ_f = fiber-matrix interfacial frictional shear stress

Thus the surface energy contribution is restricted to the matrix, since fibers do not fracture. The matrix surface energy will be shown to be a relatively minor and easily included contribution, and will be represented by a deterministic value. In keeping with sensible theoretical assumptions (Beaumont and Harris, 1972; Kelly, 1970) and experimental results (Marshall and Evans, 1985), the pull-put energy is assumed to dominate the debonding energy, and only the former term is included. The principal energy term, then, relates to the fiber pull-out from the matrix, and it is the contribution of this energy to the force-displacement integral which will be pursued.

Consider a CMC specimen of geometry (a, b, c) in the (x, y, z) directions as shown in Fig. 1. The actual fracture plane may be observed as the plane $x=A$ (see Fig. 2), with $A \epsilon$ [0, a]. The actual value of A for a given specimen is a random variable dependent on a complex series of interactions between inherent flaws, fibers, and matrix. What may be simply observed is that any fiber that crosses the plane $x=A$ has debonded and pulled out from one side of the crack surface. The difficulty is to describe how many fibers with what angles have debonded and pulled out along this plane. The fibers are assumed to be of equal length, with a known probabilistic description for center of gravity and orientation.

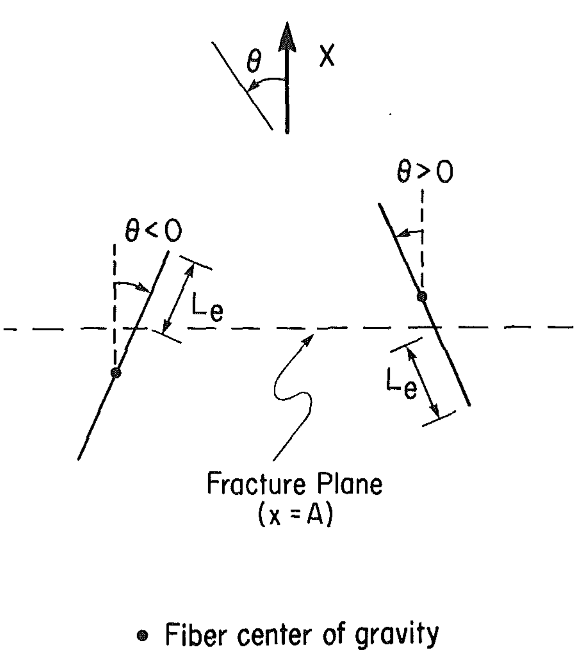

Fig. 2 Sample definitions for in-plane fiber angle and pull-out length

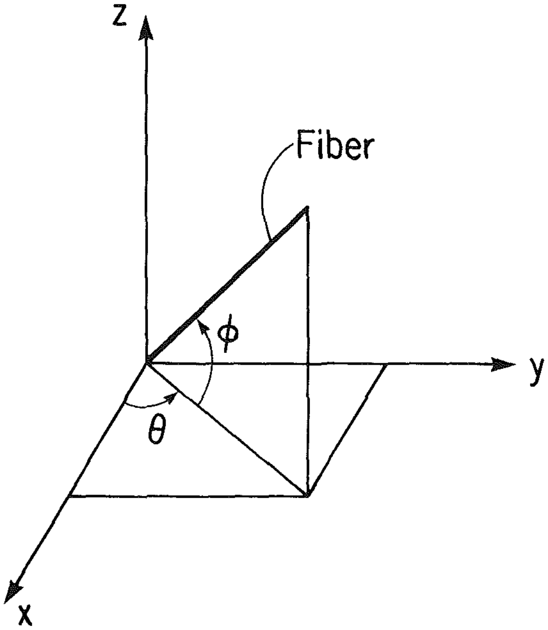

Fig. 3 Definition of planar and tilt angles

The contribution of fiber pull-out and debonding may be considered by dividing the pulled-out fibers into classes. Let the random variable n_{ijk} be the number of fibers that cross the plane $x=A$ with embedded (pull-out) length L_e described by the interval $L_e \epsilon (L_i, L_{i+1})$ in-plane orientation angle $\theta \epsilon (\theta_j, \theta_{j+1})$, and out-of-plane "pitching" angle $\phi \epsilon (\phi_k, \phi_{k+1})$. (The subscripts on all variables refer to intervals of embedded lengths and angles, and are not tensorial indices.) See Fig. 2 for sample embedded lengths and in-plane fiber orientations; see Fig. 3

for a schematic definition of fiber angles. The intervals of pull-out length and fiber orientation have been suitably divided into m, n, and q collectively exhaustive and mutually independent intervals, respectively.

$$\bigcup_{i=1}^{m} (L_i, L_{i+1}) = \left(0, \frac{l}{2}\right) \tag{4}$$

$$\bigcup_{j=1}^{n} (\theta_j, \theta_{j+1}) = \left(-\frac{\pi}{2}, \frac{\pi}{2}\right) \tag{5a}$$

$$\bigcup_{k=1}^{q} (\phi_k, \phi_{k+1}) = \left(-\frac{\pi}{2}, \frac{\pi}{2}\right) \tag{5b}$$

The limits in equation (4) reflect the fact that the shorter end of a fiber always pulls out. The random variable E of fracture energy, exclusive of the minor matrix contribution, is thus given by

$$E = \sum_{i=1}^{m} \sum_{j=1}^{n} \sum_{k=1}^{q} n_{ijk}\, e_{ijk} \tag{6}$$

where

e_{ijk} = pull-out energy for a fiber with L_e $\epsilon(L_i, L_{y+1})$ and $\theta\epsilon(\epsilon_j, \theta_{j+1})$, and $\phi\epsilon\ (\phi_k, \epsilon_{k+1})$

Since the frictional shear stress during pull-out is, to some extent, influenced by the Poisson contraction of the fiber being pulled out, it is not strictly a constant during the pull-out (Piggott et al., 1984). We shall assume here, however, that the frictional shear stress is constant along the length of the fiber, and does not vary during pull-out. Note that this may cause some overestimation of the fracture energy, depending on how the results of a frictional pull-out test are interpreted.

For a fiber with original pull-out length L_e, inclined at an angle ϕ in-plane and at an angle θ out of plane, the pull-out energy is

$$e_{ijk} = \frac{\pi}{2}\, d\ \tau_f\, \bar{L}_1^2/(\cos\bar{\theta}_j \cos\bar{\theta}_k) \tag{7}$$

where

$$\bar{L}_1^2 = \frac{L_i^2 + L_{i+1}^2}{2}$$

$$\bar{\theta}_j = \frac{\theta_j + \theta_{j+1}}{2}$$

$$\bar{\phi}_k = \frac{\phi_k + \phi_{k+1}}{2}$$

This equation arises naturally from force balance considerations for an inextensible fiber resisting the separation of the crack force (Wetherhold, 1989; Aveston and Kelly, 1973). As the crack faces separate, a force F_x along the fiber resists the separation and contributes to the work of pull-out. Both the frictional force and the normal force on the fiber as it leaves the matrix and moves into the crack opening will contribute to F_x by equilibrium. (For the normal force, it may be helpful to consider a rope moving over a pulley.) Since the fiber is assumed inextensible, the crack opening ξ over which we get a contribution is L_e. The pull-out work is thus

$$e_{ijk} = \frac{1}{\cos\theta \cos\phi} \int_0^{L_e} \tau_f \pi d\, (L_e - \xi) d\xi$$

giving the result (7).

From physical considerations, equation (7) requires modification for large angles, since there will be additional bending stresses that will cause fiber fracture rather than pull-out (Wetherhold, 1989). We thus propose a form for pull-out energy of

$$e_{ijk} = \begin{cases} \frac{\pi}{2} d\tau_f \bar{L}_i^2/\cos\bar{\theta}_j \cos\bar{\phi}_k & |\psi| < \psi_c \\ 0 & |\psi| > \psi_c \end{cases} \tag{8}$$

where $\cos\psi = \cos\theta \cos\phi$ or $\psi = \cos^{-1} \{\cos\theta \cos\phi\}$. Both the fiber inextensibility and critical angle assumptions are physically plausible; improvements in these assumptions are a subject of current research.

The fiber orientation distribution is assumed to obey the usual normalization and symmetry conditions, and the distribution of in-plane and out-of-plane angles is independent. Only the x component of the pull-out force will be considered in the integral of the force-displacement curve. These requirements may be expressed as

$$\int_{-\pi/2}^{\pi/2} \int_{-\pi/2}^{\pi/2} n(\theta, \phi)\, d\theta d\phi = 1 \tag{9a}$$

$$n(\theta, \phi) = n_\theta(\theta) n_\phi(\phi) \tag{9b}$$

$$n(\theta, \phi) = n(-\theta, \phi) = n(\theta, -\phi) \tag{9c}$$

Ideally, we should seek the entire distribution of the random variable E: its mean, variance, and all appropriate moments. It is important to realize that n_{ijk} in equation (6) are themselves random variables. Thus to recover the distribution function

$$F_E(x) \equiv P\left[\sum_{i=1}^{m} \sum_{j=1}^{n} \sum_{k=1}^{q} n_{ijk}\, e_{ijk} \le x\right] \tag{10}$$

we would need to perform an (n by m by q)-fold integration with functions as integration limits; that is, the integration is not over a product space. This integration is normally intractable. We therefore propose a simplification to recover the mean value of E. This yields more statistical information than was previously available. Recognizing that the n_{ijk} are statistically independent random variables with nonidentical distributions (Hoel et al., 1971),

$$\mu_E = \sum_{i}^{m} \sum_{j}^{n} \sum_{k}^{q} \bar{E}_{ijk} \tag{11}$$

where

$\bar{E}_{ijk}$ = average of the energy contribution $[n_{ijk}\, e_{ijk}]$

If we define the event probability p_{ijk} as follows:

$$p_{ijk} = p\{\text{fiber crosses plane } x = A \text{ with embedded length } L_e \epsilon (L_i, L_{i+1}),\ \theta\epsilon\ (\theta_j, \theta_{j+1}), \text{ and } \phi\epsilon(\phi_k, \phi_{k+1})\} \tag{12}$$

then the expected value of the energy $\bar{E}_{ijk}$ can be approximated over a very large number of independent Bernoulli trials as

$$\bar{E}_{ijk} = \bar{n}_{ijk} e_{ijk} \tag{13a}$$

where

$$\bar{n}_{ijk} = N p_{ijk} \tag{13b}$$

N = number of fibers in the sample (specimen)

Equation (13b) simply restates the fact that the random variable n_{ijk} converges to $\bar{n}_{ijk}$ over a large number of trials (Hoel et al., 1971). The remaining item is to calculate the probability p_{ijk}.

Using Bayes' theorem for the probability p_{ijk}, we may separate it into a more tractable product form

$$p_{ijk} = p_{i/jk}\, p_{jk} \tag{14}$$

where

$$p_{jk} = \int_{\theta_j}^{\theta_{j+1}} n_\theta(\theta) d\theta \int_{\phi_k}^{\phi_{k+1}} n_\phi(\phi) d\phi \tag{15a}$$

$$p_{i/jk} = p\ \{L_e\ \epsilon(L_i, L_{i+1})/\ \theta\epsilon\ (\theta_j, \theta_{j+1})\ \phi\epsilon(\phi_k, \phi_{k+1})\} \tag{15b}$$

If the fiber center of gravity is uniformly distributed ($f_x(x) = 1/a$), the conditioned event given by equation (15b) may be expressed as (Wetherhold, 1989)

Table 1 Model parameters

Property/parameter	Value
($a \times b \times c$) specimen dimensions (cm)	$10 \times 2 \times 0.5$
Cross-sectional area (cm^2)	1.0
Fiber volume fraction, Vf	0.3
Average fiber length, $l(\mu$m)	250
Average fiber diameter, $d(\mu$m)	8.0
Average fiber/matrix shear, τ_f(MPa)	2.40
Interval size for θ, ϕ	$\pi/100$
Number of L_e intervals used	100

Table 2 In-plane orientation distributions

Fiber distribution	Density function $n(\theta)$ $\Theta \epsilon [-\pi/2, \pi/2]$
Random	$1/\pi$
Cosine	$\frac{1}{2}\cos\theta$
Cosine squared	$\frac{2}{\pi}\cos^2\theta$
Aligned	$\delta(0)$

Table 3

Fiber orientation	Average energy/area, $\mu_E/(bc)$ (J/m^2)	Relative energy
Random in-plane, no out-of-plane	656	0.70
Random in-plane, $\phi' = 0.0556\pi$ (10 deg)	656	0.70
Random in-plane, $\phi' = 0.1111\pi$ (20 deg)	651	0.69
Fully random: random in-plane, $\phi' = \pi/2$ (90 deg)	385	0.40
Aligned in-plane ($n_\theta(\theta) = \delta(0)$), no out-of-plane	938	1.0
Aligned in-plane, $\phi' = 0.0556\pi$ (20 deg)	938	1.0

$$p_{i/jk} = 2\,(L_{i+1} - L_i)\cos\bar{\theta}_j \cos\bar{\phi}_k/a \tag{16}$$

It should be noticed that the probabilities p_{ijk} and $p_{i/jk}$ are insensitive to the choice of the plane A, as expected. This completes the required derivation for p_{ijk}.

Model Studies

A model SiC fiber composite was considered, with properties as given in Table 1 (Marshall and Evans, 1985; Sambell et al., 1972). The size of the intervals used for angles and embedded lengths is the result of a simple convergence study. The major classification of the results is by fiber orientation, with the in-plane orientation density functions given by Table 2.

It is useful to examine the effect of the out-of-plane tilting on the average pull-out energy μ_E for the model composite. For the out-of plane fiber orientation, we consider uniform density functions of the form

$$n_\phi(\phi) = \begin{cases} 1/(2\phi') & \phi\epsilon(-\phi', \phi') \\ 0 & \text{elsewhere} \end{cases} \tag{17}$$

The results of various fiber orientations may be seen in Table 3. For cases with no out-of-plane fiber orientation, we may consider that $n_\phi(\phi) = \delta(0)$. In agreement with fracture data from two different fiber orientations (Wetherhold, 1989; Sambell et al., 1972), we select a critical angle $\theta_c = 63$ deg.

Discussion and Conclusion

It is instructive to note that the same statistical concepts presented in Section 2 may be used to obtain the variance of the fracture energy. The results are again based on the independence of the events specified by p_{ijk} (equation (12)) together with a large number of Bernoulli trials. The variance results are

Table 4 Effect of physical variables

Variable	Average μ_E scales as	Variance $\hat{\sigma}_E^2$ scales as	COV $= \hat{\sigma}_E/\mu_E$ scales as
Volume fraction V_f	V_f	V_f	$1/\sqrt{V_f}$
Fiber length l	l^2	l^4	Independent
Fiber diameter d	$1/d$	No effect	d
Interfacial shear τ_f	τ_f	τ_f^2	Independent
Cross-sectional area $A = (bc)$	A	A	$1/\sqrt{A}$

$$\hat{\sigma}_E^2 = \sum_i^m \sum_j^n \sum_k^q \hat{\sigma}_{Eijk}^2 \tag{18}$$

where

$$\hat{\sigma}_{Eijk}^2 = Np_{ijk}(1 - p_{ijk})\, e_{ijk}^2 \tag{19}$$

We may thus systematically determine how the average, variance, and coefficient of variation (COV) are affected by altering the physical parameters one at a time. The results are given in Table 4. Several clarifications may be given. The scaling with volume fraction is like a scaling with N, the total number of fibers; this effect may be seen from equations (11), (13) and (18), (19). The dependence on fiber diameter derives from the net effect of e_{ij} as proportional to d, together with the number N as proportional to $1/d^2$. The dependence on frictional shear stress may be seen in equation (8), although we must assure ourselves that the fibers will still pull out and not fracture (equation (3)). For the length variation, it is useful to remember that we divided the fiber length up into a given number of pull-out lengths based on convergence considerations. Consider that as we change the overall fiber length from L_1 to L_2, the ith embedded length goes from $(i - 1/2)L_1/2m$ to $(i - 1/2)L_2/2m$, and that the energy e_{ijk} is a function of the length squared.

The summation (11) used for the average fracture energy contains both physical parameters and orientation parameters. This may be manipulated to separate these two factors. Since the division of $l/2$ into m segments is uniform, we have $L_i = (i-1)l/2m$. Making the appropriate substitutions and summations, with m reasonably large, we may rewrite equation (11) as

$$\mu_e = \frac{\pi d \tau_f l^2}{24} \left[\frac{V_f\, bc}{\pi d^2/4}\right] \Phi \tag{20}$$

where

$$\Phi = \sum_j^n \sum_k^q [F_\theta(\theta_{j+1}) - F_\theta(\theta_j)][F_\phi(\phi_{j+1}) - F_\phi(\phi_j)]\ \{1 - u(|\psi| - \psi_c)\} \tag{21}$$

$$F_i(x) = \int_{-\pi/2}^{x} n_i(\xi)d\xi \qquad i = \theta, \phi$$

In certain tractable cases, the summation expressed by equation (21) may be returned to the integral formulation

$$\Phi = \int_A n_\theta n_\phi\, d\phi d\theta \tag{22}$$

where

$$A = \{(\theta, \phi) : |\psi| < \psi_c\}$$

We may then take advantage of the symmetry properties (9) to evaluate equation (22) concisely. In simple cases, equation (22) may be found in closed form; otherwise, a numerical integration is required. For the case of planar fiber orientations ($n_\phi(\phi) = \delta(0)$), equation (22) will reduce simply to

$$\Phi = F_\theta(\psi_c) - F_\theta(-\psi_c) \tag{23}$$

This use of an orientation parameter for strength parallels that of the prediction of thermoelastic properties for short fiber composites (Wu and McCullough, 1977), and provides an important mechanism for comparing the toughness of different fiber orientations.

Acknowledgments

This research was supported by NASA-Lewis Research Center under Grant No. NAG3862.

References

Aveston, J., and Kelly, A., 1973, "Theory of Multiple Fracture of Fibrous Composites," *J. Mat. Sci.*, Vol. 8, p. 352.

Beaumont, P. W., and Harris, B., 1972, "The Energy of Crack Propagation in Carbon Fibre-Reinforced Resin Systems," *J. Mat. Sci.*, Vol. 7, p. 1265.

Buljan, S. T., and Sarin, V. T., 1987, "Silicon Nitride Based Composites," *Compos*, Vol. 18, p. 99.

Donald, I. W., and McMillan, P. W., 1976, "Review Ceramic Matrix Composites," *J. Mat. Sci.*, Vol. 11, p. 949.

Faber, K. T., and Evans, A. G., 1983, "Crack Deflection Processes — I. Theory," *Acta Metall.*, Vol. 31, pp. 565–576.

Gadkaree, K. P., and Chyung, K., 1986, "Silicon Carbide Whisker Reinforced Glass and Glass-Ceramic Composites," *Am. Cer. Soc. Bull.*, Vol. 65, p. 370.

Hoel, P. G., Part, S. C., and Stone, C. J., 1971, *Introduction to Probability Theory*, Houghton-Mifflin, Boston, p. 97.

Kelly, A., 1970, "Interface Effects and the Work of Fracture of a Fibrous Composite," *Proc. Roy. Soc. Lond.*, Vol. A319, p. 95.

Kelly, A., and MacMillan, N. H., 1986, *Strong Solids*, 3rd ed., Clarendon Press, Oxford.

Marshall, D. B., and Evans, A. G., 1985, "Failure Mechanisms in Ceramic Fiber/Ceramic Matrix Composites," *J. Am. Ceram. Soc.*, Vol. 68, p. 225.

Phillips, D. C., 1974, "Interfacial Bonding and the Toughness of Carbon Fibre Reinforced Glass and Glass-Ceramics," *J. Mat. Sci.*, Vol. 9, p. 1847.

Piggott, M. R., Chua, P. S., and Andison, D., 1984, "The Interface Between Glass and Carbon Fibers and Thermosetting Polymers," *Polym. Compos.*, Vol. 15, p. 19.

Sambell, R. A. J., Bowen, D. W., and Phillips, D. C., 1972, "Carbon Fibre Composites With Ceramic and Glass Matrices. Part I. Discontinuous Fibres," *J. Mat. Sci.*, Vol. 7, p. 663.

Wetherhold, R. C., 1989, "Energy of Fracture for Short Brittle Fiber/Brittle Matrix Composites With Planar Fiber Orientation," *Mat. Sci. Eng.*, Vol. A112, p. 31.

Wu, C. D., and McCullough, R. L., 1977, "Constitutive Relationships for Heterogeneous Materials," in: *Developments in Composite Materials*, G. S. Hollister, ed., Applied Science Pub., London.

S. F. Duffy[1]
Dept. of Civil Engineering and Engineering Mechanics,
Cleveland State University,
Cleveland, OH 44115

J. M. Manderscheid
Structural Integrity Branch,
NASA Lewis Research Center,
Cleveland, OH 44135

Noninteractive Macroscopic Reliability Model for Ceramic Matrix Composites With Orthotropic Material Symmetry

A macroscopic noninteractive reliability model for ceramic matrix composites is presented. The model is multiaxial and applicable to composites that can be characterized as orthotropic. Tensorial invariant theory is used to create an integrity basis with invariants that correspond to physical mechanisms related to fracture. This integrity basis is then used to construct a failure function per unit volume (or area) of material. It is assumed that the overall strength of the composite is governed by weakest link theory. This leads to a Weibull-type model similar in nature to the principle of independent action (PIA) model for isotropic monolithic ceramics. An experimental program to obtain model parameters is briefly discussed. In addition, qualitative features of the model are illustrated by presenting reliability surfaces for various model parameters.

Introduction

The potential advantages of ceramic matrix composites include increased fracture toughness as well as creep and corrosion resistance at very high service temperatures. The primary applications under consideration are advanced turbine engine composites, cutting tool bits, heat exchangers, and aerospace components (specifically those of the national aerospace plane). Considering that these composites will be produced from nonstrategic materials, it is not surprising that concerted research efforts are underway both in the field of materials science to advance processing techniques and in the field of engineering mechanics to develop design methodologies for these material systems.

The material system of interest in this paper is the whisker-toughened ceramic matrix composite. With this medium the reliability analysis must account for material symmetry imposed by whisker orientation. Duffy and Arnold (1989) presented a macroscopic model that accounted for the transversely isotropic material symmetry often encountered in hot-pressed and injection-molded whisker-toughened ceramics. A similar approach is used herein to develop a noninteractive reliability model for a material with orthotropic symmetry. This continuum approach excludes any consideration of the microstructural events that involve interactions between individual whiskers and the matrix. Other authors have addressed fracture of ceramic matrix composites on a more local scale. Wetherhold (1989) developed a model based on probabilistic principles to compute an increased energy absorption during fracture due to whisker pull-out. Faber and Evans (1983) have addressed the process of crack deflection, and Lange (1970) has modeled crack pinning. The latter two approaches are founded in deterministic fracture mechanics. Knowing that these crack mitigation processes strongly interact, it is a seemingly intractable task to detect experimentally or predict analytically the sequence of mechanisms leading to failure. A more feasible approach is the continuum-based criterion whereby reliability is computed in term of macrovariables.

As pointed out by Leckie (1981), the difference between the materials scientist and the engineer is one of scale. He notes that the materials scientist is interested in mechanisms of failure at the microstructural level and the engineer focuses on this issue at the component level. We adopt the engineer's viewpoint and present a model of practical utility that macroscopically captures the probabilistic failure phenomenon of whisker-toughened ceramics. This point of view implies that the material element under consideration is small enough to be homogeneous in stress and temperature, yet large enough to contain a sufficient number of whiskers such that the element is a statistically homogeneous continuum. This does not imply that the microscopic and macroscopic levels of focus are mutually exclusive. Indeed a close relationship must exist between the materials scientist and engineer so as to develop better failure models.

Noninteractive Reliability Model

Here we consider a continuum to be a chain comprised of links connected in series. Therefore, the overall strength of the continuum is governed by the strength of its weakest link. We further assume that the events leading to failure of an indi-

---

[1] NASA Resident Research Associate; work funded under Cooperative Agreement NCC3-81.

Contributed by the International Gas Turbine Institute and presented at the 34th International Gas Turbine and Aeroengine Congress and Exhibition, Toronto, Ontario, Canada, June 4-8, 1989. Manuscript received at ASME Headquarters January 23, 1989. Paper No. 89-GT-129.

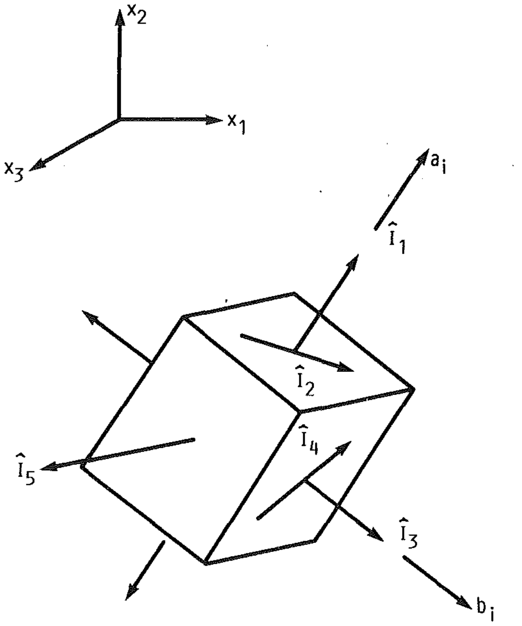

Fig. 1 Physical interpretations of invariants corresponding to fracture mechanisms

vidual link are not influenced by any other link in the chain. Defining f as the failure of an individual link, then

$$f=\psi\Delta V \tag{1}$$

where ΔV denotes an increment in volume and ψ is a failure function per unit volume of material. Taking r as the reliability of an individual link, then

$$r=1-\psi\Delta V \tag{2}$$

If the failure of an individual link is considered a statistical event, and we assume these events are independent, then the reliability of the continuum, denoted as R, is

$$R=\lim_{N\to\infty}\left[\prod_{\lambda=1}^{N} r_\lambda\right]$$

$$R=\lim_{N\to\infty}\left\{\prod_{\lambda=1}^{N}[1-\psi(x_i)\Delta V]_\lambda\right\} \tag{3}$$

Here $\psi(x_i)$ is the failure function per unit volume at position x_i within the continuum. Lower case Roman letter subscripts denote tensor indices with an implied range from 1 to 3. Greek letter subscripts are associated with products or summations with ranges that are explicit in each expression. Adopting an argument used by Cassenti (1984), the reliability of the continuum is given by the following expression:

$$R=\exp\left[-\int_V \psi\, dV\right] \tag{4}$$

For orthotropic composites the failure function must also reflect the appropriate material symmetry. This requires

$$\psi=\psi(\sigma_{ij},\, a_i,\, b_i) \tag{5}$$

where a_i and b_i are unit vectors that identify local material orientations, and σ_{ij} represents the Cauchy stress tensor. These orientations are depicted in Fig. 1.

The sense of a_i and b_i is immaterial; thus their influence is taken through the products a_ia_j and b_ib_j, i.e.,

$$\psi=\psi(\sigma_{ij},\, a_ia_j,\, b_i\, b_j) \tag{6}$$

Note that a_ia_j and b_ib_j are symmetric second-order tensors that satisfy the identities

$$a_ia_i=1 \tag{7}$$

and

$$b_ib_i=1 \tag{8}$$

Furthermore, the stress and local preferred directions may vary from point to point in the continuum. Thus, equation (6) implies that the stress field and unit vector fields, i.e., $\sigma_{ij}\,(x_k)$, $a_i\,(x_k)$, and $b_i\,(x_k)$, must be specified to define ψ.

As ψ is a scalar valued function, it must remain form invariant under arbitrary proper orthogonal transformations. Work by Reiner (1945), Rivlin and Smith (1969), Spencer (1971), and others demonstrates that through the application of the Cayley-Hamilton theorem and elementary properties of tensors, a finite set of invariants (as opposed to the work of Tsai and Wu (1971), where an infinite number of invariants are allowed) known as an integrity basis can be developed. Form invariance of ψ is ensured if dependence is taken on invariants that constitute the integrity basis, or any subset thereof. Adapting the above-mentioned work to ψ results in an integrity basis composed of 28 tensor products. Following arguments similar to those of Spencer (1984), several of these tensor products are equal and others are trivial identities such that the final integrity basis for ψ contains only the invariants

$$I_1=\sigma_{ii} \tag{9}$$

$$I_2=\sigma_{ij}\sigma_{ji} \tag{10}$$

$$I_3=\sigma_{ij}\sigma_{jk}\sigma_{ki} \tag{11}$$

$$I_4=a_ia_j\sigma_{ji} \tag{12}$$

$$I_5=a_ia_j\sigma_{jk}\sigma_{ki} \tag{13}$$

$$I_6=b_ib_j\sigma_{ji} \tag{14}$$

and

$$I_7=b_ib_j\sigma_{jk}\sigma_{ki} \tag{15}$$

A slightly different set of invariants that corresponds to physical mechanisms related to fracture can be constructed from the above integrity basis. This new set of invariants includes

$$\hat{I}_1=I_4 \tag{16}$$

$$\hat{I}_2=[I_5-(I_4)^2]^{1/2} \tag{17}$$

$$\hat{I}_3=I_6 \tag{18}$$

$$\hat{I}_4=[I_7-(I_6)^2]^{1/2} \tag{19}$$

and

$$\hat{I}_5=I_1-I_4-I_6 \tag{20}$$

Considering a uniformly stressed volume, or in the context of Weibull analysis a single link, the invariant $\hat{I}_1$ corresponds to the magnitude of the stress component in the direction of a_i, as shown in Fig. 1. $\hat{I}_2$ corresponds to the shear stress on the face normal to a_i. Similar interpretations can be made for invariants $\hat{I}_3$ and $\hat{I}_4$ and the direction b_i. Invariant $\hat{I}_5$ is the normal stress in the direction defined by the cross product of vectors a_j and b_k, i.e.,

$$d_i=e_{ijk}a_jb_k \tag{21}$$

where e_{ijk} is the permutation tensor. As proposed, these physical mechanisms are independent of I_2 and I_3. Taking

$$\psi=\psi(\hat{I}_1,\, \hat{I}_2,\, \hat{I}_3,\, \hat{I}_4,\, \hat{I}_5) \tag{22}$$

ensures ψ is form invariant.

It is assumed that compressive stresses associated with $\hat{I}_1$, $\hat{I}_3$, and $\hat{I}_5$ do not contribute to failure so that

$$\langle\hat{I}_1\rangle=\begin{cases}\hat{I}_1 & \hat{I}_1>0\\ 0 & \hat{I}_1\leq 0\end{cases} \tag{23}$$

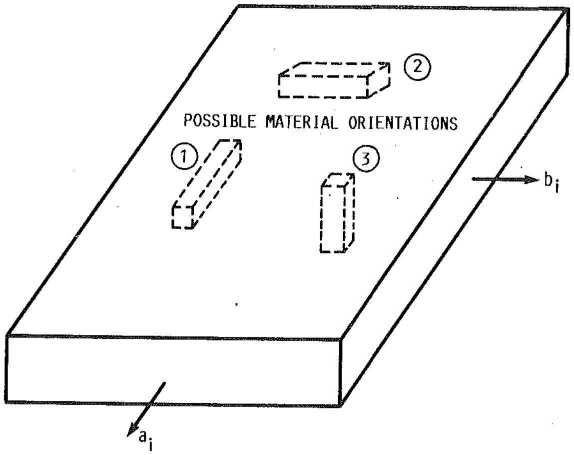

Fig. 2 Orientations of specimens for MOR bar and shear tests for full three-dimensional characterization of the Weibull parameters

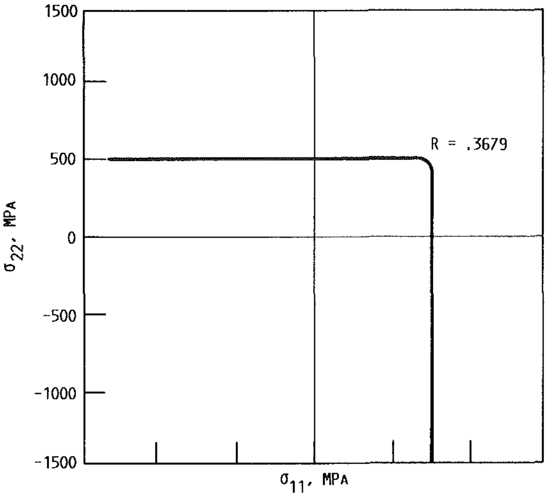

(A) BIAXIAL STRESS SPACE σ_{22}-σ_{11} WITH β_1 = 750 AND β_3 = 500.

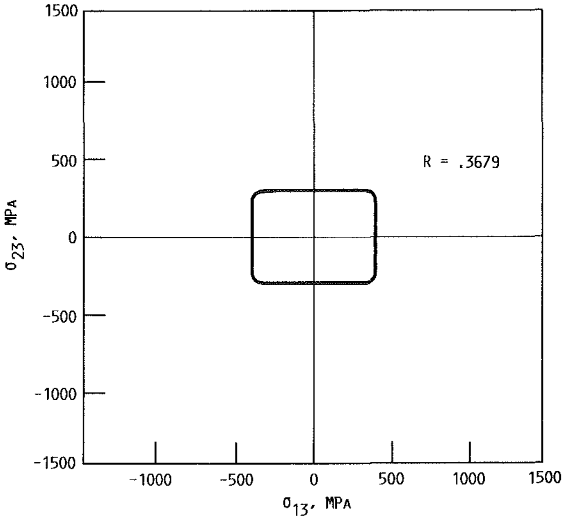

(B) SHEAR STRESS SPACE σ_{13}-σ_{23} WITH β_2 = 400 AND β_4 = 300.

Fig. 3 Reliability contours of an orthotropic continuum of unit volume with material directions a_1 and b_1 coincident with 1 and 2 directions, respectively; failure function, ψ, equal to unity

$$\langle \hat{I}_3 \rangle = \begin{cases} \hat{I}_3 & \hat{I}_3 > 0 \\ 0 & \hat{I}_3 \leq 0 \end{cases} \tag{24}$$

and

$$\langle \hat{I}_5 \rangle = \begin{cases} \hat{I}_5 & \hat{I}_5 > 0 \\ 0 & \hat{I}_5 \leq 0 \end{cases} \tag{25}$$

In addition,

$$\langle \hat{I}_2 \rangle = |\hat{I}_2| \tag{26}$$

and

$$\langle \hat{I}_4 \rangle = |\hat{I}_4| \tag{27}$$

for all values of $\hat{I}_2$ and $\hat{I}_4$. At this point we assume that the stress components identified by the invariants above act independently (i.e., a noninteractive theory) in producing failure. Following reasoning similar to Wetherhold (1983), ψ takes the form

$$\psi = \left[\frac{\langle \hat{I}_1 \rangle}{\beta_1}\right]^{\alpha_1} + \left[\frac{\langle \hat{I}_2 \rangle}{\beta_2}\right]^{\alpha_2} + \left[\frac{\langle \hat{I}_3 \rangle}{\beta_3}\right]^{\alpha_3} + \left[\frac{\langle \hat{I}_4 \rangle}{\beta_4}\right]^{\alpha_4} + \left[\frac{\langle \hat{I}_5 \rangle}{\beta_5}\right]^{\alpha_5} \tag{28}$$

Insertion of equation (28) into the volume integration given by equation (4) along with equations (23)-(27) yields a reliability model for a three-dimensional state of stress in an orthotropic ceramic composite. This model is similar in nature, yet different in form, to the PIA theory for monolithic ceramics.

In association with each invariant, the α's correspond to the Weibull shape parameters and the β's correspond to Weibull scale parameters. A variety of test methods could be used to determine these model parameters. One approach is to obtain the requisite tensile data from fast fracture of simple bend test specimens, often referred to as modulus of rupture (MOR) bars. The parameters α_1 and β_1 could be obtained from MOR bar tests conducted on specimens machined from a billet of hot pressed whisker-toughened ceramics. These specimens would be oriented along material direction a_i, shown as orientation 1 in Fig. 2. MOR bar specimens machined with orientation 2 (i.e., along b_i) could be used to determine α_3 and β_3, and similarly, orientation 3 would be used to determine α_5 and β_5. The Weibull parameters associated with shear tractions across a_i and b_i could be obtained from shear tests such as Iosipescu tests (Walrath and Adams, 1983). The parameters α_2 and β_2 could be determined from this type of test using specimens with orientation 1 in Fig. 1. Similarly, the final two parameters, α_4 and β_4, could be obtained from shear tests conducted on specimens with orientation 2.

In comparison to the transversely isotropic model (Duffy and Arnold, 1989), for which three sets of Weibull parameters are necessary, the orthotropic model requires five. However it should be noted here that, as with monolithic ceramics, it is quite possible that the surface and volume of the material will fail due to distinctly different flaw populations. These populations differ for several reasons:

1 The as-fired condition of the surface may be different due to the formation of a reaction layer:

2 grinding will change the surface and may impart subsurface damage; and

3 even if the surface flaw distribution is solely due to the intersection of internal flaws with the surface, the presence of the free surface will reduce the applied load necessary for fracture. The surface would then have different sets of Weibull parameters than the volume and equation (4) would also have to be independently evaluated over the surface area.

Implications of the Model

Subsequent to the determination of the Weibull parameters, multiaxial experiments should be conducted to assess the model's accuracy. One method is tension and/or torsion loadings

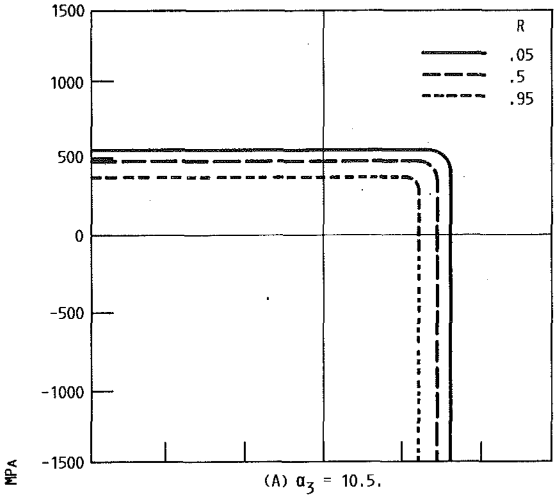

(A) α_3 = 10.5.

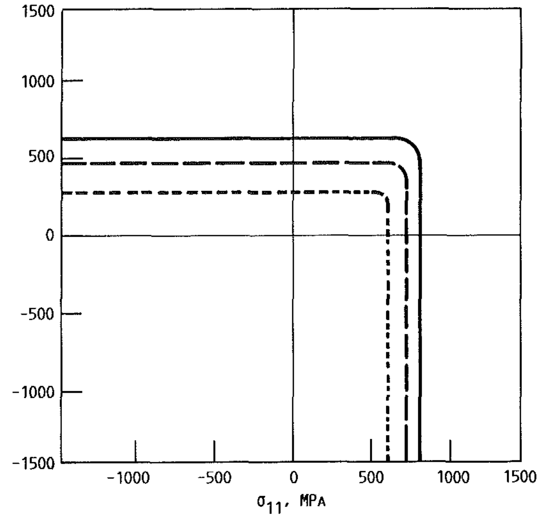

(B) α_3 = 5.

Fig. 4 Families of reliability contours depicting the effect of reducing the Weibull shape parameter α_3; material directions are the same as in Fig. 3 with $\alpha_1 = 15$. $\beta_1 = 750$, and $\beta_3 = 500$

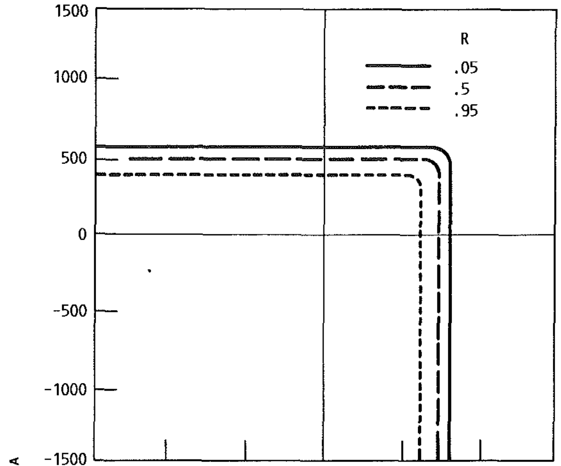

(A) a_i AND b_i COINCIDENT WITH THE 1- AND 3- DIRECTIONS RESPECTIVELY.

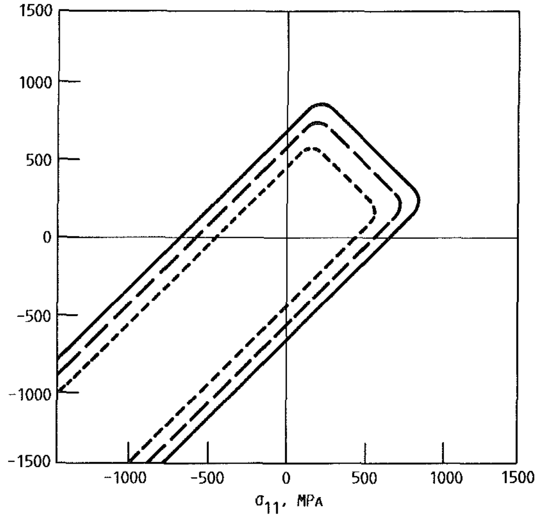

(B) MATERIAL DIRECTIONS a_i AND b_i ROTATED 45° IN THE 1-3 PLANE.

Fig. 5 Level surfaces of reliability illustrating the result of off-axis loading in a normal stress space; Weibull parameters for invariants $\hat{I}_1$ and $\hat{I}_3$ are the same as in Fig. 3(*a*), along with $\alpha_2 = 12$, $\beta_2 = 400$, $\alpha_4 = 10$, and $\beta_4 = 300$

applied to thin-walled tube specimens. The thin-walled tube ensures homogeneous, biaxial states of stress. The tubular specimen would be highly appropriate for planar applications such as heat exchangers where one of the material orientations (radial) can be ignored. Unfortunately, at the present time no data base exists to estimate model parameters, although efforts (Shaw and Bubsey, 1987) are underway to accomplish this goal. Thus an assessment of the model in comparison to experimental data is reserved for a later date, and for the examples that follow, model parameters are arbitrarily chosen for the purpose of illustration.

The calculations for the reliability contours shown herein are representative of homogeneously stressed continuum elements (or links) of unit volume. For dimensionless R, the Weibull parameter β has units of stress • (volume)$^{1/\alpha}$. Consider the material symmetry where $a_i = (1, 0, 0)$ and $b_i = (0, 1, 0)$. The uniaxial loading $\sigma_{11} \neq (\sigma_{12} = \sigma_{13} = \sigma_{22} = \sigma_{23} = \sigma_{33} = 0)$ for this orientation yields the following invariants for ψ:

$$\hat{I}_1 = \sigma_{11} \tag{29}$$

$$\hat{I}_2 = \hat{I}_3 = \hat{I}_4 = \hat{I}_5 = 0 \tag{30}$$

Hence equation (4) becomes

$$R = \exp\left[-\left(\frac{\sigma_{11}}{\beta_1}\right)^{\alpha 1}\right] \tag{31}$$

Taking $\sigma_{11} = \beta_1$ in this expression yields $R = 0.3679$. Therefore, any contour $R = 0.3679$, in a stress space containing σ_{11}, yields β_1 as the intercept along the σ_{11} axis. This can be seen in Fig. 3(*a*) where this reliability contour is plotted in the σ_{11}-σ_{22} stress space, and $\beta_1 = 750$. Also note that the intercept along the σ_{22} axis, which represents a uniaxial loading in the direction b_i, yields the Weibull parameter $\beta_3 = 500$. In a similar fashion the pure shear loading $\sigma_{13} \neq 0$ $(\sigma_{11} = \sigma_{12} = \sigma_{22} = \sigma_{23} = \sigma_{33} = 0)$ would yield β_2 as an intercept along the σ_{13} axis, and $\sigma_{23} \neq 0$ $(\sigma_{11} = \sigma_{12} = \sigma_{13} = \sigma_{22} = \sigma_{33} = 0)$ would yield β_4 as an intercept along the σ_{23} axis. This can be seen in Fig. 3(*b*) where $\beta_2 = 400$ and $\beta_4 = 300$.

Figure 4(*a*) depicts the intersection of level surfaces of R with the σ_{11}-σ_{22} stress plane for the previously mentioned material orientation. Here $\alpha_1 = 15$, $\alpha_3 = 10.5$, and as before, $\beta_1 = 750$ and $\beta_3 = 500$. The three surfaces correspond to $R = 0.95, 0.50$, and 0.05. Note that a decrease in the α's increases the spacing of the contours, which indicates a higher scatter in fracture strength. This can be seen in Fig. 4(*b*) where $\alpha_3 = 5$. The spacing between contours increases in the σ_{22} direction; however, the contours in the σ_{11} direction remain unchanged because there is no variation in α_1 or β_1. If α_3 had been in-

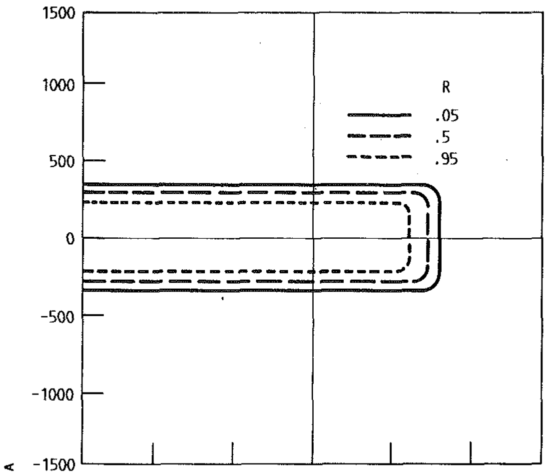

(A) a_i AND b_i COINCIDENT WITH THE 1- AND 3-DIRECTIONS RESPECTIVELY.

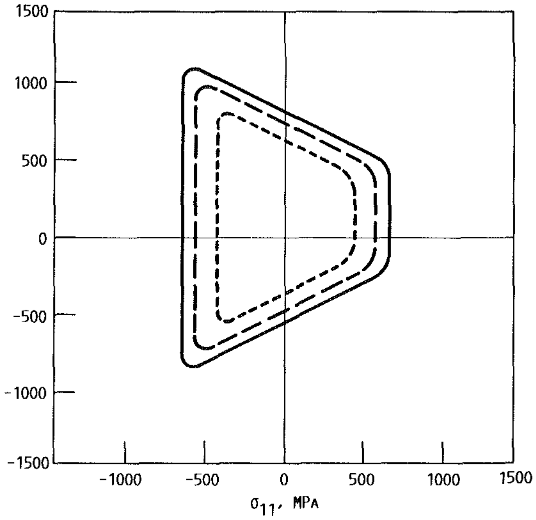

(B) MATERIAL DIRECTIONS ROTATED 45° IN THE 1-3 PLANE.

Fig. 6 Families of reliability contours comparing on- and off-axis orientations of the material directions a_i and b_i in the σ_{11}-σ_{13} stress space; the Weibull parameters for $\hat{I}_1$, $\hat{I}_2$, $\hat{I}_3$, and $\hat{I}_4$ are the same as in Fig. 5

creased, the spacing between contours would diminish, and the corners in the first quadrant would sharpen. In general, as the α's increase, eventually the reliability contours would not be distinct from each other and they would effectively map a deterministic maximum stress failure surface.

We next consider the effects of off-axis (relative to loading) material orientation. Figure 5(*a*) represents level surfaces projected onto the σ_{11}-σ_{33} stress plane for the material orientation defined by $a_i = (1, 0, 0)$ and $b_i = (0, 0, 1)$. Here $\alpha_1 = 15$, $\beta_1 = 750$, $\alpha_3 = 10.5$, and $\beta_3 = 500$, and once again three contours of reliability are depicted: $R = 0.95$, 0.5, and 0.05. Rotation of the material orientation vectors such that $a_i = (1/\sqrt{2}, 0, 1/\sqrt{2})$ and $b_i = (-1/\sqrt{2}, 0, 1/\sqrt{2})$, for the conditions identical to those associated with Fig. 5(*a*) results in the contours found in Fig. 5(*b*). Due to the new material orientation, compressive components of the stress tensor σ_{ij} contribute to failure. This does not contradict the assumption that compressive stresses along the material direction a_i (identified by $\hat{I}_1$), and along the material direction b_i (identified by $\hat{I}_3$) do not contribute to a reduction in reliability. In this case σ_{11} and σ_{33} are no longer coincident with the stresses associated with $\hat{I}_1$ and $\hat{I}_3$. Expansion of the invariants demonstrates that compressive values of σ_{11} and σ_{33} contribute to both $\hat{I}_2$ and $\hat{I}_4$ (the shear stresses across the material orientation vectors a_i and b_i, respectively) and hence cause a reduction in reliability.

Figure 6(*a*) represents level surfaces of reliability projected onto the σ_{13}-σ_{11} stress plane. Here a uniaxial compressive stress (σ_{11}) maintains a reliability of unity and the contours are symmetric with respect to the σ_{11} axis. This results from the assumptions associated with equations (23), (26), and (27). Rotation of the material orientation such that $a_i = (1/\sqrt{2}, 0, 1/\sqrt{2})$ and $b_i = (-1/\sqrt{2}, 0, 1\sqrt{2})$ results in the contours found in Fig. 6(*b*). Because the contours are closed, any state of stress that has nonzero σ_{11} or σ_{13} components would result in a nonzero probability of failure.

Concluding Remarks

In this paper we have developed a reliability model for whisker-toughened ceramic composites with orthotropic material symmetry. The model was constructed in a rational manner using an invariant formulation. Such an approach indicates the maximum number and form of the stress invariants necessary in defining the failure function ψ. A subset of the integrity basis for ψ was constructed with invariants that correspond to the macrovariables assumed to be directly related to fracture. The whiskers in each continuum element were assumed to be distributed in such a manner that three orthogonal material orientations could be identified. These material orientations are not restricted to be the same at each point in the continuum and could vary along a family of curves within a component. Thus the material is locally orthotropic with respect the local material orientation of each element (or link) of the component. This offers flexibility when modeling a component by a finite element method.

Relative to conducting experiments to determine model parameters, it was pointed out that while tubular specimens yield homogeneous states of stress, not all of the parameters could be found. However a combination of MOR and shear tests would yield all the parameters. Furthermore, several figures were presented that depicted reliability contours under different loading conditions. These figures point to behavior that requires verification in multiaxial experiments. Hence, a significant amount of experimental data must be generated before a final assessment of the theory can be made.

References

Cassenti, B. N., 1984, "Probabilistic Static Failure of Composite Material," *AIAA Journal*, Vol. 22, pp. 103-110.

Duffy, S. F., and Arnold, S. M., 1990, "Noninteractive Reliability Model for Whisker-Reinforced Ceramic Composites," *Journal of Composite Materials*, Vol. 24, pp. 293-308.

Faber, K. T., and Evans, A. G., 1983, "Crack Deflection Processes—I. Theory," *Acta Metallurgica*, Vol. 31, pp. 565-576.

Lange, F. F., 1970, "The Interaction of a Crack Front With a Second-Phase Dispersion," *Philosophical Magazine*, Vol. 22, pp. 983-992.

Leckie, F. A., 1981, "Advances in Creep Mechanics," *Creep in Structures*, A.R.S. Ponter and D. R. Hayhurst, eds., Springer-Verlag, New York, pp. 13-47.

Reiner, M., 1945, "A Mathematical Theory of Dilatancy," *American Journal of Mathematics*, Vol. 67, pp. 350-362.

Rivlin, R. S., and Smith, G. F., 1979, "Orthogonal Integrity Basis for *N* Symmetric Matrices," *Contributions to Mechanics*, D. Abir, ed., Oxford.

Shaw, N. J., and Bubsey, R. T., 1987, "Toughened Ceramics Life Prediction," proposal submitted to Oak Ridge National Laboratory—Ceramic Technology for Advanced Heat Engines Project.

Spencer, A. J. M., 1971, "Theory of Invariants," *Continuum Physics—Vol. I. Mathematics*, A. C. Eringen, ed., Academic Press, New York, pp. 239-255.

Spencer, A. J. M., 1984, "Constitutive Theory for Strongly Anisotropic Solids," *Continuum Theory of the Mechanics of Fibre-Reinforced Composites*, A. J. M. Spencer, ed., Springer-Verlag, New York, pp. 1-32.

Tsai, S. W., and Wu, E. M., 1971, "A General Theory of Strength for Anisotropic Mateirals," *Journal of Composite Materials*, Vol. 5, pp. 58-80.

Walrath, D. E., and Adams, D. F., 1983, "The Iosipescu Shear Test as Applied to Composite Materials," *Experimental Mechanics*, Vol. 23, pp. 105-110.

Wetherhold, R. C., 1983, "Statistics of Fracture of Composite Material Under Multiaxial Loading," Ph.D. Thesis, University of Delaware.

Wetherhold, R. C., 1989, "Energy of Fracture for Short Brittle Fiber/Brittle Matrix Composites With Planar Orientations," *Materials Science and Engineering*, Vol. A112, pp. 31-37.

R. Ballarini

S. Ahmed

Department of Civil Engineering,
Case Western Reserve University,
Cleveland, OH 44106

Local-Global Analysis of Crack Growth in Continuously Reinforced Ceramic Matrix Composites

This paper describes the development of a mathematical model for predicting the strength and micromechanical failure characteristics of continuously reinforced ceramic matrix composites. The local-global analysis models the vicinity of a propagating crack tip as a local heterogeneous region (LHR) consisting of springlike representations of the matrix, fibers, and interfaces. This region is embedded in an anisotropic continuum (representing the bulk composite), which is modeled by conventional finite elements. Parametric studies are conducted to investigate the effects of LHR size, component properties, interface conditions, etc. on the strength and sequence of the failure processes in the unidirectional composite system. The results are compared with those predicted by the models developed by Marshall et al. (1985) and by Budiansky et al. (1986).

Introduction

The failure characteristics of fiber-reinforced composites are dictated by various micromechanical failure processes such as matrix microcracking, slipping between matrix and fibers, delamination, and fiber breakage. This paper presents a local-global model (it combines micromechanical and macromechanical analyses), which considers the vicinity of a crack tip a "process zone" capable of modeling such phenomena. Of special interest to our study are quantities such as critical matrix cracking stresses, since such damage leads to oxidation and eventually to fiber degradation, and is therefore used as an important criterion in design. Also of interest is the global response of the system to external loads and the ultimate load that the composite can sustain.

Before presenting a detailed description of the present model, a comparative review of existing models for fracture mechanics of brittle matrix composites (BMC) is warranted. The most quoted models are those developed by Aveston et al. (1971), Marshall et al. (1985), and Budiansky et al. (1986). The following are some of the key concepts underlined in these models that we shall seek to study or validate through our model.

Marshall et al. (1985) have developed a model that can be used to predict the stress at which a matrix crack propagates across the specimen. This stress will, henceforth, be called the critical matrix cracking stress, σ_{mat}. In their analysis, a frictional bond between fibers and matrix was assumed whereby slipping takes place when the interface shear stress reaches a critical value. Using a stress intensity factor approach, they have shown that a distinction needs to be made between short and long cracks. Short cracks are those for which the entire crack length contributes to the stress intensity factor as a result of fiber bridging, and therefore propagate at a stress that depends on the crack length. Long cracks experience a crack mouth displacement that asymptotically approaches a constant value u_o. This limiting displacement is reached at a distance c_o from the crack tip. For such cracks, σ_{mat} is independent of the crack length, since the contribution to the stress intensity factor from the fibers is limited to the length c_o behind the crack tip. It is important to note that this model implicitly assumes the stress–strain diagram shown in Fig. 1(*a*), since no nonlinearities are assumed prior to the matrix cracking stress. It will be shown using the model proposed in this paper that this assumption leads to a good estimate of σ_{mat}. However, for various constituent properties the present model shows that significant nonlinearities may occur prior to σ_{mat} (Fig. 1(*b*)). These irreversible deformations, which are due to slipping between fiber and matrix and microcracking may prove to be significant for fatigue types of loading.

Budiansky et al. (1986) have considered steady-state matrix cracking stresses for two conditions: (1) unbonded, frictionally constrained fibers, where the frictional restraint is the same as in Marshall et al. (1985); and (2) initially bonded fibers, which debond due to crack tip stresses. The analysis is based on the Griffith energy criterion, which considers the change in potential energy with respect to crack growth. The critical cracking condition is associated with the upstream and downstream stress states, far ahead of and behind the crack front.

For case (1), the results generalize those of the ACK theory by considering matrix cracking stresses for conditions that lie between the no-slip and the large slip cases. They showed that the critical cracking stress, σ_{mat}, can be obtained using the graph shown in Fig. 2 in conjunction with equations (1) and (2). The procedure includes first evaluating the two parameters σ_0 and σ_1, given by

---

Contributed by the International Gas Turbine Institute and presented at the 34th International Gas Turbine and Aeroengine Congress and Exhibition, Toronto, Ontario, Canada, June 4–8, 1989. Manuscript received at ASME Headquarters January 23, 1989. Paper No. 89-GT-138.

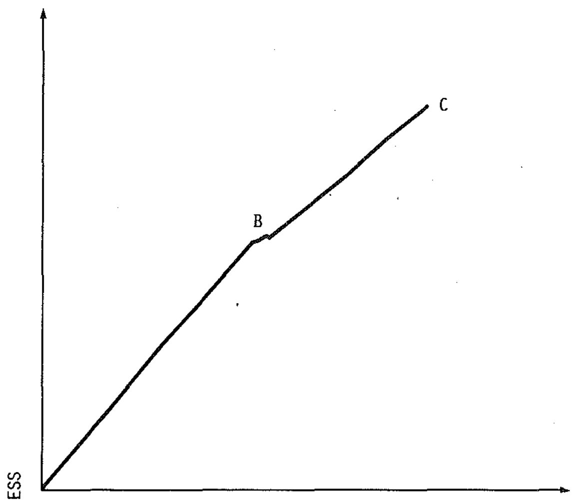

(A) LINEAR BEHAVIOR UNTIL MATRIX CRACKING.

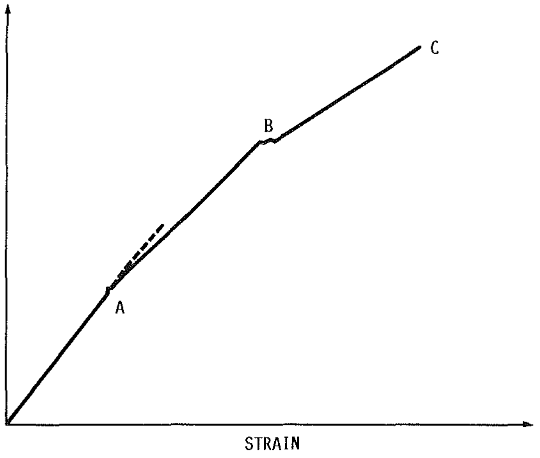

(B) OBTAINED BY USING LHR MODEL.

Fig. 1 Typical stress-strain curve for BMC

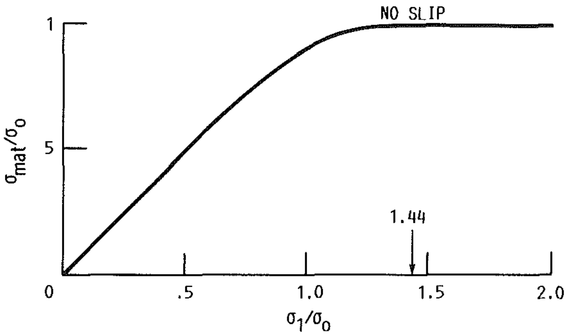

Fig. 2 Graph from Budiansky et al., for calculating matrix cracking stress

$$\frac{\sigma_0}{E}=B\left[\frac{6v_f^2E_f}{v_m^2E(1+\nu_m)}\right]^{1/4}\left[\frac{G_m}{rE_m}\right]^{1/2} \tag{1}$$

$$\frac{\sigma_1}{E}=\left[\frac{6v_f^2E_f\tau_0}{v_mEE_m}\right]^{1/3}\left[\frac{G_m}{rE_m}\right]^{1/3} \tag{2}$$

where B is a utility constant given by

$$B=\left[\frac{2v_m^3}{-6\ \ln(v_f)-3v_m(3-v_f)}\right]^{1/4}$$

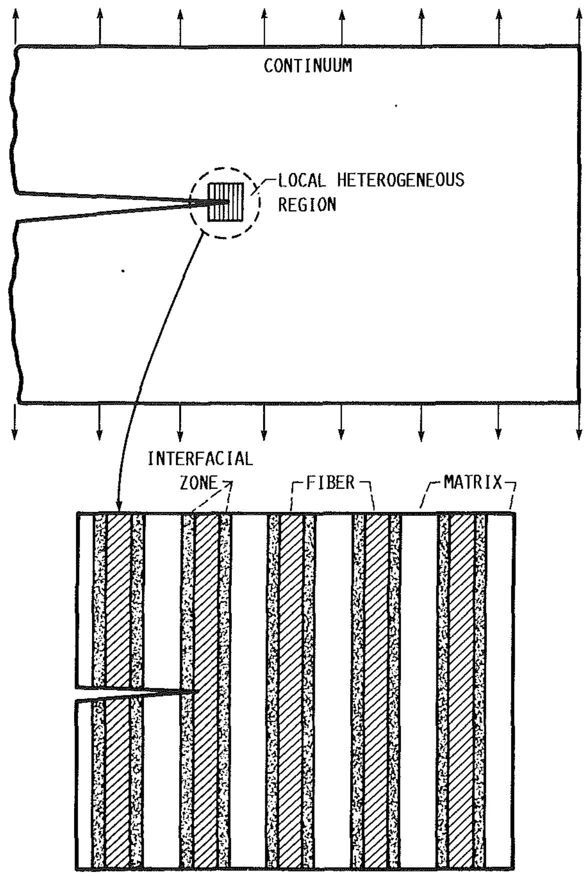

Fig. 3 Local heterogeneous region (LHR) and its components

E_f and E_m are the Young's moduli of the fiber and matrix, E is the composite modulus using the rule of mixtures, ν is the Poisson ratio, v_f and v_m are fiber and matrix volume fractions, respectively, r is the fiber radius, G_m is the critical strain energy release rate of the matrix, and τ_0 is the interface shear strength.

It is observed that for $\sigma_1/\sigma_0 \leq 1.0$, the ACK expression for large slip cracking stress is recovered, i.e.,

$$\sigma_{\mathrm{mat}}=\left[\frac{6v_f^2E_f\tau_0(K_{IC}^M)^2(1-\nu_m^2)}{v_mE_m^3Er}\right]^{1/3}E \tag{3}$$

where (K_{IC}^M) is the fracture toughness of the matrix. The ratio σ_1/σ_0 is then calculated and Fig. 2 is used to obtain the corresponding value of $\sigma_{\mathrm{mat}}/\sigma_0$.

For bonded-debonding fibers, the following expression was derived:

$$\frac{\sigma_{\mathrm{mat}}}{\sigma_0}=\left\{\frac{1+\dfrac{4v_f}{v_m}\left(\dfrac{l_d}{r}\right)\left(\dfrac{G_d}{G_m}\right)}{1+\dfrac{B^2}{v_m}\left[\dfrac{6E}{(1+\nu_m)E_f}\right]^{1/2}\left(\dfrac{l_d}{r}\right)}\right\}^{1/2} \tag{4}$$

where l_d is the debond length and G_d is the critical energy release rate of the interface.

Expressions for the slip length l_s (case (1)) and debond length l_d (case (2)) will be discussed subsequently.

This paper presents the preliminary results obtained using a model that can be used to predict the fracture characteristics of reinforced ceramic matrix composites. This model has been used to simulate an experiment in which a notched specimen is subjected to tensile stresses. The results are compared to those obtained using the aforementioned models.

Local Model

The local heterogeneous region (LHR) shown in Fig. 3 con-

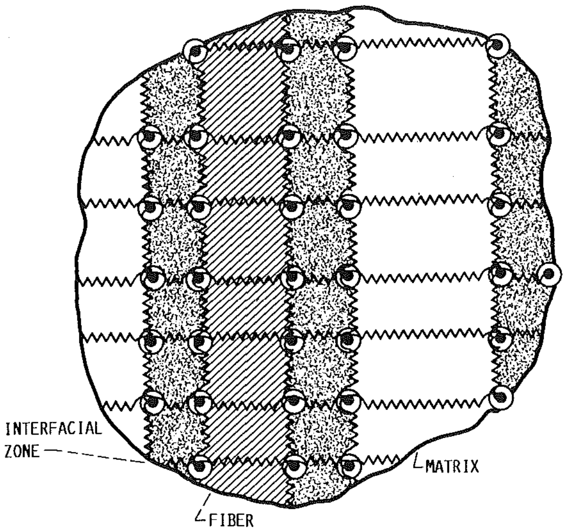

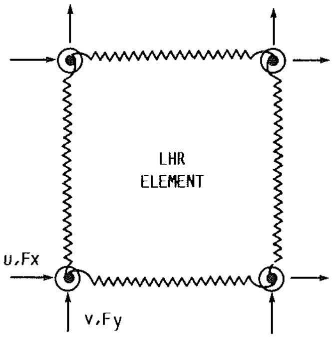

Fig. 4 Spring model of the LHR zone

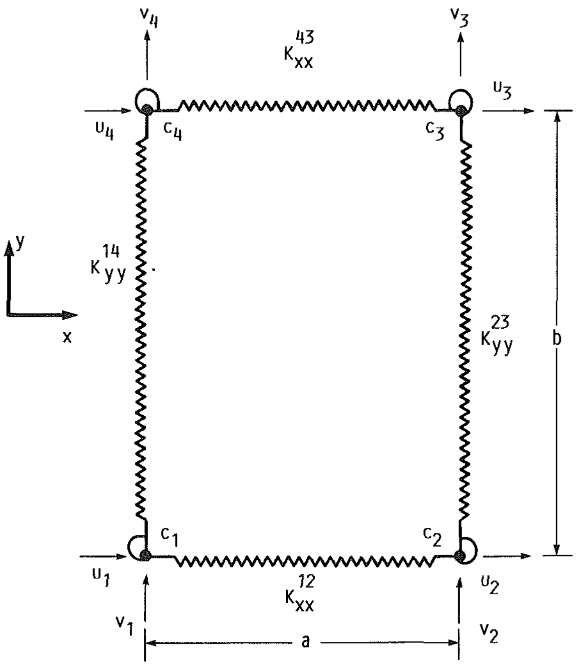

Fig. 5 LHR element stiffness components

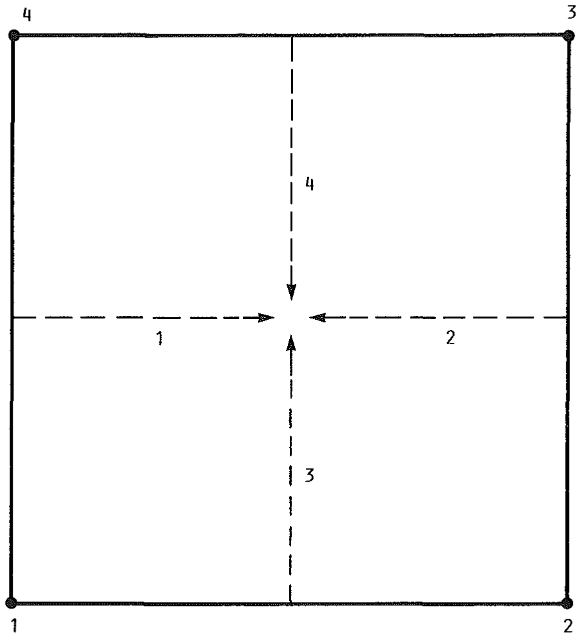

Fig. 6 Local fracture modes in an LHR element

sists of three distinct components: fibers, matrix, and fiber-matrix interface. Following Kanninen et al. (1977), each component is assumed homogeneous and isotropic and is modeled by a succession of rectangular spring elements (Fig. 4).

Each LHR spring element consists of four extensional springs and one rotary spring at each of the corner nodes. Each node has two degrees of freedom as shown in Fig. 5. An assembly of such elements behaves like a homogeneous anisotropic continuum in a state of plane deformation.

The stiffness matrix of a LHR element is given by

$$\{F\} = [K]\{d\} \tag{5}$$

where $\{F\}$ is the nodal force vector, $[K]$ is the element stiffness matrix, and $\{d\}$ is the nodal displacement vector.

The LHR element spring stiffnesses are related to the elastic properties of the material. The derivations for the spring stiffnesses and for the LHR stiffness matrix are given in Appendix A.

Each LHR fiber and matrix element is capable of fracturing in either of the four possible modes shown in Fig. 6. Modes 1 and 2 correspond to crack growth in the x direction by an amount $a/2$, while modes 3 and 4 represent cracking in the y direction within the element by a length of $b/2$, where a and b are the length and width, respectively, of an LHR element. These damage lengths have been used for the sake of simplicity in representing fracture events in the LHR elements. Each event contributes to a loss of stiffness of the element, and consequently leads to a change in the strain energy, ΔE_s, given by

$$\Delta E_s = \frac{\{u\}^T[\delta K]\{u\}}{2\Delta c} \tag{6}$$

where $\{u\}$ is the displacement vector of the element, $[\delta K]$ is the change in the element stiffness due to a fracture event, and Δc is the length of the crack in the element, i.e., $a/2$ or $b/2$. The above relationship is derived in Appendix B.

It is assumed that for each material (fiber and matrix) a critical rupture energy is known. This provides a decision rule for breakage in each separate element of the LHR.

For purposes of comparison with the results of Marshall et al. (1985), preliminary simulations were conducted assuming that fiber slipping occurs at a critical shear stress τ_0. In subsequent studies, more realistic modeling, which includes delamination and an elastic-plastic friction model, will be employed.

Local-Global Model

A schematic representation of a typical local-global model

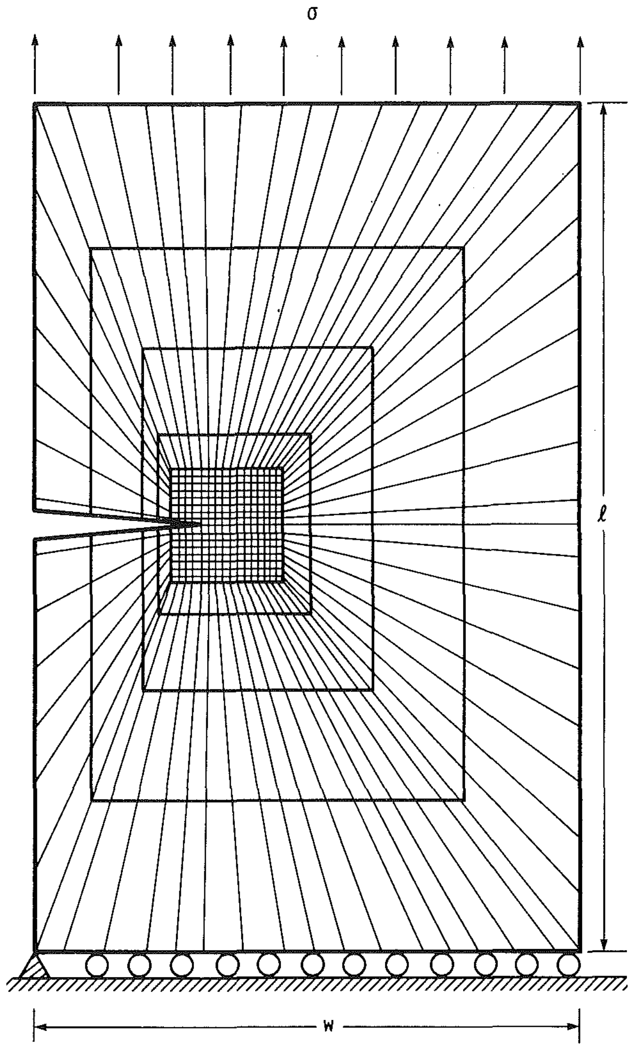

Fig. 7 Schematic of the LHR zone embedded in the finite element mesh (not to scale)

Table 1 Constitutive material properties

Constituent	Young's modulus, GPa	Poisson's ratio	K_{IC}, MPa$\sqrt{m}$
SiC fibers	390	0.3	5.0
Si_3N_4 matrix	206	.3	4.6
Interface	206	.3	---

is shown in Fig. 7 (not to scale). The notched composite specimen modeled has a length $l = 20$ cm and width $w = 5$ cm. The LHR surrounds the crack tip and is embedded in the bulk anisotropic composite, discretized by standard four-node constant strain isoparametric finite elements. The LHR and the outer zone are coupled through the enforcement of displacement compatibility at the nodes between the LHR and standard finite elements.

Analysis

The specimen is loaded incrementally in tension perpendicular to the crack plane and parallel to the direction of the fibers. Displacements are evaluated at every nodal point in the LHR, and the strain energy associated with each possible rupture event in every LHR element is calculated. The critical rupture energies of the fiber and matrix elements are obtained from their fracture toughnesses as follows:

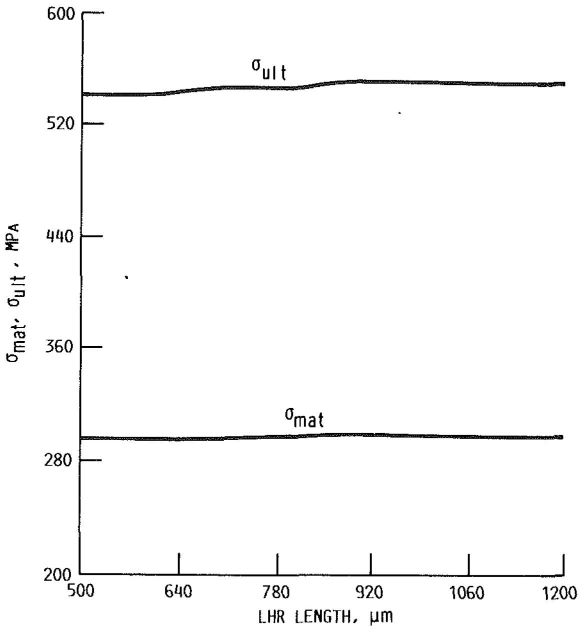

Fig. 8 Effect of LHR length on σ_{mat} and σ_{ult} ($v_f = 0.4$, $\tau_o = 10$ MPa, $K_{IC}^M = 4.6$ MPa $\sqrt{m}$).

$$(E_{cr}^{m,f}) = \frac{(K_{IC}^{M,F})^2}{(E)_{m,f}} \times (\Delta c) \times (1-\nu_{m,f}^2) \qquad (7)$$

where K_{IC}^M (K_{IC}^F) is the fracture toughness of the matrix (fiber) material, E_{cr}^m (E_{cr}^f) is the critical energy for a given length of damage growth within the matrix (fiber) LHR element; and ν_m (ν_f) is the Poisson ratio of the matrix (fiber).

The critical regions, if any exist, are allowed to fracture in any one of the four modes described earlier and appropriate modifications are made in the LHR stiffness matrix.

As stated earlier, failure of the interface elements is based on the maximum interfacial shear stress criterion. For each load level, the shear stress τ_{xy} is computed in every LHR interface element and this value is compared to the prescribed critical shear stress τ_0. If $\tau_{xy} < \tau_0$ (no-slip condition) relative displacement between the fiber and matrix is constrained. For elements where $\tau_{xy} \geq \tau_0$, the fiber is allowed to slip through the matrix and appropriate changes are made in the shear stiffness of the interface element so that slip takes place at a constant shear stress $\tau_{xy} = \tau_0$.

The solution procedure is repeated for the next load increment to reflect additional local rupture events. The progression of the main crack through the matrix (and eventually through the fibers) is followed by expanding the LHR zone continuously. The load at which the LHR elements begin to fail without any further increment of load is recorded as the ultimate strength of the composite. This is generally found to occur at a stage when the main crack has broken through four (or sometimes fewer) successive fibers.

Results

Physical Properties and Parameters. Most of the results presented in this paper assume material properties (refer to Table I) obtained from the following sources: Weeton et al. (1986), DiCarlo (1984), and Bubsey et al. (1983).

Two fiber volume fractions were considered, 0.2 and 0.4. These values were consistent with the properties of the anisotropic bulk composite:

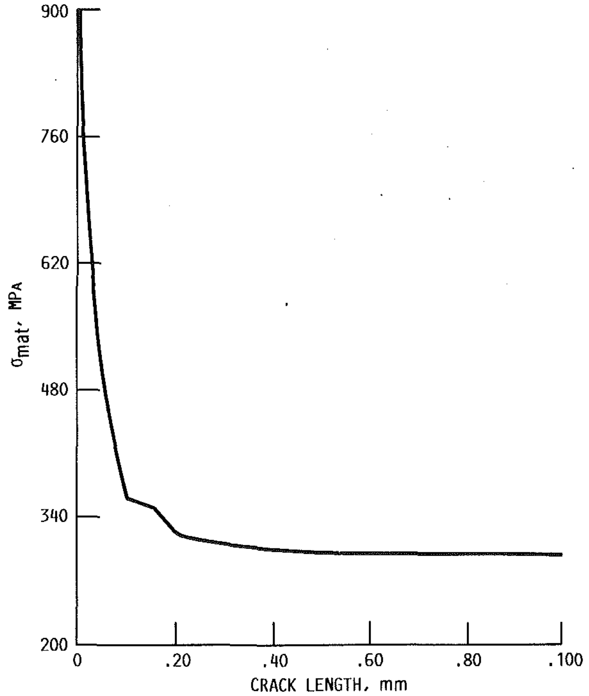

Fig. 9 **Variation of σ_{mat} with crack length c (τ_0 = 10 MPa, K_{IC}^M = 4.6 MPa $\sqrt{m}$), v_f = 0.4)**

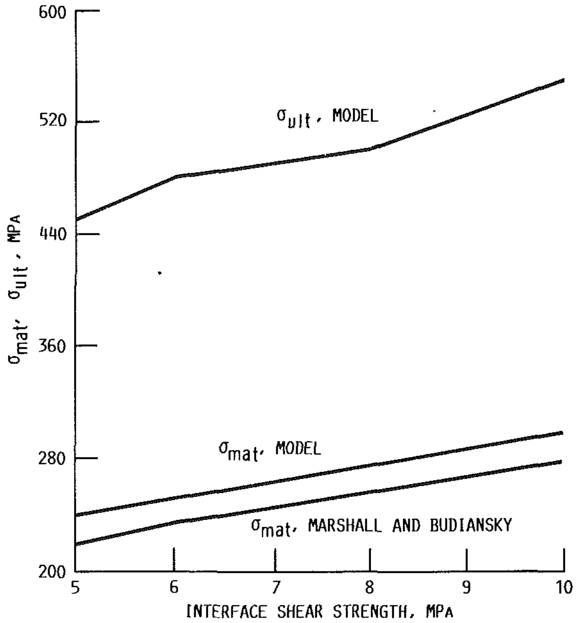

Fig. 11 **Variation of σ_{mat} and σ_{ult} with τ_0 (K_{IC}^M = 4.6 MPa $\sqrt{m}$, v_f = 0.4)**

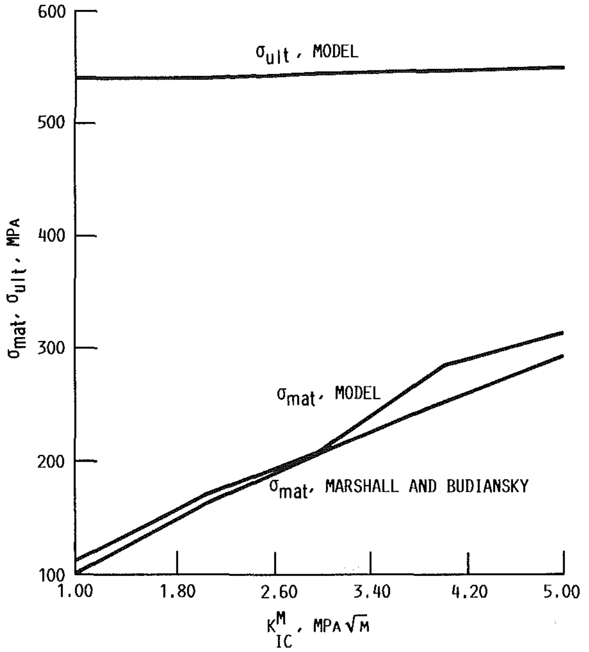

Fig. 10 **Variation of σ_{mat} and σ_{ult} with K_{IC}^M (τ_0 = 10 MPa, v_f = 0.4)**

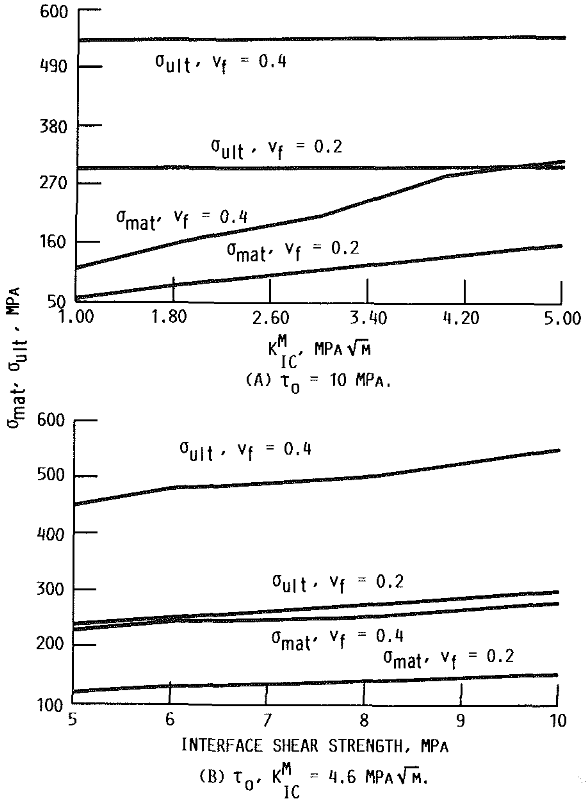

Fig. 12 **Effect of fiber volume fraction v_f on σ_{mat} and σ_{ult} variation**

$$v_f = 0.2\text{: } E_{yy} = 242.8 \text{ GPa; } E_{xx} = 227.47 \text{ GPa;}$$
$$\nu_{xy} = 0.3\text{; } G_{xy} = 100.42 \text{ GPa}$$
$$v_f = 0.4\text{: } E_{yy} = 279.6 \text{ GPa; } E_{xx} = 253.92 \text{ GPa;}$$
$$\nu_{xy} = 0.3\text{; } G_{xy} = 112.93 \text{ GPa}$$

The interface shear strength, τ_0, was varied in the practical range of 0 to 10 MPa. The fracture toughness of the matrix was also varied from 1.0 to 5.0 MPa $\sqrt{m}$.

The diameter of the SiC fibers ($2r$) was taken as 100 μm. Assumption of regular hexagonal packing arrangement gave an interfiber distance of about 213 and 150 μm (center to center) for volume fractions of 0.2 and 0.4, respectively. The interface was assumed to have a nominal thickness of 5 μm.

To investigate the convergence of the local-global model, ultimate and matrix cracking stresses were studied for various LHR sizes. Figure 8 shows the effect of starting LHR size on the ultimate stress σ_{ult} and the critical matrix cracking stress, σ_{mat}. Convergence is observed for LHR lengths greater than about 1000 μm and hence LHR sizes of the order of 1000 to 1500 μm were used throughout the study.

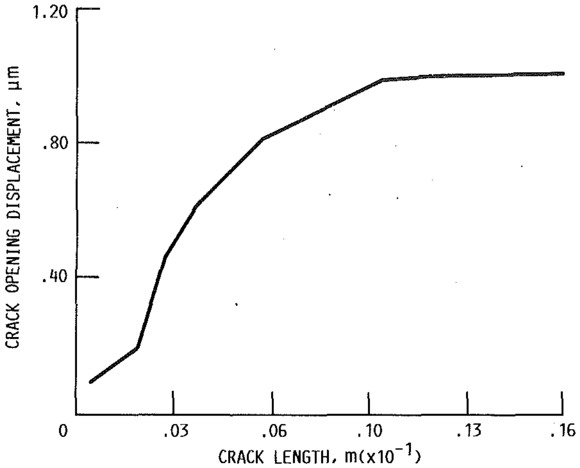

Fig. 13 Variation of crack opening displacement u_o with crack length c (τ_0 = 10 MPa, K_{IC}^M = 4.6 MPa $\sqrt{m}$, v_f = 0.4)

Comparisons With Results Obtained by Marshall et al. (1985)

Effect of Crack Length. As mentioned previously, Marshall et al. (1985) have shown that when the crack length is greater than a certain characteristic size, matrix cracking stresses are independent of the crack length c. To check this result, critical matrix cracking stresses (σ_{mat}) were calculated for various crack sizes. For the case τ_0 = 10 MPa, K_{IC}^M = 4.6 MPa $\sqrt{m}$, and $v_f = 0.4$, the results are presented in Fig. 9. Although σ_{mat} is high for small crack lengths, it is found to be independent of crack length for $c \geq 0.046$ cm. This compares favorably to the steady-state crack length proposed by Marshall et al. (1985) obtained from the relation

$$c \cong \frac{1}{3}\left(\frac{\pi}{4I^{4/3}}\right)\left[\frac{K_{IC}^M E_m v_m^2(1+\eta)r}{\tau_0 v_f^2 E_f(1-v_m^2)}\right]^{2/3} \qquad (8)$$
$$\cong 0.034 \text{ cm}$$

where $\eta = v_f E_f / v_m E_m$, K_{IC}^M is the fracture toughness of the matrix,and I is 1.2 for straight cracks.

It should be noted that equation (8) was derived by assuming that the matrix stress intensity factor, K_I^M, is related to the composite stress intensity, K_I^L, by the relation $K_I^M = K_I^L E_m / E$. This relation is not valid unless the crack length is of the order of several fiber spacings. In a future communication, the range of validity of this equation will be reported.

Effect of Matrix Fracture Toughness on σ_{mat} and σ_{ult}. Having obtained the steady-state crack length, the critical matrix cracking stress, σ_{mat}, and ultimate strength of the composite, σ_{ult}, were investigated next using an initial crack length such that steady-state conditions are obtained. The ultimate strength and σ_{mat} depend on several constituent material properties such as fracture toughness of the components, interface shear strength, fiber spacing and volume fraction of the fibers, etc. Each of these parameters is considered separately. The variation of σ_{mat} with K_{IC}^M over the range of 1.0 to 5.0 MPa $\sqrt{m}$ is studied for a notch length of 1 cm and interfacial shear strength of 10 MPa. The critical matrix cracking stress is found to increase with K_{IC}^M and the results compare well with those of Marshall et al. (1985) given by

$$\sigma_{\text{mat}} = 1.83\left[\frac{(1-v_m^2)(K_{IC}^M)^2 \tau_0 E_f v_f^2 v_m (1+\eta)^2}{E_m r}\right]^{1/3} \qquad (9)$$

The results from our model and those obtained from the above relationship are shown in Fig. 10. Since the results of Marshall et al. (1985) and Budiansky et al. (1986) are almost equivalent, they do not plot as separate curves. The ultimate strength is not affected significantly by variation in K_{IC}^M, since the ultimate strength of the composite is controlled primarily by the fiber-bundle strength. If l_u is the length of the initially uncracked ligament in the notched specimen of width w, the bundle strength is given by $\sigma_f v_f (l_u/w)$, where σ_f is the tensile strength of the fibers. For the SiC fibers, σ_f = 1.83 GPa. Hence, for a notch length of 1 cm and w = 5 cm, the theoretical bundle strength is 586 MPa for v_f = 0.4, and 293 MPa for v_f = 0.2. The ultimate composite strength, σ_{ult}, obtained using our model is slightly less than these calculated values. This is due to the sequential breakage of the fibers leading to catastrophic failure.

Effect of Interfacial Shear Strength. Since interface shear strengths are difficult to estimate, a parametric study was conducted for τ_0 ranging from 5.0 to 10.0 MPa. The variation of σ_{mat} with τ_0, shown in Fig. 11, shows good agreement with results obtained by Marshall et al. (1985) using equation (9).

Effect of Fiber Volume Fraction. Two fiber volume frac-

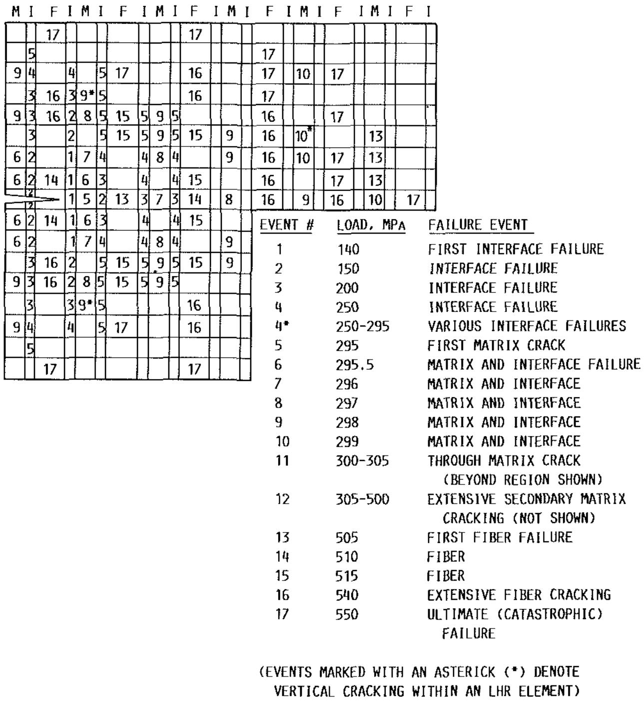

EVENT #	LOAD, MPa	FAILURE EVENT
1	140	FIRST INTERFACE FAILURE
2	150	INTERFACE FAILURE
3	200	INTERFACE FAILURE
4	250	INTERFACE FAILURE
4*	250-295	VARIOUS INTERFACE FAILURES
5	295	FIRST MATRIX CRACK
6	295.5	MATRIX AND INTERFACE FAILURE
7	296	MATRIX AND INTERFACE
8	297	MATRIX AND INTERFACE
9	298	MATRIX AND INTERFACE
10	299	MATRIX AND INTERFACE
11	300-305	THROUGH MATRIX CRACK (BEYOND REGION SHOWN)
12	305-500	EXTENSIVE SECONDARY MATRIX CRACKING (NOT SHOWN)
13	505	FIRST FIBER FAILURE
14	510	FIBER
15	515	FIBER
16	540	EXTENSIVE FIBER CRACKING
17	550	ULTIMATE (CATASTROPHIC) FAILURE

(EVENTS MARKED WITH AN ASTERICK (*) DENOTE VERTICAL CRACKING WITHIN AN LHR ELEMENT)

Fig. 14 Schematic representation of the principal failure events in the LHR zone (τ_0 = 10 MPa, K_{IC}^M = 4.6 MPa $\sqrt{m}$, v_f = 0.4)

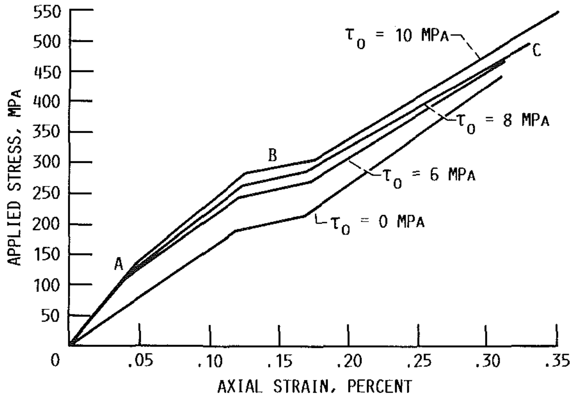

Fig. 15 Axial load deflection curve for various τ_0 values (K_{IC}^M = 4.6 MPa $\sqrt{m}$, v_f = 0.4)

tions v_f were considered, 0.2 and 0.4. The fiber volume fraction controls the interfiber spacing and its effects on σ_{mat} and σ_{ult} with respect to K_{IC}^{M} and τ_0 are presented in Figs. 12(*a*) and 12(*b*). It is observed that σ_{mat} and σ_{ult} values for $v_f = 0.2$ are approximately half of those for $v_f = 0.4$. These results agree with those obtained using equation (9).

Variation of Crack Mouth Opening Displacement With Crack Length. Another key concept introduced in the model developed by Marshall et al. (1985) is that of the equilibrium crack opening $u = u_o$ for long cracks. To study the effect of crack length on u, the crack opening displacement at the mouth of the crack was recorded for various crack lengths (Fig. 13). Although u increases with increasing crack length for crack lengths less than 1 cm, it appears to approach a constant value of approximately 1 μm for crack lengths greater than that size. This value may be compared to the limiting displacement u_o estimated by Marshall et al. (1985) by the relationship

$$u_o = \frac{\sigma^2 r}{\{4\tau_0 v_f^2 E_f(1+\eta)\}} \tag{10}$$

where σ is the far-field applied load. For $\sigma = \sigma_{\mathrm{mat}} = 300$ MPa, $\tau_0 = 10$ MPa, and $v_f = 0.4$, $u_o \approx 0.8$ μm. The agreement is quite good.

Comparison With Results Obtained by Budiansky et al. (1986)

Comparison of Critical Matrix Cracking Stress σ_{mat}. The critical matrix cracking stresses obtained using our model are compared to those obtained by Budiansky et al. (1986) for unbonded composites (equations (1)–(3)). Because their results lead to predictions equivalent to those of Marshall et al. (1985) they plot as the same curve in Figs. 10 and 11.

Comparison of Slip Lengths. For unbonded composites, the slip length has been derived by Budiansky et al. (1986) as

$$\frac{l_s}{r} = \frac{\sigma v_m E_m}{2 v_f E \tau_0} - \frac{1}{\rho} \tag{11}$$

where l_s is the slip length on either side of the crack face, σ is the applied stress, and

$$\rho = \frac{B^2}{v_m}\left[\frac{6E}{E_f(1+\nu_m)}\right]^{1/2} \tag{12}$$

For $\tau_0 = 10$ MPa, $K_{IC}^{M} = 4.6$ MPa $\sqrt{\mathrm{m}}$; and $\sigma = \sigma_{\mathrm{mat}} = 300$ MPa, $l_s = 806$ μm.

Results of our simulation are schematically presented in Fig. 14. The slip length is approximately 900 to 1000 μm on either side of the crack face, which agrees quite well with the results of Budiansky et al. (1986).

Composite Failure Sequence. While the existing models are concerned only with the steady-state condition, the present model enables a detailed study of the failure sequence as the specimen is loaded incrementally. A schematic representation of the failure events in the LHR for a notch length of 1 cm, $\tau_0 = 10$ MPa, and $K_{IC}^{M} = 4.6$ MPa $\sqrt{\mathrm{m}}$ is shown in Fig. 14. Slipping first occurs at an applied stress of 140 MPa, and the interface continues to slip with increasing load. The first matrix crack is observed around the crack tip at a stress of 295 MPa. For matrices with lower K_{IC}^{M}, some microcracking is observed around the crack tip before the growth of the main crack. The matrix crack steadily progresses through the composite section and traverses it completely at a critical matrix cracking stress of about 305 MPa (σ_{mat}). As the load is increased, several secondary matrix cracks appear in the matrix. The first fiber failure occurs at a load of 505 MPa, and in general, this occurs at a load of about 90 percent of the ultimate stress. With increasing load, the crack breaks through three successive fibers before catastrophic failure occurs at an ultimate stress of 550 MPa.

Load-Deflection Behavior. The load-deflection curves as functions of the interfacial shear strength are shown in Fig. 15. Except for the case $\tau_0 = 0$, it is observed that nonlinearities begin at point (*a*) before σ_{mat} is reached. This decrease in stiffness is a result of fiber slipping and matrix microcracking. A further reduction in stiffness occurs at region (*b*). This region corresponds to extensive matrix cracking through the section of the composite, so that the load is now essentially carried by the fibers. The ultimate failure load (σ_{ult}) is reached at (*c*).

Conclusion

A model is presented that can be used to predict the failure characteristics of fiber-reinforced composites. Preliminary results obtained using the model compare favorably with those predicted by existing models. This model may be generalized to consider more complicated geometries and loading conditions as well as the behavior of composites containing a random distribution of microflaws and strengths. It has been suggested (Dollar and Steif, 1988) that assumption of constant interface shear strength may not be accurate. The model is currently being improved through the implementation of more realistic interfacial constitutive modeling. In subsequent work, special friction interface elements developed by Plesha et al. (1987) will be used.

Acknowledgments

The authors are grateful for support from NASA Lewis Research Center (Grant NAG3-856) and for the assistance provided by Professor Robert Mullen, Civil Engineering Department, CWRU in the computational aspects of this work.

References

Aveston, J., Cooper, G. A., and Kelly, A., 1971, "Single and Multiple Fracture," *The Properties of Fibre Composites*, IPC Science and Technology Press, Guildford, United Kingdom, pp. 15–26.

Bubsey, R. T., Shannon, J. L., Jr., and Munz, D., 1983, "Development of Plane Strain Fracture Toughness Test for Ceramics Using Chevron Notched Specimens," *Ceramics for High Performance Applications III: Reliability*, E. M. Lenoe, R. N. Katz, and J. J. Burke, eds., Plenum Press, New York, pp. 753–771.

Budiansky, B., Hutchinson, J. W., and Evans, A. G., 1986, "Matrix Fracture in Fiber-Reinforced Ceramics," *Journal of the Mechanics and Physics of Solids*, Vol. 34, No. 2, pp. 167–189.

DiCarlo, J. A., 1984, "High Performance Fibers for Structurally Reliable Metal and Ceramic Composites," NASA Report, TM-86878.

Dollar, A., and Steif, P. S., 1988, "Load Transfer in Composites With a Coulomb Friction Interface," *International Journal of Solids and Structures*, Vol. 24, No. 8, pp. 789–803.

Kanninen, M. F., Rybicki, E. F., and Griffith, W. I., 1977, "Preliminary Development of a Fundamental Analysis Model for Crack Growth in a Fiber Reinforced Composite Material," *Composite Materials: Testing and Design* (*Fourth Conference*), ASTM STP 617, American Society for Testing and Materials, Philadelphia, PA, pp. 53–69.

Marshall, D. B., Cox, B. N., and Evans, A. G., 1985, "The Mechanics of Matrix Cracking in Brittle-Matrix Fiber Composites," *Acta Metallurgica*, Vol. 33, No. 11, pp. 2013–2021.

Plesha, M. E., Ballarini, R., and Parulekar, A., 1988, "A Constitutive Model and Finite Element Solution Procedure for Contact Friction Problems," submitted to the ASCE *Journal of Engineering Mechanics*.

Weeton, J. W., Peters, D. M., and Thomas, K. L., 1987, *Engineer's Guide to Composite Materials*, American Society for Metals, Metals Park, OH.

APPENDIX A

Derivation of LHR Element Stiffness

For a homogeneous isotropic material, the stress-strain relationship is given by

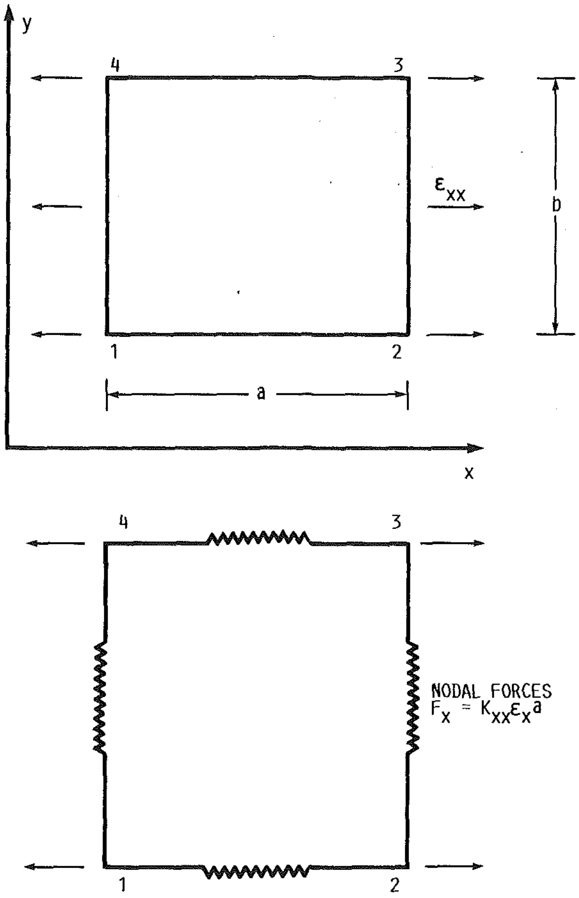

Fig. A1 Finite continuum element under uniform strain and equivalent LHR element

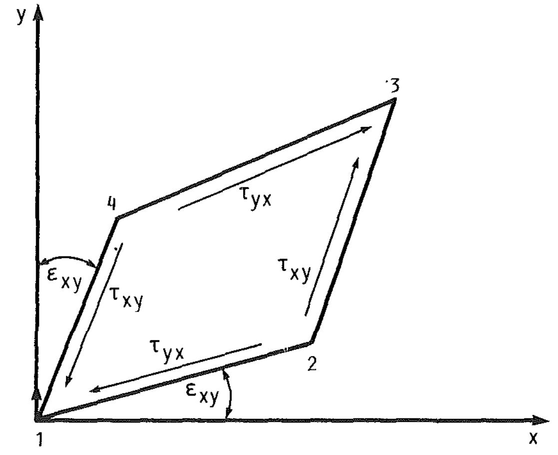

Fig. A2 Continuum element in pure shear

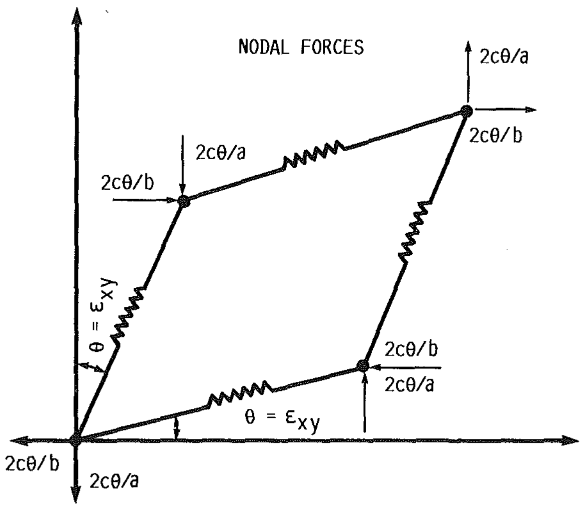

Fig. A3 LHR element in pure shear

$$\begin{Bmatrix}\sigma_{xx}\\ \sigma_{yy}\\ \tau_{xy}\end{Bmatrix} = \frac{E}{(1+\nu)(1-2\nu)}\begin{bmatrix}(1-\nu) & \nu & 0\\ \nu & (1-\nu) & 0\\ 0 & 0 & (1-2\nu)\end{bmatrix} \times \begin{Bmatrix}\epsilon_{xx}\\ \epsilon_{yy}\\ \epsilon_{xy}\end{Bmatrix} \tag{A1}$$

or

$$\begin{Bmatrix}\sigma_{xx}\\ \sigma_{yy}\\ \tau_{xy}\end{Bmatrix} = \begin{bmatrix}E_{11} & E_{12} & E_{13}\\ E_{21} & E_{22} & E_{23}\\ E_{31} & E_{32} & E_{33}\end{bmatrix}\begin{Bmatrix}\epsilon_{xx}\\ \epsilon_{yy}\\ \epsilon_{xy}\end{Bmatrix} \tag{A2}$$

The continuum is modeled by a set of spring elements as described previously. The values of the spring constants are related to the material's elastic properties by the following relationships:

$$\left.\begin{aligned} K_{xy}^{ij} &= E_{12}\\ K_{xx}^{ij} &= \frac{bE_{11}}{a}\\ K_{yy}^{ij} &= \frac{aE_{22}}{b}\end{aligned}\right\} \tag{A3}$$

$$C_i = \frac{a\bullet b\bullet E_{33}}{2} \text{ for all } i, j = 1, \ldots, 4$$

where a and b are the length (x direction) and width (y direction) of the LHR element, respectively; K_{xx}^{ij} is the extensional stiffness in the x direction between the ith and jth nodes; K_{yy}^{ij} is the extensional stiffness in the y direction between the ith and jth nodes; K_{xy}^{ij} is the cross extensional component (Poisson's contraction effect); and C_i is the rotational stiffness at each node.

The above relationships are derived as follows: Consider a finite continuum element of dimensions $a \times b$, which is modeled by an LHR spring element of the same dimensions. By forcing the spring element to behave like the continuum element, appropriate relationships may be obtained for the spring stiffnesses, K_{xx}, K_{xy}, K_{yy}, and C_i. Since the material is isotropic,

$$K_{xx}^{12} = K_{xx}^{34} = K_{xx}; \quad K_{yy}^{14} = K_{yy}^{23} = K_{yy};$$
$$K_{xy}^{12} = K_{xy}^{23} = K_{xy}^{34} = K_{xy}^{14} = K_{xy}^{14} = K_{xy}$$

and

$$C_1 = C_2 = C_3 = C_4 = C$$

Consider the continuum element under a state of uniform strain ϵ_{xx} (Fig. A1). If Δx represents the extension of the element in the x direction, then $\Delta x/a = \epsilon_{xx}$; or $\Delta x = \epsilon_{xx}a$. The stresses in the element are given by $\sigma_{xx} = E_{11}\epsilon_{xx}$ and the force in the x direction in the element is

$$F_x = \sigma_{xx}b = E_{11}\epsilon_{xx}b \tag{A4}$$

Imposing an equivalent extension in the x direction on the spring element, the forces in the x direction at the nodes 2 and

3 are given by $K_{xx}\Delta_x = K_{xx}\epsilon_{xx}a$. The total force in the x direction in the element is

$$F_x = \frac{F_{x1}+F_{x2}}{2} = K_{xx}\epsilon_{xx}a \tag{A5}$$

Hence from equations (A2) and (A3) $K_{xx} = (E_{11}b)/a$.

Similarly, by considering a uniform strain ϵ_{yy} in the y direction, it may be shown that $K_{yy} = (E_{22}a)/b$.

From equation (A1), the stress in the y direction, σ_{yy}, in the continuum element due to strain ϵ_{xx} is $\sigma_{yy} = E_{21}\epsilon_{xx} = E_{12}\epsilon_{xx}$ and the force in the y direction is

$$F_y = \sigma_{yy}a = E_{12}\epsilon_{xx}a \tag{A6}$$

If K_{xy} is the cross-extensional stiffness coefficient of the spring element, then the force in the y direction due to displacement Δx is

$$F_y = K_{xy}\Delta x = K_{xy}\epsilon_{xx}a \tag{A7}$$

From equations (A4) and (A5) we have $K_{xy} = E_{12}$.

Finally, consider the continuum element in a state of pure shear (shear strain, ϵ_{xy}), as shown in Fig. A2. The shear stress in the element is $\tau_{xx} = \tau_{yx} = E_{33}\epsilon_{xy}$. The force in the x direction on face 1-2 of the element is

$$F_x = \tau_{xy}a = E_{33}\epsilon_{xy}a \tag{A8}$$

Imposing the corresponding nodal rotations in the spring element (Fig. A3), the force in the x direction of the side 1-2 of the element is

$$F_x = \frac{2C\theta}{b} = \frac{2C\epsilon_{xy}}{b} \tag{A9}$$

Hence $C = E_{33}ab/2$.

Having obtained the spring stiffnesses in terms of the elastic constants, the stiffness matrix of an LHR element may now be formulated. The stiffness coefficients can be evaluated through energy considerations as follows. The total strain energy U stored in an element for any set of arbitrarily varied nodal displacements u_i and v_i may be written as (refer to Fig. 5 in the text)

$$\begin{aligned} U = {} & \frac{1}{2}K_{xx}(u_2-u_1)^2 + \frac{1}{2}K_{xx}(u_3-u_4)^2 \\ & + \frac{1}{2}K_{yy}(v_4-v_1)^2 + \frac{1}{2}K_{yy}(v_3-v_2)^2 \\ & + \frac{K_{xy}(v_4-v_1+v_3-v_2)(u_2-u_1+u_3-u_4)}{2} \\ & + \frac{1}{2}C\left(\frac{v_2-v_1}{a}+\frac{u_4-u_1}{b}\right)^2 + \frac{1}{2}C\left(\frac{u_3-u_2}{b}+\frac{v_2-v_1}{a}\right)^2 \\ & + \frac{1}{2}C\left(\frac{u_3-u_2}{b}+\frac{v_3-v_4}{a}\right)^2 + \frac{1}{2}C\left(\frac{u_1-u_4}{b}+\frac{v_4-v_3}{a}\right)^2 \end{aligned} \tag{A10}$$

Using Castigliano's theorem, the nodal forces can be obtained as follows:

$$\left.\begin{aligned} F_{xi} &= \frac{\partial U}{\partial u_i} \\ F_{yi} &= \frac{\partial U}{\partial v_i} \end{aligned}\right\} \tag{A11}$$

Such derivatives for each joint give the element stiffness matrix in the form

$$\{F\} = [K]\{d\} \tag{A12}$$

where $[K]$ represents the element stiffness matrix, $\{d\}$ the displacement vector, and $\{F\}$ the element force vector.

Assembly of the LHR stiffness matrix is done by standard direct stiffness methods employed in finite element practice.

APPENDIX B

Derivation of the Strain Energy Release Rate for Incipient Rupture

Consider a small virtual increase Δc in crack length in an element under a given external load. The total potential energy π is given by

$$\pi = \frac{1}{2}\{u\}^T[K]\{u\} - \{u\}^T\{b\} \tag{B1}$$

where $\{u\}$ is the nodal displacement vector, $[K]$ is the element stiffness matrix, and $\{b\}$ is the nodal force vector.

The energy release rate G is obtained from the variation of π with respect to the load, i.e.,

$$\delta\pi = \frac{1}{2}\{u\}^T[\delta k]\{u\} + \{\delta u\}^T[K]\{u\} - \{\delta u\}^T\{\mathrm{b}\} - \{\mathrm{u}\}^T\{\delta \mathrm{b}\} \tag{B2}$$

Using equilibrium and the fact that the vector $\{\delta b\}$ is null for a given load, the above simplifies to

$$\delta\pi = \frac{1}{2}\{u\}^T[\delta k]\{u\} \tag{B3}$$

Hence

$$G = -\frac{d\pi}{dc} = -\frac{1}{2}\{u\}^T\frac{d}{dc}[K]\{u\} \tag{B4}$$

If $[\delta K]$ is the change in the stiffness matrix of the element due to the incipient fracture, i.e., $[\delta K] = [K]_{\text{before}} - [K]_{\text{after}}$, then G may be written in the form

$$\Delta E_s = \frac{\{u\}^T[\delta K]\{u\}}{2\Delta c} \tag{B5}$$

J. T. DeMasi-Marcin

K. D. Sheffler

S. Bose

Pratt & Whitney Materials Engineering,
E. Hartford, CT 06108

Mechanisms of Degradation and Failure in a Plasma-Deposited Thermal Barrier Coating

Failure of a two-layer plasma-deposited thermal barrier coating is caused by cyclic thermal exposure and occurs by spallation of the outer ceramic layer. Spallation life is quantitatively predictable, based on the severity of cyclic thermal exposure. This paper describes and attempts to explain unusual constitutive behavior observed in the insulative ceramic coating layer, and presents details of the ceramic cracking damage accumulation process, which is responsible for spallation failure. Comments also are offered to rationalize the previously documented influence of interfacial oxidation on ceramic damage accumulation and spallation life.

Introduction

A thermal barrier coating (TBC) is a thin layer of ceramic insulation applied to the external surface of hollow, internally cooled turbine airfoils and platforms. A TBC provides performance, efficiency, and durability benefits by reducing turbine cooling air requirements and lowering metal temperatures (Ruckle, 1980; Miller et al., 1980; Duvall and Ruckle, 1982). Calculations indicate that a 10 mil (250 μm) thick layer of zirconia can reduce metal temperature as much as 300°F (about 170°C), depending on local heat flux. It is estimated that efficiency gains resulting from the application of a TBC to all high turbine airfoils in a typical modern gas turbine engine could result in annual fuel savings as high as ten million gallons for a 250-aircraft fleet (Sheffler and Gupta, 1988).

Premature spallation of the insulative ceramic layer is a significant concern in the utilization of TBC on gas turbine components (Miller and Lowell, 1982; Grisaffe and Levine, 1979; Ruckle, 1979). Ceramic spallation is caused by cyclic thermal stresses resulting from differential thermal expansion of ceramic and metal. Fortunately, the amount of cyclic thermal exposure required to cause spallation appears to be deterministically related to the number and severity of applied thermal cycles, and can be predicted quantitatively with the same degree of reliability as metallic failure from creep, fatigue, etc. (Miller, 1984, 1988; Cruse et al., 1988).

Most current TBC applications use a two-layer coating system incorporating an inner oxidation-resistant metallic layer and an outer insulative ceramic layer, both applied by the plasma spray process. Examination of failed components indicates that spallation occurs as the result of cracking in the ceramic layer parallel and adjacent to, but not coincident with, the very rough metal–ceramic interface. Phenomenological assessment of factors that cause plasma-deposited ceramic spallation indicates two independent but apparently interactive degradation modes (Miller and Lowell, 1982; Miller, 1984; Cruse et al., 1988). The first involves mechanical damage, which is attributed to cyclic inelastic strain in the ceramic. The second appears to involve gradual interfacial oxidation of the metallic coating layer. The purpose of this paper is to comment on the occurrence and possible causes of significant inelastic deformation in a nominally brittle ceramic coating, and to present recent observations that more fully characterize the accumulation of ceramic cracking damage.

Coating System Description

The investigated coating system is used on turbine vanes in several commercial engines, including the JT9D, PW2037, PW4000, and V2500. As shown in Fig. 1, it incorporates a nominal 5 mil (130 μm) inner "bond coat" of highly oxidation resistance Low-Pressure Plasma-Sprayed (LPPS) NiCoCrAlY and a nominal 10 mil (250 μm) air plasma-deposited outer layer of 7 percent yttria partially stabilized zirconia. X-ray diffraction analysis indicates 55 to 60 volume percent (v/o) tetragonal, 40 to 45 v/o cubic, and no detectable monoclinic phase in the as-deposited ceramic. This nonequilibrium phase distribution results from very rapid solidification in the deposition process (Miller et al., 1983). The ceramic structure is porous and extensively microcracked (Fig. 1*c*). This contributes significantly to the unusual ceramic mechanical behavior described in the following section. The interface between ceramic and metal possesses a very complex topology characteristic of the original LPPS NiCoCrAlY surface. As shown in Figs. 1(*b*) and 2, this surface includes many small, almost free-standing "peninsular" metal deposits, which penetrate relatively deeply into and are almost completely surrounded by ceramic. This feature creates many re-entrant angles and pockets, which promote mechanical interlocking between ceramic and metal. This interface also has a high specific surface area. Because of the high degree of interpenetration and interlocking, the ceramic–metal interface can be viewed as a narrow "graded zone" about

---

Contributed by the International Gas Turbine Institute and presented at the 34th International Gas Turbine and Aeroengine Congress and Exhibition, Toronto, Ontario, Canada, June 4–8, 1989. Manuscript received at ASME Headquarters January 23, 1989. Paper No. 89-GT-132.

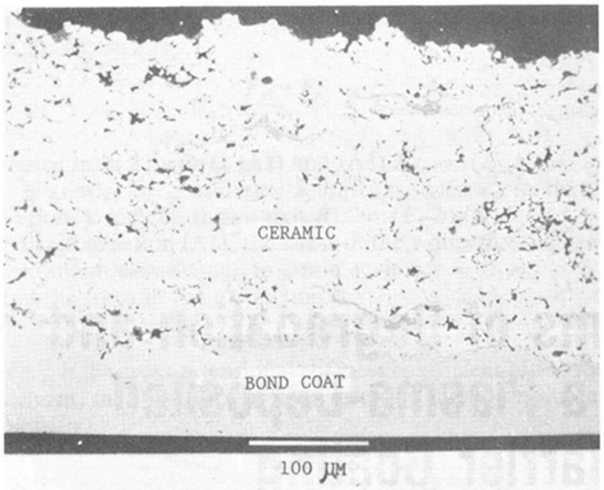

A) OVERVIEW

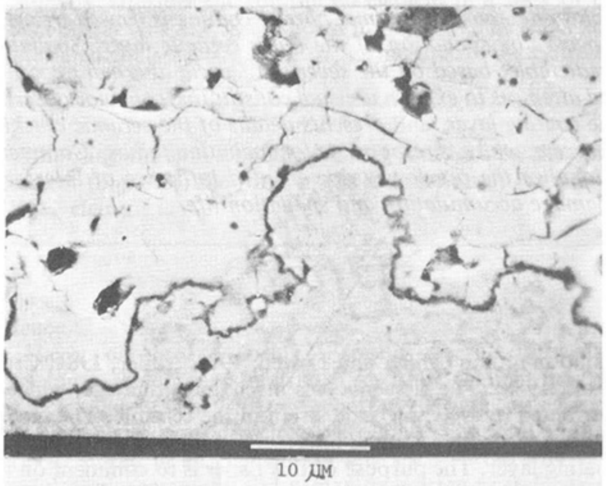

B) MAGNIFIED VIEW OF INTERFACE SHOWING METAL SURFACE DEPOSITS SURROUNDED BY CERAMIC

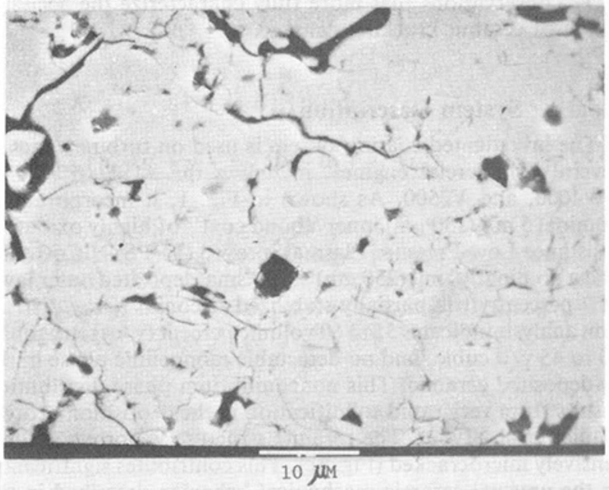

C) MAGNIFIED VIEW OF CERAMIC POROSITY AND MICROCRACKING

Fig. 1 Plasma-deposited thermal barrier coating microstructure

one mil (25 μm) thick. This concept of a graded zone of extremely high metal surface area, incorporating many almost free-standing peninsular surface deposits, is important to subsequent interpretation of the relationship between oxidation and ceramic cracking.

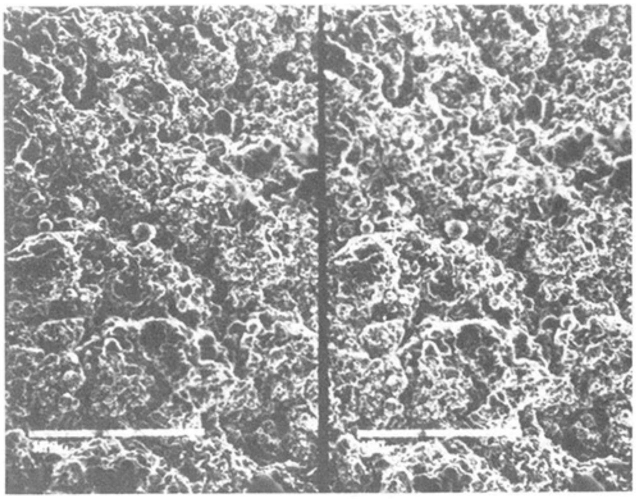

Fig. 2 Stereographic pair of photomicrographs of as-deposited MCrAlY bond coat surface; note that a special viewer is required to superimpose these images optically for true three-dimensional viewing

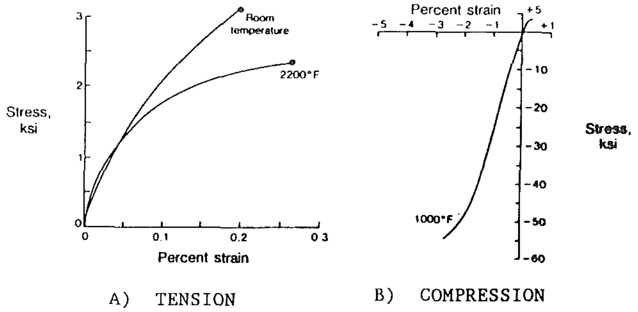

A) TENSION B) COMPRESSION

Fig. 3 Uniaxial tensile and compressive deformation of bulk plasma-deposited ceramic at various temperatures

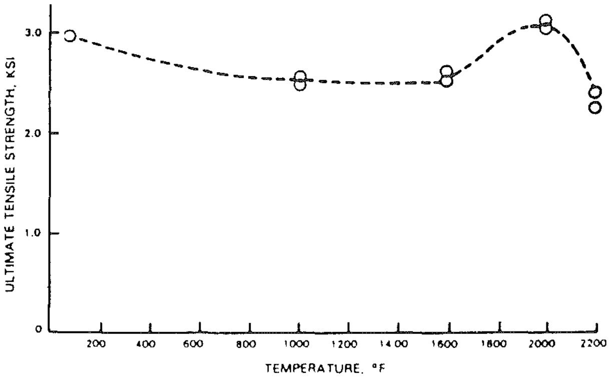

Fig. 4 Influence of temperature of tensile strength of bulk plasma-deposited ceramic

Ceramic Mechanical Behavior

Because spallation occurs by cracking in the ceramic layer, substantial effort was devoted to characterization of ceramic mechanical behavior. Four-point bend, uniaxial tensile, compression, creep, and pseudotensile disk fatigue tests (Shaw et al., 1973) were conducted on specimens machined from bulk plasma deposited ceramic. Loads were applied in a direction to produce maximum principal stress in the plane of the splat structure. Deposition parameters were the same as those used to deposit TBC and produced essentially identical microstructure. Some of these data are reported by Cruse et al. (1988); details of the ceramic microstructure and test methods are reported by DeMasi et al. (1989).

The most significant finding of this work is the observation of substantial reversed inelastic deformation at all temperatures investigated (ambient to 2200°F/1204°C). This is very unusual behavior for a ceramic material. Most ceramics are

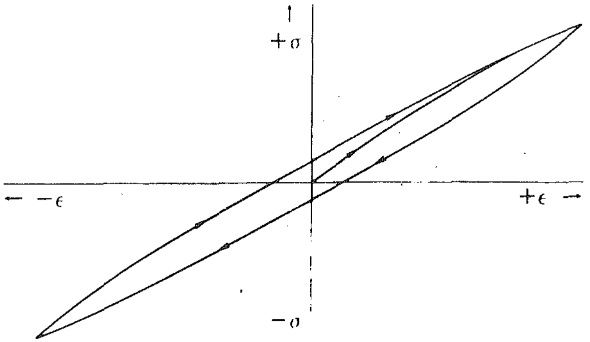

Fig. 5 Ambient temperature hysteresis loop obtained by successive reversal of strain-gaged bend specimen

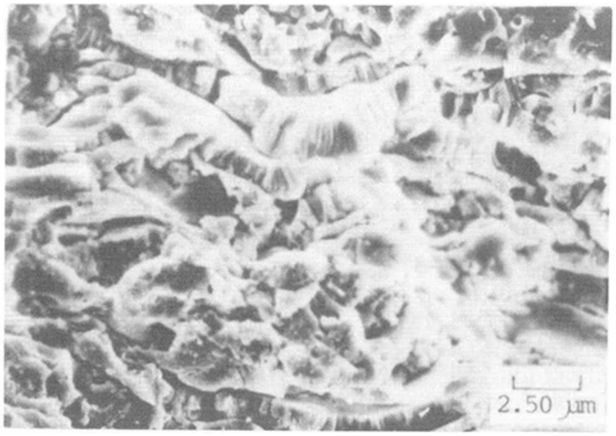

Fig. 6 Tensile fracture surface of bend test specimen

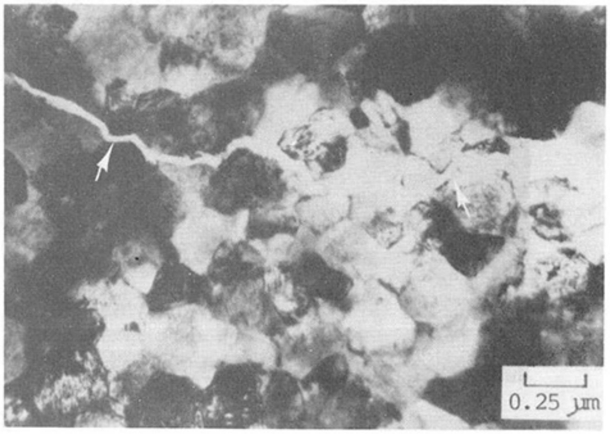

Fig. 7 Transmission electron micrograph showing submicron scale crack surface roughness produced by microcracking at grain boundaries (arrows); plane of micrograph is parallel to plane of coating

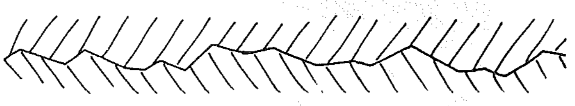

A) UNSTRESSED MICROCRACK

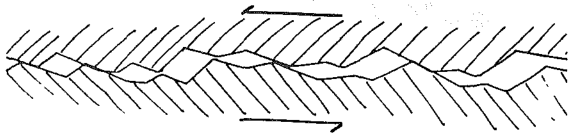

B) SLIDING OF MICROCRACK UNDER STRESS

Fig. 8 Illustrating hypothesized stick-slip sliding behavior of rough microcrack such as shown in Fig. 7

brittle, exhibiting only liner elastic deformation at low and intermediate temperatures. The excellent cyclic thermal durability of plasma-deposited ceramic is attributed primarily to this unusual reversed inelasticity. As shown in Fig. 3(*a*), uniaxial tensile curves for the plasma-deposited ceramic are nonlinear even at very low stress levels, with no clearly definable elastic segment. Ultimate tensile strength and fracture strain are quite low, on the order of 7 ksi (48 MPa) and 0.25 percent, respectively. Fracture toughness also is quite low, on the order of 0.5 ksi root-inch (0.55 MPa root-meter). Only a slight decline of strength is seen between ambient temperature and 1800°F (982°C), with an apparent slight increase of strength at 2000°F (1094°C) (Fig. 4). Above this temperature, strength starts to decline rapidly. Uniaxial compression exhibits a combination of linear and nonlinear behavior, with significantly higher strength than in tension (Fig. 3*b*). Substantial permanent offset was measured on a strain-gaged four-point bend specimen from which load was removed prior to failure. No visually observable cracking was seen on the tensile face of this specimen, indicating that the curvature in Fig. 3 represents truly inelastic behavior. A hysteresis loop obtained by reversing the orientation of this specimen at zero load exhibits significant reversed inelastic strain (Fig. 5). Evidence of significant creep at 1800°F (982°C) and above, and of exceptionally stress sensitive fatigue behavior (stress exponent on the order of 50) also are found.

The proposed explanation for the metal-like behavior described above is based on the nature of the plasma-deposited ceramic structure shown in Fig. 1. The development of this plasma splat structure is nicely illustrated by Herman (1988). It can be idealized as an assembly of independent segments that are mechanically interlocked in an interpenetrating network almost analogous to a three-dimensional jigsaw puzzle. A better appreciation of this layered, interpenetrating "puzzle structure" is provided by a fractograph obtained from the tensile face of a four-point bend failure (Fig. 6). This fractograph also shows a columnar substructure within the splats.

Microcracking has been known to induce nonlinear stress-strain behavior in ceramics (Fu and Evans, 1984). In the present investigation, it is hypothesized that reversed inelastic deformation results from a form of stick-slip behavior between adjacent interpenetrating elements of the microcracked ceramic structure. This stick-slip behavior results in turn from an attempt of surfaces that are rough on a very fine scale to slide past one another, which requires them to be forced very slightly apart. As shown by the transmission electron micrograph in Fig. 7, microcracks in the plasma-deposited ceramic are inherently rough on the submicron scale as a result of the intergranular crack morphology.

The stick-slip concept is illustrated schematically in Fig. 8. As force is initially applied, surfaces with very small asperities slide first at very low stresses. As stress increases, surfaces with progressively larger asperities slide to a new "stuck" position. This progressive increase of cumulative amounts of sliding with increasing stress accounts for the shape of the tensile curve shown in Fig. 3. Behavior in compression is analogous, except that stress required to cause relative movement across adjacent shear boundaries is much greater because movement of these boundaries is restrained by direct abutment of interfaces normal to the maximum principal stress. Hence relative movement of adjacent structural elements requires substantial elastic deformation of abutting segments before sufficient strain is accumulated to permit discontinuous displacement of adjacent shear surfaces. The occurrence of reversed inelasticity is easily accounted for by this model, and in fact the nonlinear nature of the unloading and compressive reloading curves can be rationalized by an argument identical to that put forward to account for initial tensile nonlinearity. Further refinements can

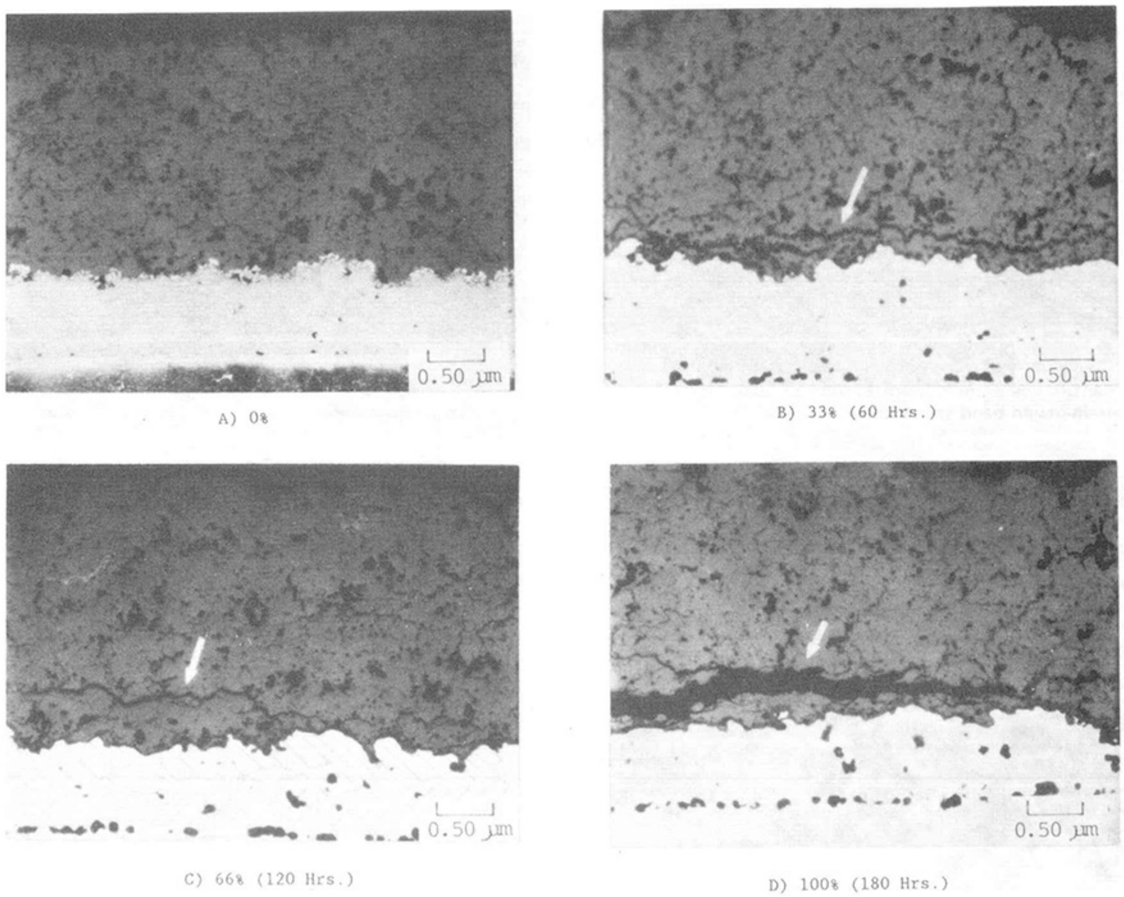

A) 0%

B) 33% (60 Hrs.)

C) 66% (120 Hrs.)

D) 100% (180 Hrs.)

Fig. 9 Cracking damage in specimens suspended from test at various fractions of spallation life

be formulated to account for the cyclic strain "softening" seen with repeated strain cycling. These refinements might involve localized fracture of smaller asperities, which would permit adjacent surfaces to slide more freely on subsequent cycles.

There are several lines of further investigation that might be pursued to gain additional understanding of the proposed deformation mechanism. The use of internal friction and/or acoustic emission is proposed, as is more detailed phenomenological characterization, including additional studies of cyclic strain softening behavior and strain rate sensitivity. The influence of microcrack roughness level, which could be varied by manipulation of deposition parameters and hence crystalite size, would be of great interest in the above studies. Additional microstructural characterization is needed, especially fractography of fatigue crack surfaces to search for evidence of abrasion damage.

Behavior of the ceramic above 1800°F is attributed to the presence of glassy phase(s) at splat and possibly grain boundaries. The classic indication of this phase is the reduction of strength above the temperature where softening and consequent boundary sliding initiate. Typically, at the temperature where the phase just becomes viscous, there is an initial increase in strength and toughness resulting from crack blunting. Such an increase has been observed in many systems (Tsai and Raj, 1981). While a similar strength versus temperature increase has been attributed to aging effects in partially stabilized zirconia (Hannink and Swain, 1986), specimens in the present study were at temperature for less than one hour, which is not sufficient time to experience aging at the investigated temperatures (Miller et al., 1981). To demonstrate this, furnace-exposed specimens were examined by x-ray diffraction. These specimens showed very little change from the as-deposited phase distribution for times up to 60 h at 2200°F (1204°C). The apparent slight increase in strength seen in Fig. 4 near 2000°F thus is attributed to glassy phase(s) arising from the presence of glass forming impurities in the original spray powder, which was analyzed to contain 0.53 percent silica. The decline of strength above this temperature is attributed to further softening of the hypothesized boundary phase(s). Additional transmission electron microscopy will be required to confirm the presence of this phase.

To summarize, reversible, nonlinear, inelastic behavior is observed at ambient and elevated temperatures in plasma-deposited 7 percent yttria partially stabilized zirconia. This reversible inelasticity is attributed to a form of "stick-slip" behavior in the heavily microcracked plasma splat structure. This stick-slip behavior involves the accumulation of discrete, discontinuous displacements across adjacent shear loaded surfaces in the interpenetrating, mechanically interlocked microcrack structure, as illustrated schematically in Fig. 8. Above 1800°F (982°C), glassy boundary phases soften, leading to strength reduction and creep.

Ceramic Damage Accumulation

Results of stress analyses based on the above constitutive properties indicate that thermal cycling of the TBC on gas turbine airfoils produces substantial reversed inelastic deformation in the ceramic coating layer (Cruse et al., 1988). To determine the influence of this reversed inelastic strain cycling on the nature and accumulation of ceramic damage, interrupted laboratory thermal cycling tests were conducted in a jet fueled burner rig (details reported elsewhere by DeMasi et al., 1989). Behavior of the ceramic in this test correlates well with engine behavior.

Ceramic cracking damage found in selected specimens re-

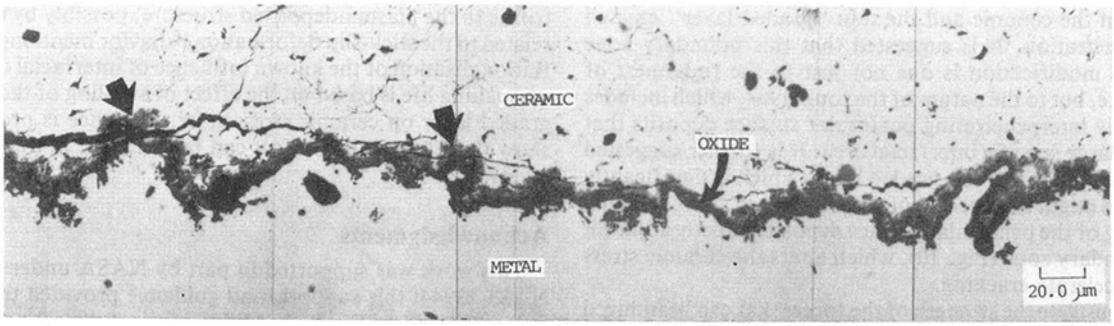

Fig. 10 Morphology of interfacial oxide; note substantial lateral growth at sides of oxidized "peninsular" surface deposits (arrows)

moved from test at various fractions of the cyclic thermal spalling life is shown in Fig. 9. It is clear from these and other fractionally exposed samples that ceramic cracking commences early, on the order of one-quarter to one-third of the total exposure required to spall the coating. Careful examination of crack morphology at successively increasing life fractions suggests that ceramic spallation may result from progressive link-up of adjacent subcritical cracks, rather than from subcritical growth of a single dominant crack. Quantitative measurement of average crack length shows a progressive increase with increasing exposure. "Young" specimens contain cracks on the order of 2 to 3 mils (50 to 80 µm); longer exposure times yield average crack lengths of about 6 to 10 mils (160 to 250 µm). The number of cracks also appears to increase with exposure time. "Old" specimens exhibit large isolated cracks on the order of 13 mils (330 µm) together with shorter cracks about 2 to 3 mils (50 to 80 µm) long. The "oldest" unfailed specimen examined (90 percent life) showed one major crack 38 mils (970 µm) long and several shorter cracks (about 7 mils/180 µm).

An observation that is consistent with the stick-slip hypothesis proposed earlier is the presence of detectable monoclinic phase on the surface of spalled coating chips. X-ray diffraction analysis of failed specimens indicates very little change of "bulk" coating phase distribution, with essentially no monoclinic phase detectable in the bulk ceramic coating after cyclic thermal exposure. However, analysis of the spalled surfaces does indicate small but detectable quantities of monoclinic. Strain-induced transformation from tetragonal to monoclinic has been observed on abraded surfaces of bulk partially stabilized zirconia (Reed and Lejus, 1977). While the importance of this effect is not well understood for plasma-sprayed zirconia, it seems reasonable to expect that sliding surfaces in the stick-slip model might exhibit detectable monoclinic content.

To summarize, the accumulation of ceramic damage occurs by progressive cracking directly adjacent to the ceramic-metal "graded zone." Significant cracking is seen as early as one-fourth of the spallation life, and seems to accumulate by a mechanism of multiple crack link-up rather than by monotonic propagation of a single dominant crack. The issue of crack initiation is addressed in the following section.

The Role of Oxidation

As noted in the introduction, previously published phenomenological evidence clearly demonstrates a significant influence of oxidation on spallation life. Based on this evidence, substantial effort was devoted to investigating the relationship between ceramic cracking and the growing oxide scale. This scale can be discerned in Figs. 9(*b–d*) as a very thin dark layer at the ceramic–metal interface. Because of the very rough nature and high specific surface area of the interface, this oxide layer is highly irregular, with numerous accumulations of uncharacteristically thick oxide build-up resulting from partial or total oxidative consumption of the previously noted peninsular metallic surface deposits (Fig. 10). As discussed earlier, most ceramic cracking occurs parallel and very close to the interface, touching the tops of the highest metallic protrusions (Figs. 9*b–d*).

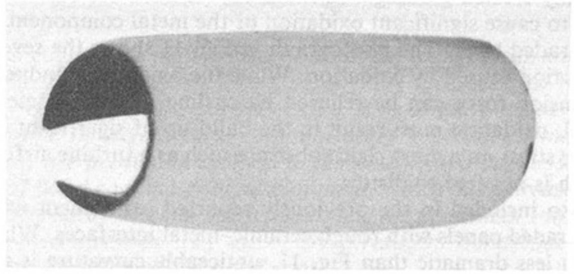

Fig. 11 Severe curling resulting from thermal exposure of an initially flat panel with an intentionally graded metal-ceramic interface

Considerable effort was devoted to identification of ceramic crack initiation sites. Based on the clear phenomenological link between oxidation and life, it seems reasonable to speculate that the swelling associated with oxidation, especially of the peninsular deposits, might directly initiate cracking. Electron microscope examinations did find a few isolated cases of what might be interpreted as scale-initiated cracking. However, these examples were sufficiently infrequent as to lead to the conclusion that this is not the major initiation mode. Scale-initiated cracking was easier to find in "older" specimens, occurring in the same structure together with larger numbers of well-developed longer cracks, which appear, at least in the two-dimensional section, to be isolated from the interface. This observation would suggest that the thicker oxide scale developed at longer exposure times can initiate cracks, but that this is not the critical damage mode in the sense that these are not the cracks that link and propagate to failure.

Based on the above observations, it is hypothesized that "initiation" really is a process involving near-threshold growth of pre-existing microcracks. It is further hypothesized that this near-threshold growth is facilitated by the accumulation of abrasion damage resulting from the previously discussed stick-slip behavior. Additional quantitative metallographic studies of specimens with very small exposure times will be required to confirm this hypothesis. Also of value would be fractographic studies to characterize abrasion damage on spallation crack surfaces.

In the absence of clear evidence for oxide-initiated cracking, the question naturally arises as to the mechanism by which interfacial oxidation accelerates the accumulation of ceramic fatigue damage. Following the lead of other investigators, it is assumed that oxidation affects spallation life by altering ceramic stress state in the region where cracking occurs (Miller and Lowell, 1982; Miller, 1984). This region is not easily defined, but appears to be coincident with a hypothetical boundary between the ceramic and the thin "graded layer" created by interpenetration. It is suggested that this boundary zone stress state modification is due not just to the roughness of the interface, but to the nature of the roughness, which includes many highly interpenetrating peninsular surface deposits that produce a large specific interfacial area. It is further suggested that it is the swelling of this graded layer, which is significantly greater than might be expected of a flat interface, and especially the swelling of the peninsular surface deposits directly adjacent to the boundary zone (Fig. 10), which alters the ceramic stress state to accelerate cracking.

To demonstrate the strength of the forces that can be induced by oxidative expansion of a graded ceramic-metal layer, a previously reported experiment (Duvall and Ruckle, 1982) is reproduced in Fig. 11. A flat sheet metal panel with intentionally created grading was thermally exposed for sufficient time to cause significant oxidation of the metal component in the graded layer. The photograph in Fig. 11 shows the severe distortion caused by oxidation. While the oxidatively induced expansion force can be relieved by curling of a sheet metal panel, oxidation must result in the build-up of significant ceramic stress on a more rigid substrate such as a turbine airfoil, which is not free to distort.

Also included in the previously reported experiment were nongraded panels with rough ceramic-metal interfaces. While much less dramatic than Fig. 11, noticeable curvature is apparent on careful observation of these panels (Fig. 2 of Duval and Ruckle, 1982). A suggested approach to quantify the magnitude of ceramic stress produced by interfacial oxidation would be to measure the amount of distortion produced with varying times, temperatures, and substrate thicknesses.

Other investigators have used highly idealized sinusoidal finite element models of the ceramic-metal interface to study the effect of interfacial oxidation of the ceramic stress state (Chang et al., 1987). Results show that simulated oxide growth at the interface can significantly alter stress.

Summary

Failure of a two-layer plasma-deposited thermal barrier coating is caused by cyclic thermal exposure and occurs by spallation of the outer ceramic layer. Spallation life is quantitatively predictable, based on the severity of cyclic thermal exposure. This paper describes and attempts to explain unusual constitutive and cracking behavior observed in the insulative ceramic coating layer. Reversible, nonlinear, inelastic ceramic deformation is attributed to a stick-slip type of behavior in the heavily microcracked, mechanically interlocked plasma-deposited splat structure. Elevated temperature strength reductions and creep are attributed to softening of grain boundary glassy phase(s). Ceramic spallation is shown to result from progressive accumulation of ceramic cracking damage parallel and directly adjacent to a narrow (about 1 mil/25 μm) pseudo-graded zone created by interpenetration of ceramic and metal at the very rough interface. Cracking damage is seen as early as 25 percent of life, and appears to accumulate by progressive link-up of multiple small cracks rather than by monotonic propagation of a single dominant crack.

Previously published work has shown a strong influence of interfacial oxidation on spallation life. Extensive metallographic examination failed to show evidence of significant direct oxide-induced ceramic crack initiation. It is thus hypothesized that crack "initiation" really is a process of near-threshold growth of pre-existing microcracks, which are intrinsic to the plasma-deposited structure, possibly by a process related to the stick-slip deformation behavior mentioned above. Rationalization of the known influence of interfacial oxidation on spalling life is based on the effect of swelling of the pseudo-graded layer on ceramic stress state. Evidence is provided to show that the swelling effect can be dramatic in thick graded layers.

Acknowledgments

This work was supported in part by NASA under Contract NAS3-23944; this support, and guidance provided the NASA Project Manager, Dr. R. A. Miller, is gratefully acknowledged. For helpful discussions concerning the behavior of partially stabilized zirconia we thank Susan L. Manning. Also appreciated is the technical support provided by Messrs. Russell Shenstone and Merritt Wight.

References

Chang, G. C., Phucharoen, W., and Miller, R. A., 1987, "Behavior of Thermal Barrier Coatings for Advanced Gas Turbine Blades," *Surface and Coatings Technology*, Vol. 30, p. 13.

Cruse, T. A., Stewart, S. E., and Ortiz, M., 1988, "Thermal Barrier Coating Life Prediction Model Development," ASME Journal of Engineering for Gas Turbines and Power, Vol. 110, p. 611.

DeMasi, J. T., Ortiz, M., and Sheffler, K. D., 1989, "Thermal Barrier Coating Life Prediction Model Development," Final Report, NASA Contract NAS3-23944 (Pratt & Whitney, in press).

Duvall, D. S., and Ruckle, D. L., 1982, "Ceramic Thermal Barrier Coatings for Turbine Engine Components," ASME Paper No. 82-GT-332.

Fu, Y., and Evans, A. G., 1985, "Some Effects of Microcracks on the Mechanical Properties of Brittle Solids—I, Stress-Strain Relations," *Acta Met.*, Vol. 33, p. 1515.

Grisaffe, S. J., and Levine, S. R., 1979, *Proceedings of First DOE/EPRI Conference on Advanced Materials for Alternate Fuel Capable Directly Fired Heat Engines*, Castine, ME, p. 680.

Hannink, R. H., and Swain, M. V., 1986, "Particle Toughening in Partially Stabilized Zirconia: Influence on Thermal History," in: *Tailoring Multiphase and Composite Ceramics: Materials Science Research, Vol. 20*, R. E. Tressler, G. L. Messing, C. G. Pantano, and R. E. Newnham, eds., Plenum Press, New York, p. 259.

Herman, H., 1988, "Plasma-Sprayed Coatings," *Scientific American*, Vol. 259, p. 112.

Miller, R. A., Levine, S. R., and Stecura, S., 1980, "Thermal Barrier Coatings for Aircraft Gas Turbines," AIAA Paper No. 80-0302.

Miller, R. A., Smialek, J. L., and Garlick, R. G., 1981, "Phase Stability in Plasma-Sprayed Partially Stabilized Zirconia-Yttria," in: *Advances in Ceramics, Vol. 3, Science and Technology of Zirconia*, The American Ceramic Society, p. 241.

Miller, R. A., and Lowell, C. E., 1982, "Failure Mechanisms of Thermal Barrier Coatings Exposed to Elevated Temperatures," *Thin Solid Films*, Vol. 99, p. 265.

Miller, R. A., Garlick, R. G., and Smialek, J. L., 1983, "Phase Distributions in Plasma Sprayed Zirconia-Yttria," *American Ceramic Society Bulletin*, Vol. 62, p. 1355.

Miller, R. A., 1984, "Oxidation Based Model for Thermal Barrier Coating Life," *Journal of the American Ceramic Society*, Vol. 67, p. 517.

Miller, R. A., 1988, "Life Modeling of Thermal Barrier Coatings for Aircraft Gas Turbine Engines," in: *Toward Improved Durability in Advanced Aircraft Engine Hot Sections*, ASME, New York.

Reed, J. S., and Lejus, A., 1977, "Effect of Grinding and Polishing on Near Surface Phase Transformations in Zirconia," *Mater. Res. Bull.*, Vol. 12, p. 949.

Ruckle, D. L., 1979, "Evaluation of Plasma Sprayed Ceramic Coatings for Turbine Engine Components," *Thin Solid Films*, Vol. 64, p. 327.

Ruckle, D. L., 1980, "Plasma Sprayed Ceramic Thermal Barrier Coatings for Turbine Vane Platforms," *Thin Solid Films*, Vol. 73, p. 455.

Shaw, M. C., Braiden, P. M., and DeSalvo G. J., 1975, "The Disk Test for Brittle Materials," ASME *Journal of Engineering for Industry*, Vol. 97, pp. 77-87.

Sheffler, K. D., and Gupta, D. K., 1988, "Current Status and Future Trends in Turbine Application of Thermal Barrier Coatings," ASME Journal of Engineering for Gas Turbines and Power, Vol. 110, p. 605.

Tsai, R. L., and Raj, R., 1981, "Creep Fracture in Ceramic Containing Small Amounts of a Liquid Phase," *Acta Met.*, Vol. 30, p. 1043.

D. J. Wortman

E. C. Duderstadt

W. A. Nelson

GE Aircraft Engines,
Cincinnati, OH 45215

Bond Coat Development for Thermal Barrier Coatings

The use of thermal barrier coatings on high-pressure turbine components can improve gas turbine efficiency through reduction of cooling airflow. However, to reduce cooling airflow, a highly reliable thermal barrier coating is required. This increased reliability will be achievable through several complimentary approaches: material and process development, life prediction method development, and engine service experience. The results of bond coat material development, which has increased the thermal cycle life of plasma spray thermal barrier coatings, are presented. Improvements were achieved by two methods: (1) use of creep-resistant bond coat compositions, and (2) overaluminiding of the bond coat.

Introduction

The effort to increase gas turbine engine efficiency has received added impetus in recent years because of the sharp increase in fuel cost and the requirements for increased turbine performance. Several generations of superalloys have been developed over the years to permit increases in turbine inlet gas temperatures to increase engine efficiency, but the practical temperature limits make this increasingly difficult and expensive. The use of thermal barrier coatings (TBCs) has the potential to increase engine efficiency by permitting increased gas inlet temperatures at present metal temperatures, or maintaining current gas inlet temperatures and reducing coolant requirements and the efficiency penalties associated with cooling air usage. Alternatively, TBCs can be utilized to reduce metal temperatures and extend life.

Thermal barrier coatings are now commonly used on combustors, afterburner flameholders, and other low-risk applications to extend the useful lives of those components significantly. Also, TBCs have been successfully tested on several high-pressure turbine (HPT) nozzles and blades. The occasional loss of some of the ceramic insulating layer of the TBC from combustors and flameholders is not unduly harmful to engine operation or life, and the ability to predict coating life in such applications is not essential. On the other hand, the reliability of coatings used on HPT components is more critical. Loss of the coating from such components has the potential to shorten component life to less than that of uncoated parts, particularly if cooling air has been reduced to obtain engine efficiency. Thus the long-term use of TBCs on HPT hardware under engine operating conditions where safe metal temperatures must be maintained requires a highly reliable coating and predictable life.

Two methods for thermal barrier coating application are available: (1) plasma spray, and (2) physical vapor deposition. The present paper deals only with plasma spray TBCs. For HPT components, where bond coat temperatures may exceed 1000°C (1832°F), a vacuum plasma spray process is generally used to apply bond coats rather than the initially developed air plasma spray process. The reduced porosity and oxide inclusion content with vacuum plasma spray (VPS) produces a bond coat with greater oxidation resistance. A typical plasma spray TBC consists of a 125-μm (5-mil) thick MCrAlY bond coat, applied by VPS, and a 250–380-μm (10–15-mil) thick partially stabilized (6–8 percent Y_2O_3) zirconia top coat applied by air plasma spray (APS). The primary failure mode of TBCs is spallation, typically on cool down from use temperatures (Hillery et al., 1988). Another failure mode, erosion loss, may be relevant from some applications as well (Bennett et al., 1987).

Thermal cycle spallation occurs within the ceramic near the metal–ceramic interface. Major spallation stresses result during thermal cycling from the large difference in coefficient of thermal expansion of the ceramic insulating layer, the metallic bond coat, and the substrate alloy. Several other phenomena may contribute to spallation:

1 sintering or other thermal processes within the ceramic, which reduce its thermal shock resistance;

2 accumulation of damage (microcracking) during repeated thermal cycling (DeMasi and Sheffler, 1986);

3 creep of the substrate or bond coat; and

4 oxidation of the bond coat resulting in growth of an Al_2O_3 scale between the bond coat and ceramic top coat, which increases the strain within the ceramic.

Development of life prediction models using these failure modes and tools such as finite element analysis is being conducted (Chang et al., 1986).

In the materials and process development areas, plasma spray parameters have been developed at the various application centers to achieve optimum results. These include selection of powder and plasma spray parameters to achieve the desired structure and properties. Bond coat process development has led to high-density bond coats for oxidation resistance while achieving adequate roughness for adherence of the ceramic top coat. Bond coat compositions have generally been adapted from the MCrAlY (M = Ni or NiCo) overlay coatings developed

---

Contributed by the International Gas Turbine Institute and presented at the 34th International Gas Turbine and Aeroengine Congress and Exhibition, Toronto, Ontario, Canada, June 4–8, 1989. Manuscript received at ASME Headquarters January 23, 1989. Paper No. 89-GT-134.

Table 1 Nominal Ni, Co, Cr, Al, and Y contents of TBC bond coats*

	Content (wt%)				
	Ni	Co	Cr	Al	Y
NiCrAlY	bal	—	22.0	10.0	0.3
NiCoCrAlY	bal	32.0	20.0	8.0	0.3
BC51	bal	4.0	9.0	6.0	0.3
BC52	bal	10.0	18.0	6.5	0.3

*BC51 and BC52 contain several additional elements to provide solid solution and grain boundary strengthening (Goldman, 1983).

for oxidation and hot corrosion resistance. In the present work, newly developed thermal fatigue resistant overlay coatings have been adapted for use as TBC bond coats.

Experimental Procedure

Disk specimens (0.32 cm thick by 2.5 cm dia) were machined from cast substrates of René N4 and René 80. The René N4 was cast as monocrystal slabs and the specimens were machined such that the faces were parallel to the ⟨100⟩ orientation. The René 80 was conventionally cast as a polycrystalline rod and specimens were sliced from the rod. Prior to bond coat application, specimens were given the standard alloy solution heat treatment. The 125-μm-thick bond coats were applied to one face of the disk specimens by vacuum plasma spraying. The bond coat powders were produced by argon atomization and screened to a $-200/+325$ mesh size. This size has been found to provide (1) adequate surface roughness for ceramic coating adherence, and (2) good density (less than 5 percent porosity) for oxidation resistance. Four bond coat compositions were utilized: NiCrAlY, NiCoCrAlY, BC51, and BC52. All four are based on the Ni(Co)CrAlY systems (Table 1); however, the BC51 and BC52 were modified by Goldman (1983) for improved strengthening by (1) reducing Al content to produce a γ-γ' microstructure, (2) adding solid solution strengthening elements, and (3) adding grain boundary modifiers. Some of the bond coats were aluminide coated by the Codep B pack aluminide process to enrich the outer surface in aluminum content and thereby improve oxidation resistance. The aluminide layers were approximately 50 μm (2 mils) thick.

The ceramic top coatings were applied to a 250-μm (10-mil) thickness over the bond coats by air plasma spray. The ceramic coating material was ZrO_2 with 8 wt% Y_2O_3 stabilizer made by sintering, crushing, and screening to a $-200/+325$ mesh size.

Thermal Cycle Spallation Testing

Spallation resistance of the coatings was determined by thermal cycle testing in air. Testing was performed in a furnace equipped with a programmable temperature controller. To provide uniform testing, the specimens were set in shallow grooves with their faces nearly vertical. The 65-min thermal cycle (Fig. 1) consisted of a 10-min heat up from 200°C (390°F) to the test temperature, a 45-min hold at test temperature, followed by cooling to approximately 200°C in 10 min. The cooling cycle is produced by automatically lowering the specimen tray from the furnace and forced air cooling. Up to 60 specimens can be tested simultaneously by this method. Specimen positions are rotated at each inspection period (20 cycles) to assure similar thermal histories. Inspection was performed measuring the coating spallation as a percentage of coating surface area. Specimens were removed for test when they showed 10 percent ceramic coating spallation.

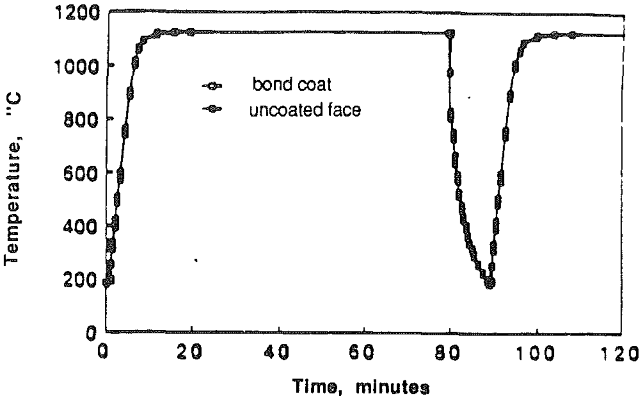

Fig. 1 Temperature history of coated specimens. Curves shown are for thermocouples located directly beneath the ceramic coating (within the bond coat) and along the uncoated specimen face. Emissivity corrected pyrometer measurements showed the temperature history of the ceramic surface to be within 10°C of that given for the uncoated face (from Holmes and Pilsner, 1987).

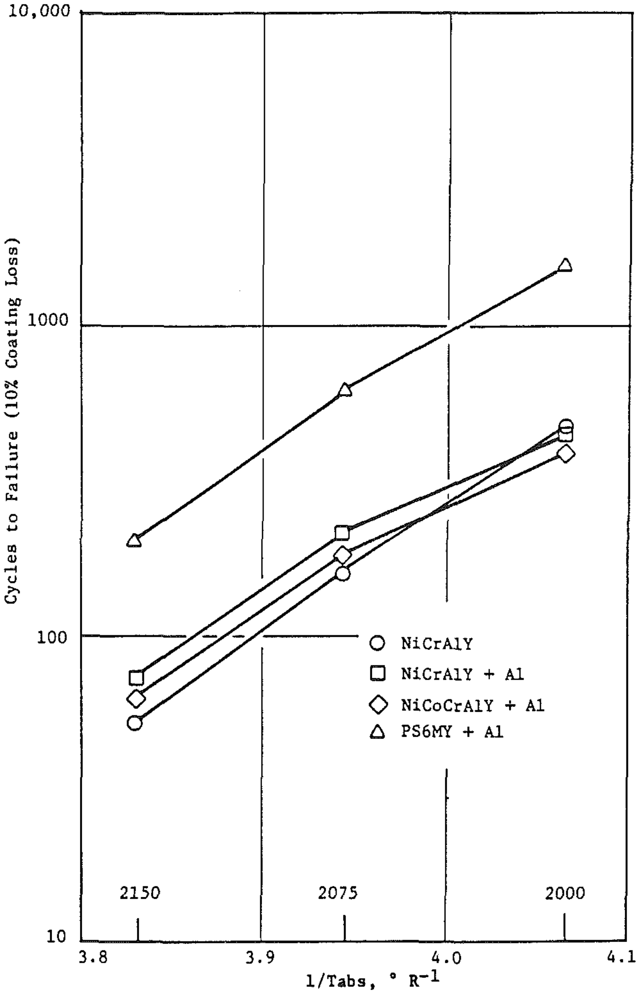

Fig. 2 Thermal cycle test lives of TBCs with various bond coat systems on René N4 specimens

Results and Discussion

Results of the initial testing at three temperatures, 1093°C (2000°F), 1135°C (2075°F), and 1177°C (2150°F), are shown in Fig. 2. Spalling occurred at the typical location around the periphery of the specimen. The lives of all TBC systems increased with decreasing temperatures. The differences in lives of TBCs with NiCrAlY, NiCrAlY + Al, and NiCoCrAlY + Al bond coats were small. The BC51 + Al bond coat TBC however had approximately three times the life of the other systems.

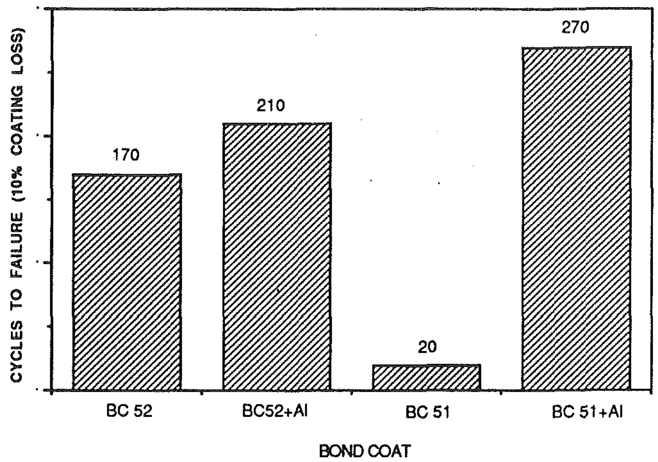

Fig. 3 Thermal cycle test lives at 1135°C (2075°F) of TBCs with various bond coats on René 80 specimens

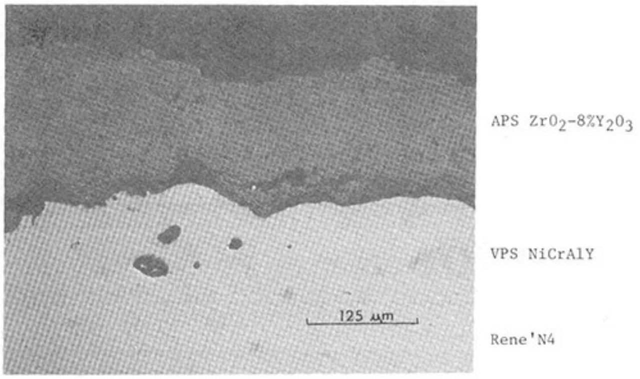

Fig. 4 Microstructure of TBC with NiCrAlY bond coat after 500 thermal cycles to 1093°C (2000°F); note absence of beta phase in bond coat

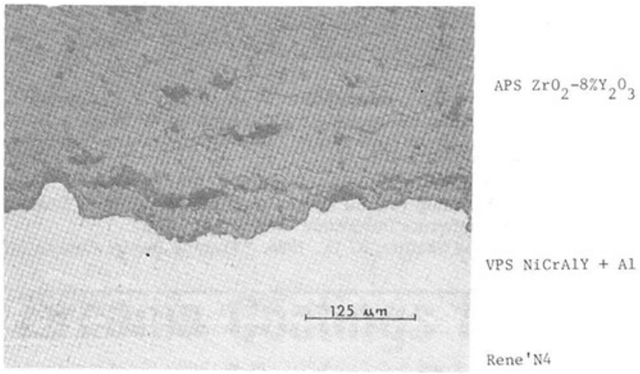

Fig. 5 Microstructure of TBC with NiCrAlY+Al bond coat after 480 thermal cycles to 1093°C (2000°F); note remaining beta phase adjacent to bond coat/substrate interface

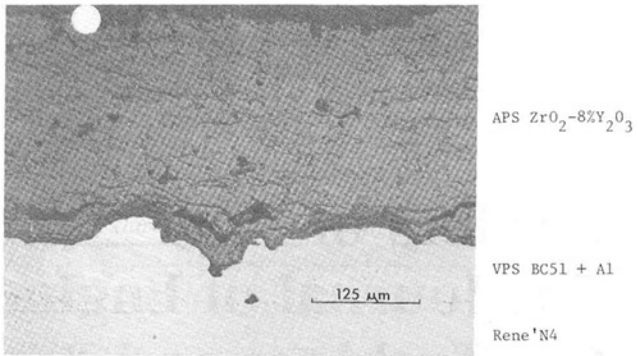

Fig. 6 Microstructure of TBC with BC51+Al bond coat after 1720 thermal cycles to 1093°C (2000°F); note remaining beta phase

In subsequent testing at 1135°C (2075°F) with BC51 and BC52 bond coats, both aluminided and unaluminided (Fig. 3), the unaluminided BC51 bond coat TBC had extremely short life; more than 10 percent spallation had occurred at the first inspection cycle. The BC52+Al bond coat thermal cycle lives were comparable to the BC51+Al bond coat TBC lives (210 versus 270 cycles). When BC52 was used as a bond coat unaluminided, the lives were still good (170 cycles). The lives reported on René 80 are less than on René N4. This effect has been observed with several other bond coats as well. When BC52+Al is tested on René N4, lives comparable to BC51+Al have been achieved by Nelson (1988).

These results suggest the following: (1) Overaluminiding provides benefit to strengthened bond coats, and (2) bond coat strength is a factor on TBC spallation. The improvement in lives afforded by aluminiding is believed to be due to the relatively low aluminum content (6-6.5 percent) of BC51 and BC52. Based on the low aluminum, it is likely that BC51 is a marginal alumina former and the enrichment of the outer layer with 20-30 percent Al helps the bond coat form alumina.

After 500 cycles of testing at 1093°C (2000°F), the NiCrAlY bond coat had been depleted of the high-aluminum β phase by alumina scale growth and interdiffusion with the substrate. The oxide scale was approximately 5 μm thick (Fig. 4). The NiCrAlY+Al bond coat, after approximately the same number of cycles (480), had an oxide thickness of only 2 μm and the β phase was still present over most of the scale-metal interface (Fig. 5).

Microcrack link-up could be seen in the unspalled areas of the ceramic at the failure times. The BC51+Al bond coat specimens tested at 1093°C for 1720 cycles (Fig. 6) had an oxide scale thickness of approximately 9 μm. Within the margin of error in the oxide thickness measurement, the parabolic growth rate of the oxide on the BC51+Al bond coat is similar to that of the NiCrAlY+Al bond coat, and greater than that of the NiCrAlY bond coat. This suggests that the improved life of TBCs with the strengthened bond coats is not due to superior oxidation resistance. TBC modeling efforts using a finite element mechanics approach has predicted the opposite result for a bond coat with increased creep resistance (Hillery et al., 1988); therefore the reasons for the improved lives are still unclear.

Summary

Two new bond coats, BC51+Al and BC52+Al, have been identified that have provided improved thermal cycle lives for TBCs in laboratory testing. These bond coats are NiCoCrAlYs, which have been modified for improved creep strength. Overaluminiding is necessary to improve the oxidation resistance of the surface of BC51; however, BC52 can still provide improved lives without overaluminiding. Thermal barrier coatings with these new bond coats are now being engine tested on HPT blades and nozzles. The improved spallation resistance provided by these bond coats is expected to, in part, help produce the high reliability that will be required for future gas turbine application.

Acknowledgments

The authors wish to recognize the technical assistance in applying coatings by Dr. B. K. Gupta and Mr. Bob Zimmerman and the assistance in testing and evaluation by Mr. Art Losekamp and Mr. Brad Williamson.

References

Bennett, A., Toriz, F. C., and Thakker, A. B., 1987, "A Philosophy for Thermal Barrier Coating Design and Its Corroboration by 10,000 h Service Experience on RB211 Nozzle Guide Vanes," *Surface and Coatings Technology*, Vol. 32, pp. 359–375.

Chang, G. C., Phucharoen, W., and Miller, R. A., 1986, "A Study on Thermal Barrier Coatings Including Thermal Expansion Mismatch and Bond Coat Oxidation," NASA Conference Publication 2444, pp. 415–434.

DeMasi, J. T., and Sheffler, K. D., 1986, "Thermal Barrier Coating Life Prediction Model Development," NASA Conference Publication 2444, pp. 469–483.

Goldman, E. H., 1983, personal discussion.

Hillery, R. V., Pilsner, B. H., McKnight, R. L., Cook, T. S., and Hartle, M. S., 1988, "Thermal Barrier Coating Life Prediction Model Development," NASA Contractor Report 180807, Nov.

Holmes, J. W., and Pilsner, B. H., 1987, "Cerium Oxide Stabilized Thermal Barrier Coatings," *Thermal Spray: Advances in Coating Technology*, D. L. Honk, ed., Proceedings of ASM's 1987 National Spray Conference, Orlando, FL, Sept. 14–17.

Nelson, W. A., 1988, "Development of a Highly Reliable High Performance Thermal Barrier Coating," AFWAL-TR-88-4079, June.

T. E. Strangman

J. L. Schienle

Garrett Auxiliary Power Division,
Allied-Signal Aerospace Company,
Phoenix, AZ 85010

Tailoring Zirconia Coatings for Performance in a Marine Gas Turbine Environment

Zirconia coatings represent an advanced materials technology that offers significant durability and performance benefits for marine gas turbines. Thin zirconia coatings offer superior resistance to hot corrosion attack from fuel (sulfur, vanadium, and sodium) and air (sea salt) impurities present in marine engine environments. Thicker zirconia coatings reduce transient thermal stresses and heat transferred into air-cooled components. This paper describes the development of zirconia coatings, applied by the electron beam evaporation-physical vapor deposition process, that are tailored to provide superior durability in a marine engine environment.

Introduction

The high-quality diesel fuel required for marine gas turbine applications has sometimes been limited in worldwide availability; however, fuel supplies will be significantly increased if fuels with greater impurity concentrations (i.e., sulfur and vanadium) can be burned without affecting engine durability.

Unfortunately, current predictions indicate permitting high concentrations of sulfur and vanadium in marine diesel fuels will adversely affect the lives of gas turbine components. Predicted life trends for superalloy components with a CoCrAlY coating for various fuel sulfur and vanadium contents are illustrated in Fig. 1. Increasing the sulfur concentration over current fuel specification limits would result in a large reduction in coating life for turbine components with metal temperatures near 700°C. Similarly, increasing the vanadium concentration of marine diesel fuel to 2 parts per million (ppm) is predicted to result in further reductions in component lives in the 700 to 800°C temperature range. Consequently, there is a continuing demand for improved protective coatings for the structural alloys used in marine gas turbines.

Burner rig testing conducted by the Garrett Auxiliary Power Division (GAPD) Strangman, 1987) and marine engine testing conducted by General Electric (Wortman and Nagaraj, 1987) indicates that yttria-stabilized zirconia (YSZ) coatings can provide superior hot corrosion resistance to molten sulfate salt deposits, relative to conventional diffusion aluminide and overlay coatings. Studies conducted at the University of Pittsburgh (Warnes et al., 1988) have indicated that YSZ also will be effective in inhibiting hot corrosion when sodium vanadate is present in the molten sulfate salts; laboratory studies have indicated that YSZ is about twenty times more resistant to hot corrosion by sodium vanadate than is alumina.

Current YSZ coatings, applied by electron beam evaporation-physical vapor deposition (EB-PVD) and plasma spray processes, have high levels of porosity for strain tolerance. The microstructure of the EB-PVD ceramic coating is composed of columnar grains with intercolumnar gaps, which permit cyclic thermal and coating-superalloy thermal expansion mismatch strains to be accommodated by almost-free expansion. This virtually unstressed microstructure has resulted in coatings with superior lives in a cyclic oxidation environment (Strangman et al., 1987). Superior durability EB-PVD zirconia thermal barrier coated turbine airfoils have been reported for aircraft engine applications, where salt ingestion is minimal (Strangman, 1982; De Masi and Sheffler, 1986).

Unfortunately, GAPD has observed that wicking of salt deposits into porous zirconia coatings can compromise strain-tolerance, resulting in premature spalling (Strangman et al., 1987). The magnitude of the life reduction observed in a current generation EB-PVD YSZ coating is illustrated in Fig. 2. Molten salt film damage to the zirconia microstructure is illustrated in Fig. 3.

Therefore, to realize the full benefit of the superior hot corrosion resistance of zirconia coatings, the microstructure of the coatings must be further optimized, to preclude wicking of molten salt into the coatings. The following paragraphs describe the status of a development effort to achieve this goal.

Ceramic Coating Development

A viable coating for marine engine applications must be tailored to function in the complex marine thermal-mechanical-corrosive engine environment. Fig. 4 schematically illustrates a coating system designed to meet these requirements. The coating system consists of a ceramic coating layer and a metallic bond coating, which forms an adherent oxide scale that inhibits additional oxidation.

The ceramic layer must be engineered to have good adhesion to the oxide scale, accommodate high thermal expansion mismatch strains with the substrate, be stable in combustion environments, and inhibit penetration of corrosive molten salts. Stabilized zirconia coatings applied by EB-PVD can be tailored

---

Contributed by the International Gas Turbine Institute and presented at the 34th International Gas Turbine and Aeroengine Congress and Exhibition, Toronto, Ontario, Canada, June 4-8, 1989. Manuscript received at ASME Headquarters February 13, 1989. Paper No. 89-GT-269.

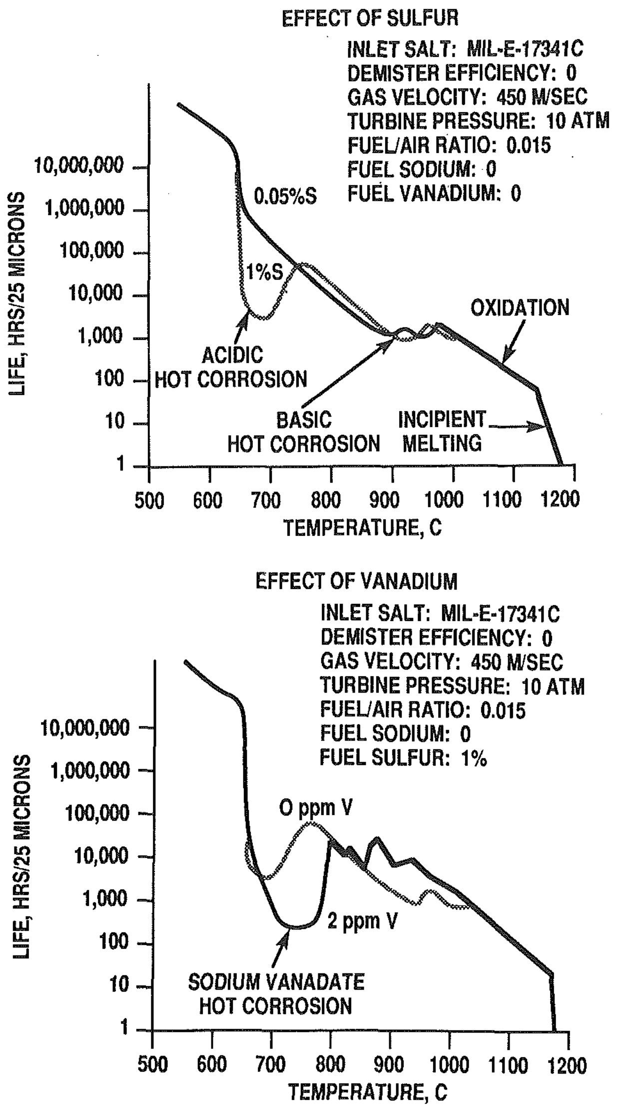

Fig. 1 Increased levels of fuel contaminants (*S*, *V*) are predicted to result in large reductions in low-temperature hot corrosion lives of CoCrAlY-coated superalloy components

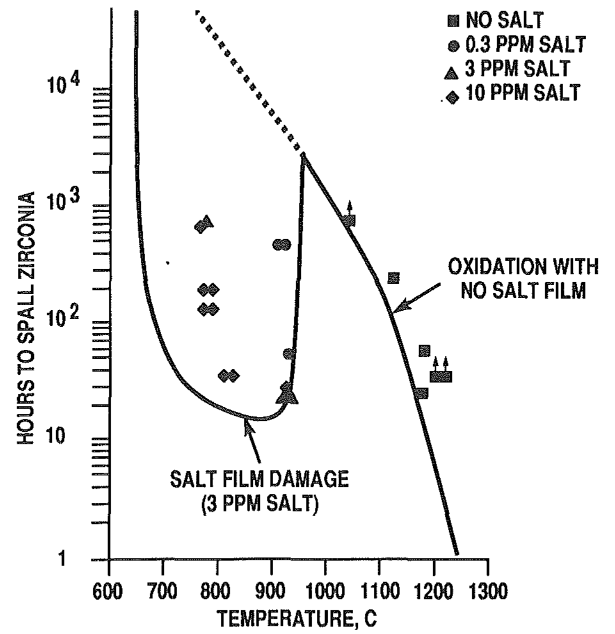

Fig. 2 Zirconia spalling is accelerated by the presence of molten salt films

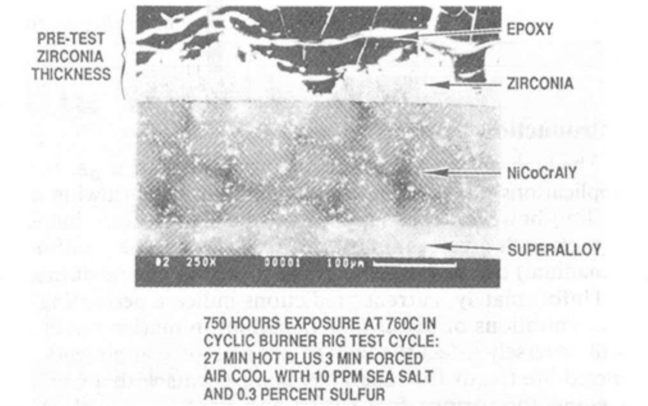

Fig. 3 Sulfate salt films wicking into the microstructure damage columnar-grained EB-PVD zirconia coatings

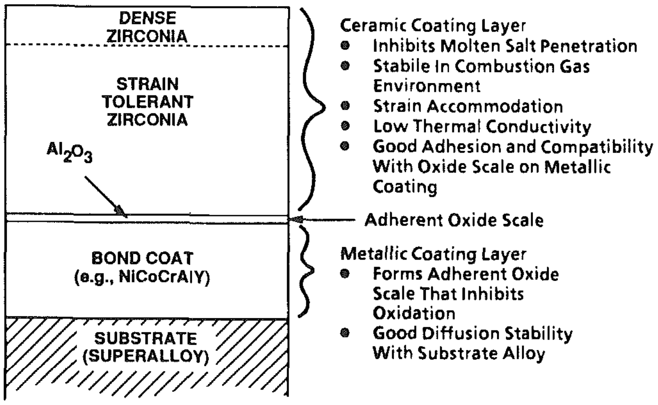

Fig. 4 Coatings for marine gas turbine applications must be engineered to function in a complex thermal-mechanical-corrosive environment

to meet all of these requirements. The selection of both zirconia and the EB-PVD process was dictated by these considerations.

Selection of Yttria-Stabilized Zirconia. Stabilized zirconia was selected for the ceramic layer, due to its superior hot corrosion resistance and thermal stress resistance. Burner rig hot corrosion tests, with sea salt ingestion into the combustion air, indicated that 8 to 20 weight percent yttria-stabilized zirconia is at least five times more resistant to molten sulfate salt (predominantly sodium and magnesium sulfates) attack than the protective alumina scales formed on metallic coatings currently used for corrosion resistance. In a General Electric LM2500 engine test, CoCrAlY coated turbine blades exhibited extensive hot corrosion after 1077 hours of marine service, whereas EB-PVD YSZ coated blades concurrently tested in the same rotor indicated no evidence of hot corrosion attack (Wortman and Nagaraj, 1987). Also, as previously noted, lab-

Nomenclature

°C = degrees Celsius
CoCrAlY = cobalt, chromium, aluminum, yttria
CVD = chemical vapor deposition
EB-PVD = electron beam evaporation–physical vapor deposition
GAPD = Garrett Auxiliary Power Division
IN738 = nickel-based alloy
MAR-M 247 = nickel-based alloy
ppm = parts per million
YSZ = yttria-stabilized zirconia

oratory tests have indicated that YSZ has the potential to be about 20 times more resistant to molten $NaVO_3$ than alumina is (Warnes et al., 1988).

For thermal stress resistance, YSZ has a relatively high thermal expansion coefficient, relative to other hot corrosion resistant oxides (e.g., silica, zircon, and mullite). The higher expansion coefficient of zirconia helps minimize stresses due to ceramic–superalloy thermal expansion mismatch strains.

Selection of the EB–PVD Process. The EB–PVD process was selected for deposition of the ceramic coating, since it produces the most strain-tolerant microstructure (columnar grains with intercolumnar porosity). This columnar microstructure accommodates high thermal strains and provides superior performance in cyclic oxidation environments, relative to other candidate processes such as plasma spraying (Strangman, 1987; Strangman et al., 1987). Also, the EB–PVD process provides the opportunity to engineer the coating microstructure at critical interfaces; i.e., the bond coating-zirconia interface and the gas path surface. EB–PVD process parameters can be changed during deposition to tailor both the bond interface, for high interfacial toughness, and the gas path surface, for resistance to penetration of corrosive molten salt deposits and erosion. EB–PVD provides cost advantages for small turbine airfoils as well: several components can be coated concurrently. Also, microstructural modifications can be achieved during EB–PVD zirconia deposition, avoiding requirements for expensive secondary process steps, such as sputtering or laser glazing.

Bond Coating. The bond coating must form an adherent oxide scale, to inhibit additional oxidation and to provide a suitable bonding surface for the zirconia. Bond coating compositions are typically selected to form a stable, adherent alumina scale. The alumina scale provides a stable interface and inhibits additional oxidation for several thousand hours under marine engine operating conditions. It also provides an increment of hot corrosion resistance in the event that the ceramic layer is locally damaged.

Oxide scale adhesion to the substrate can be enhanced by adding elements such as yttrium and hafnium in the bond coating. Alumina adhesion can be further enhanced by the presence of yttrium, hafnium, and zirconium in the superalloy substrate, which subsequently diffuse into the bond coating.

High-purity alumina scales are an excellent bonding surface for EB–PVD zirconia coatings. This is particularly true for crystallographically stable alpha alumina; in high-temperature exposure tests (Demaray, 1985), zirconia coatings remained adherent to single-crystal sapphire (alpha alumina) specimens after 200 hours at 1200°C, with interfacial toughness in the order of 3 $MPa \cdot m^{1/2}$. Consequently, the composition and processing of the bond coating are selected to assure a high-purity alumina scale is achieved.

The development of strain-tolerant columnar grained zirconia coatings has been discussed previously (Strangman, 1982, 1987). Consequently, the remainder of this paper focuses on engineering the ceramic coatings for both high interfacial toughness and resistance to molten salt penetration.

Coating Interfacial Toughness. As previously noted, for optimum interfacial toughness, a high-purity alpha-alumina scale is highly desirable. The presence of unstable gamma-alumina in the oxide scale must be avoided since it is a potential contributor to void formation at the bond interface; a volume change occurs during the phase transformation to the denser alpha-alumina (Smialek and Gibala, 1983).

Several approaches for achieving higher purity alpha-alumina scales are being evaluated. For baseline coatings, the oxide scale is formed during the EB–PVD deposition of the zirconia layer (the background pressure of oxygen in the EB–PVD process is adequate for thermal oxidation of the metallic bond coating). Although this approach for scale forming is inexpensive, the oxide scale typically contains small amounts of transient oxides of nickel, cobalt, and chromium, which can adversely affect interface stability at high temperatures. High EB-PVD zirconia deposition temperatures (near 1100°C) favor thermal growth of full alpha-alumina scales on the bond coating.

Other options for forming higher purity alpha-alumina scales include preoxidation of the bond coating in wet hydrogen, and deposition of a chemical vapor deposition (CVD) alumina layer on the bond coating prior to deposition of the EB–PVD zirconia layer. Bond coating heat treatments in wet hydrogen are designed to inhibit the formation of transient oxides; the dew point is controlled to make transient oxides thermodynamically unstable so that only alumina, yttria, and hafnia can form. Also, the heat treatment temperature is controlled to favor alpha–alumina formation. A chemically pure alumina layer can be applied by CVD. Again, the deposition temperature is selected to favor formation of the crystallographically stable alpha phase.

Interfacial microporosity must also be avoided to achieve high interfacial toughness. Microporosity has been found previously at the bond coating/zirconia interface in cases where poor interfacial toughness was exhibited. Consequently, the EB–PVD process and interfacial composition of the EB–PVD zirconia are tailored to inhibit interfacial microporosity. For the baseline EB–PVD process, the initial few microns of EB–PVD zirconia are deposited under substoichiometric conditions (Zr rich). This produces a relatively dense microcrystalline structure at the interface and good adhesion (Demaray, 1987). It has been speculated (Strangman, 1987) that the substoichiometric zirconia deposition promotes adhesion by "cleaning" the interface; i.e., substoichiometric zirconia reduces transient nickel and cobalt oxides present on the surface of the alumina and permits them to diffuse into the adjacent zirconia, away from the interface.

To further improve adhesion, other approaches are possible. Electrically biasing the substrate increases the energy of zirconia ions produced in the EB–PVD process. Also, the zirconia can be doped with elements that can improve adhesion. These approaches are currently being evaluated.

Development Results to Date

Evaluation of the parameters described above has been initiated and the results to date are discussed in the following paragraphs.

Coating Adhesion. Two nickel-based superalloys, IN738 and MAR-M 247, were evaluated as substrate materials to assess the effects of substrate composition (Table 1) on bond coating–zirconia adhesion. Alumina scale forming procedures predicted to yield higher purity alumina scales were used in these initial investigations. Also, the effect of electrical biasing on interfacial toughness was evaluated.

Specimens were prepared and evaluated for interfacial toughness using a modified bond strength test (Strangman, 1987; Strangman et al., 1987). The interfacial toughness of the coated specimens was characterized in both the as-coated condition, and after 100 hours exposure in air at 900°C, to verify coating toughness stability. Each test specimen was a coated button, which had an artificial flaw (e.g., a sputtered carbon dot) located at the bond coat–zirconia interface. To test coating adherence, the button was epoxy bonded between two pull rods and pulled in tension to failure. All fracture surfaces were examined optically. Scanning electron microscopy and energy dispersive x-ray analyses were performed on selected specimens to characterize the crack propagation modes.

The overall results were encouraging, since many of the EB–

Table 1 **Nickel-based superalloys evaluated as coating substrates: Composition by weight, percent**

Alloy	Ni	Co	Cr	Al	Ti	Ta	Cb	W	Mo	Si	Zr	C	B	La	Hf
IN738	(bal)	8.5	16.0	3.4	3.4	1.7	0.9	2.6	1.7	--	0.10	0.17	0.010	--	--
MAR-M 247	(bal)	10.0	8.4	5.5	1.1	3.0	--	10.0	0.6	--	0.05	0.15	0.015	--	1.4

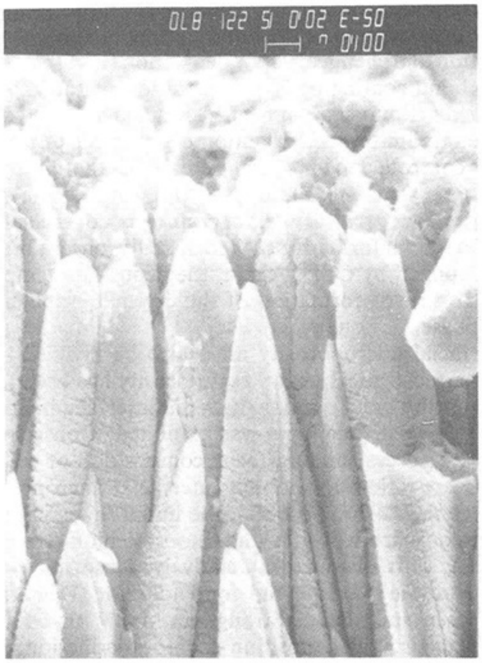

Fig. 5 Electrical biasing produced a thin, dense surface layer that bridged the intercolumnar porosity of the EB-PVD ZrO_2

PVD coatings significantly exceeded the cohesive toughness of plasma spray zirconia coatings, which is typically about 1 MPa•$m^{1/2}$. The interfacial toughness of the best EB-PVD zirconia coatings was typically around 2 MPa•$m^{1/2}$; toughness values as high as 3.5 MPa•$m^{1/2}$ were observed.

Substrate composition does have a significant effect on interfacial toughness. MAR-M 247 substrates tended to promote better zirconia adhesion than IN738. This observation suggests that the 1.4 percent hafnium in the MAR-M 247 superalloy contributes to enhanced toughness of the ceramic-metal interface.

Another trend observed was that electrically biasing the substrate during the initial zirconia deposition increases interfacial toughness in the as-coated condition.

For interfacial stability (retained toughness after 100 hours air exposure at 900°C), the CVD alumina and wet hydrogen heat treatments at 1120°C for 2 hours resulted in good toughness retention after oxidation exposures. Wet hydrogen heat treatments conducted at 1000°C and 1050°C resulted in significantly reduced adhesion. Analysis of these low-toughness specimens identified the presence of some gamma-alumina in the fine-grained zirconia region between the alpha-alumina scale and the columnar-grained zirconia.

Ceramic Surface Densification. To improve the corrosion resistance of EB-PVD stabilized zirconia coatings, wicking of molten salt deposits into the coating intercolumnar porosity must be minimized to avoid premature spallation. The approach to inhibit salt penetration into the coating is to produce a dense zirconia surface layer, which bridges the porosity of the strain-tolerant EB-PVD microstructure. Preferred methods involve modification of the EB-PVD process to produce a dense zirconia closeout layer. Other methods for densifying the surface of the EB-PVD coating, such as laser glazing and sputtering, have also been considered (Strangman et al., 1987; Prater and Courtright, 1987). However, from an economic standpoint, these methods are not as desirable since additional equipment and process steps are required.

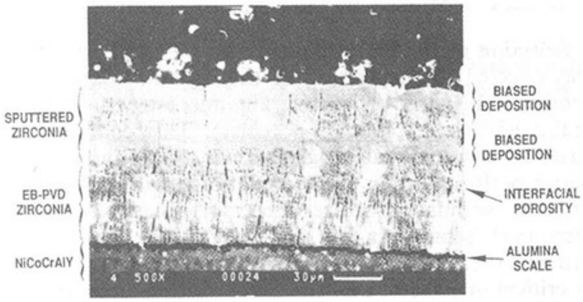

Fig. 6 Sputtered zirconia coating with dense electrically biased layers inhibited penetration of salt into underlying columnar-grained EB-PVD zirconia during 1285 hours of cyclic burner rig testing at 870°C

Process parameters with the potential to promote a transition to a dense surface EB-PVD microstructure are being evaluated. Initial efforts have focused on combinations of zirconia stoichiometry, electrical biasing, and deposition rate. Other parameters that are expected to influence surface density are specimen rotation rate and doping of the zirconia vapor with secondary oxides that promote sintering.

Preliminary EB-PVD coating trials to evaluate electrical biasing have been performed. The EB-PVD deposition rate was reduced while electrically biasing the substrate during the last few minutes of deposition. The microstructure of the electrically biased zirconia coating is illustrated in Fig. 5. The results indicate that surface densification was achieved via the electrical biasing. As shown in the figure, slightly less than 1 μm of densified zirconia was deposited. Although a nominal goal for the dense layer thickness is 5 μm, the results were encouraging; i.e., the dense layer bridged the intercolumnar porosity of the EB-PVD coating in this preliminary run. Increased thickness of the dense surface can be achieved by increasing the biased deposition time. Experiments are currently underway to determine the combination(s) of coating process parameters that readily accomplish the goal of a dense surface layer.

Corrosion Resistance of Zirconia Coatings. To verify the hot corrosion benefits of a dense surface layer, an electrically biased sputtering process was used to apply dense (8 percent) yttria-stabilized zirconia coating layer(s) onto burner rig specimens coated with EB-PVD columnar-grained yttria-stabilized zirconia (Fig. 6). Specimens with and without dense sputtered surface layers were tested for up to 1285 hours in a cyclic (27 min hot plus 3 min forced air cooling) burner rig hot corrosion test at 870°C (20 ppm salt in air, 0.3 percent sulfur in fuel).

All of the coatings exhibited some spalling within the zirconia layer. In the case of the specimens that were overcoated with dense layers, spalling was frequently associated with a line of voids at the interface between the EB-PVD and sputtered zirconia layers (Fig. 6). Small areas of zirconia spalling were also observed in the EB-PVD coated baseline specimens; in most instances, spalling occurred within the zirconia layer and did not damage the interface. It is expected that this damage can be avoided with uninterrupted EB-PVD processing, which transitions the zirconia coating from the strain-tolerant microstructure to a dense surface.

Microstructural analysis indicated that virtually no salt pen-

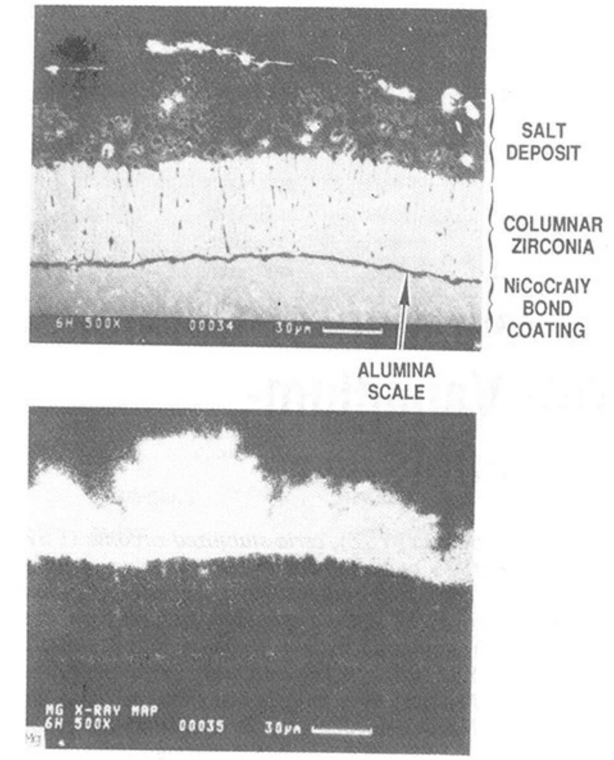

Fig. 7 Without a dense surface layer, molten salt is wicked into the columnar zirconia layer; specimen was exposed for 1285 hours in an 870°C cyclic corrosion burner rig test

etrated through the dense sputtered layer(s) where they remained adherent. In contrast, salt permeated the EB-PVD zirconia microstructure to the bond coating interface where intercolumnar gaps within the EB-PVD zirconia layer were exposed to the surface (Fig. 7).

Conclusions

Stabilized zirconia coatings offer superior hot corrosion resistance for turbine engine components in marine environments.

A dense surface layer can be produced by application of an electrical bias to the component during deposition of sputtered and EB-PVD zirconia coatings.

Dense surface layers inhibit molten salt wicking into the strain-tolerant columnar grained zirconia microstructure.

EB-PVD zirconia coatings have been identified with superior interfacial adhesion, relative to plasma-sprayed zirconia coatings.

Acknowledgments

Development of corrosion-resistant zirconia coatings has been partially supported by the U.S. Navy under Contract N00167-86-C-0097, "Corrosion Resistant Ceramic Coating Development Program for Marine Gas Turbine Application." The Navy Program Manager is Mr. R. Clarke. Corrosion studies to support coating development have been conducted at the University of Pittsburgh (Mr. B. Warnes and Dr. F. Pettit) and Ohio State University (Mr. S. Scarberry and Dr. R. Rapp). Transmission electron microscope studies of ceramic-metal interfaces have been performed at Case Western Reserve University (Drs. O. Unal and A. Heuer). EB-PVD coatings have been applied by Temescal, Inc., under the direction of Mr. D. Lee. Sputtered zirconia coatings were applied by Battelle Pacific Northwest Laboratory under the direction of Drs. E. Courtright and J. Prater. This program has also received significant support from Mrs. P. Solfest, Ms. A. Comfort, Mr. G. Capek, and Mr. J. McIver at Garrett.

References

DeMasi, J. T., and Sheffler, K. D., 1986, "Thermal Barrier Coating Life Prediction Model Development," Contract NAS3-23944, presented at Turbine Engine Hot Section Technology 1986, Cleveland, OH.

Demaray, R. E., 1985, private communication.

Demaray, R. E., 1987, "Adherent Ceramic Coatings," U.S. Patent No. 4,676,994.

Prater, J. T., and Courtright, E. L., 1987, "Ceramic Thermal Barrier Coatings With Improved Corrosion Resistance," presented at the International Conference on Metallurgical Coatings, San Diego, CA.

Smialek, J. L., and Gibala, R., 1983, "Structure of Transient Oxides Formed on NiCrAl Alloys," *Metallurgical Transactions A*, Vol. 14A, pp. 2143-2161.

Strangman, T. E., 1982, "Columnar Grain Ceramic Thermal Barrier Coatings," U.S. Patent No. 4,321,331.

Strangman, T. E., 1987, "Development and Performance of Physical Vapor Deposition Thermal Barrier Coating Systems," *Proceedings of the 1987 Coatings for Advanced Heat Engines Workshop*, Maine Maritime Academy, Castine, ME, July 27-30, pp. III-63 to III-71.

Strangman, T. E., Neumann, J., and Liu, A., 1987, "Thermal Barrier Coating Life-Prediction Model Development," NASA Report CR-179648.

Warnes, B., Meier, G. H., and Pettit, F. S., 1988, "Hot Corrosion of Yttria Stabilized Zirconia by Deposits Containing Vanadium," presented at the 1988 Annual Meeting of the Metallurgical Society of AIME, Phoenix, AZ.

Wortman, D. J., and Nagaraj, B. A., 1987, "Advanced Ceramic Coatings for Marine Gas Turbine Engines," *Proceedings of the 1987 Coatings for Advanced Heat Engines Workshop*, Maine Maritime Academy, Castine, ME, July 27-30, pp. III-49 to III-62.

Burner Rig Evaluation of Ceramic Coatings With Vanadium-Contaminated Fuels

B. A. Nagaraj

D. J. Wortman

General Electric Aircraft Engines
Cincinnati, OH 45215

The performance of yttria-stabilized zirconia (YSZ), ceria-stabilized zirconia (CSZ), and magnesia-stabilized zirconia (MSZ) coatings was evaluated using an atmospheric burner rig; test environment contained compounds of vanadium, sodium, and sulfur. The coatings were deposited by plasma spraying and electron beam physical vapor deposition (EB-PVD); sputtered sealant layers of hafnia, alumina, and platinum were deposited on the YSZ coating. The tests were performed for up to 500 hours at 1650°F and 1300°F. The tests were designed to simulate the deposit chemistry and sulfur trioxide partial pressures expected in a marine gas turbine engine operating on contaminated fuel. YSZ, CSZ, and MSZ coatings all underwent reaction in the burner rig environment; the reaction products and their effects on spallation were varied. MSZ was by far the most reactive, readily forming $MgSO_4$ *in both 1650°F and 1300°F tests. The observed reaction products provided a measure of "protection" for the bond coat by preventing molten salt infiltration for the duration of the test. The mechanism of ceramic spallation is discussed. Sputtered overlayers of platinum, hafnia, and alumina did not prevent salt infiltration and reaction with the underlying ceramic, although no reaction product between the overlayer and the salt was observed.*

Introduction

A US Navy sponsored program for development of ceramic coatings for marine gas turbine hot-section blades and vanes as used in engines of greater than 5000 hp is currently underway at General Electric. The fuels of interest in this program are diesel fuels with a higher impurity (Na, V, S) content than currently allowed in the specifications of the US Navy and General Electric. The contaminated fuels, in addition to being cheaper, are available more widely on a worldwide basis than the higher quality fuels currently specified.

In gas turbine engines designed for electric power generation, contaminated fuels can often be tolerated by adding magnesium-containing corrosion inhibitors to the fuel. These inhibitors act by reaction with the vanadium to form magnesium vanadates, which have high melting points (in excess of 2000°F). In this process, relatively large quantities of solids are generated that would block cooling holes in the turbine blades of aircraft derivative gas turbine engines. Thus corrosion-resistant coatings must be employed in these engines if contaminated fuels are to be utilized. In addition to improving corrosion resistance, the ceramic coatings may also provide a significant thermal barrier effect, which could be used to reduce the cooling air flow and increase the engine efficiency and/or hot section component lives.

YSZ is the state-of-the-art ceramic material that is utilized for thermal barrier coating applications. However, previous work at General Electric (McKee et al., 1978) and elsewhere (Hamilton and Nagelberg, 1984; Lau and Bratton, 1983; Barkalow and Pettit, 1979; Hodge et al., 1980) has shown that YSZ can be destabilized by reactions of the ceramic with vanadium compounds to form yttrium vanadate. CSZ was expected to possess good corrosion resistance in environments containing vanadium compounds because ceria had been found to be relatively invulnerable to vanadium attack (Siemers and McKee, 1982). However, recent work (Jones et al., 1987) has shown that CSZ may react more rapidly with vanadium compounds than YSZ. In order to explore these conflicting data further and obtain a better understanding of the spallation mechanism of ceramic coatings, the performances of a number of ceramic coatings have been evaluated using a burner rig burning vanadium-contaminated fuel.

Table 1 Fuel composition

	V(ppm)	Na(ppm)	S (wt%)
GT12	5	2	2

CALCULATED PARAMETERS* FOR BURNER RIG TESTS

Fuel	Temp. F	Deposition Rate	V in fuel (ppm wt)	Sea Salt in air (ppm wt)	SO_2 in Air (% Vol.)
GT12'	1650	1X	5.4	3.2	1.93
		10X	31.6	29.6	1.93
	1300	1X	19.4	3.2	1.05
		10X	163.3	33.7	1.05

Contributed by the International Gas Turbine Institute and presented at the 34th International Gas Turbine and Aeroengine Congress and Exhibition, Toronto, Ontario, Canada, June 4–8, 1989. Manuscript received at ASME Headquarters February 1989. Paper No. 89-GT-270.

Table 2 Parameters used in burner rig tests

Test No.(1)	Objective	Test Temp. °F	V in Fuel (ppm wt.) (aimed for)	V in Fuel (ppm wt.) (actual)(2)	Sea Salt in Air (ppm wt.)	Equiv. Na in Fuel (ppm wt.)	Vol. % SO$_2$ In Air
1	Baseline	1650	0	0	3.2	25.6	1.93
2	GT12' 1X	1650	5.4	5.2	3.2	25.6	1.93
3	GT12' 10X	1650	31.6	32.7	29.6	232.8	1.93
4	GT12' 10X	1650	31.6	35.4	29.6	232.8	1.93
5	GT12' 1X	1300	19.4	20.3	3.2	25.6	1.05
6	GT12' 10X	1300	163.3	89.6	33.7	264	1.05

1. Specimens in Test Nos. 1, 2, and 5 were cooled to room temperature every 24 hours; specimens in Test Nos. 3, 4 and 6 were run isothermally for 100 hours.

2. Actual values were measured downstream the fuel nozzle at the end of the 100 hour test.

Table 3 Processes used for deposition of ceramic coatings

Process	Coating Composition Wt%	Thickness (mils)	Comments
EB-PVD	8% YSZ	5.0	Relatively dense structure
EB-PVD	8% YSZ	2.5	Relatively dense structure
EB-PVD	45% CSZ	3.5	Columnar structure, relatively high ceria content (40 to 45%)
EB-PVD Sputtering	8% YSZ + HfO$_2$	5.0 + 1.8	Dense structure of the sputtered overlayer
EB-PVD Sputtering	8% YSZ + Al$_2$O$_3$	5.0 + 0.3	Dense structure of the sputtered overlayer
EB-PVD Ion Plating	8% YSZ + Pt	5.0 + 0.3	Dense structure
Plasma Sprayed	8% YSZ	5.0	Typical plasma sprayed structure with splats and porosity
Plasma Sprayed	18% CSZ	5.0	Typical plasma sprayed structure with splats and porosity
Plasma Sprayed	24% MSZ	5.0	Typical plasma sprayed structure, relatively dense coating
Plasma Sprayed	CeO$_2$	5.0	Typical plasma sprayed structure, relatively porous coating

Experimental Procedure

Design of Test Parameters. The test parameters are designed to simulate the same deposit chemistry for a one atmosphere test as in the General Electric LM2500 engine. To determine the test parameters, the deposit chemistry expected on the first stage vanes in the LM2500 engine was calculated for one selected fuel, GT-12. GT-12 and GT-12′ are empirical designations and not part of any fuel specification. The fuel contaminant levels (designated GT-12′) required to produce the same deposit chemistry in one atmosphere tests were back calculated. These calculations were performed both for the deposition rate expected in an LM2500 engine and for ten times the expected deposition rate. The 10× deposition rates were used since the tests were of relatively short duration. The calculation procedure is described by Luthra (1982, 1989). The calculated and experimental fuel compositions are listed in Tables 1 and 2, respectively.

The Burner Rig. The corrosion tests were carried out in a one atmosphere burner rig using a clean distillate fuel (JP5) doped with vanadium naphthanate. Sulfur dioxide gas was injected into the rig immediately after the point of fuel combustion.

The design and operation of the burner rig have been described by Doering and Bergman (1969). Briefly, fuel is combusted with air at one end of a ceramic tube; the combustion products are mixed with additional air and passed through the tube, where the temperature of the gas mixture is adjusted to the desired value by electrical resistance heaters. An atomized spray of synthetic sea water is injected into the combustion chamber. The combustion products and contaminants flow past cylindrical pin specimens, which are mounted vertically on a rotating ceramic platform. The rig operates at atmospheric pressure with a linear gas velocity of 25 m/s.

Six 100-hour tests were carried out. The test parameters and the specimens tested are listed in Table 2.

Ceramic Coated Specimens. YSZ, CSZ, and MSZ coatings were deposited using a number of processes. The processes utilized and the thicknesses of the coatings are listed in Table 3.

The specimens were 2.3 in. long by 0.25 in. in diameter. René 80 was the substrate. Bond coats were selected based on General Electric experience in developing ceramic thermal barrier coatings. Bond coats with a rough surface finish (greater than 300 μin.) are required to provide mechanical adhesion for plasma-sprayed ceramic coatings, whereas a smooth surface finish (approximately 30 μin.) of the bond coat is necessary to achieve the strain-tolerant columnar structure of the physical vapor deposited ceramic coatings. A vacuum plasma sprayed superalloy-type bond coat (with a coarse particle size, $-200/+325$ mesh) with an aluminide overcoat was used as the bond coat for plasma-sprayed ceramic top coats. Vacuum plasma-sprayed CoCrAlHf (with a fine particle size, -400 mesh) was polished to a surface finish of approximately 30 μin. and used as the bond coat for PVD ceramic coatings.

In an attempt to seal the porosity in the ceramic coatings, thin layers of hafnia, alumina, and platinum were sputtered

Table 4 Summary of burner rig corrosion results

Coating*	Total Duration (hours of Test	Test Temperature (°F)	Post-Test Observations
EB-PVD YSZ (5 mils thick)	400	1650	Ceramic attacked, but not spalled. Major amounts of YVO_4 on the surface. Local spots of yttrium sulfate.
EB-PVD YSZ (2.5 mils thick)	400	1650	Most of the ceramic attacked, consumed, and spalled. Remnants of zirconia, fully depleted of Y on the surface; bond coat visible on the specimen surface.
EB-PVD YSZ +Pt	300	1650	Pt layer was not impermeable. Local spots of yttrium vanadate on the surface. Pt and ceramic spalled on a part of the specimen surface.
EB-PVD YSZ + Al_2O_3	100	1300	Al_2O_3 layer was not impermeable. Local spots of yttrium vanadate on the surface.
EB-PVD YSZ + HfO_2	100	1650	HfO_2 layer was not impermeable, even though it was much thicker than alumina or Pt. HfO_2 and YVO_4 spalled on a part of the surface.
Plasma Sprayed YSZ	400	1650	Ceramic reacted, but not spalled. Major amounts of YVO_4 on the surface. Local spots of yttrium sulfate.
Plasma sprayed YSZ	200	1300	Ceramic reacted, but not spalled. Yttrium vanadate and yttrium sulfate on the surface.
Plasma sprayed CSZ	400	1650	Ceramic reacted, but not spalled.
Plasma sprayed CSZ	200	1300	Ceramic reacted, and spalled. Major amounts of cerium sulfate and minor amounts of cerium vanadate on the surface.
Plasma sprayed CeO_2	100	1300	Ceramic reacted and cracked/spalled. Major amounts of cerium sulfate and minor amounts of cerium vanadate on the surface.
Plasma sprayed MSZ	200	1300	Ceramic reacted but not spalled. Major amounts of magnesium sulfate and minor amounts of magnesium vanadate on the surface.

* See Table 3 for coating thickness.

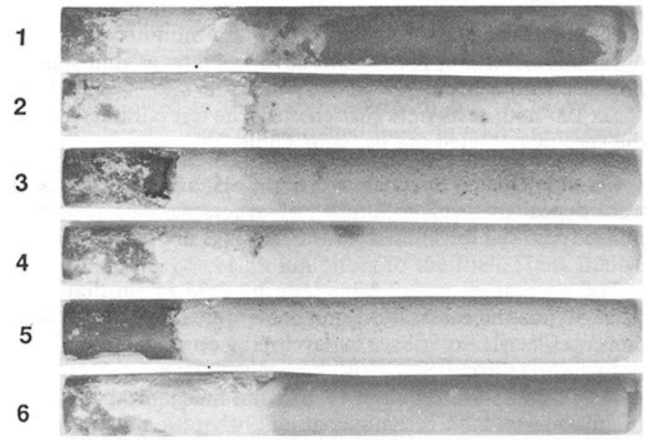

1 ⇒ PVD 8% YSZ (2.5 mils) TEST #'s 1-4 ⇒ 400 hrs
2 ⇒ PVD 8% YSZ (5 mils) TEST #'s 1-4 ⇒ 400 hrs
3 ⇒ PLASMA SPRAYED 8% YSZ TEST #'s 1-4 ⇒ 400 hrs
4 ⇒ PLASMA SPRAYED18% CSZ TEST #'s 1-4 ⇒ 400 hrs
5 ⇒ PLASMA SPRAYED 24% MSZ TEST # 4 ⇒ 100 hrs
6 ⇒ PVD 8% YSZ & SPUTT. HfO_2 TEST # 4 ⇒ 100 hrs

Fig. 1 Macrophotographs of ceramic coated specimens, burner rig corrosion tested up to 400 h at 1650°F (see Table 2 for details)

on the PVD YSZ coatings. In view of the surface roughness of plasma-sprayed ceramic coatings, it is difficult to sputter uniform sealant layers onto such coatings; therefore only the PVD ceramic coatings were used with the sputtered sealant layers.

Results and Discussion

The corrosion test results are summarized in Table 4. The macroscopic appearance of post-test coatings is illustrated in Figs. 1 and 2. Analyses of water rinsings of tested specimens are listed in Table 5.

YSZ. Plasma-sprayed and PVD YSZ coatings both performed well, with no spallation after 400 hours at 1650°F and 200 hours at 1300°F. The surfaces of both the plasma-sprayed and PVD coatings were fully covered with a layer of yttrium vanadate at both temperatures. The yttrium vanadate was identified by x-ray diffraction to be the body-centered-tetragonal phase of YVO_4. Vanadium was not observed in water rinsings (Table 5), indicating that yttrium vanadate is virtually insoluble in water. Yttrium vanadate has a high melting point (3290°F) and would be expected to be solid at the YSZ/YVO_4 interface. It is postulated that this solid phase retards penetration of the ceramic by the molten salt and thereby extends the coating life; however, YVO_4 can dissolve in a liquid salt mixture containing V at the YVO_4/salt interface as indicated by the Y_2O_3–V_2O_5 phase diagram (Levin, 1967).

Significant amounts of soluble yttrium and sulfate were detected in the water rinsings (Table 5), indicating that YSZ

Table 5 Water soluble constituents (mg) in salt deposits on burner rig specimens

Element Analyzed	Plasma CSZ	Plasma MSZ	Plasma YSZ	Plasma CeO_2	PVD YSZ	PVD CSZ	PVD YSZ+Pt
Yttrium	0.010	<0.001	0.332	0.010	1.90	0.001	0.977
Vanadium	<0.001	0.009	<0.001	<0.001	0.001	<0.001	<0.001
Sodium	0.284	1.30	0.590	0.376	0.768	0.301	0.690
Magnesium	0.036	6.74	0.043	0.041	0.034	0.026	0.035
Cerium	0.081	<0.001	<0.001	3.68	<0.001	0.687	<0.001
Sulfate	0.68	48.9	3.04	5.07	6.43	1.85	3.15

Specimen area ~ 9.5 cm^2

*Specimens were tested for 100 hours in Test #5 (See Table 2)

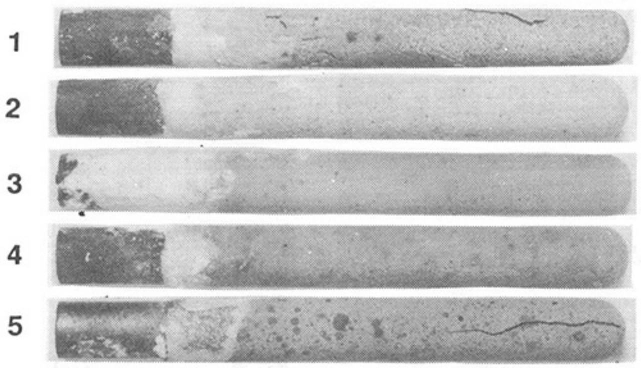

1 ⇒ PLASMA SPRAYED18% CSZ TEST#'s 5&6 ⇒ 200 hrs
2 ⇒ PLASMA SPRAYED 24% MSZ TEST#'s 5&6 ⇒ 200 hrs
3 ⇒ PVD 8% YSZ TEST#'s 5&6 ⇒ 200 hrs
4 ⇒ PLASMA SPRAYED 8% YSZ TEST#'s 5&6 ⇒ 200 hrs
5 ⇒ PLASMA SPRAYED CeO_2 TEST # 6 ⇒ 100 hrs

Fig. 2 Macrophotographs of ceramic coated specimens, burner rig corrosion tested up to 200 h at 1300°F (see Table 2 for details)

undergoes an additional reaction to form yttrium sulfate solute at 1300°F (SO_3 partial pressure 0.0043 atmosphere). Crystals containing yttrium and sulfur were observed on the surface of plasma-sprayed YSZ specimens tested at 1300°F (Fig. 3). The YVO_4 had a needlelike crystalline appearance (Fig. 4), whereas blocky crystals contained both yttrium vanadate and sulfate (Fig. 3); isolated crystals of yttrium sulfate were not observed. The quantities of water-soluble yttrium and sulfate (Table 5) indicate that the yttrium sulfate formed contains an excess of sulfate, probably as $Y_2(SO_4)_3$. The 5-mil-thick PVD YSZ coatings performed significantly better than 2.5 mil thick PVD YSZ coatings (Table 4).

Examination of the specimens in cross section showed no bond coat corrosion. In Na_2SO_4 + 20 w/o $NaVo_3$ sprayed deposit furnace corrosion tests at 1650°F, where an SO_3 partial pressure of 0.0005 atmosphere was maintained, there was no evidence of yttrium sulfate formation (Nagaraj and Wortman, 1988).

The observed yttrium vanadate (YVO_4) and yttrium sulfate can be explained by the following reactions:

The formation of YVO_4 would invariably cause local depletion of yttrium and destabilization of zirconia; however, this did not result in the spallation of the ceramic for the limited durations of the current tests. If the test durations were longer, or if the tests had involved more thermal cycles, the ceramic might have spalled. Clearly, "some" destabilization of zirconia would not result in immediate spallation.

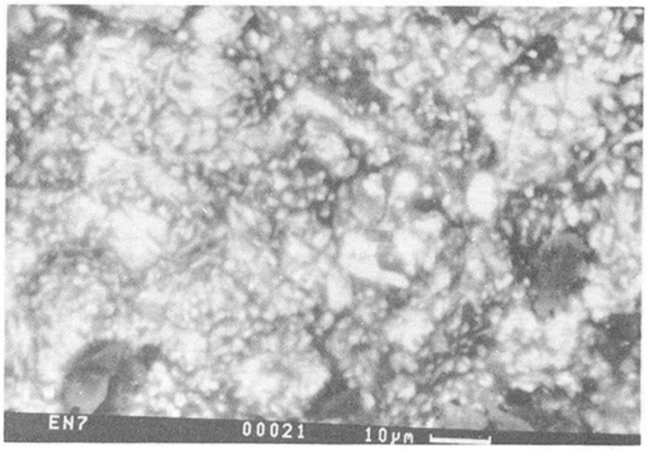

Fig. 3 Surface of plasma-sprayed YSZ, burner rig corrosion tested for 200 h at 1300°F (see Table 2 for details); white crystals contain yttrium vanadate and yttrium sulfate

CSZ and Ceria. Plasma-sprayed and PVD CSZ coatings both performed well, with no spallation after 400 hours in 1650°F tests. The surface was covered with crystals of cerium vanadate (dark brown) and "free" ceria (Fig. 5). The cerium vanadate was identified by x-ray diffraction to the body-centered-tetragonal phase of $CeVO_4$. In the 1300°F tests, the surfaces of

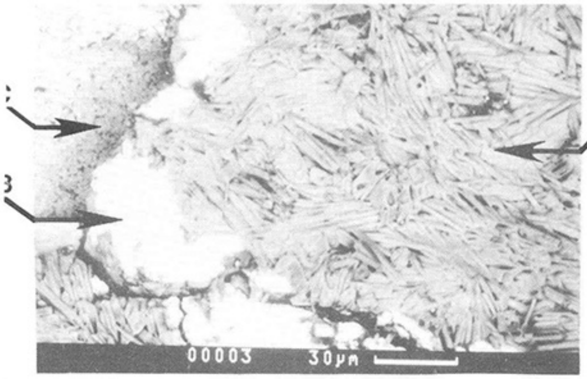

Fig. 4 (A) YVO_4 crystals; (B) remnants of HfO_2; (C) zirconia (fully depleted of Y); surface of PVD YSZ + sputt. HfO_2, burner rig corrosion tested for 100 h at 1650°F (see Table 2 for details); HfO_2 has spalled; YVO_4 has formed and spalled with the HfO_2 (except in local areas); surface is predominantly zirconia, which has not spalled with the YVO_4 and HfO_2

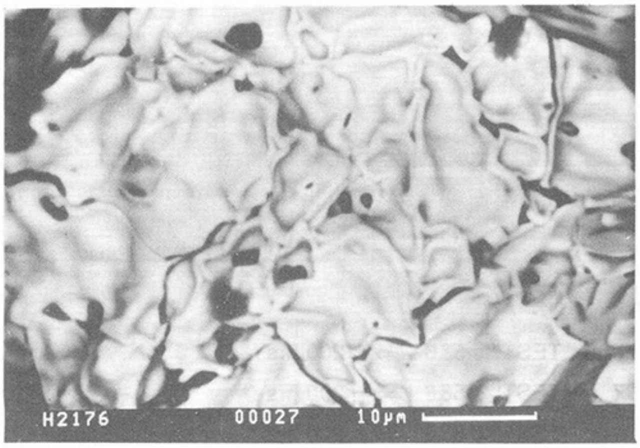

'free ceria'

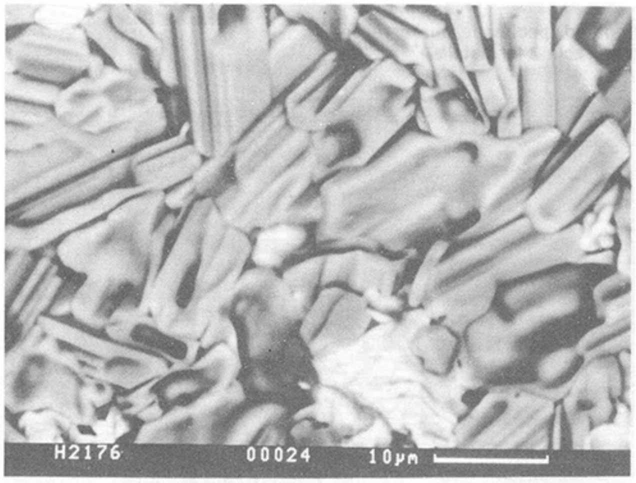

cerium vanadate

Fig. 5 Surface of plasma-sprayed CSZ, burner rig corrosion tested for 400 h at 1650°F (see Table 2 for details)

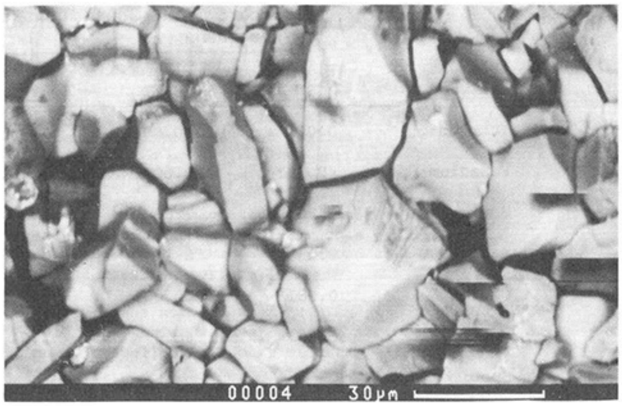

UNSPALLED SURFACE

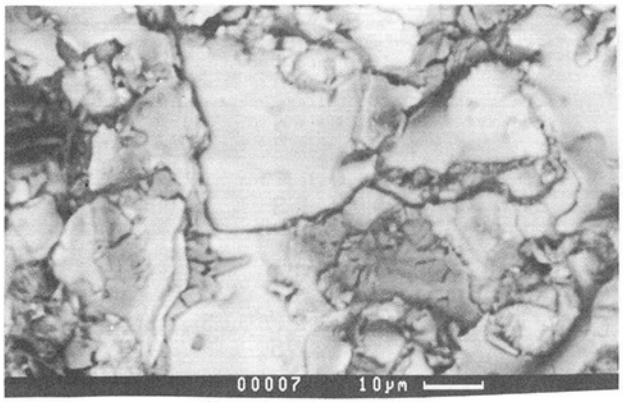

SPALLED SURFACE

Fig. 6 Surface of plasma-sprayed CSZ, burner rig corrosion tested for 200 h at 1300°F (see Table 2 for details); unspalled surface is covered with cerium sulfate crystals; spalled surface is zirconia (depleted in Ce) with remnants of cerium sulfate

Table 6 Thermal cycle* lives of YSZ coating

Powder Type	Coating Composition % Mono	Tetra	Cubic	Thermal Cycles to Failure
Spray dried	20	75	5	700
Spray dried	47	53	0	285
Spray dried	59	41	0	40
Sintered	22	75	<5	660

* 2075°F tests Ref. 18

plasma-sprayed CSZ, ceria, and PVD CSZ were covered predominantly with cerium sulfate (light brown) (Fig. 6), and minor amounts of $CeVo_4$ (dark brown). Bond coat corrosion was not observed in areas where the ceramic had not spalled, indicating that the cerium sulfate reaction product is "protective" (Fig. 7); however, in areas where the ceramic had spalled, bond coat corrosion was observed (Fig. 8). Jones et al. (1985) have determined the equilibrium SO_3 partial pressure for the sulfation of CeO_2 to be approximately 10^{-3} atmosphere at 1300°F and 2.3×10^{-3} atmosphere at 1380°F. Furthermore, lower SO_3 pressures are adequate to form cerium sulfate as a solute with reduced activity in the liquid deposit solution. The burner rig operating parameters are designed to produce an equilibrium SO_3 partial pressure of 4.3×10^{-3} atmosphere in the 1300°F tests and 1.65×10^{-3} atmosphere in the 1650°F tests. Thus the observed formation of cerium sulfate in the 1300°F tests was expected, even though the gas residence times in the burner rig are short and complete equilibrium would not be expected.

The cerium sulfate apparently caused the spallation of plasma-sprayed CSZ. Vanadium was not observed in water rinsings (Table 5), indicating that cerium vanadate is insoluble in water. Cerium and sulfate were detected in water rinsings (Table 5); $Ce_2(SO_4)_3$ is known to be water soluble.

Clearly, CSZ and ceria undergo additional reactions to form

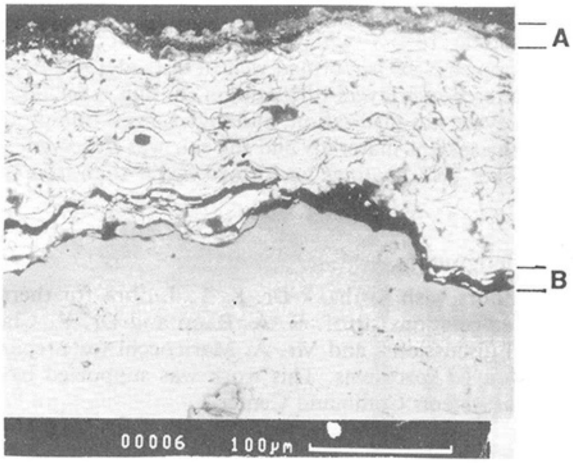

Fig. 7 Cross section of plasma-sprayed cerium oxide, burner rig tested for 100 h at 1300°F (see Table 2 for details): (A) outer layer of cerium sulfate; (B) negligible corrosion of bond coat

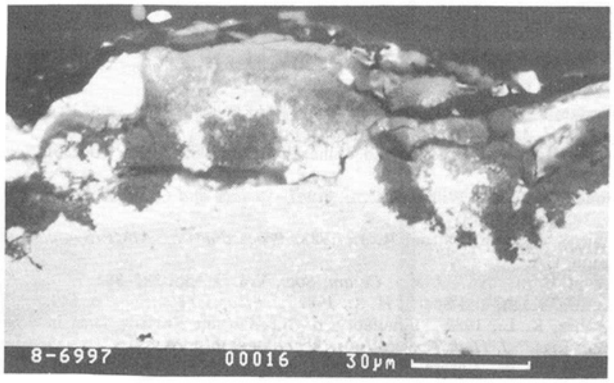

Fig. 8 Cross section of plasma-sprayed CSZ, tested for 200 h at 1300°F (see Table 2 for details); bond coat corrosion where ceramic has spalled

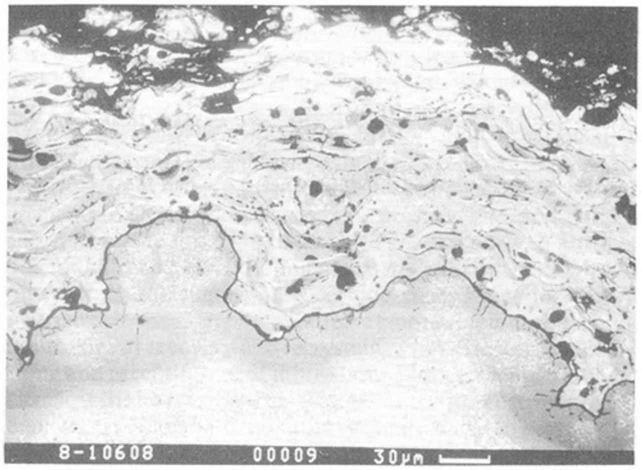

Fig. 9 Cross section of plasma-sprayed MSZ, burner rig corrosion tested for 200 h at 1300°F; bond coat not corroded; ceramic has undergone reaction

cerium sulfate at 1300°F (SO_3 partial pressure 0.0043 atmosphere). In Na_2SO_4 + 20 w/o $NaVO_3$ sprayed deposit furnace corrosion tests at 1650°F, where an SO_3 partial pressure of 0.0005 atmosphere was maintained, there was no evidence of cerium sulfate formation (Nagaraj and Wortman, 1988).

The observed cerium vanadate and cerium sulfate can be explained by the following reactions:

A number of cerium sulfates are known to exist, including $CeOSO_4$, $Ce_2(SO_4)_3$, and $Ce(SO_4)_2$. The amounts of cerium and sulfate in the rinsings of CSZ and CeO_2 specimens (Table 5) are such that the observed cerium sulfate is likely to be $CeOSO_4$.

Although both cerium vanadate and cerium sulfate were stable in the test environment at 1300°F, it is likely that the observed "free" ceria in the 1650°F test was precipitated by the dissociation of some of the cerium vanadate; some cerium vanadate was also observed in the 1650°F tests.

MSZ. Plasma-sprayed MSZ coatings did not spall in 100 hours of testing at 1300°F and 1650°F, although they underwent extensive reaction at both temperatures. The principal reaction product was magnesium sulfate. From all the ceramic coatings tested, MSZ was by far the most reactive, and relatively large amounts of magnesium and sulfate were detected in water rinsings (Table 5). It is surprising that the ceramic did not spall in spite of the magnesia depletion caused by the reactions. Bond coat corrosion was not observed (Fig. 9), suggesting that the reaction product (primarily magnesium sulfate) "protected" the bond coat from contact with the molten salt deposit.

Sputtered Sealant Layers. None of the three materials that were utilized as sputtered sealant layers, viz., platinum, hafnia, and alumina, reacted in the burner rig environment. The platinum and alumina layers were approximately 0.3 mil thick, whereas the hafnia layer was approximately 1.8 mil thick. However, none of them, not even the thick hafnia layers, proved to be impervious. Local regions of yttrium vanadate were found at the YSZ/sealant layer interface. The hafnia and the yttrium vanadate layers spalled, leaving behind the ceramic whose surface was depleted in yttrium (Fig. 4). It is encouraging that the remaining YSZ did not spall with the yttrium vanadate.

Mechanism of Ceramic Spallation

There are three possible principal mechanisms for explaining the molten salt induced spallation of ceramic coatings. These are:

1 **Bond Coat Corrosion.** Metallographic examination of post-test specimens has clearly shown that there is no bond coat corrosion in the cases of several specimens where the ceramic coatings have spalled (Wortman and Nagaraj, 1987) in test durations of up to 105 hours. On the other hand, when a PVD YSZ specimen was tested at 1650°F with a sodium chloride deposit, local bond coat corrosion accompanied by ceramic spallation was observed in only 2 hours of testing. These observations suggest that bond coat corrosion is a sufficient, but not necessary, cause for ceramic spallation.

2 **Melting and Freezing of Salts Within the Ceramic.** Since the burner rig tests described above did not involve a large number of thermal cycles, it is difficult to draw conclusions regarding the importance of melting and freezing of salts (within the ceramic) on the spallation of the ceramic coating. However, in addition to the corrosion tests described above, burner rig tests were carried out on plasma-sprayed and EB-PVD YSZ coatings at 1700°F in an atmosphere containing 5 ppm sea salt and no vanadium. Both the EB-PVD and plasma sprayed YSZ coatings performed very well, with lives in excess of 1000 hours (the specimens were cooled to room temperature every 24 hours). These results agree with the work of Tjong and Wu (1987) who found that plasma-sprayed YSZ coatings resisted spallation in molten sodium sulfate immersion tests. Clarke and Dapkunas (1974) have reported that, in crucible tests, there was no massive attack of YSZ by molten sodium sulfate. Clearly, the YSZ coatings have shown good resistance to spallation induced by melting and freezing of Na_2SO_4.

3 **Reaction of Salts With Ceramic.** Yttria, ceria, and magnesia (the oxides that stabilize zirconia) react to form sulfates and vanadates of yttrium, cerium, and magnesium. Among

the three oxides, magnesia is by far the most reactive, reacting readily to form magnesium sulfate at both 1300°F and 1650°F, at relatively low SO_3 partial pressures. It also forms magnesium vanadate. Ceria and yttria, on the other hand, form sulfates only at relatively high SO_3 partial pressures. Localized regions of unstabilized zirconia did not cause immediate spallation of the ceramic; extensive reaction would result in the destabilization of the *bulk* of zirconia and lead to spallation during thermal cycling. It has been reported (Rigney et al., 1987) that YSZ coatings with moderate (up to 47 percent) amounts of monoclinic phase perform well in thermal cycle tests at 2075°F, whereas those with excessive amounts of monoclinic phase had short lives.

In addition to the destabilization effect (which has been observed by several investigators), the observations in the current work suggest two other important effects associated with the reaction of the salts with the ceramic. These are:

(*a*) "Protection" of the bond coat by the solid reaction product at the ceramic/salt interface. The solid reaction product can be sulfate and vanadate of Ce, Y, or Mg. Although this protection might not be permanent, it was beneficial for the duration of the current tests (400 hours at 1650°F and 200 hours at 1300°F).

(*b*) Dissociation of cerium vanadates, and possibly sulfates and precipitation of "free" ceria. "Free" ceria has been observed on the surface of CSZ in 1650°F tests (Fig. 8). "Free" ceria has also been observed in the cross section of PVD and plasma-sprayed CSZ in Na_2SO_4 + 20 w/o $NaVO_3$ sprayed deposit furnace corrosion tests at 1650°F (Nagaraj and Wortman, 1988).

Conclusions

1 YSZ, CSZ, and MSZ coatings all underwent reaction in burner rig tests with vanadium-contaminated fuel. The reaction products and their effects on spallation were varied. YSZ formed solid YVO_4 at both 1300°F and 1650°F; it also formed dissolved yttrium sulfate at 1300°F but less at 1650°F. CSZ formed solid $CeVO_4$ at both temperatures; the $CeVO_4$ and CSZ tended to decompose to free ceria at 1650°F. CSZ formed cerium sulfate solute at 1300°F but not at 1650°F. Among all the coatings tested, MSZ was the most reactive, readily forming $MgSO_4$ at both temperatures. The observed reaction products provided a measure of "protection" for the bond coat by preventing molten salt infiltration for the duration of the test.

2 PVD and plasma-sprayed YSZ and CSZ coatings performed moderately well in burner rig tests with vanadium-contaminated fuel. Plasma-sprayed CSZ and YSZ performed well in tests at 1650°F with no spallation after 400 hours. Plasma-sprayed YSZ performed well in tests at 1300°F.

3 Sputtered overlayers of platinum, hafnia, and alumina did not prevent salt infiltration, although no reaction product between the sealant materials and the salt was observed.

4 Thicker YSZ coatings performed better than thin coatings.

Acknowledgments

The authors wish to thank Dr. K. L. Luthra for thermodynamic calculations, Prof. R. A. Rapp and Dr. R. Clarke for useful discussions, and Mr. A. Maricocchi for preparing plasma-sprayed specimens. This work was supported by the Naval Sea Systems Command Center.

References

Barkalow, R. H., and Pettit, F. S., 1979, *Proceedings of 1st Conf. Advanced Materials for Alternate-Fuel Capable Directly Fired Heat Engines*, CONF-790749, NTIS, Springfield, VA, p. 704.

Clarke, R. J., and Dapkunas, S. J., 1974, "Behaviour of Stabilized Zirconia in Molten Sodium Sulfate," Report No. 4406.

Doering, H. V., and Bergman, P., 1969, *Materials Research and Standards*, Vol. 9, No. 9, p. 135.

Hamilton, J. C., and Nagelberg, A. S., 1984, *J. Am. Ceram. Soc.*, Vol. 67, p. 686.

Hodge, P. E., Stecura, S., Gedwill, M. A., Zaplatynsky, I., and Levine, S. R., 1980, *J. Mater. for Energy Systems*, pp. 47-58.

Jones, R. L., Jones, S. R., and Williams, C. E., 1985, *J. Electrochem. Soc.*, pp. 1498-1501.

Jones, R. L., and Williams, C. E., 1987, *Surface and Coatings Technology*, Vol. 32, pp. 349-358.

Lau, S. K., and Bratton, R. J., 1983, *Proceedings of AIME Symposium*, Atlanta, GA.

Levin, E. M., 1967, *J. Am. Ceram. Soc.*, Vol. 50, pp. 381-382.

Luthra, K. L., and Spacil, H. S., 1982, *J. Electrochem. Soc.*, p. 649.

Luthra, K. L., 1989, "Simulation of Gas Turbine Environments in Small Burner Rigs," *J. High Temperature Technology*, in press.

McKee, D. W., Luthra, K. L., and Palko, J., 1978, *Proceedings of AIME Symposium*, St. Louis, MO, p. 82.

Nagaraj, B. A., and Wortman, D. J., 1988, paper presented at the International Conference on Metalurgical Coatings, San Diego, CA.

Nagelberg, A. S., 1985, *J. Electrochem. Soc.*, Vol. 132, p. 2502.

Rigney, D. V., Mantkowski, T. E., and Froning, M. J., 1987, paper presented at the DOE Workshop on Ceramic Coatings for Heat Engines, Castine, ME.

Siemers, P. A., and McKee, D. W., 1982, "Method of Coating a Superalloy Substrate, Coating Compositions, and Composites Therefrom," U.S. Patent No. 4,328,285.

Tjong, S. C., and Wu, C. S., 1987, *Surface and Coatings Technology*, Vol. 31, pp. 289-295.

Wortman, D. J., and Nagaraj, B. A., 1987, paper presented at the DOE Workshop on Ceramic Coatings for Heat Engines, Castine, ME.

Metallurgical Characterization of a High-Pressure Rotor for Remaining Service Life Assessment After 26 Years of Service

N. S. Cheruvu
Principal Engineer,
Westinghouse Electric Corporation,
Orlando, FL 32826

L. R. Malmfeldt
Plant Engineer,
Pacific Gas and Electric Co.
San Francisco, CA 94106

In-service material degradation of a high-pressure rotor steel has been investigated for remaining service life assessment. The samples for this study were taken from the cold and hot locations of a rotor that had operated for approximately 167,500 hours. The test results have indicated that the rotor steel is slightly softened and temper embrittled as a result of service exposure. Based on isostress creep rupture data of the rotor steel in the service-exposure. Based on isostress creep rupture data of the rotor steel in the service-exposed condition, it is concluded that crack initiation due to creep is not a concern in the near future. Considering the uncertainties associated with the extrapolation of short-time rupture data on remaining service life assessment, the rotor material should be re-evaluated for degradation of properties after the next 10 years of operation.

Introduction

High-pressure (HP) and intermediate-pressure (IP) steam-turbine rotors typically operate over a temperature range of 390 to 550°C (572 to 1022°F). Prolonged service exposure at these temperatures leads to deterioration of properties, due to aging (Cheruvu et al., 1985; Viswanathan and Jaffe, 1983; Qu and McMahon, 1983; Viswanathan and Brumer, 1985). The deterioration of properties is due to segregation of residual elements such as phosphorus, tin, arsenic, and antimony in the steel at the grain boundaries (Viswanathan and Brumer, 1985) and changes in the microstructure (Sellars, 1983). The microstructural changes are carbide coarsening, increase in interparticle spacing, precipitation of more stable carbides, and occurrence of recovery and recrystallization. The carbide coarsening and precipitation of more stable carbides deplete alloying elements in the matrix. The changes in the microstructure and depletion of alloying elements in the matrix lead to degradation of yield, tensile, and creep strengths. The extent of aging and subsequent deterioration in properties depends upon operating temperature, material composition, and original heat treatment of the rotor. Segregation of residual elements at the grain boundaries embrittles the rotor steel, leading to degradation of toughness and an increase in fracture appearance transition temperature (FATT) of the steel. This phenomenon is known as temper embrittlement. The temper embrittlement problem and consequent degradation of toughness affect the rotor life, reliability, availability, and efficiency of the steam turbine (Viswanathan and Jaffee, 1983).

The degradation in material properties of service-exposed rotors coupled with scatter in the material property data is one of the major sources of uncertainty in the remaining life assessment. Therefore, the properties of the rotor in its service-exposed condition must be determined for improved life assessment.

As part of total plant life extension study at Pacific Gas and Electric, Pittsburg Unit 5, material samples were removed from the HP rotor for metallurgical characterization. The purpose of this study is to determine the current material properties of the HP rotor and to evaluate the extent of in-service property degradation based on the original material properties for remaining service life assessment.

Metallurgical Background of the Rotor Forging

The HP rotor was fabricated from a CrMoV steel forging. The steel for the ingot was melted in a basic electric arc furnace in late 1957. At that time ladle metallurgy was primarily limited to composition adjustment of the steel. Ladle refining techniques for controlling the residual elements such as phosphorus, sulfur, tin, etc., were not available (Steiner et al., 1983; Swaminathan et al., 1982). The steel was poured into the ingot mold in air. Subsequent oxidation of steel during pouring and ingot solidification results in oxide inclusions in the ingot. These inclusions are detrimental for the toughness. The vacuum stream degassing process was known in those days but not applied to rotor forgings until the early 1960s. Thus, the

---

Contributed by the Power Division and based on a paper presented at the Joint Power Generation Conference, Miami, Florida, October 4-8, 1987. Paper No. 87-JPGC-Pwr-53. Manuscript received by the Power Division August 1, 1988; revision received October 16, 1989.

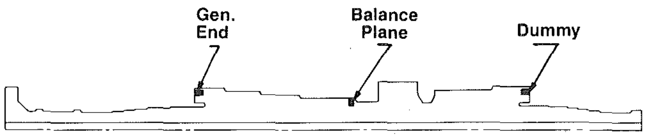

Fig. 1 Schematic of a HP rotor forging showing test sample locations

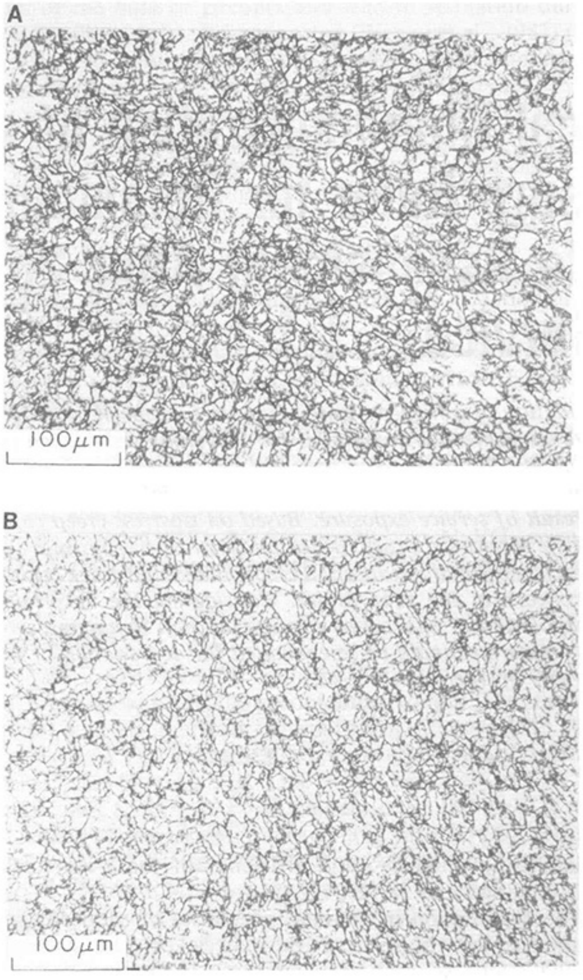

Fig. 2 Grain boundary etching behavior of (A) as-received and (B) de-embrittled samples from the dummy

steel melting practice used for the subject rotor forging was the state-of-the-art process in the late 1950s. The forging was austenitized at 954°C (1750°F) for 26 hours, air cooled, and then tempered at 666°C (1230°F) for 32 hours and air cooled.

Material and Test Conditions

Material samples for this study were drilled from the HP dummy, the generator end balance holes, and the impulse chamber zone (center balance plane) of the rotor (Fig. 1). The long axis of the samples was oriented approximately parallel to the axis of the rotor at the HP dummy and the generator end balance hole locations. The samples at the center balance plane location were oriented in the radial direction. The operating metal temperatures at the HP dummy, generator end balance hole, and center balance plane locations were 438°C (820°F), 354°C (670°F), and 493°C (920°F), respectively. Hereafter the generator end balance hole and center balance plane locations are referred to as the cold and hot locations, respectively.

Charpy V notch specimens were machined from the samples obtained from the dummy and the cold locations to determine in-service temper embrittlement. Half of the Charpy specimens from each location were given a de-embrittling treatment comprising of heating the specimens for one hour to 638°C (1180°F) and air cooling from this temperature. Impact transition temperatures were determined in the as-received and de-embrittled conditions, using the Charpy specimens.

Table 1 Chemical composition of rotor, wt. percent

Element	Hp Dummy	Cold End	Test Report	ASTM-A470* Class 8
Carbon	0.31	0.32	0.34	0.25–0.35
Manganese	0.89	0.90	0.90	1.00 Max
Phosphorus	0.011	0.013	0.012	0.015 Max
Sulfur	0.008	0.009	0.010	0.018 Max
Silicon	0.33	0.33	0.31	0.15–0.35
Nickel	0.08	0.09	0.10	0.75 Max
Chromium	1.08	1.09	1.07	0.90–1.50
Molybdenum	1.20	1.25	1.22	1.00–1.50
Vanadium	0.24	0.24	0.24	0.20–0.30
Tin	0.009	0.01	–	–

*Current ASTM A470-82 specification for rotor forgings.

Although CrMoV rotors operate over the entire critical range of temperatures for temper embrittlement, severe temper embrittlement in the rotors normally occurs in service around 427°C (800°F) (Cheruvu et al., 1985; Qu and McMahon, 1983). Therefore, Charpy specimens were not removed from the hot location of the rotor.

Tensile and creep rupture specimens were machined from the samples taken from the hot location since maximum softening in service due to thermal aging generally occurs at the hottest location of the rotor. Tensile tests were conducted only at room temperature. Smooth-notch bar creep rupture specimens were used for both isothermal and isostress rupture tests. This combination specimen facilitates evaluating the notch sensitivity of the rotor steel. All creep rupture tests were conducted in air over a range of temperatures and stresses.

Results and Discussion

Rotor Chemistry. The samples from the cold location and the HP dummy were analyzed for chemistry. The results are presented in Table 1 along with the supplier test report results and current ASTM specification requirements for turbine rotor forgings for comparison.

The present chemical analysis results are in good agreement with the supplier test results. The chemistries of the samples taken from both locations are almost identical, suggesting that the rotor has uniform composition along the axis. During the early 1960s, ASTM material specification for rotor forgings allowed phosphorus and sulfur levels as high as 0.02 percent (each element). The phosphorus promotes susceptibility to temper embrittlement in-service. Sulfur is present in the steel as manganese sulfide inclusions, which are detrimental to toughness. Hence, the maximum levels of phosphorus and sulfur were reduced to 0.015 percent in the current ASTM specification. Although the rotor was forged in the late 1950s, the phosphorus and sulfur levels in the rotor are within present ASTM specification requirements. However, both phosphorus and sulfur levels of the rotor were higher than the values typically achieved in the current forgings (Swaminathan et al., 1982).

Metallography. Microsections for metallography were cut from the samples obtained from the dummy and the cold and hot locations of the rotor. These sections were mechanically polished and etched in 2 percent nital to reveal microstructure. Woodfine (1953) and Capus (1962) have shown that when temper embrittled steels were etched in aqueous picric acid, the prior austenite grain boundaries etched preferentially to the interior of the grain. Nonembrittled steels are free from such preferential attack. Therefore, microsections were also

Table 2 Comparison of Room Temperature Tensile Properties of Pittsburgh 5 Rotor with the Supplier Test Results

Property	Original (Supplier test results)	Hot Location (After service)
Tensile strength, MPa (ksi)	837.1 (121.5)	812.3 (117.9)
Yield strength, MPa (ksi)	675.2 (98.0)	646.3 (93.8)
Percent elongation	17.0	18.0
Percent reduction in area	48.9	47.8

Table 3 Impact properties of rotor before and after service

	Before service	After service			
		Cold location		Dummy	
		As-Received	De-embrittled	As-Received	De-embrittled
Room temperature impact energy, Joules	11.2	10.5	7.7	9.8	9.8
(ft-lb)	(8.0)	(7.5)	(5.5)	(7.0)	(7.0)
FATT, °C	93	104	104	118	104
(°F)	(200)	(220)	(220)	(245)	(220)
Upper shelf energy, Joules	109.9	109.9	109.9	95.2*	108.5
(ft-lb)	(78.5)	(78.5)	(78.5)	(68*)	(77.5)

---

*Estimated value corresponds to 0 percent brittle fracture.

etched in 2 percent picric acid at 79°C (175°F) to determine the extent of grain boundary attack due to embrittlement.

Manganese sulfide inclusions were observed in all samples in the as-polished condition. No differences in inclusion content were noted among the samples. The inclusion content was normal for a rotor forging made in the late 50s and the amount of inclusions was not considered excessive. However, it should be noted that these samples were taken close to the periphery of the rotor. In heavy forgings such as rotors, more inclusions are present at the center than at the periphery of the forging. Hence, more inclusions are expected near the rotor bore. Samples were not taken from the rotor bore for evaluation.

All samples from the dummy and the cold and hot locations exhibited a bainitic microstructure. This microstructure is expected in air-cooled CrMoV rotor steels. The samples exhibited a very fine grain size and the average grain size is comparable to that of ASTM grain size #8 to 9. No discernible differences in the microstructure are observed between the samples from the cold and the hot locations under an optical microscope. However, differences in carbide size, type, and distribution existing between the cold and hot locations of the rotor can only be identified by transmission electron microscopy.

Grain boundary attack in picric acid etching in the as-received and de-embrittled samples from the HP dummy are shown in Fig. 2. No significant difference in the grain boundary etching behavior is observed between the samples.

Temper embrittlement of low alloy steel is due to segregation of impurity elements on the grain boundaries. Among the impurity elements in the rotor steels, phosphorus, silicon, tin, and arsenic are the most potential embrittling elements (Viswanathan and Brumer, 1983). Qu and McMahon (1983) have shown that the shift in FATT due to temper embrittlement was directly related to phosphorus segregation on the grain boundaries of CrMoV steels. Phosphorus segration in low alloy steels accelerates grain boundary attack when they are etched in picric acid solution. Depth of grain boundary penetration is related to the grain boundary phosphorus levels (Ogwa et al., 1980). The absence of preferential grain boundary attack in the as-received sample suggests that little or no phosphorus segregated to the grain boundaries in service.

Tensile Properties. Room temperature tensile properties of the rotor material after service are summarized in Table 2 along with the original properties for comparison. The yield and tensile strengths decreased approximately 4 and 3 percent, respectively, as a result of service exposure. This decrease in strength is attributed to thermal softening, since the samples were taken from a low-stress region of the rotor.

Thermal softening is due to microstructural changes, such as carbide coarsening, precipitation of more stable carbides, etc., that takes place in service at elevated temperatures. The extent of softening of a rotor in service depends on its original properties, operating temperature, and operating time. The original properties in turn are controlled by the chemistry and heat transfer of the rotor. The extent of softening increases with increasing operating temperature and time (Cheruvu et al., 1985; Qu and McMahon, 1983).

Rotors heat-treated to higher strength levels are more susceptible to softening than those heat-treated to lower strength levels (Argo and Seth, 1977). The rotors are tempered prior to service at a temperature significantly higher than their service exposure temperatures in order to delay the onset of softening. Thus, there is an incubation time for CrMoV rotors to soften in service. The observation of a 29.0 MPa (4.2 ksi) drop in the yield strength suggests that the operating time of the rotor has exceeded the incubation time for softening. Hence, the rotor is expected to degrade with operating time in the future. This observation is consistent with recent findings (Fujii et al., 1982).

Impact Properties. As stated earlier, the Charpy specimens were taken from the cold and the dummy locations of the rotor, and the service temperature at these locations was 354°C (670°F) and 438°C (820°F), respectively. The Charpy specimens were tested in the as-received and de-embrittled conditions.

Impact properties of the rotor steel before and after service are shown in Table 3. Figure 3 shows the variation of impact energy and percent brittle failure with the test temperature for the samples taken from the cold and the dummy locations, respectively. The lower shelf (room temperature) impact energy values after service in the as-received and de-embrittled conditions are comparable to the original values measured prior to service. Therefore, service exposure did not affect room temperature energy. However, upper shelf energy after service in the as-received condition was lower than the original value. This decrease in upper shelf energy can be attributed to temper embrittlement. The loss in upper shelf energy as a result of service-induced temper embrittlement was recovered by the de-embrittling treatment at 638°C (1180°F). However, essentially no loss in upper shelf energy was observed in the samples obtained from the cold location of the rotor. The shift in FATT

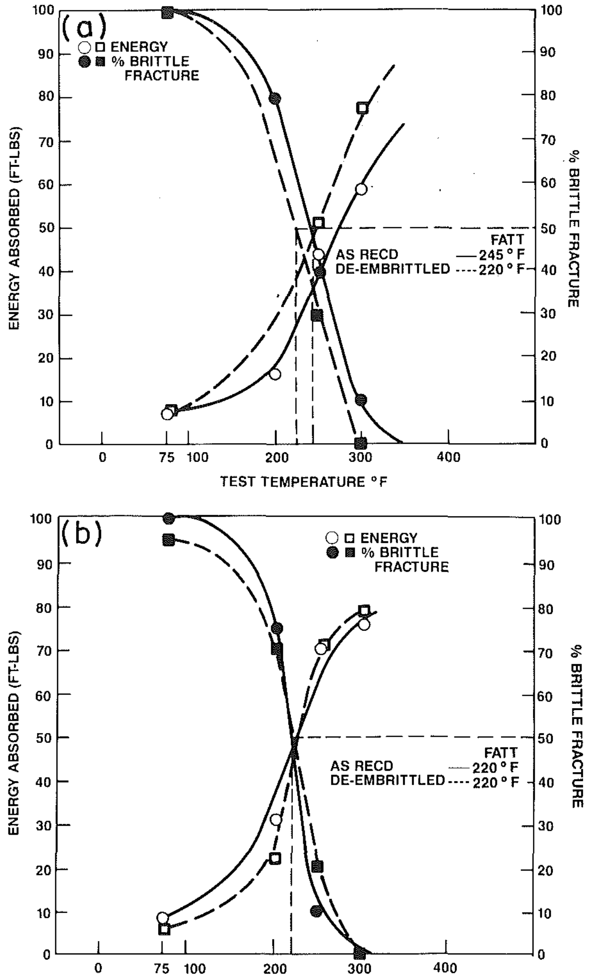

Fig. 3 Variation of impact energy and percent brittle fracture with the test temperature for the as-received and de-embrittled samples removed from the (A) dummy and (B) cold locations. Circles and squares denote as-received and de-embrittled conditions, respectively.

in as-received samples from the cold and dummy locations is 11 °C (20 °F) and 25 °C (45 °F) higher, respectively, than original FATT measured prior to service.

The shift in FATT is a measure of temper embrittlement susceptibility. Thus, the results indicate that the rotor has become slightly embrittled in service. However, the degree of temper embrittlement is not significant enough to cause any concern regarding the reliability of the rotor in the present condition.

The as-received and de-embrittled broken Charpy impact specimens from the dummy tested at room temperature were examined in the scanning electron microscope. In both cases the fracture surface exhibited cleavage mode fracture. Segregation of residual elements, particularly phosphorus, at the grain boundaries weakens the boundaries and thus results in intergranular failure in a rotor steel. The observation of cleavage failure suggests that the grain boundaries are not weakened due to phosphorus segregation in service. This observation is consistent with metallographic results.

Although the amount of intergranular failure is a measure of temper embrittlement susceptibility, occurrence of grain boundary failure not only depends on the grain boundary composition but also on the grain size (Capus, 1962) hardness (Viswanathan and Joshi, 1975), and test temperature (Yu and McMahon, 1985).

For a given shift in the FATT the amount of intergranular failure increases with increasing grain size or hardness. Furthermore, experiments by Viswanathan and Joshi (1985) have shown that for a comparable shift in FATT and hardness, the martensitic structure results in larger amount of intergranular fracture than the bainitic structure. In CrMo and CrMoV steels, significant temper embrittlement may result in only small amounts of intergranular failure (Yu and McMahon, 1985). A small shift in FATT, fine grain size, and bainitic microstructure are responsible for not observing any intergranular fracture in the as-received condition.

In addition to residual elements in the steel, the other major variables that affect temper embrittlement susceptibility of CrMoV rotors in service are grain size, service temperature, and operating time. Argo and Seth (1977) have investigated temper embrittlement behavior of two CrMoV rotors after 15 years of operation. These rotors were forged from the same ingot and had identical chemistry. One rotor was austenitized at a higher temperature than the other. High-temperature austenitization treatment leads to coarse grain size. Their results have shown that the coarse grain rotor was more temper-embrittled in service than the fine grain rotor.

The effect of service temperature on FATT of CrMoV rotors was investigated by Cheruvu (1985), Qu et al. (1983), and Fujii et al. (1982). These investigations have revealed that in both coarse and fine-grain rotors the maximum embrittlement occurred at a service temperature of approximately 427 °C (800 °F). Based on the results of these investigations, it can be assumed that the observed shift in FATT in the samples obtained from the dummy represents maximum degradation due to temper embrittlement in-service.

There have been no systematic studies of the effects of service time on temper embrittlement kinetics of CrMoV steels. However, the temper embrittlement kinetics for NiCrMoV steel at 399 °C (750 °F) indicated three distinct regions: incubation region, an intermediate region where the embrittlement rate increased rapidly, and finally a region where the embrittlement rate has decreased (Viswanathan and Brummer, 1985). Assuming that the temper embrittlement kinetics for CrMoV steel also exhibits these three regions, the subject rotor will continue to temper embrittle in service with time. It is not possible to predict future embrittlement rate without knowing the embrittlement kinetics of CrMoV steel.

Temper embrittlement in service also deteriorates the material toughness. The toughness is an important material property that controls critical crack size. The critical crack size, for a given operating stress, is directly related to the square of the toughness. Any degradation of toughness due to temper embrittlement thus decreases the rotor life, and increases risk of brittle failure during a cold start. Therefore, it is necessary to determine the toughness of the rotor for remaining service life assessment. The fracture toughness can be estimated from Charpy energy (Logsdon and Begley, 1977; Rolfe and Novak, 1970). The relationship between toughness and the upper shelf Charpy energy absorption is given by the equation

$$\left(\frac{K_{Ic}}{\sigma_y}\right)^2=\frac{5}{\sigma_y}\left(\mathrm{CVN}-\frac{\sigma_y}{20}\right)$$

where

K_{Ic} = plane strain fracture toughness
σ_y = yield strength
CVN = uppershelf energy

This equation was originally developed by Rolfe and Novak (1970) and was verified by Logsdon and Begley (1977) for a CrMoV steel. Using this equation, the K_{Ic} of the rotor is estimated to be 184 MPa $\sqrt{\mathrm{m}}$. (168 ksi $\sqrt{\mathrm{in.}}$) at the upper shelf

Table 4 Creep rupture data at operating temperature (isothermal) of 975°F (524°C)

Specimen No.	Stress, MPa (ksi)	Rupture time, h	Elongating, percent	RA, percent	Minimum strain rate in./in./hr
4-1-5	276.0 (40.0)	1840	25.8	69.5	2.55×10^{-5}
4-1-6	293.3 (42.5)	681	27.0	62.1	7.26×10^{-5}
4-1-7	310.5 (45.0)	274	22.0	68.6	1.66×10^{-4}
4-1-8	327.8 (47.5)	75	22.9	55.5	6.32×10^{-4}

Table 5 Creep rupture data at operating stress (isostress) of 12 ksi (82.8 MPa)

Specimen No.	Test Temperature, °C (°F)	Rupture time, h	Elongation, percent	RA, percent	Minimum strain rate, in./in./hr
4-1-1	649 (1200)	785	34.3	77.3	7.58×10^{-5}
4-1-2	635 (1175)	1683	33.8	80.4	2.74×10^{-5}
4-1-3	621 (1150)	3576	33.7	73.5	1.47×10^{-5}
4-1-4	607 (1125)	7511	29.1	79.3	5.02×10^{-6}

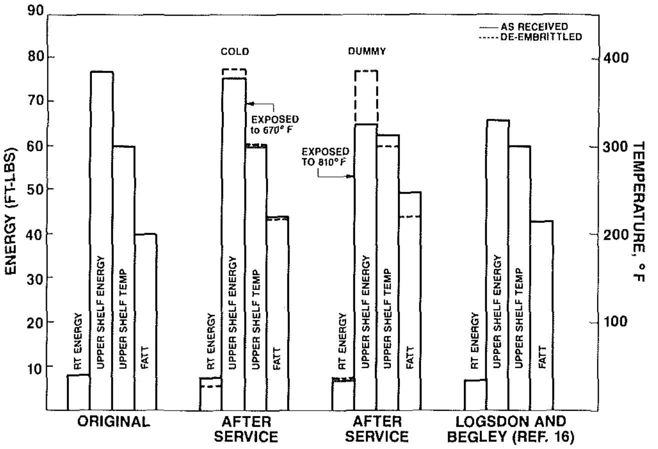

Fig. 4 Comparison of impact properties before and after service

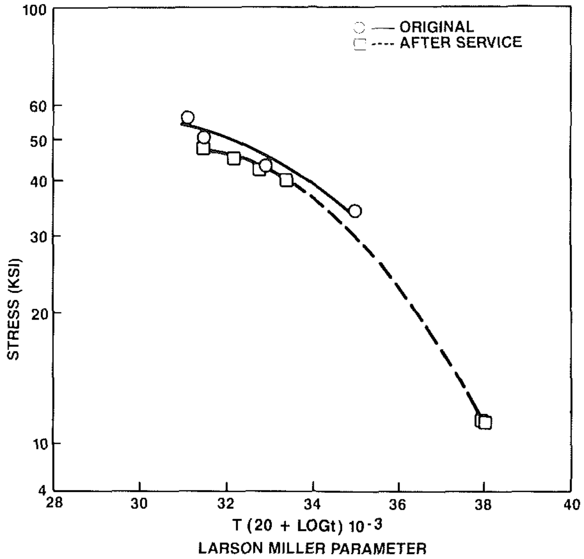

Fig. 6 Comparison of creep rupture strength before and after service

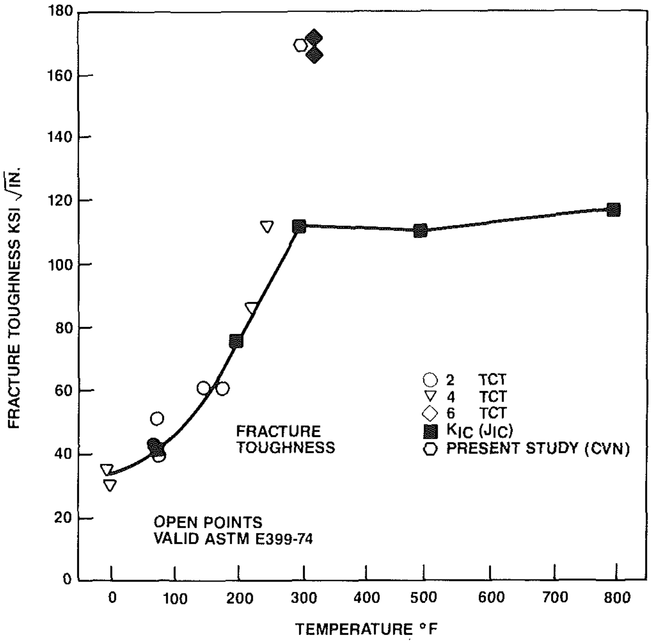

Fig. 5 Temperature dependency of fracture toughness of CrMoV steel

temperature of 156°C (312°F). From this equation it is not possible to estimate room temperature toughness. In order to estimate the room temperature toughness of the rotor, the impact results of this investigation are compared in Fig. 4 with those reported by Logsdon and Begley (1977). It can be seen from the figure that the Charpy energy values of the as-received samples taken from the dummy are in excellent agreement with their results. Hence, the toughness of the subject rotor can be assumed to be comparable to the values reported by Logsdon and Begley. They have shown variation in fracture toughness for a CrMoV rotor steel with temperature (Fig. 5). From Fig. 5, the room temperature toughness of the subject rotor is estimated to be 38.5 MPa $\sqrt{\mathrm{m}}$ (35 ksi $\sqrt{\mathrm{in.}}$).

Creep Rupture. Creep rupture tests on service-exposed material at stresses and temperatures similar to service conditions will give more accurate remaining life estimates. These tests, however, run for an extremely long time and, therefore, accelerated tests are needed for remaining life assessment. Creep tests can be accelerated by increasing the stress at the service temperature (isothermal) or raising the temperature at the service stress (isostress). In this study, accelerated rupture tests were conducted under both isothermal and isostress conditions on the samples obtained from the hot location. The creep rupture results under isothermal and isostress conditions are shown in Tables 4 and 5, respectively. All creep rupture specimens failed in the smooth bar section, indicating that the material was not notch sensitive.

Figure 6 shows the effect of service exposure on creep rupture strength. The service exposure lowered creep rupture strength slightly. The drop in creep strength is a result of thermal softening. These results are consistent with the drop in tensile and

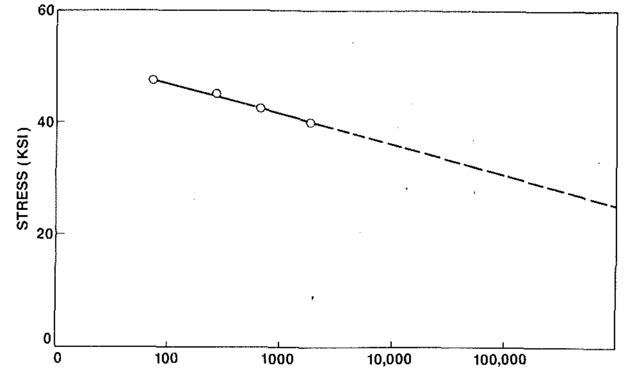

Fig. 7 Stress versus rupture time data at operating temperature (isostress) of 524°C (975°F)

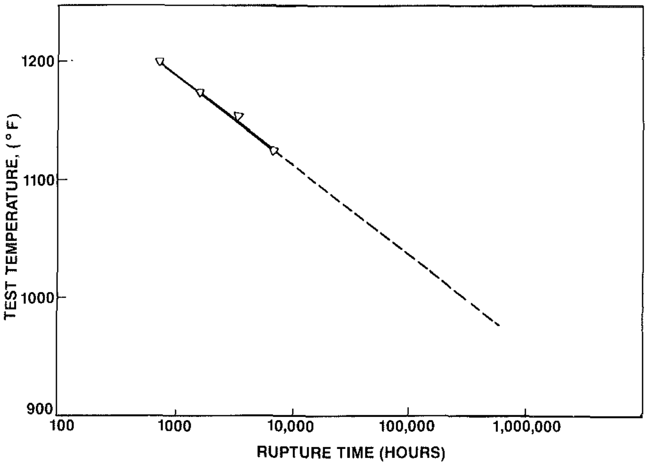

Fig. 8 Isostress rupture data at operating stress

yield strengths. Furthermore, a comparison of creep rate with the results of Saxena et al. (1984) has revealed that the service exposure slightly increased the creep rate. From the time-temperature (Larson-Miller) parameter that corresponds to the operating stress of 82.8 MPa (12 ksi), the crack initiation time is estimated as 269 years.

The results of increased stress (isothermal) tests at service temperature are shown in Fig. 7. Limited creep rupture data indicate a linear relationship between the stress and logarithum of rupture time. Extrapolation of the line through the data points to the service stress of 82.8 MPa (12 ksi) (maximum creep tangential stress near the bore[1]) gives a crack initiation time of 600 years. It is well known that any future microstructural changes that occur in service will change the slope of this line and reduce the life (Dieter, 1976). Hence, straight line extrapolation of the plot stress against rupture life appears to overestimate crack initiation life of the rotor.

The isostress creep rupture test results are shown in Fig. 8. The straight line extrapolation of the plot test temperature against rupture time gives crack initiation time of 68 years for the rotor. Material property degradation, particularly softening, during this period will reduce initiation time. Furthermore, in-service creep damage at critical locations of the rotor and creep fatigue interaction will also reduce initiation time.

Hart (1976) has investigated the validity of accelerated creep rupture tests for remaining service life evaluation by performing the tests on the samples taken from a service-exposed component under isothermal, isostress, and service conditions. His results indicated that the remaining life can be more accurately predicted from the isostress test results. Contrary to the results observed in this study, Hart (1976) reported that the isothermal test data underestimated residual life.

This discrepancy can be explained by considering two major differences existing between these investigations. First, the samples for this study are taken from a low-stress region of the rotor exposed to high temperature. In-service creep damage in this region is negligible. Therefore, effect of service-induced creep deformation on rupture life is not considered in this study. On the other hand the test material used by Hart was exposed to both elevated temperature and stress. Second, the microstructure of rotor steel may not be thermodynamically stable over the range of extrapolation.

Extrapolation of short-time test (stress versus rupture) data significantly overestimates residual life (Johnson and Glen, 1974) when the microstructure is not stable. It is, therefore, necessary to re-evaluate material degradation after 10 more years of operation. The microstructure of the material used by Hart was relatively more stable over the time period of measured life. Hart extrapolated 2000 hour isothermal creep rupture data to 10,000 hours life. In order for the life predictions to be reasonably accurate, long-time test data are needed for the materials that are susceptible to aging in service (Williams, 1977).

Conclusions

Material tests were conducted to evaluate in-service degradation on the samples taken from the high-pressure rotor, which had operated for 167,500 hours. The following conclusions can be drawn from the results of this study:

1 Although the rotor was fabricated in the late 1950s, its chemistry satisfied current ASTM specification (A470 Class 8) requirements for rotor forgings.

2 The yield and tensile strengths decreased 4 and 3 percent, respectively, as a result of service exposure. This decrease in strength was attributed to thermal softening.

3 The service exposure increased FATT due to temper embrittlement. The extent of temper embrittlement was not significant enough to cause any concern regarding the reliability of the rotor in the present condition.

4 The creep strength decreased slightly due to the thermal softening.

5 Accelerated creep rupture tests at the service temperature overestimated the remaining life.

6 A straight line extrapolation of isostress rupture data gave a crack initiation life of 68 years for the rotor. Material property degradation during this period of service leads to lower creep life.

7 The rotor steel will continue to soften and temper embrittle with operating time. Therefore, the rotor should be re-evaluated for material degradation after 10 more years of operation.

Acknowledgments

The authors wish to thank Dr. R. L. Novak for his support and encouragement during the course of this project; Mrs. L. Fredda for her efforts in preparing the graphics; and Mrs. J. Mackay for excellent work in formatting and printing this document on the word processor. This work was funded by Electric Power Research Institute under project No. RP2556-6.

References

Argo, H. C., and Seth, B. B., 1977, "Fracture Mechanics Analysis of Ultrasonic Indications in CrMoV Alloy Steel Turbine Rotors," in: *Case Studies in Fracture Mechanics*, T. P. Rich and D.J. Cartrigert, eds., Army Materials Research Center MS77-5.

Bruemmer, S. M., et al., 1985, "Grain Boundary Composition and Inter-

---

[1] The maximum creep tangential stress is relaxed stress or maximum steady-state stress under creep conditions. The long-term creep deformation of the rotor bore depends on the steady-state stress.

granular Fracture of Steels, Vol. 1: Detection of Grain Boundary Segregation in Steels," EPRI Report RP 3859, Project RP 2257-1.

Capus, J. M., 1962, "Austenite Grain Size and Temper Brittleness," *Journal of the Iron and Steel Institute*, Vol. 196, p. 922.

Cheruvu, N. S., Howard, W. E., and Beasley, O.W., 1985, "Life Analysis of Oklahoma Gas Electric Co., Mustang 3, HP-IP Rotor," ASME Paper No. 85-JPGC-Pwr-29.

Dieter, G. E., 1976, *Mechanical Metallurgy*, 2nd ed., McGraw-Hill, New York, p. 483.

Fujii, H., et al., 1982, "Changes in Material Properties and Life Management of Steam Turbine Components Under Long Term Service," *MHI Technical Review*, Vol. 19, p. 202.

Hart, R.V., 1976, "Assessment of Remaining Creep Life Using Accelerated Stress Rupture Tests," *Metals Technology*, Vol. 3, p. 1.

Johnson, R. F., and Glen, J., 1974, "Creep Strength in Steel and High Temperature Alloys," *J. Metals Society*, London, p. 37.

Logsdon, W. A., and Begley, J. A., 1977, "Uppershelf Temperature Dependence of Fracture Toughness for Four Low to Intermediate Strength Ferritic Steels," *Eng. Fract. Mechanics*, Vol. 9, p. 460.

Ogwa, T., Makino, A., and Matsumoto, T., 1980, *Scripta Metallurgica*, Vol. 14, p. 887.

Qu, Z., and McMahon, C. J., 1983, "The Effects of Tempering Reactions on Temper Embrittlement of Alloy Steels," *Metallurgical Transactions A*, Vol. 14A, p. 1101.

Rolfe, S. T., and Novak, S. R., 1970, "Slow Bend K1F Testing of Medium Strength High Toughness Steels," ASTM STP Vol. 463, p. 124.

Saxena, A., Shih, T. T. and Ernst, H. A. 1984, "Wide Range Creep Crack Growth Behavior of A470 Class 8 (CrMoV) Steel Fracture Mechanics," *15th Symposium*, R. J. Sanford, ed., ASTM STP Vol. 833, p. 516.

Sellars, C. M., 1983, "Creep Strength of Steels and High Temperature Alloys," *J. Metals Society*, London, p. 20.

Steiner, J. E., et al., 1983, "Advanced Steel Melting Processes for Rotor Forgings," EPRI Final Report RP 3336.

Swaminathan, V. P., Steiner, J. E., and Jaffee, R. I., 1982, "High Temperature Turbine Rotor Forgings by Advanced Steel Melting Technology," ASME Paper No. 82-JPGC-Pwr-24.

Viswanathan, R., and Joshi, A., 1975, "Effect of Microstructure on the Temper Embrittlement of CrMoV Steels," *Metallurgical Transactions A*, Vol. 6A, p. 2289.

Viswanathan, R., and Jaffee, R. I., 1983, ASME *Journal of Engineering Materials and Technology*, Vol. 105, p. 235.

Viswanathan, R., and Bruemmer, S. M., 1985, "In Service Degradation of Toughness of Steam Turbine Rotors," ASME *Journal of Engineering Materials and Technology*, Vol. 107, pp. 316.

Williams, R., 1977, "Effect of Microstructural Instability on the Creep and Fracture Behavior of Ferritic Steels," *Materials Science and Eng.*, Vol. 28, p. 289.

Woodfine, B. C., 1953, *Journal of the Iron Steel Institute*, Vol. 173, p. 240.

Yu, J., and McMahon, C. J., 1985, "Variation of the Fracture Mode in Temper Embrittled 2.25 Cr 1 Mo Steel," *Metallurgical Transactions A*, Vol. 16A, p. 1325.

Automated Welding of Turbine Blades

J. Liburdi

P. Lowden

C. Pilcher

Liburdi Engineering, Ltd.,
Hamilton, Ontario, Canada

The welding of superalloys has been regarded, generally, as an art requiring the highest degree of welder skill and discipline. These highly alloyed materials are prone to micro-cracking and, in some cases, even the best welders cannot achieve satisfactory results. Now, however, advances in automation technology have made it possible to program precisely the complex airfoil shapes and the welding parameters. Consequently, turbine blades can be welded in a repeatable manner, with a minimum of heat input, resulting in better metallurgical quality both in the base metal and the weld deposit. The application of this technology to the automated welding of high-pressure compressor turbine blade tips and the refurbishment of low-pressure turbine blade shrouds are presented in this paper.

Introduction

Before the introduction of automated welding, many difficulties were encountered in the welding of high-temperature materials used in turbine blades because these materials are primarily engineered for creep and oxidation resistance, rather than weldability. In fact, highly alloyed compositions of nickel, cobalt, chromium, aluminum, titanium, molybdenum, and tungsten are prone to cracking by a variety of complex mechanisms, and are generally labeled in the literature as "nonweldable" or, at best, "difficult to weld" (Hucke, 1985).

The industry, however, has learned to cope with these difficulties and has developed techniques to weld repair and hard face a wide variety of turbine blades. However, these procedures require a high degree of operator skill in order to maintain the tight arc and the low heat input required to weld these alloys. Consequently, the quality and degree of rework will vary considerably and productivity is relatively low.

In spite of these problems, the turbine industry, although technically sophisticated, has lagged behind in the development of automated welding processes. This is especially true considering the advances that have taken place in CNC machining, and their widespread use in aerospace industries. Weld automation, however, has been limited to relatively simple circumferential welds and seal buildup, probably as a result of shortcomings in earlier machines, which lacked the sophistication and accuracy to deal with airfoil shapes. These earlier attempts at welding automation did not have the required consistency, and results were disappointing.

However, advances in computerization, robotics, power supplies, and integration software have now made it possible to re-examine the automated welding of turbine blades. This paper will review examples of shroud and airfoil welds produced on a current state-of-the-art system. The discussions will include a metallurigical examination of weld quality, and an outline of the required programming and fixturing.

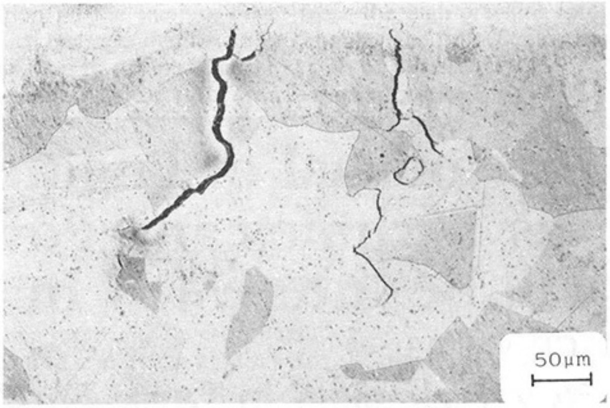

Fig. 1 Micrograph showing typical HAZ microcracking in a superalloy weldment (alloy: IN738LC)

Metallurgical Observations

Cracking Mechanisms. The weldability of the superalloys used in the manufacture of turbine blades is limited principally by their tendency to form cracks during, or after, welding. Two distinct types of cracking have been identified: heat affected zone (HAZ) cracking, which occurs in the solid base metal adjacent to the weld pool, and postweld heat treatment cracking, commonly referred to as strain age cracking, which occurs principally in the HAZ during heat treatment (Owczarski, 1977). Other generic weld defects, such as lack of fusion, oxide inclusions, weld zone cracking, poor bead shape, and porosity may also be present in superalloy weldments. However, unlike HAZ or strain age cracking, these defects are not specific to superalloys.

From a metallurgical point of view, HAZ cracking in superalloys results from phase transformations occurring along the grain boundaries adjacent to the melted zone. In this region, the material is exposed to a range of high temperatures approaching the liquidus of the alloy. These temperatures can have a profound effect on the carbides, borides, and elemental segregation found along the grain boundaries of superalloys. As a consequence, localized melting or liquefaction can occur

---

Contributed by the International Gas Turbine Institute and presented at the 34th International Gas Turbine and Aeroengine Congress and Exhibition, Toronto, Ontario, Canada, June 4–8, 1989. Manuscript received at ASME Headquarters February 21, 1989. Paper No. 89-GT-307.

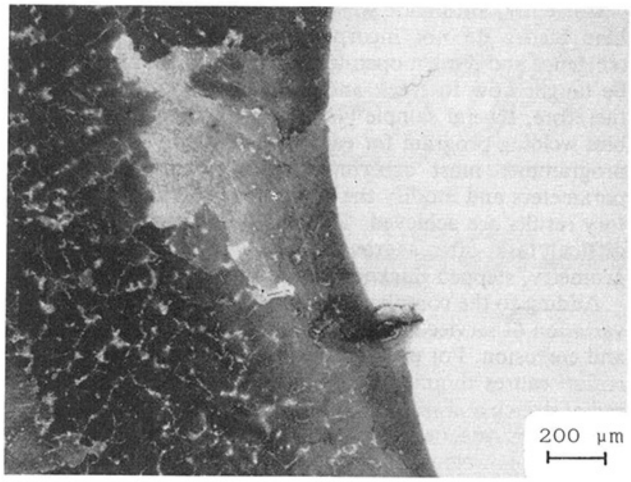

Fig. 2 Typical acceptable defects in a turbine blade (alloy: B1900)

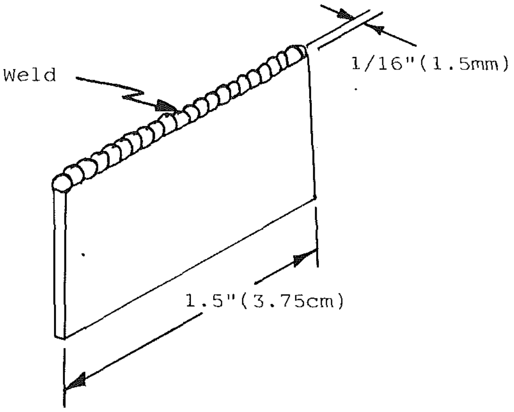

Fig. 3 Sketch showing the geometry of IN738LC samples used in welding trials; welds were prepared along top and bottom edges

Table 1 Crack density of manual and automatic GTA welds (cracks/in.)

	Before heat treatment		After heat treatment	
	Mean	95% C.I$^+$	Mean	95% C.I.
Automatic	0*	-	0.6	0.6
Manual	0.1	0.2	2.3	1.9

$^+$ Confidence interval.
* No detectable cracks.

in certain phases or areas of the grain boundaries, which have a lower melting point than the bulk alloy (Liburdi and Lowden, 1985). HAZ cracks can result in these locally melted regions by two mechanisms: Either thermal strains induced during welding act on the liquid layer at the grain boundaries and pull them apart; or, upon solidification, a brittle structure may form in the resolidified zone, which cracks on cooling as residual stress levels increase (Duvall and Owczarski, 1967). HAZ cracks can range in size from less than 0.005 in. (0.1 mm) to over 0.100 in. (2.5 mm) (Fig. 1).

In comparison, strain age cracking in superalloys is not as well understood (Thamburaj et al., 1983). This phenomenon occurs after the welding has been completed and the blades are given heat treatments designed to relieve stresses and develop mechanical properties in the base alloy. During the reheat treatment cycle, intergranular cracks ranging in size from 0.010 in. (0.3 mm) to several inches can form in the HAZ next to the weld. It is generally accepted that the cracking occurs as a result of residual stresses from the weld thermal cycle, and from stresses, related to the precipitation of the gamma prime strengthening phase, in the HAZ. In addition, intermediate temperature embrittlement along the grain boundaries may play a role in the mechanism.

A number of factors influence the susceptibility of a superalloy weld to HAZ and strain age cracking. Among the most important factors are the base metal chemistry and the weldment design. In general, higher strength alloys with high Al and Ti content and coarser-grained structures show increased cracking tendencies. Weldments made with a high degree of restraint, or on thicker sections, show a markedly increased susceptibility to cracking. Also, preweld heat treatment such as solutioning and overaging can be used to soften the alloy and reduce the sensitivity to cracking.

Although most factors are fixed in a given welding or hard facing situation, a variation in heat input has been shown to influence cracking significantly. Even if the literature indicates that there may be exceptions (Thamburaj et al., 1983), in general, low heat inputs have been found to be beneficial. Thus for a given set of conditions, there will be a specific level of heat input that minimizes or eliminates HAZ cracking.

It should be noted that some level of microscopic cracking is likely to be evident in higher strength blade alloys, regardless of the parameters chosen. However, provided that the defects are sufficiently small, and the welds are located in regions of low stress, the stress intensity at the crack tips will be too low for crack propagation to occur in service. Because of this, repair specifications for aeroturbine blades allow some level of microcracking (typically <0.030 in.) (0.8 mm) to be present in noncritically stressed locations. Figure 2 shows a typical defect in a repaired aeroturbine blade.

Further defects that can be formed during the welding of superalloys are common to other types of materials. Lack of fusion, oxide or tungsten inclusions, weld zone cracking, porosity, and poor weld profile are problems generally resulting from poor execution or repeatability, which can be eliminated by adequate control of the welding process.

The principal goals of automation should be the elimination of defects related to welding repeatability and improved control of the welding process. By accurately controlling the heat input, it also should be possible consistently to minimize the level of cracking and improve the quality of blade weld repairs.

Welding of IN738. In order to investigate the potential for an automated welding system to reduce cracking, a group of five specimens was prepared by manual Gas Tungsten Arc (GTA) welding system described below. The samples were prepared from IN738LC alloy to the geometry shown in Fig. 3 and were given a standard solution heat treatment prior to welding. A two-pass weld was deposited on opposite edges of each specimen. After welding, the samples were given the standard full heat treatment for IN738 alloy. Measurements of crack density (cracks/in.) were made by fluorescent penetrant inspection immediately after welding, and after the postweld heat treatment.

The results, shown in Table 1, indicate that automatic welding, when compared to manual welding, has not only considerably reduced the scatter, particularly after heat treatment, but has lowered the mean crack density as well.

The large reduction in scatter suggests that, as expected, much of the scatter is due to variability in the manual welding process, rather than in the material itself. The superior ability of the automatic system to maintain the arc length and current has likely resulted in more uniform heat input. This decrease in scatter has significant implications for a practical repair process. Since many specifications will limit both the size and

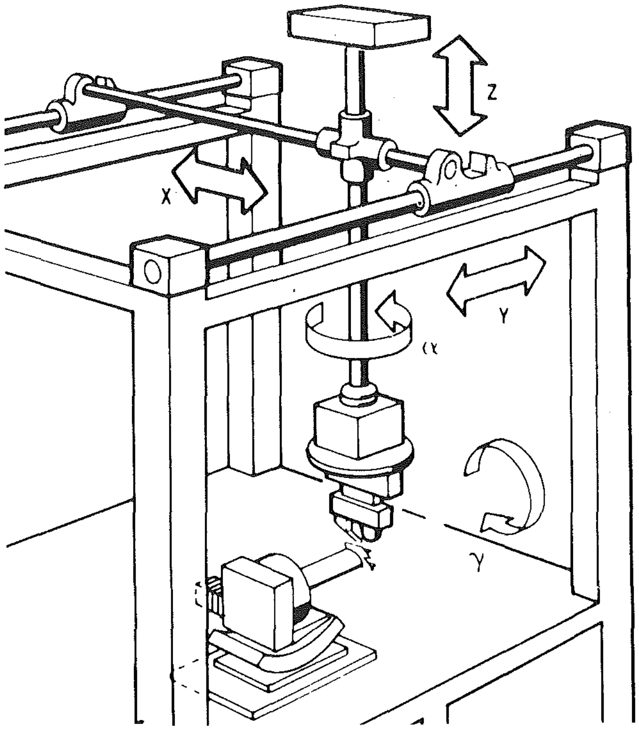

Fig. 4 Sketch showing the control axes utilized in the automatic blade welding system

frequency of cracking, it should be possible to obtain a higher production yield with automatic welds.

Influence of Power Sources. Although the apparatus used in this study employs a GTA or plasma arc torch as the source of heating for welding, and a cold wire feed for introducing filler metal, similar results can be obtained using other processes. For example, the use of lasers and electron beams as heating sources and the use of metal powder as filler material have been suggested as means of reducing crack sensitivity, and in some cases, have been shown to result in improvements over manual welding (Weerasinghe and Steen, 1987; Hughes and Berry, 1967). This benefit, however, is largely due to the use of lower heat inputs, which cannot be achieved by manual welding techniques. Given the metallurgical basis of the cracking phenomena discussed previously, there is no reason to believe that one source of heat or filler will result in different behavior for a given heat and mass input. The region adjacent to the weld pool will reach a similar temperature and the same metallurgical reactions will occur in all cases. Thus, one of the principal advantages of automating the gas tungsten arc and plasma welding processes is the ability to achieve consistent low heat inputs similar to those achieved by other heat sources.

Blade Welding Automation

Process Control. Control systems are generally classified as closed-loop or open-loop. In a closed-loop system, parameters are adjusted on the basis of feedback, while in an open-loop system, parameters are preprogrammed.

In manual welding, the human brain controls the ultimate closed-loop system. Skilled GTA welders can maintain a tight weld arc as they maneuver the welding torch across complex shapes, while simultaneously introducing filler wire into the weld pool and adjusting the current. Feedback and adjustments in the process are based on the welder's visual observation of both the weld pool and the position of the torch relative to the work piece.

Currently, automatic welding systems used in welding turbine blades do not incorporate feedback or adaptive intelligence and remain open-loop systems. Such machines must be taught how to track and weld each configuration, and, therefore, several sample blades are required to generate the best welding program for each turbine blade type. The robot programmer must experiment with a variety of welding parameters and modify the computer program until satisfactory results are achieved. This can be a time-consuming and difficult task, often aggravated by the complexity to the blade geometry, stepped thickness variations, and tight corners.

Adding to the complexity of blade geometry is dimensional variation of serviced turbine blades as a result of wear, creep, and corrosion. For example, in shrouded turbine blades, corrosion causes thinning of the shroud, while creep results in radial stretch and shroud lift. Thickness variations must be addressed by categorizing the blades into ranges for which a single set of welding parameters is acceptable. Radial stretch and shroud lift create a change in the position of the weld path the robot must follow. Properly designed fixturing can be used to eliminate the effects of blade stretch; however, shroud lift can only be overcome by changing the weld path to the new position. Without the aid of a feedback system capable of measuring the new weld path, each blade must be categorized by dimensional analysis into similar weld path groups, then welded using the appropriate program. Once an optimum welding program has been developed, the robot will give repeatable results.

A description of the equipment used, the programming techniques, and some examples are outlined in the following sections.

Equipment Features. The Computapath II welding system utilized in this development is configured around a high-precision gantry robot holding a welding torch and wire feed. The Dimetrics welding power supply allows control over all of the necessary welding parameters such as pulse frequency, wave shape, current, and voltage. Servomotors allow accurate control of the wire feed rate in both the primary and background part of the wave. The welding power supply controller communicates with the robot, which, in turn, controls the movement of the axes.

The welding system has five axes of control (Fig. 4): the three Cartesian coordinates (x, y, z), yaw for the torch head, and roll of the blade. Movement is provided by an overhead gantry system using d-c servomotors and optical encoders. The gantry system provides excellent accuracy in movement and the location of the welding sites; however, the blades must be fixtured properly to ensure repeatability. It is important that the fixtures be properly designed not only to permit accurate location of the blade, but also to allow the welding torch to have access to the weld face without hindering its travel.

Computer Programming. The Computapath II uses Adaptive Assembly Machine Programming Language (AAMPL), which has been developed solely for robot control. In order to attain enough flexibility to control both robot motion and the welding power supply, AAMPL structures the programming into site locations, welding parameter segments, and program movement.

Site location data dictate the point-to-point weld path the torch head will follow. Each site is assigned a name, such as W1, and consists of the three Cartesian coordinates (x, y, z), yaw, pitch, and roll. In order to teach the site locations, the torch head is moved to the appropriate location and the program is told this is site W1. The number of sites chosen influences the accuracy of the curve fitting for shape following, while their location can be used to demarcate welding parameter segments.

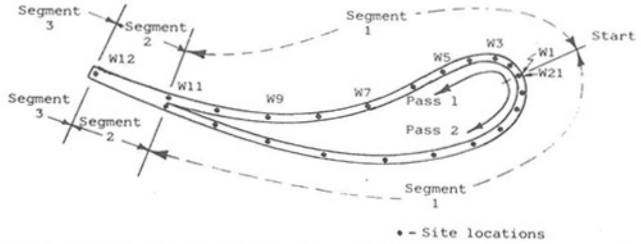

Fig. 5 Sketch showing the location of sites and welding segments used for squealer tip repair of a CF6-50 HP blade

• - Site locations

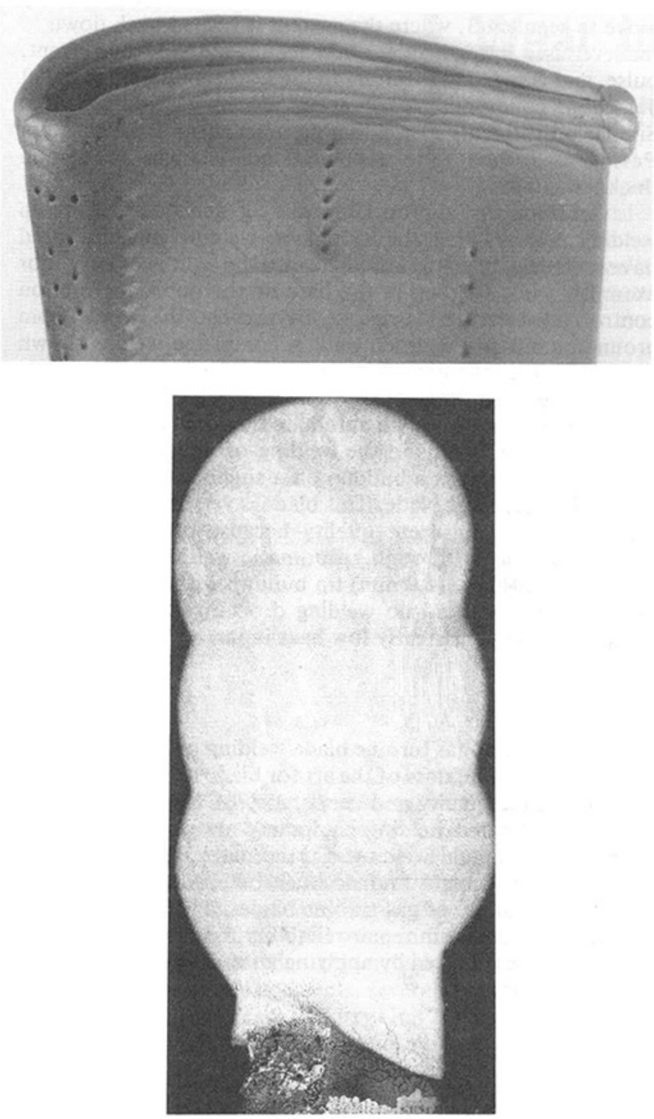

Fig. 6 Photograph and micrograph illustrating the quality of repair achieved on a CF6-50 HP blade and squealer tip

Welding parameter segments contain the welding power supply control parameters for a particular section of the weld path. The duration of a segment is controlled by either timing the segment or by specifying an end site. The parameters controlled are current slope rate (seconds), current (primary and background), voltage (primary and background), pulse frequency, wire speed (primary and background), and torch velocity (ipm).

The program movement section ties together the sites and welding parameter segments. It tells the torch to begin welding at a site, turns on the curve-fitting function, initiates pauses in the required areas, controls the changing of one weld

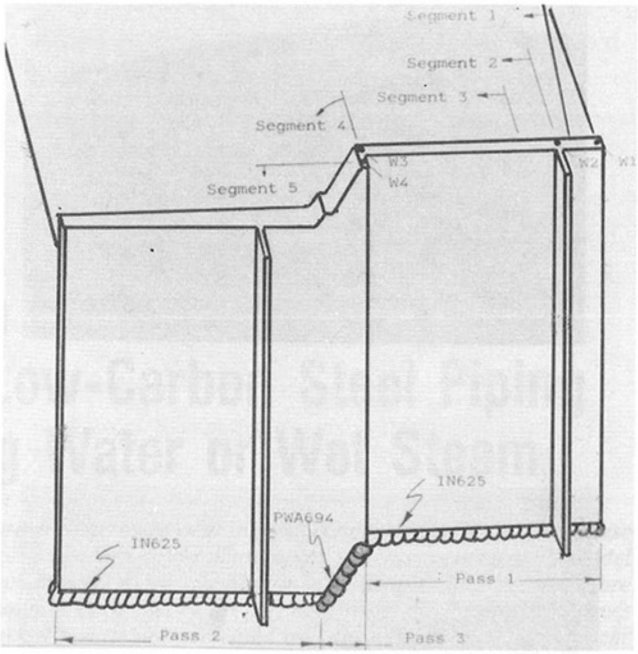

Fig. 7 Sketch showing the three passes required for hardfacing of JT8D LP blades and details or welding sites and segments for Pass 1

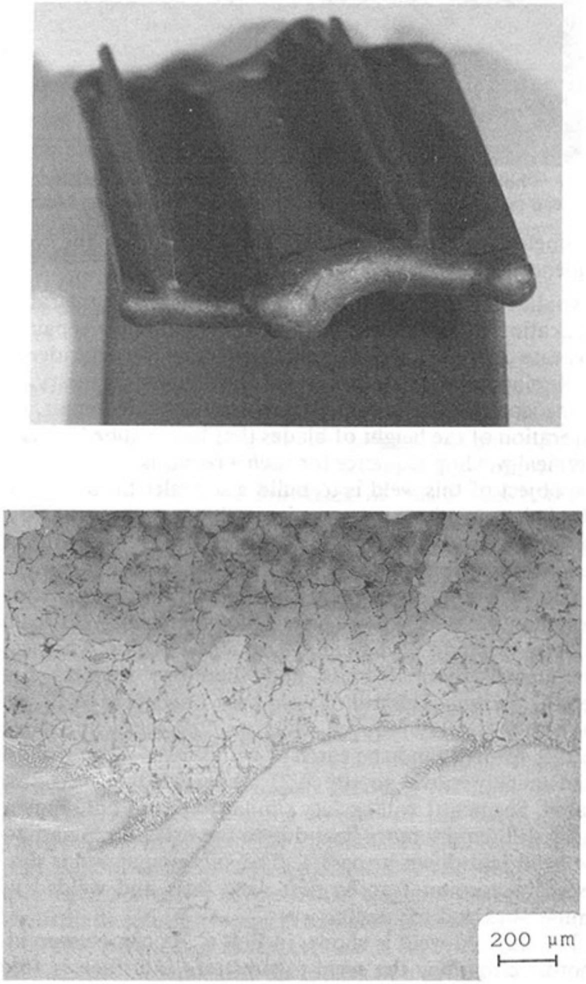

Fig. 8 Photograph and photomicrograph showing a completed shroud Z-notch weld on a JT8D LP turbine blade

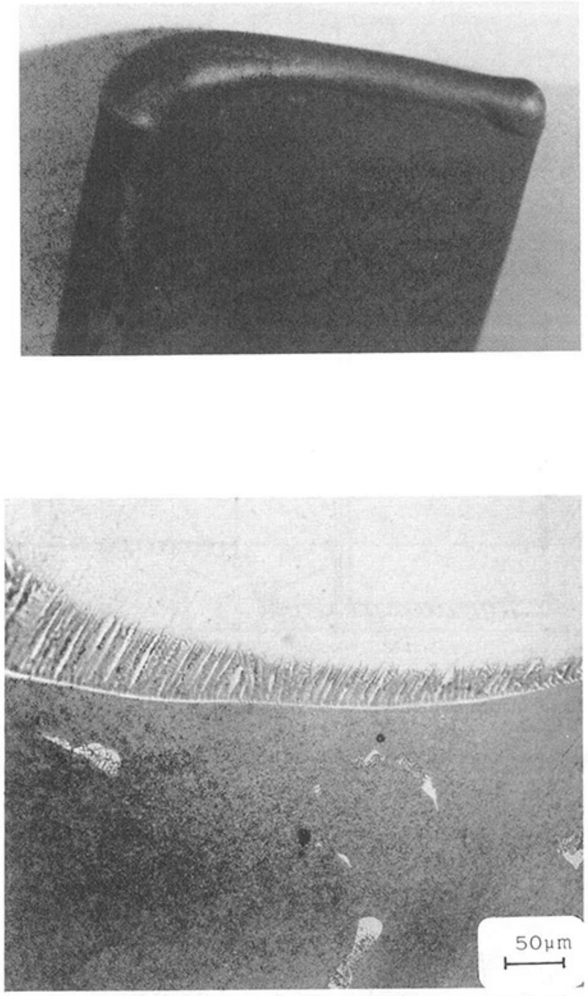

Fig. 9 Photograph and photomicrograph showing the quality of weld achieved on a single-crystal air-cooled JT9D HP first-stage blade

parameter segment to another, and shuts down the welding sequence.

Applications. The following examples demonstrate the application of automated welding to actual blade repairs and illustrate some of the factors that must be considered in developing appropriate programs for a given geometry.

One common requirement in turbine blade repair is the restoration of the height of blades that have rubbed in service. A typical welding sequence for such a repair is shown in Fig. 5. The object of this weld is to build a squealer tip on a CF6-50 HP blade using three passes, with each pass split into two subpasses. Pass number 1 starts at site W1 by using the weld parameters set by weld segment 1. Before welding is initiated at site W1, the curve-fitting (shape-following) function is turned on. Sites W1 to W11 are following using weld segment 1. Upon reaching W11 welding segment 2 begins. This section has greater thermal mass and therefore requires higher welding current. The end of weld pass 1 occurs at W12, where the heat is quickly reduced using welding segment 3, a small bead is formed, and the torch is withdrawn. Then, the torch head quickly moves to site W21 where welding pass 2 is initiated. Segment 1 will be very similar to pass 1 but segments 2 and 3 will require more heat due to the extra thermal mass of the bead laid down in pass 1. The subsequent welds are adjusted to account for the first weld pass and welded using similar sites and segments.

The finished weld is shown in Fig. 6. As can be seen in the photomicrograph, the weld-to-substrate interface is free of cracks and excellent interpass quality has been maintained. Total weld time in this case was approximately six minutes.

Another common repair requirement is to restore the correct shroud dimensions on shrouded blades that have worn in service. An example is the requirement for hardfacing the Z notch of JT8D LP blades. The welding of these must be divided into six different passes (three per side). Each side consists of two passes using Inconel 625 filler wire and one pass using PWA 694 for the hardfacing, as shown in Fig. 7. As in squealer tip welding, different weld segments are used to accommodate the stepped changes in shroud thickness. Pass 1 begins at site W1 using welding segment 1. The extra thermal mass of the air seal, located at site W2, necessitates the use of higher welding current. In order to minimize the number of sites, segment 2 is initiated using a timing sequence. When the preset duration of segment 2 is reached, it will automatically move to segment 3, where the current is turned back down to the level used in segment 1. On reaching site W3, the current, pulse, and wire feed are turned to the level set by weld segment 4. The end conditions are met at site W4 using weld segment 5. Similar adjustments to welding parameters must be made in Pass 2 and Pass 3 to accommodate changes in section thickness.

In addition to appropriate welding schedules, Z-notch welding requires that the automatic welding machine used have sufficient agility to articulate into the tight geometry. For example, when welding in the base of the notch the motion control must be very accurate to prevent the torch from grounding out on the notch wall. A completed weld is shown in Fig. 8, demonstrating the capability of existing equipment to meet these requirments.

A final instance in which automated welding has significant technical advantages is in the welding of extremely thin sections. Figure 9 shows a buildup on a single-crystal air-cooled JT9D HP first-stage blade. This blade is very difficult to weld manually with consistent quality because of the thin cap, which often melts through. Automatic welding was able to produce a 0.040-in. (1.0 mm) tip buildup with a minimum of substrate dilution and no welding drop through on the cap because of the consistently low heat input.

Conclusions

Automation of gas turbine blade welding provides a significant advance in the state of the art for blade repair. It has been shown that the quality and consistency of welds prepared by existing automated welding equipment are superior to those prepared by manual welding. Furthermore, the same equipment has the control and accuracy to produce equivalent results on a variety of gas turbine blades. Therefore, a meaningful improvement in repair reliability, quality, and productivity could be achieved by applying automated welding to gas turbine repairs.

References

Duvall, D. S., and Owczarski, W. A., 1967, "Further Heat-Affected Zone Studies in Heat Resistant Nickel Alloys," *Welding Research Supplement*, Sept.

Hucke, H. J., ed., 1985, *Aerospace Structural Metals Handbook*, Metals and Ceramics Information Centre, Columbus, OH, Vol. 4 and Vol. 5, pp. 4101-4218.

Hughes, W. P., and Berry, T. F., 1967, "A Study of the Strain-Age Cracking Characteristics in Rene 41—Phase I," *Welding Research Supplement*, Aug., pp. 361s-370s.

Liburdi, J., and Lowden, P., 1985, "Repair Technologies for Gas Turbine Components," *AGARD Conference Proceedings No. 398, Advanced Joining of Aerospace Metallic Materials*, Sept., pp. 22.1-22.12.

Owczarski, W. A., 1977, "Process and Metallurgical Factors in Joining Superalloys and Other High Service Temperature Materials," *AGARD Lecture Series No. 91, Advanced Manufacturing Techniques in Joining Aerospace Materials*, Sept., pp. 3.1-3.32.

Thamburaj, R., Wallace, W., and Goldak, J. A., 1985, "Post Weld Heat Treatment Cracking in Superalloys," *International Metals Review*, Vol. 28(1), pp. 1-22.

Weerasinghe, J. M., and Steen, W. M., 1987, "Laser Cladding With Blown Powder," *Metal Construction*, Oct., pp. 581-585.

R. G. Keck[1]

P. Griffith

Department of Mechanical Engineering,
Massachusetts Institute of Technology,
Cambridge, MA 02139

Prediction of Erosive-Corrosive Wear in Low-Carbon Steel Piping Conveying Water or Wet Steam

Techniques to predict erosive-corrosive wear in pipes conveying single and two-phase water in low-carbon steel secondary power plant piping systems are presented. Model equations for two mechanisms, oxide dissolution and droplet impingement, are introduced and the terms in each theory are defined in detail. Parametric curves showing dissolution model results are presented and the effects of localized wear enhancement due to flow geometries are discussed.

Introduction

Secondary piping systems of many nuclear and fossil power plants around the world have experienced high rates of material wear due to erosion-corrosion. The piping is generally composed of low-carbon steel and transports high-temperature water (feedwater piping) or steam (extraction piping) over lengths of roughly one hundred meters inside the plant. The pipes are between 0.25 and 1.0 m in diameter and the flow is highly turbulent. The system water chemistry is maintained at very low oxygen levels (below 20 ppb) and alkaline pH (between 7 and 10). In these systems the steel corrodes, forming magnetite (Fe_3O_4), an adherent iron oxide that protects the pipe from the corrosive environment. Through an interaction with the flowing fluid, the magnetite layer is damaged and subsequently removed, exposing bare metal to the corrosive environment. The metal then corrodes to form new oxide, which is then removed by the flow, and so on. This cycle of continual oxide growth and removal accelerates pipe wall thinning and decreases the mechanical integrity of the system. The consequences of this rapid material wear in power plants over the last 15 years have included minor leaks, unscheduled plant outages and piping replacements, several catastrophic in-service failures and, in the case of Surry Unit 2, personnel fatalities.

Efforts to understand the mechanisms causing the wear and to develop reasonable predictive methods are hindered by three important wear characteristics. First, the wear is greatest at changes in flow direction (such as bends, tees, and fittings), which correspond to the most complex hydrodynamic conditions. Since the bulk flow is usually highly turbulent, these complex local flow conditions are not easily modeled. Second, the wear often occurs in small (20–40 mm diameter), seemingly random, nonuniform patches that are immediately adjacent to protected regions with the original pipe wall thickness. These small length scales make both wear measurement and prediction extremely difficult, and subject to large error. The third characteristic is the temperature dependence, shown in Fig. 1, in which the wear increases with temperature up to 150°C, at which point it reaches a maximum value and declines rapidly. Analytic models must identify and quantify the effects that cause this nonmonotonic temperature dependence.

Observations (Vu, 1982; Keck, 1987) show there are two dominant erosive mechanisms in these systems: (1) oxide dissolution enhanced by convective mass transport, and (2) entrained droplet impingement. Dissolution is known to occur on the inner radii of bends (Vu, 1982; Sanchez, 1988) and can occur in both single and two-phase lines. Droplet impingement, only possible in two-phase lines, occurs on the outer radii of bends (Vu, 1982; Keck, 1987). Neither cavitation nor solid particle damage were observed in the two-phase lines inspected by Keck (1987).

Keller (1974) first identified the temperature dependence shown in Fig. 1 and presented an empirical model for impingement wear. The model included the characteristic temperature curve and the effect of pipe geometry as multiplicative factors to a base wear estimate that was a function of flow velocity and quality. One drawback of this model is that it does not contain any material or system chemistry properties. Berge (1982) and Bignold (1982) developed analytic models for the dissolution wear, but use of these models is limited by the absence of values for the dissolution reaction rate constant assumed to be the limiting kinetic process. More advanced empirical methods were presented at an EPRI conference (EPRI, 1987).

Sanchez (1984) postulated that, in two-phase lines, both dissolution and impact erosive mechanisms were present, and developed analytical models to predict the wear in these systems. The Sanchez droplet impact model is valid only in two-phase flows and describes the fatigue of the oxide due to repeated droplet impingement. The Sanchez dissolution model is valid in both single and two-phase flows and describes the flow-assisted corrosion of the oxide. Sanchez experimentally verified this dissolution model in a single-phase flow apparatus. Keck (1987) performed an experimental study of the droplet impact model, incorporated the effects of alloying and oxygen concentration into the two models, and examined the relative benefits of various strategies to mitigate high wear conditions.

---

[1] Present address: Arco Oil and Gas Co., Plano, TX 75075.

Contributed by the Power Division and presented at the ASME/IEEE Joint Power Generation Conference, Miami, Florida, October 4–8, 1987. Manuscript received at ASME Headquarters January 2, 1990.

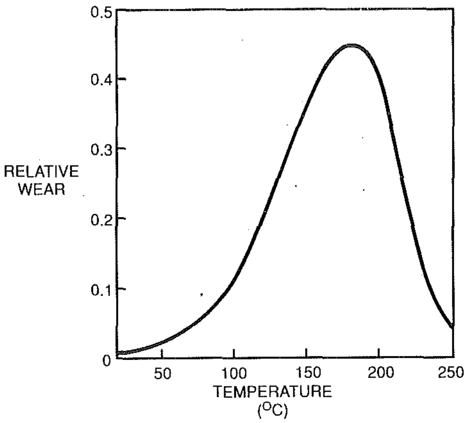

Fig. 1 **Corrosion-erosion wear rate as a function of temperature showing peak wear at approximately 150°C**

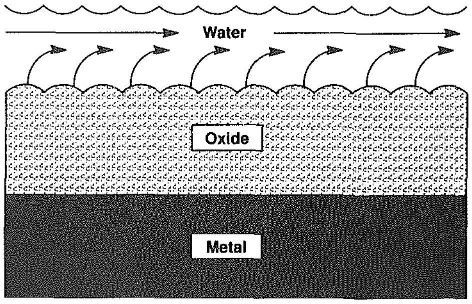

Fig. 2 **Schematic representation of the convection-assisted oxide dissolution wear mechanism**

This paper focuses on application of the Sanchez theories to predict the extent of erosive-corrosive wear caused by oxide dissolution and droplet impingement. The paper begins by presenting (without derivation) equations to predict the uniform wear caused by these two mechanisms. The terms in these equations are then defined and expressions necessary to evaluate the terms are provided. The subject of localized wear enhancement is then introduced and methods to account for the increased wear in these locations with the models are presented. Comparison of model predictions with plant measurements shows the equations provide reliable indications of relative wear rates in a given plant, but that absolute wear rates are at best a factor of two to three lower than plant values and are often up to an order of magnitude low.

Dissolution Wear Model

We start with the Sanchez dissolution model, derivations of which may be found in Sanchez (1984, 1988). Figure 2 is a schematic representation of this mechanism, in which the flow of the liquid over the oxide surface accelerates oxide dissolution. The Sanchez equation for this condition is given by

$$\dot{m}'' = \frac{C_e \theta}{\frac{1}{K} + (1-f)\left(\frac{L}{D} + \frac{1}{h_D}\right)} \qquad (1)$$

where $\dot{m}''$ is the material wear rate in kg/m^2-s, C_e is the equilibrium concentration (solubility) of magnetite in kg/m^3, θ is the oxide porosity (unitless), K is the corrosion reaction rate in m/s, L is the oxide thickness in m, D is the ferrous ion diffusivity in water in m^2/s, h_D is the convective mass transfer coefficient in m/s, and f is a constant equal to 0.5.

This model is based on three processes: (1) a corrosion process taking place at the metal/oxide interface, (2) a diffusion process occurring in the oxide pores, and (3) a convection process in the free water stream outside the oxide layer. In the equation presented above, the equilibrium concentration is the dissolved oxide concentration at the metal/oxide interface. It is implictly assumed in the model that the free-stream concentration of dissolved ions is zero.

In the sections below, each of these terms is defined in detail and the methods to calculate the values are provided.

Solubility of Magnetite (C_e). Sweeton and Baes (1970) determined that magnetite dissolves in high-temperature oxygenless water into four dominant ferrous species. These four solubility equations can be written in compact form as:

$$Fe_3O_4 + 3(2-b)H^+ + H_2(g) <==> 3Fe(OH)_b^{(2-b)+} + (4-3b)H_2O \qquad (2)$$

where b takes on values of 0, 1, 2, and 3 corresponding to each of the ferrous hydroxide ionic species.

The solubility of magnetite is a function of the equilibrium constant for the above reactions and the concentrations of hydrogen ion and hydrogen gas in the aqueous solution. The equilibrium constant is given by:

$$K_b = [Fe(OH)_b^{(2-b)+}]/([H^+]^{(2-b)}[H_2]^{\frac{1}{3}}) \qquad (3)$$

where K_b is the equilibrium constant for the bth ferrous species, $[H_2]$ is the concentration of hydrogen gas in atmospheres, and $[H^+]$ is the concentration hydrogen ions in mol/cm^3.

The numerator in the above equation is the solubilty, abbreviated by C_e:

$$C_e \equiv [Fe(OH)_b^{(2-b)+}] \qquad (4)$$

Sweeton and Baes experimentally determined values of K_b over a wide range of temperatures and developed best-fit equations of the form

$$K_b = \exp([-A_b/T + B_b[\ln((T)-1)] + D_b])/R) \qquad (5)$$

where T is temperature in K, R is the universal gas constant in J/kg mol-K, and A_b, B_b, and D_b are dimensional constants with values tabulated by Sweeton and Baes.

To evaluate the solubility, one must also determine the hydrogen gas and hydrogen ion concentrations. The former can be computed from knowledge of the bulk concentration in the piping system, with adjustments for solubility as a function of temperature as given by Himmelblau (1960). The latter is dependent on the concentrations of other species in the system, and is given by Sweeton and Baes as

$$[H_2]^{\frac{1}{3}}(2K_0[H^+]^3 + K_1[H^+]^2 + K_3) + [H^+]^2 - [A][H^+] = K_w \qquad (6)$$

where $[A]$ is concentration of ions used for water chemistry control and K_w is the solubility product of water.

This equation determines the *bulk flow* hydrogen ion concentration from the *bulk flow* hydrogen gas concentration. Equation (1), however, is valid at the metal/oxide interface, where the concentrations will differ from the bulk values. Due to the continuous corrosion process occurring at the metal/oxide interface, the hydrogen gas concentration will locally be higher than the bulk (due to cathodic production) and the hydrogen ion concentration will be lower than the bulk (due to anodic consumption). For the sake of simplicity, and to avoid a more complicated iterative expression to solve equation (1), we neglect these differences for purposes of making wear predictions with equation (1). Guidelines that compensate for this assumption are provided later in the discussion section.

To close the system of equations, an equation for K_w as a function of temperature is required. Rose (1961) provides an empirical equation that spans the given temperature range, given by:

$$-\log(K_w) = 4471/T + 0.017067T - 6.0875 \tag{7}$$

where T is temperature in K.

The above discussion is valid if magnetite is the stable form of iron oxide, which implicitly assumes the system is essentially free of dissolved oxygen. If significant levels of dissolved oxygen are present, hematite (Fe_2O_3) will form and the solubility expressions given above are not applicable.

Porosity of Magnetite (θ). Field and Holmes (1965) used transmission electron microscopy to obtain an order of magnitude measurement of the porosity of magnetite. In the derivation of equation (1), Sañchez (1984, 1988) postulated a slight decrease in the porosity of magnetite over the range 150 to 175°C. A mechanism for this decrease based on an interpore chemical reaction was proposed by Keck (1987), but direct verification of the temperature and extent of porosity decrease were not obtained. The recommended values of porosity are therefore a combination of Field and Holmes' order of magnitude and Sanchez's assumed decrease above 150°C, given by

$$\theta = 0.03 \quad (T < 150^\circ\mathrm{C}) \tag{8}$$

$$\theta = -0.004T + 0.15 \quad (150^\circ\mathrm{C} \le T \le 175^\circ\mathrm{C}) \tag{9}$$

$$\theta = 0.01 \quad (T > 300^\circ\mathrm{C}) \tag{10}$$

where temperature is in °C.

Reaction Rate (K). Sanchez empirically determined the value of the reaction rate and verified that it obeyed an Arrhenius expression as a function of temperature. The equation is

$$K = 8.45 \times 10^{17} \exp\left(\frac{-17{,}869}{T}\right) \tag{11}$$

with temperature in K.

Diffusion Coefficient (D). The value of the diffusion coefficient for the dissolved ferrous species is obtained using a modification (Sanchez, 1984, 1988) of an expression given by Rohsenow and Choi (1962). The general form of this equation includes the atomic volume of the diffusing species, which will vary slightly for the four ferrous species. This difference is so slight as to be unimportant for calculations. The equation is

$$D = 1.04 \times 10^{-7} T/\mu_f \tag{12}$$

where μ_f is the dynamic viscosity of the water in kg/m-s and T is in K.

Oxide Thickness (L). Values of the thickness of magnetite in an actively wearing region have been widely reported in the literature, with cited values between 1 and 40 μ. SEM observations by Keck (1984) of worn power planting piping showed oxide thickness around 10 μ, which is the value recommended for use in equation (1).

Mass Transfer Coefficient (h_D). The mass transfer coefficient is the one term in the dissolution model that requires separate calculations for single and two-phase flows. The brief section below provides equations for fully developed flows in pipes; increased mass transfer due to developing flow conditions found in bends is discussed later in the localized geometry section.

Single Phase Systems. Berger and Hau (1978) have developed an expression for the mass transfer in a turbulent pipe flow that uses the Reynolds and Schmidt numbers as parameters. The Reynolds number is given by

$$\mathrm{Re} = \frac{\bar{u}d}{\nu_f} \tag{13}$$

where $\bar{u}$ is the average fluid velocity in m/s, d is the pipe diameter in m, and ν_f is the liquid (water) viscosity in m^2/s.

The average fluid velocity is given by

$$\bar{u} = \frac{4\dot{m}}{\pi \rho_f d^2} \tag{14}$$

The Schmidt number is given by

$$\mathrm{Sc} = \frac{\nu_f}{D} \tag{15}$$

where D is the diffusion coefficient calculated from equation (12).

The Berger and Hau expression is

$$h_D = \frac{D}{d}\left(2.0 + a\mathrm{Re}^b \mathrm{Sc}^{\frac{1}{3}}\right) \tag{16}$$

where $a = 0.86 - 10.0/(4.7 + \mathrm{Sc})^3$ and $b = 0.0165 - 0.011\,\mathrm{Sc}\exp(-\mathrm{Sc})$.

In the parametric curves for the disssolution wear model presented later, the characteristic flow velocity is the friction velocity. For single-phase turbulent flow, Schlichting (1968) provides the following approximate relation for the friction velocity:

$$u^* = \left(\frac{\bar{u}}{7}\right)^{\frac{7}{8}} \left(\frac{2\nu}{d}\right)^{\frac{1}{8}} \tag{17}$$

where u^* is the friction velocity in units of m/s.

Two-Phase Flows. For two-phase flows, the mass transfer coefficient depends upon the given system flow regime. In most steam extraction piping systems, the mass flow rate of vapor is very large compared with that of liquid, and the two-phase mixture is in the annular flow regime. The equations for mass transfer in two-phase flows given below are valid only in the annular flow regime.

To calculate the mass transfer coefficient for fully developed annular flow, first compute the liquid only friction factor, given by Collier (1978) as

$$f_{fo} = 0.079 \left(\frac{Gd}{\mu_b}\right)^{-0.25} \tag{18}$$

where G is the mass velocity in units of kg/m^2-s, given by

$$G = \frac{4\dot{m}}{\pi d^2} \tag{19}$$

Second, compute the homogeneous friction multiplier

$$\Phi_{fo}^2 = \left(1 + x\left(\frac{v_{fg}}{v_f}\right)\right) \left(1 + x\left(\frac{\mu_{fg}}{\mu_f}\right)\right)^{-0.25} \tag{20}$$

The third step is to compute the wall shear stress, given by

$$\tau_w = 0.5 f_{fo} G^2 \nu_f \Phi_{fo}^2 \tag{21}$$

Finally, the friction velocity is given by

$$u^* = \sqrt{\tau_w/\rho_f} \tag{22}$$

Kunz and Yerazunis (1969) determined the heat transfer coefficient for annular two-phase flows over a wide range of Reynolds and Prandtl numbers. Using the Colburn analogy (Rohsenow and Choi, 1961), these results can be applied to mass transfer problems as well (Keck, 1987). At sufficiently high Reynolds numbers, the transposed Kunz and Yerazunis results become independent of Reynolds number and are a function of only the Schmidt number and friction velocity. Over the range of Schmidt numbers likely to be found in power plants, the mass transfer coefficient can be computed from

$$h_D = \frac{u^*}{\mathrm{Sc}}(0.07607\ln(\mathrm{Sc}) + 0.16) \tag{23}$$

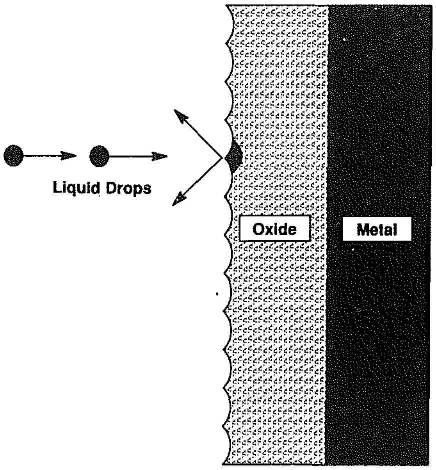

Fig. 3 Schematic representation of the droplet impingement fatigue wear mechanism

Droplet Impact Wear Equations

Figure 3 is a schematic of the wear of the oxide due to repeated droplet impacts normal to the oxide surface. The Sanchez droplet impact model is an adaptation for liquid droplets of the approach by Hutchins (1980) for impacts of solid spheres at normal impingement angles. The Sanchez model assumes that the wear occurs once the total strain of an element of the oxide exceeds the critical strain to fracture. The model also assumes that 100 percent of the drop energy is converted to plastic deformation, and that the oxide resists deformation proportional to its indentation hardness. To complete the model, a mass balance on the number of drops entrained in the two-phase pipe flow is performed over the impacted region. The final form of the Sanchez wear equation is

$$\dot{m}'' = \frac{C\rho_f \dot{m}_{\text{tot}}(1-x)V_d^4 F_e F_h}{(P\epsilon_c)^2 A_c} \tag{24}$$

where $\dot{m}''$ is the wear rate in kg/m^2=s, C is a dimensionless wear coefficient, ρ_f is the liquid density in kg/m^3, $\dot{m}_{\text{tot}}$ is the total mass flow rate in kg/s, x is the thermodynamic quality, V_d is the drop velocity in m/s, F_e is the entrainment fraction (unitless), F_h is the hitting fraction (unitless), P is the indentation hardness in N/m^2, ϵ_c is the critical strain to fracture (unitless), and A_c is the characteristic wear area in m^2.

In the sections below, each of these terms is defined and a method for calculating the values is provided.

Mass Flow Rate ($\dot{m}_{\text{tot}}$): The total mass flow rate of liquid and vapor in the given line in kg/s.

Quality (x): The thermodynamic quality of the two-phase mixture (unitless).

Drop Velocity (V_d): The drop velocity is assumed to be equal to the superficial gas velocity, given by Collier (1978) as

$$V_d = \frac{4\dot{m}_{\text{tot}}x}{\pi\rho_g d^2} \tag{25}$$

Liquid Density (ρ_f): Density of the liquid phase, kg/m^3.

Oxide Hardness (P): Indentation hardness of the oxide being impacted. McClintock and Argon (1960) cite the hardness of magnetite as 650 N/mm^2. (Note: This value was incorrectly reported as 6500 by Keck (1987) and Keck and Griffith (1987).)

Critical Strain to Fracture (ϵ_c): Strain required to fracture the oxide. No literature values for magnetite were found, but the empirical studies of Keck (1987), upon which the nondimensional wear coefficient's values cited below are based, use a value of 0.03 (unitless).

Hitting Factor (F_h): Fraction of entrained drops that impact at normal angles on the characteristic area. This dimensionless quantity depends on how the characteristic area is defined, and has values ranging from zero to unity. Using the definition of A_c given below, the value is unity. However, as is discussed in the next section on wear enhancement, values of Keller's geometry factors can be included in the droplet impact model through this term.

Characteristic Area (A_c): The area over which the entrained drops impact normally to the oxide surface. Values vary considerably with flow geometry, but for a standard radius 90-deg bend, the following equation is recommended:

$$A_c = 1.5d^2 \tag{26}$$

Entrainment Fraction (F_e): The fraction of liquid present in the system that is entrained in the core vapor flow. This unitless quantity, which can have values from zero to one, must be obtained from correlations available in the literature. We recommend using the Wallis (1968) correlation. For a maximum wear prediction, the entrainment fraction is unity.

Wear Coefficient (C): Nondimensional wear coefficient. Keck (1987) performed a series of experiments at room temperature in which magnetite-coated steel specimens were impacted with an air-water mixture at velocities between 100 and 150 m/s. These experiments were designed to check the wear dependence on velocity and to measure the corresponding value of C. Results showed that the velocity dependence was to the 3.4 power, slightly lower than predicted by the Sanchez theory. For predictions using the theory, the maximum value wear coefficient measured was 1.0×10^{-8}. (Note that due to the incorrect reporting of oxide hardness by Keck (1987) and Keck and Griffith (1987) as noted above, the value of this coefficient as earlier reported is also incorrect.)

Localized Wear Enhancement

Localized flow effects enter the dissolution model via the mass transfer coefficient, which must be modified to account for developing flows present in non-straight pipe sections. In the droplet impact model, the entrainment fraction (F_e) and the hitting fraction (F_h) will both be changed due to local hydrodynamic effects. This section discusses how these effects are incorporated in the two models and cites values available for the resultant increased wear.

Analytical expressions for the increased mass transfer in bends and other complex flow geometries are not common for single or two-phase flows, but some isolated empirical results do exist. Gill et al. (1982) and Coney et al. (1983) found dissolution of 90 deg plaster-of-paris pipe bends in high quality air-water mixtures at room temperature to be 3 to 5 times greater than that in straight pipes. Similar experiments by DeFreitas (1988) over flow obstructions and protrusions in the flow yielded factors from 1.4 to 2.8. In the absence of additional evidence, maximum mass transfer coefficient increases of a factor of three do not seem unreasonable. There do not, however, seem to be data for the relative enhancement between components, such as that in a 90 deg miter bend versus that in a short-radius 45 deg bend.

For the droplet impact model, there is some information on how the hitting factor (F_h) will change with flow geometry, but there appear to be no expressions for non-fully developed entrainment (F_e). Localized hitting factor values can be extracted from the geometry factors that Keller (1974) presented. These factors, which range from a low of 1 to a high of 25, can be used in the droplet impact model if one simply normalizes the values relative to a maximum value of 1. Thus the Keller value of 25 becomes a hitting factor of unity, while the Keller minimum value of 1 becomes a hitting factor of 0.04.

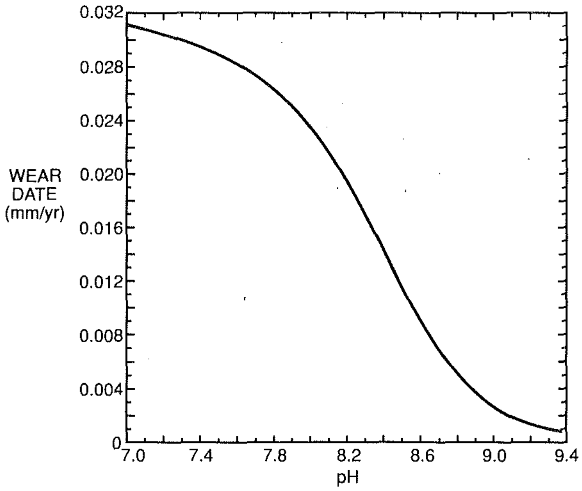

Fig. 4 Dissolution wear rate per unit area as a function of pH at 125°C

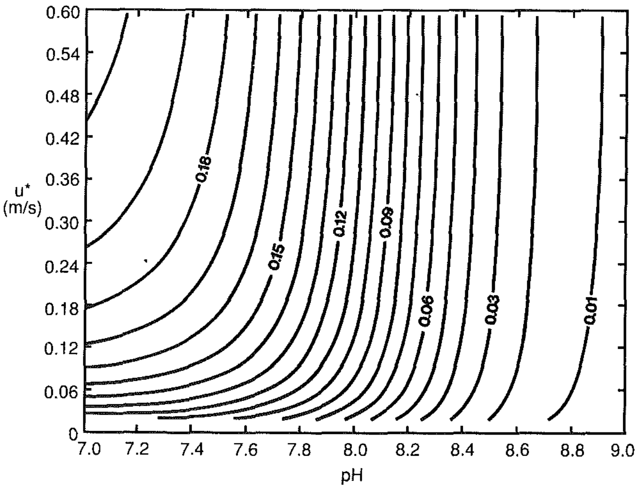

Fig. 6 Dissolution wear rate (in mm/yr) at 175°C as a function of pH and friction velocity

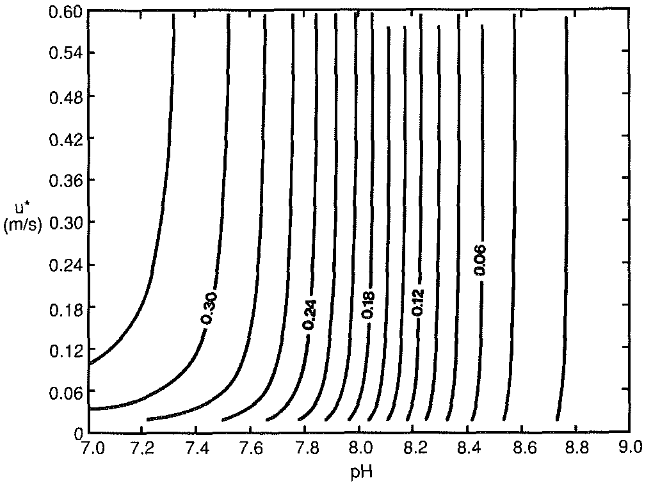

Fig. 5 Dissolution wear rate (in mm/yr) at 150°C as a function of pH and friction velocity

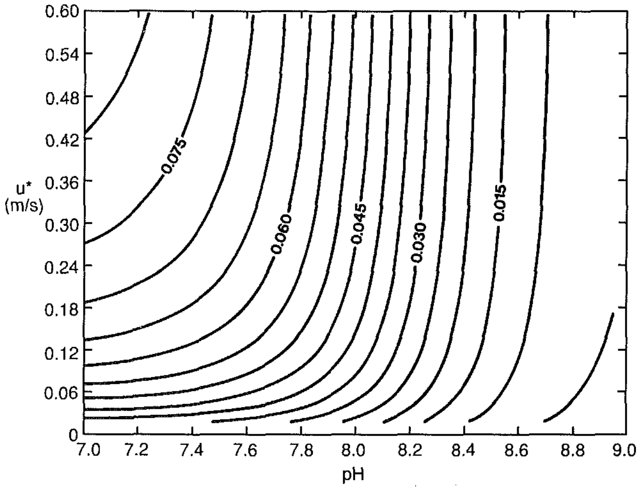

Fig. 7 Dissolution wear rate (in mm/yr) at 200°C as a function of pH and friction velocity

Model Results and Discussion

Since predictions using the droplet impact model only require solution of an algebraic expression, we focus in this section on results from the dissolution model, which is quite cumbersome to solve by hand.

The dissolution model contains five system parameters required as input: (1) temperature, (2) pH, (3) mass flow rate, (4) pipe diameter, and (5) quality. Of the terms in the dissolution model, C_e, θ, K, D, and h_D are all temperature dependent. The only term that is pH dependent is C_e. The last three parameters, all flow properties, only affect h_D. With the desire to present sample results for a range of input parameters, we thus lump the effects of the flow variables into a single parameter, the friction velocity. (For single-phase systems, the friction velocity is calculated from equation (17); for two-phase systems, from equation (22).)

Figures 4–7 provide solutions of equation (1) at temperatures of 125, 150 175, and 200°C, respectively, generated with pH and friction velocity as parameters. Figure 4 shows the wear rate per unit area as a function of pH (the friction velocity dependence drops out at low temperatures, as is discussed below). Figures 5–7 show wear iso-lines, with both pH and u^* as parameters.

Equation (1) is in a form that has the driving force in the numerator and a sum of resistances in the denominator. For this problem, the driving force is the equilibrium concentration. The results presented in Figs. 4–7 show how the relative magnitudes of these denominator resistances vary with temperature. At temperatures below 150°C, the reaction rate K is small and its resistance dominates. Thus, as shown in Fig. 4, the effect of the mass transfer process is negligible despite variations in friction velocity. As the temperature increases, the reaction rate rises exponentially, ultimately becoming negligible relative to the other terms, and the effect of velocity becomes more pronounced. The increased dependence on friction velocity at low pH as one moves from Fig. 5 to Fig. 7 illustrates this point. This result has direct implications in power plants as it suggests that the effect of increased flow velocity due to turbulence in elbows and tees will only adversely influence the wear at temperatures above the 150°C peak temperature.

In using the dissolution model to make wear predictions, we recommend the following rules of thumb for simplifications in the model. First, to compensate for the use of the bulk-flow hydrogen concentrations (as discussed below equation (6)) and to correct for pH excursions that might yield off-design water chemistry in PWRs with volatile amines, we recommended basing predictions on a pH one-half unit below the design value. Second, to account for non-fully developed flows and localized turbulence in pipe bends, we recommend using a friction velocity three times the bulk value.

Predictions from the two wear models are generally factors of two to three lower than plant values and are often an order of magnitude below measurements. One reason for these low predictions is the fact that the laboratory values of the dissolution (Sanchez, 1984, 1989) wear were about an order of magnitude below plant values. While it is possible that plant transients, off-design operating conditions, and water chemistry excursions might explain the differences between laboratory and plant wear rates, the lack of quantitative oxygen control in the Sanchez experiments might also contribute to the errors.

Due to the differences between the measured and predicted values, the models are commonly used to predict relative wear rates, which are then used to design inspection and mitigation strategies. Dyrness et al. (1989) developed inspection guidelines for an operating BWR and report very satisfactory predictions of relative wear with the models.

Conclusion

This paper has presented equations for predicting erosive-corrosive wear in low-oxygen power plant piping due to the mechanisms of dissolution and droplet impact wear. Using the definitions and equations provided in the main sections of the paper, full calculations of predicted wear rates are possible. From a theoretical view there are considerable obstacles to completely accurate wear predictions. The effects of transient off-design operations, start-up and shut-down procedures, pH excursions, and localized flow conditions must all be better understood before more accurate predictions can be made. Models presented here are reasonable engineering tools that can be used to prioritize inspection locations and to study the effect of design parameters on the resulting wear rate.

References

Berge, P., and Khan, F., 1982, "Summary and Conclusions of the Specialists Meetings on Corrosion-Erosion of Steels in High Temperature Water and Wet Steam," EdF, Les Renardiers, France.

Berger, F. P., and Hau, K., 1977, *Heat and Mass Transfer*, Vol. 20, p. 1185.

Bignold, G. J., et al., 1981, "Tackling Erosion-Corrosion in Nuclear Power Generating Plants," *Nuclear Engineering International*, Vol. 26, No. 314, pp. 37-41.

Collier, J. G., 1972, *Convective Boiling and Condensation*, McGraw-Hill, New York.

Coney, M. W. E., et al., 1982, "Thermal Hydraulic Effects on Mass Transfer Behaviour and on Erosion-Corrosion Metal Loss Rates," presented at the Specialists' Meeting on Corrosion-Erosion, EdF, Les Renardiers, France.

DeFreitas, G., 1986, "Dissolution Wear Rates in the Wake of a Welding Backup Ring," M.E. Engineers Degree Thesis, MIT, Cambridge, MA.

Dyrness, A. D., Watts, T. N., and Keck, R. G., 1989, "The Use of the Sanchez Models to Predict and Monitor Erosive/Corrosive Wear in Power Plant Piping," presented at The Power Conference, New Orleans, LA.

Himmelblau, D. M., 1960, "Solubilities of Inert Gases in Water," *Journal of Chemical Engineering Data*, Vol. 5, No. 1, pp. 10-15.

Hutchings, I. M., 1981, "A Model for the Erosion of Metals by Spherical Particles at Normal Incidence," *Wear*, Vol. 70, pp. 269-281.

EPRI, 1985, "Erosion-Corrosion in Nuclear Plant Steam Piping: Causes and Inspection Program Guidelines," EPRI Report NP-3944, Palo Alto, CA.

EPRI, 1987, "EPRI Workshop on Erosion-Corrosion of Carbon Steel Piping," held at L'Enfant Plaza Hotel, Washington, DC.

Field, E. M., and Holmes, D. R., 1965, "Nucleation and Growth of Magnetite Films on Pure Iron in High Temperature Water," *Corrosion Science*, Vol. 5, pp. 361-370.

Gill, G. M., et al., 1982, "The Effects of Oxygen and Iron in Feedwater on Erosion-Corrosion of Mild Steel Tubing," presented at the Specialists' Meeting on Corrosion-Erosion, EdF, Les Renardiers, France.

Keck, R. G., 1987, "Prediction and Mitigation of Erosive-Corrosive Wear in Steam Extraction Piping Systems," M.E. Ph.D. Thesis, MIT, Cambridge, MA.

Keck, R. G., and Griffith, P., 1987, "Models and Equations for the Prediction of Erosive-Corrosive Wear in Steam Extraction Piping," ASME Paper No. 87-JPGC-Pwr-35.

Keller, V. H., 1974, "Erosion-Corrosion in Wet Steam Turbines," *VGB Krafwerktechnik*, Vol. 62, No. 5, pp. 12-21.

Kunz, H. R., and Yerazunis, S., 1969, "An Analysis of Film Condensation, Film Evaporation, and Single-Phase Heat Transfer for Liquid Prandtl Numbers From 10^{-3} to 10^4," ASME *Journal of Heat Transfer*, Vol. 91, pp. 413-420.

Rohsenow, W. M., and Choi, H., 1961, *Heat, Mass and Momentum Transfer*, Prentice Hall, Englewood Cliffs, NJ.

Rose, J., 1961, *Dynamic Physical Chemistry*, Wiley, New York, p. 403.

Sanchez-Caldera, L. E., 1984, "Mechanisms of Corrosion-Erosion in Steam Extraction Lines of Power Stations," M.E. Ph.D. Thesis, MIT, Cambridge, MA.

Sanchez-Caldera, L. E., Griffith, P., and Rabinowicz, E., 1988, "The Mechanism of Corrosion-Erosion in Steam Extraction Lines of Power Stations," ASME JOURNAL OF ENGINEERING FOR GAS TURBINES AND POWER, Vol. 110, pp. 180-185.

Schlichting, H., 1968, *Boundary Layer Theory*, 6th ed., McGraw-Hill, New York.

Sweeton, F. H., and Baes, C. F., 1970, "The Solubility of Magnetite and Hydrolysis of Ferrous Ion in Aqueous Solutions at Elevated Temperatures," *Journal of Chemical Thermodynamics*, Vol. 2, pp. 479-502.

Vu, H., 1982, "Erosive-Corrosive Wear in Steam Extraction Lines of Power Plants," M.E. M.S. Thesis, MIT, Cambridge, MA.

Wallis, G. B., 1969, *One Dimensional Two-Phase Flow*, McGraw-Hill, New York.

W. E. Wright

J. C. Hall

Advance Technology Control Systems,
General Electric Aircraft Engines,
Cincinnati, OH 45215

Advanced Aircraft Gas Turbine Engine Controls

With the advent of vectored thrust, vertical lift, and fly-by-wire aircraft, the complexity of aircraft gas turbine control systems has evolved to the point wherein they must approach or equal the reliability of current quad redundant flight control systems. To advance the technology of high-reliability engine controls, one solution to the Byzantine General's problem (Lamport et al., 1982) is presented as the foundation for fault tolerant engine control architecture. In addition to creating a control architecture, an approach to managing the architecture's redundancy is addressed.

Background

Present day military and commercial engine controls are generally concerned with five or fewer engine-manipulated variables. Control of core engine functions (fuel flow, stators, etc.) has until recently been a hydromechanical function. In the early 1960s, engines like the J79 in the F4 Phantom used a single hydromechanical control for fuel flow and stators. With the advent of transistorized circuitry, the 1960s and 1970s saw engines using analog electronic controls in conjunction with hydromechanical main fuel controls. The 1980s brought sufficient advances in data acquisition and microcessor technologies to allow replacement of analog controls with a digital processor based unit on the GE F110 engine for the F16 Falcon. Commercial aircraft are now flying with full authority digital engine controls, usually in a dual configuration to allow continued engine operation upon the event of a single component failure. The Advanced Tactical Fighter (ATF) and other advanced programs have identified performance advantages from further usage of electronics. Dual, Triplex, and Quad control processing designs are all potential candidates that will allow the removal of the hydromechanical control. The progression in control system architectures is illustrated in Fig. 1.

Systems Approach

A typical aircraft gas turbine control system encompasses five areas requiring a systems design approach. These areas include sensors, actuators, control/computational hardware and software, and integration with the Vehicle Management System (VMS). Each area requires a system design that stresses maintainability, reliability, performance, and life cycle cost. The VMS is becoming increasingly important to the aircraft as the technology for fully integrated aircraft control system develops. Incorporation of that portion of the aircraft systems, which are truly flight critical, into an integrated Vehicle Management System will result in reduced component maintenance while improving aircraft performance.

Byzantine Resilience

The term "Byzantine Resilience" (Lamport et al., 1982; Dolev, 1982) applies to the ability of a multichannel control to accommodate any arbitrarily malicious fault. The resulting architecture contains the fault within the channel and prohibits the fault from propagating into other control computations. Many fault-tolerant control system concepts are subject to single-point failures. As an example, commercial aircraft are now in operation using two redundant computing channels within the engine control. The reliability of such a system is sufficient for aircraft wherein the use of multiple engines allows continued flight upon the loss of an entire engine control. Two engine aircraft are limited on over-water flight durations because the reliability of the engine control becomes a critical factor subsequent to the loss of one engine. With only two operable channels, the health of an individual channel can only be assessed by itself. This severely limits the control's ability to provide 100 percent first-failure coverage.

Flight critical aircraft functions have traditionally relied on quaternary redundancy to provide proper control operation. Voting among channels is the means of determining proper operation of individual control channels. The General Electric Aircraft Engines Advance Technology Controls organization has, through the auspices of the Air Force sponsored Integrated Reliable Control for Engines (INTERFACE I and INTERFACE II—L) programs, accomplished an in-depth study of engine control fault-tolerance considerations.

Fault-tolerance requirements as applied to engine controls are generally derived from the MTBF/MTBR (mean time between failure/repair) and other mission requirements of the engine. The INTERFACE programs addressed the reliability/fault tolerance engine control issues without regard to a specific engine application. The issue of fault tolerance in multichannel computing systems has been studied in many industry and government programs. The most promising architecture for

---

Contributed by the International Gas Turbine Institute and presented at the 34th International Gas Turbine and Aeroengine Congress and Exhibition, Toronto, Ontario, Canada, June 4-8, 1989. Manuscript received at ASME Headquarters October, 1989.

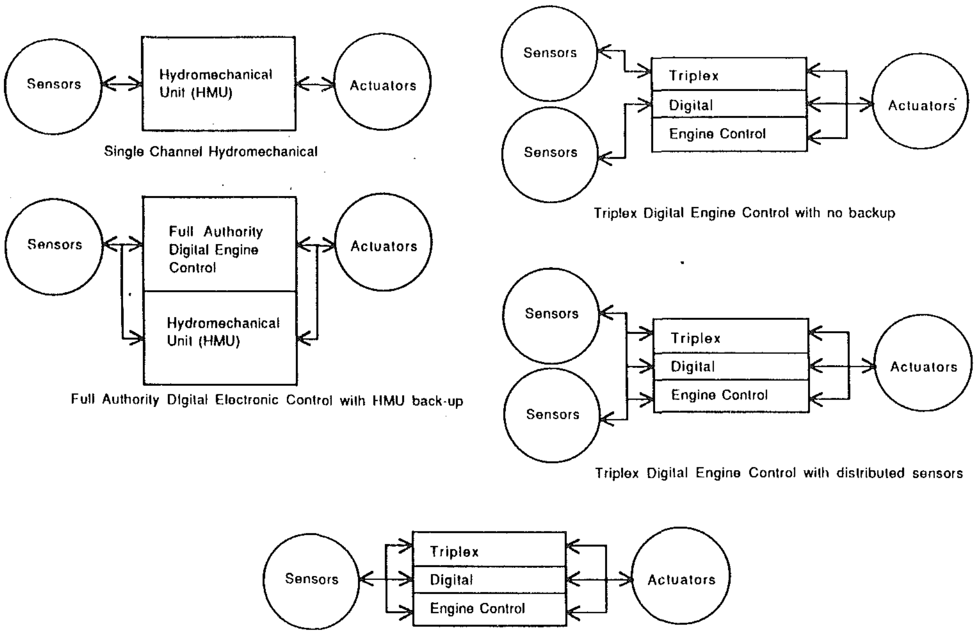

Single Channel Hydromechanical

Full Authority Digital Electronic Control with HMU back-up

Triplex Digital Engine Control with no backup

Triplex Digital Engine Control with distributed sensors

Fig. 1 Control system architectures

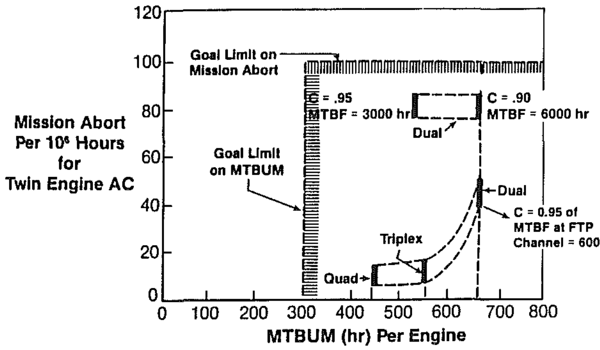

Fig. 2 Dual, triplex, and quad comparisons

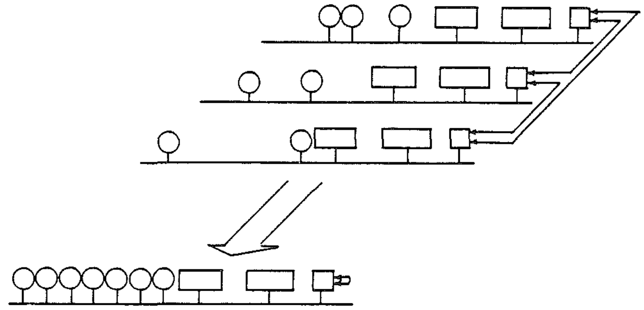

Fig. 3 Draper fault-tolerant architecture

engine control applications was determined to be the Byzantine Resilient Fault-Tolerant Multi-Processor (FTMP) concept (Smith et al., 1986; Nelson et al., 1986) developed by the Charles Stark Draper Laboratories. The issue of triplex versus quad redundancy within the engine control was decided in favor of triplex architecture subsequent to evaluation of cost and complexity versus reliability requirements. As illustrated in Fig. 2, the additional decrease in mission aborts of a quaternary control versus a triplex control cannot be justified when compared to the increase in control maintenance. The parameter *C* in Fig. 2 refers to the coverage of the first fault as a percentage achieved in the selected architecture.

INTERFACE I Control

The INTERFACE I control was a triplex machine and incorporated a DOD 1750A processor. Draper microframe synchronous Byzantine Resilient architecture was incorporated into the control and the control was programmed in JOVIAL. The control was completed and tested in early 1985. The fault-tolerant capabilities of the microframe synchronous Draper architecture were demonstrated; however control throughput was not up to requirements because of the inherent limitations of those microprocessors that complied with the 1750A instruction set. The inability of the 1750 processor to satisfy engine control throughput requirements and a lost channel recovery time exceeding 100 ms required further design development. Several other control advancements such as bubble memory and optical data buses were demonstrated by the INTERFACE I control.

INTERFACE II—L Control

The INTERFACE II—L contract was awarded to General Electric on July 30, 1985. The object of this program was to carry forward the Draper architecture developed in INTERFACE I. In order to challenge the Draper architecture and support the use of Mil-std 1815A Ada as the control language, 20 mHz Motorola 68020 32 bit processors were incorporated into the design of the control. Because of the previously noted limitations of the 1750A instruction set and the growing interest in Ada, the operating system and application software were programmed in Ada. Fabrication of the INTERFACE II—L control is now complete and the control testing phase is in progress. Results to date indicate no problems with the control architecture. The microframe synchronous characteristics of the Draper architecture permit the change from simplex to triplex control operation with no software modifications. The only concern remains the inefficiency of the Ada language as applied to real-time control systems.

Reliability

The fault-tolerant core of the General Electric INTERFACE II—L engine control is a set of three tightly synchronized M68020 processors utilizing hardware voting with fault containment and error detection mechanisms. As illustrated by

Fig. 3, to the application software, the system appears as a single control processor. This feature is important because it permits the utilization of a General Electric developed analytic redundancy program (Vizzini et al., 1980; Spang et al., 1977; Linebrink et al., 1982) known as FICA (failure indication and corrective action). Analytical redundancy is defined as the development, by analytic means, of synthesized values for various engine, sensor, and effector values. These synthesized values are continuously updated based upon engine operating parameters and are compared with actual sensor values in preparation for furnishing information to the control upon loss of a sensor. The architecture within the control permits transmittal of channel information to all other channels. This information is voted and passed on to other channels for computational purposes (Polley et al., 1988).

The availability of a synthesized set of operating parameters permits full triplex control operation with only two sets of control input sensors. The synthesized set constitutes the third sensor set. The actuator set is equipped with triple coil actuator drives. Each coil possesses sufficient drive capability to control each actuator independently. Each coil is driven by a control channel with the output drive magnitude determined by the number of operable channels. This feature permits full engine control capability with only one operational channel.

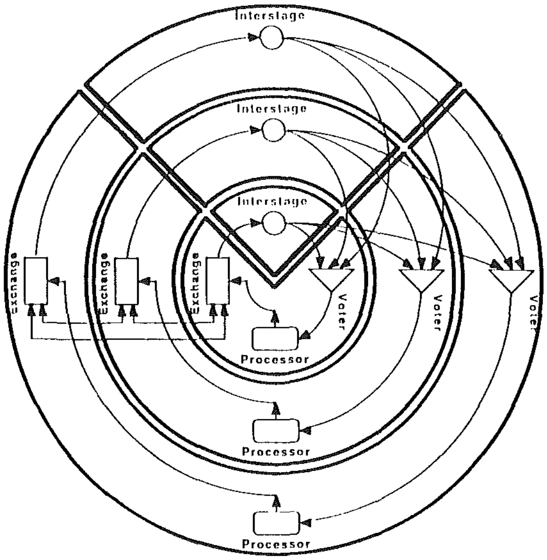

Fig. 4 Fault containment regions of the FTP

Architecture

The INTERFACE II—L program used Markov modeling to perform the reliability analyses that led to the selection of the Charles Stark Draper Laboratory (CSDL) Byzantine Resilient fault-tolerant processing design shown in Fig. 4. This triplex control design satisfied the requirements for 100 percent first failure coverage and resulted in reliability figures of merit of better than 10^{-8}. This processing architecture is the result of several CSDL programs (Hopkins et al., 1985). The original NASA fault-tolerant processing research program took two different design approaches: SIFT (Software Implemented Fault Tolerance) and FTMP. In this program the FTMP design was found to be preferable for engine controls because it resulted in an implementation with minimal operating system overhead. The SIFT design however is software intensive and results in less verifiable fault tolerance and more operating system overhead. The FTMP design led to the Advanced Information Processing System (AIPS, a NASA follow-on fault-tolerant research program) and INTERFACE architectures. Both approaches use tightly synchronous processors and utilize an interstage and voter to provide fault-tolerant hardware partitioning.

To assure operation during any single failure, a triplex set of all flight critical sensors and a duplex set of engine critical sensors is required. In the event of a discompare between the sensor values, the embedded engine model is used to arbitrate. Recent reliability studies have identified enhanced performance opportunities from a dual sensor set distributed across the three channels.

Advances in engine modeling from the Analytical Redundancy Technology for Engine Reliability Improvement (ARTERI, Brown, 1984) program are leading to reduced-size minimal-sensor sets. This reduction enables a set of dual sensors to be distributed across three channels where each channel has sufficient sensors for normal engine operation. This technology provides an increased capability for second failure operation. As engine modeling matures, a return to a single sensor set may be feasible as shown by Fig. 3. This ability would reduce weight and cost while maintaining the capability for second failure operation. Analytical redundancy technology will also enable safe engine operation after an actuation system failure. This is accomplished by the ability to identify a failure

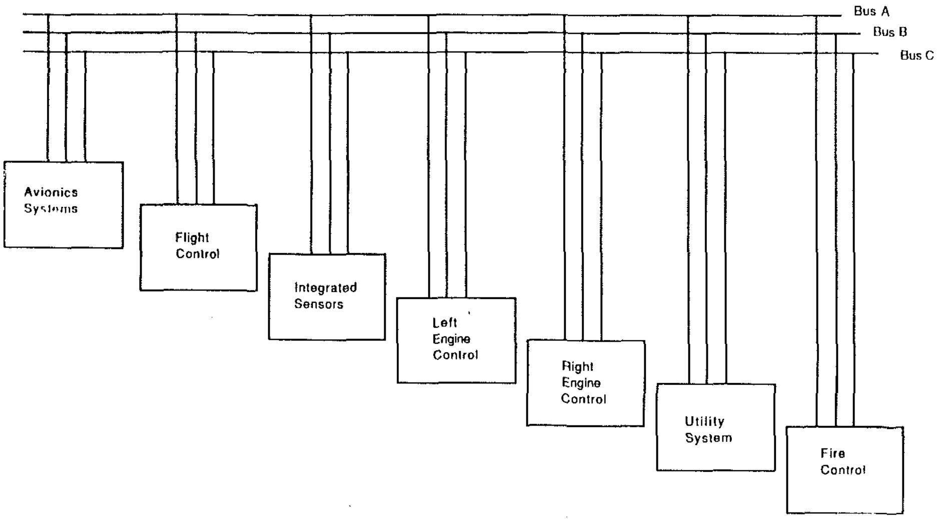

Fig. 5 Vehicle management system (VMS)

and then switch over to battle damage accommodation schedules.

Vehicle Management System (VMS)

In order to obtain greater performance from future aircraft and reduce pilot workload, integration of presently independent systems will be required. An enabling technology for integration is a communications network with the ability to perform high-speed reliable data exchange. This ability will allow for many new functionally integrated modes such as Integrated Flight/Propulsion Control (IFPC), Integrated Flight/Fire Control (IFFC), Terrain Following/Terrain Avoidance/Obstacle Avoidance (TF/TA/OA), Performance Seeking Control (PSC), and Battle Damage Accommodation concepts. Without the high-speed VMS network, illustrated in Fig. 5, the above modes could incur unacceptable data transfer delays (system phase lag). The delays would severely impact the system's transient response/performance.

In present production aircraft the engine is a wholly independent subsystem and communicates with other systems over analog or other low bandwidth networks. Proposed Advanced Tactical Fighter (ATF) and preliminary supersonic short takeoff and vertical land (STOVL) concepts will result in an engine design that will be integrated and dependent on other systems. Technologies such as shared electric power, shared hydraulic power, and dynamic reprogramming of the entire aircraft software (for different response characteristics/missions) will provide performance benefits in future aircraft.

Having all flight critical functions communicating on a fault-tolerant bus connecting distributed components will provide for enhanced logistics support. Data access will be easier and communication hardware commonality will make fault isolation and repair simpler.

Conclusions

In the past, aircraft engines, with their associated control systems, could be applied by the airframer with very little attention needed to engine control system capabilities since thrust was the primary engine concern. Airframe flight controls achieved the required fault tolerance/reliability through multichannel implementation. The requirement for vectored thrust from the engine exhaust nozzles, the emphasis on vertical lift capabilities, and other flight critical functions have placed new requirements on the engine. As a result, the control and its interface with the airframe air data computer/flight control system has become flight critical. General Electric Aircraft Engine's approach to meeting this challenge is the triplex engine control incorporating the Byzantine resilient computer architecture developed by the Charles Stark Draper Laboratories. This is certainly not the only fault-tolerant computer architecture in existence but it is considered to be the best architecture for embedded engine controls.

These concepts have been proven in the INTERFACE I and II programs. Future plans for these concepts include parallel and distributed Byzantine resilient control systems.

Acknowledgments

The developments reported in this paper were conducted under contract numbers F33657-82-C-2265, F33657-85-C-2131, and N00140-83-C-9046 for the Air Force Aeropropulsion Laboratory and the Naval Air Propulsion Center. The authors wish to acknowledge the contributions provided by P. T. Adams, T. J. Lewis, Z. D. Gastineau, and R. W. Vizzini of these sponsoring offices.

References

Brown, H., 1984, "Analytical Redundancy Technology for Engine Reliability Improvement," Quarterly Technical Progress Report, Apr.; Contract No. NAS 3-9046.

Dolev, D., 1982, "The Byzantine Generals Strike Again," *Journal of Algorithms*, Vol. 3, No. 1, pp. 14–30.

Hopkins, A. J., Smith, T. B., III, and Lala, J. M., 1985, "FTMP Highly Reliable Fault-Tolerant Multiprocessor for Aircraft," *Proceedings of the IEEE*, Vol. 66, No. 10, pp. 1221–1239.

Lamport, L., Shotak, R., and Pease, M., 1982, "The Byzantine Generals Problem," *ACM Transactions on Programming Languages and Systems*, Vol. 4, No. 3, pp. 382–401.

Linebrink, K. L., and Vizzini, R. W., 1982, "FADEC-Augmented Fighter Engine Demonstration," AIAA Paper No. 821371; Contract No. N00019-76-C-0423.

Nelson, S., Stanton, W., and Volp, J., 1986, "A Fault-Tolerant 1750A Engine Controller," presented at the AIAA/SAE/ASEE 22nd Joint Propulsion Conference, Huntsville, AL, June 16–18.

Polley, J. A., Adibhatla, S., and Hoffman, P. J., 1987, "Multivariable Turbofan Engine Control for Full Flight Envelope Operation," ASME JOURNAL OF ENGINEERING FOR GAS TURBINES AND POWER, Vol. 111, pp. 130–137.

Smith, T. B., III, et al., 1986, *The Fault-Tolerant Multiprocessor Computer*, Noyes Publishers, Parkridge, NJ, ISBN 0-8155-1087-X CR, p. 782.

Spang, H. A., and Corley, R. C., 1977, "Failure Detection and Correction for Turbofan Engines," presented at the Joint Automatic Control Conference, San Francisco, CA, June.

Vizzini, R. W., and Toot, P. D., 1980, "FADEC Application to a Variable Cycle Engine," presented at the Aerospace Congress and Exposition, Los Angeles, CA, Oct. 13–15, Contract No. N00019-76-C-0423.

Development of the HIDEC Inlet Integration Mode

J. D. Chisholm

S. G. Nobbs

McDonnell Aircraft Company,
McDonnell Douglas Corporation,
St. Louis, MO 63166

J. F. Stewart
NASA—AMES/Dryden,
Edwards Air Force Base, CA 93523

An integrated flight propulsion control mode called Inlet Integration has been developed and will be flight demonstrated on an F-15 test aircraft in the Highly Integrated Digital Electronic Control (HIDEC) program. The HIDEC program is conducted by the NASA Ames/Dryden Flight Research Center. The development of the Inlet Integration mode is described in this paper, including the Inlet Integration concept, the control law, its implementation on the test bed aircraft, and the predicted performance benefits. The Inlet Integration system will increase excess thrust (thrust-drag) during supersonic operation. This improvement in aircraft performance is accomplished by utilizing a calculation of engine corrected airflow from the Digital Electronic Engine Control (DEEC) to improve the scheduling of the inlet ramp positions in real time. The improvement in scheduled ramp positions will result in increased inlet performance, hence aircraft performance, while maintaining stable inlet operation. Analyses have shown the Inlet Integration system can increase excess thrust by as much as 13 percent at Mach 2.3, 40,000 ft. This thrust increase will result in increased supersonic acceleration. Inlet integration has the additional feature of improving aircraft supportability by eliminating the need for replacing inlet controllers when higher thrust derivative engines are installed in the F-15.

Introduction

The Inlet Integration mode is the last of four integrated flight propulsion control modes to be developed in the NASA HIDEC program, in which McDonnell Aircraft Company (MCAIR) is the prime contractor and Pratt & Whitney (P & W) is the principal subcontractor. In the Inlet Integration mode, additional aircraft performance is realized through a unique real-time scheduling of the inlet ramp positions using an onboard calculation of engine corrected airflow (WAC). Initial HIDEC concepts were first reported by Burcham and Haering (1984) and Yonke et al. (1984). The first three integrated flight propulsion modes are: (1) the Adaptive Engine Control System (ADECS) mode, (2) the Trajectory Guidance mode, and (3) and the Extended Engine Life mode. In the ADECS mode, additional engine thrust is obtained by increasing engine pressure ratio when excess stall margin is available. In the Trajectory Guidance mode, optimal trajectories are generated on board the aircraft to minimize fuel usage or minimize time.

In the Extended Engine Life mode, the turbine operating temperatures are decreased while maintaining constant thrust, thereby reducing wear on the engine. This is accomplished by increasing engine pressure ratio while simultaneously decreasing engine airflow. The ADECS and Trajectory Guidance modes have been developed and flown. The development and flight demonstration of the ADECS mode was reported by Putnam et al. (1985), Landy et al. (1987), and Yonke et al. (1985, 1987). The Extended Engine Life mode has been developed and will be flown in conjunction with Inlet Integration.

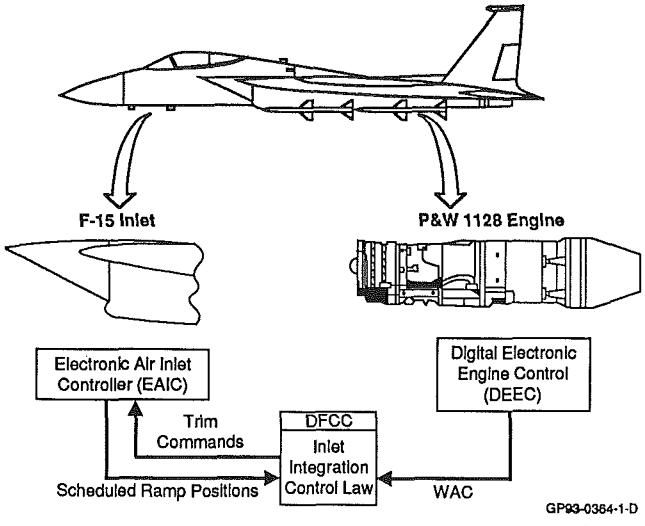

Fig. 1 Inlet integration mode

The test bed for the Inlet Integration mode is the NASA F-15 flight test aircraft, which was used in demonstration of the previous HIDEC modes. The aircraft is equipped with P&W 1128 engines, a growth version of the F100 engine. A key feature on the P&W 1128 engine is a Digital Electronic Control (DEEC) that communicates with the aircraft Digital Flight Control Computer (DFCC). In addition, the aircraft Electronic Air Inlet Controllers (EAIC) have been modified to communicate on the 1553 Mux bus with the DFCC.

The operation of the Inlet Integration mode is illustrated in Fig. 1. The Inlet Integration control law is programmed in the

---

Contributed by the International Gas Turbine Institute and presented at the 34th International Gas Turbine and Aeroengine Congress and Exhibition, Toronto, Ontario, Canada, June 4–8, 1989. Manuscript received at ASME Headquarters October 1989.

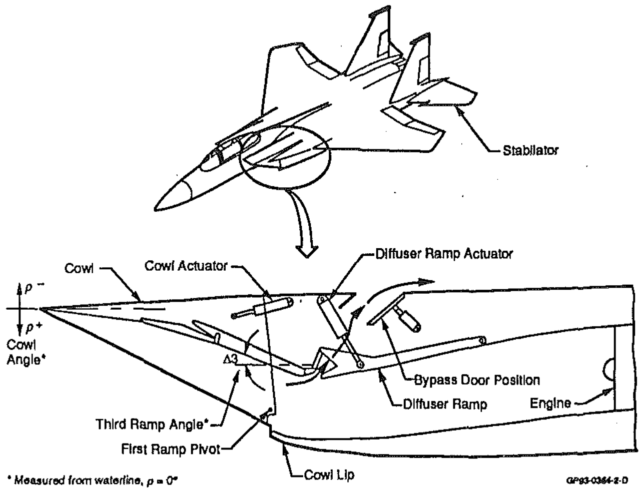

Fig. 2 F-15 air induction system

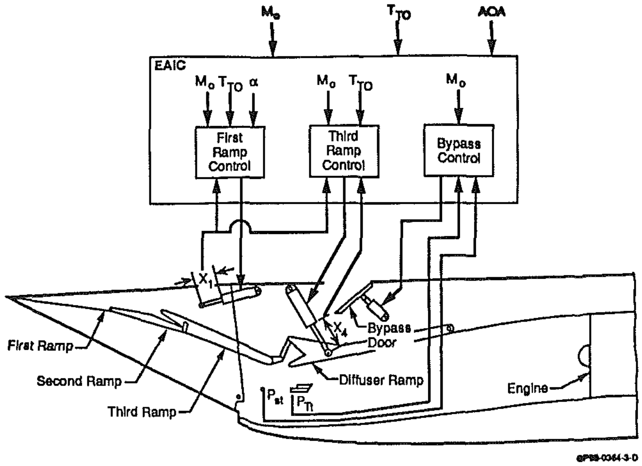

Fig. 3 Inlet control system

DFCC. It uses DEEC calculated engine corrected airflow (WAC), the EAIC base scheduled ramp positions, and the flight condition information available to the DFCC to determine optimal trim commands for the inlet ramps. The control law is designed for supersonic operation only. At subsonic conditions the inlet ramps are always positioned wide open for the best performance and, therefore, are not a candidate for integration.

The development of the Inlet Integration mode is described in this paper, including the Inlet Integration concept, the control law, its implementation on the test bed aircraft, and the predicted performance benefits. Prior to this description, a review of the current F-15 production inlet system is provided.

F-15 Production Inlet System

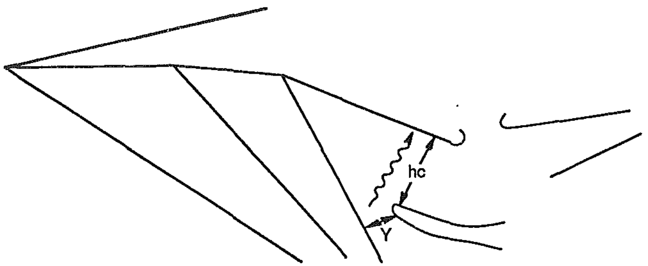

Shock Displacement Ratio = $\frac{Y}{hc}$

Y = Perpendicular distance the 3rd shock stands from the cowl lip

hc = Capture height

GP93-0364-4-D

Fig. 4 Shock displacement ratio

The F-15 inlet, illustrated in Fig. 2, is a two-dimensional, three-ramp, external compression design with partially cut back sideplates. During supersonic operation, compression is accomplished through three oblique shocks and one terminal normal shock. The three compression ramps are all variable. Separate cowl diffuser ramp actuators provide independent control of the first and third ramps. The second ramp position is dependent on the first and third ramp positions. This approach gives the F-15 inlet a unique variable capture feature that minimizes inlet spill drag. The inlet also incorporates a variable bypass system for inlet/engine matching.

Each inlet is controlled by a separate EAIC. The EAIC control logic positions the actuators to yield the scheduled cowl, third ramp, and bypass door positions for the given flight condition and angle-of-attack (AOA). The inlet control system is illustrated in Fig. 3. The first ramp is scheduled with aircraft Mach number, free-stream total temperature, and AOA. The third ramp is scheduled with aircraft Mach number and free-stream total temperature. The bypass door is scheduled with free-stream Mach number and inlet duct Mach number. The cowl and third ramp schedules are designed to maximize inlet and aircraft performance while maintaining stable inlet operation. The bypass door schedule is designed to provide additional inlet stability when it is required.

Inlet performance refers to the quality of the flow the inlet provides to the engine in terms of total pressure and the effect of the inlet on aircraft performance in terms of drag. Inlet performance can be quantified in terms of three components. The first component, inlet drag, is incurred mainly by the spillage of compressed flow over the cowl lip and the discharge of ramp bleed and bypass flows overboard. The second component, total pressure recovery (ratio of total pressure at the engine face to the free-stream total pressure) is a measure of the inlet's efficiency in supplying compressed airflow to the engine. The large final component is stabilator time drag. The large cowl surfaces on the F-15 impart a pitching moment on the aircraft when positioned away from zero AOA. Stabilator trim drag (D_{trim}) is the aircraft drag incurred by the stabilator in counteracting this pitching moment. The inlet drag and pressure recovery are bookkept as part of this aircraft's net propulsive force (FNP). Therefore, supersonic inlet performance can be defined in terms of FNP-D_{trim}.

Nomenclature

ADECS = Adaptive Engine Control System
AOA = Angle of Attack
DEEC = Digital Electronic Engine Control
DFCC = Digital Flight Control Computer
D_{trim} = stabilator trim drag
EAIC = Electronic Air Inlet Controller
FNP = Net Propulsive Force
FTIT = Fan Turbine Inlet Temperature
HIDEC = Highly Integrated Digital Electronic Control
IFTD = In-Flight Thrust Deck
MCAIR = McDonnell Aircraft Company
MUX = Multiplex
NASA = National Aeronautics and Space Administration
NCI = Navigation Control Indicator
P&W = Pratt & Whitney
TT2 = Total Temperature Engine Face
WAC = Engine Airflow, Corrected

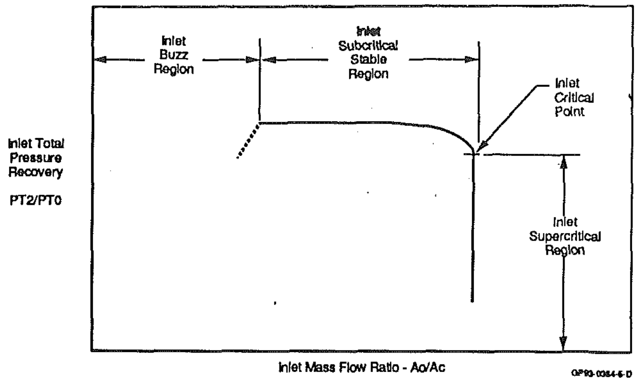

Fig. 5 **Inlet flow stability regions**

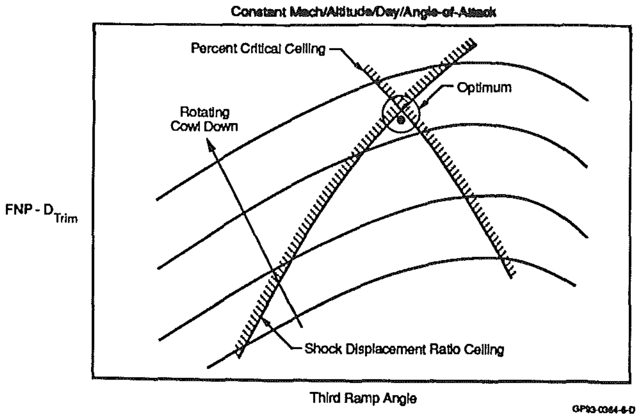

Fig. 6 **Optimizing supersonic installed performance**

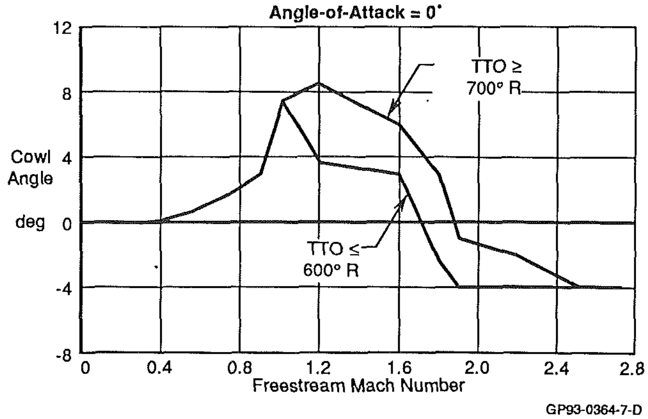

Fig. 7 **1128 base cowl schedule**

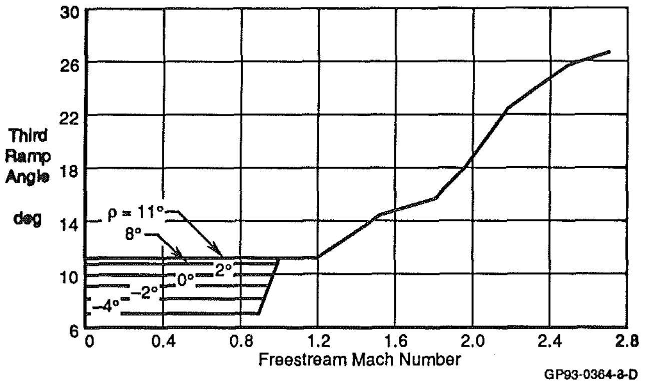

Fig. 8 **1128 base third ramp schedule**

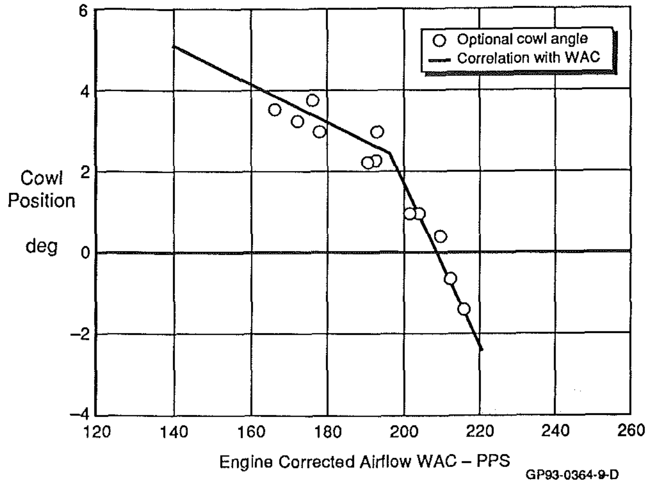

Fig. 9 **Correlation of optimal cowl angle with WAC at Mach 1.8**

Inlet stability refers to the condition of the flow in the inlet duct. Unstable flow produces large variations in the total pressure distribution at the engine face, i.e., high inlet distortion. Two important inlet stability parameters during supersonic operation are shock displacement ratio and percent critical mass flow ratio. Shock displacement ratio, illustrated in Fig. 4, is the perpendicular distance that the third oblique shock stands off the cowl lip divided by the capture height. The capture height is the perpendicular distance from the third ramp to the cowl lip. For stable inlet operation, the shock displacement ratio must remain positive. A negative shock displacement ratio indicates the final oblique shock has been ingested by the inlet producing a slipstream associated with the intersection of the normal and oblique shocks in the inlet duct. The resulting flow instability produces high dynamic distortion at the engine face. The inlet ramps are scheduled to maintain a positive shock displacement ratio.

The inlet percent critical mass flow ratio is also a measure of inlet stability. Percent critical is the ratio of the operating mass flow ratio to the critical mass flow ratio. To illustrate the effect of mass flow ratio on inlet stability, inlet recovery is plotted as a function of mass flow ratio in Fig. 5. The regions of inlet stability are shown. In the inlet buzz region, the low inlet mass flow causes a flow instability resulting in an organ pipe resonance in the inlet duct. In the supercritical region (or inlet critical point), the engine airflow demand exceeds the inlet capacity, causing the normal shock to be ingested and producing high inlet dynamic distortion. In the intermediate subcritical region, stable inlet operation occurs. The inlet bypass door is scheduled to open at the onset of buzz. This will raise the mass flow ratio and stabilize the flow. The inlet ramps are scheduled to avoid supercritical operation.

Supersonic inlet performance and stability are affected by flight condition, engine corrected airflow (WAC), ambient temperature, and AOA. For any set of operating conditions, a set of optimal ramp angles exists that maximizes inlet performance while maintaining stability. To illustrate this, FNP–D_{trim} is plotted for various combinations of cowl and third ramp angles in Fig. 6. Stability ceilings are placed on the plot by setting limits on percent critical and shock displacement ratio. The optimal set of ramp angles is at the maximum FNP–D_{trim} located within the stable region.

The EAIC has inherent limitations, which prevent the optimization of inlet performance across the range of aircraft operation. First, the EAIC receives limited information about aircraft operation (only Mach, TTO, and AOA) and no information about engine operation (WAC). As a consequence, an indirect scheduling method must be used in the EAIC. In this method, parameters that directly affect inlet performance and stability (such as WAC) are represented with indirect parameters (such as TT2). Second, the EAIC is severely limited

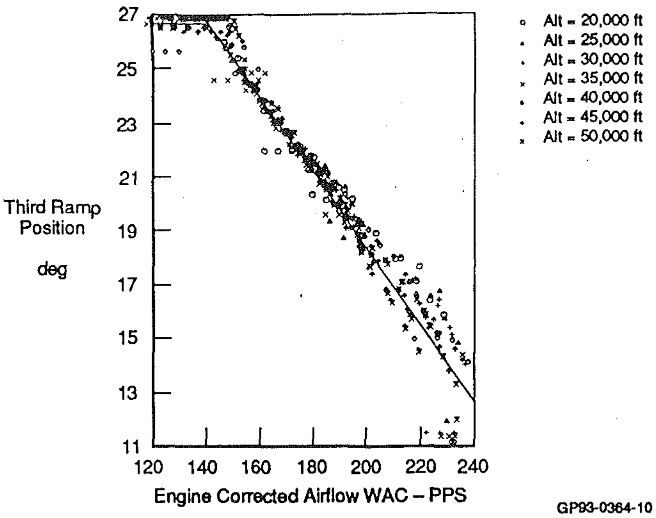

Fig. 10 Correlation of optimal third ramp angles with WAC

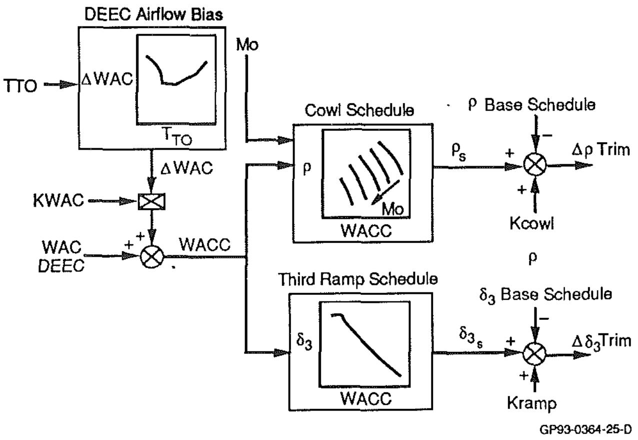

Fig. 11 Inlet integration control law

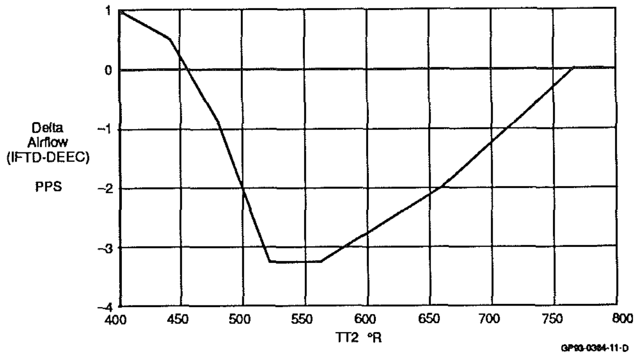

Fig. 12 DEEC airflow bias

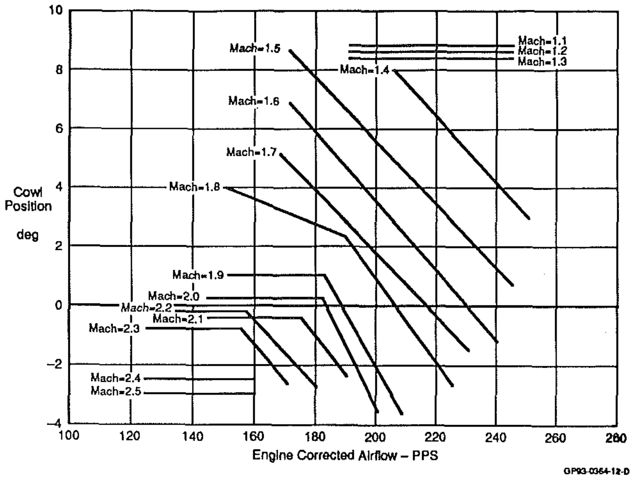

Fig. 13 Inlet integration cowl schedule; angle-of-attack = 0 deg

in the amount of memory allocated for the schedules. This limits the size of the schedules, thereby reducing their accuracy.

Within these limitations, the EAIC schedules are designed to maximize inlet performance while maintaining stability. The schedules are tailored to a specific engine type with its unique WAC demand. The schedules are designed at 36,089 feet on a cold day where the highest engine airflows occur. Here, optimal angles are determined over the range in Mach number at a zero AOA. These angles are used to form base schedules. Then, these schedules are adjusted and biased with TTO and AOA to achieve full flight envelope and temperature range capability. In this process, inlet performance is comprised in order to maintain stability over the expected range of aircraft and engine operation. The resulting base cowl and third ramp schedules for the P&W 1128 are shown in Figs. 7 and 8. These schedules produce suboptimal inlet performance due to the inherent EAIC limitations.

Inlet Integration Concept

In the NASA HIDEC program, the goal of the Inlet Integration mode is to obtain optimal inlet performance throughout the supersonic flight envelope, over the full range of ambient temperatures. The potential to realize this goal has been greatly increased with the recent advances in integrated controls on the HIDEC program. By integrating the EAIC with the DEEC and the DFCC, additional aircraft and engine information is available for use in the Inlet Integration mode.

To accomplish our goal, a digital simulation was developed and used to determine the optimal ramp angles at several hundred different supersonic operating conditions. The simulation was performed with TDINLET, MCAIR's highest fidelity analytical/empirical representation of the F-15 inlet, and a P&W 1128 engine performance model. An optimization routine was also added to the simulation to automate the process. This simulation was then run across the supersonic flight envelope for various levels of engine airflow at standard, hot, and cold day temperatures. The resulting data base of optimal ramp angles was analyzed for correlation parameters. The optimal cowl angle was found to correlate well with WAC and Mach number. This is illustrated for 1.8 Mach in Fig. 9. In this figure, the optimal cowl angle is plotted against WAC for various combinations of day temperatures, altitudes, and levels of WAC. The correlation formed for the cowl angle at 1.8 Mach is sketched on the plot. The optimal third ramp angle was found to correlate solely with WAC as illustrated in Fig. 10. In this figure, the optimal third ramp is plotted against WAC at various altitudes. For each altitude, the optimal angles are plotted for the range in Mach number at various day temperatures and at different levels of WAC. The linear correlation formed for the third ramp angle is sketched on the plot and shows good agreement with the data. These correlations were curve fit to produce schedules for Inlet Integration.

The Inlet Integration scheduling technique has several advantages over the current EAIC scheduling. The new technique uses the parameters that directly affect inlet performance to schedule the ramps. This simplifies the scheduling logic while increasing its accuracy. The performance of the two techniques is compared later in this paper in the Performance Improvements section. Further, the Inlet Integration schedules, although developed for the P&W 1128, are good for any engine derivative installed in the F-15. Since the schedules were developed as a function of engine airflow demand, they are no

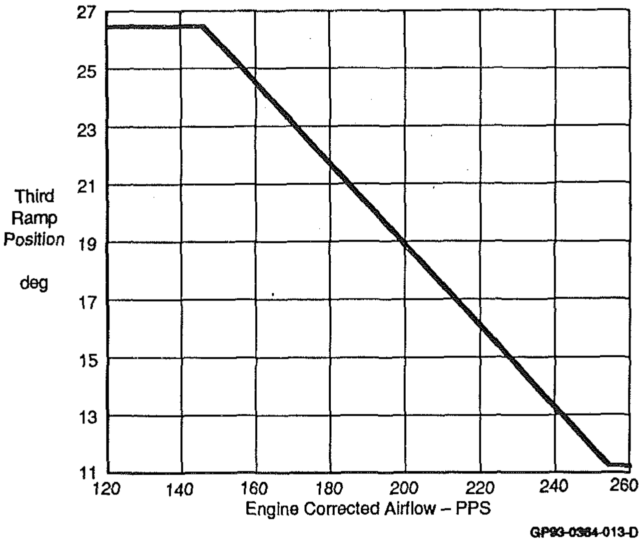

Fig. 14 Inlet integration third ramp schedule

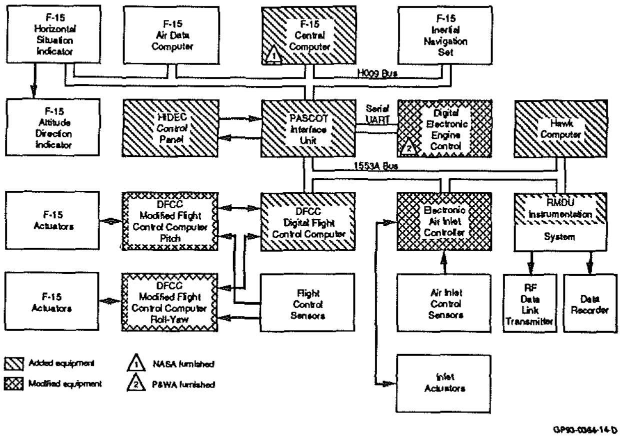

Fig. 15 Inlet integration avionic architecture

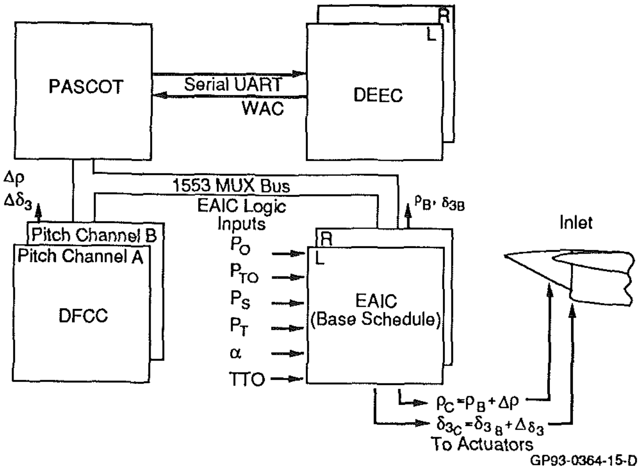

Fig. 16 Inlet integration communication

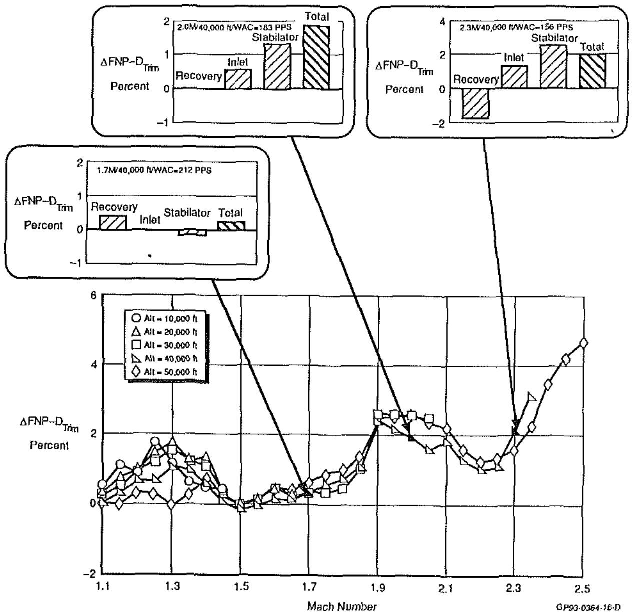

Fig. 17 Inlet integration performance improvements—standard day

longer tailored to a specific engine type. The transferability of the Inlet Integration schedules has been proven in digital propulsion simulations with several engine types: F100-PW-220, F100-PW-229, F119-PW-100, GE-129, and GE-F120/21C2.

Inlet Integration Control Law

A control law has been developed to implement the Inlet Integration concept in the DFCC on the test bed aircraft. This control law is depicted in Fig. 11. The DEEC calculation of WAC is adjusted for an airflow bias. This bias is an inaccuracy in the WAC calculation caused by simplifying assumptions in the DEEC. It was quantified with the in-flight thrust deck (IFTD) during the ADECS testing and was correlated with total temperature, as illustrated in Fig. 12. The bias ranges from 1 lb/sec to just under −3 lb/sec.

The improved airflow calculation (WACC) is used to schedule the ramp angles. The Inlet Integration cowl schedule, shown in Fig. 13, is a function of WACC and Mach number. The Inlet Integration third ramp schedule, shown in Fig. 14, is a function of WAC only. The base scheduled angles from the EAIC are subtracted from the Inlet Integration scheduled angles to produce trim commands.

The control law was structured to take advantage of the capability to reprogram the DFCC during flight test. This will allow the flight test program to be structured such that the concept and technology can be demonstrated prior to refining the system performance. During the flight demonstration of the system, the Inlet Integration scheduled ramp positions can be varied using adders, Kcowl and Kramp, as seen in Fig. 11. Values for Kcowl and Kramp are selected by the pilot via the Navigation Control Indicator (NCI). This will permit a fine tuning of the schedules. In addition, the magnitude of the DEEC airflow bias can be varied with a multiplier, KWAC, if discrepancies are discovered.

Inlet Integration Implementation

The avionic architecture on the test bed aircraft is illustrated in Fig. 15. The equipment that has been modified or added to the baseline F-15 for the HIDEC program is shaded appropriately. The HIDEC control panel is located in the cockpit and is used by the pilot to engage the various HIDEC modes. Communication between the various equipment occurs across three buses: the aircraft standard H009 bus, the Serial UART bus, and the 1553A bus. The Programmable Asynchronous Serial Communication Translator (PASCOT) has been installed to permit the interchange of information between the three data buses and the HIDEC Control Panel. The equipment of particular relevance to the Inlet Integration mode is the DEEC, DFCC, and the EAIC.

The DEEC has been modified to communicate over the Serial

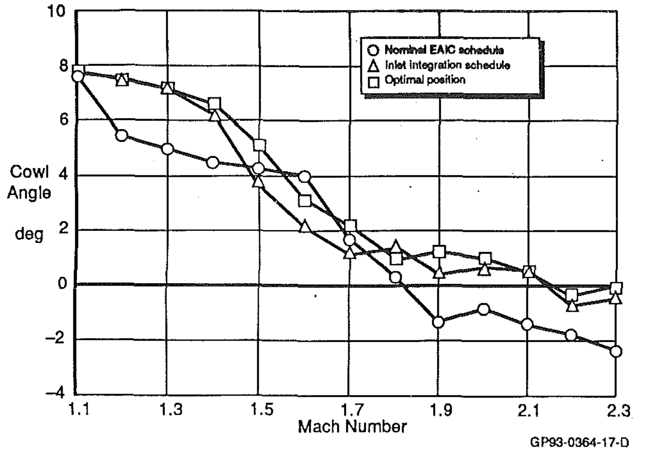

Fig. 18 Comparison of the scheduled cowl angles; standard day—40,000 ft

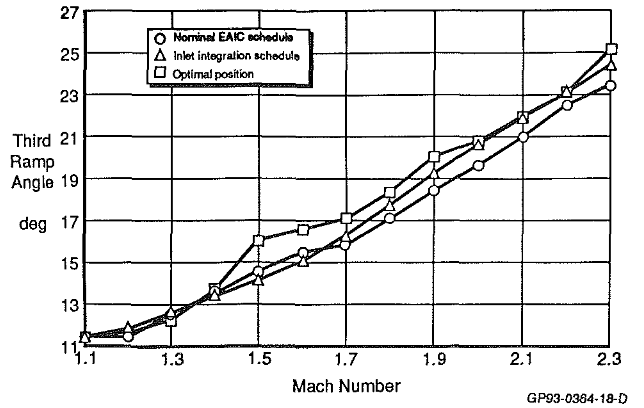

Fig. 19 Comparison of the scheduled third ramp angles; standard day—40,000 ft

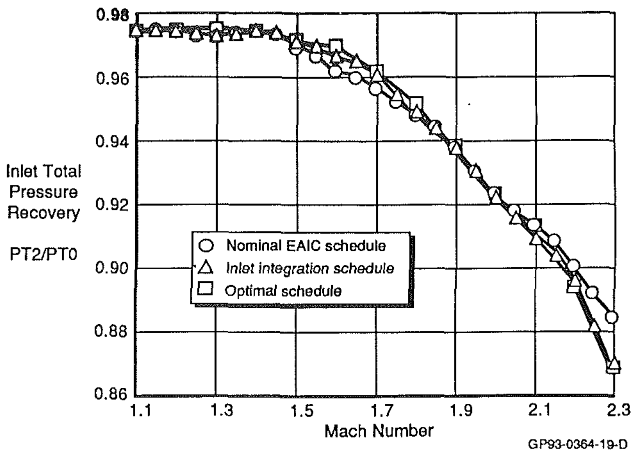

Fig. 20 Comparison of inlet recoveries; standard day—40,000 ft

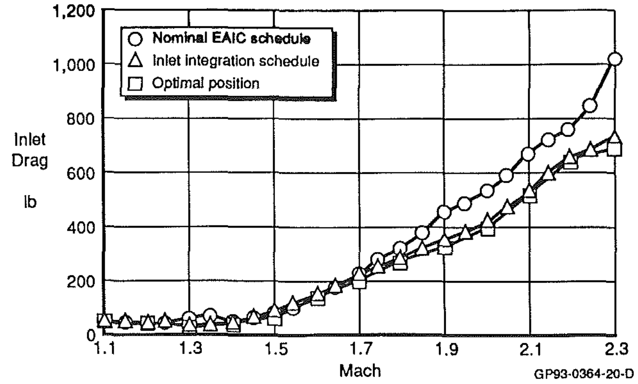

Fig. 21 Comparison of inlet drag; standard day—40,000 ft

UART bus. The DEEC outputs a 100-word message consisting of scheduled, measured, diagnostic, and calculated engine parameters. This message includes the calculation of WAC.

The DFCC and the modified analog pitch and roll/yaw computers have replaced the F-15 analog Control Augmentation System (CAS). The DFCC is a four-channel microprocessor featuring parallel processing. Redundant pitch control laws are contained in two channels and redundant roll/yaw control laws are in the remaining two channels.

The EAIC consists of three major components: the digital computer, the pressure sensors, and the input (analog-to-digital) and output (digital-to-analog) interfaces. For Inlet Integration, the EAIC digital computer has been modified for communication with the 1553 Bus. The EAIC output message consists of base schedule ramp angles, command ramp angles, and the ramp feedback positions. The EAIC accepts delta trims to the cowl and third ramp base schedules within the EAIC, the times are added to the baseline schedules. The resulting cowl angle is adjusted for AOA. The commanded angles are range limited for safety.

The communication between the equipment for the Inlet Integration system is illustrated in Fig. 16. The Inlet Integration control law resides in the DFCC Pitch Channels. Pitch Channel A is dedicated to the left inlet and Pitch Channel B to right inlet. The WAC calculations from the left and right DEEC are sent to the PASCOT across the two Serial UART Buses. The PASCOT directs the DEEC information to the appropriate Channels in the DFCC. The control laws calculate the trim commands to the inlet ramp angles. These commands are then sent across the 1553A mux bus to the appropriate EAIC.

Inlet Integration Performance Improvements

The primary benefit of the Inlet Integration mode is an increase in inlet performance (FNP-D_{trim}) during supersonic operation. The performance improvements discussed below are predicted values for the testbed aircraft configuration. These predictions are based on the actual Inlet Integration control logic that will be flight demonstrated. The Inlet Integration performance improvements on a standard day are shown in Fig. 17. Here, the change in FNP-D_{trim} relative to the nominal EAIC schedules is plotted against Mach number with lines of constant altitude. The performance improvements range from 0 percent at 1.5 Mach to over 4 percent at 2.5 Mach. In all cases, Inlet Integration maintained stable inlet operation. The component breakdown of the performance improvements is shown at 40,000 ft for 1.7 Mach, 2.0 Mach, and 2.3 Mach. At 1.7 Mach, Inlet Integration trims the inlet ramps to obtain better total pressure recovery at a slight cost in stabilator trim drag. At 2.0 Mach, Inlet Integration trims the inlet ramps to reduce inlet and stabilator trim drag. At 2.3 Mach, Inlet Integration reduces stabilator trim and inlet drag while compromising inlet total pressure recovery.

To understand these performance improvements better, a comparison was made between the nominal EAIC base schedules, the Inlet Integration schedules, and the optimal ramp positions at 40,000 feet. Comparisons of the cowl and third ramp positions are presented in Figs. 18 and 19. In Fig. 18, the Inlet Integration scheduled cowl angle closely tracks the optimal position. The optimal and Inlet Integration angles are seen to cross over the nominal between 1.5 and 1.7 Mach. In Fig. 19, the Inlet Integration ramp angle closely tracks the optimal angle except for a region between Mach 1.4 and 1.7.

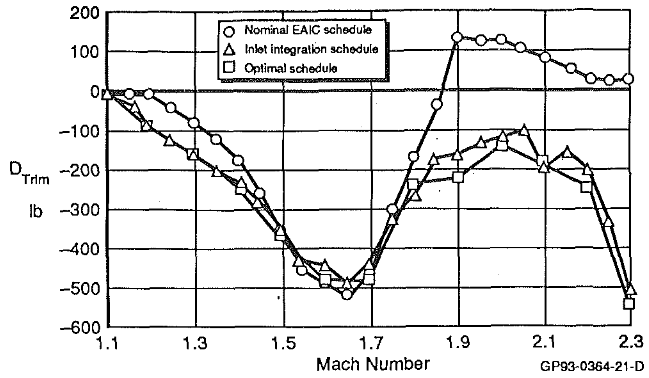

Fig. 22 Comparison of stabilator trim drag; standard day—40,000 ft

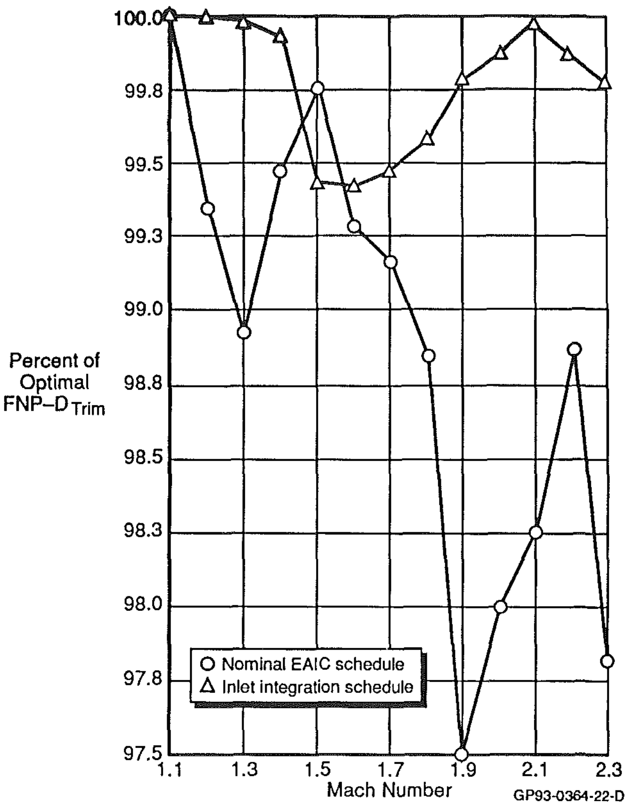

Fig. 23 Comparison of total inlet performance; standard day—40,000 ft

In this region, the linear correlation that comprises the Inlet Integration third ramp schedule yields a slightly off-optimal position. The crossover in the cowl schedule and the off-optimal third ramp position explain the lack of performance improvement seen in Fig. 17 between Mach 1.5 and 1.7.

Next, the performance improvements are compared for the three sets of ramp positions at 40,000 feet. The inlet recovery resulting from each set of ramp positions is compared in Fig. 20. Here, the recovery from the optimal and Inlet Integration is seen to be higher than the nominal between 1.5 and 1.8 Mach and lower than the nominal at Mach numbers greater than 2.1. This was seen in the component breakdown of performance improvements in Fig. 17. The inlet drag resulting from each set of ramp positions is compared in Fig. 21. At Mach numbers greater than 2.2, the optimal and Inlet Integration have substantially less drag than the nominal. In Fig. 22, the stabilator trim drag resulting from each set of ramp positions is compared. The optimal and Inlet Integration have substantially

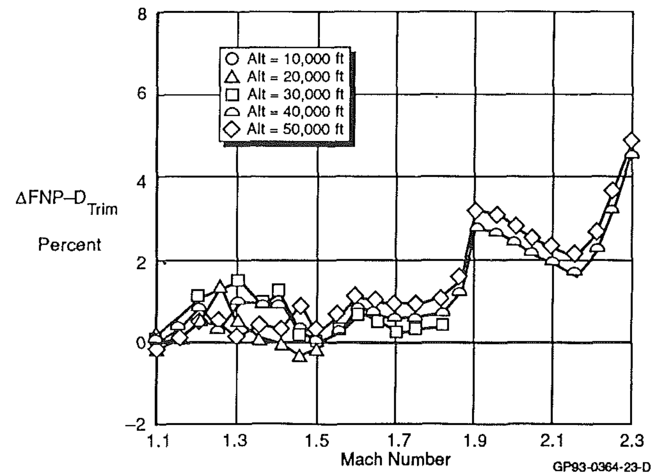

Fig. 24 Inlet integration performance improvements—hot day

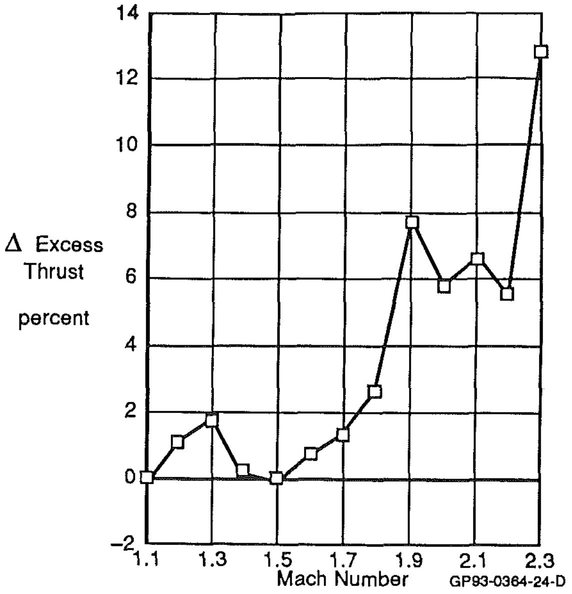

Fig. 25 Performance improvements translate into increased aircraft acceleration; standard day—40,000 ft

less stabilator trim drag than the nominal everywhere except between 1.5 Mach and 1.7 Mach.

The overall performance of the nominal and Inlet Integration schedules is compared to the optimum in Fig. 23. The percent of optimal FNP-D_{trim} is shown for the Inlet Integration and the nominal schedules. The Inlet Integration schedules achieve at least 99.4 percent of the optimal performance across the Mach sweep. The nominal schedule performance improvements are seen to be more erratic than Inlet Integration. This is a result of the indirect scheduling method. The suboptimal performance of the nominal schedules is due to several factors. The nominal schedules were designed at the highest engine airflows (36,089 ft/cold day). At 40,000 ft, on a standard day the engine airflows are lower. The temperature bias in the nominal schedules cannot fully account for this large airflow variation. Further, in the high Mach region, Inlet Integration achieves a significant reduction in inlet drag and stabilator trim drag, which was not realized by the nominal schedules.

The Inlet Integration performance improvements on a hot day are shown in Fig. 24. Slightly higher performance benefits are seen than on a standard day. On a hot day, the engine airflow demand is reduced. The nominal schedules are biased with TTO in an attempt to account for the reduced WAC.

Due to the limitations of this method, the nominal EAIC angles move further from the optimal angles. The Inlet Integration schedules, utilizing the DEEC WAC calculation, maintain their accuracy. Other changes in operating conditions, such as engine deterioration, have been shown to decrease the nominal schedules' accuracy, thereby increasing the performance improvements available to Inlet Integration. With a deteriorated engine on a hot day, Inlet Integration has been shown to achieve up to an additonal 5 percent increase in FNP-D_{trim} over the standard day, nominal engine benefits.

During supersonic operation, the performance benefits (in terms of FNP-$D_{\rm trim}$) will translate into significant increases in aircraft acceleration (in terms of excess thrust: FNP-$D_{\rm aircraft}$). In Fig. 25, the increase in excess thrust is shown at 40,000 ft over the Mach range. A 13 percent increase in excess thrust is available at Mach 2.3. This increase will translate into significant decreases in aircraft acceleration times. Our six-degree-of-freedom simulation predicts the aircraft will accelerate from Mach 1.4 to 2.2 at 40,000 feet in 8 percent less time with Inlet Integration. After completing the flight demonstration, the actual performance improvements will be compared with the prediction.

Conclusion and Future Effort

The Inlet Integration mode will be flight demonstrated in the NASA HIDEC program. In this mode, the F-15 inlet control system will be coupled with the P&W 1128 engine control system to obtain additional performance. The Inlet integration control law will trim the inlet ramp positions based upon engine corrected airflow demand. Our digital simulations show the Inlet Integration control logic schedules the inlet for lower inlet drag and stabilator trim drag. Excess thrust improvements as great as 13 percent are anticipated during supersonic flight. These thrust improvements will result in significant decreases in aircraft acceleration times. After demonstrating performance improvements with nominal P&W 1128 engines, the engines' airflow demand will be reduced to simulate another engine type. New thrust improvements will be demonstrated with the reduced airflow engines to demonstrate the transferability of the Inlet Integration control law.

By integrating the inlet and engine controllers, significant supersonic thrust improvements can be realized. These thrust increases can be attained without size or weight increases to the aircraft. In addition, this integration will result in supportability benefits by eliminating the need to replace inlet controllers when different engine types are installed in the same aircraft.

In Inlet Integration, the inlet controls (ramp positions) are optimized by using information from the other aircraft systems (the DEEC and DFCC). As the control of each system is integrated with the other systems, it becomes increasingly difficult to optimize the performance of the total system. Therefore, following Inlet Integration, an integrated control process called Performance Seeking Controls (PSC) will be implemented on the NASA F-15. In PSC, the engine and inlet control effectors will be trimmed by a real-time optimization designed to maximize aircraft performance. This optimization will account for engine degradation using real-time parameter identification techniques. To accomplish this, a Kalman filter will process engine data to update an on-board model of the engine for use in the optimization process. The PSC program involves some high technical risks but promises to develop key technology for future aircraft.

References

Burcham, F. W., Jr., and Haering, E. A., Jr., 1984, "Highly Integrated Digital Engine Control System on an F-15 Airplane," AIAA Paper No. 84-1259.

Landy, R. J., Yonke, W. A., and Stewart, J. F., 1987, "Development of HIDEC Adaptive Engine Control Systems," ASME JOURNAL OF ENGINEERING FOR GAS TURBINES AND POWER, Vol. 109, pp. 146–151.

Putnam, T. W., and Burcham, F. W., Jr., Andries, M. G., and Kelly, J. G., 1985, "Performance Improvements of a Highly Integrated Digital Electronic Control System for an F-15 Airplane," NASA TM-86748.

Yonke, W. A., Landy, R. J., and Cushing, J. M., 1984, "Integrated Flight/Propulsion Control: HIDEC Modes," NAECON Paper.

Yonke, W. A., Terrell, L. A., and Myers, L. P., 1985, "Integrated Flight/Propulsion Control: Adaptive Engine Control System Mode," AIAA Paper No. 85-1425.

Yonke, W. A., Landy, R. J., and Stewart, J. F., 1987, "HIDEC Adaptive Engine Control System Flight Evaluation," ASME Paper No. 87-GT-257.

Simulation of Bird Strikes on Turbine Engines

E. Niering
Turbinen-Union
Munich, Federal Republic of Germany

External components of aeroengines, such as casings and intake blades, must be capable of withstanding bird strikes. Various methods of computer simulation that have been developed are presented in summary. The most accurate and meaningful results are obtained with finite element programs specifically developed for impact events. Bird and component are divided into finite elements. The component model must allow for great elastic-plastic deformation, where the yield strength is a function of the strain rate. A model shape and a homogeneous substitute material must be defined for the complicated and nonhomogeneous structure of the bird. Bird strikes on a rotating spinner and an intake blade are investigated with the finite element program DYNA3D.

1 What Is Bird Strike?

The impingement of birds on flying aircraft — the so-called "bird strike" — seriously jeopardizes flight safety as regards component stresses and frequency of events.

1.1 Stresses. According to Mattingly (1976), the impact force exerted by a 1.8-kg bird on an aircraft flying at 485 km/h is 127 kN. At a speed of 970 km/h, the impact force increases to 510 kN. In the tests conducted by Wilbeck (1981), the birds were shot onto rigid, flat plates by means of pressure-gas operated guns. Two typical pressure curves as measured in the impact centers are shown in Fig. 1.

The pressure waves originating at the impact location and propagating through the bird produce the pressure peaks, the so-called "Hugoniot pressures." The pressure maximum at the beginning of the event is dissipated by relaxation waves propagating from the free surface of the bird.

The final "stagnation pressure" yields the plateau-type pressure curves shown in Fig. 1. All in all, the behavior of impinging birds resembles that of a fluid. The pressure values for various bird masses and impact velocities summarized in Table 1 are also taken from graphs of Wilbeck (1981).

1.2 Frequency of Events. According to the investigations by Hild (1974, 1981), approximately 600 bird strike events occur in the Federal Republic of Germany each year with the resultant damage amounting to some ten million Deutschmarks. It is assumed that at least 50 military jets and some commercial or passenger jets have crashed because of bird strike since the introduction of jet propulsion. According to Mattingly (1976), the US Air Force alone registered an annual rate of 400 bird strike events in the ten years before 1974 with a resultant damage of more than ten million dollars. Eleven pilots died and 19 aircraft were lost. McCarty (1984) estimates the damage to the US Air Force due to the loss of aircraft at 980 million dollars for the period 1966 to 1977. He reports six crew members who died. Comprehensive material on bird strike events and the damage to aviation of various industrial nations was compiled in tabular form by Hild (1974).

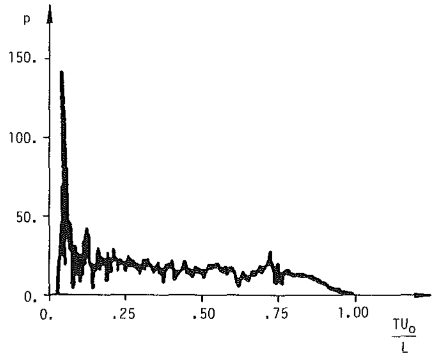

Fig. 1(*a*) U_o = 197 m/s

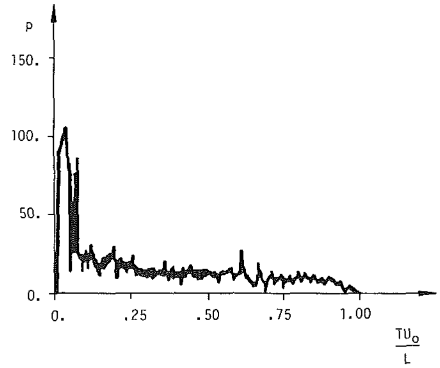

Fig. 1(*b*) U_o = 225 m/s

Fig. 1 Two pressure curves as measured in the impact centers; U_o = impact velocity; T = impact duration; L = bird length; p = pressure in MPa

---

Contributed by the International Gas Turbine Institute for publication in the JOURNAL OF ENGINEERING FOR GAS TURBINES AND POWER. Manuscript received by the International Gas Turbine Institute October 1988.

Table 1 Hugoniot pressure and stagnation pressure for various impact conditions

Bird mass in kg	Impact velocity in m/s	Hugoniot pressure in MPa	Stagnation pressure in MPa
0.5 - 0.6	120	45	3 - 7
0.5 - 0.6	200	110 - 140	12 - 19
2.	160	80	17
4.	160	70 - 130	12

Near the ground, i.e., in particular during takeoff and landing, the risk of a bird strike is greater than during flight at higher altitudes. According to Mattingly (1976), 75 percent of all birds spend their whole life flying at altitudes below 150 m. Small birds fly only at low altitudes. Large birds, such as the crane, goose, and eagle, however, have been observed as high as 6000 m above sea level. Therefore, the less frequent strikes at higher altitudes are particularly dangerous. The same author also states that 43 percent of all bird strikes occur at altitudes below 150 m, 17 percent at altitudes between 150 and 300 m, 27 percent between 300 and 600 m, and the remainder at higher altitudes.

1.3 Jeopardized Aircraft Components. Aircraft components that are particularly jeopardized by bird strikes include the intake blades of turbine engines, propellers, windscreens, and plastic items. The velocity of impact on stationary components is determined by the velocity of the aircraft, which in the case of military aircraft may be in the sonic range in low-level flight or even beyond at higher altitudes. The higher the speed of the aircraft, the greater the damage on the stationary component. In the case of rotating engine components, the relative speed between bird and component depends also on the speed of revolution. For this reason, the damage on rotating components is more extensive at medium aircraft speed.

This paper deals mainly with bird strikes on turbine engines. In this case, the resultant stresses, in particular of the intake blades, are of such a degree that freedom of damage, or even function, can generally not be ensured for all physically possible impact conditions. The bird strike capability is defined in the engine specification. A main requirement on the blading is that no parts are knocked off. The hard parts passing through the engine and the resultant rotor imbalance would endanger the engine more than the bird body. Casings must be dimensioned such that they at least maintain their structural function after an impact "acceptable" as per specification has occurred.

1.4 Bird Strike Organizations. The danger of bird strike has increased with higher flight speeds and the use of jet engines. This has led to the foundation of national and international organizations. In 1964, the "Deutsche Ausschuß zur Verhütung von Vogelschlägen" (German Bird Strike Committee) was founded (Keil, 1981; Hild, 1981). Since 1966, the "Bird Strike Committee Europe BSCE" has been working on a European level (Dahl, 1984). The "International Civil Aviation Organization" has been working worldwide and has prepared the data base "IBIS," the "International Bird Strike Information System" (NN., 1982).

2 Survey of the Paper

Aircraft and engine manufacturers endeavor to design their products as bird-proof as possible. Mathematical analysis and simulation on modern computer systems provide information on component stresses as early as in the design phase. Test-associated calculations provide information that otherwise could hardly be obtained because of the considerable metrological problems involved.

The following sections define the physical and mathematical problems involved. Section 4 reports the history of usual calculation methods. It is followed by a summary of test reports from the literature, which can be useful for the development of calculation methods. Section 6 presents the simulation of bird strikes by the currently most efficient procedure, the finite element method, as performed by the author.

3 Requirements for Calculation Procedures

3.1 Bird Model. The definition of a suitable bird model is the main problem in the simulation of bird strike. It should be capable of representing measured stress developments as shown in Fig. 1. For continuum-mechanics calculations, a model shape must be found and the nonhomogeneous structure of real birds must be homogenized. Suitable mean values for compressibility and density of the fluid model must yield the same stresses as the real bird. Since high compression and shear rates occur in the bird material upon impact, internal friction may also have to be taken into account. Because of the high degree of deformation, a geometric nonlinear calculation is required, i.e., the Euler or Lagrange formulation of continuum mechanics must be applied.

3.2 Component Model. The component model must allow for great elastic and plastic deformation, and must therefore be of nonlinear design in terms of geometry and material. Here, the Lagrange notation common for solid body mechanics is appropriate. With the high deformation rates involved, the yield strength must be definable as a function of the strain rates. It should also be possible to simulate the separation of fragments of the blade.

3.3 Contact Conditions. The impact and sliding conditions at the contact point must also be established mathematically. Numerical contact algorithms require considerable computer time. Therefore, these calculations are normally performed on vector computers.

4 Calculation Procedures and History

In the past, many attempts have been made to calculate bird strike events. The procedures applied often insufficiently fulfill the requirements per section 3. Recent finite-element methods however provide for very accurate calculations.

In parallel with impact tests against rigid walls, simple unidimensional analytical estimates are often made, which have been described by Wilbeck (1978, 1981) and Cassenti (1979). For a perpendicular impact, the Hugoniot pressure is

$$p_H = \rho_o v_s v_o$$

where ρ_o is the initial density, v_o is the initial velocity, and v_s the velocity of sound in the bird material. The stagnation pressure is obtained as

$$p_s = \frac{1}{2} \rho_o v_o^2$$

With these formulas, the pressure development in the impact center can be roughly estimated.

To assess the strain of components such as engine blades, three-dimensional calculations are required. Initially, only linear calculations were made in which the blade is represented either by its modal data, by a spring-mass system, or by a simple bar. The shock wave and thus the Hugoniot pressure in the bird are neglected. For the calculation of the stagnation pressure it is assumed that the bird is substitutable by a series of incompressible fluid jets connected in parallel. The calculation of the diversion pressure in the fluid jets is based on work by Schach (1934, 1935). To enable representation of the nonlinear behavior of the blade in terms of geometry and material, the fluid jet model was later included in nonlinear FE programs.

Table 2 Mathematical procedures for investigation of bird strike problems

Author (Year)	Blade model	Bird model	Calculating program
Cornell (1976)	Spring-mass-system	Fluid jet	-
Denke (1977), Eide (1977), Morris (1977)	Finite elements, modal	Fluid jet	IMPACT
Alexander (1981)	Finite elements, modal	Fluid jet	NASTRAN
Engblom (1980)	Finite elements, elastic-plastic	Fluid jet	MARC
McCarty (1980, 1983, 1984) Nash (1983) Brockman (1984)	Finite elements, elastic-plastic	Fluid jet	MAGNA
Storace (1982)	Finite elements, elastic-plastic	Fluid jet	NONSAP
Lawson (1987)	Finite elements, elastic-plastic	Finite elements, water friction-free	DYNA3D
Niering (1988)	Finite elements, elastic-plastic	Finite elements, viscous water-air mixture	DYNA3D

Table 3 Bird strike test reports

Author (year)	Type of tests performed
Barber, Taylor, Wilbeck (1975, 1978) Wilbeck (1978, 1981)	Perpendicular shots against flat rigid plates
Challita, Barber (1978)	Oblique shots against flat rigid plates
Barber, Taylor, Wilbeck (1979)	Shots against resilient plates
Ikeda, Miyachi, So Fue (1985) Bertke (1982) Ravenhall, Salemme (1978) Graff, Stoltze, Varholak (1976) Johns (1974)	Shots against engine blades
Gourley, Littel (1983) West (1980) Coker, Magnusson (1978) Simmons, Stenger (1983) Fonden, Persson (1983) Pinnel (1983) Heath, Gould (1983)	Shots against cockpits and windscreens
Welsh, Centonze (1986) Wilbeck (1981)	Development of synthetic birds

A further improvement is achieved by dividing the bird into finite elements. Thus, the geometric impact conditions can be established more accurately. With the use of a material law that accounts for compressibility, representation of the Hugoniot pressure in the bird becomes possible. The publications summarized in Table 2 indicate the history of bird strike calculation methods.

5 Literature on Test Results

Test results are required for the development of a continuum-mechanics substitute model for birds and for the testing of mathematical procedures. Table 3 shows a listing of applicable publications.

Some of these reports provide measurement results of perpendicular bird strikes against flat rigid plates. Measured pressure curves for the impact center and sometimes also for measuring points located radially outward are presented. Parameters are the bird mass and the impact speed. The test setup is normally described and high-speed photographs of approaching and impinging bird bodies enclosed.

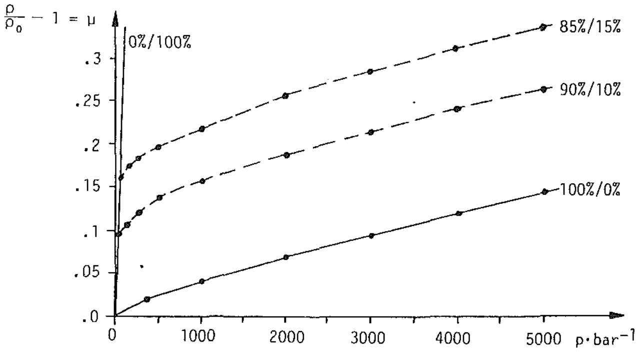

Fig. 2 Compressibility of bird substitute materials and their water/air content

Papers on impact test of components such as engines, blades, cockpits, and windscreens of aircraft have been published in great number.

The average masses and sizes of the most frequent bird types are summarized in a report by Hild (1947). Some authors have investigated the suitability of synthetic birds made of gelatin.

6 Finite-Element Calculations

Currently the most efficient method for the mathematical simulation of bird strikes is the finite-element method. This section presents the investigations performed by the author with the calculation program DYNA3D.

6.1 Calculation Program. DYNA3D is a finite-element program in Lagrange formulation developed by Halquist (1983, 1986) specifically for high-speed impact events. It contains contact algorithms and a high number of material laws, which connect Jaumann stress rates $\overset{\nabla}{\sigma}_{ij}$ with strain rates $\dot{\epsilon}_{kl}$

$$\overset{\nabla}{\sigma}_{ij} = C_{ijkl}\dot{\epsilon}_{kl} \tag{1}$$

Various elastic-plastic material laws for the modeling of components are available. For the modeling of the bird, the "null material," a friction-free hydrodynamic material law can be used, which corresponds essentially to Euler's equations of fluid mechanics. This model was used for the majority of calculations. A fluidic material law with compression and shear viscosity was included in the program as a result of minor deviations from test results and numerical problems.

Calculation of rotating components must account for the centrifugal force. Two methods were included by modification and new development of subroutines. In the first method, the axis of rotation of the component is modeled. For the nodes of the component model, the velocities of a rotary motion are specified as initial conditions. In the case of the second method, the centrifugal forces are calculated and added to the existing nodal forces of the stationary component only. A suitable rotational speed characteristic to simulate the starting procedure without causing centrifugal force shocks was developed by Niering (1989).

6.2 Modeling. In contrast to the blade model, a suitable shape and the fineness of division into finite elements of the bird model is initially unknown. Furthermore, a homogeneous substitute must be defined for the complex and nonhomogeneous structure of the bird body.

Comprehensive measurements made by Wilbeck (1981) and

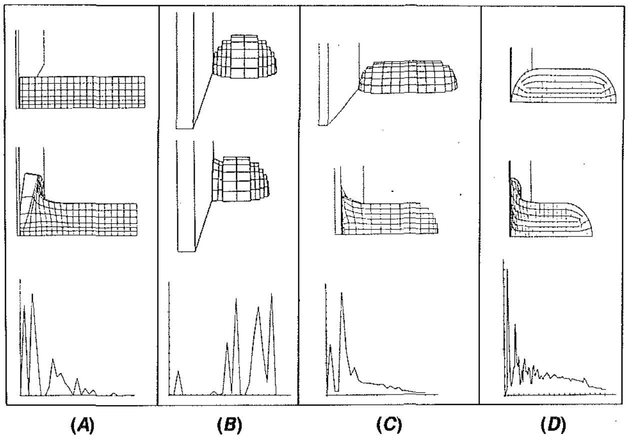

Fig. 3 Test of various FE bird models by calculation of the pressure curves for perpendicular bird strikes against a flat rigid plate in the impact center.

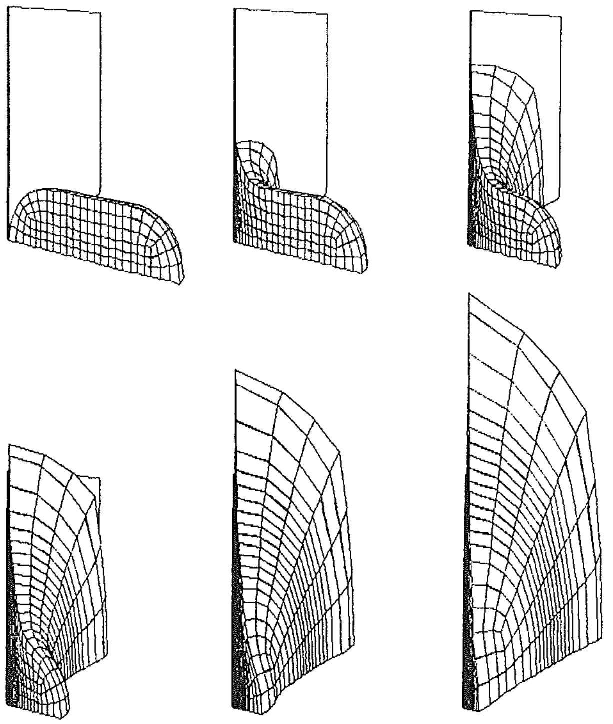

Fig. 4 Mathematical simulation of perpendicular impacts against a rigid flat wall using a quarter-model

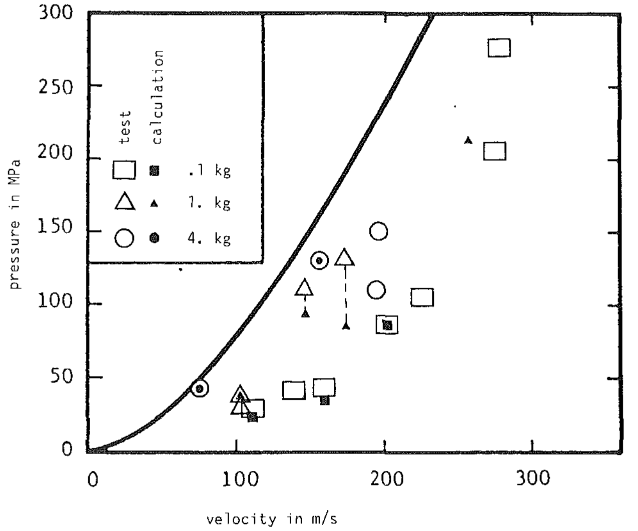

Fig. 5 Calculated and measured Hugoniot pressures for perpendicular bird strikes against a flat rigid plate

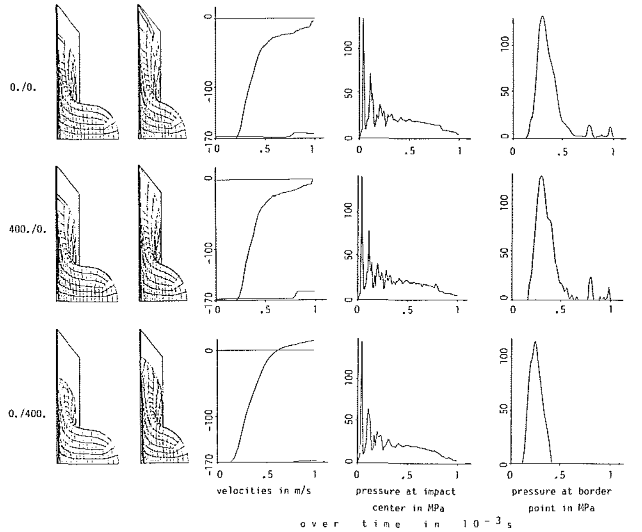

Fig. 6 Effects of volume and shear viscosity in the simulation of perpendicular impacts on flat rigid walls; shear viscosity/pressure viscosity shown at left of each row of figures; basic units kg, m, s

Welsh and Centonze (1985) indicate that a substitute material should consist of 85 to 90 percent by volume of water and the remainder of air. Use of the "null material" in DYNA3D requires knowledge of the compressibility of the mixture. Figure 2 shows the compressibilities μ of water, air, and two mixtures as a function of pressure.

Test results indicated by Wilbeck (1981) were recalculated with a substitute of 90 percent water and 10 percent air and bird models of different shapes (Fig. 3). The pressure curves for models A, B, and C differ significantly from the measured curves (Fig. 1). In particular, several strong compression waves occur upon impact of the steps of models B and C, which were not observed in the test. Only with the use of model body D, a cylinder with hemispherical ends, were realistic pressure curves achieved.

It is known that in metal parts substantial strain is induced by the stagnation pressure, whereas the Hugoniot pressure as an extremely short-time impulse is often negligible. Here, the accuracy at which such pressure peaks can be calculated is generally only a reflection of the efficiency of the calculating procedure. If the Hugoniot pressure is presented accurately, it can be assumed that the more easily representable stagnation pressure is also calculated correctly. In the case of fiber-reinforced plastics, shock waves may result in delamination, as explained by Garg (1988) in a summarizing representation. The Hugoniot pressure may cause initial damage and reduction in component strength, and the subsequent stagnation pressure may cause complete degradation. With the bird model D per Fig. 3 and the substitute of 90 percent water and the remainder of air, the Hugoniot pressures for impacts of various bird masses and impact velocities were calculated (Fig. 4). In the graph in Fig. 5, the calculation results are plotted against the test results by Wilbeck (1981). With one exception, the calculation results are within the scatter range of the test.

In bird strike calculations with a bird substitute material without internal friction, the pressure maxima occur at the rim of the impact areas and not in the impact centers as indicated by the measurements of Wilbeck (1981). Furthermore, this model material continues to flow during the calculation until the calculation crashes due to destroyed elements. Both problems will be resolved in the future by a viscous material law,

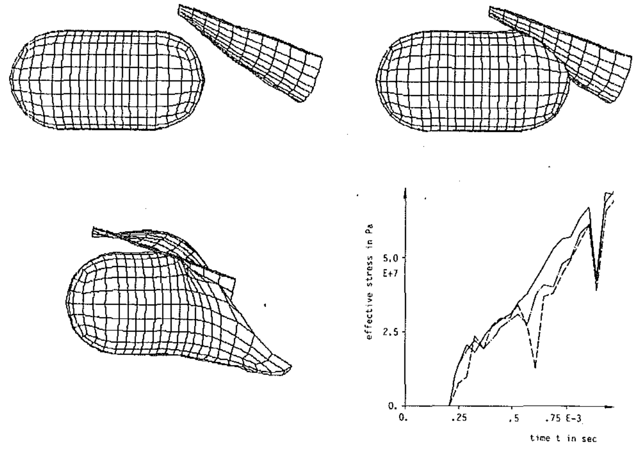

Fig. 7 Simulation of a bird strike on the rotating spinner of an aeroengine: structural patterns and von Mises effective stresses in the three points of the spinner impact area

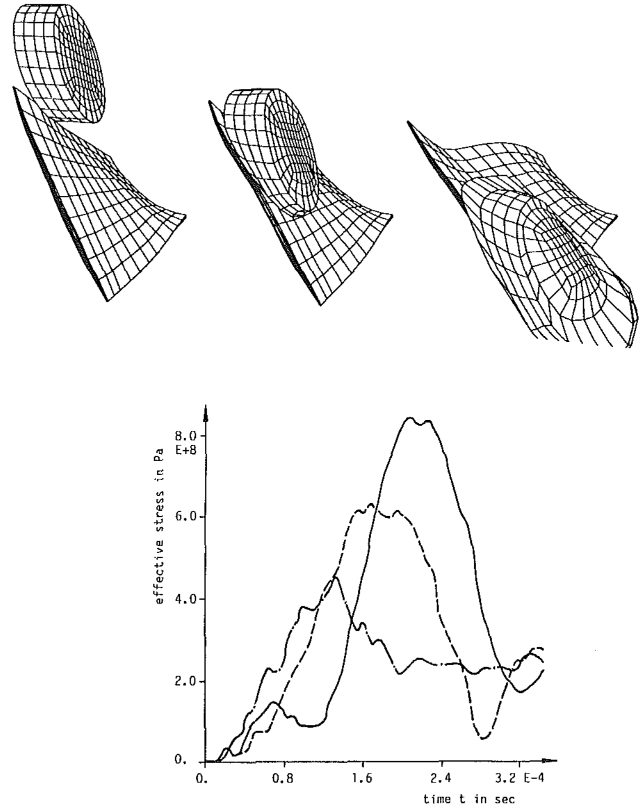

Fig. 8 Calculation of a bird strike on the intake blade of an engine: structural patterns and von Mises effective stresses in three points of the blade impact area

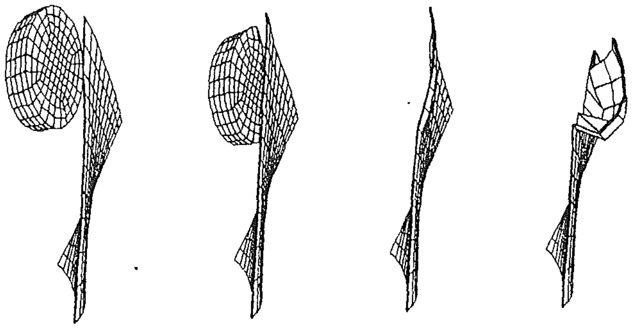

Fig. 9 Blade corner knocked off by bird strike

which has been implemented in DYNA3D. A short description is provided in the appendix. Figure 6 shows a first qualitative study on the effect of volume and shear viscosity on the impact event.

6.3 Simulation of Bird Strikes on Engine Components

6.3.1 Rotating Spinner. Figure 7 shows the simulation of the strike of a 1 kg bird against a rotary spinner in $TiCu_2$ with 4-mm-thick walls at an impact velocity of 170 m/s. The three structural patterns represent the deterioration of the component. To save computer time, symmetry of the event was assumed and the calculation performed with a half model. The rotating spinner was modeled only partly and the environment assumed to be rigid. The deterioration of the component is also represented by the curve at the bottom right of Fig. 7, which shows the von Mises effective stress in three points of the impact area, which were formally calculated far beyond the ultimate stress.

6.3.2 Intake Blade. Birds impinging on the blade row of an engine are cut into slices. The influence of the evasive movement of the blade on the thickness of the bird slice is neglected. Figure 8 shows the simulation of the impact of such a slice on the respective blade. A bird with a total mass of 442 g flies at a speed of 100 m/s relative to the aircraft. The blade, which is made of TiAl6V4, has a circumferential tip speed of 400 m/s. The von Mises effective stresses were calculated in three points of the impact area and are shown in Fig. 8. They reach far into the plastic range. Figure 9 shows a first attempt to simulate the separation of blade fragments.

7 Conclusions

Considering the historical development, far-reaching results can be obtained by using modern finite element programs like DYNA3D. However, further improvements are necessary.

Large distortions of the bird mesh affect the precision of calculations and give rise to wishes for a rezoning capability. Viscous substitute bird materials also permit improvements. Very great values of viscosity have lead to numerical instabilities.

Failure prediction for parts made of reinforced plastics is hardly practicable. Current failure theories were developed for static load cases and suitable impact criteria are not known.

With respect to calculations done on parts and described in section 6.3, one can say that the results are qualitative and numerical in the range of tests as far as known. Calculations for parts development are practicable. Nevertheless further correlations with test results have to be carried out. On this occasion the influence of the blade evasive movement to the mass of the cut bird part should be taken into consideration. This can be done by increasing the density of the bird material in a suitable way.

References

Alexander, A., 1981, "Interactive Multi-Mode Blade Impact Analysis," presented at the ASME Gas Turbine Conference & Products Show, Houston, TX.

Barber, J. P., Taylor, H. R., and Wilbeck, J. S., 1975, "Characterization of Bird Impacts on a Rigid Plate," AFFDL-TR-75-5, Dayton, OH.

Barber, J. P., Taylor, H. P., and Wilbeck, J. S., 1978, "Bird Impact Forces and Pressures on Rigid and Compliant Targets," AFFDL-TR-77-60, Dayton, OH.

Bertke, R. S., 1982, "Local Leading Edge Damage From Hard Particle and Soft Body Impacts," General Electric Co., OH.

Brockman, R. A., 1984, "Finite Element Analysis of Soft Body Impact," AFWAL-TR-84-3035, Dayton, OH.

Cassenti, B. N., 1979, "Hugoniot Pressure Loading in Soft Body Impacts," AIAA Paper No. 79-0782.

Challita, A., and Barber, J. P., 1979, "The Scaling of Bird Impact Loads," AFFDL-TR-79-3042, Dayton, OH.

Coker, M. J., and Magnusson, R. H., 1978, "High Speed Bird Impact Testing of Aircraft Transparencies," Douglas Aircraft Co., Long Beach, CA.

Cornell, R. W., 1976, "Elementary Three-Dimensional Interactive Rotor Blade Impact Analysis," ASME JOURNAL OF ENGINEERING FOR POWER, Vol. 98, pp. 480–486.

Dahl, H., 1984, *Bird Strike Committee Europe, Proceedings, Conference and Training Workshop on Wildlife Hazards to Aircraft*, Charleston.

Denke, P. H., 1977, "Aircraft Windshield Bird Impact Mathematical Model, Part 1, Theory and Application," Wright-Patterson AFB, OH.

Eide, G. R., 1977, "Aircraft Windshield Bird Impact Mathematical Model, Part 2. User's Manual," AFFDL-TR-77-99-PT-2, Long Beach, CA.

Engblom, J. J., 1980, "Coupled Fluid/Structure Response Predictions for Soft Body Impact of Airfoil Configurations," presented at the Emerging Technology Conference, San Francisco, CA.

Fonden, B. P., and Persson, K. I., 1983, "Investigations Concerning Improvements of the SAAB 37 Windshield Bird Strike Resistance," Saab-Scanid, A. B., Linkoeping.

Garg, A. C., 1988, "Delamination — A Damage Mode in Composite Structures," *Engineering Fracture Mechanics*, Vol. 29, pp. 557–584.

Gourley, W. E., and Littell, H. E., Jr., 1983, "Development of Lightweight Commercial Aircraft Windshields With New High Strength Glasses," PPG Industries Inc., Pittsburgh, PA.

Graff, J., Stoltze, L., and Varholak, E. M., 1976, "Fiber Composite Fan Blade Impact Improvement," Hamilton Standard Div., Windsor Locks.

Halquist, J. O., 1983, "Theoretical Manual for DYNA3D," Lawrence Livermore Lab, CA.

Halquist, J. O., and Benson, D. J., 1986, "DYNA3D User's Manual," Lawrence Livermore Lab, CA.

Heath, J. B. R., and Gould, R. W., 1983, "Degradation of the Bird Impact Resistance of Polycarbonate," National Research Council of Canada, Ottawa.

Hild, J., 1974, "Das Vogelschlagproblem in der Verhütung von Störungen, Zwischenfällen und Unfällen mit Luftfahrzeugen der Bundeswehr, Fachliche Mitteilungen," *Amt für Wehrgeophysik*, Vol. 176.

Hild, J., 1981, "Vogelschlag und Flugsicherheit," *Aerokurier*, Vol. 10, pp. 1286–1288.

Ikeda, T., Miyachi, T., and So Fue, Y., 1985, "Fundamental Investigation on the Impact Strength of Hollow Fan Blades," National Aerospace Laboratory, Tokyo.

Johns, R. H., 1974, "FOD Impact Testing of Composite Fan Blades," National Aeronautics and Space Administration, Cleveland, OH.

Keil, W., 1981, "Die Entwicklung des Deutschen Ausschusses zur Verhütung von Vogelschlägen im Luftverkehr," *Vogel und Luftverkehr*, Vol. 1, pp. 6–10.

Lawson, M., 1987, "Supersonic Simulation of a Bird Strike on a Turbofan Aero Engine," *Finite Element News*, pp. 10–11.

Mattingly, A., 1976, "Reducing the Bird Strike Hazard," *Airport Forum*, Vol. 4, pp. 13–28.

McCarty, R. E., 1980, "Finite Element Analysis of F-16 Aircraft Canopy Dynamic Response to Bird Impact Loading," AIAA Paper No. 80-0804.

McCarty, R. E., 1983, "MAGNA (Materially and Geometrically Nonlinear Analysis) Computer Simulation of Bird Imapct on the F-15 Aircraft Canopy," Wright-Patterson AFB, OH.

McCarty, R. E., 1984, "Aircraft Transparency Bird Impact Analysis Using the MAGNA Computer Program," *Proceedings, Conference and Training Workshop on Wildlife Hazards to Aircraft*, Charleston.

Morris, R. C., 1977, "Aircraft Windshield Bird Impact Mathematical Model, Part 3, Programming Manual," AFFDL-TR-77-99-PT-3, Long Beach, CA.

Nash, R., 1983, "Parametric Studies of the T-38 Student Windshield Using the Finite Elements of Code MAGNA (Materially and Geometrically Nonlinear Analysis)," Dayton University, Dayton, OH.

Niering, E., 1988, "Berechnung von Vogelschlägen mit DYNA3D," interner MTU-Bericht, Munich, Federal Republic of Germany.

Niering, E., 1989, "How to Start Transient Response Calculations for Rotating Structures Without Causing Centrifugal Force Shocks," ASME *Journal of Vibration, Acoustics, Stress, and Reliability in Design*, Vol. 111, pp. 386–391.

NN., 1982, "Manual on the ICAO Bird Strike Information System (IBIS)," International Civil Aviation Organization, Montreal.

Pinnell, W. R., 1983, "In-Flight Measurement of Pressure Distribution over T-38 Student Canopy," Wright-Patterson AFB, OH.

Ravenhall, R., and Salemme, C. T., 1978, "Program for Impact Testing of Spar-Shell Fan Blades," General Electric Co., Cincinnati, OH.

Schach, W. von, 1934, "Umlenkung eines freien Flüssigkeitsstrahles an einer ebenen Platte," *Ingenieur-Archiv*, Vol. 5, pp. 245–265.

Schach, W. von, 1935, "Umlenkung eines kreisförmigen Flüssigkeitsstrahles an einer ebenen Platte, senkrecht zur Strömungsrichtung," *Ingenieur-Archiv*, Vol. 6, pp. 51–59.

Simmons, R., and Stenger, G. J., 1983, "Bird Impact Evaluation of the F/RF-4 Transparency System," Wright Patterson AFB, OH.

Storace, A. F., 1982, "Foreign Object Impact Design Criteria," AFAPL-TR-78-81, Cincinnati, OH.

Welsh, C. J., and Centonze, V., 1986, "Aircraft Transparency Testing — Artificial Birds," Arnold Engineering Development Center, TN.

West, B. S., 1980, "Alternate T-38 Transparency Development, Part II," Dayton University, Dayton, OH.

Wilbeck, J. S., 1978, "Bird Impact Loading," *Proc. Shock and Vibration Bulletin*, Vol. 48, pp. 115–122.

Wilbeck, J. S., 1981, "The Development of a Substitute Bird Model," ASME JOURNAL OF ENGINEERING FOR POWER, Vol. 103, pp. 725–730.

APPENDIX

Fluidic Material Law With Shear and Volume Viscosity

In DYNA3D the Cauchy stresses t_{ij} are divided into the deviator s_{ij} and the ball part $-p\delta_{ij}$ with the mean pressure p as usual

$$t_{ij} = s_{ij} - p\delta_{ij}, \qquad p = -1/3 t_{kk} \tag{1}$$

For both shares, an own material law is assumed. The Jauman stress rates, marked by $\triangledown$, can be defined separately

$$\dot{s}_{ij} = \overset{\triangledown}{s}_{ij} + s_{ik}w_{jk} + s_{jk}w_{ik} \tag{2}$$

$$\dot{p}\delta_{ij} = \overset{\triangledown}{p}\,\delta_{ij} + p\delta_{ik}w_{jk} + p\delta_{jk}w_{ik}$$

$$\dot{p} = \overset{\triangledown}{p} \tag{3}$$

where w_{ij} is the spin tensor. The deviatoric stress tensor s_{ij} is connected with the deviator $\dot{\epsilon}'_{ij}$ of the strain rates by the hypoelastic material law

$$\overset{\triangledown}{s}_{ij} = C_{ijkl}\dot{\epsilon}'_{kl} \tag{4}$$

$$\dot{\epsilon}'_{ij} = \dot{\epsilon}_{ij} - \frac{1}{3}\dot{\epsilon}_{kk}\delta_{ij} \tag{5}$$

C_{ijkl} is a material tensor. The pressure p is assumed as a function of the specific internal energy E in the form of a general, nonlinear equation of state

$$p = f(E) \tag{6}$$

The numerical integration of equations (2) and (4) leads to

$$s_{ij}^{n+1} = s_{ij}^{n} + \left(C_{ijkl}\dot{\epsilon}'^{\,n+1/2}_{kl} + s_{ip}^{n}w_{jp}^{n+1/2} + s_{jp}^{n}w_{ip}^{n+1/2}\right)\Delta t^{n+1/2} \tag{7}$$

The use of stresses s_{ij}^{n} at "full" base points n in lieu of "half" base points $n + 1/2$ is necessary since in the numerical concept used in DYNA3D the stresses are only calculated at "full" base points. Therefore equation (7) contains mixed central and forward differences. The integration of equations (3) and (6) to get p^{n+1} can be adopted as defined in the theory manual (Halquist, 1983).

From equation (1), the total stress tensor at the time t^{n+1} results as

$$t_{ij}^{n+1} = s_{ij}^{n+1} - p^{n+1}\delta_{ij} \tag{8}$$

Equations (8) and (7) must be modified to assume the form of the Navier Poisson law for compressible fluids with volume viscosity λ and shear viscosity μ

$$t_{ij}^{n+1} = -p^{n+1}\delta_{ij} + \lambda\dot{\epsilon}_{kk}^{n+1}\delta_{ij} + 2\mu\dot{\epsilon}_{ij}^{n+1} \tag{9}$$

The first, third, and fourth sum and the factor $\Delta t^{n+1/2}$ on the right-hand side of equation (7) are to be deleted. $C_{ijkl}\,\dot{\epsilon}'^{\,n+1/2}_{kl}$ is to be substituted by $\lambda\dot{\epsilon}_{kk}^{n+1}\,\delta_{ij} + 2\mu\,\dot{\epsilon}_{ij}^{n+1}$.

The strain rates in DYNA3D are calculated at half support points. Therefore, the approximation

$$t_{ij}^{n+1} = -p^{n+1}\delta_{ij} + \lambda\dot{\epsilon}_{kk}^{n+1/2}\delta_{ij} + 2\mu\,\dot{\epsilon}_{ij}^{n+1/2}$$

must be implemented in lieu of the more accurate equation (9). The error is in the same range as if changing from central to forward differences.

S. K. Chen

A. H. Lefebvre

Thermal Science and Propulsion Center,
Purdue University,
West Lafayette, IN 47907

J. Rollbuhler

NASA-Lewis Research Center,
Cleveland, OH 44135

Influence of Geometric Features on the Performance of Pressure-Swirl Atomizers

The spray characteristics of several different simplex pressure-swirl nozzles are examined using water as the working fluid. Measurements of mean drop size, drop-size distribution, effective spray cone angle, and circumferential liquid distribution are carried out over wide ranges of injection pressure. Eight different nozzles are employed in order to achieve a wide variation in the length/diameter ratio of the final discharge orifice. Generally, it is found that an increase in discharge orifice length/diameter ratio (l_o/d_o) *increases the mean drop size in the spray and reduces the spray cone angle. The circumferential liquid distribution is most uniform when* $l_o/d_o=2$. *If* l_o/d_o *is raised above or lowered below this optimum value, the circumferential uniformity of the liquid distribution is impaired. The observed effects of* l_o/d_o *on spray characteristics are generally the same regardless of whether the change in* l_o/d_o *is accomplished by varying* l_o *or* d_o.

Introduction

A pressure-swirl nozzle is one in which the liquid to be atomized is fed into a swirl chamber through a number of helical or tangential passages that impart to the liquid a high angular velocity. The liquid then emerges through the final discharge orifice with both tangential and axial components, thereby producing a hollow conical sheet, which rapidly disintegrates into ligaments and then drops. The advantages of the pressure-swirl nozzle include simplicity of construction, reliability, good atomization, and low pumping power requirements. These advantages have resulted in numerous practical applications, including spray coating, humidification, gas washing, fire protection, crop spraying, and spray cooling, as well as in various types of spray drying systems, where they are used to atomize a wide range of solutions, suspensions, and slurries of food and chemical products.

Pressure-swirl nozzles are also used extensively for injecting liquid fuel into a wide range of aircraft, marine, and industrial gas turbine combustors. The many widely used types of pressure-swirl nozzles for gas turbine applications include simplex, duplex, dual-orifice, and spill-return designs.

The practical importance of pressure-swirl atomizers is evidenced by a large number of publications covering both theoretical and experimental studies on all aspects of their design and performance. If consideration of these publications were confined to the past decade, it would include studies on the influence of liquid properties on mean drop size by Simmons (1980), Jasuja (1979), Jones (1982), Kennedy (1986), and Wang and Lefebvre (1987). Studies on the effects of ambient air properties on mean drop size and/or spray cone angle include those of Parsons and Jasuja (1986), DeCorso and Kemeny (1957), Dodge and Biaglow (1986), and Lefebvre (1987). Other workers have investigated the effects of variations in atomizer geometry on several facets of pressure-swirl nozzle performance. The most detailed and comprehensive of these studies are those undertaken by Elkotb et al. (1978), Babu et al. (1982), Kennedy (1986), and Jones (1982). The nozzles tested by Jones were generally of large flow capacity, of the size employed in large-scale industrial furnaces. Kennedy's investigation was also confined to nozzles of large flow capacity. In the present study, emphasis is placed on simplex nozzles of low flow number, of the type that are generally used in small gas turbines and that also serve as "primary" or "pilot" atomizers in the dual-orifice and hybrid airblast injectors fitted to large turbojet engines. Such nozzles are of special interest because relatively small variations in certain critical dimensions can have a disproportionately large impact on spray characteristics. In this context, the most critical geometric feature is the final discharge orifice, since this is where the liquid attains its maximum velocity before it is ejected from the nozzle in the form of a conical spray. As viscous losses tend to be high in this region of maximum flow velocity, normal design practice is to make the length/diameter ratio of the final discharge orifice (l_o/d_o) as small as possible, without creating a sharp edge that would be difficult to manufacture consistently and would also be susceptible to damage during handling.

The experimental work described in this paper is focused on the influence of the final discharge orifice l_o/d_o ratio on several key aspects of spray nozzle performance, including Sauter mean diameter (SMD), drop-size distribution, radial liquid distribution, and circumferential liquid distribution. It is hoped that the results of this study will be of interest and value to both designers and users of pressure-swirl atomizers. One useful application of the results obtained could be in the

---

Contributed by the International Gas Turbine Institute and presented at the ASME Twelfth Annual Energy-Sources Technology Conference and Exhibition, Houston, Texas, January 22–25, 1989. Manuscript received at ASME Headquarters September 1, 1989.

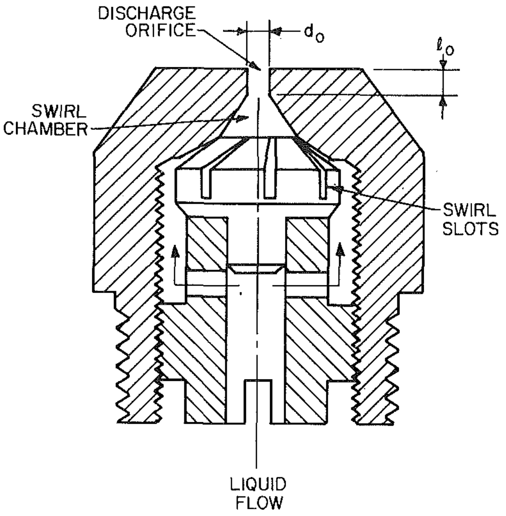

Fig. 1 Simplex swirl atomizer

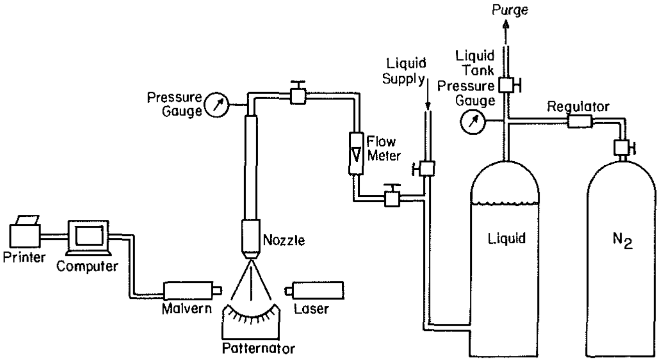

Fig. 2 Schematic diagram of test facility

selection of an optimum value of l_o/d_o for any given nozzle application.

Experimental

The type of atomizer employed is shown in Fig. 1. Five nozzles conforming to this basic design were manufactured by the Delavan Company, having discharge orifice length/diameter ratios of 0.5, 1.0, 2.0, 3.0, and 4.0. For all five nozzles the flow number is 8×10^{-8} m^2.

The apparatus used to measure spray characteristics is shown schematically in Fig. 2. Water is supplied to the nozzle from a nitrogen-pressurized tank. The amount of water ejected from the nozzle is controlled by a hand-operated valve located in the bypass line. A number of valves, pressure gages, and flow meters are located in the nozzle feed line to provide the desired nozzle operating conditions in terms of liquid injection pressure and mass flow rate.

Mean drop sizes are measured using a Malvern particle size analyzer. This instrument is based on the Fraunhofer diffraction theory of a collimated laser beam scattered by moving drops. The principle of operation of the Malvern instrument has been reviewed by Swithenbank et al. (1977) and Dodge and Cerwin (1984), while the accuracy and limitations of the instrument have been discussed by Hirleman et al. (1984) and Dodge (1984).

All measurements are carried out at a distance of 150 mm downstream of the nozzle with the laser beam passing through the centerline of the spray. Centerline measurements ensure that the laser beam encompasses both the smaller drops located at the center of the spray as well as the larger drops at the spray periphery.

The "effective" angle of the spray is measured using a patternator of the type illustrated in Fig. 2. This patternator is 1.27 cm deep and 31.75 cm wide. The sampling tubes were formed by cutting slots into the opaque white plastic base over which a clear thin sheet of plastic is glued. The outer edges that form the openings to the tubes are filed to sharp edges so that each tube has a well-defined sampling area. The tubes are almost square in cross section, each tube having an area of 0.504 cm^2. There are a total of 29 sampling tubes, spaced 4.5 deg apart along a radius of curvature of 10 cm.

Before a spray sample is taken the water flow rate is adjusted until the nozzle is operating at the desired conditions. At this point a container into which the water has been flowing is removed, and the sampling tubes begin to fill. When one of the tubes is nearly full, the water supply is turned off and the residual flow is diverted away from the patternator.

The volume of liquid in each tube is measured by visually locating the meniscus between lines scribed into the clear plastic of the patternator. Liquid distribution curves are made by plotting liquid volume as the ordinate and the corresponding angular location of the sampling tubes as the abscissa. The method has been fully described by DeCorso and Kemeny (1957) and Ortman and Lefebvre (1985).

In order to describe more succinctly the effects of changes in operating parameters on liquid distribution, the curves of liquid volume versus angular position can be reduced to a single numerical value called the "effective spray angle." The effective spray angle is the sum of two angles, $\phi=\phi_L+\phi_R$, which are calculated using the following equation:

$$\phi_L(\text{or }\phi_R)=\frac{\Sigma y\theta\Delta\theta\sin\theta}{\Sigma y\Delta\theta\sin\theta}=\frac{\Sigma y\theta\sin\theta}{\Sigma y\sin\theta}$$

L and R represent the left and right lobes of the liquid distribution curve, respectively, θ is the angular location of the sampling tubes, $\Delta\theta$ the angle between the sampling tubes, and y the liquid volume measured at the corresponding tubes. The physical meaning of the effective spray angle is that ϕ_L(or ϕ_R) is the value of θ that corresponds to the position of the center of the mass of a material system for the left- (or right-) hand lobe of the distribution curve.

Circumferential liquid distribution in the spray is measured using a plexiglass cylinder divided into 16 equal wedges. Liquid is sprayed into the patternator until it nears the top of one of the cells. The level of the liquid in each cell is then measured and recorded. The values are normalized against the average of the levels in all the cells, and the standard deviation of the normalized values is calculated. This yields a normalized standard deviation σ, which is indicative of the irregularity of the nozzle spray.

Results

In the course of this investigation a large amount of data was collected on the effects of liquid injection pressure and

Nomenclature

b = Rosin-Rammler size distribution parameter
d_o = diameter of final discharge orifice, m
FN = flow number of atomizer, m^2
l_o = length of final discharge orifice, m
ΔP_L = nozzle injection pressure differential, Pa
q = Rosin-Rammler size distribution parameter
SMD = Sauter mean diameter, m

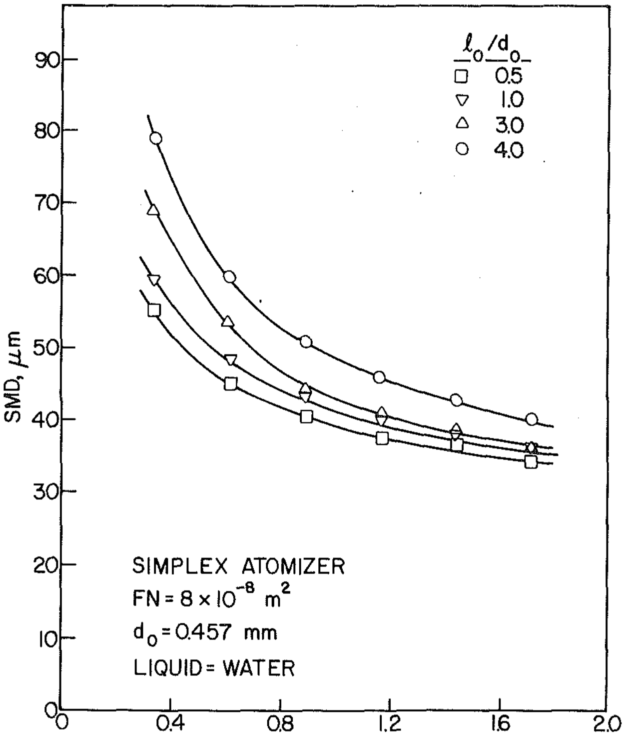

Fig. 3 Influence of injection pressure on mean drop size

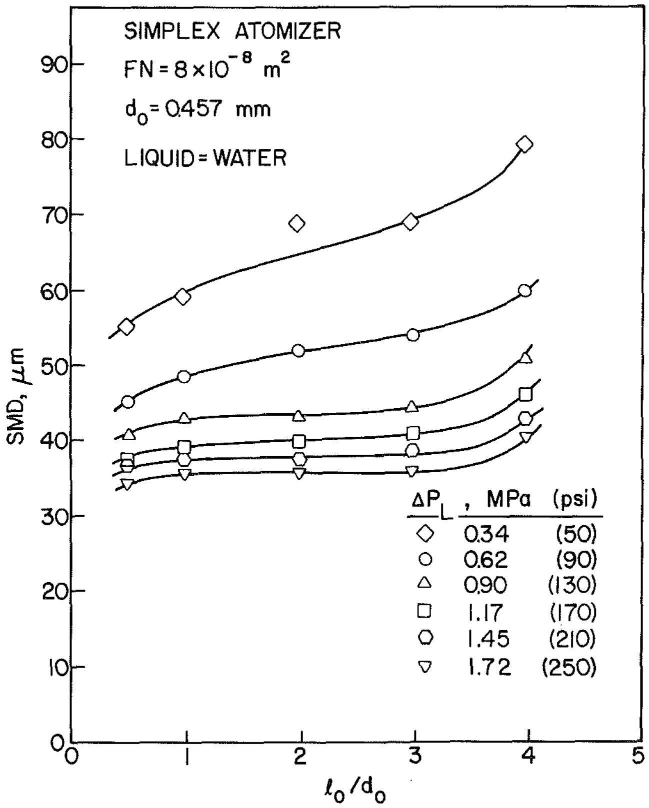

Fig. 4 Influence of discharge orifice length/diameter ratio on mean drop size

discharge orifice length/diameter ratio on mean drop size, drop-size distribution, effective spray cone angle, and circumferential liquid distribution. These various aspects are discussed below in turn.

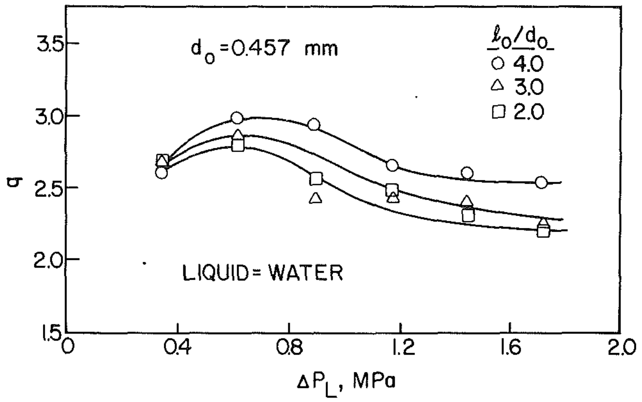

Fig. 5 Influence of injection pressure and l_o/d_o on Rosin-Rammler drop size distribution parameter

Mean Drop Size. Figure 3 shows the influence of liquid injection pressure (ΔP_L) on Sauter mean diameter for various values of final discharge orifice length/diameter ratio (l_o/d_o). The results indicate that SMD declines with increase in injection pressure according to the relationship SMD $\propto \Delta P_L^{-n}$, where n varies from 0.30 to 0.40 as l_o/d_o is raised from 0.5 to 4.0.

The effect of discharge orifice dimensions on mean drop size is shown more directly in Fig. 4, in which SMD is plotted against l_o/d_o for values of ΔP_L ranging from 0.34 to 1.72 MPa (50 to 250 psi). This figure shows that the influence of l_o/d_o on SMD is very small at the highest levels of injection pressure, but becomes more pronounced as the injection pressure is reduced.

Drop-Size Distribution. Of the many drop-size distribution parameters contained in the literature, the most widely used is one that was originally developed for powders by Rosin and Rammler (1933). It may be expressed in the form

$$1 - v = \exp(-bx)^q$$

where v is the fraction of the total volume contained in drops of diameter less than x, and b and q are constants. Thus, by applying the Rosin-Rammler relationship to sprays, it is possible to describe the drop-size distribution in terms of the two parameters b and q. The exponent q provides a measure of the spread of drop sizes. The higher the value of q, the more uniform is the spray. If q is infinite, the drops in the spray are all the same size. For most practical sprays the value of q lies between 2 and 4.

Although it assumes an infinite range of drop sizes, the Rosin-Rammler expression has the virtue of simplicity. Moreover, it permits data to be extrapolated into the range of very fine droplets, where measurements are most difficult and least accurate.

The variation of q with injection pressure and discharge orifice length/diameter ratio is illustrated in Fig. 5. This figure shows that q generally declines with increase in ΔP_L. When Fig. 5 is examined alongside Fig. 3, it is apparent that for simplex nozzles the effect of an increase in injection pressure is to reduce the mean drop size in the spray and, at the same time, produce a broader range of drop sizes. This expansion in drop-size distribution is accomplished by the creation of many more droplets in the smallest size range.

Figure 5 also shows that the effect of an increase in l_o/d_o is to produce a more uniform distribution of drop sizes in the spray. This is attributed to a thickening of the liquid film within the final discharge orifice as the orifice length is increased. It has been shown elsewhere (Lefebvre, 1987) that an increase in initial film thickness generally leads to an increase in mean drop size and a narrowing of dropsize distribution.

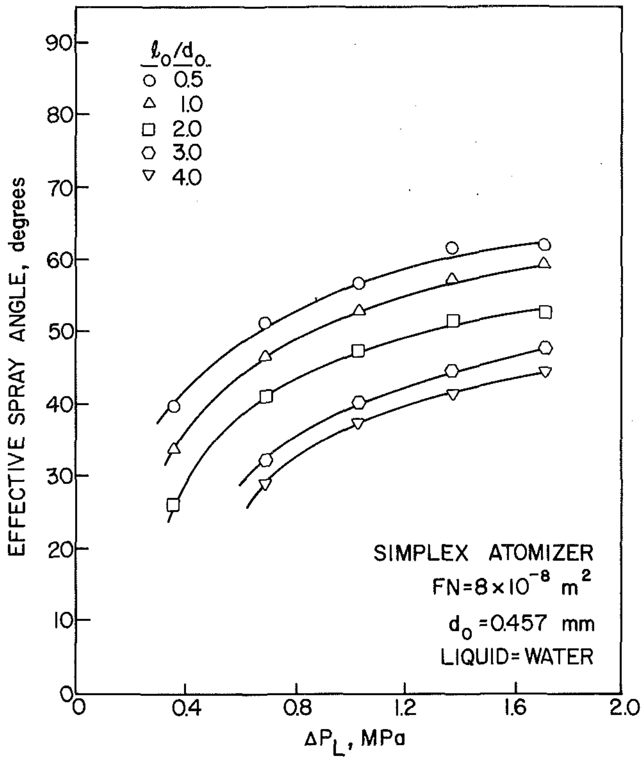

Fig. 6 Influence of injection pressure on spray cone angle

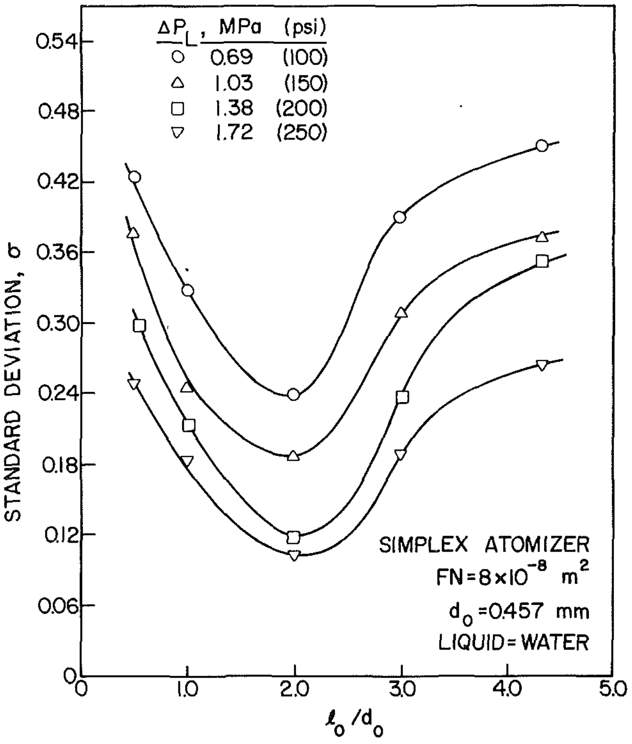

Fig. 8 Influence of discharge orifice length/diameter ratio on uniformity of circumferential liquid distribution

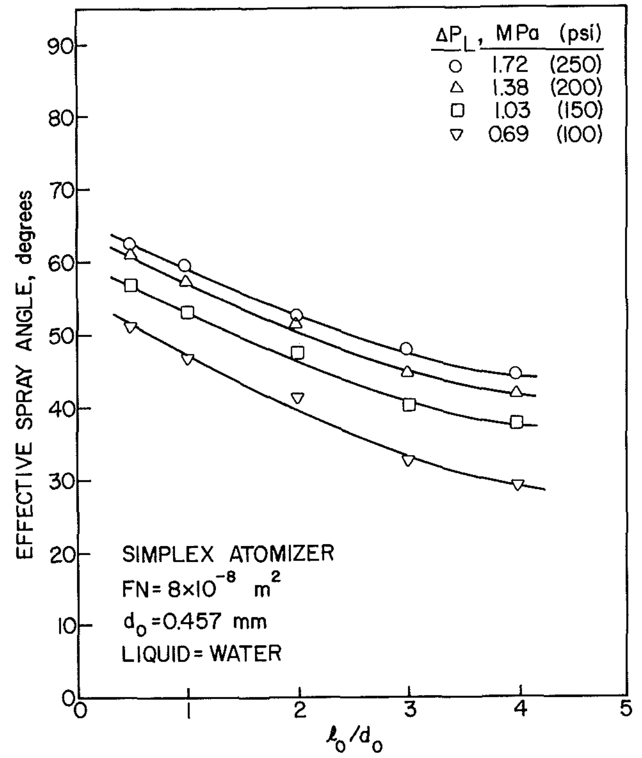

Fig. 7 Influence of discharge orifice length/diameter ratio on spray cone angle

This it does by eliminating the smallest droplets from the spray.

Spray Cone Angle. The effects of injection pressure and discharge orifice length/diameter ratio on effective spray cone angle are illustrated in Figs. 6 and 7. Figure 6 shows that, over the range of injection pressures covered in these experiments, the effective spray angle increases with increase in ΔP_L. This, incidentally, is one of the reasons why the SMD declines with increase in ΔP_L (Lefebvre, 1987). It may also be observed in Fig. 6 that, over the range of l_0/d_0 ratios covered in these experiments, a reduction in l_0/d_0 always results in an increase in effective spray cone angle. This effect of l_0/d_0 on effective spray angle is also clearly evident in Fig. 7.

In connection with Fig. 6, it should be noted that the effective spray angle does not continue to increase indefinitely with increase in ΔP_L. Previous work, for example, Ortman and Lefebvre (1985), has shown that the effective spray angle widens as ΔP_L is raised until the angle attains a maximum value. Any further increase in ΔP_L beyond this point causes the effective spray angle to contract.

Circumferential Liquid Distribution. The results obtained on the effects of injection pressure and discharge orifice length/diameter ratio on circumferential liquid distribution are presented in Fig. 8. This figure shows, for all values of ΔP_L, that increase in l_0/d_0 over the range from 0.5 to 2.0 causes the standard deviation σ to decline, i.e., the circumferential liquid distribution becomes more uniform. However, further increase in l_0/d_0 beyond a value of around 2 has an adverse effect on the uniformity of the circumferential liquid distribution. The reasons for this observation are unclear. At the outset of the test program it had been anticipated that continual increase in orifice length would produce a thicker and more uniform film at the orifice exit, thereby creating a more uniform circumferential distribution of liquid in the spray. One of the authors (AHL) made a similar observation some years ago when attempting to determine the optimum length for the prefilming surface of an airblast atomizer. It was noted that striations in the liquid sheet, caused by the feed jets emerging from a finite number of slots onto the prefilming surface, almost disappeared at a certain distance along the prefilming surface, only to reappear again in the flow region farther downstream. At that time it was concluded that either too long or too short a prefilming surface would result in nonuniformities in the thickness of the liquid film formed at the prefilming edge, but no attempt was

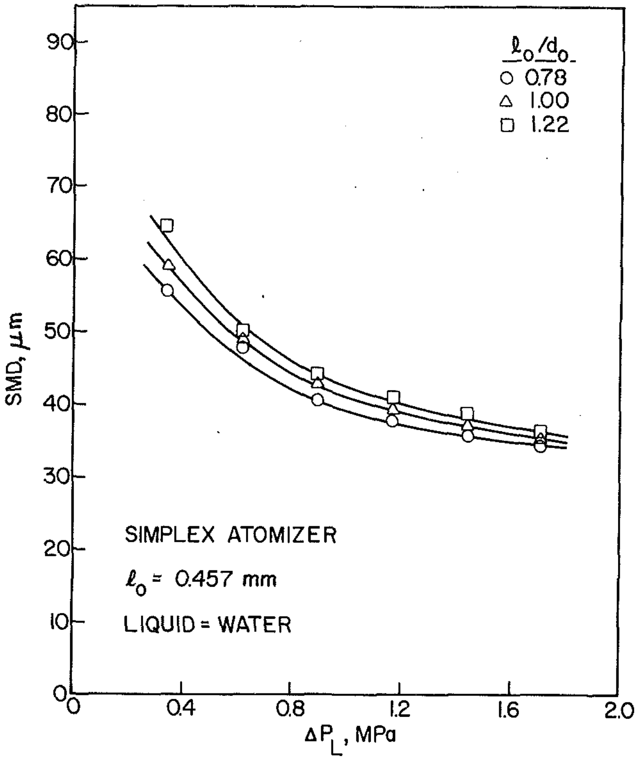

Fig. 9 Influence of injection pressure and discharge orifice length/diameter ratio on mean drop size

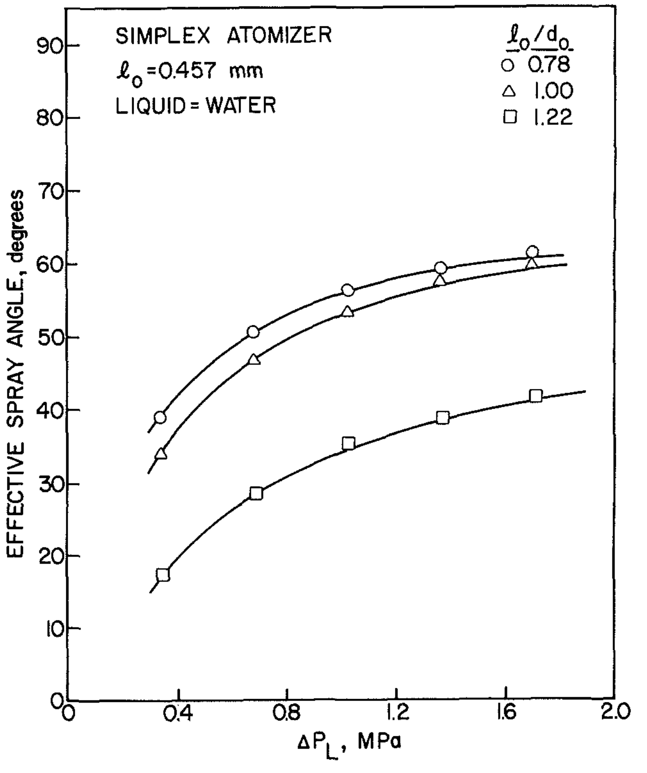

Fig. 10 Influence of injection pressure and discharge orifice length/diameter ratio on effective spray angle

made to determine the optimum prefilming length for any given number of feed slots, or how this optimum length might be affected by changes in liquid flow rate and liquid properties. It is possible that a similar phenomenon is responsible for the results outlined above on the influence of discharge orifice length/diameter ratio on circumferential liquid distribution.

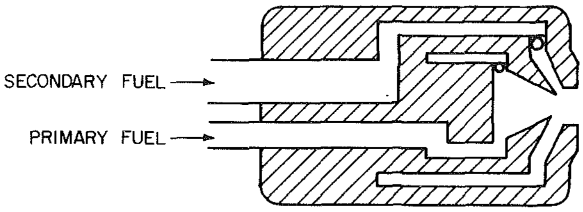

Fig. 11 Schematic diagram of dual-orifice fuel atomizer

Additional Tests. In the test program described above, the diameter of the discharge orifice was maintained constant at a value of 0.457 mm and variation in l_0/d_0 was achieved by varying the length of the discharge orifice. This raises the question as to whether similar results would have been obtained if l_0 had been kept constant and the variation in l_0/d_0 accomplished by using different values of d_0. The results obtained over a limited range of l_0/d_0 values by following this alternative approach are shown in Figs. 9 and 10. Figure 9 illustrates the influence of injection pressure and length/diameter ratio on mean drop size, while Fig. 10 shows the effects of these same parameters on effective spray angle. Without discussing these results in detail, it is clear from inspection of Figs. 9 and 10 alongside Figs. 3 and 6, respectively, that the effects of l_0/d_0 on mean drop size and effective spray angle are generally the same, regardless of whether the change in l_0/d_0 is accomplished by changing l_0 or d_0.

Discussion

Some of the results obtained in this investigation have special relevance and importance to the design of dual-orifice atomizers for aircraft gas turbines. A major drawback of the simplex atomizer in its application to gas turbines is that its flow rate varies as the square root of the injection-pressure differential. Thus, doubling the fuel flow rate demands a fourfold increase in fuel-injection pressure. For kerosine the minimum injection pressure for satisfactory atomization quality is about 100 kPa. This means that an increase in fuel flow rate to some 20 times the minimum value would require an injection pressure of 40,000 kPa. This basic drawback of the simplex atomizer has led to the development of various *wide-range atomizers*, of which the most important and most widely used is the dual-orifice atomizer, as illustrated in Fig. 11. Essentially, it is comprised of two simplex nozzles that are fitted concentrically, one inside the other. At low fuel flows all the fuel is supplied from the inner, primary nozzle, which has a low flow number. As the fuel flow increases, its pressure eventually reaches some predetermined value at which a pressurizing valve opens and admits fuel to the outer, secondary nozzle, which has a high flow number. It is normal design practice to make the length/diameter ratio of the discharge orifices of both nozzles as short as possible, without creating a sharp edge that would be susceptible to erosion and to damage during handling. In some nozzles this length/diameter ratio is as small as 0.2.

The results obtained in this investigation suggest that, for aircraft applications, it would be better design practice to retain a small length/diameter ratio of around 0.5 or less for the primary nozzle, and to increase the length/diameter ratio of the secondary nozzle to a value of around 2.0. This arrangement provides some important advantages. By retaining a small l_0/d_0 for the primary nozzle, good atomization is assured at the low fuel injection pressures associated with operation at high altitudes, where all the fuel is supplied from the primary nozzle, and where good atomization is of paramount importance to the attainment of wide stability limits and good relight performance. Figure 4 shows that atomization performance is very dependent on l_o/d_o. Thus, for the primary nozzle, a small l_o/d_o is essential.

If, however, the atomizer is operating at high fuel flow rates, where most of the fuel emanates from the secondary nozzle, an important additional requirement is that the fuel spray distribution should be circumferentially uniform. Experience has shown that nonuniformities in the circumferential spray distribution often give rise to a maldistribution of temperature in the combustor exhaust gases (poor pattern factor), hot streaks along the liner walls, and excessive pollutant emissions. Figure 8 shows clearly that the circumferential fuel distribution is most uniform when l_o/d_o is 2.0. Furthermore, Fig. 4 shows that increasing l_o/d_o from 0.5 to 2.0 incurs virtually no penalty in atomization performance at the high fuel pressures at which the secondary nozzle normally operates.

Based on these observations, a dual-orifice atomizer having values for l_o/d_o of 0.2 to 0.5 for the primary nozzle and 2.0 for the secondary nozzle would appear to be ideal for aircraft gas turbines.

Conclusions

From measurements of spray characteristics carried out on several different simplex atomizers, all conforming to the same basic design but having different values of discharge orifice length/diameter ratio, the following conclusions are drawn:

1 The mean drop size in the spray declines with increase in liquid injection pressure according to the relationship SMD α ΔP_L^{-n}, where the value of n varies from 0.3 to 0.4 as the length/diameter ratio of the final discharge orifice (l_o/d_o) is raised from 0.5 to 4.0.

2 The influence of l_o/d_o on mean drop size is very small at the highest injection pressure tested (1.72 MPa, or 250 psi), but becomes more pronounced at lower injection pressures.

3 An increase in l_o/d_o produces a more uniform distribution of drop sizes in the spray.

4 Increase in l_o/d_o always reduces the effective spray cone angle.

5 Increase in l_o/d_o from 0.5 to 2.0 causes the circumferential liquid distribution to become more uniform. However, further increase in l_o/d_o, in the range from 2.0 to 4.0, has an adverse effect on the uniformity of the circumferential liquid distribution.

6 The effects of variations in l_o/d_o on mean drop size and effective spray angle are generally the same regardless of whether the variation in l_o/d_o is accomplished by varying l_o or d_o.

Acknowledgments

The authors wish to express their gratitude to Delavan Incorporated, and in particular to Mr. Darrell Bobzin, for providing the specially manufactured nozzles employed in this investigation.

References

Babu, K. R., Narasimhan, M. V., and Narayanaswamy, K., 1982, "Prediction of Mean Drop Size of Fuel Sprays From Swirl Spray Atomizers," *Proceedings of the 2nd International Conference on Liquid Atomization and Sprays*, Madison, WI, pp. 99–106.

DeCorso, S. M., and Kemeny, G. A., 1957, "Effect of Ambient and Fuel Pressure on Nozzle Spray Angle," *ASME Transactions*, Vol. 79, No. 3, pp. 607–615.

Dodge, L. G., 1984, "Change in Calibration of Diffraction-Based Particle Sizers in Dense Sprays," *Optical Engineering*, Vol. 23, No. 5, pp. 626–630.

Dodge, L. G., and Biaglow, J. A., 1986, "Effect of Elevated Temperature and Pressure on Sprays From Simplex Swirl Atomizers," ASME JOURNAL OF ENGINEERING FOR GAS TURBINES AND POWER, Vol. 108, pp. 209–215.

Dodge, L. G., and Cerwin, S. A., 1984, "Extending the Applicability of Diffraction-Based Drop Sizing Instruments," in: *Liquid Particle Size Measurement Techniques*, J.M. Tishkoff, R.D. Ingebo, and J.B. Kennedy, eds., ASTM STP 848.

Elkotb, M. M., Rafat, N. M., and Hanna, M. A., 1978, "The Influence of Swirl Atomizer Geometry on the Atomization Performance," *Proceedings of the 1st International Conference on Liquid Atomization and Spray Systems*, Tokyo, pp. 109–115.

Hirleman, E. D., Oechsel, V., and Chigier, N. A., 1984, "Response Characteristics of Laser Diffraction Particle Size Analyzers: Optical Sample Volume Extent and Lens Effects," *Optical Engineering*, Vol. 23, No. 5, pp. 610–619.

Jasuja, A. K., 1979, "Atomization of Crude and Residual Fuel Oils," ASME JOURNAL OF ENGINEERING FOR POWER, Vol. 101, No. 2, pp. 250–258.

Jones, A. R., 1982, "Design Optimization of a Large Pressure-Jet Atomizer for Power Plant," *Proceedings of the 2nd International Conference on Liquid Atomization and Spray Systems*, Madison, WI, pp. 181–185.

Kennedy, J. B., 1986, "High Weber Number SMD Correlations for Pressure Atomizers," ASME JOURNAL OF ENGINEERING FOR GAS TURBINES AND POWER, Vol. 108, pp. 191–195.

Lefebvre, A. H., 1987, "The Prediction of Sauter Mean Diameter for Simplex Pressure-Swirl Atomizers," *Atomization and Spray Technology*, Vol. 3, No. 1, pp. 37–51.

Ortman, J., and Lefebvre, A. H., 1985, "Fuel Distributions from Pressure-Swirl Atomizers," *AIAA Journal of Propulsion and Power*, Vol. 1, No. 1, pp. 11–15.

Parsons, J. A., and Jasuja, A. K., 1986, "Effect of Air Pressure Upon Spray Angle/Width Characteristics of Simplex Pressure Swirl Atomizers," ASME Paper No. 86-GT-176.

Rosin, P., and Rammler, E., 1933, "The Laws Governing the Fineness of Powdered Coal," *J. Inst. Fuel*, Vol. 7, No. 31, pp. 29–36.

Simmons, H. C., 1980, "The Prediction of Sauter Mean Diameter for Gas Turbine Fuel Nozzles of Different Types," ASME JOURNAL OF ENGINEERING FOR POWER, Vol. 102, No. 3, pp. 646–652.

Swithenbank, J., Beer, J. M., Taylor, D. S., Abbot, D., and McCreath, G. C., 1977, "Experimental Diagnostics in Gas Phase Combustion Engines," *Prog. Aeronaut. Astronaut.*, B.T. Zin, ed., AIAA, Vol. 53, p. 421.

Wang, X. F., and Lefebvre, A. H., 1987, "Mean Drop Sizes From Pressure-Swirl Nozzles," *AIAA Journal of Propulsion and Power*, Vol. 3, No. 1, pp. 11–18.

Conversion of Sulfur Dioxide to Sulfur Trioxide in Gas Turbine Exhaust

B. W. Harris
Los Alamos National Laboratory,
Los Alamos, NM 87545

Acid dewpoints were calculated from SO_2-to-SO_3 conversion in gas turbine exhaust. These data can be used as guidelines in setting feedwater temperatures in combined-cycle systems. Accurate settings can prevent corrosion of heat-exchanger (boiler) tubes, thus extending their life time. This study was done using gas turbine engines and a laboratory generator set. The units burned marine diesel or diesel No. 2 fuel with sulfur contents up to 1.3 percent. The exhaust from these systems contained an excess of 20 percent oxygen, and 3–10 percent water vapor. Exhaust temperatures ranged from 728 to 893 K (455 to 620°C).

Introduction

Combined-cycle systems have three major parts: (1) a gas turbine engine, (2) a steam-generating unit (boiler), and (3) a steam turbine. The hot exhaust from the gas turbine engine is vented into a unit of finned metal tubes filled with water. The heat converts the water into steam that is vented into a steam turbine where it does useful work (Fig. 1) [1].

Efficiency and durability are essential in combined-cycle steam systems. Both are affected substantially by corrosive components in the flue gases, the most severe of which is sulfuric acid, H_2SO_4. Minimizing sulfuric-acid corrosion in the boiler unit of a combined-cycle system can greatly extend the lifetime of the boiler, and make the entire system more cost effective. The first step is to determine how much sulfur dioxide (SO_2) is converted into sulfur trioxide (SO_3) in gas turbine exhaust. This information is used to estimate acid dewpoints, which are valuable in determining feedwater temperature settings for the boiler. Given in this paper are: (A) a review of some of the basic theories for the formation of H_2SO_4 in gas turbine exhaust; (B) the percentage conversion of SO_2 to SO_3 in the exhaust of three systems: (1) a large stationary gas turbine (G.E. LM2500), (2) a Centaur combined-cycle system, and (3) a Laboratory Experimental Combustor Boiler-Loop unit; and (C) acid dewpoints estimated from the amount of sulfuric acid in the engine exhaust.

During the combustion of diesel fuels, oxides of sulfur and sulfuric acid are produced by the following reactions:

$$S + O_2 \rightarrow SO_2 \qquad (1)$$

$$SO_2 + H_2O \rightleftharpoons H_2SO_3 \qquad (2)$$

$$SO_2 + 1/2\,O_2 \rightleftharpoons SO_3 \qquad (3)$$

$$SO_3 + H_2O \rightleftharpoons H_2SO_4 \qquad (4)$$

$$H_2SO_4 + 2H_2O \rightleftharpoons 2H_3O^+ + SO_4^= \qquad (5)$$

The extent of these reactions depends upon the engine type and operating conditions. Turbine engines are capable of causing reaction (1) to go to completion because sulfur does not exist in the zero oxidation state in turbine exhaust. Also, more than 90 percent of the sulfur is in the +4 oxidation state as SO_2, but a small percentage can be converted to SO_3.

The SO_2 sulfidation–oxidation, i.e., "hot corrosion" of nickel-based alloys, such as the ones being proposed for present-day heat-exchanger systems, is expected to be retarded by the more than 20 percent excess oxygen in the exhaust [2].

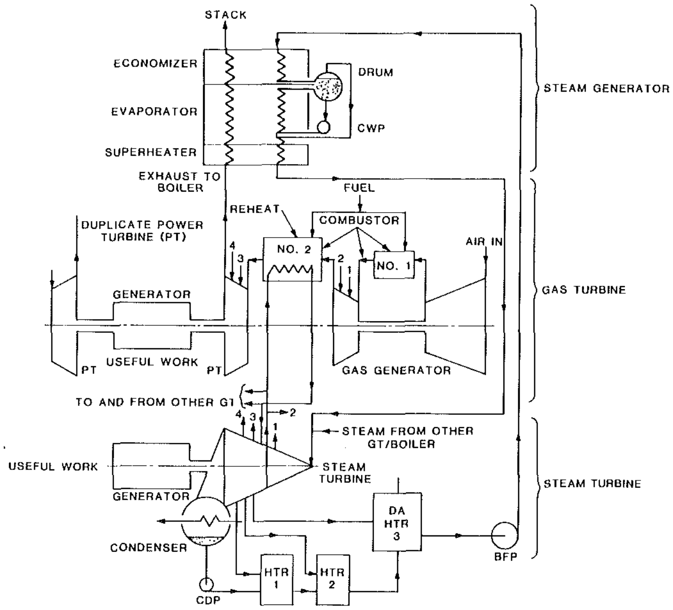

Fig. 1 Schematic flow diagram of reheat gas turbine combined-cycle system showing extraction steam points numbered 1–4 for gas turbine vane and blade cooling

---

Contributed by the International Gas Turbine Institute for publication in the Journal of Engineering for Gas Turbines and Power. Manuscript received at ASME Headquarters October 1989.

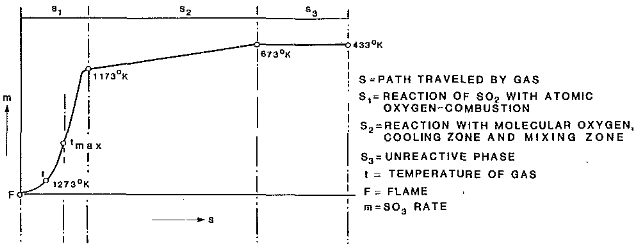

Fig. 2 Phases of conversion of SO_2 to SO_3 in flue gas for gas turbines

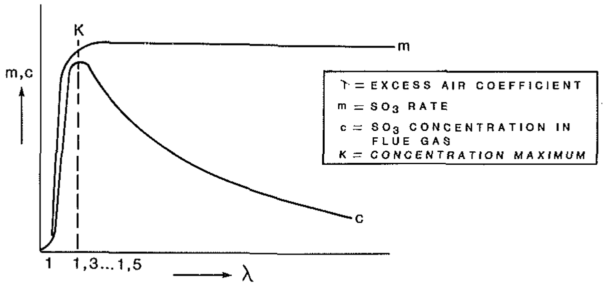

Fig. 3 SO_3 rate and concentration as a function of excess air for gas turbines and combined gas and steam turbine plants

Also, researchers have concluded that the amount of SO_2 converted to sulfurous acid (H_2SO_3) does not pose a serious corrosion problem [2]. The solubility of SO_2 in water is 10 wt% at 293.15 K (20°C) and 1.013×10^5 Pa (1 atm). The solubility decreases with increasing temperatures, 0.00058 kg/0.1 kg (0.58 wt%) H_2O at 363 K (90°C) [3]. Solutions of H_2SO_3 are largely hydrogen sulfite ions, HSO_3^-, with a small percentage of sulfite ions, $SO_3^=$, present (reactions (6) and (7)). *Further reaction of* H_2SO_3 *with molecular oxygen can cause* sulfuric acid or metal sulfates (M_xSO_4) to be formed, especially in the presence of ferrous and arsenite ions.

$$H_2O + H_2SO_3 \rightleftharpoons HSO_3^- + H_3O^+ \qquad (6)$$

$$H_2O + HSO_3^- \rightleftharpoons H_3O^+ + SO_3^= \qquad (7)$$

In gas turbines the amount of excess air, and therefore excess oxygen, is greater than it is in boilers. The reaction of both molecular and atomic oxygen with SO_2 to form SO_3 first occurs downstream from the primary zone, with an additional 10 percent formed at the entrance of the turbine transition duct. Other factors remaining constant, the formation of SO_3 increases with increasing oxygen content and pressure to a given level (Figs. 2 and 3). Beyond this level, excess air will dilute the flue gases and lower the partial pressures of sulfuric acid and water, thus lowering the dewpoint. Work done by S. C. Hunter gives more information on the reaction kinetics of SO_3 formation in turbine exhaust [4].

Most research in this area has been focused on limiting the amount of sulfur in fuel and thus limiting the amount of sulfur trioxide formed in reaction (3) that could be deposited as sulfuric acid (reactions (4) and (5)). Sulfates of platinum and nickel, and oxides of tungsten, vanadium, molybdenum, chromium, nitrogen, and iron are well-known catalysts for reaction (3). This reaction is exothermic, but SO_2 and O_2 do not combine at a measurable rate at room temperature. Even at temperatures of 673-938 K (400-665°C), where the uncatalyzed reaction rate is significant, the yield of SO_3 is believed to be small (Fig. 2) [5].

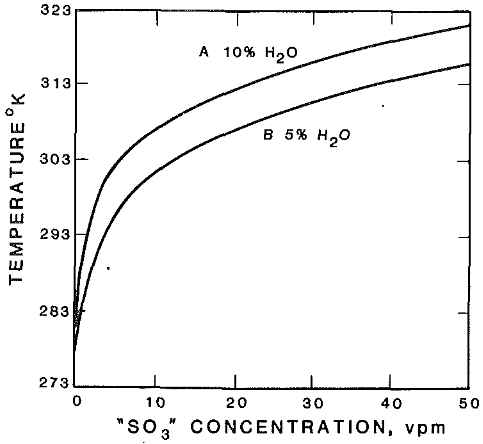

Fig. 4 Acid dewpoint versus H_2SO_4 concentration for two levels of H_2O (from Verhoff and Banchero)

Factors important in determining the percentage conversion of SO_2 to SO_3 in flue gases are: (1) excess oxygen, (2) sulfur content in the fuel, (3) catalytic substances, (4) combustion and mixing processes, (5) dwell time of the flue gases in the system, and (6) the presence of solid particles such as soot.

Because most of these factors have been determined for gas turbines, the present study was directed toward determining the amount of SO_3 produced from the combustion of liquid fuels in these engines with sulfur contents ranging from 0.18 to 1.3 percent. Acid dewpoints were calculated from these data. The systems studied were not at equilibrium.

The acid dewpoint is the highest temperature at which H_2SO_4 vapor ($SO_3 + H_2O$) is in equilibrium with H_2SO_4 liquid at a given pressure. The acid dewpoint increases as the amounts of SO_3 and moisture in the exhaust increase (Fig. 4) [6, 7].

In many cases, experimental measurements of the partial pressures of SO_3 and H_2SO_4 vapors above H_2SO_4 solution do not agree with those calculated from thermodynamic data. However, Verhoff and Banchero have taken data from several experimentalists and formulated an equation for acid dewpoints [7]

$$\begin{aligned}\frac{1}{T_{DP}} &= 0.002276 - 0.00002943 \ln (P_{H_2O}) \\ &- 0.0000858 \ln (P_{H_2SO_4}) \\ &+ 0.00000620 (\ln P_{H_2SO_4}) (\ln P_{H_2O}), \qquad (8)\end{aligned}$$

where T_{DP} = dewpoint, K; P = partial pressure, mm Hg. Equation (8) was used to calculate the acid dewpoints in the exhaust of the systems studied.

Experimental

We used three gas turbine engines in these experiments: (1) a G. E. LM2500 (FFG-7), 1B) gas turbine engine located at NAVSSES—Philadelphia, (2) a Centaur engine made by Solar Turbine, Inc., and (3) a Laboratory Subscale-Hot Loop. As a general profile, our system's fuel/air ratio ranged from 45 to 88 percent with the excess oxygen in the exhaust exceeding 20 percent. Samples were extracted isokinetically, but not at equilibrum conditions, for SO_2, SO_3, and O_2. The temperature of the sampling zone ranged from 645 to 727 K (372 to 454°C). The amount of water vapor in the exhaust was 3-10 percent.

Nomenclature

EPA = Environmental Protection Agency
NAVSEC = Navy Ship Engineering Center
NAVSSES = Navy Systems Engineering Station
H_2SO_3 = sulfurous acid
H_2SO_4 = sulfuric acid
SO_2 = sulfur dioxide
SO_3 = sulfur trioxide

Table 1 Experimental conditions for exhaust sampling, SO_2/SO_3 FFG-7, G.E. LM2500, NAVASSES, Philadelphia

Power turbine speed, rpm	Power turbine inlet temperature, K	Power turbine pressure, kPa	Gas generator speed, rpm	Gas generator total pressure, kPa	Gas generator total temperature, K	Shaft power, W × 10^6
700	109.35	18.8	5750	14.8	333.45	0.373
2500	1349.75	37.6	8200	14.6	335.05	7.833
2500	1424.95	42.4	8300	14.7	333.15	10.966
2900	1584.65	51.3	8800	14.6	332.95	15.442

Table 2 Atmospheric conditions from the Philadelphia weather bureau, May 18-20, 1983, 12:00 noon

Parameter	W	Th	F
Percent relative humidity	23	39	93
H_2O dewpoint, K	298.15	313.15	336.15
Ambient air temperature, K	337.15	339.15	337.15
Ambient air pressure, Pa	1.0158E+6	1.0158E+6	1.0192E+6

Table 3 Concentrations of anions in exhaust gas samples from the laboratory subscale test loop; measurements made by ion chromatography [a,b]

	Concentration of Anions (ppm)			
Collection zone	Cl^-	NO_3^-	$SO_3^=$	$SO_4^=$
Condenser				<1.0
Impinger No. 1	<0.25	<1.55	7.2	7.4
Impinger No. 2	<0.25	<1.55	None	26.5
Impinger No. 3	<0.25	<1.55	None	1.0

---

[a] Sulfite ions were measured by a wet chemical method.

[b] Analyses were performed by the analytical staff at San Diego Gas and Electric and Analytical Technologies, Inc., San Diego, CA.

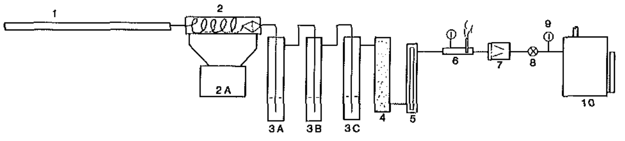

1. HEATED QUARTZ LINED PROBE
2. CONDENSER
   (a) CONDENSER HEATER & PUMP
3. IMPINGERS
   (a) 80% AQUEOUS ISOPROPANOL
   (b) 3% AQUEOUS H_2O_2
   (c) 3% AQUEOUS H_2O_2
4. DESICCANT-SILICA GEL
5. FLOW METER
6. DRY GAS - PRESSURE & TEMPERATURE
7. FILTER & CONTROL ORIFICE
8. SYSTEM FLOW SHUT OFF VALVE
9. VACUUM PUMP CHECK GAUGE
10. VACUUM PUMP

Fig. 5 SO_2 - SO_3 controlled condensation system

Table 4 Measurements of SO_2/SO_3 concentrations in gas turbine exhaust[a]: Engines tested were G. E. LM 2500 (FFG-7 NO. 1B, NAVSSES—Philadelphia) and Centaur gas turbine, San Diego, CA

Engine horsepower	Percent H_2O	SO_3, ppm	Percent conversion	Dewpoint, K
500	3.7	1.9	3.4	374.55
10,500	5.05	5.5	8.3	403.16
14,700	4.74	6.2	8.4	387.60
20,500	4.24	5.7	5.6	385.94
Centaur	4.46	3.7	5.3	383.66

---

[a] The LM-2500 SO_2 concentration ranged from 54 to 75 ppm with a questionable 98.7 ppm at full power. The calculated air/fuel ranged from ratio 47 to 66. Sample collection time was 1.0 hour for all runs, except full power, which had a collection time of 20 minutes.

The concentrations of SO_2 measured were 54–75 ppm.

The G. E. LM2500 burned marine diesel fuel, air/fuel ratio 48–58, and was operated from idle to full-load conditions while samples were extracted from the exhaust at specific settings. Atmospheric and engine operating conditions are listed in Tables 1 and 2. The Centaur engine operated on diesel fuel No. 2 at 2.9800×10^4 W (4000 hp) and with an air/fuel ratio of 66. The exhaust temperature ranged from 727 to 894 K (454 to 621°C). This engine was connected to a heat exchanger. Sulfur oxides were extracted from the exhaust and analyzed. The Laboratory Subscale Hot Loop System burned Diesel fuel No. 2; its operating parameters were: fuel consumption 2.0188 E^{-5} m^3/s (0.320 gal/min), airflow rate 0.1512 kg/s (1200 lb/h), fuel/air ratio 88, exhaust gas temperature 711–728 K (438–455°C), and hp 0.1260 kg/s (1000 lb/h) steam. Exhaust gas samples were extracted and analyzed.

EPA Method 8 was modified and used to separate and collect SO_2 and SO_3 from the turbine exhaust. Exhaust gas samples were taken with a Corbett/Flint–Goksyr/Ross collection apparatus and a quartz-lined stainless-steel probe (Fig. 5). The probe [0.9144 m × 0.0222 m (36 in. × 7/8 in.)] was positioned midway in the exhaust stream, which was above the eductor on the G. E. LM2500. The probe was maintained above 465.0 K (192°C) to prevent premature condensation of SO_3. The exhaust gases were drawn into a condenser heated to 350 K (77°C) through a probe with the aid of a pump. Concentrated H_2SO_4 was collected in the condenser. After the condenser were three impingers: The first one contained 80 percent isopropanol for removing additional SO_3 and H_2SO_4; the second and third contained 3 percent hydrogen peroxide for collecting SO_2 and converting it into H_2SO_4.

A $BaSO_4$ precipitation method and ion chromatograph were used to determine the amount of H_2SO_4 obtained from SO_3 and SO_2. The balance between fuel sulfur and sulfur oxides was improved by washing the collection tubes with water and adding the solution to the appropriate container.

On-line systems were used to measure concentrations of NO_x, CO, CO_2, O_2, hydrocarbons (HC), and SO_2 in the exhausts. Concentrations of SO_2 were made using a TECO Model 40 Pulsed Fluorescent Analyzer (manufactured by Thermo Electron Corp. of Holkinton, MA). This unit tended to give low values because of a loss of SO_2 in condensed water even though a permeation dryer was used.

Results and Discussions

One of the first tasks was to identify the acids being collected in each impinger. Selected samples were sent to independent laboratories for analysis. The composition of the first impinger was about 50 percent $SO_3^=$ and 50 percent $SO_4^=$ from dissolved SO_2 and SO_3, respectively. Laboratory experiments with H_2SO_3 showed that under the stated experimental conditions it is not converted to H_2SO_4. Therefore, the 50/50 mixture was not produced from H_2SO_3-to-H_2SO_4 conversion in solution. Our purpose had been to collect only SO_3 in impinger No. 1 and we expected only $SO_4^=$ ions in solution. However, we used the experimentally determined concentrations for the species in

Table 5 Conversion of SO_2 to SO_3 in the exhaust of a laboratory subscale test loop[a,b]; the average of three runs from each sampling period is reported

Fuel sulfur	Concentration $SO_4^=$ (ppm)						Percent conversion[c]
	Probe	Condenser	Impinger 1	Impinger 2	Impinger 3	Total	
0.48	0.4	0.0	11.9	39.8	14.6	66.7	9.5
0.46	0.1	0.0	10.9	43.6	13.7	68.3	8.2
0.56	0.8	0.1	12.9	44.9	15.6	74.3	10.0

---

[a] The apparatus was covered and the probe insulated. The temperature of the water in the condenser was 355.4 K.

[b] Fuel consumption 2.020 × 10^{-5} M^3/s, airflow 2.832 × 10^{-1} M^3/s, air/fuel = 88, exhaust temperature 727 K, steam consumption 1.260 × 10^{-1} kg/s, 3 percent water vapor in the exhaust.

[c] The average percentage conversion of SO_2 to SO_3 is 9.2.

Table 6 Conversion of $SO_2 \rightarrow SO_3$ in gas turbine exhaust and in the exhaust of the laboratory subscale test loop; typical runs from the three systems are reported[a,b,c]

Test equipment	Percent sulfur in fuel	Concentration of anions, ppm					Percent conversion
		Condenser	Impinger 1	Impinger 2	Impinger 3	Total $SO_4^=$	
Centaur	0.43	2.2	3.0	48.9	10.8	69.3	5.3
GE-LM-2500	0.18	0.4	3.2	46.5	5.0	55.1	3.6
Test loop[a]	0.48	0.4	11.9	39.8	14.6	66.7	9.4

---

[a] Engine shaft horsepower 3899, 15,000, and 15,000.

[b] Water vapor concentration 3-5 percent.

[c] Calculations are based upon known composition of impingers.

Table 7 SO_2 and SO_3 measurement aboard the GTS Adm. Callaghan during east/west voyages in the Atlantic Ocean[a]

Voyage	Engine	Percent sulfur in fuel	SO_2 ppm (V)	Percent Conversion $SO_3/(SO_2 + SO_3)$ by volume (Impinger only)	(Impinger + line rinse)
142	1	0.75	110	6.5	39.0
142	2	0.82	117	4.5	22.0
152	1	0.45	93	2.0	4.1
152	2	0.42	51	2.1	3.0
172	2	0.17	38	8.1	10.0
172	1	0.86	103	3.6	4.9
172	2	0.86	99	10.5	29.3
			Average	5.3	14.6

Combined average 9.96

---

[a] Sulfur content of diesel fuels available to ships is likely to be higher if purchased in less-developed countries.

solution for our calculations (Table 3). The Cl^- and NO_3^- ion concentrations were negligible by comparison to the other anions. Therefore, hydrochloric acid (HCl) and nitric acid (HNO_3) did not contribute significantly to the overall acidity of the solution in the impingers.

The SO_3 *concentration* was 3.7 ppm *in the exhaust of the* Centaur turbine engine (fuel: diesel No. 2, (0.43% sulfur). This represented a 5.3 percent conversion of SO_2 to SO_3 and a calculated acid dewpoint of 383.7 K (110.5°C) (Table 4). The exhaust of the G.E. LM-2500, burning marine diesel fuel, was also tested, and the hp was changed from idle to full load 3.73 × 10^5 - 1.5293 × 10^7 W (500-20,500 hp), the SO_3 concentration changed from 2 to 6 ppm, which represented a 3-8 percent conversion of SO_2 to SO_3. The calculated acid dewpoints were 374-403 K (101-130°C) with a moisture content of 5 percent (Table 4). These data were in agreement with the 8 and 10 percent average conversions reported by other companies (Tables 7 and 8). Also, the calculated acid dewpoints were of the same order as those reported in the Russian literature by Romanov et al.: 388 to 393°K (115-120°C) [8].

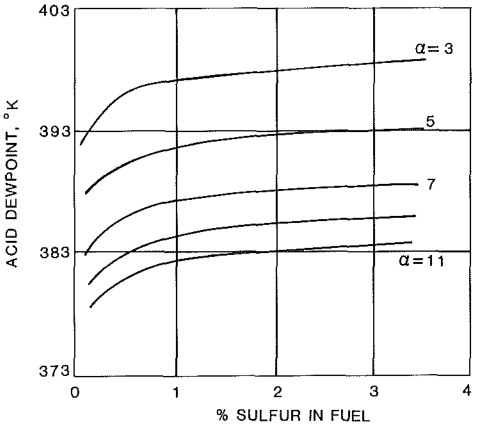

Fig. 6 ***Sulfuric acid vapor dewpoint as function of fuel sulfur content for various excess air ratios α***

The sulfur content was slightly higher in the fuel used in the Laboratory Test Unit than in the fuels of the Centaur or LM2500. Also, the air/fuel ratio was increased more than 15 percent by comparison. However, *the percentage conversion* of SO_2 to SO_3 was in the same range (Table 5).

General Electric Corporation measured SO_2, SO_3, and total hydrocarbon content in the exhaust of two G.E. LM2500 gas turbines, burning marine diesel, aboard the GTS Adm. Wm. M. Callaghan [9]. The fuel's sulfur content ranged from 0.17 to 0.86 percent. The conversion of SO_2 to SO_3 varied from 2-22 percent with a high value above 30 percent. The average conversion was 10 percent (Tables 6 and 7). Possible causes for the variability of the data, listed by G. E., were:

> "Variation in SO_3 concentration was due mostly to the heterogeneous processes in the combustion chamber and slow rate of SO_3 formation."
>
> "Samples were extracted for several hours with the engine operating over a range of power settings."
>
> "Experimental conditions required long sample lines from the engine to the NAVSEC trailer when specimens were transported to Evendale for analysis."

Table 8 Percent conversion of SO_2 to SO_3 in gas turbine exhaust from the combustion of liquid fuel

Company	Percent sulfur in fuel	Engine	Percent conversion
A	0.48	Test loop	9.5
A	0.43	Centaur	5–7
B	0.18	G. E. LM-2500	3–8
C	0.37	Large stationary turbine	2–14
D	0.17–0.86	G. E. LM-2500	2–22

KVB, Inc. has presented data with a conversion of SO_2 to SO_3 of 2–14 percent, which increases to 20 percent at the combustor exit [4]. Their collection method was similar to the one described under the experimental section of this paper. However, they used two impingers instead of three with 3 percent hydrogen peroxide in each. The engine was a large stationary gas turbine burning oil distillate, 0.37 percent sulfur [5].

Romanov et al. reported an acid dewpoint of 388–393 K (115–120°C) from analytical determinations of H_2SO_4 in the combustion products of a combined cycle system. The research was done at the Leningrad "Order of Lenin Shipbuilding Institute." A KUP-1300 steam generator was connected to an M-25 gas turbine that burned diesel special fuel (GOST 4749-73) with a sulfur content of 0.1–3 percent and excess air of 3–11 percent. The acid dewpoints seem to decrease with increased excess air (Fig. 6). Data were also taken from a steam generator burning fuel oil with sulfur content up to 3 percent. Gas turbine fuels sometimes reach 2.5 percent (GOST 10433-75) and higher acid dewpoints would be expected [8].

A summary of the test results shows that the percentage conversion is not dependent solely upon the fuel sulfur content (Table 8). A combination of parameters should be studied before making a decision about SO_2-to-SO_3 conversion in gas turbine exhaust. Air/fuel ratio, engine operating power conditions, water content in the exhaust, and combustor design are major factors.

Sulfuric acid causes corrosion in Ni-based superalloys, such as those used in present-day boiler designs [10, 11]. Therefore, H_2SO_4 formation must be controlled. With each unit first determine its present rate of sulfur-oxide conversion, then modify the design or take steps to reduce the fuel sulfur. Some research laboratories are using bacteria to reduce the amount of sulfur in fuel [12].

Sulfuric acid also seems responsible for the glue or resin found in the soot that sticks to surfaces that are in contact with the exhaust. Catalytic action of H_2SO_4 with alloys is thought to cause the fouling [13].

Conclusions

The percent conversion of SO_2 to SO_3 in gas turbine exhaust is unique to a particular kind of engine, its combustion system, its operating conditions, and its fuel sulfur. The percentage conversion averaged less than 10 percent for the G.E. LM2500 and Centaur engines. Both burned diesel fuel No. 2 with a sulfur content of 0.18 and 0.43 percent, respectively, which gave a calculated acid dewpoint range of 388.71–399.82 K (115.56–126.67°C). Feedwater settings above this range should greatly reduce acid corrosion of heat-exchanger surfaces of combined-cycle systems utilizing these engines. Also, these settings should extend the lifetime of the boiler unit, making the overall system more cost effective.

Acknowledgments

The author gratefully acknowledges T. L. Johnson and H. A. Cook for their contribution to this work. The United States Department of the Navy funded the project, which was conducted in San Diego, CA.

References

1 Rice, R. G., "The Reheat Gas Turbine Combined Cycle," *Mechanical Engineering*, Vol. 104, No. 4, 1982, p. 50.

2 Viswanathan, R., and Sprengler, C. J., *Corrosion*, Vol. 26, 1970, p. 29.

3 Weast, R. C., and Astle, M. J., *Handbook of Chemistry and Physics*, CRC Press, FL, 1962.

4 Hunter, S. C., "Formation of SO_3 in Gas Turbines," ASME JOURNAL OF ENGINEERING FOR POWER, Vol. 104, 1982, pp. 44–51.

5 Bodenstein, M., and Pohl, W., *Z. Electrochem.*, Vol. II, 1904, p. 373.

6 Peacock, C. R., "Methods of Measuring Sulfuric Acid Dewpoints," presented at the 23rd Annual ISA Analysis Instrumentation Symposium, IBSN 87664-361-6, May 1977.

7 Verhoff, F. H., and Banchero, J. T., "Predicting Dewpoints of Flue Gases," *Chem. Eng. Progress*, Vol. 70, 1974, pp. 71–78.

8 Romanov, V. A., Dmitrieve, G. I., Shcherbinkin, V. I., and Protsenko, G. V., *Energomashinostroenie*, Vol. 8, 1978, p. 22.

9 General Electric Company, Document No. 7A003CIP235, 1980.

10 Zurich, D. L., *Brown Boveri Review*, BBC Brown Boveri and Co., Ltd., Baden, Switzerland, G5, 1978, p. 691.

11 Radway, J. E., and Exley, X. X., "A Practical Review of the Causes and Control of Cold End Corrosion and Acid Stack Emission in Oil-Fired Boilers," ASME Paper No. 85-WA/CO-8, 1985.

12 Alper, J., *High Technology*, Vol. 4, 1984, p. 32.

13 Part 2 of this Research project.

The Impact of Atmospheric Conditions on Gas Turbine Performance

A. A. El Hadik
Assistant Professor,
Mechanical Engineering Department,
Faculty of Technological Studies,
Kuwait

In a hot summer climate, as in Kuwait and other Arabian Gulf countries, the performance of a gas turbine deteriorates drastically during the high-temperature hours (up to 60°C in Kuwait). Power demand is the highest at these times. This necessitates an increase in installed gas turbine capacities to balance this deterioration. Gas turbines users are becoming aware of this problem as they depend more on gas turbines to satisfy their power needs and process heat for desalination due to the recent technical and economical development of gas turbines. This paper is devoted to studying the impact of atmospheric conditions, such as ambient temperature, pressure, and relative humidity on gas turbine performance. The reason for considering air pressures different from standard atmospheric pressure at the compressor inlet is the variation of this pressure with altitude. The results of this study can be generalized to include the cases of flights at high altitudes. A fully interactive computer program based on the derived governing equations is developed. The effects of typical variations of atmospheric conditions on power output and efficiency are considered. These include ambient temperature (range from −20 to 60°C), altitude (range from zero to 2000 m above sea level), and relative humidity (range from zero to 100 percent). The thermal efficiency and specific net work of a gas turbine were calculated at different values of maximum turbine inlet temperature (TIT) and variable environmental conditions. The value of TIT is a design factor that depends on the material specifications and the fuel/air ratio. Typical operating values of TIT in modern gas turbines were chosen for this study: 1000, 1200, 1400, and 1600 K. Both partial and full loads were considered in the analysis. Finally the calculated results were compared with actual gas turbine data supplied by manufacturers.

Introduction

Over the last three decades, gas turbines have played a unique role in the power industry. Because of their relatively low initial cost, gas turbines are frequently used for emergency services and handling daily peak loads on a power plant system. In many systems gas turbines are also operated in the spinning reserve mode.

Recent improvements in gas turbine performance have led to increases in gas turbines efficiency. Many researchers have worked on the evaluation of gas turbine performance. Recently, Yousef et al. (1987) re-evaluated the thermophysical properties of the combustion gases of the gas turbine engines using the Soave–Redlich–Kwong (SRK) equation of state. The properties considered in their work were density, specific heat at constant pressure, enthalpy, entropy, viscosity, and thermal conductivity. The SRK equation of state generally predicted better values for thermophysical properties than those predicted by the virtual equation of state. In addition, the thermodynamics of compression and expansion process in turbomachinery is reanalyzed by Sergio et al. (1986).

The present study is carried out on the impact of atmospheric conditions on a gas turbine performance. It is well known that gas turbine performance is affected by varying atmospheric conditions, such as the temperature, pressure, and relative humidity. A computer program is especially designed to calculate overall thermal efficiency and the specific net work from the simple-cycle gas turbine. These calculations were carried out for various combustor discharge temperatures (TIT) and pressure ratios. Partial loads are considered as well as full load during these calculations.

Theoretical Analysis

Due to the simplicity in design of the simple-cycle gas turbine, it is the most-used topping cycle in today's combined plants. The arrangement illustrated schematically in Fig. 1(*a*) shows the flow diagram for the cycle under consideration, and its thermodynamic state points are illustrated on temperature–entropy coordinates in Fig. 1(*b*).

The fuel is assumed to be methane. All gaseous mixtures considered in the calculations may be treated as mixtures of

---

Contributed by the International Gas Turbine Institute for publication in the JOURNAL OF ENGINEERING FOR GAS TURBINES AND POWER. Manuscript received at ASME Headquarters October 1989.

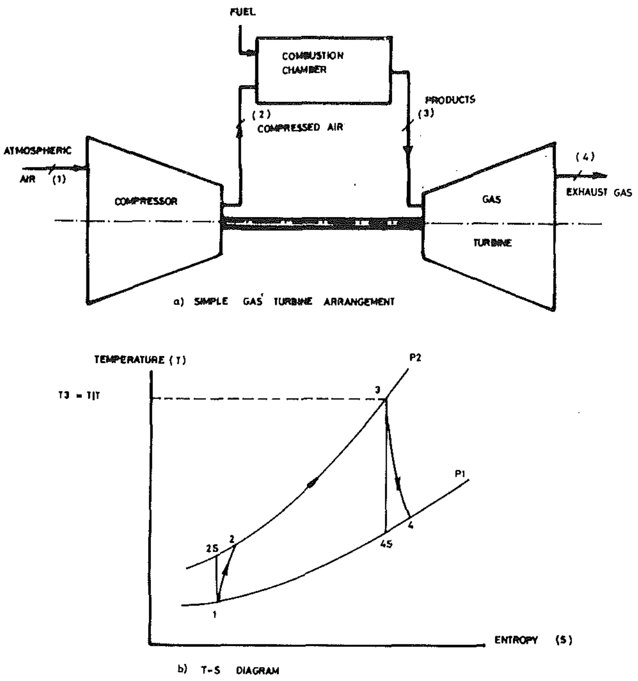

Fig. 1 Basic gas turbine engine

varying proportions of three components. These components are: air (77.44 percent N_2, 20.76 percent O_2, 0.92 percent Ar, 0.85 percent H_2O, 0.03 percent CO_2); water (100 percent H_2O); and stoichiometric gases (70.16 percent N_2, 19.58 percent H_2O, 9.43 percent CO_2, 0.83 percent Ar). Polynomial fits for the specific heats of each of those three components as a function of temperature are used in the calculations. The specific enthalpy is treated as the sum of chemical components and thermomechanical components.

The operating principle of a gas turbine is simplified as follows. Basically ambient air is drawn into a multistage compressor when it is compressed to about 10 times atmospheric pressure. The compressed air then passes through the combustion chamber where fuel is injected and burned. The products of combustion enter the turbine and expand to approximately atmospheric pressure. Part of the work developed by the turbine is used to drive the compressure, while the remainder is delivered to equipment external to the gas turbine.

Therefore, the gas turbine performance varies significantly with compressor inlet air conditions, mainly the atmospheric temperature, pressure, and relative humidity. Gas turbine design ratings are usually based upon standard conditions. The standard conditions differ from country to country. One popular standard is that of the International Standards Organization (ISO). The site conditions at this standard case are: sea level altitude (101.325 kPa, 15°C, and 60 percent relative humidity).

In the present study the effect of atmospheric conditions on the gas turbine performance was taken into consideration. A computer program is designed especially for calculating the overall thermal efficiency and specific output work. The governing equations are:

(a) Compression Process: For a given polytropic efficiency, the pressure ratio, temperature, and thus other state variables for each stream can be calculated. The specific enthalpy can be calculated from the specific heat polynomials

$$h=\int_{T_1}^{T_2} CP_a(T)dt \tag{1}$$

where

$$CP_a = CP_d + H * CP_s \tag{2}$$

$$CP_d = [28.11 + 0.001967T + 0.4802 \times 10^{-5}T^2 - 1.966 \times 10^{-9}T^3]/28.97 \tag{3}$$

where 28.97 is the molecular weight of dry air;

$$CP_s = [32.24 + 0.001923T + 1.055 \times 10^{-5}T^2 - 4.187 \times 10^{-9}T^3]/18.015 \tag{4}$$

where 18.015 is the molecular weight of vapor.

Humidity ratio

$$H = 0.622\,\frac{P_v}{P_d} = 0.622\,\frac{P_{ss}\bullet\Phi}{P_a - P_v} \tag{5}$$

Steam mass fraction

$$(\text{SMF}) = \frac{H}{1+H} \tag{6}$$

Air mass fraction

$$(\text{AMF}) = 1 - \text{SMF} \tag{7}$$

Molecular weight of mixture

$$(\text{MMW}) = \frac{1}{\dfrac{\text{SMF}}{18.015} + \dfrac{\text{AMF}}{28.97}} \tag{8}$$

Nomenclature

CP = specific heat of working substances at constant pressure, kJ/kg K
f = theoretical fuel/air ratio, kg fuel/kg air
$\bar{f}$ = actual fuel/air ratio, kg fuel/kg air
H = humidity, kg moisture/kg air
h = enthalpy, kJ/kg
LHV = lower heating value (enthalpy of reactions), kJ/kg
M = molecular weight
MMW = mixture molecular weight
R = gas constant, kJ/kg K
$\bar{R}$ = universal gas constant, kJ/kg mol K
RH = relative humidity of air, percent
P = pressure, N/m^2
PR = pressure ratio (compression or expansion)
T = temperature, K
TIT = maximum turbine inlet gas temperature, K
W = specific net work (net work per unit mass of air), kJ/kg of air
γ = specific weight of substances, N/M^3
η = overall thermal efficiency, percent
ρ = density, kg/m^3
Φ = relative humidity, percent

Subscripts

a = ambient air
c = compressor
d = dry air
f = fuel
m = mixture
P = products
s = moisture
ss = saturated vapor
t = turbine
V = vapor
1, 2, 3, 4 = cycle state points, Fig. 1(*b*)

Gas constant of mixture

$$(R_{\text{mixture}}) = \frac{\bar{R}}{\text{MMW}} = \frac{8.3143}{\text{MMW}} \tag{9}$$

Mean specific heat at constant pressure

$$(C_{pm}) = \frac{Cp_1 + Cp_2}{2} \tag{10}$$

Mean specific heat at constant volume

$$(Cv_m) = Cpm - R_{\text{mixture}} \tag{11}$$

Isentropic exponent

$$(k) = \left(\frac{Cp}{Cv}\right)_m \tag{12}$$

$$T_{2s} = T_1 (PR)^{\frac{K-1}{K}} \tag{13}$$

By assuming constant isentropic efficiency η_{is} for the compression process, then

$$T_2 = \frac{T_{2s}}{\eta_{is}} + T_1 \left(1 - \frac{1}{\eta_{is}}\right) \tag{14}$$

where η_{is} can be considered equal to 0.87 (see Yousef et al., 1987). Then the required work per unit mass for the compressor is equal to

$$W_c = Cp_m \left[\frac{T_{2s}}{\eta_{is}} + T_1 \left(1 - \frac{1}{\eta_{is}}\right) - T_1\right] \tag{15}$$

(b) Combustion Process: The specific heat of mixture at the combustion chamber entrance is defined as follows.

(*b.1*) *Before Combustion:*

$$C_{pm} = C_{pa2} + (f/a) C_{pf} \tag{16}$$

where f/a is the fuel/air ratio, C_{pa2} is the specific heat of moist air at compressor outlet, and C_{pf} is the specific heat of fuel at combustion chamber inlet.

(*b.2*) *After Combustion:* The specific heat of gaseous products after combustion may be determined by using a mathematical model formulated using regression analysis to relate combustion temperature and fuel-to-air ratio to the specific heat of gaseous products. The values of Cp for different fuel air ratios given by Keenan and Kage (1984) were calculated in the form of the following equations:

$$C_{p_p} = 1.01 + 0.32 \left(\frac{T_3 - 400}{1400}\right) - 0.04 \left(\frac{T_3 - 400}{1400}\right)^2 \quad (\text{for } f/a = 0) \tag{17}$$

$$C_{p_p} = 1.03 + 0.32 \left(\frac{T_3 - 400}{1400}\right) - 0.02 \left(\frac{T_3 - 400}{1400}\right)^2 \quad (\text{for } f/a = 0.0135) \tag{18}$$

$$C_{p_p} = 1.05 + 0.34 \left(\frac{T_3 - 400}{1400}\right) - 0.02 \left(\frac{T_3 - 400}{1400}\right)^2 \quad (\text{for } f/a = 0.027) \tag{19}$$

Any value in between these range limits can be interpolated to get the exact value of C_p gas.

Hence, the values of $C_{p\,\text{mixture}}$, after combustion, can be determined by using the following relation:

$$C_{pm3} = C_{pp3} + HC_{ps3} \tag{20}$$

Then, the heat transfer per unit mass into the combustion chamber can be calculated this way

$$Qin = \int_{T_2}^{T_3} [C_{pm3}(T) * T_3 - C_{pm2}(T) * T_2] dT \tag{21}$$

(c) Gas Turbine: The actual gas turbine work is given by

$$W_{T.ac} = \frac{W_{T.The}}{0.95 + (f/a)} \tag{22}$$

where $W_{T.ac}$ is the actual work per unit mass of the combustor product, $W_{T.The}$ is the theoretical work per unit mass of air inlet to the compressor, 0.95 is the ratio of the air after combustion assuming 5 percent air loss from compressor, and f/a is the fuel-to-air ratio

$$\frac{T_3}{T_{4s}} = \left(\frac{P_3}{P_4}\right)^{\frac{K-1}{K}} \tag{23}$$

where $(P_3/P_1) = PR * 0.97$ (0.97 is considered to account for the duct pressure loss); $P_4 = 101.325/0.99$ (0.99 is considered to account for the exit pressure loss); T_{4s} is the isentropic temperature at turbine exit.

$$C_{pm.g} = (C_{p_{p3}} + C_{p_{p4}})/2 \tag{24}$$

$$C_{V\ m.g} = C_{p\ m.g} - R_p \tag{25}$$

$$k_{m.g} = (C_{p\ m.g}/C_{v\ m.g})_p \tag{26}$$

Therefore

$$T_{4s} = T_3/(P_3/P_4)^{\frac{K-1}{K}} \tag{27}$$

Hence, the turbine output work is given by

$$WT.ac = C_{p\ m.g} * 0.95 + (f/a) * (T_3 - T_{4s}) * T \tag{28}$$

Then

$$\eta_{th} = (W_{T.ac} - Wc)/Qin \tag{29}$$

Finally the computer program is written in FORTRAN language and run at Kuwait University Computing Centre.

The results of equations (1)-(29) were repeated to get the converged results. Each computer run is stored until the new result comes out. A check between the new and old results is printed out. Otherwise the iteration process takes place.

Results and Discussion

The effect of atmospheric conditions (temperature, pressure, and relative humidity) on gas turbine performance has been studied. For this purpose a full computer program is constructed using the formulas derived from the previous section. The effect of atmospheric pressure is studied on the basis of change of altitude from zero to 2000 m above sea level. Also the range of study for the ambient temperature and relative humidity are considered from −20 to 60°C, and zero to 100 percent, respectively. Net specific work and overall thermal efficiency are calculated for various values of maximum turbine inlet temperature (TIT) and pressure ratio. The values of maximum turbine inlet temperature are taken as 1000, 1200, 1400, and 1600 K, while the values of pressure ratio considered in the calculation are 2, 4, 6, 8, 10, 12, 14, and 16.

Figure 1 shows the simple-cycle gas turbine arrangement considered in this study. Natural gas is assumed to be used in this analysis. However, the properties of any type of fuel can be fed to the computer program to get the exact results. Also the efficiencies of the compressor, the gas turbine, and the combustion chamber are assumed equal to 87, 89, and 97 percent, respectively. The values of the duct pressure loss and

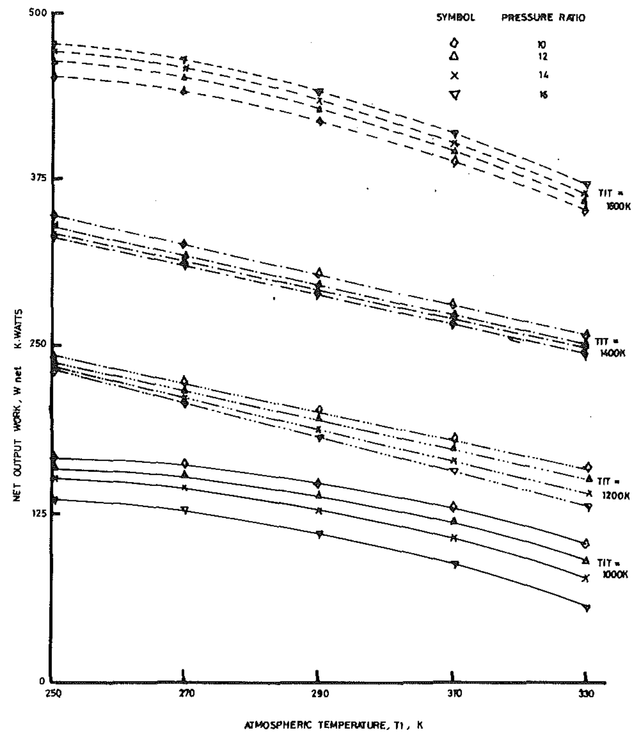

Fig. 2 Net output power with various maximum turbine inlet temperatures (TIT)

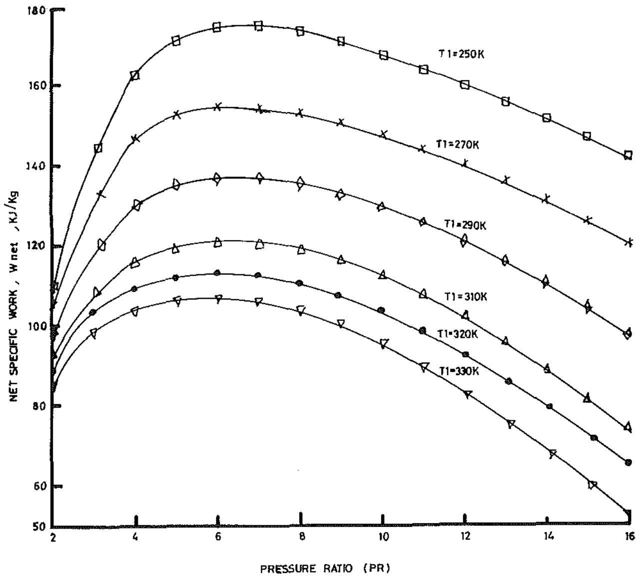

Fig. 3 Net specific work (W_{net}) with various atmospheric temperatures and constant turbine inlet temperature (TIT = 1000 K)

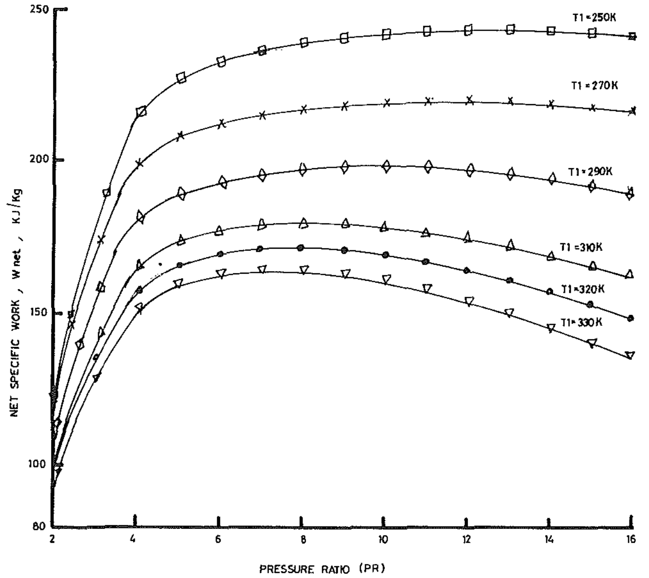

Fig. 4 Net specific work (W_{net}) with various atmospheric temperatures, and constant turbine inlet temperature (TIT = 1200 K)

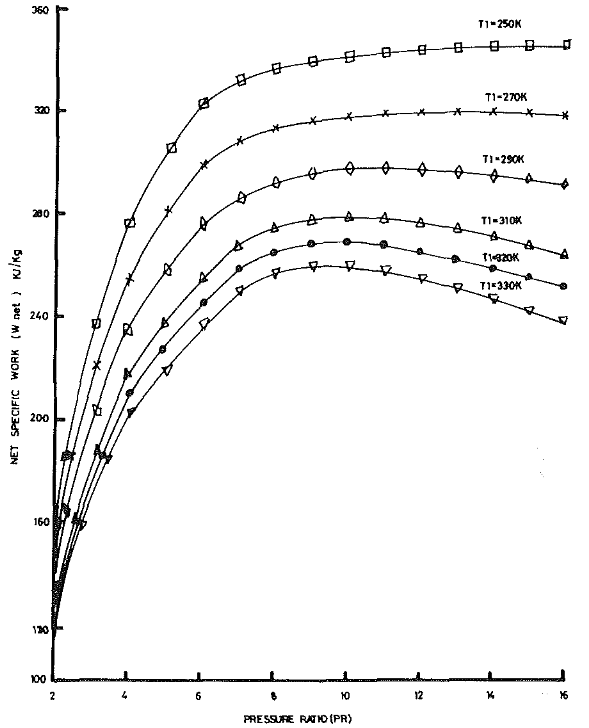

Fig. 5 Net specific work (W_{net}), with various atmospheric temperatures and constant turbine inlet temperature (TIT = 1400 K)

exit pressure gain are also assumed to be 97 and 99 percent, respectively. These assumptions have been taken from manufacturer's catalogues to approach the real results.

Figure 2 shows the net work at various ambient temperatures and different maximum inlet temperatures (TIT). The increase of the maximum inlet temperature (TIT) increases the net work. These net work values decrease as the atmospheric air temperature increases for the same TIT. The effect of the atmospheric air temperature on the thermal efficiency is also indicated through Figs. 7, 8, 9, and 10. Similarly, the effect of atmospheric air temperature on the thermal efficiency is seen to follow the same trend of the net work.

The effects of pressure ratio on both net work and thermal efficiency are clearly shown in Figs. 3–6 and Figs. 7–10, respectively.

Figure 3 shows the change of net work with various values of pressure ratio at a constant maximum turbine inlet temperature of 1000 K, and various atmospheric temperatures. In this figure, an increase of the pressure ratio to 5 increases the net work for all considered atmospheric temperatures. Beyond a pressure ratio equal to 5, an increase in the pressure ratio decreases the net work output. However, the decreasing rate is lowered by decreasing the atmospheric temperatures.

Figure 4 indicates how the net work varies with the pressure ratio when the maximum turbine inlet temperature is at a constant value of 1200 K, while the atmospheric temperature values are varied. The net work is increased with the increase

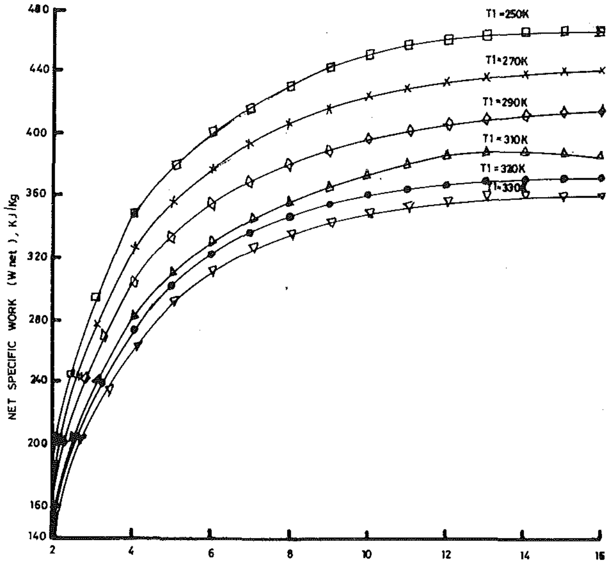

Fig. 6 Net specific work (W_{net}), with various atmospheric temperatures and constant turbine inlet temperature (TIT = 1600 K)

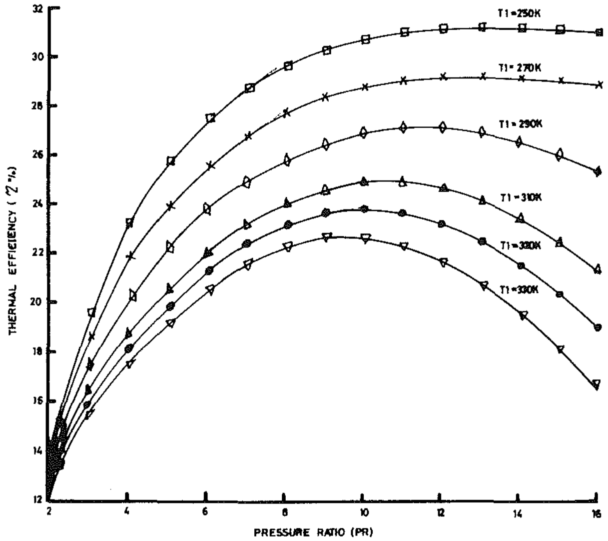

Fig. 7 Overall thermal efficiency with various atmospheric temperatures, and constant turbine inlet temperature (TIT = 1000 K)

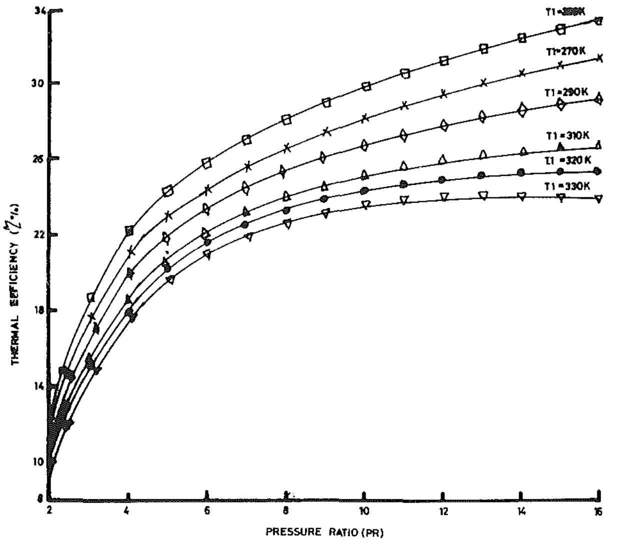

Fig. 8 Overall thermal efficiency with various atmospheric temperatures, and constant turbine inlet temperature (TIT = 1200 K)

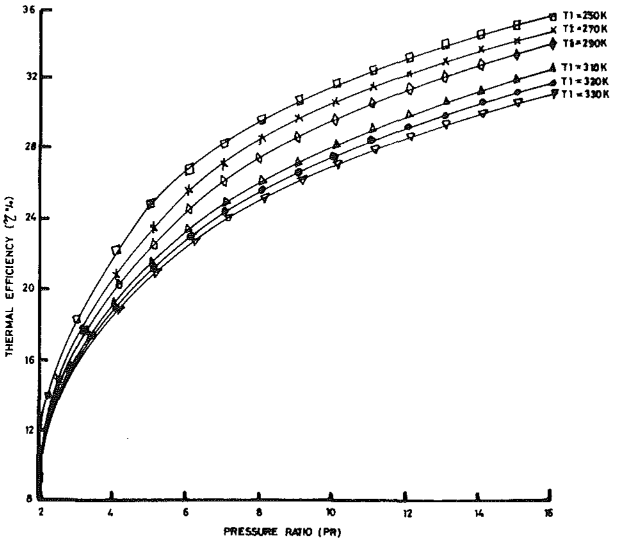

Fig. 9 Overall thermal efficiency with various atmospheric temperatures, and constant turbine inlet temperature (TIT = 1400 K)

of pressure ratio when the latter is less than 8. An increase in the pressure ratio beyond 8 decreases the net work for atmospheric temperature of 310, 320, and 330 K. However, an increase in the pressure ratio beyond 8 does not affect the net work for atmospheric temperatures of 270 and 280 K.

The same effects on the net work were observed, as shown in Fig. 5, with a change in pressure ratio for constant maximum turbine inlet temperature of 1400 K, and variable atmospheric temperatures. However, Fig. 6 shows that the increase in pressure ratio increases the net work values at all considered atmospheric temperatures, and at constant maximum turbine inlet temperature of 1600 K.

Figures 9 and 10 show the thermal efficiency at various pressure ratios and atmospheric temperatures and constant maximum turbine inlet temperatures of 1400 and 1600 K, respectively. The increase of pressure ratio increases the thermal efficiency in all the considered cases. For a pressure ratio range less than 9, the increase of this pressure ratio causes an increase in the thermal efficiency for constant maximum inlet temperature of 1000 K as shown in Fig. 7. Beyond a pressure ratio equal to 9, the increase of this pressure ratio decreases the thermal efficiency again at all considered values of the assumed atmospheric temperature. However, at higher values of atmospheric temperature, the rate of the thermal energy increase with the pressure ratio becomes smaller.

Figure 8 shows the same trend of thermal efficiency with the pressure ratio for maximum turbine inlet temperature of 1200 K. In Fig. 8 the increase of pressure ratio, in the range beyond 10 has little effect on the thermal efficiency values when the atmospheric temperature values are equal to 250 and 270 K, but the values of thermal efficiency decrease as the pressure ratio increases when the atmospheric values are in the range of 290–330 K. The atmospheric pressure has no real effect on the efficiency and work output per unit mass. However, the atmospheric pressure has a noticeable effect on the specific power output per unit volume. The importance of this point comes from the fact that the compressor sucked almost a constant volume. An increase of the specific volume (due to lowering atmospheric pressure) decreases the mass of air intake and consequently the power output. This means that decreasing the compressor inlet pressure (by changing the altitude above sea level) improves the gas turbine arrangement thermal efficiency.

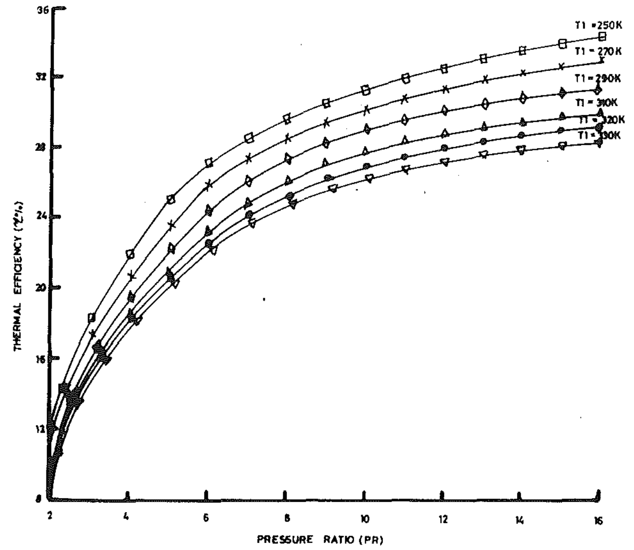

Fig. 10 Overall thermal efficiency with various atmospheric temperatures, and constant turbine inlet temperature (TIT = 1600 K)

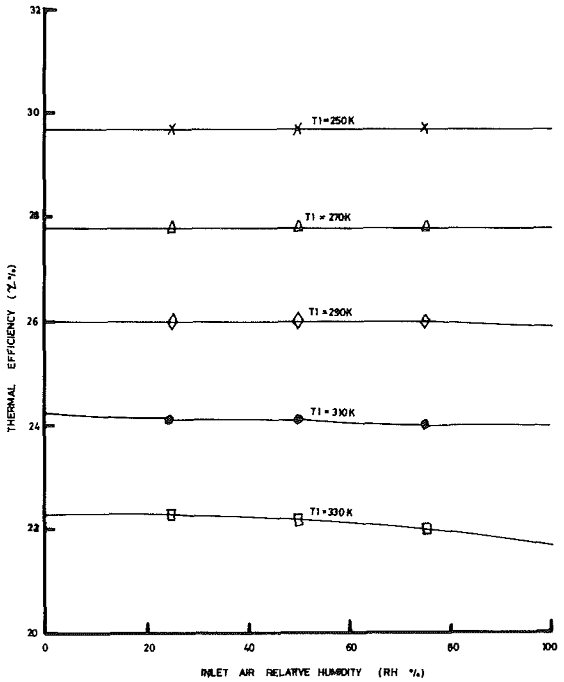

Fig. 11 Overall thermal efficiency with various atmospheric air temperatures, and relative humidities, and at constant pressure ratio (*PR* = 10) and constant turbine inlet temperature (TIT = 1200 K)

The effects of the relative humidity on thermal efficiency and net work of the gas turbine arrangement are presented in Figs. 11 and 12, respectively. In both figures no effect is noticed for atmospheric temperatures of 250, 270, and 290 K, while at higher atmospheric air temperatures (greater than 310 K), the increase in relative humidity decreases the net work values and increases the thermal efficiency values.

The effects of atmospheric temperature on thermal efficiency and the net work of the gas turbine arrangement, when partial loads are considered, are shown in Figs. 14 and 15, respectively. The increase in atmospheric air temperature decreases both thermal efficiency and net work at all partial-load values.

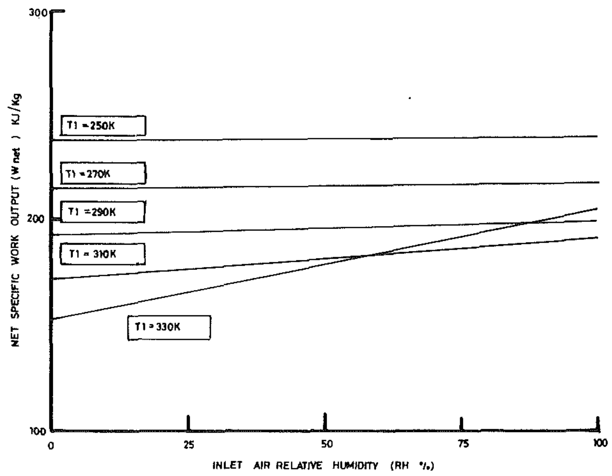

Fig. 12 Net specific work (W_{net}) with various atmospheric air temperatures, and relative humidities, and at constant pressure ratio (*PR* = 10) and constant turbine inlet temperature (TIT = 1200 K)

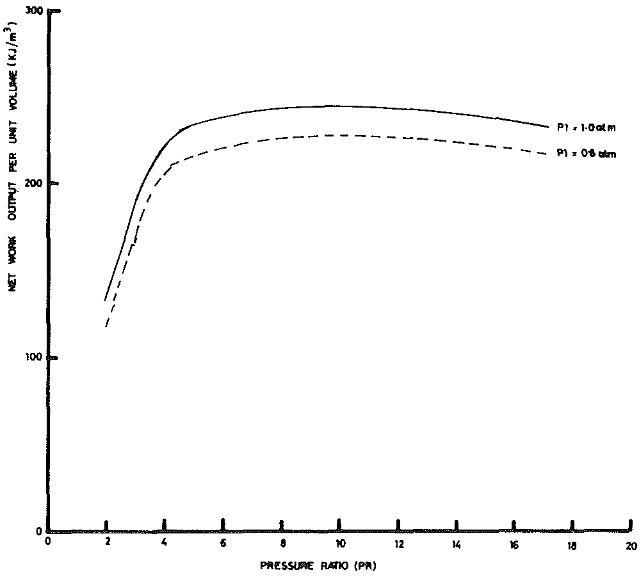

Fig. 13 Net work per unit volume with various pressure ratios, and at constant atmospheric temperature (T_1 = 280 K) and inlet turbine temperature (TIT = 1200 K)

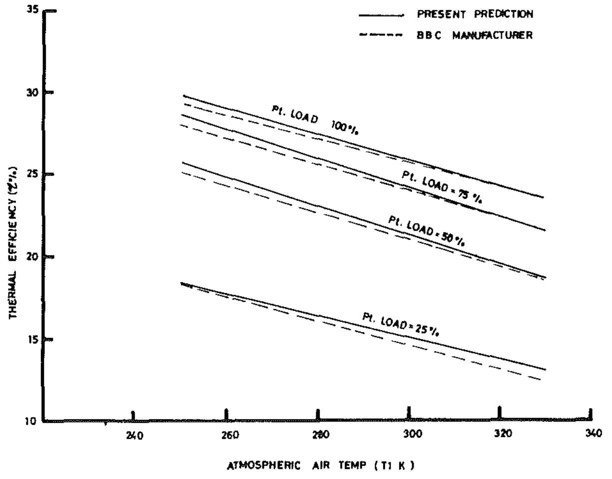

Fig. 14 Overall thermal efficiency with various partial load, and at constant turbine inlet temperature (TIT = 1200 K) and pressure ratio (*PR* = 10)

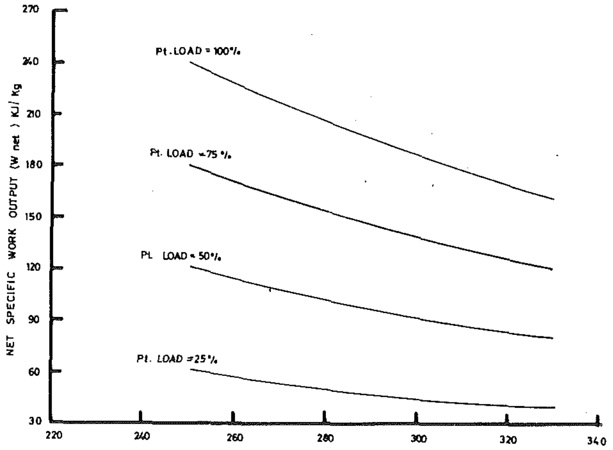

Fig. 15 **Net specific work (W_{net}), with various partial loads, at constant turbine inlet temperature (TIT = 1200 K) and pressure ratio (PR = 10)**

Figure 13 also shows the comparison results between the new predictions along with Brown Boveri Company (BBC) manufacture. Both results are shown clearly in good agreement.

Conclusion

The performance of gas turbines is greatly affected by atmospheric weather conditions, such as ambient temperature, pressure, and relative humidity. Among the three, ambient temperature has the greatest effect on gas turbine efficiency and net work. This effect seems to increase with increasing turbine inlet temperature and pressure ratio. The ambient pressure affects the work output per unit volume only, and has no effect on either the net work per unit mass nor thermal efficiency. The relative humidity also has a negligible effect on both thermal efficiency and net work per unit mass, at low atmospheric temperatures. However, decreases in efficiency and increases in net work at higher values of atmospheric air temperature and turbine inlet temperature are noted.

Finally, the effect of atmospheric air temperature and relative humidity on the net work output per unit mass and thermal efficiency of a gas turbine arrangement are computed and studied.

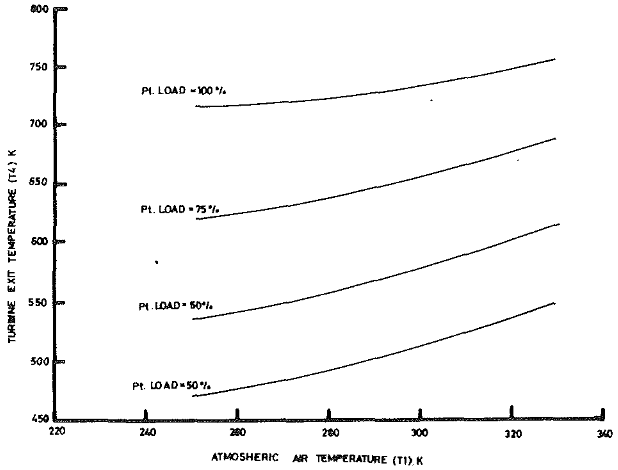

Fig. 16 **Turbine exit temperature with various partial loads, at constant turbine inlet temperature (TIT = 1200 K) and constant pressure ratio (PR = 10)**

References

Baughn, J. W., McKillop, A. A., and Treleven, K., 1983, "An Analysis of the Performance of Gas Turbine Cogeneration Plant," ASME JOURNAL OF ENGINEERING FOR POWER, Vol. 105, pp. 816-821.

El-Masri, M. A., 1987, "Exergy Analysis of Combined Cycles: Part 1—Air Cooled Brayton-Cycle Gas Turbine," ASME JOURNAL OF ENGINEERING FOR GAS TURBINES AND POWER, Vol. 109, pp. 228-236.

Frusshi, H. U., 1980, "The Relationship of Power and Heat Production With Closed Cycle Gas Turbines," ASME JOURNAL OF ENGINEERING FOR GAS TURBINES AND POWER, Vol. 102, pp. 288-291.

Horii, S., Ito, K., Pak, P. S., and Suzuki, Y., 1987, "Optimal Planning of Gas Turbine Co-Generation Plants Based on Mixed-Integer Linear Programming," *Int. Journal of Energy Research*, Vol. 11, pp. 507-518.

Keenan, J. H., and Kaye, J., 1984, *Gas Tables—Thermodynamic Properties of Air Products of Combustion and Component Gases—Compressible Flow Functions*, Wiley, New York.

Sergio, S., Stecco, X., and Giampolo, M., 1986, "Energy Analysis of Compression and Expansion Processes," *Int. Journal of Energy*, Vol. 11, No. 6, pp. 573-577.

Ushiyama, I., 1976, "Theoretical Estimating the Performance of Gas Turbines Under Varying Atmospheric Conditions," ASME JOURNAL OF ENGINEERING FOR POWER, Vol. 98, pp. 69-78.

Yousef, S. H., and Najjar, 1986, "GIBBS Function as a Correlating Performance Parameter for Fuel Used in Gas Turbines," *Int. Journal of Energy Research*, Vol. 10, pp. 47-57.

Yousef, S. H., Najjar, S. H., and Mansour, A. R., 1987, "Evaluation of SRK Equation of State in Calculating the Thermophysical Properties of Gas Turbine Combustion Gases," *Int. Journal of Energy Research*, Vol. 11, pp. 459-477.

On-Line Determination of Unburned Carbon in Airborne Fly Ash

R. C. Brown

A. R. Dona

Department of Mechanical Engineering,
Iowa State University,
Ames, IA 50011

Knowledge of the carbon content of fly ash is important for calculating combustion efficiency in coal-fired boilers. However, present methods of measuring carbon content of fly ash are tedious and time consuming. Thus, we are investigating photoacoustic absorption spectroscopy (PAS) as a method for on-line monitoring of carbon in fly ash. Photoacustic absorption spectroscopy is capable of detecting very weak absorptions and is unaffected by light scattering in a particulate-laden gas flow. Accordingly, PAS has good potential for distinguishing small amounts of carbon from mineral matter suspended in flue gas. Experiments have been performed on fly ash samples of variable carbon content suspended in a gas flow. A 35-mW HeNe laser was able to detect carbon loadings of 0.75 g/m^3*. Order-of-magnitude improvements in detection sensitivity are expected with higher power lasers or improved PAS cell design.*

Introduction

Carbon emitted from combustors can generally be classified as either grit or soot. Grit, usually defined as material retained on a 200-mesh U.S.A. sieve (nominal aperture of 75 μm), represents unburned char. Knowledge of the carbon content of fly ash is important for calculating combustion efficiency in coal-fired boilers. The amount of mass in unburned char is much more significant than the mass of soot, which is composed of particles less than 1 μm in diameter and is formed by gas phase processes. The mass of soot leaving a combustor is too small to affect combustion efficiency greatly. Unburned carbon in fly ash is presently measured by a tedious and sometimes inaccurate procedure [1]. Flue gas is sampled from the exhaust of a combustor, and a particulate filter is used to remove fly ash from the flow. The fly ash is dried and weighed before being placed in a furnace for several hours in order to burn off the carbon. The fly ash is then reweighed to find the percent carbon. This analytical procedure often consumes several hours. Rarely does filtering yield a large enough sample of fly ash to investigate transient phenomena in a combustor. The accuracy of this technique is limited by problems associated with isokinetic sampling and filtration techniques [2].

We are investigating photoacoustic absorption spectroscopy (PAS) as a method for on-line monitoring of carbon in the exhaust gas of coal-fired boilers. Photoacoustic absorption spectroscopy is based on the periodic heating of a gas when intensity-modulated, optical light radiation is absorbed by the gas or by particles suspended in the gas [3]. This periodic heating produces an acoustical wave that can be detected by a microphone. Although isokinetic sampling is still required, PAS has two important features that make it especially suitable for detection of carbon in flue gas. The first of these is the ability to detect very weak absorptions. Secondly, the PAS signal is unaffected by light scattering in a particle-laden gas flow; the acoustical signal arises only from light absorption. Consequently, only particles with a large absorptive component in the complex refractive index, such as soot or char, contribute to the signal. Major constituents of mineral matter scatter light with small absorptive component. Accordingly, PAS has good potential for distinguishing unburned carbon from mineral matter that is suspended in flue gas. The technique has already been used to measure instantaneous mass concentrations of soot in the exhaust of diesel engines [4, 5]. We are attempting to extend this technique to the measurement of grit in gas flows that are heavily laden with particles.

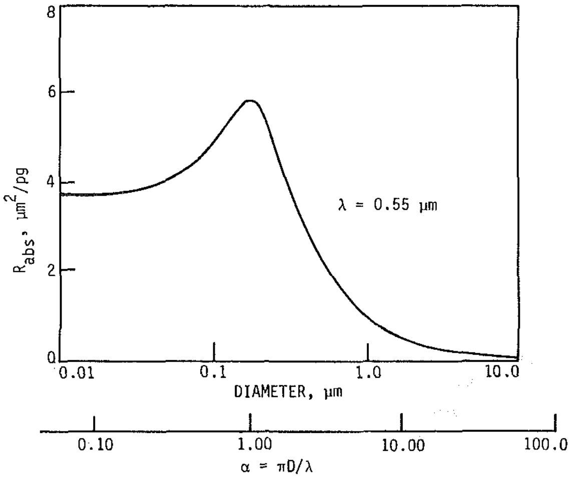

Fig. 1 Absorption coefficient for carbon particles at 550 nm (from [6])

Contributed by the Fuels and Combustion Technologies Division for publication in the JOURNAL OF ENGINEERING FOR GAS TURBINES AND POWER. Manuscript received by the Fuels and Combustion Technologies Division February 1989.

Background

In the measurement of particulate mass loadings, it is convenient to define optical properties on a mass basis [6]. For example, the absorption cross section, C_{abs}, is rewritten in terms of a mass-specific cross section.

$$R_{\mathrm{abs}} = C_{\mathrm{abs}}/\rho\left(\frac{\pi}{6}D^3\right) \tag{1}$$

where ρ is the particle density and D is the particle diameter. Assuming that the refractive index of carbon is $n = 1.95 - 0.66\,i$, Faxvog and Roessler [6] have generated a plot of absorption cross section per unit mass as a function of carbon particle diameter. This plot is shown in Fig. 1 for an incident wavelength λ of 0.55 μm. For particles in the Rayleigh range ($D \ll \lambda$), R_{abs} is independent of particle diameter. Soot particles come close to satisfying this condition and studies on soot particles emitted from diesel engines show that Rayleigh scattering is reasonably well approximated [4, 5].

Carbon in the size range of grit is large enough to give R_{abs} values that are inversely proportional to D. Accordingly, the PAS signal will be a function of the integrated mass-specific absorption coefficient of the suspended char particles [6]

$$\gamma = \int_0^\infty R_{\mathrm{abs}}(D)m(D)dD \Big/ \int_0^\infty m(D)dD \tag{2}$$

The particle mass distribution, $m(D)$, is given by

$$m(D) = \frac{\pi}{6}\rho D^3 N f(D) \tag{3}$$

where $f(D)$ is the diameter frequency distribution and N is the number of particles per unit volume.

If the char particles are distributed lognormally in size, then γ will be a function of the log mean diameter and the log standard deviation of the particle distribution. A lognormal distribution is assumed, even though char distributions from some combustors are known to be nonlognormal and even sometimes bimodal. Faxvog and Roessler [6] have numerically evaluated the integral in equation (2) for several standard deviations to give the mass-specific optical properties of carbon as a function of geometric-mean particle size. The effect of the distribution of particle sizes for small particles ($D \ll \lambda$) is to raise the absorption coefficient, making the optical properties slightly dependent on the geometric mean diameter and the geometric standard deviation. For large particles ($D \gg \lambda$) the effect of a lognormal distribution is to decrease slightly the specific absorption and decrease the slope of the specific absorption versus mean diameter plot. As a result, the specific absorption is less sensitive to the geometric mean diameter [6, 7]. It is evident from Fig. 1 that for particles of interest in this study ($D > 50\,\mu$m) the absorption coefficient will be only weakly dependent on particle diameter; however, the magnitude of the absorption coefficient will be significantly smaller than that for soot. If log mean diameter and log standard deviations are not strongly dependent on combustor operating conditions, then PAS can be used to determine the quantity of carbon emitted as grit from a combustor.

For low light absorption, the PAS signal response in volts [7] is given by

$$S = RP_o\gamma ML \tag{4}$$

where R is the cell response (dependent on cell geometry and light modulation frequency), P_o is the incident power, M is the mass per unit volume of absorbing particles, and L is the length of the cell.

The cell response R (in volts per watt) is related to the cell geometry, modulation frequency, and the density and specific heat of the gaseous medium. The cell response R for nonresonant operation can be approximated by [7]

$$R = 4(k-1)\sigma_m/\pi\omega V\sqrt{2} \tag{5}$$

where k is the ratio of specific heats, σ_m is the sensitivity in volts per unit pressure of the microphone and amplifier, ω is the angular modulation frequency, and V is the cell volume.

Equation (5) shows that low frequencies give the highest sensitivity; however, it has been found that less background noise exists at higher frequencies [5]. The theoretical upper limit for the modulation frequency is given by the thermal time constant

$$\tau = \frac{r^2 C_p}{3\lambda_g} \tag{6}$$

where r is the particle radius, C_p is the heat capacity per unit volume of the particle, and λ_g is the thermal conductivity of the surrounding medium [8]. This limit on modulation frequency assumes that the whole particle changes temperature. This condition is satisfied for very small particles ($D \ll 0.1\,\mu$m); however, work done with soot particles ($D \approx 0.1\,\mu$m) showed that frequencies higher than allowed by equation (6) can be employed if the particles are relatively large. Under these circumstances, only the surface of the particle, rather than the whole volume, is heated by the incident light.

The objective of our current research is to determine whether PAS can be applied to measurements of carbon emitted from combustors as grit in the presence of particulate mineral matter. Experiments have been performed with "synthetic" fly ash to evaluate the usefulness of PAS in this application.

Experimental Apparatus and Procedure

The photoacoustic cell, machined from solid aluminum, is illustrated in Fig. 2. The cell has been constructed especially for measuring photoacoustic signals generated by large particles suspended in dusty gas flows. Photoacoustic cells are usually constructed for horizontal flow of gas through the cell. However, the terminal velocity of the largest (75-μm-diameter) particles passing through the cell is 0.15 m/s. Gravitational

Nomenclature

C_{abs} = absorption cross section, m^2
C_p = heat capacity per unit volume of particle, J/m^3•K
D = particle diameter, m
$\bar{D}$ = average particle diameter, m
f = diameter frequency distribution
k = ratio of specific heats for gaseous medium
L = length of cell, m
m = particle mass distribution
M = mass concentration of char particles, kg/m^3
n = complex refractive index
N = number of particles per unit volume, m^{-3}
P_o = incident laser power, W
r = particle radius, m
R = cell response, V/W
R_{abs} = mass-specific cross section, m^2/kg
S = signal response, V
V = cell volume, m^3
γ = integrated mass-specific adsorption coefficient, m^2/kg
λ = wavelength of incident radiation, m
λ_g = thermal conductivity of gaseous medium, W/m•K
ρ = particle density, kg/m^3
σ_m = sensitivity of the microphone and amplifier, V/Pa
τ = thermal time constant of particles, s
ω = angular modulation frequency, s^{-1}

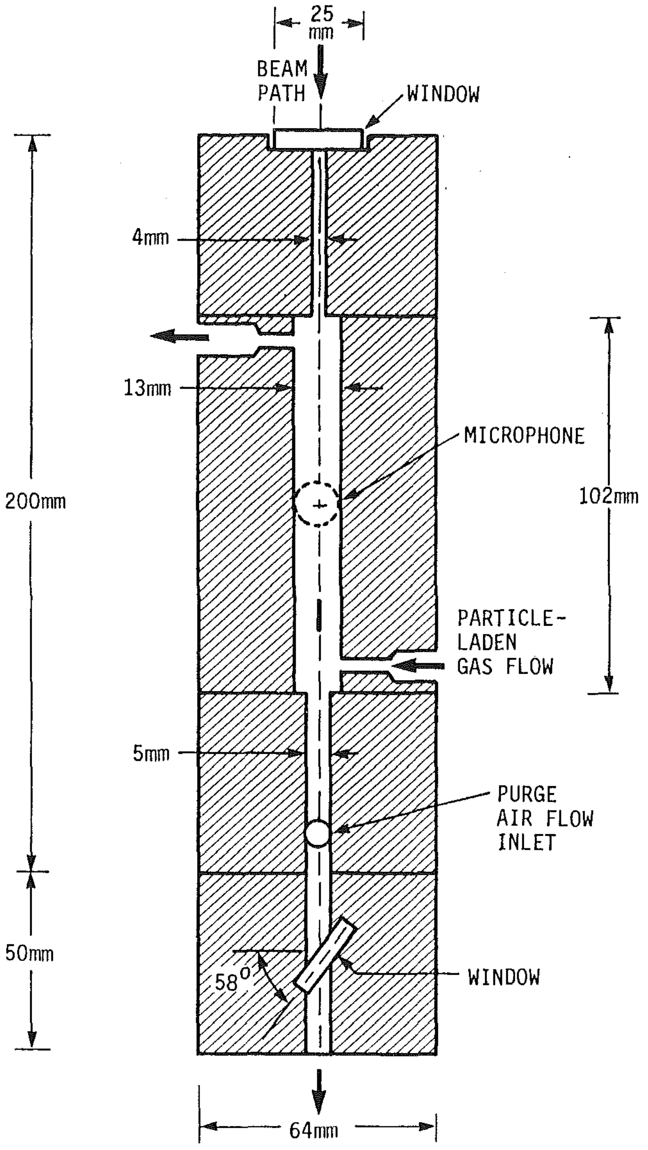

Fig. 2 Photoacoustic cell

settling of particles within a horizontal cell would be unacceptable even for very high gas flow rates through short cells. Furthermore, Osada et al. [9] have shown that photoacoustic response is independent of gas flow rate only for relatively low flow velocities. They suggest that flow velocities should be less than 0.40 m/s through the cell. We have adopted a vertical flow configuration with upward flow velocities slightly higher than the terminal velocity for the largest particles expected in the gas flows. This configuration allows us to retain a long cell length (10.2 cm) and operate at relatively low flow velocities.

The particle-laden gas flows through a 1.3-cm dia. cylindrical chamber machined in the center of the aluminum block. The beam enters this chamber through a 0.4-cm-dia. hole drilled through the top of the aluminum block; it exits through a similar but slightly larger hole at the bottom of the block. Windows at the top and bottom of the assembly are isolated from the gas flow in this manner to prevent particles from hitting and coating the windows.

The cell windows are made of high quality optical glass to minimize the absorption, which generates background acoustical noise. The beam exits through a Brewster angle window set at 58 deg. This arrangement reduces reflection of light back into the cell where it would be absorbed by the walls and create acoustical noise. Although the upward flow velocity should be sufficient to keep particles from settling onto the bottom window, an additional precaution has been included. A small flow of air can be admitted to the narrow passage that transmits the light beam to the lower window. This flow prevents particles from reaching the lower window. No particles were deposited on the upper window during the tests we performed.

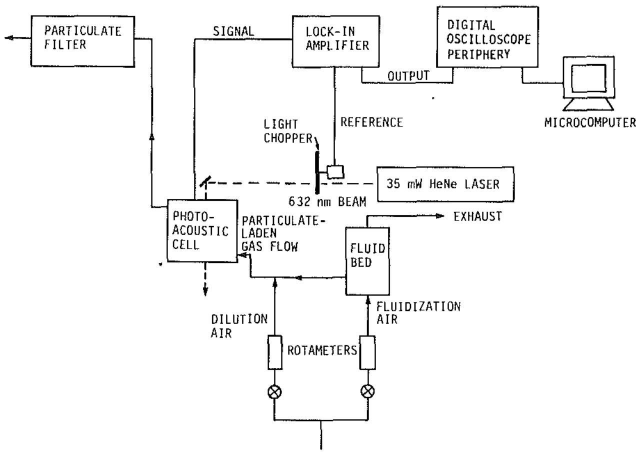

Fig. 3 Schematic of photoacoustic absorption spectroscopy apparatus

Multiple scattering of light [10] is avoided in the photoacoustic cell by assuring that mass loadings satisfy

$$M<1/\gamma L \tag{7}$$

In the limit of large particles, the absorption coefficient can be estimated as [10]

$$\gamma \simeq \frac{3}{2}\left(\frac{1}{\rho \bar{D}}\right) \tag{8}$$

where ρ is the particle density. Particles of fly ash are estimated to have an average diameter $\bar{D}=20$ μm and particle density of 2000 kg/m^3. Accordingly, mass loadings in the cell must be less than 130 g/m^3. Particulate emissions from pulverized coal combustors are well below this number [2]; thus, dilution of the gas flow before the photoacoustic cell will rarely be necessary.

The microphone is recessed into the cell wall about halfway up the cell as shown in Fig. 2. It is part of a General Radio model 1933 precision sound-level meter and analyzer. This half-inch electret condenser microphone has a sensitivity of -43 dB referenced to 1 V/Pa. The use of a high-quality microphone that can detect low-level signals is essential in these experiments. Fine fabric covering the microphone face prevented particle deposition. Acoustic isolation is achieved by mounting the cell in a metal enclosure that is packed with acoustic shielding material.

The complete experimental apparatus is illustrated schematically in Fig. 3. A varible-speed mechanical chopper was used to modulate the light beam from a 35-mW HeNe laser. Acoustic signals were processed by a narrow band prefilter to reject background noise. The signal was then processed by a lock-in amplifier and displayed and stored on a microcomputer using a Rapid Systems 4×4 digital oscilloscope peripheral. The cell response, R, as a function of light modulation frequency, was determined by calibration with 462 ppm of NO_2 in nitrogen gas. The absorption coefficient at 632.8 nm for this concentration of NO_2 is estimated to be 0.0162 ± 0.0026 m^{-1} from Hsu et al. [11].

The particulate supply system is similar to the device described by Altenkirch et al. [12]. Particle-laden flows were generated with a 3.8-cm-dia. fluidized bed of fly ash mixed with unburned carbon. "Synthetic" fly ash samples of variable carbon content were prepared by mixing small quantities of Illinois No. 5 coal screened to 270 × 325 mesh with a pulverized-

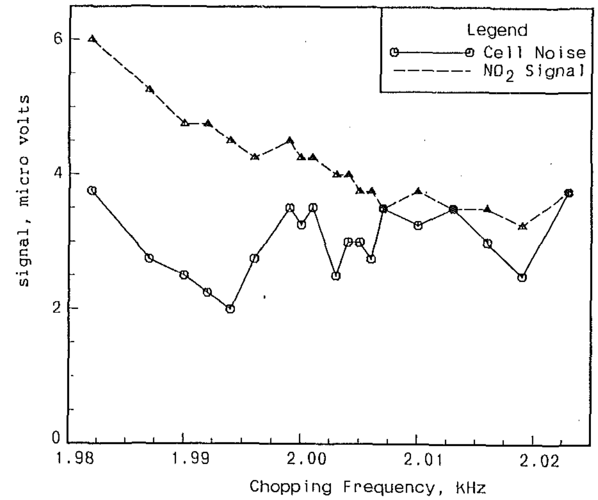

Fig. 4 Cell noise and NO_2 signal versus chopping frequency

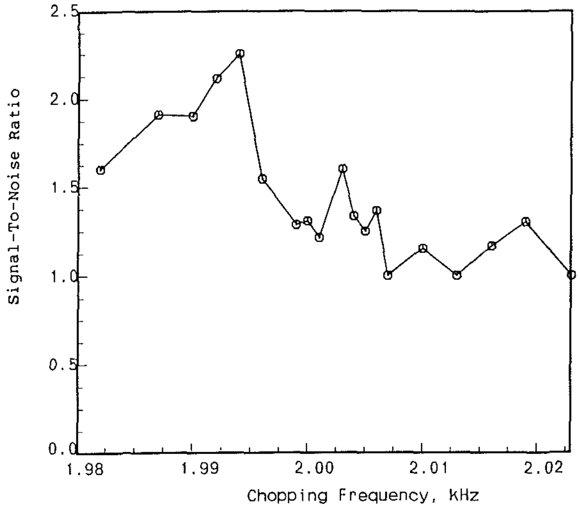

Fig. 5 Signal-to-noise ratio versus chopping frequency

Table 1 Photocoustic signal from carbon in fly ash

Test No.	Mass Loading (g/m^3)	Carbon Loading (g/m^3)	% Carbon	Signal S(μV)
1	2.044	2.044	100.00	12.25
2	2.060	1.893	91.90	11.25
3	2.067	1.740	84.12	10.5
4	1.930	1.490	77.23	8.75
5	2.081	1.337	64.25	8.0
6	2.075	1.215	58.56	7.25
7	2.041	1.024	50.19	6.25
8	2.036	0.953	46.81	5.75
9	2.036	0.929	45.64	5.50
10	2.052	0.834	40.65	4.75
11	2.041	0.760	37.22	4.00
12	2.065	0.691	33.46	4.75
13	2.057	0.606	29.47	3.50
14	2.061	0.0	0.00	3.00

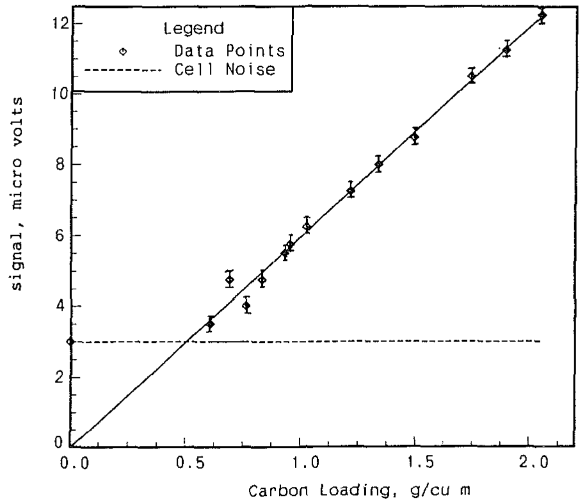

Fig. 6 Photoacoustic signal versus carbon loading

coal fly ash that had been previously heated in an oxidizing environment to remove all carbon. Particles suspended in the bed are extracted through a small orifice in the side of the bed and diluted with additional air before flowing to the photoacoustic cell. Fluidization and dilution air flows were simultaneously adjusted to set the desired particulate loading of the gas flow entering the photoacoustic cell.

The fly ash particles, with an averge diameter of 35 μm, are small enough to be classified as class C particles. Class C particles are characterized by interparticle forces strong enough to interfere with smooth fluidization; the bed usually collapses in a short time and crevasses form through which air bypasses the bed. To overcome this behavior, we needed to disturb the bed periodically by tapping or shaking. The bed was fluidized in this manner without causing excessive acoustical noise by vibrating it with a B&K Vibration Exciter type 4808, which operated at 20 Hz.

Particles leaving the cell were captured on a Balston microfiber filter. Total particulate loading was determined by weighing the fly ash accumulated on the filter. Carbon loading was determined by heating the filter in an oven to 500°C for two hours and by measuring the weight loss for the sample.

Results and Discussion

The results of the cell response tests are shown in Fig. 4 as plots of signal and noise versus chopping frequency. This shows that the signal from the NO_2 generally decreases as the chopping frequency increases, as would be expected from the response relationship given by equation (5). From these data, a signal-to-noise ratio versus chopping frequency plot can be made. This plot (Fig. 5) shows the optimal frequency for testing to be 1996 Hz, where the signal-to-noise ratio has a peak of 2.25. The NO_2 photoacoustic signal of 4.5 μV at 1996 Hz yields a cell response of 75.5 mV/W by using equation (4). This measured value is significantly larger than the predicted value of 15 mV/W obtained from equation (5).

The results of tests for unburned carbon in fly ash are shown in Table 1. These data show that the total particulate loading was kept nearly constant as the carbon loading was varied. The photoacoustic signal changed with the carbon loading and was not affected by the amount of mineral matter in the gas flow. Figure 6 shows the photoacoustic signal versus the carbon loading. A linear regression analysis of these data shows a slope of 6.0 $\mu V \cdot m^3/g$ and an intercept of -0.043 μV (that is, nearly zero) with a correlation coefficient of 0.992. The sensitivity of this cell, per unit laser power, is 171.4 $\mu V \cdot m^3/g \cdot W$. These results indicate that the signal is unaffected by mineral matter and is linearly proportional to the mass of carbon in the gas flow. The slope corresponds to an absorption coefficient, γ, of 0.022 ± 0.004 m^2/g, which is in excellent agreement with equation (8). Assuming average coal particle size of 50 μm and density of 1310 kg/m^3, we predict with equation (8) an absorportion coefficient of 0.023 m^2/g. The measured absorption coefficient also agrees to within 25 percent of the value found by Japar and Szkarlat [4], who found an absorption coefficient of 8.9 ± 0.5 m^2/g in their work with soot particles ($D \approx 0.1$ μm). Assuming the absorption coefficient is inversely proportional to the average particle diameter, Japar and Szkarlat's [4] data for soot can be extrapolated to an absorption coefficient of 0.018 ± 0.001 m^2/g for char particles ($\bar{D} \approx 50$ μm).

The uncertainty associated with photoacoustic signals arises from two sources: the unsteady nature of the particulate loading in these experiments and the presence of random acoustical noise in the room. The particulate supply system has many problems that complicate its operation. The particulate supply system relies on uniform fluidization of very small particles that have different diameters and densities. These differences make it difficult to keep the bed fluidized and well mixed, which resulted in an unsteady flow of particles to the photoacoustic cell. These problems were overcome, in part, by using a high fluidization velocity. At high fluidization velocities there was violent mixing in the bed and the bed became slightly pressurized. Problems associated with acoustical noise can be reduced by improved acoustical isolation of the photoacoustic cell.

Improved sensitivity is not to be expected by employing an alternative laser wavelength. The absorption of light by carbon particles, which behave approximately as blackbody radiators, is not dependent on the excitation wavelength. Shorter wavelengths would ease calibration of the photoacoustic cell with NO_2. The absorption by NO_2 gas at 514 nm (the wavelength of an Ar-ion laser) is approximately 14 times larger than the absorption at the 632-nm wavelength of our HeNe laser.

Improved sensitivity can be attained by either increasing laser power or increasing response of the photoacoustic cell. Increasing the power of the laser would raise both signal and noise levels. Noise would increase because the higher power laser would make the cell more sensitive to particles deposited on the windows. Improvements in the acoustic isolation of the cell would help reduce some of the cell noise caused by outside sources such as the chopper, mirrors, and the ambient surroundings.

The response R of our cell was relatively low compared to the cells constructed by other researchers for soot measurements. Some of these cells had responses as high as 1500 mV/W compared to only 75 mV/W for our cell. Part of this difference arises from the lower frequencies used by these researchers; cell response is inversely proportional to modulation frequency. Better acoustical isolation of our cell would allow us to operate at lower frequencies. However, even after correcting for differences in modulating frequency, some of these cells were ten times more responsive than our own. Further improvements require geometric changes or a more sensitive microphone.

The minimum detectable carbon loading in these experiments was 0.75 g/m^3, which is near the upper limit of carbon loading expected for flue gas emitted from coal combustors. However, there appear to be no major obstacles to reducing this detection limit below 0.1 g/m^3 by either increasing laser power or improving cell response.

Conclusions

The standard method for detecting unburned carbon in fly ash is a long and tedious process that is incapable of detecting transients in particle loadings. This work showed that photoacoustic absorption spectroscopy is capable of measuring real-time carbon mass loading of 0.75 g/m^3 in the presence of particulate mineral matter. At least an order of magnitude improvement is expected by employing either a higher power laser or a photoacoustic cell with higher response. Future work should be done with particles sampled directly from a combustor. Whether particle size and size distribution are sufficiently constant for a particular combustor were not investigated in this study. These questions must be resolved before quantitative measurements of unburned carbon in flue gas can be reliably performed using the photoacoustic effect.

Acknowledgments

This work was supported by the Assistant Secretary for Fossil Energy, Division of Coal Utilization, through the Ames Laboratory. Ames Laboratory is operated for the U.S. Department of Energy by Iowa State University under Contract W-7405-Eng82. The assistance of the Iowa State University Engineering Research Institute in preparing this paper is also appreciated.

References

1 *Annual Book of ASTM Standards*, "Standard Test Method for Ash in the Analysis Sample of Coal and Coke," ASTM Standard No. d3174-82, Vol. 05.05, Section 5, ASTM, 1988.

2 Hawksley, P. G. W., Badzioch, S., and Blackett, J. H., *Measurement of Solids in Flue Gases*, The Institute of Fuel, London, 1977.

3 Rosencwaig, A., *Photoacoustics and Photoacoustic Spectroscopy*, Wiley, New York, 1980.

4 Japar, S. M., and Szkarlat, A. C., "Measurement of Diesel Vehicle Exhaust Particulate Using Photoacoustic Spectroscopy," *Combustion Science and Technology*, Vol. 24, 1981, pp. 215–219.

5 Faxvog, F. R., and Roessler, D. M., "Optoacoustic Measurements of Diesel Particulate Emissions," *Journal of Applied Physics*, Vol. 50, 1979, pp. 7880–7882.

6 Faxvog, F. R., and Roessler, D. M., "Carbon Aerosol Visibility versus Particle Size Distribution," *Applied Optics*, Vol. 17, 1978, pp. 2612–2616.

7 Roessler, D. M., and Faxvog, F. R., "Optoacoustic Measurement of Optical Absorption in Acetylene Smoke," *Journal of the Optical Society of America*, Vol. 69, 1979, pp. 1699–1704.

8 Terhune, R. W., and Anderson, J. E., "Spectrophone Measurements of the Absorption of Visible Light in the Atmosphere," *Optics Letters 1*, Vol. 70, 1977, pp. 70–72.

9 Osada, H., Okayama, J., Ishida, K., and Saitoh, O., "Real-Time Measurement of Diesel Particulate Emissions by the PAS Method Using a CO_2 Laser," SAE Paper No. 820461, 1983.

10 Jones, A. R., "Scattering of Electromagnetic Radiation in Particulate Laden Fluids," *Progress in Energy and Combustion Science*, Vol. 5, 1979, pp. 73–96.

11 Hsu, D., Monts, D., and Zare, R., *Spectral Atlas of Nitrogen Dioxide 5530 to 6480Å*, Academic Press, New York, 1978.

12 Altenkirch, R. A., Peck, R. E., and Chen, S. L., "Fluidized Bed Feeding of Pulverized Coal," *Powder Technology*, Vol. 20, 1978, pp. 189–196.

A Solution for the Temperature Distribution in a Pipe Wall Subjected to Internally Stratified Flow

W. R. Smith
Tennessee Valley Authority,
Sequoyah Nuclear Plant,
Daisy, TN
Mem. ASME

D. S. Cassell
Mem. ASME

E. P. Schlereth

University of Tennessee—Chattanooga,
Chattanooga, TN 37403

Stratified flow in a pipe is a phenomenon in which two distinct fluids flow simultaneously through a pipe with little or no mixing. Under certain conditions the flow stratification will result in a dramatic temperature variation within the pipe wall. This paper presents a solution for the temperature distribution in a pipe wall subjected to internally stratified flow by solving Laplace's equation in cylindrical coordinates using a finite Fourier cosine transform. The top and bottom sections are treated separately and coupled by boundary conditions at the interface. A one-dimensional approximation for the temperature distribution in the pipe at the interface is developed to uncouple the top and bottom sections, thereby avoiding the necessity for simultaneous solution of two partial differential equations. Results from the solution for a case study of a particular physical situation were compared to the solution obtained using the ANSYS finite element computer program. The solution agreed with the finite element solution to within approximately 2.4 percent throughout the pipe wall and was within 0.4 percent for most of the pipe.

Introduction

Stratified flow in a pipe is a phenomenon in which two distinct fluids flow simultaneously through a pipe with little or no mixing. The fluid is divided into two distinct layers with the denser fluid occupying the lower position. This phenomenon is typical of laminar flow perpendicular to a gravitational field (i.e., horizontal). Examples of stratified flow in a pipe are: (1) two phases of a saturated fluid flowing together such as water and steam, (2) two immiscible fluids flowing together such as oil and water, and (3) two fluids of the same phase flowing together without mixing such as hot and cold water. Differences in the fluid temperatures and heat transfer coefficients will lead to temperature gradients in the pipe wall in both the circumferential and radial directions. These gradients produce thermal stresses in the pipe wall, which can lead to pipe cracking or failure. Numerous cases of pipe cracking and failure as a result of flow stratification have occurred in steam generator feedwater lines at nuclear power plants throughout the United States and Japan as reported by the NRC [9]. Industry experience indicates that flow stratification occurs primarily during hot standby conditions and during startup and shutdown when feedwater heaters are not in use. The effect of the stratification and the resulting circumferential temperature gradient is that the pipe is subjected to high alternating thermal shear stresses. Thermal fatigue effects coupled with shear stresses and operating dynamic loadings, especially at regions of stress concentration such as weld joints, nozzle transitions, etc., may lead to pipe cracking and subsequent pipe failure.

Considerable research has been performed by Bejan and Tien, Hong, Kimura and Bejan, and Yih [2, 4, 5, 10] to model the thermal/hydraulic aspects of stratified flow. These efforts toward finding the temperature distribution in the pipe wall, however, have been limited primarily to laboratory testing of particular geometries, to obtaining field data, or to numerical studies. No closed-form analytical solution for the temperature distribution is known to exist even though such a solution is of considerable practical and theoretical importance.

Presented in this paper is an analytical solution for the steady state temperature distribution in a pipe wall subjected to internally stratified flow (although the solution is developed in terms of an infinite series using an approximate boundary condition, the term "analytical" will be used to differentiate the solution obtained herein from a purely numerical solution). The solution is developed using the integral transform technique and a one-dimensional approximation for the interface temperature profile. A case study involving the numerical solution of the temperature field for a particular physical situation is then developed. A detailed comparison is made between the results of the analytical and the ANSYS [1] computer code solutions.

Analytical Solution

The steady-state temperature distribution in a two-dimensional (r, Θ) homogeneous cylinder with no internal heat generation and constant physical properties is given by Laplace's equation in cylindrical coordinates as [6, p. 85]

Contributed by the Nuclear Engineering Division and presented at the Joint ASME/ANS Nuclear Power Conference, Myrtle Beach, South Carolina, April 17-20, 1988. Manuscript received by the Nuclear Engineering Division May 4, 1988; revision received August 1989.

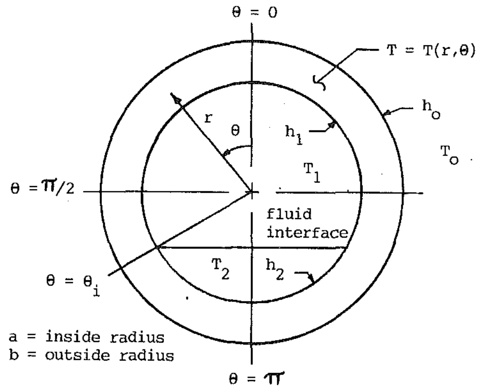

Fig. 1 Physical parameters and coordinate system

$$\frac{\partial^2 T}{\partial r^2}+\frac{1}{r}\frac{\partial T}{\partial r}+\frac{1}{r^2}\frac{\partial^2 T}{\partial \Theta^2}=0 \qquad (0\le\Theta\le\pi) \qquad (1)$$

where the physical parameters and coordinate system are defined in Fig. 1. It is assumed that axial conduction through the pipe wall may be neglected, the two fluids do not mix, each fluid is well mixed with a uniform temperature, and there is no heat transfer between the two fluids. Since the temperature distribution in the bottom of the pipe will differ from the temperature distribution in the top, the top and bottom sections must be treated separately. Letting $T(r, \Theta)$ be the temperature distribution in the top section ($\Theta \le \Theta_i$) and $G(r, \Theta)$ be the temperature distribution in the bottom section ($\Theta \ge \Theta_i$), equation (1) applied to each section becomes

$$\frac{\partial^2 T}{\partial r^2}+\frac{1}{r}\frac{\partial T}{\partial r}+\frac{1}{r^2}\frac{\partial^2 T}{\partial \Theta^2}=0 \qquad \text{for } \Theta\le\Theta_i \qquad (2)$$

and

$$\frac{\partial^2 G}{\partial r^2}+\frac{1}{r}\frac{\partial G}{\partial r}+\frac{1}{r^2}\frac{\partial^2 G}{\partial \Theta^2}=0 \qquad \text{for } \Theta\ge\Theta_i \qquad (3)$$

Equations (2) and (3) require four boundary conditions (BCs) each. The required BCs may be obtained by application of the principle of conservation of energy to each bounding "surface." The bounding surfaces and applicable BCs are shown in Fig. 2.

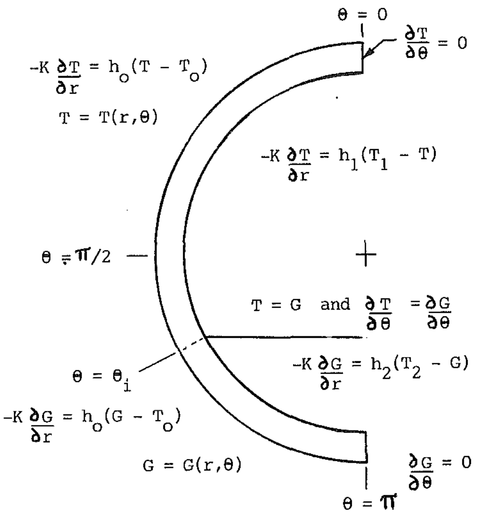

Fig. 2 Boundary conditions for the ideal model

An exact analytical solution may be found by solving equations (2) and (3) subject to the eight BCs. This exact solution requires the simultaneous solution of two partial differential equations (PDEs) subject to eight BCs. Since the solution of each of these PDEs results in a solution involving infinite series, a simultaneous solution is not analytically practical.

Since the difficulty in finding an exact analytical solution is the simultaneous solution of two PDEs, a means for uncoupling the two PDEs would allow an independent solution for each PDE. A reasonable approach for uncoupling the PDEs is to prescribe a temperature profile at the interface. Although this interface temperature profile cannot be prescribed exactly, an approximation can be developed. As a minimum, the approximation for the interface temperature function must:

1 satisfy the PDEs and

2 reduce to the solution for the one-dimensional case given by Carslaw and Jaeger [3, p. 333] when $h_1 = h_2$ and $T_1 = T_2$.

It is easily shown that these conditions are satisfied by an equation of the form

$$f(r) = A + B \ln r \qquad (4)$$

Nomenclature

A = constant, °C
a = inside pipe radius, m
B = constant, °C
b = outside pipe radius, m
f_1 = constant, °C/m
f_2 = constant, °C/m
$f(r)$ = one-dimensional approximation of interface temperature profile, °C
$G(r, \Theta)$, G = temperature distribution in bottom section of pipe, °C
g_1 = constant, $(\mathrm{m})^{\beta-1}$
g_2 = constant, $\mathrm{m}^{-\beta-1}$
g_3 = constant, $\mathrm{m}^{\beta-1}$
g_4 = constant, $\mathrm{m}^{-\beta-1}$
h_1 = inside convection coefficient in top section of pipe, W/m^2°C
h_1 = inside convection coefficient in bottom section of pipe, W/m^2°C
h_0 = convection coefficient on outside of pipe, W/m^2°C
K = thermal conductivity, W/m°C
m = summation index
N = constant, m^{-1}
P = constant, m^{-1}
r = radius, m
$\bar{T}(r, \beta)$, $\bar{T}$ = transform temperature, °C
$T(r, \Theta)$, T = temperature distribution in top section of pipe, °C
T_1 = inside bulk fluid temperature in top section of pipe, °C
T_2 = inside bulk fluid temperature in bottom section of pipe, °C
$T_B(r)$ = one-dimensional interface temperature, °C
T_N = constant, °C
T_0 = bulk temperature of fluid outside of pipe, °C
T_P = constant, °C
Z = special function
β = eigenvalues
Θ = angle, rad (except as noted in deg)
Θ_i = fluid interface angle, rad (except as noted in deg)

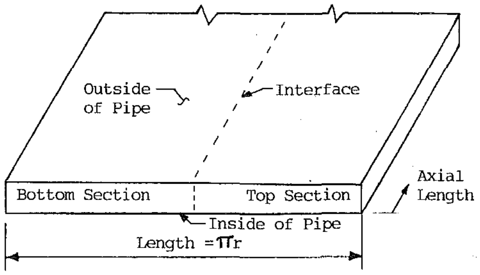

Fig. 3 One-dimensional pipe model

A reasonable approximation of the constants A and B may be developed using a one-dimensional approximation by "straightening" the pipe wall, as shown in Fig. 3, and treating the opened pipe as a fin. The results as given by Smith [8] are

$$A=\frac{T_B(a)\ln b-T_B(b)\ln a}{\ln(b/a)} \tag{5}$$

$$B=\frac{T_B(b)-T_B(a)}{\ln(b/a)} \tag{6}$$

where

$$T_B(r)=\frac{T_N N\tanh(Nr(\pi-\Theta_i))+T_P P\tanh(Pr\Theta_i)}{N\tanh(Nr(\pi-\Theta_i))+P\tanh(Pr\Theta_i)} \tag{7}$$

$$T_N=\frac{h_2T_2+h_oT_o}{h_2+h_o} \tag{8}$$

$$N^2=\frac{h_2+h_o}{K(b\text{-}a)} \tag{9}$$

$$T_P=\frac{h_1T_1+h_oT_o}{h_1+h_o} \tag{10}$$

$$P^2=\frac{h_1+h_o}{K(b\text{-}a)} \tag{11}$$

The top and bottom sections are uncoupled by application of equation (4) at the interface ($\Theta=\Theta_i$). To summarize, the following equations and corresponding BCs identify the modified analytical problem to be solved:

(1) For the top section ($\Theta\le\Theta_i$):

$$\text{PDE:}\quad \frac{\partial^2T}{\partial r^2}+\frac{1}{r}\frac{\partial T}{\partial r}+\frac{1}{r^2}\frac{\partial^2T}{\partial\Theta^2}=0 \tag{12}$$

$$\text{BC 1:}\quad \frac{\partial T}{\partial\Theta}=0\quad\text{at }\Theta=0 \tag{13}$$

$$\text{BC 2:}\quad -K\frac{\partial T}{\partial r}=h_o(T-T_o)\text{ at }r=b \tag{14}$$

$$\text{BC 3:}\quad -K\frac{\partial T}{\partial r}=h_1(T_1-T)\text{ at }r=a \tag{15}$$

$$\text{BC 4:}\quad T=A+B\ln r\quad\text{at }\Theta=\Theta_i \tag{16}$$

(2) For the bottom section ($\Theta\ge\Theta_i$):

$$\text{PDE:}\quad \frac{\partial^2G}{\partial r^2}+\frac{1}{r}\frac{\partial G}{\partial r}+\frac{1}{r^2}\frac{\partial^2G}{\partial\Theta^2}=0 \tag{17}$$

$$\text{BC 1:}\quad \frac{\partial G}{\partial\Theta}=0\quad\text{at }\Theta=\pi \tag{18}$$

$$\text{BC 2:}\quad -K\frac{\partial G}{\partial r}=h_o(G-T_o)\text{ at }r=b \tag{19}$$

$$\text{BC 3:}\quad -K\frac{\partial G}{\partial r}=h_2(T_2-G)\text{ at }r=a \tag{20}$$

$$\text{BC 4:}\quad G=A+B\ln r\quad\text{at }\Theta=\Theta_i. \tag{21}$$

The solution to each of the above systems is obtained by applying an integral transform to the PDE resulting in an ordinary differential equation. This ordinary differential equation is solved using classical solution techniques and then inverted using the appropriate inversion formula.

The appropriate transform (the finite Fourier cosine transform), inversion formula, and eigenvalues recommended by Ozisik [7, p. 169] are

Transform:

$$F\{\mathbf{T}\}=\bar T(r,\beta)=\int_0^{\Theta_i}T(r,\Theta)\sqrt{\frac{2}{\Theta_i}}\cos\beta\Theta\,d\Theta \tag{22}$$

Inversion:

$$T(r,\theta)=\sum_\beta\bar T(r,\beta)\sqrt{\frac{2}{\Theta_i}}\cos\beta\Theta \tag{23}$$

Eigenvalues:

$$\cos\beta\Theta_i=0 \tag{24}$$

The first step in the solution is to apply the integral transform to the PDE and BCs. Applying the transform to the PDE subject to BCs 1 and 4 yields

$$r^2\frac{d^2\bar T}{dr^2}+\frac{r d\bar T}{dr}-\beta^2\bar T=-\sqrt{\frac{2}{\Theta_i}}(A+B\ln r)\beta(-1)^m \tag{25}$$

where $\bar T$ is the transform of the temperature function in accordance with equation (22) and

$$\beta=\frac{(2m+1)\pi}{2\Theta_i},\qquad m=0,1,2,3,\ldots \tag{26}$$

Solving equation (25) subject to BCs 2 and 3 gives

$$\bar T=\frac{(g_2f_2-g_4f_1)r^\beta+(g_3f_1-g_1f_2)r^{-\beta}}{g_2g_3-g_1g_4}+ZA+ZB\ln r \tag{27}$$

where

$$Z=\sqrt{\frac{2}{\Theta_i}}\frac{(-1)^m}{\beta} \tag{28}$$

$$g_1=\beta b^{\beta-1}+\frac{h_0b^\beta}{K} \tag{29}$$

$$g_2=\frac{h_0b^{-\beta}}{K}-\beta b^{-\beta-1} \tag{30}$$

$$g_3=\beta a^{\beta-1}-\frac{h_1a^\beta}{K} \tag{31}$$

$$g_4=\frac{-h_1a^{-\beta}}{K}-\beta a^{-\beta-1} \tag{32}$$

$$f_1=\frac{h_0T_0Z}{K}-\frac{ZB}{b}-\frac{h_0ZA}{K}-\frac{h_0ZB\ln b}{K} \tag{33}$$

$$f_2=\frac{-h_1T_1Z}{K}-\frac{ZB}{a}+\frac{h_1ZA}{K}+\frac{h_1ZB\ln a}{K} \tag{34}$$

Application of the inversion formula to equation (27) results in

$$T(r,\theta)=A+B\ln r+\sum_{m=0}^{\infty}\frac{2}{\Theta_i}(-1)^m\frac{\cos\beta\Theta}{\beta}$$

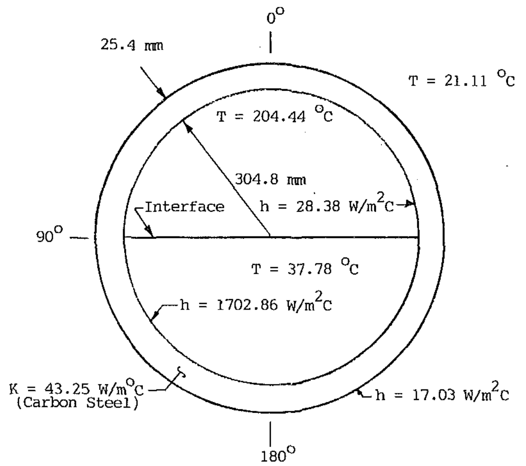

Fig. 4 Physical parameters and geometry for the case study problem

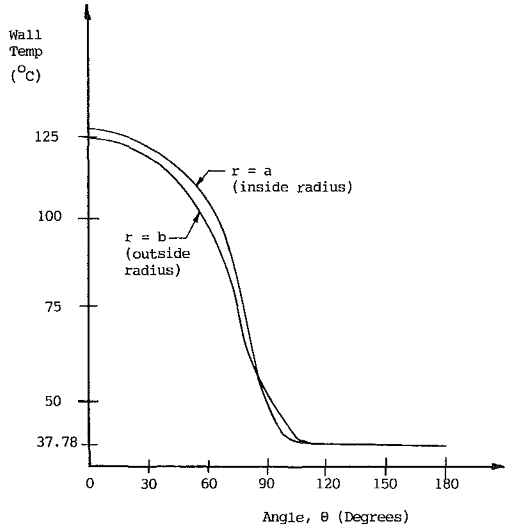

Fig. 5 Wall temperature profile for the case study problem

$$\left\{\left[\left(\frac{r}{b}\right)^{\beta}\left(\frac{h_o}{K}-\frac{\beta}{b}\right)-\left(\frac{b}{r}\right)^{\beta}\left(\frac{\beta}{b}+\frac{h_o}{K}\right)\right]\left[\frac{-h_1T_1}{K}-\frac{B}{a}\right.\right.$$
$$\left.+\frac{h_1A}{K}+\frac{h_1B\ln a}{K}\right]+\left[\left(\frac{r}{a}\right)^{\beta}\left(\frac{h_1}{K}+\frac{\beta}{a}\right)\right.$$
$$\left.+\left(\frac{a}{r}\right)^{\beta}\left(\frac{\beta}{a}-\frac{h_1}{K}\right)\right]\left[\frac{h_oT_o}{K}-\frac{B}{b}-\frac{h_oA}{K}\right.$$
$$\left.\left.-\frac{h_oB\ln b}{K}\right]\right\}\left\{\left(\frac{a}{b}\right)^{\beta}\left(\frac{h_o}{K}-\frac{\beta}{b}\right)\left(\frac{\beta}{a}-\frac{h_1}{K}\right)\right.$$
$$\left.+\left(\frac{b}{a}\right)^{\beta}\left(\frac{h_1}{K}+\frac{\beta}{a}\right)\left(\frac{\beta}{b}+\frac{h_o}{K}\right)\right\}^{-1} \quad (35)$$

Equations (35) and (26) describe the total solution for the temperature distribution in the top section of the pipe. Because of the symmetry of the problem, the temperature distribution for the bottom section may be obtained by replacing $T(r, \Theta)$ by $G(r, \Theta)$, h_1 by h_2, T_1 by T_2, and Θ_i by $(\pi-\Theta_i)$.

Results

Case Study: Analytical Results. The temperature distribution in the pipe wall as given by equations (35) and (26) will be presented in the form of a case study for a particular physical situation. The problem chosen for analysis is shown in Fig. 4. This example represents the physical situation of a gas at 204.44°C (400°F) flowing at a low velocity in the top half of an uninsulated pipe with a liquid at 37.78°C (100°F) flowing in the bottom half of the pipe. It is assumed that two fluids do not mix, that each fluid is well mixed with a uniform temperature, and that there is no heat transfer between the two fluids. The temperature gradient in the Θ direction will be significant since the inside heat transfer coefficients and fluid temperatures differ significantly between the top and bottom sections. The solution procedure is as follows:

Table 1 Temperature comparison for case study

r (mm)	Θ (DEG)	T_{ANSYS} (°C)	$T_{ANAL.}$ (°C)	% DIFF
304.8	0.0	126.08	126.03	.040
	22.5	123.88	123.81	.057
	45.0	115.81	115.65	.138
	67.5	96.45	96.12	.343
	78.75	78.98	78.48	.637
	84.375	67.21	66.62	.886
	90.0	50.78	51.27	-.956
	95.625	41.42	41.20	.534
	101.25	38.93	38.85	.206
	112.5	37.77	37.76	.026
	135.0	37.61	37.61	0
	157.5	37.60	37.60	0
	180.0	37.60	37.60	0
330.2	0.0	124.92	124.86	.048
	22.5	122.71	122.63	.065
	45.0	114.61	114.46	.131
	67.5	95.20	94.87	.348
	78.75	77.68	77.18	.648
	84.375	65.92	65.31	.934
	90.0	52.50	51.29	2.359
	95.625	43.11	42.77	.795
	101.25	39.42	39.31	.280
	112.5	37.68	37.66	.053
	135.0	37.43	37.43	0
	157.5	37.43	37.43	0
	180.0	37.43	37.43	0

1 determine the interface temperature profile (equation (4))
2 substitute physical constants into equations (35) and (26)
3 choose arbitrary values for r and Θ
4 perform the summation in equation (35)

This procedure must be performed for both the top and bottom sections using the appropriate physical constants depending on the particular section of pipe being considered.

The results obtained from the analytical solution using 200 terms of the series are plotted in Fig. 5. It is interesting to note that the curves intersect at two points, and the $r=b$ curve is actually above the $r=a$ curve between these points of intersection. The significance of this observation is that even though the inside fluids are hotter than the outside fluid, the inside surface is colder than the outside surface in this region. In fact, the inside surface temperature of the pipe is actually hotter than the inside fluid temperature between $\Theta=90$ deg and $\Theta=111.5$ deg. This means that the heat flux is from outside to inside in this region. This phenomenon occurs as a result of the heat flux in the pipe wall in the Θ direction across the interface.

The sharp temperature gradient in the top section of the pipe is a result of the small inside convective heat transfer coefficient in the top section. Likewise, the flat profile in the bottom section is a result of the large inside convective heat transfer coefficient in that section.

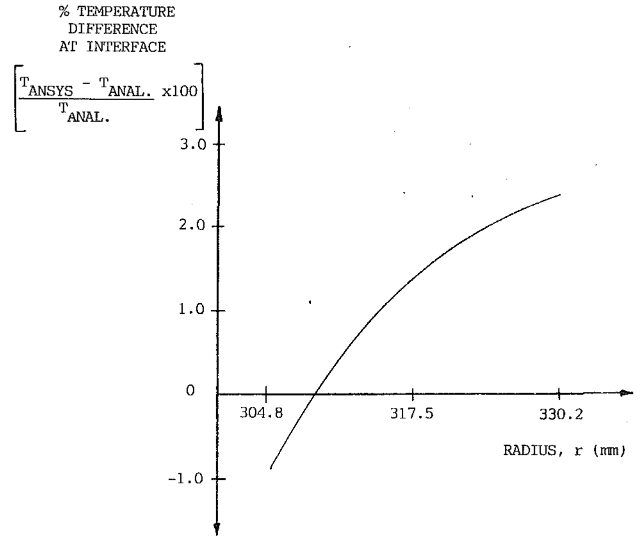

Fig. 6 Comparison of analytical and ANSYS solutions at the interface

The relatively constant interface temperature profile as predicted by the analytical solution is a consequence of the arbitrary selection of thermophysical properties and convective coefficients for the case study. A judicious choice of these parameters would result in nontrivial gradients.

Comparison With Numerical Results. The same case was analyzed using the finite element computer code ANSYS [1]. A comparison between the analytical and ANSYS solutions at various radii and angular positions for the case study is presented in Table 1.

As is indicated in Table 1, the maximum temperature difference between the analytical and ANSYS solutions is 1.21°C at the outer surface at $\Theta = 90$ deg, which represents a difference of 2.359 percent (based on degrees Celsius). At an angle of 5 deg or more from the interface, the temperature difference is less than 1.0 percent. For most of the pipe the temperature difference is less than 0.4 percent. Over a range of wall temperatures of almost 90°C, this agreement is well within the range required for most engineering applications.

Figure 6 is a comparison of the analytical and finite element solutions at the interface for the case study problem. As shown on the figure, the difference between the two solutions is greatest at the outside radius. The slight difference between the analytical and ANSYS solutions is primarily a result of the interface temperature approximation in the analytical solution.

Conclusions

An analytical solution for the temperature distribution in a pipe wall subjected to internally stratified flow has been developed using the integral transform technique and a one-dimensional approximation for the interface temperature profile. The temperature field predicted by the analytical solution of a selected physical model compared favorably with that from a finite element solution using the ANSYS computer code.

Although finite-element methods have been successfully applied to calculation of temperature distributions in pipe walls subjected to stratified flow, the analytical solution developed in this paper offers several advantages over the finite element technique. One obvious advantage of the analytical method is that it allows the design engineer to predict with relative ease the sensitivity of the temperature distribution to various thermal and physical properties, fluid levels, and flow conditions. Additionally, the analytical method is easily adapted to use on a personal computer as opposed to larger machines required by most finite element methods. One further advantage of the analytical solution is its applicability to the inverse solution; that is, given a small sample of temperature data from thermocouples attached to the pipe o.d., the fluid interface level and detailed wall temperature distribution may be predicted. The inverse solution, which may require a large number of solution iterations, would be much more convenient and inexpensive to perform using the analytical solution method.

References

1 ANSYS, "Engineering Analysis System," Rev. 4.2B, Swanson Analysis Systems, Inc., Houston, PA.

2 Bejan, A., and Tien, C. L., "Fully Developed Natural Counterflow in a Long Horizontal Pipe With Different End Temperatures." *Int. Journal of Heat and Mass Transfer*, Vol. 21, 1978, pp. 701-708.

3 Carslaw, H. S., and Jaeger, J. C., *Conduction of Heat in Solids*, Clarendon Press, London, 1959, p. 333.

4 Hong, S. W., "Natural Circulation in Horizontal Pipe." *Int. Journal of Heat and Mass Transfer*, Vol. 20, 1977, pp. 685-691.

5 Kimura, S., and Bejan, A., "Numerical Study of Natural Circulation in a Horizontal Duct With Different End-Temperatures," *Warme- und Stoffubertragung*, No. 14, 1980, pp. 269-280.

6 Kreith, F., *Principles of Heat Transfer*, Harper and Row, New York, 1973, p. 85.

7 Ozisik, M. N., *Boundary Value Problems of Heat Conduction*, Int. Textbook Company, Scranton, PA, 1968, p. 169.

8 Smith, W. R., "An Analytical Solution for the Temperature Distribution in a Pipe Wall Subjected to Internally Stratified Flow," M.S. Thesis, The University of Tennessee at Chattanooga, Aug. 1987, pp. 37-43.

9 U.S. Nuclear Regulatory Commission, "Investigation and Evaluation of Cracking Incidents in Piping in Pressurized Water Reactors," NUREG 0691, Sept. 1980.

10 Yih, C.-S., *Stratified Flows*, Academic Press, New York, 1980.

S. G. Bankoff
Fellow ASME

T. E. Rehm[1]
Department of Chemical Engineering,
Northwestern University,
Evanston, IL 60208

Convective Boiling in Narrow Concentric Annuli

An experimental apparatus was used to simulate the annulus formed by a single tube passing through a tube support plate (TSP) in the steam generator of a PWR nuclear power plant. It was found that the extent of thin film evaporation, compared to nucleate boiling, is larger for smaller annuli, with a transition at 0.203 mm gap width to a local dryout/rewet condition. A model was developed that predicts an increasing extent of surface dryout/rewet prior *to critical heat flux (CHF). A CHF correlation was developed by modification of a pool boiling CHF correlation, and the Chen (1966) correlation was modified to allow prediction of the two-phase heat transfer coefficient.*

Introduction

Two-phase flow and heat transfer studies have received much attention in recent years, due primarily to problems encountered in steam generators of PWR nuclear power plants. Green and Steininger (1980) reported tube thinning, denting, and failure in 25 percent of steam generators with less than ten years' service. These problems resulted from accelerated corrosion due to dryout occurring within the narrow annuli formed by the tube and the tube support plates (TSP) or tube sheet.

To understand the mechanisms associated with dryout in narrow annuli, an experimental apparatus was designed and constructed to simulate a single tube passing through a TSP. The design maintained a concentric tube orientation within the TSP hole, thereby minimizing tangential components of flow and heat transfer.

A similar study (Bankoff et al., 1982; Johnston et al., 1983a, 1983b; Johnston and Bankoff, 1985; Tong et al., 1985) used an eccentric tube orientation, producing a line contact between the tube and the TSP. In the eccentric orientation a stable vapor patch (dryout region) existed in the vicinity of line contact between the tube and the TSP. Vapor within the patch periodically swept across a thin liquid film through a region of very small crevice dimensions.

Existence of thin liquid films and alternate dryout/rewet within these thin films prior to critical heat flux (CHF) have been observed in studies of pool boiling in vertical concentric annuli. Ishibashi and Nishikawa (1969) studied heat transfer to coalesced bubbles and observed a liquid-deficient region prior to CHF in which rising liquid periodically rewetted dry surfaces. In studying the transition heat flux from nucleate boiling to alternate dryout/rewet, Aoki et al. (1982) photographed the dryout and rewet of thin liquid films prior to CHF.

In the presence of thin liquid films, heat transfer coefficients in narrow annuli are inversely proportional to the thickness of the annulus. Aoki et al. (1982) observed that the heat transfer coefficient increased with decreasing annulus thickness over the range $0.2<\delta<1.5$ mm. In a study of pool boiling and dryout in short horizontal annuli, Jensen et al. (1977) reported that annular heat transfer coefficients were as much as 230 percent greater than those measured for normal pool boiling, and increased with decreasing gap size. They postulated that this behavior was due to a thin film evaporation mechanism.

Fiori and Bergles (1970) proposed that dryout is initiated by nucleating bubbles, which disrupt the thin liquid film. Even in unrestricted pool boiling, alternate dryout/rewet occurs prior to CHF. Ishigai and Kuno (1966) proposed that an increasing occurrence of intermittent local surface dryout accounts for the shape of the conventional boiling curve, which is smooth and continuous through CHF into transition boiling. Kusada and Nishikawa (1967) experimentally studied boiling in thin liquid films and concluded that the best heat transfer occurred when 70 percent of the surface was wetted (i.e., 30 percent was intermittently dry).

Many empirical correlations have been developed for the boiling heat transfer coefficient. Cooper (1982) attempted to reduce ten correlations of nucleate boiling in unrestricted pools by collapsing them into one correlation, using reduced properties. Another study by Stephan and Abdelsalam (1980) involved correlation of 5000 nucleate boiling data points gathered from 53 researchers.

A common approach to data correlation is superposition. Rohsenow (1952) defined an overall heat transfer coefficient as the sum of boiling and convective components. Wang et al. (1982) used this principle to correlate transition boiling data taken in a vertical annulus ($\delta = 5$ mm). Chen (1966) developed a correlation for convective two-phase heat transfer coefficients by superposition of "micro-convective" and "macro-convective" components. Similarly, Hall et al. (1981) developed a correlation involving the superposition of a forced convective vaporization component and a nucleate boiling component.

In regards to correlation of CHF, Kutateladze and Leontiev (1966) proposed that for unrestricted convective boiling, CHF

---

[1] Present address: Amoco Chemical Co., Naperville, IL.

Contributed by the Power Division for publication in the JOURNAL OF ENGINEERING FOR GAS TURBINES AND POWER. Manuscript received by the Power Division August 7, 1987; revision received October 3, 1989.

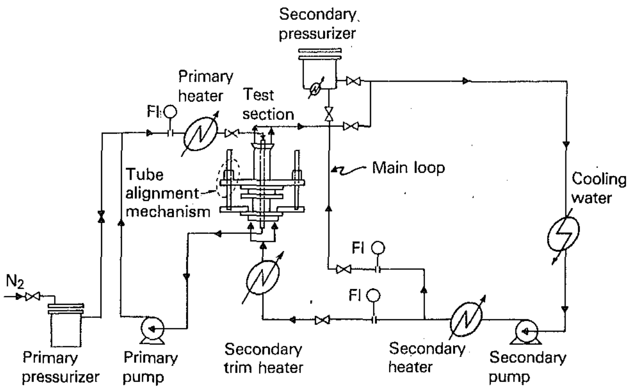

Fig. 1 Experimental apparatus

can be represented as the sum of a pool boiling CHF component and the heat flux required for the generated vapor to cause boundary layer separation. Green (1982) developed a CHF correlation for convective boiling in vertical tubes, Merilo (1979) for convective boiling in horizontal tubes, and Jensen et al. (1977) for pool boiling in narrow annuli.

Turning to CHF correlations for convective boiling within annuli, two studies are noted. Shah (1980) developed a graphic method for CHF in vertical annuli. A parameter Y is calculated and used to determine a boiling number Bo, and two factors F_1 and F_2, from which CHF is determined. Katto (1979) also developed a correlation for CHF in vertical annuli. He constructed a CHF regime map, which consisted of three regimes defined by two dimensionless groups, L/D_{hp} and $\sigma\rho_1/G^2L$. A parameter K was determined to be a function of the CHF regimes.

The study by Bankoff et al. (1982) illustrates the effect of thin film evaporation. In modeling the extent of vapor patch in the vicinity of line contact, the two-phase region was modeled as a homogeneous mixture. The model successfully predicted the extent of vapor patch but failed to predict the temperature profile for a segment of the annulus over which an intermittent vapor sweep was observed. Over this vapor-sweep region, the model overpredicted the wall superheat substantially. As in the Ishibashi/Nishikawa model, the effect of thin film evaporation under the vapor sweep was underestimated.

In an attempt to model the mechanism of thin film evaporation, Merte et al. (1982) used an eccentric annular geometry, so that the growth of a single coalesced bubble could be observed at the minimum radial gap width. The major assumptions were that (1) the heat transfer is dominated by liquid film evaporation and (2) the liquid film is spatially uniform. The authors state that the " . . . developed analytical model qualitatively predicts the trends found in the data but does not adequately predict the quantitative trends." They conclude that the assumption of spatial uniformity of the thin film was at fault.

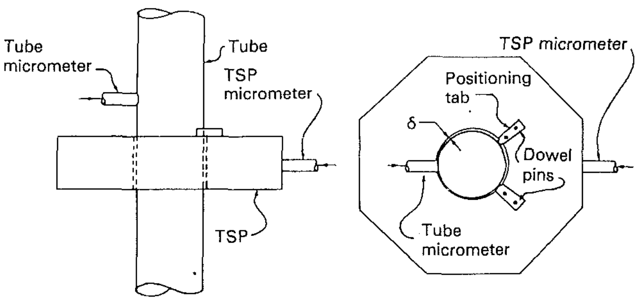

Fig. 2 Tube-tube support plate geometry

Experimental Work

A schematic of the equipment is presented in Fig. 1.

In order to view the phenomena, an attempt was made to secure quotes on the manufacture of quartz or glass tube support plates (TSP). One specification for proper tube-TSP alignment was prohibitive due to the narrowness of the annulus. As such, all TSPs, excepting the 0.203 mm TSP, were cut from stainless steel. The 0.203 mm TSP was used by Bankoff et al. (1982) and was available.

From the main secondary water loop a small slipstream fed the test section. This consisted of two parallel piping runs, each with a set of orifice plates and valves. The valves were low flow valves, each designed for a 345 kPa drop in order to minimize the detrimental effect of TSP Δp fluctuation on the accuracy of the fluid metering.

Due to the narrowness of the space dimension, precautions were taken to ensure that during the placement of a TSP, the test section would not be misaligned prior to rebolting. In order to minimize misalignment, a tube alignment mechanism was installed (Fig. 1). The roller bushings used within the mechanism had a tolerance of 0.0051 mm. To ensure that the tube did not shift during a run, positioning tabs affixed to the downstream surface of the TSP were used, in conjunction with micrometers to lock the tube and TSP in position (Fig. 2).

Nomenclature

Bo = Bond number $= d^2\rho g/\sigma$
CHF = critical heat flux
c_p = specific heat
D = diameter
F = convective boiling factor
F_{Chen} = Chen's convective boiling factor
G = mass flux
g_c = acceleration due to gravity
h = individual heat transfer coefficient
Ja = Jakob number $= \rho_1 c_p \Delta T_{\text{sat}}/\rho_v \lambda_{\text{vap}}$
k = thermal conductivity
L = length of annulus
P = pressure
ΔP_{sat} = differential pressure corresponding to ΔT_{sat}

Pr = Prandtl number $= c_p\mu/k$
q'' = heat flux, kW/m^2
Re = Reynolds number $= DG/\mu$
S = nucleate boiling factor
S_{tt} = Martinelli parameter
T = temperature, °C
TSP = tube support plate
ΔT_{sat} = wall superheat, °C
w = length of annulus in CHF correlation, equation (5)
x = thermodynamic quality
Z_2 = axial location at initial dryout (thin film model)
δ = radial gap width
η = thin film thickness
λ – latent heat of vaporization
μ = viscosity
ρ = density

σ = surface tension
ϕ^2 = two-phase pressure drop multiplier
χ = dimensionless gap width

Subscripts

cr = critical
hp = heated perimeter; equation (20)
l = liquid
o = outside
sat = saturated
sp = single phase
tl = total flow, liquid properties
tp = two phase
v = vapor
vap = vaporization

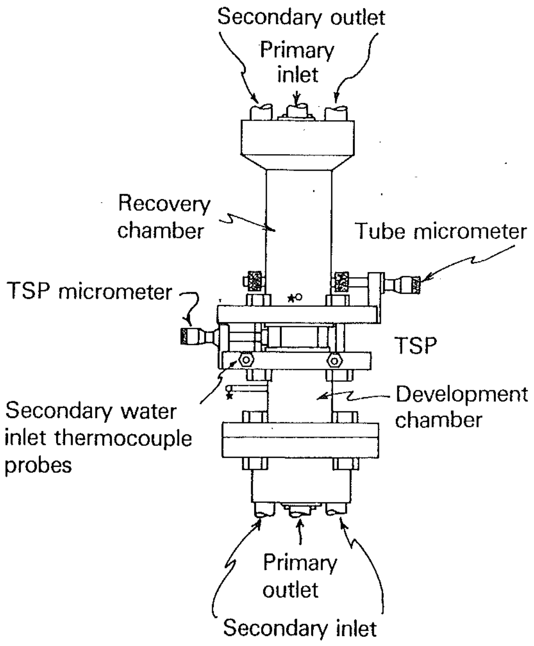

*Pressure taps

Fig. 3 Test section

At the maximum primary water temperature, thermal expansion of the tube would lead to 0.0005 mm decrease in the radial gap width, 1 percent of the smallest annulus.

The test section is detailed in Fig. 3. Due to the very low flow rates attainable in these narrow annuli, it wsa necessary to minimize the error in the inlet conditions. Two steps were taken to do so. A Teflon tube insert was made to fit snugly over the primary tube inside the development chamber, such that an annulus of 3 mm witdth remained for passage of the secondary water. The second step consisted of the installation of three thermocouples immediately above the Teflon tube. The junctions of the thermocouples were positioned such that the secondary water only had 6 mm of tube surface (axial length) to traverse before entering the annulus. Even with this design, temperature rises of up to 3°C had to be accounted for in estimating the inlet conditions at the lowest experimental flow rate.

The primary water loop was pressurized with compressed nitrogen. A limiting operating temperature of 205°C was required in order to provide the primary water pump with sufficient NPSH. The secondary water loop was designed to be pressurized with its own vapor. However all data were taken at atmospheric pressure in order to maximize the heat flux within the limitations of the primary loop.

The temperature of the tube wall was measured with seven 1.02 mm o.d. iron-constantan thermocouple probes embedded within the wall. The junctions of these probes were at various axial and azimuthal locations within the tubewall. Three junctions were downstream of the annulus, three were in the annulus, and one was upstream of the annulus.

Data acquisition requirements were divided into two categories. In the first were the secondary flow rate and inlet conditions, which were held approximately constant during an experimental run. Inlet subcooling was held constant during a run by measuring the annulus upstream pressure, estimating the heat pickup between the three thermocouples in the development chamber and the annulus inlet, and adjusting the secondary trim heater to achieve the inlet subcooling. The primary water temperature was varied throughout each run. Temperatures of the primary water and the instrumented tube were recorded by an Esterline Angus PD2064 data logger. This instrument could record temperatures at a speed of 1 channel per second, which was slow relative to the frequency of oscillation in the TSP pressure drop measurements. Therefore, the tube wall temperatures and subsequent heat flux calculations could only be time-averaged.

A thick-walled (3.175 mm) stainless steel, 19 mm o.d. tube was used such that channels could be cut for placement of the wall thermocouples without distortion of the roundness of the tube.

Since the tube-wall thermocouple probes were composed of various materials (iron, constantan, magnesium oxide, and a stainless steel sheath), while a solder amalgam (lead-tin) was used to cover the probes, there were a number of thermal conductivity discontinuities in the vicinity of the thermocouple junction. Consequently, the temperature profile through the wall at the location of each junction was distorted from the profile that would have been present in a solid stainless-steel tube wall. Therefore, a critical element in error minimization was a calibration of the "virtual" location, r_v, of each tube-wall thermocouple. r_v was defined as the location that the junction would have if the wall were solid stainless steel.

An annulus of 3.18 mm gap width was used in the calibration to allow the use of the data of Kays and Leung (1963) for calculation of the annular film coefficient. The primary water film coefficient was calculated using the Dittus-Boelter correlation. A set of calibration data consisted of temperatures and flow meter readings for both the primary and secondary water loops, and temperature readings for all tubewall probes. Calculation of the virtual location of every probe was easily determined for each calibration run. 119 calibration runs were conducted over a range of secondary water flow rate (500-2200 kg/m^{2}s), secondary water temperature (82-116°C), and primary water temperature (88-178°C). The calibration resulted in a linear correlation of r_v with a dimensionless probe temperature ξ.

$$r_v = a + b\xi$$

where

$$\xi = \frac{T_T - T_2}{T_p - T_2}$$

Experimental Procedure

The radial gap width (δ), secondary flow rate, and degree of inlet subcooling were varied systematically. The ranges of operation were

$$0.0508 < \delta < 0.406 \text{ mm}$$
$$20 < \text{subcooling} < 3\,^\circ\text{C}$$
$$300 < G < 2540 \text{ kg/m}^2\text{s}$$

A typical set of data was generated by varying the primary water temperature from 110°C to 200°C for a given TSP and secondary water inlet condition.

Treatment of Data

The most important sources of concern in evaluation of the data were: (1) proper calibration of the tubewall thermocouple probes, (2) estimation of the actual inlet condition, (3) determination of the axial pressure profile through the annulus, and (4) calculation of the axial location at which saturated boiling is certain. The first item has been discussed.

2 Three thermocouples were positioned in the secondary water bulk flow so that their junctions were 6 mm upstream from the annulus inlet. The heat transfer over that 6 mm length of fluid travel was calculated by use of an "unrestricted" heat transfer coefficient; "unrestricted" identifies flow as external to the annulus. Calibration of the "unrestricted" heat transfer coefficient was accomplished by running the test section with the secondary water in single

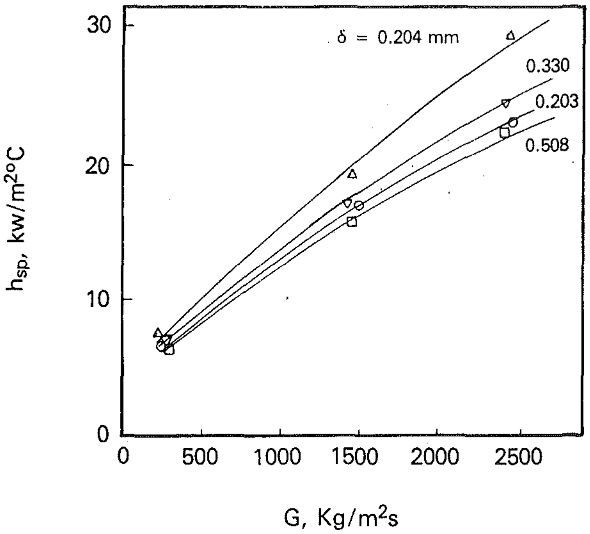

Fig. 4 Annular single-phase heat transfer calibration

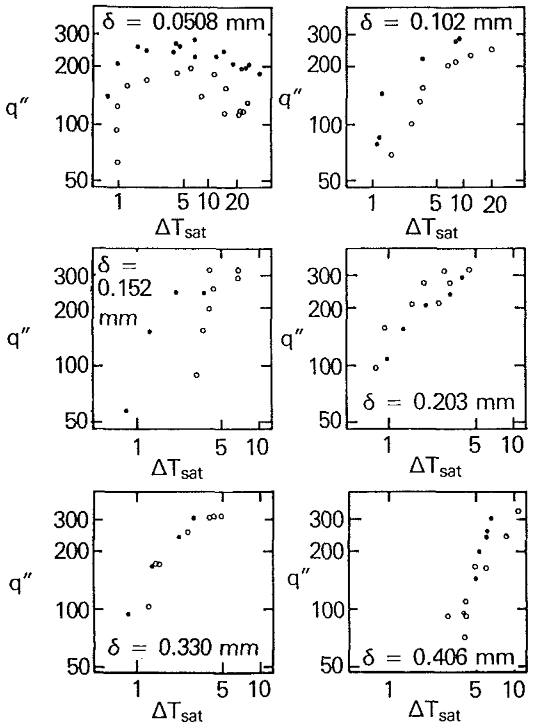

Fig. 5 Experimental results of saturated boiling

phase and measuring the secondary water bulk temperature adjacent to embedded tubewall probes.

3 The TSP pressure drop was not negligible as it affected the treatment of the data. The limiting factor on permissible maximum flow rates was the differential pressure transducer, which has a range of 0-69 kPa. In addition, pressure drops varied significantly over a single run such that a single boiling curve does not correspond to a single value of annulus pressure. The highest pressure drop was 83 kPa, exceeding the range of the test section differential pressure transducer. This corresponds to an inlet saturation temperature of 123°C, 15°C higher than at the start of the run. Therefore the effect of pressure drop was not negligible. To account for the axial pressure gradient, a simple linear pressure profile was used in data reduction. This was used in light of the stochastic nature of the phenomena.

4 In order to characterize the boiling as saturated or subcooled, the axial location at which the bulk liquid is saturated, L_{sat}, was calculated. In order to calculate L_{sat}, a calibration was performed for each combination of TSP and secondary flow rate for the purpose of estimating the heat transfer coefficient to the liquid phase in single-phase heat transfer, H_{sp} (Fig. 4). The total heat flux, q_t'', was considered to be a superposition of heat flux from single-phase heat transfer, q_{sp}'', and heat flux from vaporization, q_{vap}''. L_{sat} was determined by calculating the single-phase temperature, T_{sp}, as a function of axial length and by use of the assumed linear pressure profile to calculate a saturation temperature profile over the length of the annulus. Prior to L_{sat}, the boiling was assumed to be subcooled.

Table 1 $Re_{\ell l}$ **of experimental data**

δ, mm	$(Re_{\ell l})_{min}$	$(Re_{\ell l})_{max}$
0.0508	318	667
0.102	318	880
0.152	331	860
0.203	442	1839
0.330	730	2940
0.406	920	3680

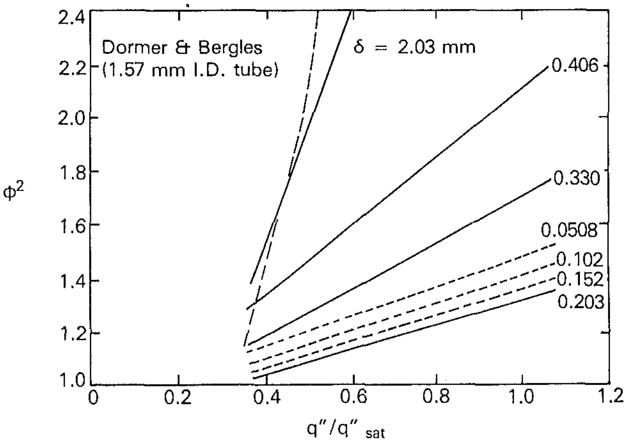

Fig. 6 Two-phase mutliplier for subcooled boiling pressure drop

Experimental Results

Results corresponding to saturated boiling are shown in Fig. 5; values of Re_{tl} are given in Table 1. Heat flux was calculated from data taken on the primary water inside the tube and the temperature of the embedded tubewall probes. In Fig. 5, low data values of Re_{tl} are represented by open circles, high data values by solid circles.

Note that data for radial gaps of 0.203 mm and greater indicate little sensitivity to $Re_{\ell l}$, whereas data taken for gaps under 0.203 mm yield a definite Reynolds number effect. This distinction is explained by an increasing domination of thin film evaporation over nucleate boiling for thinner annuli.

Subcooled boiling data provide insight into the dominance of thin film evaporation for flow in narrow channels. This is illustrated by studying the pressure drop during subcooled boiling as a function of gap width.

The two-phase multiplier, ϕ_2, for subcooled boiling in narrow flow channels is presented in Fig. 6. ϕ_2 is the ratio of the pressure drop during subcooled boiling to the pressure drop for single-phase flow without heat transfer. Due to the narrowness of the flow channel, vapor generated by subcooled boiling is not intimately mixed with subcooled liquid, and therefore, subcooled boiling in narrow spaces is a partially stratified flow phenomena. The abscissa of Fig. 6 is the actual heat flux divided by the heat flux required to achieve saturated conditions at the exit of the flow channel.

The results for subcooled boiling pressure drop are compared with the results of Dormer and Bergles (1964), who studied pressure drop in very small diameter tubes, the smallest diameter being 1.57 mm i.d. The results shown in Fig. 6 are linear least-squares fits (7.2 percent std. dev.) of the data.

Subcooled boiling in narrow channels occurs by both nucleate boiling and thin film evaporation. Flow over a surface of nucleating bubbles results in a higher pressure drop than that for the separated flow of a thin film evaporation mechanism. Referring to Fig. 6, thin film evaporation varies from a minor effect for the 2.03-mm annulus to a major effect for annuli of 0.203 mm and under. For annuli under 0.203 mm, increasing levels of alternating dryout/rewet lead to increasing pressure drop.

The method of Kline and McClintock (1953) was used to estimate the uncertainty in a calculated result based on the uncertainties of its components.

Local heat flux

±6.6 percent at 44 kJ/m^2
±4.9 percent at 88 kJ/m^2
±4.5 percent at 132 kJ/m^2
±4.4 percent at 175 kJ/m^2
±4.3 percent at 219 kJ/m^2

Outside wall surface temperature

$\pm 0.7^\circ\mathrm{C}$ at $(T_p - T_l) < 10^\circ\mathrm{C}$
$\pm 0.8^\circ\mathrm{C}$ at $(T_p - T_l) = 20^\circ\mathrm{C}$
$\pm 0.9^\circ\mathrm{C}$ at $(T_p - T_l) = 30^\circ\mathrm{C}$
$\pm 1.1^\circ\mathrm{C}$ at $(T_p - T_l) = 40^\circ\mathrm{C}$
$\pm 1.3^\circ\mathrm{C}$ at $(T_p - T_l) = 50^\circ\mathrm{C}$

Modification of Chen Correlation

Chen's correlation of forced convective boiling film coefficients has been accepted as one of the best (1966). Chen used data from a number of researchers in developing his correlation. The data were derived from (*a*) vertical flow in tubes with inside diameters ranging from 2.95 mm to 25.4 mm and (*b*) vertical flow in annular test sections having radial gap widths of 6.35 mm and greater. The fluids used by these researchers were water and organic liquids. No subcooled boiling data or horizontal flow data were used.

Chen proposed that the heat transfer coefficient could be determined as

$$h = h_{\mathrm{mic}} + h_{\mathrm{mac}}$$

where $h_{\mathrm{mic}} = 0.00122(\Delta T_{\mathrm{sat}})^{0.24}(\Delta P_{\mathrm{sat}})^{0.75} S\phi$,

$$\phi = \left[\frac{(k_1)^{0.79}(Cp_1)^{0.1415}(\rho_1)^{0.49}(g_c)^{0.25}}{\sigma^{0.5}(\mu_1)^{0.29}\lambda^{0.24}(\rho_v)^{0.24}}\right]$$

and $h_{\mathrm{mac}} = 0.023(k_1)/D(\mathrm{Re}_{tl})^{0.8}(\mathrm{Pr}_1)^{0.4}F$. h_{mic} is based on the work of Forster and Zuber (1955) and h_{mac} on the Dittus–Boelter correlation.

$$F = 1; \qquad 1/X_{tt} \le 0.1$$

$$F = 2.35(1/X_{tt} + 0.213)^{0.736}; \quad 1/X_{tt} > 0.1$$

$$S = 1/[1 + 2.53(10^{-5})\mathrm{Re}_{tp}^{1.17}]$$

For a clear understanding of the following development, Chen's F will be referred to as F_{Chen} and the modified form of F_{Chen} will be referred to as F.

In the development of a modified Chen correlation, the calculated value of h_{mic} in narrow annuli was less than 5 percent of the experimental two-phase heat transfer coefficient for all the experimental data (and less than 1 percent for $\delta < 0.203$ mm). Since the primary mechanism for boiling in narrow annuli is thin film evaporation, the nucleate boiling contribution in Chen's correlation requires no modification. Therefore, Chen's S function was used, reducing the procedure to a calculation of F for each data point.

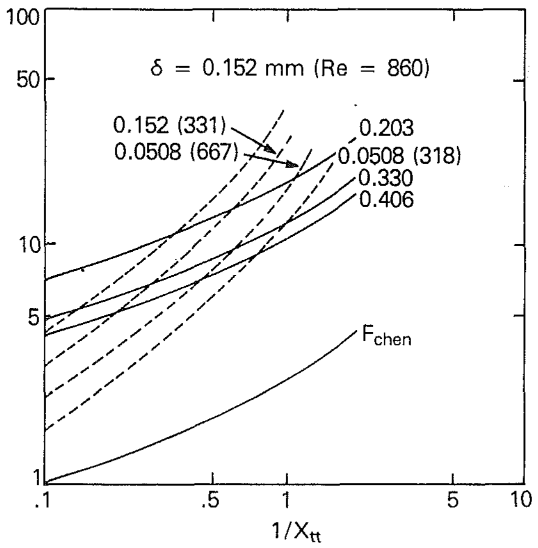

Fig. 7 Convective boiling factor for modified Chen correlation

The radial gap width was characterized by a dimensionless length χ

$$\chi = \mathrm{Bo}^{0.5} = d_h(\rho g/\sigma)^{0.5} = 2\delta(\rho g/\sigma)^{0.5}$$

The form of F used in the modification was:

$$F = l\psi(\chi)F_{\mathrm{Chen}}$$

where

$$\psi(\chi) = 1 + \operatorname{csch}\chi$$

and

$$l = a(1/X_{tt})^b; \quad l = 1 \text{ for } \delta > 0.203 \text{ mm}$$

$$a = 1 + a_1\gamma + a_2\gamma^2$$

$$a_1 = -6.55 + 0.038(\mathrm{Re})$$

$$a_2 = -4.7 - 0.3(\mathrm{Re})$$

$$b = 16.4\gamma(1 - 6.43\gamma)$$

$$\gamma = \chi^* - \chi; \quad \gamma = 0 \text{ for } \delta > 0.203 \text{ mm}$$

$$\chi^* = \chi(\delta^*)$$

$$\delta^* = 0.203 \text{ mm}$$

l provides (*a*) a flow rate effect, (*b*) a steeper slope of the F function, and (*c*) an asymptotic value of $l = 1.0$ as the radial gap width increases to 0.203 mm. $\psi(\chi)$ permits the value of F asymptotically to approach F_{Chen} as δ increases. In fact, at a value of $\chi = 2.54$, which corresponds to a radial gap width of approximately 6.35 mm, $F = 1.01F_{\mathrm{Chen}}$. This value of χ agrees roughly with the limit of the data available to Chen. Figure 7 graphically illustrates the correlation (22.1 percent std. dev.).

Thin Film Evaporation Model

High-speed film (700 frames/s) was taken of boiling within the 0.203 mm annulus. Figure 8 is a sequence of line drawings of frames taken from the film. A subcooled condition exists at the inlet of the annulus for each frame. This sequence shows (roughly) one cycle involving the annulus being 75 percent full

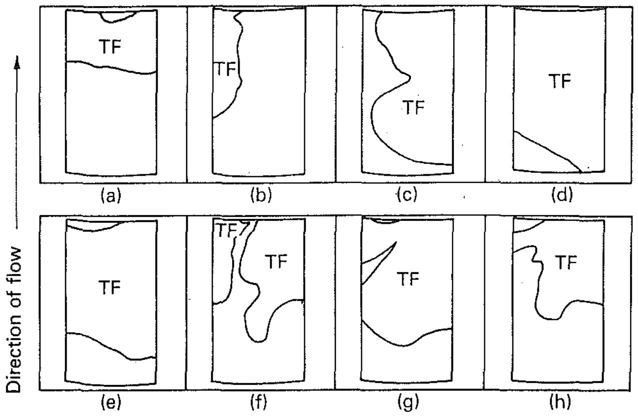

Fig. 8 Stochastic nature of boiling (TF = thin film; other regions are liquid filled)

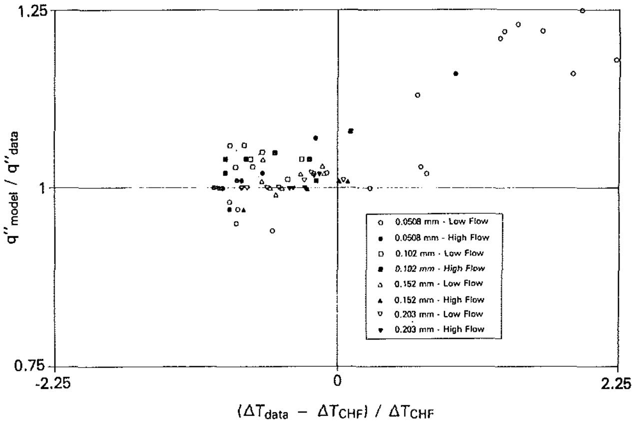

Fig. 9 Prediction of heat flux by thin film evaporation model

of liquid [in (*a*)] followed by various degrees of thin film (TF) coverage. The entire sequence occurred within a time span of 0.08 s.

It is obvious that the flow pattern is neither steady nor periodic. The data in this experiment were not taken at a frequency that would permit modeling of the cycle indicated by Fig. 8. In addition to this difficulty, approximately eight cycles, such as in Fig. 8, correspond to one cycle of pressure drop fluctuation. Therefore, the periodicity conditions and the coupling of the momentum and energy equations are complex. A simplified model was attempted in order to study the effect of thin film evaporation and the extent of dryout.

The model includes an inlet zone, Zone I, which is simply a liquid-filled, nonboiling, convective heat transfer zone. The liquid within this zone increases in temperature until saturation is reached, at which point a vapor phase begins to form. A second zone, Zone II, is completely modeled by thin film evaporation. The vapor phase is positioned above a thin liquid film, which thins axially until local dryout occurs. Dryout occurs when the thickness of the thin film equals the parameter used in the model, η^*. Zone III consists of a growing dryout region. The wetted portion of this zone is a thin film region having a thin film thickness equal to H^*.

The correlation for H^* was developed by use of the thin film evaporation model. For each data point, various values of η^* were used to generate q'', ΔT_{sat}, Ja, Re_{tl}, and Z_2. This array of simulated data was then fitted to η^*; i.e., $q''(\eta^*)$, and so on. An error function f_e was then minimized to determine the best value of η^* for the experimental data point.

$$f_e = [(1 - q''/q''_{\text{data}})^2 + (1 - \Delta T/\Delta T_{\text{data}})^2]^{1/2}$$

Table 2 η^* required to force the model to predict CHF

δ, mm	G, kg/m^{2}s	η^*/δ
0.203	310	0.250
0.203	1233	0.357
0.152	307	0.352
0.152	763	0.468
0.102	430	0.392
0.102	765	0.538
0.0508	858	0.478
0.0508	1721	0.653

The resulting array of H^* values was related to Ja, Re_{tl}, and χ, in order to develop the η^* correlation. η^* was observed to be a function of the radial gap width, the Reynolds number, and the wall superheat. As such, the correlation was determined as

$$\eta^*/\delta = 0.191(\text{Ja})^{1.5}(\text{Re}_{tl})^{0.5}(\chi)^{-2.79}$$

The model was designed to predict the complete boiling curve. Unfortunately, the model fails to predict CHF. The ability of the model to predict heat flux is represented by Fig. 9. The abscissa is the approach to CHF based on the value of ΔT_{data} (ΔT_{sat} of data point) relative to ΔT_{CHF} (ΔT_{sat} at CHF, determined from experimental data). The ordinate is the heat flux calculated by the model, divided by the heat flux calculated from the data. The model fails to predict CHF because it overpredicts the heat flux for data points past CHF.

By taking note of the regression coefficients, however, qualitative conclusions can be made. The most significant factor is the radial gap width. This is logical in that linear velocities of the escaping vapor must necessarily increase with thinner annuli, thereby increasing the interfacial shear stress at the vapor/liquid interface of the thin film. The Jakob number, a measure of the wall superheat, has an understandably significant effect, in that as the boiling curve is traversed, the wall superheat increases. This increase in wall superheat parallels an increase in the temperature gradient across the thin film, contributing to thin film destabilization. Even though the Reynolds number has the least significant effect relative to the other factors, it is still a significant factor, particularly in light of the narrow range of flow rates used in this study.

Values of η^*/δ required to force the model to predict CHF were determined and are presented in Table 2. For the 0.0508-mm annulus, alternate dryout/rewet occurs at a thin film, which exceeds half the annular space. The prevalence of alternate dryout/rewet prior to CHF decreases with increasing annulus gaps, as evidenced by decreasing values of η^*/δ in Table 2.

These results corroborate the findings of other researchers in that alternate dryout/rewet occurs prior to critical heat flux.

Correlation of CHF

Inasmuch as the thin film evaporation model was inadequate in predicting the boiling curve, it was necessary to use a different approach in predicting CHF. The narrow-annulus pool boiling correlation of Jensen et al. (1977) was used. The CHF correlation (9.4 percent std. dev.) herein presented reduces to the pool boiling correlation in the limit as Re_{tl} goes to zero.

The form of the correlation is

$$\left[\frac{q''_{cr} w(D_o/\delta)}{2\lambda_{\text{vap}}\mu_v[1+(D_o/\delta)]}\right]\left[\frac{D_o}{2\delta}\right]\left[\frac{\rho_1-\rho_v}{\rho_v}\right]^{0.78} = (f_{\text{conv}})2.994(10^5)(\delta/w)^{-0.213}$$

Table 3 Convective factor f_{conv} in CHF correlation

δ	Re_{tl}	f_{conv}
0.0508	318	2.85
0.0508	667	4.10
0.102	318	2.47
0.102	880	2.92
0.152	331	2.17
0.152	860	2.20
0.203	1140 *	1.79
0.330	1835 *	1.24

* Average value of Re_{tl}.

where f_{conv} is a factor that modifies the pool boiling correlation for the effect of convective flow.

The values of f_{conv} necessary to yield experimental values of CHF are given in Table 3.

The form of f_{conv} provides a limit of one as Re_{tl} approaches zero.

$$F_{\mathrm{conv}} = \exp[a(\mathrm{Re}_{tl}/\chi)^{0.5}]$$

$$\text{where } a = \begin{cases} 0.011; & \chi < 0.122 \\ -(0.012 + 0.018 \ln \chi)\,; & \chi > 0.122 \end{cases}$$

Conclusions

In annuli over 0.203 mm thick, both nucleate boiling and thin film evaporation occur. Under 0.203 mm, thin film evaporation is the dominant mechanism. A thin film evaporation model was developed that simulates the boiling in three axial zones: (1) a nonboiling convective heat transfer zone, (2) a thin-film evaporation zone, and (3) a growing dryout zone. The model was used to correlate the thickness of a thinning thin film (η^*) at the first instance of dryout. The values of η^* at CHF indicate the existence of alternate dryout/rewet prior to CHF, with increasing prevalence at smaller annuli.

The Chen correlation for convective boiling heat transfer was modified to allow its use in narrow annuli. Similarly, the Jensen correlation for CHF in narrow annuli pool boiling was modified for convective boiling. In both correlations, modification involved convective factors, whose final forms corroborate an increasing domination of thin film evaporation with decreasing annulus.

All data taken in this study were at atmospheric pressure. In a PWR nuclear power plant, the secondary water pressure is 7000 kPa. Although the results of this study should not be used quantitatively, the mechanism of thin film evaporation will contribute to convective boiling in narrow annuli at elevated pressure.

Acknowledgments

This work was supported by the Office of Basic Energy Sciences, Department of Energy.

References

Aoki, S., et al., 1982, "Experimental Study on the Boiling Phenomena Within a Narrow Gap," *Int. J. Heat Mass Transfer*, Vol. 25, pp. 985–990.

Bankoff, S. G., et al., 1982, "Boiling Heat Transfer in a Narrow Eccentric Annulus," EPRI NP-2610, Research Project S133-1, Final Report, Electric Power Research Institute, Palo Alto, CA.

Chen, J. C., 1966, "Correlation for Boiling Heat Transfer to Saturated Fluids in Convective Flow," *I&EC Proc. Des. & Develop.*, Vol. 5, pp. 322–328.

Cooper, M. G., 1982, "Correlations for Nucleate Boiling—Formulation Using Reduced Properties," *PCH PhysicoChemical Hydrodynamics*, Vol. 3, pp. 89–99.

Dormer, J., Jr., and Bergles, A. E., 1964, "Pressure Drop With Surface Boiling in Small Diameter Tubes," Report No. M.I.T. 8767-31, Dept. of Mech. Eng., M.I.T., Cambridge, MA.

Fiori, M. P., and Bergles, A. E., 1970, "Model of Critical Heat Flux in Subcooled Flow Boiling," *Proc. Fourth Intl. Heat Transfer Conf.*, Vol. 6, p. B6.3.

Forster, H. K., and Zuber, N., 1955, "Dynamics of Vapour Bubbles and Boiling Heat Transfer," *AIChE Journal*, Vol. 1, pp. 531–543.

Green, S. J., and Steininger, D. A., 1980, "Pressurized Water Steam Generators—Problems and Progress," *ASME Century 2 Nuclear Engineering Conference*, San Francisco, CA.

Green, W. J., 1982, "A Flow Boiling Critical Heat Flux Correlation for Water and Freon-12 at Low Mass Fluxes," *Nuclear Engr. and Design*, Vol. 72, pp. 381–393.

Hall, G. R., et al., 1981, "Correlation of Forced Convection Boiling Heat Transfer Data," *Int. J. Heat Mass Transfer*, Vol. 25, pp. 753–759.

Ishibashi, E., and Nishikawa, K., 1969, "Saturated Boiling Heat Transfer in Narrow Spaces," *Int. J. Heat Mass Transfer*, Vol. 12, pp. 863–893.

Ishigai, S., and Kuno, T., 1966, "Experimental Study of Transition Boiling on a Vertical Wall in an Open Vessel," *Bull. J.S.M.E.*, Vol. 9, pp. 361–368.

Jensen, M. K., Cooper, P. E., and Bergles, A. E., 1977, "Boiling Heat Transfer and Dryout in Restricted Annular Geometries," *AIChE Symposium Series*, Vol. 73, pp. 205–211.

Katto, Y., 1979, "Generalized Correlations of Critical Heat Flux for the Forced Convection Boiling in Vertical Uniformly Heated Annuli," *Int. J. Heat Mass Transfer*, Vol. 22, pp. 575–586.

Kays, W. M., and Leung, E. Y., 1963, "Heat Transfer in Annular Passages—Hydrodynamically Developed Turbulent Flow With Arbitrarily Prescribed Heat Flux," *Int. J. Heat Mass Transfer*, Vol. 6, pp. 537–557.

Kline, S. J., and McClintock, F., 1953, "Describing Uncertainties in Single Sample Experiments," *Mech. Engrg.*, Vol. 3, pp. 3–8.

Kusada, H., and Nishikawa, K., 1967, "A Study of Nucleate Boiling in Liquid Film," *Mem. Fac. Engng. Kyushu Univ.*, Vol. 27, pp. 155–173.

Kutateladze, S. S., and Leontiev, A. I., 1966, "Some Applications of the Asymptotic Theory of the Turbulent Boundary Layer," *3rd Intl. Heat Transfer Conf.*, Vol. 3, pp. 1–11.

Merilo, M., 1979, "Fluid-to-Fluid Modeling and Correlation of Flow Boiling Crisis in Horizontal Tubes," *Int. J. Multiphase Flow*, Vol. 5, pp. 313–325.

Merte, H., et al., 1982, "Boiling in Narrow Crevices in Steam Generators," EPRI NP-2638, Project S1134-1 Final Report.

Rohsenow, W. M., 1952, *Heat Transfer—A Symposium*, Engrg. Research Inst., Univ. of Michigan, Ann Arbor, MI.

Shah, M. M., 1980, "A General Correlation for Critical Heat Flux in Annuli," *Int. J. Heat Mass Transfer*, Vol. 23, pp. 225–234.

Stephan, K., and Abdelsalam, M., 1980, "Heat-Transfer Correlations for Natural Convection Boiling," *Int. J. Heat Mass Transfer*, Vol. 23, pp. 73–87.

Wang, S., Kao, Y. K., and Weisman, J., 1982, "Studies of Transition Boiling Heat Transfer With Saturated Water at 1-4 Bar," *Nuclear Eng. and Design*, Vol. 70, pp. 223–229.